frontiers | Research Topics

New molecular pathways in thyroid cancer and pathophysiology: Role of coding and noncoding genes

Edited by
Cesar Seigi Fuziwara, Murilo Vieira Geraldo and Juan Pablo Nicola

Published in
Frontiers in Endocrinology
Frontiers in Oncology

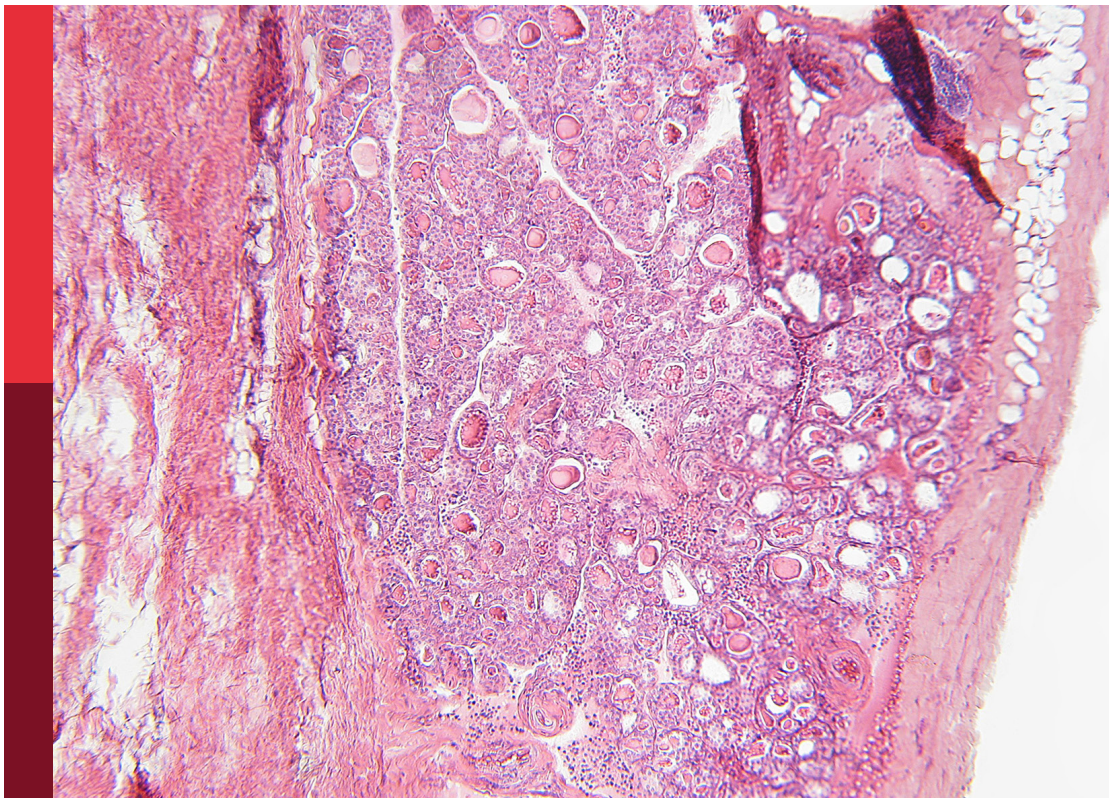

ISSN 1664-8714
ISBN 978-2-8325-4782-3
DOI 10.3389/978-2-8325-4782-3

About Frontiers

Frontiers is more than just an open access publisher of scholarly articles: it is a pioneering approach to the world of academia, radically improving the way scholarly research is managed. The grand vision of Frontiers is a world where all people have an equal opportunity to seek, share and generate knowledge. Frontiers provides immediate and permanent online open access to all its publications, but this alone is not enough to realize our grand goals.

Frontiers journal series

The Frontiers journal series is a multi-tier and interdisciplinary set of open-access, online journals, promising a paradigm shift from the current review, selection and dissemination processes in academic publishing. All Frontiers journals are driven by researchers for researchers; therefore, they constitute a service to the scholarly community. At the same time, the *Frontiers journal series* operates on a revolutionary invention, the tiered publishing system, initially addressing specific communities of scholars, and gradually climbing up to broader public understanding, thus serving the interests of the lay society, too.

Dedication to quality

Each Frontiers article is a landmark of the highest quality, thanks to genuinely collaborative interactions between authors and review editors, who include some of the world's best academicians. Research must be certified by peers before entering a stream of knowledge that may eventually reach the public - and shape society; therefore, Frontiers only applies the most rigorous and unbiased reviews. Frontiers revolutionizes research publishing by freely delivering the most outstanding research, evaluated with no bias from both the academic and social point of view. By applying the most advanced information technologies, Frontiers is catapulting scholarly publishing into a new generation.

What are Frontiers Research Topics?

Frontiers Research Topics are very popular trademarks of the *Frontiers journals series*: they are collections of at least ten articles, all centered on a particular subject. With their unique mix of varied contributions from Original Research to Review Articles, Frontiers Research Topics unify the most influential researchers, the latest key findings and historical advances in a hot research area.

Find out more on how to host your own Frontiers Research Topic or contribute to one as an author by contacting the Frontiers editorial office: frontiersin.org/about/contact

New molecular pathways in thyroid cancer and pathophysiology: Role of coding and noncoding genes

Topic editors

Cesar Seigi Fuziwara — University of São Paulo, Brazil
Murilo Vieira Geraldo — State University of Campinas, Brazil
Juan Pablo Nicola — National University of Cordoba, Argentina

Citation

Fuziwara, C. S., Geraldo, M. V., Nicola, J. P., eds. (2024). *New molecular pathways in thyroid cancer and pathophysiology: Role of coding and noncoding genes*. Lausanne: Frontiers Media SA. doi: 10.3389/978-2-8325-4782-3

Table of contents

frontiers | Frontiers in Endocrinology

TYPE Editorial
PUBLISHED 05 April 2024
DOI 10.3389/fendo.2024.1404305

OPEN ACCESS

EDITED AND REVIEWED BY
Antonino Belfiore,
University of Catania, Italy

*CORRESPONDENCE
Cesar Seigi Fuziwara
cesar.fuziwara@usp.br

RECEIVED 20 March 2024
ACCEPTED 25 March 2024
PUBLISHED 05 April 2024

CITATION
Fuziwara CS, Nicola JP and Geraldo MV (2024) Editorial: New molecular pathways in thyroid cancer and pathophysiology: role of coding and noncoding genes.
Front. Endocrinol. 15:1404305.
doi: 10.3389/fendo.2024.1404305

Editorial: New molecular pathways in thyroid cancer and pathophysiology: role of coding and noncoding genes

Cesar Seigi Fuziwara[1]*, Juan Pablo Nicola[2,3] and Murilo Vieira Geraldo[4]

[1]Department of Cell and Developmental Biology, Institute of Biomedical Sciences, University of São Paulo, São Paulo, Brazil, [2]Department of Clinical Biochemistry, Faculty of Chemical Sciences, National University of Córdoba, Córdoba, Argentina, [3]Clinical Biochemistry and Immunology Research Center - National Scientific and Technical Research Council (CIBICI-CONICET), Córdoba, Argentina, [4]Department of Structural and Functional Biology, State University of Campinas, São Paulo, Brazil

KEYWORDS

thyroid cancer, coding genes, noncoding genes, molecular marker, omic analyses, mutation–genetics

Editorial on the Research Topic
New molecular pathways in thyroid cancer and pathophysiology: role of coding and noncoding genes

Thyroid cancer is the most common endocrine malignancy arising from different cell types that compose thyroid gland, namely, follicular cells and C-cells or parafollicular cells. Within the follicular cell-derived thyroid cancer, several variants can be identified that exhibit heterogeneous behavior ranging from indolent papillary thyroid cancer (PTC) to very aggressive and lethal anaplastic thyroid cancer (ATC), turning thyroid cancer into a fruitful field for investigation of tumor biology. In this context, the Research Topic "*New molecular pathways in thyroid cancer and pathophysiology: role of coding and noncoding genes*" compiled several articles that provided novel aspects of thyroid cancer biology, adding new layers to the complexity of the disease.

Regarding the oncogenesis aspect, new molecular players have been identified using animal models, human samples and proteomic analysis. For example, Minna et al. reported mutations in *DICER1* in follicular-patterned RAS-like tumors without any oncogenic activation of the MAPK pathway. Dicer1 is an endoribonuclease that processes endogenous miRNA precursors into mature miRNA, and mutations that alter Dicer's functionality impair this process, with consequences for cell biology. Didier-Mathon et al. reported that the *Borealin* gene (*CDCA8*), discovered in a patient with congenital hypothyroidism due to thyroid dysgenesis, is involved in thyroid cell biology. Inactivation of Borealin induces goiter and the formation of papillary-like structures that overactivate ERK signaling and induce a BRAF-like gene expression signature in transgenic mice, resembling mutation in human Borealin. Zhou et al. investigated the genetics of the non-classical PTC and revealed a high prevalence of gene fusions involving *NTRK* and *RET*, suggesting a common genetic signature among patients without BRAF or RAS mutations. Huang et al. conducted proteomic profiling of follicular-pattern thyroid tumors, and identified proteins that

discriminate follicular thyroid cancer from the follicular-variant of papillary thyroid cancer. Among these proteins, ANXA1 was validated as a novel biomarker in thyroid tumors.

Currently, an array of open-access databases generated from large-scale studies are available for researchers to explore, re-analyze, and gain new insights into thyroid cancer progression. In particular, Zhang et al. used available microarray datasets to detect differentially expressed genes in metastatic PTC and identified a signature of four genes associated with iodine metabolism in metastatic PTC that were associated with poor overall survival. Liu et al. conducted bioinformatic analysis in The Cancer Genome Atlas database for thyroid cancer to identify genes associated with lymph node metastasis potential. Among a twelve-gene signature, ERBB3 (HER3) overexpression was detected in patients with lymph node metastasis or advanced stage disease, which was associated with reduced ERBB3 gene methylation.

Response to radioiodine is essential for thyroid cancer treatment and new molecular insights into the histopathology of aggressive tumors could lead to a better management in clinical practice. In this extent, Bogdanova et al. investigated aggressive radioiodine-refractory recurrent PTC and showed that while primary metastases and radioiodine-refractory metastases are less differentiated and show similar architecture with solid trabecular structure and increased p16 staining, the primary tumors are more differentiated with papillary structure. Huang et al. investigated the relationship between $BRAF^{V600E}$ mutation and iodine avidity in distant lung metastases and showed that lymph node metastases are more likely to lose radioiodine avidity when the primary tumor harbors the $BRAF^{V600E}$ oncogene. In addition, Mukhtar et al. investigated the association of $BRAF^{V600E}$ and *TERT* promoter mutation in the stratification of differentiated thyroid cancer, and confirmed that only *TERT* promoter mutations, either alone or in combination with $BRAF^{V600E}$, correlate with a high-risk disease.

To identify new vulnerabilities of aggressive thyroid cancer cells, Sriramareddy et al. and Pita et al. have investigated the efficacy of targeting DNA repair and CDK phosphorylation. Using an approach to block the DNA repair mechanism in ATC cells, Sriramareddy et al. showed that the treatment with a DNA ligase inhibitor enhanced apoptosis in doxorubicin-treated ATC cells *in vitro* and reduced tumor growth *in vivo* in nude mice. On the other hand, Pita et al. explored the potential of CDK4/6 inhibition in a comprehensive panel of thyroid cancer cell lines and observed a synergistic antitumoral effect when blocking CDK together with MAPK signaling in CDK-sensitive cells, while testing an 11-gene signature tool to detect CDK insensitivity.

Overall, we hope that these 11 articles published in the Research Topic "*New molecular pathways in thyroid cancer and pathophysiology: role of coding and noncoding genes*" have shed new light on the understanding of thyroid biology and pathogenesis, while provided new insights into this molecular field that is emerging from the interpretation of data generated in the omics era.

Author contributions

CF: Writing – original draft, Writing – review & editing. JN: Writing – review & editing. MG: Writing – review & editing.

Conflict of interest

The authors declare that the research was conducted in the absence of any commercial or financial relationships that could be construed as a potential conflict of interest.

The author(s) declared that they were an editorial board member of Frontiers, at the time of submission. This had no impact on the peer review process and the final decision.

Publisher's note

frontiers | Frontiers in Endocrinology

ORIGINAL RESEARCH
published: 06 July 2022
doi: 10.3389/fendo.2022.854611

Proteotypic Differences of Follicular-Patterned Thyroid Neoplasms

Dongdong Huang[1], Huifang Zhang[1], Lu Li[2,3,4,5], Weigang Ge[6], Wei Liu[2,3,4], Zhen Dong[2,3,4], Jinlong Gao[2,3,4], Nan Yao[6], Wenxin Fu[6], Lingling Huang[6], Tiannan Guo[2,3,4], Yaoting Sun[2,3,4] and Xiaodong Teng[1]**

[1] The First Affiliated Hospital, Zhejiang University School of Medicine, Hangzhou, China, [2] Westlake Laboratory of Life Sciences and Biomedicine, Key Laboratory of Structural Biology of Zhejiang Province, School of Life Sciences, Westlake University, Hangzhou, China, [3] Institute of Basic Medical Sciences, Westlake Institute for Advanced Study, Hangzhou, China, [4] Research Center for Industries of the Future, Westlake University, Hangzhou, China, [5] College of Pharmaceutical Sciences, Zhejiang University, Hangzhou, China, [6] Westlake Omics (Hangzhou) Biotechnology Co., Ltd., Hangzhou, China

The diagnosis of follicular-patterned thyroid tumors such as follicular thyroid adenoma (FA), follicular thyroid carcinoma (FTC), and follicular variant of papillary thyroid carcinoma (FvPTC) remains challenging. This study aimed to explore the molecular differences among these three thyroid tumors by proteomic analysis. A pressure cycling technology (PCT)-data-independent acquisition (DIA) mass spectrometry workflow was employed to investigate protein alterations in 52 formalin-fixed paraffin-embedded (FFPE) specimens: 18 FA, 15 FTC, and 19 FvPTC specimens. Immunohistochemical (IHC) analysis of 101 FA, 67 FTC, and 65 FvPTC specimens and parallel reaction monitoring (PRM) analysis of 20 FA, 20 FTC, and 20 FvPTC specimens were performed to validate protein biomarkers. A total of 4107 proteins were quantified from 52 specimens. Pairwise comparisons identified 287 differentially regulated proteins between FTC and FA, and 303 between FvPTC and FA and 88 proteins were co-dysregulated in the two comparisons. However, only 23 discriminatory proteins between FTC and FvPTC were detected. Additionally, the quantitative results for ANXA1 expression based on IHC staining and PRM-MS quantification were consistent with the proteomic results, showing that ANXA1 can be used to distinguish FvPTC from FA and FTC. The differentially regulated proteins found in this study can differentiate FA from FvPTC. In addition, ANXA1 is a promising biomarker for differentiating FvPTC from the other thyroid tumors.

Keywords: follicular thyroid adenoma, follicular thyroid carcinoma, follicular variant papillary thyroid carcinoma, data-independent acquisition, mass spectrometry

OPEN ACCESS

Edited by:
Yuji Nagayama, Nagasaki University, Japan

Reviewed by:
Aysel Ozpinar, Acıbadem University, Turkey
Giulia Capitoli, University of Milano Bicocca, Italy

***Correspondence:**
Yaoting Sun
sunyaoting@westlake.edu.cn
Xiaodong Teng
teng1102069@zju.edu.cn

Specialty section:
This article was submitted to Thyroid Endocrinology, a section of the journal Frontiers in Endocrinology

Received: *15 March 2022*
Accepted: *31 May 2022*
Published: *06 July 2022*

Citation:
Huang D, Zhang H, Li L, Ge W, Liu W, Dong Z, Gao J, Yao N, Fu W, Huang L, Guo T, Sun Y and Teng X (2022) Proteotypic Differences of Follicular-Patterned Thyroid Neoplasms. Front. Endocrinol. 13:854611. doi: 10.3389/fendo.2022.854611

INTRODUCTION

Thyroid nodules, encompassing adenomatous nodules, nodular goiters, follicular thyroid adenoma (FA), follicular thyroid carcinoma (FTC), and follicular variant of papillary thyroid carcinoma (FvPTC), are a common finding in adults and exhibit follicular morphological characteristics (1). Given that ultrasound-guided fine-needle aspiration (FNA) biopsy is less traumatic than open surgical resection, it is still the gold standard screening method to validate the characteristics of

tumors (2). However, the diagnosis and identification of follicular-patterned thyroid nodules such as FA, FTC, and FvPTC have always been formidable challenges to cytopathologists because of overlapping cytological features and the lack of evidence of capsular or vascular invasion.

Given these difficulties in diagnosing follicular-patterned thyroid neoplasms, ancillary tools are necessary and helpful. Proteomics is a promising approach for identifying biological systems and functions by quantifying and validating large numbers of proteins. This approach has enabled the evaluation and acquisition of some target molecular markers and specific signaling pathways in thyroid pathology. For instance, aiming to identify biomarker candidates to distinguish FA from FTC, Lai et al. discovered several biomarker candidates by a comprehensive mass spectrometry-based analysis; these candidate biomarkers included SUCLG2, with a sensitivity of 75% and a specificity of 80% (3). However, the specific proteomic variants of other follicular-patterned thyroid tumors, such as FvPTC, have not been validated.

FvPTC has been deemed to be entirely or almost entirely composed of follicles, with cells showing nuclear characteristics of classical papillary thyroid carcinoma (cPTC), including intranuclear pseudoinclusions, nuclear grooves, and overlapping nuclei (4). As early as 1960, Lindsay proposed that FvPTC is a distinct subtype of FTC, sharing some biological behaviors with cPTC. However, it was still classified as cPTC during the 1980s, despite the dominance of the follicular pattern (5). A previous study advocated that encapsulated FvPTC behaved like FA or FTC and carried no risk of recurrence or death. In contrast, infiltrative FvPTC was regarded as similar to infiltrative cPTC in terms of biological behaviors and morphological features (6). In addition, the Cancer Genome Atlas research network revealed that the FvPTC group of neoplasms, both infiltrative and noninfiltrative, had the molecular signature of *RAS* mutations, while cPTC exhibits a high prevalence of $BRAF^{V600E}$ mutation (7). There is still debate as to which pathological type FvPTC is closer to. Therefore, research on new potential markers for thyroid pathology, particularly markers enabling FA, FTC, and FvPTC to be distinguished, remains worth conducting.

Recently, pressure cycling technology (PCT) has been developed for semiautomatic processes with small-volume clinical tissues. PCT-data-independent acquisition (DIA) results in higher quantitative accuracy, provides deeper proteome coverage, and is less time-consuming than conventional approaches (8). In this work, we performed the method mentioned above to compare FA, FTC, and FvPTC, gleaning enhanced insights into similarities and differences in protein levels in these three thyroid tumors.

METHODS

Thyroid Tissue Specimens

As shown in **Table 1**, 345 formalin-fixed paraffin-embedded (FFPE) specimens, specifically, 139 FA, 102 FTC, and 104 FvPTC specimens were obtained from the First Affiliated Hospital of the College of Medicine, Zhejiang University, with approval from the hospital ethics committee. Among the specimens, 18 FA, 15 FTC, and 19 FvPTC specimens were analyzed by the PCT-DIA method to investigate the protein alterations in these three thyroid tumors. These 52 specimens were a subset of our previously analyzed dataset (9). Additionally, immunohistochemical (IHC) analysis of 101 FA, 67 FTC, and 65 FvPTC samples and parallel reaction monitoring (PRM) analysis of 20 FA, 20 FTC, and 20 FvPTC specimens were performed to validate the selected proteins. Two pathologists (X.T. and H.Z.) independently confirmed the pathological diagnosis in the above tissues in accordance with the World Health Organization Classification of Tumors of Endocrine Organs.

TABLE 1 | Clinical characteristics in DIA-MS, PRM-MS, and IHC analyses.

	Discovery set	Validation set	
	DIA-MS	PRM-MS	IHC
Histopathology diagnosis			
FA	18	20	101
FTC	15	20	67
FvPTC	19	20	65
Gender			
Female (%)	35 (67.3%)	41 (68.3%)	160 (68.7%)
Male (%)	17 (32.7%)	19 (31.7%)	73 (31.3%)
Age at diagnosis			
Mean	46.77	44.13	46.36
Range	33.24 - 60.3	30.13 – 58.13	32.61 – 60.11
<55 y (%)	34 (65.4%)	44 (73.3%)	157 (67.4%)
≥55 y (%)	18 (34.6%)	16 (26.7%)	76 (32.6%)
Nodule size			
Mean	2.76	2.71	2.66
Range	1.13 – 4.39	1.29 – 4.12	1.11 – 4.20
<1 cm (%)	7 (13.4%)	7 (11.7%)	33 (14.2%)
1 - 4 cm (%)	34 (65.4%)	41 (68.3%)	168 (72.1%)
>4 cm (%)	11 (21.2%)	12 (20.0%)	32 (13.7%)

Proteomic Analysis

Samples (0.6-1.2 mg) were punched from FFPE blocks according to the histopathological areas of interest marked by pathologists (D.H. and H.Z.). FFPE sample preparation was performed using the FFPE-PCT-DIA workflow, as described previously (10, 11). Briefly, FFPE samples were dewaxed and hydrated with heptane and an ethanol gradient (100%, 90%, and 75%). Next, samples were processed by incubation in 0.1% formic acid at 30°C for 30 min and Tris-HCl solution (pH=10, 100 mM) at 95°C for 30 min for decrosslinking. Tissues were subjected to a PCT lysis protocol in 6 M urea and 2 M thiourea buffer. Reduction and alkylation were conducted in 10 mM tris(2-carboxyethyl) phosphine (TCEP) and 40 mM iodoacetamide (IAA). Extracted proteins were digested using LysC (enzyme-to-substrate ratio, 1:40; Hualishi Scientific, China) and trypsin (enzyme-to-substrate ratio, 1:50; Hualishi Scientific, China) by PCT. Digested peptides were desalted on C18 columns (The Nest Group, United States). The chemical reagents described above were purchased from Sigma–Aldrich.

Cleaned peptides (0.4 μg) from each sample were separated on an in-house-developed analytical column (75 μm × 150 mm, 1.9 μm, 100 Å C18 particles) in an Ultimate 3000 HPLC nanoflow system over 45 min in a linear gradient concentration of 3-25% buffer B (buffer A: 2% acetonitrile and 0.1% formic acid in HPLC-grade water; buffer B: 98% acetonitrile and 0.1% formic acid in HPLC-grade water). Eluted peptides were quantified in an Orbitrap (Thermo Q Exactive™ HF) with resolutions of 60,000 and 30,000 (at *m/z* 200 Th) for full MS scans and MS/MS scans, respectively, in DIA mode. For MS/MS scans, we used a series of 24 variable DIA windows to cover the precursor mass over an *m/z* range of 400 to 1200 Th. Each sample was acquired and analyzed by MS with two technical replicates. Therefore, we collected 104 raw DIA data files, which were part of our previous released dataset (9). All DIA data were re-searched by Spectronaut™ (version 13.5) against a thyroid-specific spectral library (12), including 157,548 peptide precursors, 121,960 peptides, and 9941 proteins with a false discovery rate of 0.01. The other parameters were set to the default values.

Construction of Tissue Microarrays and Immunohistochemical Analysis

Tissue microarray (TMA) blocks for further validation were constructed using samples from the First Affiliated Hospital of College of Medicine, Zhejiang University. Cores (1-mm) were punched from each of the collected specific paraffin-embedded tissue blocks from 101 cases of FA, 67 cases of FTC, and 65 cases of FvPTC and were embedded into new TMAs for subsequent IHC staining. For the current study, some prominent IHC markers, i.e., LUC7L, NUP214, PTK7, DPY30, SYNPO, CDC42EP1, ANXA1, RBM10, FAM50A, MAP2, and CD74, whose differential expression ratio were at least four in each group, were chosen to be verified based on the availability of antibodies for IHC staining. The core from each TMA block was subjected to IHC staining with a specific antibody, verified for accurate specific staining, and scored independently by two pathologists (X.T. and H.Z.). Additionally, a Leica image analysis system was used to measure the staining intensity of each TMA block, which was finally presented as a specific value.

PRM Quantification and Data Analysis

PRM analysis was performed on 20 FA, 20 FTC (2 specimens were from the same patient), and 20 FvPTC specimens in the Thermo Q Exactive™ HF system connected to a nanoflow DIONEX UltiMate 3000 RSLCnano System. Eighty proteins, including those identified above by IHC staining, whose differential expression ratio was at least eight in each group, were further verified by PRM. Seventy-seven peptide precursors from 65 proteins were successfully programmed for the PRM assay with these criteria applied: unique peptide, no dynamic modification, no missed cleavage, appropriate sequence length, and clear mass-fragment spectrum. Peptides were separated at 300 nL/min along a 60 min 10%–30% linear LC gradient of buffer B. The PRM acquisition method was applied following our previous publication (12).

Bioinformatical and Statistical Analysis

Statistical diagrams for proteomic data analysis were generated by R software (4.0.2). The coefficients of variation (CVs) were calculated as the ratio of the standard deviation to the mean. Two-tailed paired Student's *t* test was used to determine probability and was adjusted by the Benjamini and Hochberg (BH) method for generation of volcano plots. The *P* values of the three groups' comparisons were calculated by one-way analysis of variance (ANOVA). The heatmap was generated with the pheatmap R package, and the proteins in each row were subjected to unsupervised clustering. Pathway enrichment analysis was conducted with Ingenuity Pathway Analysis (IPA) software. The protein network was constructed based on the STRING database and plotted with Cytoscape (version 3.8.2). The network edges indicate the interactions with high confidence, with a required minimum interaction score of 0.700. The disconnected nodes in the network were hidden. The Mann–Whitney U test was used to evaluate statistically significant differences in the staining intensity between FA, FTC, and FvPTC specimens for each chosen marker. SPSS version 22 (IBM Corp., Armonk, NY, USA) was used for statistical analyses, and the statistical significance level was set to 0.05.

RESULTS

Patient Characteristics and Study Design

In the present study, we established two sets of subjects: one contained 52 specimens from 51 patients for proteomic analysis, and the other contained 293 samples from 246 patients for validation by IHC (n=233) and PRM (n=60) analyses. Samples for proteomic analysis were processed *via* a PCT-DIA workflow as described in the *Methods* section (**Figure 1A**).

More details of the clinical characteristics are summarized in **Table 1** and **Table S1**. The histopathological characteristics are shown in **Figure 1B**. FAs are well-encapsulated thyroid nodules without typical invasiveness and abnormal nuclear features,

whereas FTCs frequently exhibit capsular disruption, vascular invasion, extrathyroidal extension, and even distant metastasis. In addition, although glandular nuclei, intranuclear inclusions, and nuclear grooves are visible, the histological pattern of infiltrative FvPTC tends to be follicular rather than papillary.

Proteomic Data Analysis Based on Discovery Group

Two technical replicates of each sample in the discovery set were analyzed for further robustness evaluation of the proteome maps generated from the FFPE tissues. In summary, 52 specimens were analyzed by MS with two technical replicates, and 104 DIA files were subsequently obtained. We identified 4107 proteins based on the 104 proteomic data files. The numbers of identified peptides and proteins in each MS file are shown in **Figures S1A, B**.

For the three groups' comparisons by one-way ANOVA, *P* values of 799 and 444 proteins are less than 0.05 and 0.01, respectively (**Table S2**). The Venn diagram in **Figure 2A** shows the number of identified proteins displaying significantly quantitative similarities and differences among the three groups. There were 3830, 3753, and 3883 proteins identified in FA, FTC, and FvPTC, respectively. A total of 3522 proteins were shared by all three groups, demonstrating that a large set of overlapping proteins (85.8%) was detected, which validated the robustness of the proteome maps to some extent. In addition, 94 and 63 proteins were only identified in FA and FTC, respectively, while 113 proteins identified in FvPTC were observed in neither FA nor FTC.

In addition, the protein abundance distribution of the two biological replicates of all 52 samples was compared by Pearson correlation analysis (**Figure S1C**), showing the high robustness and reliability of the current comprehensive research. Additionally, principal component analysis (PCA) using 4107 proteins grouped by tissue type (**Figure 2B**) and gender (**Figure S1D**) revealed that FTC is more similar to FvPTC than FA. However, there was no significant difference in gender among these three groups.

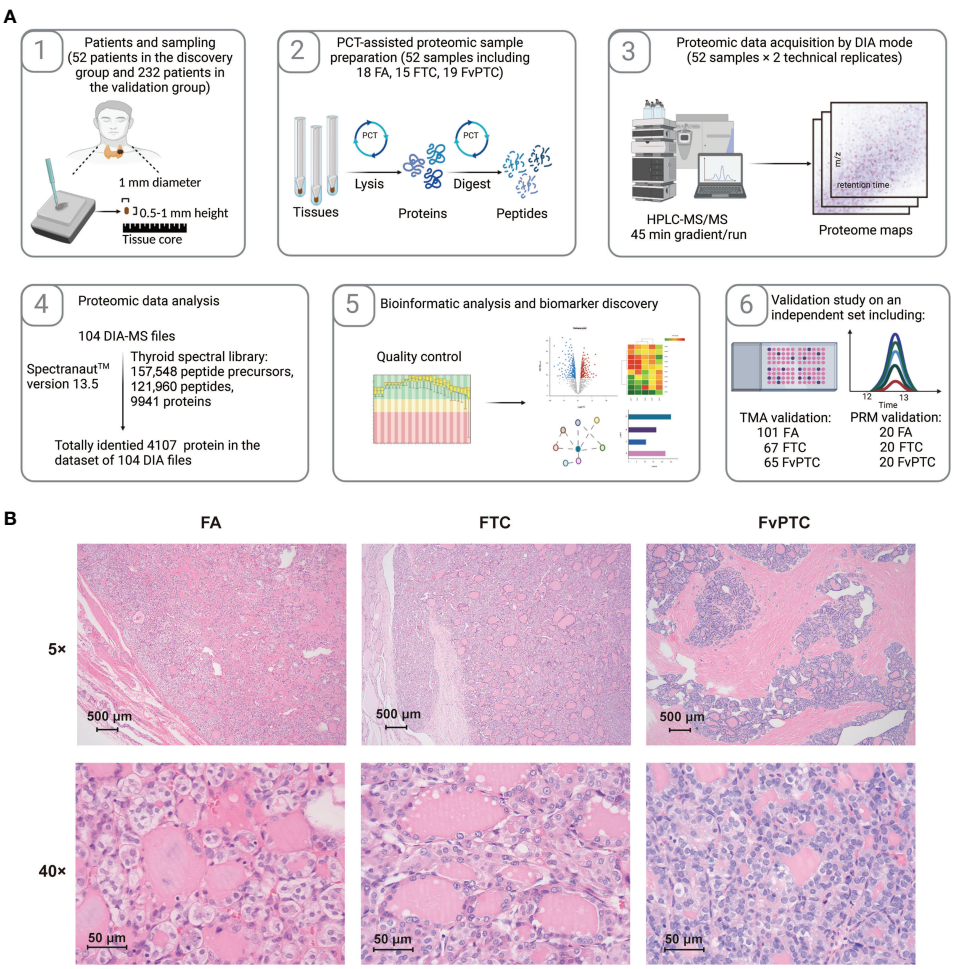

FIGURE 1 | Schematic of the study. **(A)** Workflow of the current study. **(B)** The histopathological characteristics of FA, FTC, and FvPTC.

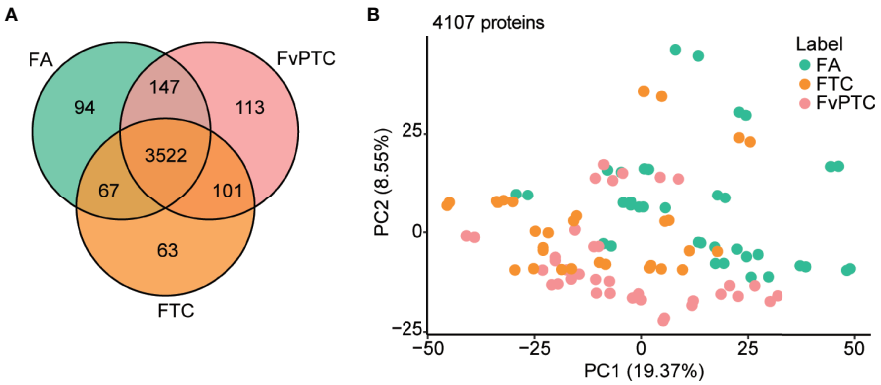

FIGURE 2 | Global proteomic analysis. **(A)** Venn diagram showing protein identification in FA, FTC, and FvPTC. **(B)** Principal component analysis (PCA) using 4107 proteins grouped by tissue type.

Difference Analysis of Proteomic Profile for the Follicular-Patterned Thyroid Tumors

Pairwise comparisons of the differential expression of multiple proteins in the FA, FTC, and FvPTC samples were performed to explore apparent similarities and distinctions among the three groups. We first processed proteome profiles showing significantly and differentially altered proteins between FA and FTC. As the volcano plots in **Figure 3A**, by setting a cutoff value of a two-fold change and a threshold adjusted *P* value of less than 0.05, we identified 287 differentially expressed proteins (DEPs), specifically, 253 upregulated and 34 downregulated proteins in FTC. In addition, the comparison showed 303 DEPs in FA and FvPTC, with 256 upregulated proteins and 47 downregulated proteins in FvPTC (**Figure 3B**). Interestingly, only 23 discriminatory proteins were detected between FTC and FvPTC (**Figure 3C**), a much lower number than found in the other comparative analyses. These pairwise analyses of protein expression also showed an apparent separation of FA from FTC and FvPTC, whereas FvPTC showed no apparent distinction from FTC. These results indicated that the two malignant tumors exhibited similar proteotypes but were distinct from the benign tumor FA. Subsequently, we performed PCA (**Figure 3D**) using 506 discriminatory proteins, the combined set of dysregulated proteins from the three volcano plots. These DEPs could distinguish samples from different tumor types better than the complete set of 4107 proteins (**Figure 2B**). In the unsupervised clustering protein heatmap, the protein diversity and abundance were higher in the malignant tumors (FTC and FvPTC) than in FA (**Figure 3E**).

To further investigate the biological function of malignant follicular tumors, we performed pathway and network analyses based on the DEPs. Based on the 287 proteins identified by comparison of FTC and FA (**Figure 3F**), AMPK signaling, which participates in cell growth, autophagy, and metabolism, was the most significantly enriched pathway (13). However, based on the 303 DEPs between FvPTC and FA (**Figure 3G**), RhoA signaling was substantially enriched. Signaling by Rho family GTPases was the most activated pathway, whereas RhoGDI signaling was the most inhibited pathway. In addition, the VEGF signaling pathway was significantly enriched.

Biological Analysis for the Three Types of Tumors

As indicated above, 253 and 256 proteins were upregulated but 34 and 47 proteins were downregulated in FTC and FvPTC, respectively, compared with FA. The analysis further indicated that FTC and FvPTC shared 78 upregulated and ten downregulated proteins compared with FA (**Figures 4A, B**). These proteins were related to thyroid cancers and their expressions were shown in the heatmap (**Figure 4C**). Of the 88 co-dysregulated proteins, 30 of them were with *P* value less than 0.01 estimated by one-way ANOVA. We further explored the protein-protein interactions of the 88 overlapping proteins by mapping to the STRING database. The largest mapped cluster is shown in **Figure 4D**. The 88 proteins were involved in three major biological functions or processes, namely, spliceosomal snRNP complex (FDR 8.3 e-9), mRNA processing (FDR 2.5 e-12), and mRNA transport (FDR 1.6 e-6), as annotated around the nodes. The key proteins in the center of the network were PRPF3, SNRPB2, SNRPA, LSM2, LSM8, FIP1L1, NCBP1, WBP11, CDC5L, and CPSF7.

Immunohistochemistry and PRM-MS Quantification for Validation

Furthermore, we validated the selected proteins as mentioned in the IHC and PRM-MS quantification methods in the two independent sets. Of note, the differential expression levels of ANXA1 in all three tumors were consistent across all three methods including DIA-MS, PRM-MS and IHC. In addition, interestingly, NUP214 presented higher expression as determined by DIA and PRM in FTC compared with FA and FvPTC, although IHC analysis showed different results (**Figure 5**).

DISCUSSION

Thyroid nodules exhibiting follicular histological features mainly include FA, FTC, and FvPTC. Since there is a wide range of

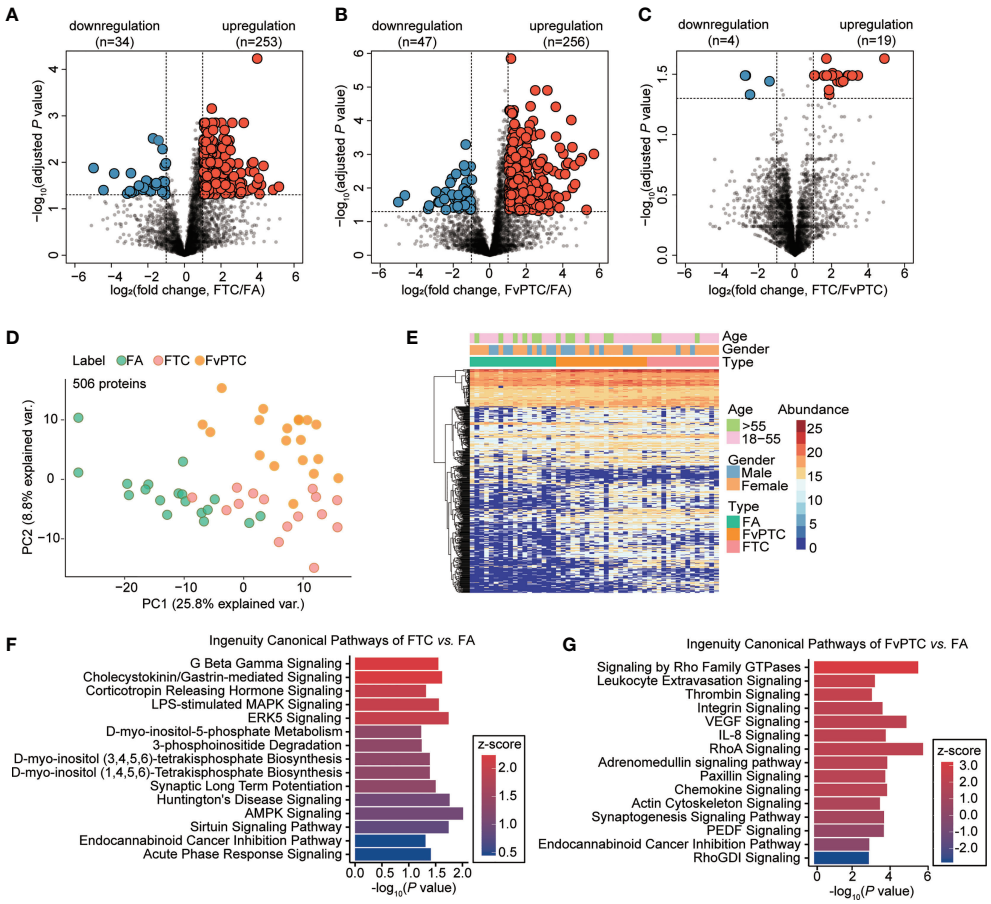

FIGURE 3 | Dysregulated protein expression analysis. **(A-C)** Volcano plot showing dysregulated proteins in **(A)** FTC vs. FA, **(B)** FvPTC vs. FA, and **(C)** FvPTC vs. FTC with a two-fold-change cutoff and an adjusted P value threshold less than 0.05. **(D)** PCA of samples from different tumor types using 506 dysregulated proteins. **(E)** Heatmap showing the protein expression profiles of 52 follicular-patterned thyroid tumor tissue specimens. 506 proteins (rows) are clustered without supervision. Samples (columns) are arranged based on the tissue type. The color indicates the $\log_2$-transformed intensity of each protein in each sample. Ingenuity canonical pathway analysis was used to enrich pathways from differentially expressed proteins (DEPs) in FTC vs. FA **(F)** and FvPTC vs. FA **(G)**. The top 15 enriched canonical pathways with *P* value <0.05 are ordered based on the z-score values.

benign to malignant differentiated subtypes, there is no doubt that diagnosing a relatively solitary nodule with follicular morphological characteristics, such as FA, FTC, or FvPTC, is always an enormous challenge for pathologists.

As mentioned above, various studies have recently developed additional methods to provide useful information for diagnosing and treating follicular neoplasms. Based on matrix-assisted Laser Desorption/Ionization (MALDI) Mass Spectrometry Imaging (MSI), a complementary tool with a combination of mass spectrometric data and histology, Yasemin et al. differentiated noninvasive follicular thyroid neoplasms with papillary-like nuclear features (NIFTP) from normal thyroid parenchyma (14). They also revealed that the peptide profiles of NIFTP and encapsulated and infiltrative FV-PTC were similar. In the current work, we utilized PCT-DIA-MS (11) to compare proteomic similarities and differences between FA, FTC, and FvPTC.

Concerning FvPTC, a previous study revealed that encapsulated FvPTC behaves like FA (15). However, microarray expression profiling validated a series of candidate genes involved in molecular mechanisms that differentiate FvPTC from FA (16). Regarding ultrasound characteristics, Ng *et al.* believed that FvPTC and FTC were more likely to be well-defined and noncalcified isoechoic lumps with relatively regular margins (17). In our analysis, 287 and 303 differentially regulated proteins were identified in FTC and FvPTC, respectively, compared to FA. In comparison, only 23 discriminatory proteins were found between FTC and FvPTC, which indicated that these neoplasms share significant similarity with each other and are apparently distinct from FA.

In the comparison of FTC and FA, pathway analysis demonstrated several prominent alterations, such as activated AMPK signaling in FTC. This finding was consistent with a previous study revealing that activation of the AMPK and mTOR pathways can exist simultaneously in FTC (18).

Regarding the biological differences in FvPTC in comparison with FA, our analysis found that RhoA signaling, which

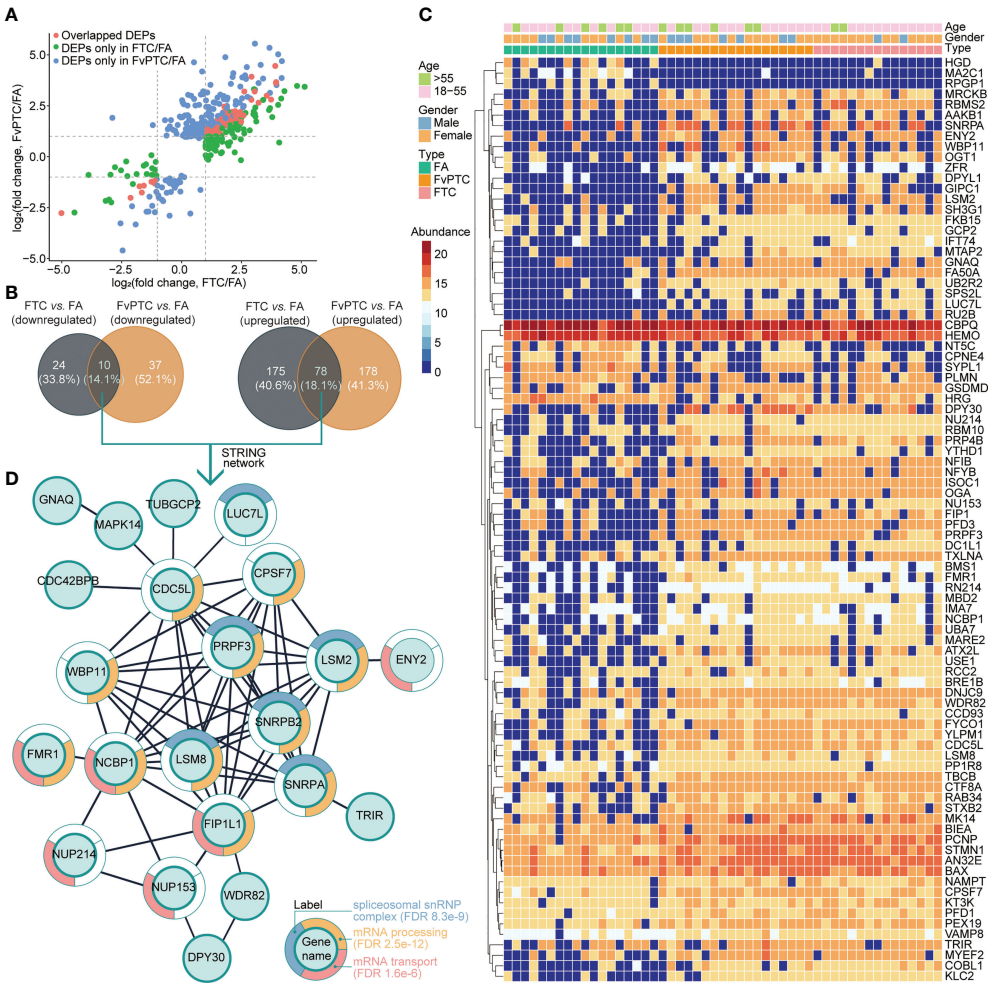

FIGURE 4 | Differentially expressed proteins in malignant tumors vs. the benign tumor and their biological analysis. **(A)** The differentially regulated proteins in FTC vs. FA and FvPTC vs. FA are distributed in the scatter plots. The overlapped DEPs in the two paired comparisons are colored in red, while the unique DEPs in the FTC vs. FA and FvPTC vs. FA are colored in green and blue, respectively. **(B)** Venn diagrams showing the total number of DEPs in FvPTC vs. FA and FTC vs. FA. **(C)** The heatmap exhibited the expression of 88 overlapped dysregulated proteins (panels **A, B**). **(D)** Functional analysis of the largest cluster was obtained by the overlapping upregulated- and downregulated proteins [panels **(A, B)**] using the STRING database. The top-three enriched biological process (BP) terms of gene ontology (GO) after redundancy filtering are visualized on split donut charts around the nodes annotated with those terms.

haspreviously been reported to be involved in the proliferation and carcinogenesis of thyroid cancer modulated by miR-128, miR-154-3p, and miR-487-3p, was substantially enriched (19, 20). Interestingly, VEGF signaling was also significantly enriched. Joaquim et al. expounded the role of VEGF signaling in thyroid carcinomas of follicular origin (21). They showed that coexpression of VEGF and two high-affinity tyrosine kinase receptors in VEGF signaling, namely, VEGFR-1/Flt-1 and VEGFR-2/KDR, were expressed in papillary thyroid carcinomas (PTCs), including follicular variants. Notably, VEGFR2 was critical for maintaining thyroid vascular integrity, and its blockade triggered inhibition of vascular remodeling and follicular hypertrophy (22).

Interestingly, the roles of top-ranked discriminatory proteins such as SNRPB2, PRPF3, and LSM8 in other diseases have been investigated for years, although there is limited evidence about the associations between these molecules and malignant thyroid tumors. For example, high expression levels of PRPF3 and SNRPB2 were observed in hepatocellular carcinoma and related to poor prognosis (23, 24). Additionally, LSM8 was significantly correlated with the development of Hashimoto's thyroiditis, which commonly triggers thyroid cancer (25). Consequently, we hypothesize that the abovementioned costimulatory molecules might trigger oncogenic effects in malignant thyroid tumors.

Besides, in addition to being the most prominent candidate according to the IHC staining and PRM-MS quantification results, ANXA1 has previously been reported in thyroid tumors (26). Its identification in serum and saliva combined with clinical biopsy may distinguish different thyroid nodules, including FTC and cPTC. Regarding NUP214, although there have been few studies on its

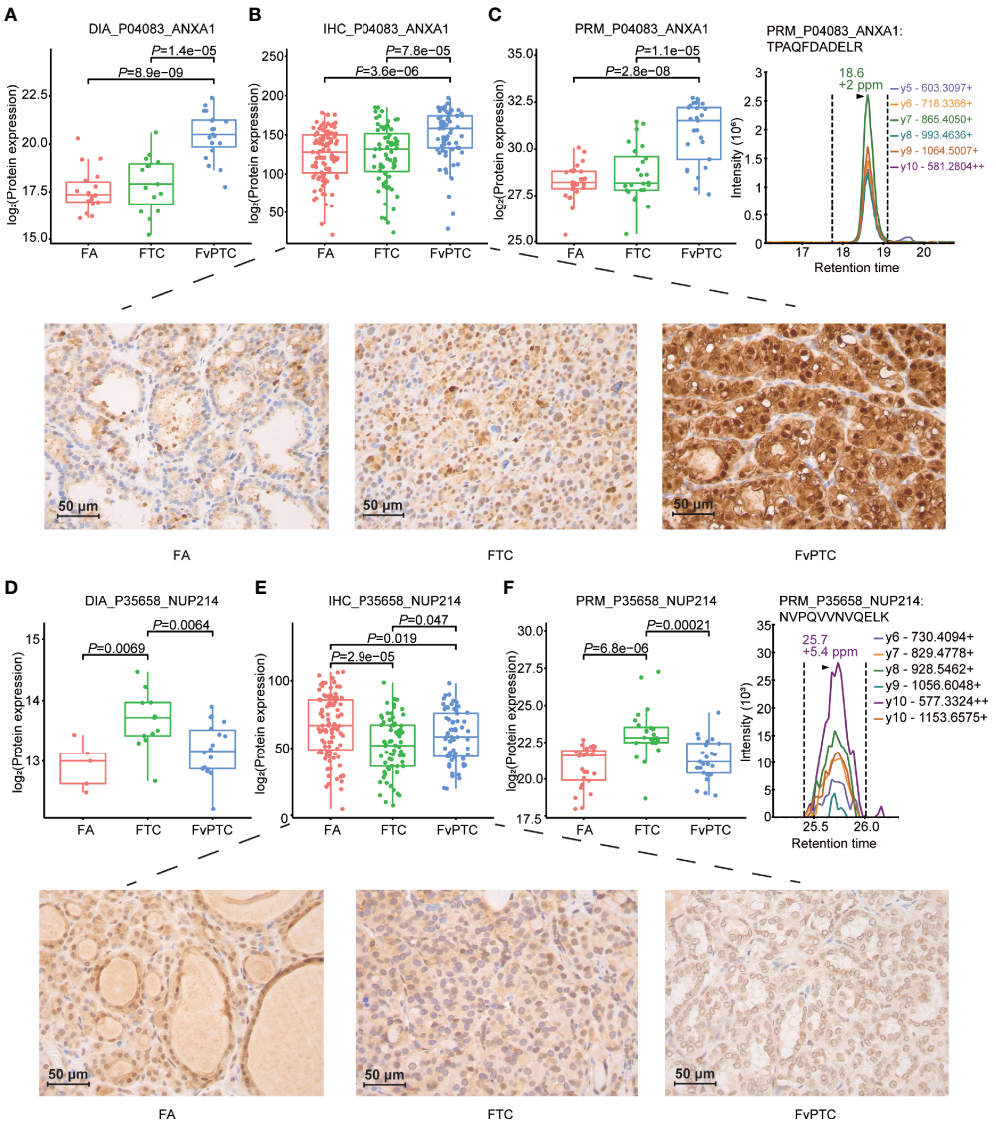

FIGURE 5 | Validation study. Representative results of PCT-DIA, PRM-MS, and immunohistochemical staining of ANXA1 **(A–C)**, NUP214 **(D–F)** in FA, FTC and FvPTC specimens.

relationship with thyroid tumors, chromosomal translocations involving the NUP214 locus were found to be recurrent in acute leukemia. Specifically, the C-terminal region of NUP214 is frequently fused with SET and DEK, and these two chromatin remodeling proteins are related to the regulation of transcription (27), which may be associated with the tumorigenesis and progression of FvPTC.

Limitations

In the current work, although some potential markers for follicular-patterned thyroid tumors were discovered, there are still several limitations. First, at present, it is difficult to differentiate the follicular-pattern thyroid tumors no matter at the pre- and post-surgery. Considering that histopathology is the gold standard for diagnosis, we explored the difference in the FFPE samples instead of FNA samples, which have a clear diagnosis by the experienced pathologist. Without a doubt, the current study is our first step to finding the protein marker candidates for distinguishing the follicular-pattern thyroid tumors. In the next step, we would verify the biomarker candidates in a larger cohort of samples from multiple clinical centers including FNA samples. Second, other follicular-patterned thyroid neoplasms, i.e., Hürthle cell tumors, NIFTP and well-differentiated tumors of uncertain malignant potential, and thyroid nodules with different backgrounds, i.e., hashimoto's thyroiditis and goiter were not analyzed, which will be analyzed in the further study. Third, the current study lacked comprehensive and integrated analyses combining multi-omic platforms with morphological

characteristics based on histopathology or medical ultrasonics, which could be further applied to improve the accuracy and efficacy of diagnostic and prognostic.

CONCLUSION

In conclusion, the current proteomic analysis of FA, FTC, and FvPTC identified certain protein signatures that can distinguish various thyroid nodules with different follicular morphological characteristics. Specifically, clusters of proteins demonstrated a marked ability to differentiate FA from FTC and FvPTC. However, more research needs to be carried out to further cull and validate potential biomarker candidates. These findings may provide deeper insight for improving the diagnostic accuracy and efficiency of follicular-patterned thyroid neoplasms.

DATA AVAILABILITY STATEMENT

The mass spectrometry proteomics data have been deposited to the iProX with the dataset identifier IPX0003973000.

ETHICS STATEMENT

The studies involving human participants were reviewed and approved by Clinical Research Ethics Committee, The First Affiliated Hospital, Zhejiang University School of Medicine. Written informed consent for participation was not required for this study in accordance with the national legislation and the institutional requirements.

AUTHOR CONTRIBUTIONS

XT, DH, and YS designed the project. XT, DH, and HZ revised the slides and collected the FFPE samples. YS, LL, and WL performed the experiments for discovery set. NY and WF performed the targeted proteomic sample preparation and analysis. DH and HZ did the IHC validation study. YS, WG, and LH conducted proteomic data analysis. DH and YS wrote the manuscript with inputs from all co-authors. TG supported the data analysis and data presentation in the manuscript. XT and YS supervised the project. All authors contributed to the article and approved the submitted version.

FUNDING

This work is supported by grants from the National Key R&D Program of China (No. 2021YFA1301601, 2021YFA1301602, 2020YFE0202200), Zhejiang Provincial Research Center for Cancer Intelligent Diagnosis and Molecular Technology (JBZX-202003), China Postdoctoral Science Foundation (2021TQ0283) and International Postdoctoral Exchange Fellowship Program (Talent-Introduction Program) (YJ20210170).

SUPPLEMENTARY MATERIAL

The Supplementary Material for this article can be found online at: https://www.frontiersin.org/articles/10.3389/fendo.2022.854611/full#supplementary-material

Supplementary Figure 1 | Data quality control analysis. **(A)** Identified peptide and **(B)** protein numbers in each DIA run. **(C)** Pearson correlation analysis of technical replicates for each paired sample. **(D)** Principal component analysis (PCA) using 4107 proteins grouped by gender.

Supplementary Figure 2 | IHC images of ANXA1 and NUP214 in FA, FvPTC, and FTC specimens.

Supplementary Table 1 | Details of the clinical characteristics.

Supplementary Table 2 | Protein expression comparison among the FA, FTC, and FvPTC.

REFERENCES

1. Chmielik E, Rusinek D, Oczko-Wojciechowska M, Jarzab M, Krajewska J, Czarniecka A, et al. Heterogeneity of Thyroid Cancer. *PAT* (2018) 85:117–29. doi: 10.1159/000486422
2. Haugen BR, Alexander EK, Bible KC, Doherty GM, Mandel SJ, Nikiforov YE, et al. 2015 American Thyroid Association Management Guidelines for Adult Patients With Thyroid Nodules and Differentiated Thyroid Cancer: The American Thyroid Association Guidelines Task Force on Thyroid Nodules and Differentiated Thyroid Cancer. *Thyroid* (2016) 26:1–133. doi: 10.1089/thy.2015.0020
3. Lai X, Umbricht CB, Fisher K, Bishop J, Shi Q, Chen S. Identification of Novel Biomarker and Therapeutic Target Candidates for Diagnosis and Treatment of Follicular Carcinoma. *J Proteomics* (2017) 166:59–67. doi: 10.1016/j.jprot.2017.07.003
4. Yoon JH, Kwon HJ, Kim E-K, Moon HJ, Kwak JY. The Follicular Variant of Papillary Thyroid Carcinoma: Characteristics of Preoperative Ultrasonography and Cytology. *Ultrasonography* (2016) 35:47–54. doi: 10.14366/usg.15037
5. Tallini G, Tuttle RM, Ghossein RA. The History of the Follicular Variant of Papillary Thyroid Carcinoma. *J Clin Endocrinol Metab* (2017) 102:15–22. doi: 10.1210/jc.2016-2976
6. Chai YJ, Kim S, Kim SC, Koo DH, Min HS, Lee KE, et al. BRAF Mutation in Follicular Variant of Papillary Thyroid Carcinoma Is Associated With Unfavourable Clinicopathological Characteristics and Malignant Features on Ultrasonography. *Clin Endocrinol* (2014) 81:432–9. doi: 10.1111/cen.12433
7. Agrawal N, Akbani R, Aksoy BA, Ally A, Arachchi H, Asa SL, et al. Integrated Genomic Characterization of Papillary Thyroid Carcinoma. *Cell* (2014) 159:676–90. doi: 10.1016/j.cell.2014.09.050
8. Zhu Y, Guo T. High-Throughput Proteomic Analysis of Fresh-Frozen Biopsy Tissue Samples Using Pressure Cycling Technology Coupled With SWATH Mass Spectrometry. *Methods Mol Biol* (2018) 1788:279–87. doi: 10.1007/7651_2017_87
9. Sun Y, Selvarajan S, Zang Z, Liu W, Zhu Y, Zhang H, et al. Protein Classifier for Thyroid Nodules Learned From Rapidly Acquired Proteotypes. *medRxiv* (2020) 2020:4.09.20059741. doi: 10.1101/2020.04.09.20059741
10. Zhu Y, Weiss T, Zhang Q, Sun R, Wang B, Yi X, et al. High-Throughput Proteomic Analysis of FFPE Tissue Samples Facilitates Tumor Stratification. *Mol Oncol* (2019) 13:2305–28. doi: 10.1002/1878-0261.12570
11. Guo T, Kouvonen P, Koh CC, Gillet LC, Wolski WE, Röst HL, et al. Rapid Mass Spectrometric Conversion of Tissue Biopsy Samples Into Permanent Quantitative Digital Proteome Maps. *Nat Med* (2015) 21:407–13. doi: 10.1038/nm.3807

12. Sun Y, Li L, Zhou Y, Ge W, Wang H, Wu R, et al. A Comprehensive Mass Spectral Library for Human Thyroid Tissues. *Mol Oncol* (2022) 16:1611–24. doi: 10.1101/2021.05.27.445992
13. Mihaylova MM, Shaw RJ. The AMP-Activated Protein Kinase (AMPK) Signaling Pathway Coordinates Cell Growth, Autophagy, & Metabolism. *Nat Cell Biol* (2011) 13:1016–23. doi: 10.1038/ncb2329
14. Ucal Y, Tokat F, Duren M, Ince U, Ozpinar A. Peptide Profile Differences of Noninvasive Follicular Thyroid Neoplasm With Papillary-Like Nuclear Features, Encapsulated Follicular Variant, and Classical Papillary Thyroid Carcinoma: An Application of Matrix-Assisted Laser Desorption/Ionization Mass Spectrometry Imaging. *Thyroid : Off J Am Thyroid Assoc* (2019) 29:1125–37. doi: 10.1089/thy.2018.0392
15. Nikiforov YE, Seethala RR, Tallini G, Baloch ZW, Basolo F, Thompson LDR, et al. Nomenclature Revision for Encapsulated Follicular Variant of Papillary Thyroid Carcinoma. *JAMA Oncol* (2016) 2:1023–9. doi: 10.1001/jamaoncol.2016.0386
16. Schulten H-J, Al-Mansouri Z, Baghallab I, Bagatian N, Subhi O, Karim S, et al. Comparison of Microarray Expression Profiles Between Follicular Variant of Papillary Thyroid Carcinomas and Follicular Adenomas of the Thyroid. *BMC Genomics* (2015) 16:S7. doi: 10.1186/1471-2164-16-S1-S7
17. Ng S-C, Kuo S-F, Hua C-C, Huang B-Y, Chiang K-C, Chu Y-Y, et al. Differentiation of the Follicular Variant of Papillary Thyroid Carcinoma From Classic Papillary Thyroid Carcinoma: An Ultrasound Analysis and Complement to Fine-Needle Aspiration Cytology. *J Ultrasound Med* (2018) 37:667–74. doi: 10.1002/jum.14377
18. Kari S, Vasko VV, Priya S, Kirschner LS. PKA Activates AMPK Through LKB1 Signaling in Follicular Thyroid Cancer. *Front Endocrinol (Lausanne)* (2019) 10:769. doi: 10.3389/fendo.2019.00769
19. Zheng X, Wang S, Hong S, Liu S, Chen G, Tang W, et al. CXCR4/RhoA Signaling Pathway Is Involved in miR-128-Regulated Proliferation and Apoptosis of Human Thyroid Cancer Cells. *Int J Clin Exp Pathol* (2017) 10:9213–22.
20. Fan X, Luo Y, Wang J, An N. miR-154-3p and miR-487-3p Synergistically Modulate RHOA Signaling in the of Thyroid Cancer. *Biosci Rep* (2020) 40: BSR20193158. doi: 10.1042/BSR20193158
21. Vieira JM, Santos SCR, Espadinha C, Correia I, Vag T, Casalou C, et al. Expression of Vascular Endothelial Growth Factor (VEGF) and its Receptors in Thyroid Carcinomas of Follicular Origin: A Potential Autocrine Loop. *Eur J Endocrinol* (2005) 153:701–9. doi: 10.1530/eje.1.02009
22. Jang JY, Choi SY, Park I, Park DY, Choe K, Kim P, et al. VEGFR2 But Not VEGFR3 Governs Integrity and Remodeling of Thyroid Angiofollicular Unit in Normal State and During Goitrogenesis. *EMBO Mol Med* (2017) 9:750–69. doi: 10.15252/emmm.201607341
23. Liu Y, Yang Y, Luo Y, Wang J, Lu X, Yang Z, et al. Prognostic Potential of PRPF3 in Hepatocellular Carcinoma. *Aging (Albany NY)* (2020) 12:912–30. doi: 10.18632/aging.102665
24. Luo Y, Lin J, Zhang Y, Dai G, Li A, Liu X. LncRNA PCAT6 Predicts Poor Prognosis in Hepatocellular Carcinoma and Promotes Proliferation Through the Regulation of Cell Cycle Arrest and Apoptosis. *Cell Biochem Funct* (2020) 38:895–904. doi: 10.1002/cbf.3510
25. Brčić L, Barić A, Gračan S, Torlak V, Brekalo M, Škrabić V, et al. Genome-Wide Association Analysis Suggests Novel Loci Underlying Thyroid Antibodies in Hashimoto's Thyroiditis. *Sci Rep* (2019) 9:5360. doi: 10.1038/s41598-019-41850-6
26. Ciregia F, Giusti L, Molinaro A, Niccolai F, Mazzoni MR, Rago T, et al. Proteomic Analysis of Fine-Needle Aspiration in Differential Diagnosis of Thyroid Nodules. *Trans Res* (2016) 176:81–94. doi: 10.1016/j.trsl.2016.04.004
27. Mendes A, Fahrenkrog B. NUP214 in Leukemia: It's More Than Transport. *Cells* (2019) 8:76. doi: 10.3390/cells8010076

Conflict of Interest: TG is a shareholder of Westlake Omics Inc. WG, YN, WF. and LH are employees of Westlake Omics Inc.

The remaining authors declare that the research was conducted in the absence of any commercial or financial relationships that could be construed as a potential conflict of interest.

Publisher's Note: All claims expressed in this article are solely those of the authors and do not necessarily represent those of their affiliated organizations, or those of the publisher, the editors and the reviewers. Any product that may be evaluated in this article, or claim that may be made by its manufacturer, is not guaranteed or endorsed by the publisher.

frontiers | Frontiers in Endocrinology

TYPE Original Research
PUBLISHED 02 November 2022
DOI 10.3389/fendo.2022.959089

OPEN ACCESS

EDITED BY
Loredana Pagano,
University of Turin, Italy

REVIEWED BY
Stefan Sponholz,
Agaplesion Markus Krankenhaus, Germany
Hongye Chen,
Quzhou Kecheng People's Hospital, China
Lu Zhao,
Huazhong University of Science and Technology, China

*CORRESPONDENCE
Rui Huang
huang_rui@scu.edu.cn
Yuan Tang
1202ty@163.com

†These authors have contributed equally to this work

SPECIALTY SECTION
This article was submitted to Thyroid Endocrinology, a section of the journal Frontiers in Endocrinology

RECEIVED 01 June 2022
ACCEPTED 17 October 2022
PUBLISHED 02 November 2022

CITATION
Huang S, Qi M, Tian T, Dai H, Tang Y and Huang R (2022) Positive *BRAF*V600E mutation of primary tumor influences radioiodine avidity but not prognosis of papillary thyroid cancer with lung metastases. *Front. Endocrinol.* 13:959089. doi: 10.3389/fendo.2022.959089

Positive *BRAF*V600E mutation of primary tumor influences radioiodine avidity but not prognosis of papillary thyroid cancer with lung metastases

Shuhui Huang[1†], Mengfang Qi[1†], Tian Tian[1], Hongyuan Dai[1], Yuan Tang[2*] and Rui Huang[1*]

[1]Department of Nuclear Medicine, West China Hospital of Sichuan University, Chengdu, China, [2]Department of Pathology, West China Hospital of Sichuan University, Chengdu, China

Purpose: This study investigated the relationship between *BRAF*V600E mutation of the primary tumor and radioiodine avidity in lung metastases (LMs) and then further evaluated the impact of *BRAF*V600E mutation and radioiodine avidity status on the prognosis of papillary thyroid cancer (PTC) with LMs.

Methods: Ninety-four PTC patients with LMs after total thyroidectomy and cervical lymph node dissection between January 2012 and September 2021 were retrospectively included. All patients received *BRAF*V600E mutation examination of primary tumors and radioactive iodine (RAI) therapy. The therapeutic response was evaluated by Response Evaluation Criteria in Solid Tumors (RECIST) assessments (version 1.1). For patients with target lesions, the response was divided into complete response (CR), partial response (PR), stable disease (SD), and progressive disease (PD); for patients without target lesions, the response was divided into CR, non-CR/non-PD, and PD. In therapeutic response, PR and SD were classified as non-CR/non-PD for analysis. The chi-square test and logistic regression were used to analyze the impact factor on PD and mortality. Progression-free survival (PFS) and overall survival (OS) curves were constructed by the Kaplan–Meier method.

Results: It was found that 21.2% (7/33) of patients with positive *BRAF*V600E mutation and 62.3% (38/61) of patients with negative *BRAF*V600E mutation had radioiodine-avid LMs (χ^2 = 14.484, p = 0.000). Patients with positive *BRAF*V600E mutation are more likely to lose radioiodine avidity; the odds ratios (ORs) were 5.323 (95% CI: 1.953–14.514, p = 0.001). Finally, 25 patients had PD, and six patients died; loss of radioiodine avidity was the independent predictor for PD, and the ORs were 10.207 (95% CI: 2.629–39.643, p = 0.001); *BRAF*V600E mutation status was not correlated with PD (p = 0.602), whether in the radioiodine avidity group (p = 1.000) or the non-radioiodine avidity group (p = 0.867). Similarly, *BRAF*V600E mutation status was not correlated with

mortality; only loss of radioiodine avidity was the unfavorable factor associated with mortality in univariate analyses (p = 0.030).

Conclusion: Patients with LMs of PTC were more likely to lose radioiodine avidity when their primary tumor had positive *BRAF*V600E mutation; however, only radioiodine avidity and not *BRAF*V600E mutation status affected the clinical outcome of patients with lung metastatic PTC.

KEYWORDS

papillary thyroid carcinoma, BRAFV600E mutation, lung metastases, radioiodine avidity, prognosis

Introduction

Differentiated thyroid cancer (DTC) is the most common endocrine malignancy, accounting for 90% of all thyroid cancers (1). Although most cases of DTC can be curable with a favorable prognosis, 5% to 25% of patients still have distant metastases (DMs), with a 10-year survival rate of only approximately 50% (2, 3). Radioactive iodine (RAI) therapy is the mainstay treatment option for DTC patients with DMs. However, when patients with DMs are resistant to RAI, their 10-year survival rate is less than 10% (4). The ability of DMs to trap iodine is essential to the efficiency of RAI. The sodium iodide symporter (NIS) actively transports iodide from plasma against its concentration gradient (5). Therefore, the level of NIS expression and its correct location on cancer cells are very important for RAI accumulation.

NIS expression is regulated by genetic and epigenetic alterations. *BRAF*V600E is the most frequent genetic aberration in papillary thyroid cancer (PTC), occurring in 29%–83% of PTC but basically missing in follicular thyroid cancers (FTCs) (6). Transgenic mice with *BRAF*V600E mutation showed tumorigenic potential to rapidly and consistently develop PTC that in the majority of cases displayed a poorly differentiated phenotype with decreased NIS expression and radioiodine refractoriness (RAI-R) (7). Preclinical and clinical studies of *BRAF*V600E inhibitors (dabrafenib and vemurafenib) restored or enhanced partial lesions concentrating I-131 (8–10). However, *BRAF* mutation is genetically heterogeneous within PTC tumor cells, and the relationship between *BRAF*V600E mutation and the aggressiveness and prognosis of patients with PTC is controversial (11–13). We demonstrated that *BRAF*V600E mutation had no effect on radioiodine ablation and adjuvant therapy for PTC without DMs, similar to another study demonstrating that the clinical response to RAI therapy was not inferior in *BRAF*V600E mutation PTC patients without DM (11, 14). A recent clinical study demonstrated that the addition of selumetinib to adjuvant RAI failed to improve the complete response rate for PTC patients when compared with RAI alone (15).

When referring to DMs from PTC, *BRAF*V600E was demonstrated to influence the ability to accumulate RAI (16). However, the effect of *BRAF*V600E mutation on the prognosis of metastatic PTC patients needs to be further illustrated. Moreover, not all patients with *BRAF*V600E mutation of the primary tumor have lost the ability to accumulate RAI (16). Whether *BRAF*V600E mutation can affect clinical outcomes in metastatic PTC patients with radioiodine avidity and non-radioiodine avidity also needs to be clarified. Thus, this study was designed to assess the proportion of radioiodine avidity and the prognosis of lung metastatic PTC patients with *BRAF*V600E mutation of primary tumors and then compare them with DMs coming from non-*BRAF*V600E mutation PTC patients.

Patients and methods

Patients

During enrollment, 1,360 patients with *BRAF*V600E mutation testing results from our hospital from January 2012 to September 2021 were reviewed. The inclusion criteria were as follows: 1) patients with lung metastases (LMs) based on pathological biopsy-proven assessment, chest CT, or imaging of treatment dose whole-body scan; 2) no other distant metastases, such as bone, liver, and muscle; 3) patients older than 20 years at diagnosis. Ultimately, a total of 94 patients with LMs of histological confirmation as PTC with *BRAF*V600E mutation testing results of the primary tumor were retrospectively enrolled. All the patients were divided into a positive *BRAF*V600E mutation group and a negative *BRAF*V600E group according to the status of *BRAF*V600E mutation. In addition, all patients also were divided into the radioiodine avidity group and non-radioiodine avidity group according to the status of radioiodine uptake. The study was

approved by our institutional review board, and the requirement for informed consent was waived.

The disease stages of PTC were defined according to the eighth edition of the American Joint Committee on Cancer TNM staging (17). Risk stratification was performed based on the 2015 American Thyroid Association guidelines (18).

*BRAF*V600E mutational analysis

The method for determining the *BRAF*V600E mutation status of primary PTC tumors was described previously (14). Briefly, genomic DNA extracted from primary tumors was used to amplify the fragment of *BRAF* gene containing the T1799A hot spot. *BRAF*V600E was identified on sequencing electropherograms.

Radioactive iodine therapy protocol

All patients underwent total thyroidectomy with at least central neck dissection and radioiodine therapy, followed by thyroid-stimulating hormone (TSH) suppression. One to six months after surgery, RAI therapy was administered according to the patients' examination. Before each RAI therapy, to ensure that the TSH level was above 30 mIU/L, levothyroxine withdrawal was maintained for at least 3 weeks. For the dose of RAI, the fixed radioactivity of 3.7 to 7.4 GBq was administered, and 5.5 to 7.4 GBq was given to repeated RAI therapy for patients with radioiodine-avid LMs. Levothyroxine was given on the third day of radioiodine therapy. ^{131}I whole-body scan was performed 3–5 days after radioiodine therapy. According to the results of the posttherapy ^{131}I whole-body scan, PTC patients with radioiodine-avid LMs included patients in whom partial or all pulmonary nodules could accumulate radioiodine; non-radioiodine-avid LMs included those patients in whom no pulmonary nodules could accumulate radioiodine.

Evaluation of therapeutic response

All patients were evaluated for LMs according to chest CT every 6 to 12 months. If there was at least one measurable pulmonary nodule (the longest diameter ≥1 cm), Response Evaluation Criteria in Solid Tumors (RECIST) 1.1 criteria (19) for target lesions were used to evaluate the therapeutic response as follows: 1) complete response (CR) if all lesions disappear and suppressed serum thyroglobulin level is undetectable, 2) partial response (PR) if the sum of the diameters of target lesions decreased more than 30%, 3) stable disease (SD) if the sum of the diameters of target lesions decreased less than 30% or increased less than 20%, and 4) progressive disease (PD) if new lesions developed or the sum of the diameters of target lesions increased more than 20% and absolute increase at least 5 mm. If there were no measurable pulmonary nodules, RECIST 1.1 criteria for non-target lesion was used, as follows: 1) CR if all lesions disappeared and the suppressed serum thyroglobulin level was undetectable, 2) non-CR/non-PD if one or more lesions existed persistently, and 3) PD if the number of lesions increased or there is an occurrence of distant metastases in other sites. Here, the PR and SD of measurable lesions were classified as non-CR/non-PD. Patients evaluated as CR or non-CR/non-PD were defined as non-PD.

Progression-free survival (PFS) was defined as the interval time between the first found LMs and the detection of PD. Overall survival (OS) was defined as the interval time from the time when LMs were first found to death.

Statistical analysis

Statistical analysis was performed using SPSS 26.0 for Mac, Prism 9.0 was used for survival curves, a histogram was drawn in Excel, and an alluvial diagram was drawn by RStudio. The numeric variables are described as the mean, standard deviation, maximum, and minimum. Frequency or percentage is used to describe categorical variables. The chi-square test or Fisher's test was used to identify the differences in subgroups in univariate analyses, and logistic regression was performed for multivariate analyses. PFS plots and OS plots were constructed by the Kaplan–Meier method. The alluvial diagram showed the relationship between *BRAF*V600E mutation status, radioiodine avidity, and clinical outcome. $p < 0.05$ was considered statistically significant.

Results

All patient characteristics

Ninety-four PTC patients identified with LMs from January 2012 to September 2021 met the inclusion criteria. The median age of all patients was 42 years (ranging from 20 to 77 years), and 70.2% (66/94) of them were female (Table 1).

According to the *BRAF*V600E mutation testing results, 33 patients with a median age of 51 years (25–77 years) were assigned to the positive *BRAF*V600E mutation group, and 61 patients with a median age of 37 years (20–69 years) were assigned to the negative *BRAF*V600E group. The overall prevalence of *BRAF*V600E mutation was 35.1% (33/94). As shown in Figure 1, in the positive *BRAF*V600E mutation group, 21.2% (7/33) of patients had radioiodine-avid LMs, and 78.8% (26/33) of patients had non-radioiodine-avid LMs, while in the negative *BRAF*V600E group, 62.3% (38/61) of patients had radioiodine-avid LMs, and 37.7% (23/61) of patients had non-radioiodine-avid LMs.

TABLE 1 Clinical characteristics of all patients.

Characteristics	N
Age (years)	
≥55	22 (23.4%)
<55	72 (76.6%)
Gender	
Male	28 (29.8%)
Female	66 (70.2%)
Multifocality	
Yes	26 (27.7%)
No	55 (58.5%)
NA	13 (13.8%)
Bilaterality	
Yes	34 (36.2%)
No	52 (55.3%)
NA	8 (8.5%)
CI	
Yes	72 (76.6%)
No	5 (5.3%)
NA	17 (18.1%)
ETE	
Yes	54 (57.5%)
No	27 (28.7%)
NA	13 (13.8%)
T stage*	
T1/T2/T3	40 (42.6%)
T4	35 (37.2%)
Tx†	19 (20.2%)
N stage*	
N0	0 (0.0%)
N1a	12 (12.8%)
N1b	77 (81.9%)
Nx†	5 (5.3%)
*BRAF*V600E	
Positive	33 (35.1%)
Negative	61 (64.9%)
Radioiodine uptake	
Radioiodine-avid	45 (47.9%)
Non-radioiodine-avid	49 (52.1%)

CI, capsule invasion; NA, non-available; ETE, extrathyroidal extension.
*TNM staging was determined by the 8th American Joint Cancer Committee TNM stage system.
†Indicates that information about that characteristic was not available.

Factors impacting the status of radioiodine avidity

According to the status of radioiodine avidity, 49 and 45 patients were assigned to the non-radioiodine avidity group and radioiodine avidity group, respectively. The characteristics, including age, sex, multifocality, capsular invasion, bilaterality, extrathyroidal extension (ETE), TN stage, and the status of *BRAF*V600E mutation, were evaluated for their effects on radioiodine avidity. All characteristics were independent of radioiodine avidity except age and the status of *BRAF*V600E mutation, as shown in Table 2. Meanwhile, positive *BRAF*V600E mutation was the only predictor of radioiodine avidity loss in multivariate analysis; the odds ratios (ORs) were 5.323 (95% CI: 1.953–14.514, p = 0.001, Table 2).

Clinical characteristics between positive and negative *BRAF*V600E patients in radioiodine-avid and non-radioiodine-avid subgroups

In the radioiodine avidity subgroup of 45 patients, there were no significant differences in clinicopathological characteristics between the positive and negative *BRAF*V600E mutation groups (Table 3). In the non-radioiodine avidity subgroup, the median age of patients with positive *BRAF*V600E mutation was older than that in the mutation-negative group (53.5 *vs.* 35.0 years, Z = −3.629, p = 0.000); then, no significant differences in other clinicopathological characteristics between patients with positive and negative *BRAF*V600E mutation were found (Table 3).

Predictors of progressive disease of papillary thyroid cancer patients with lung metastases in univariate and multivariate analyses

After a median 29-month (range from 3 to 151 months) follow-up, 25 patients (26.6%) were defined as PD, and 51 patients (54.3%) were defined as non-PD. Eighteen (19.1%) patients were not evaluated due to a follow-up time of less than 12 months or an inability to assess LMs. Consequently, 76 PTC patients were enrolled in the analysis; the cumulative PFS rates at 5 and 10 years were 68.7% and 41.0%, respectively. Univariate analyses found that the status of *BRAF*V600E mutation was not significantly associated with PD (Table 4, p = 0.365), although the median PFS of positive *BRAF*V600E was shorter than that of negative *BRAF*V600E (78.0 *vs.* 93.0 m; Figure 2A, p = 0.602), whereas the status of radioiodine avidity and bilaterality of primary tumor were the predictors of PD. In the multivariate analyses, the status of radioiodine avidity was only the independent predictor of PD (ORs: 10.207, 95% CI: 2.629–39.643, p = 0.001), as shown in Table 4. The median PFS of the non-radioiodine avidity group *vs.* radioiodine avidity group was 57.0 m *vs.* not reached (log-rank = 18.256, p = 0.000), as shown in Figure 2B.

In addition, a subgroup analysis in the radioiodine avidity group and non-radioiodine avidity group was used to analyze the relationship between *BRAF*V600E mutation status and PD.

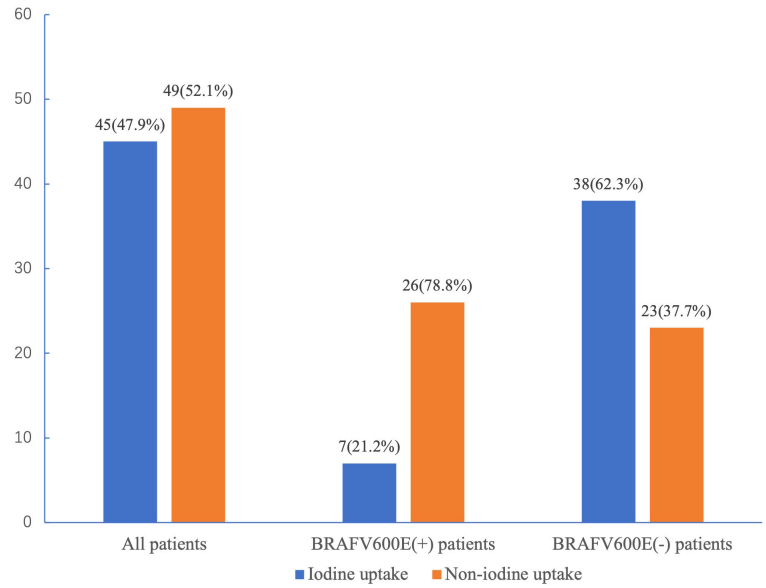

FIGURE 1
*BRAF*V600E mutation status and radioiodine avidity status in all patients.

In the radioiodine avidity subgroup, all positive *BRAF*V600E patients (7/7) remained non-CR/non-PD; as for patients with *BRAF*V600E negative mutation, the rates of CR, non-CR/non-PD, and PD were 0% (0/28), 89.3% (25/28), and 10.7% (3/28), respectively (p = 1.000, Table 5). Similarly, in the non-radioiodine avidity subgroup, no patients achieved CR. The rate of non-CR/non-PD and PD in positive and negative *BRAF*V600E mutation patients were 47.6% (10/21) and 52.4% (11/21) *vs.* 45.0% (9/20) and 55.0% (11/20), respectively (p = 0.867, Table 5).

When combining the status of *BRAF*V600E mutation and the status of radioiodine avidity into the survival analysis of PFS, we found that patients with positive *BRAF*V600E mutation and non-radioiodine-avid LMs had the shortest median PFS (p = 0.000, Figure 3). The relationship among *BRAF*V600E mutation status, radioiodine avidity, and PD were shown by an alluvial diagram (Figure 4A).

Predictors of mortality of papillary thyroid cancer patients with lung metastases in univariate analyses

Of 94 patients, eight were excluded from the analysis due to a follow-up time of less than 12 months. Therefore, 86 patients were enrolled in the analysis. After a median 56.5-month (range from 12 to 164 months) follow-up time, the mortality rate of all patients was 7.0% (6/86). The cumulative 5- and 10-year OS rates were 92.9% and 90.4%, respectively. Applying the chi-square test for the univariate analyses of death rate (Table 6), the mortality rates of non-radioiodine-avid patients and radioiodine-avid patients were 14.3% (6/42) and 0.0% (0/44), respectively (χ^2 = 4.735, p = 0.030). In total, 1/29 (3.4%) and 5/57 (8.8%) mortalities were observed in the positive BRAFV600E mutation patients and mutation-negative patients, respectively (χ^2 = 0.219, p = 0.639). The status of iodine uptake was the only factor associated with the death rate. Similarly, patients with radioiodine-avid LMs may have longer OS than that non-radioiodine avidity LMs, although they did not achieve the median OS (p = 0.011, Figure 5A). The status of *BRAF*V600E mutation did not influence the OS of PTC patients (p = 0.277, Figure 5B). An alluvial diagram that showed the correlation among *BRAF*V600E mutation status, radioiodine avidity, and PD is listed in Figure 4B.

Discussion

*BRAF*V600E mutation is the most common genetic alteration in thyroid carcinogenesis, which occurs in approximately 45% of PTC patients (6). However, a previous study by Sancisi et al. (20) found that 29.8% of PTC patients with DMs and 44.0% of PTC patients without DMs had positive *BRAF*V600E mutations. In another study by Yang et al. (16), there were 26.0% of metastatic PTC patients with positive *BRAF*V600E mutation. Similarly, 35.1% of metastatic PTC patients had positive *BRAF*V600E mutation in our study, and 66.0% of patients without DMs had positive *BRAF*V600E

10.3389/fendo.2022.959089

TABLE 2 The relationship between clinical features and the loss of radioiodine avidity.

Characteristics	Non-radioiodine-avid	Radioiodine-avid	χ^2	p	OR	p
No. patients	49 (52.1%)	45 (47.9%)				
Age (years)			4.884	0.027		
≥55	16 (72.7%)	6 (27.3%)			1	
<55	33 (45.8%)	39 (54.2%)			2.146 (0.691–6.661)	0.186
Gender			0.402	0.526		
Male	16 (57.1%)	12 (42.9%)				
Female	33 (50.0%)	33 (50.0%)				
Multifocality			2.366	0.124		
Yes + NA	24 (61.5%)	15 (38.5%)				
No	25 (45.5%)	30 (54.5%)				
CI			0.000	1.000		
Yes + NA	46 (51.7%)	43 (48.3%)				
No	3 (60.0%)	2 (40.0%)				
Bilaterality			2.908	0.088		
Yes + NA	26 (61.9%)	16 (38.1%)				
No	23 (44.2%)	29 (55.8%)				
ETE			0.240	0.624		
Yes + NA	36 (53.7%)	31 (46.3%)				
No	13 (48.1%)	14 (51.9%)				
T stage			0.011	0.917		
T1/T2/T3/Tx	31 (52.5%)	28 (47.5%)				
T4	18 (51.4%)	17 (48.6%)				
N stage			0.214	0.644		
N1a/Nx	8 (47.1%)	9 (52.9%)				
N1b	41 (53.2%)	36 (46.8%)				
*BRAF*V600E			14.484	0.000		
Positive	26 (78.8%)	7 (21.2%)			1	
Negative	23 (37.7%)	38 (62.3%)			5.323 (1.953–14.514)	0.001

CI, capsule invasion; NA, non-available; ETE, extrathyroidal extension.

mutation in our previous study (14). These results indicated that PTC patients with DMs may have a lower mutation frequency of *BRAF*V600E than patients without DMs.

*BRAF*V600E mutation has been found to repress NIS expression by impairing thyroid-specific transcription factor (PAX8) binding to the NIS promotor by activating transforming growth factor-β/Smad3 signaling. It was also demonstrated that this mutation prevents NIS transcription by driving histone deacetylation of the H3 and H4 lysine residues of the NIS (21–23). The Cancer Genome Atlas (TCGA) sequencing divided PTC into *BRAF*-like and RAS-like groups. *BRAF*-like PTC is associated with reduced expression of key genes involved in iodine metabolism (24). Based on these molecular mechanisms, many previous studies have explored the relationship between *BRAF*V600E mutation and the ability to trap iodine in PTC. A study by Durante et al. (25) found that the transcript level of positive *BRAF*V600E mutation patients reduced NIS expression by 82% compared to wild-type *BRAF*V600E patients. They assumed that the *BRAF*V600E mutation in PTC altered the effectiveness of radioiodine therapy. Similarly, Ricarte et al. (26) also revealed that RAI-refractory metastatic thyroid cancers are enriched with *BRAF*V600E mutation (62%). A respective study by Liu et al. (27) revealed higher RAI avidity loss in the positive *BRAF*V600E mutation group than in the wild-type group (80.4% *vs.* 33.9%). In addition, Yang et al. (16) reported that 93.4% of distant metastases in PTC patients with positive *BRAF*V600E mutation of primary tumors were more likely to be non-radioiodine avidity. In our study, positive *BRAF*V600E mutation patients are also more likely to lose radioiodine avidity than negative *BRAF*V600E mutation patients (78.8% *vs.* 37.7%); ORs were 5.323 (95% CI: 1.953–14.514).

On the one hand, we found that not all patients with positive *BRAF*V600E mutation lost radioiodine avidity, as 21.2% of patients retained RAI uptake in our study. Further evaluation of the clinical outcome in *BRAF*V600E mutation-negative and *BRAF*V600E mutation-positive patients respectively in the radioiodine-avid and non-radioiodine-avid LM subgroups

TABLE 3 Clinical characteristics of *BRAF*V600E(+) and *BRAF*V600E(–) patients in radioiodine avidity subgroup and non-radioiodine avidity subgroup.

Characteristics	Radioiodine avidity			Non-radioiodine-avidity		
	*BRAF*V600E (+)	*BRAF*V600E (–)	p	*BRAF*V600E (+)	*BRAF*V600E (–)	p
No. patients	7 (15.6%)	38 (84.4%)		26 (53.1%)	23 (46.9%)	
Age (years)			1.000			0.032
≥55	1 (16.7%)	5 (83.3%)		12 (75.0%)	4 (25.0%)	
<55	6 (15.4%)	33 (84.6%)		14 (42.4%)	19 (57.6%)	
Gender			0.129			0.765
Male	4 (33.3%)	8 (66.7%)		8 (50.0%)	8 (50.0%)	
Female	3 (9.1%)	30 (90.9%)		18 (54.5%)	15 (45.5%)	
Multifocality			1.000			0.321
Yes/NA	2 (13.3%)	13 (86.7%)		11 (45.8%)	13 (54.2%)	
No	5 (16.7%)	25 (83.3%)		15 (60.0%)	10 (40.0%)	
CI			1.000			1.000
Yes/NA	7 (16.3%)	36 (83.7%)		24 (52.2%)	22 (47.8%)	
No	0 (0.0%)	2 (100.0%)		2 (66.7%)	1 (33.3%)	
Bilaterality			1.000			0.303
Yes/NA	2 (12.5%)	14 (87.5%)		12 (46.2%)	14 (53.8%)	
No	5 (17.2%)	24 (82.8%)		14 (60.9%)	9 (39.1%)	
ETE			1.000			0.947
Yes/NA	5 (16.1%)	26 (83.9%)		19 (52.8%)	17 (47.2%)	
No	2 (14.3%)	12 (85.7%)		7 (53.8%)	6 (46.2%)	
T stage			1.000			0.390
T1/T2/T3/Tx	4 (14.3%)	24 (85.7%)		15 (48.4%)	16 (51.6%)	
T4	3 (17.6%)	14 (82.4%)		11 (61.1%)	7 (38.9%)	
N stage			0.918			0.564
N1a/Nx	2 (22.2%)	7 (77.8%)		3 (37.5%)	5 (62.5%)	
N1b	5 (13.9%)	31 (86.1%)		23 (56.1%)	18 (43.9%)	
Cycles of RAI	2 (1–3)	1 (1–5)	0.304	NA	NA	NA
Cumulate dose of ^{131}I (GBq)	14.8 (3.7–22.2)	7.4 (3.7–37.0)	0.487	NA	NA	NA

CI, capsule invasion; NA, non-available; ETE, extrathyroidal extension; RAI, radioactive iodine.

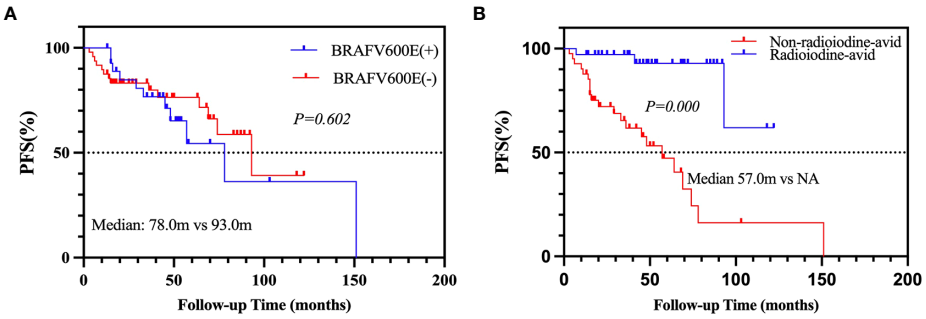

FIGURE 2
Kaplan–Meier analysis of PFS in PTC patients according to *BRAF*V600E mutation status **(A)** and radioiodine avidity status **(B)**. PFS, progression-free survival; PTC, papillary thyroid cancer.

10.3389/fendo.2022.959089

TABLE 4 Univariate and multivariate analyses of predictors of progressive disease in 76 patients.

Characteristics	No. of PD	χ^2	p	OR	p
No. patients	25 (32.9%)				
Age (years)		3.126	0.077		
≥55	9 (50.0%)			1	
<55	16 (27.6%)			0.554 (0.159–1.935)	0.355
Gender		0.901	0.343		
male	9 (40.9%)				
female	16 (29.6%)				
Multifocality		1.529	0.216		
Yes + NA	12 (41.4%)				
No	13 (27.7%)				
CI		–	1.000		
Yes + NA	24 (32.9%)				
No	1 (33.3%)				
Bilaterality		4.168	0.041		
Yes + NA	15 (45.5%)			1	
No	10 (23.3%)			0.502 (0.164–1.532)	0.226
ETE		0.016	0.899		
Yes + NA	18 (33.3%)				
No	7 (31.8%)				
T stage		1.168	0.280		
T1/T2/T3/Tx	14 (28.6%)				
T4	11 (40.7%)				
N stage		0.004	0.947		
N1a/Nx	4 (28.6%)				
N1b	21 (33.9%)				
*BRAF*V600E		0.820	0.365		
Positive	11 (39.3%)				
Negative	14 (29.2%)				
Radioiodine uptake		17.388	0.000		
Radioiodine-avid	3 (8.6%)			1	
Non-radioiodine-avid	22 (53.7%)			10.207 (2.629–39.643)	0.001

PD, progressive disease; CI, capsule invasion; NA, non-available; ETE, extrathyroidal extension.

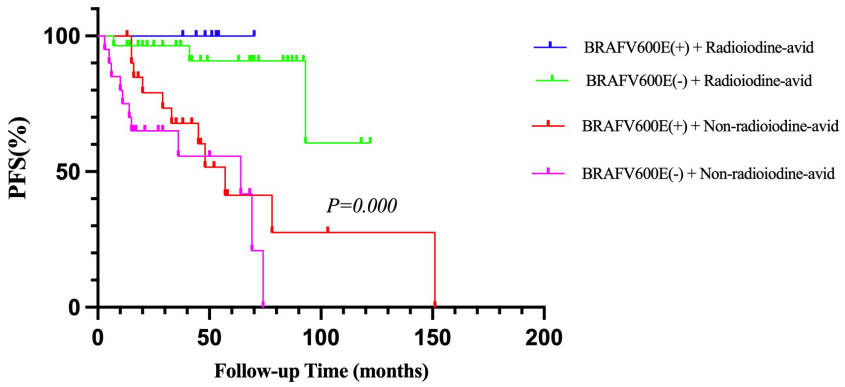

FIGURE 3
Kaplan–Meier analysis of PFS in PTC patients according to *BRAF*V600E mutation status combined with radioiodine avidity status. PFS, progression-free survival; PTC, papillary thyroid cancer.

TABLE 5 Association between progressive disease and *BRAF*V600E mutation status in radioiodine avidity subgroup and non-radioiodine avidity subgroup.

*BRAF*V600E mutation	Clinical outcome							
	Radioiodine avidity				Non-radioiodine-avidity			
	CR	Non-CR/non-PD	PD	p	CR	Non-CR/non-PD	PD	p
Positive	0 (0.0%)	7 (100.0%)	0 (0.0%)	1.000	0 (0.0%)	10 (47.6%)	11 (52.4%)	0.867
Negative	0 (0.0%)	25 (89.3%)	3 (10.7%)		0 (0.0%)	9 (45.0%)	11 (55.0%)	

CR, complete response; PD, progressive disease.

found no significant differences between those groups. TCGA sequencing also showed that partial positive *BRAF*V600E mutation patients reserved the expression of NIS transcription (28). This may be due to tumor heterogeneity, in which primary PTC tumors were composed of a mixture of positive *BRAF*V600E mutation tumor cells and negative *BRAF*V600E mutation tumor cells, and the metastatic tumor did not genetically gain *BRAF*V600E mutation (29). Quantitative sequencing analyses demonstrated that *BRAF*V600E mutation was detected only in a subset of tumor cells (approximately 5.1% to 44% of total alleles) (30). Another reason is that in all of the above studies, the gene results of primary tumors were used for analysis; however, in the Melo et al. (31) study, when comparing the gene concordance of primary tumors and DMs, they found significant discrepancies in primary PTC and DMs, with mutation frequencies of 44.6% and 23.8%, respectively.

On the other hand, in this study, 37.7% of patients with negative *BRAF*V600E mutation could not accumulate radioiodine.

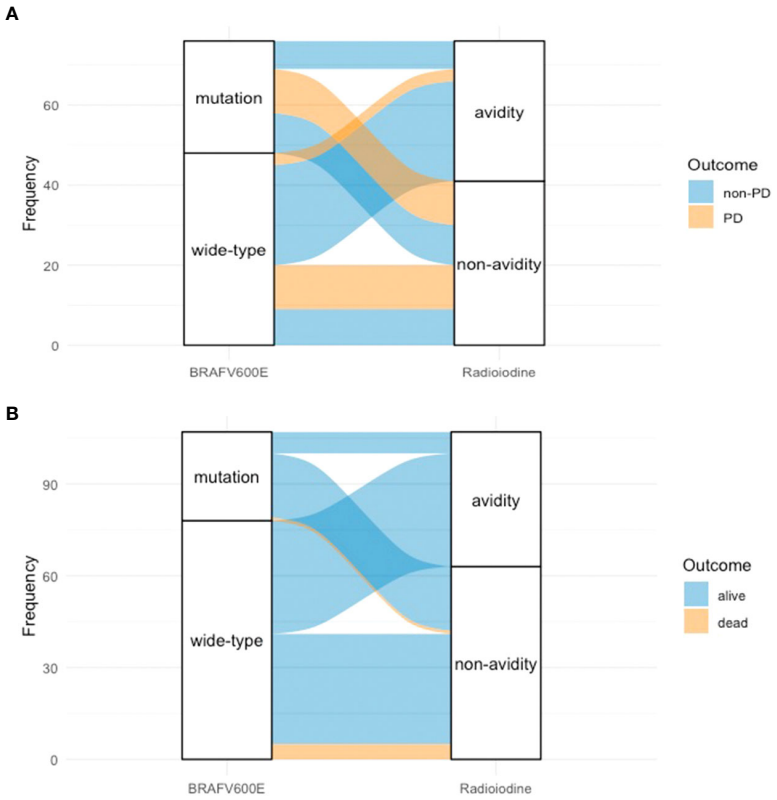

FIGURE 4
Alluvial diagram of PTC patients showed the relationship between *BRAF*V600E mutation status, radioiodine avidity status, and outcome. **(A)** *BRAF*V600E mutation status, radioiodine avidity status, and PD. **(B)** *BRAF*V600E mutation status, radioiodine avidity status, and mortality. PTC, papillary thyroid cancer; PD, progressive disease.

10.3389/fendo.2022.959089

TABLE 6 Univariate chi-square analysis of prognostic factors of mortality in 86 patients.

Characteristics	No. of death	χ^2	p
No. patients	6 (7.0%)		
Age (years)		0.001	0.973
≥55	2 (9.5%)		
<55	4 (6.2%)		
Gender		2.679	0.102
Male	4 (16.0%)		
Female	2 (3.3%)		
Multifocality		0.012	0.912
Yes + NA	3 (8.8%)		
No	3 (5.8%)		
CI		–	1.000
Yes + unknown	6 (7.4%)		
No	0 (0.0%)		
Bilaterality		0.719	0.396
Yes + NA	4 (11.1%)		
No	2 (4.0%)		
ETE		1.467	0.226
Yes + NA	6 (10.0%)		
No	0 (0.0%)		
T stage		1.390	0.238
T1/T2/T3/Tx	2 (3.6%)		
T4	4 (12.9%)		
N stage		0.174	0.676
N1a/Nx	2 (12.5%)		
N1b	4 (5.7%)		
*BRAF*V600E		0.219	0.639
Positive	1 (3.4%)		
Negative	5 (8.8%)		
Radioiodine uptake		4.735	0.030
Radioiodine-avid	0 (0.0%)		
Non-radioiodine-avid	6 (14.3%)		

CI, capsule invasion; NA, non-available.

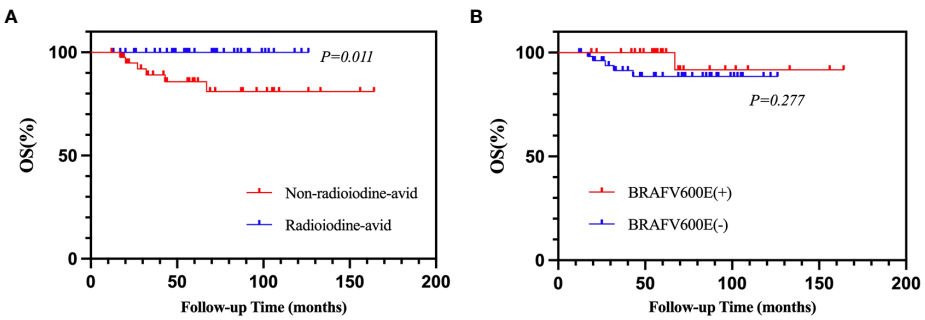

FIGURE 5
Kaplan–Meier analysis of OS in PTC patients according to radioiodine avidity status **(A)** and *BRAF*V600E mutation status **(B)**. OS, overall survival; PTC, papillary thyroid cancer.

We assumed the reason may be that other gene aberrations exist, such as RAS mutation and RET rearrangements of thyroid cancer, which have been reported to activate the MAPK pathway, followed by the dedifferentiation of DTCs (32). Liu et al. (27) demonstrated that 55.6% of patients with TERT mutation alone would be non-radioiodine-avid. In addition, metastatic lesions have a median of 62% somatic mutations corresponding to primary tumor samples that do not have (33).

The effect of *BRAF*V600E mutation on the prognosis of PTC patients is controversial. Many studies have illustrated the relationship between *BRAF*V600E mutation and the prognosis of PTC patients. A 15-year median follow-up study by Elisei et al. (34) that included 102 PTC patients found that *BRAF*V600E mutation was an independent factor correlated with the worst outcomes in a higher risk of not being cured and death. In a multicenter study of 219 PTC patients, Xing et al. (35) found that positive *BRAF*V600E mutation may be associated with the recurrence of tumors (25% *vs.* 9%); this study also indicated that PTC patients with positive *BRAF*V600E mutation may have a worse prognosis than those patients with a negative mutation. Another retrospective and multicenter study including 1,849 patients by Xing et al. (13) revealed that the presence of *BRAF*V600E mutation was associated with an increased mortality rate in PTC patients based on the difference in mortality rate in *BRAF*V600E-positive mutation patients and *BRAF*V600E-negative mutation patients (5.3% *vs.* 1.1%). However, when clinicopathological features such as lymph node metastases, extrathyroidal extension, and distant metastases were included in the analysis model, *BRAF*V600E mutation was no longer associated with mortality caused by PTC. A meta-analysis by Vuong et al. (36) including 35 studies with 17,732 patients revealed that *BRAF*V600E mutation was significant in a short-term follow-up because *BRAF*V600E mutation increased the risk of recurrence (HR = 1.63; 95% CI = 2.40–3.96) but was independent of cancer mortality rate (HR = 1.41; 95% CI = 0.90–2.23).

In our study, we found that *BRAF*V600E mutation-positive patients had shorter PFS than *BRAF*V600E mutation-negative patients, but there were no significant differences (median: 78.0 *vs.* 93.0 m in the positive group *vs.* the negative group). At the same time, we found that positive *BRAF*V600E mutation was also not associated with OS in metastatic PTC patients, although neither reached a median OS due to the short follow-up time. The mortality rate of all patients was 7.0% in our study, which was consistent with the reported result (13). The findings of Pu et al. (24) may explain the controversy regarding *BRAF*V600E mutation in predicting the prognosis of PTC by using single-cell transcriptomic analysis and refining bulk molecular subtyping. *BRAF*-like patients can be further divided into *BRAF*-like-A and *BRAF*-like-B subclasses, and *BRAF*-like-B patients had a lower thyroid differentiation score, advanced staging, and a significantly compromised prognosis (24). In our study, we found that the status of radioiodine avidity was associated with clinical outcome and *BRAF*V600E mutation was one of the factors influencing radioiodine avidity. However, not all patients with positive *BRAF*V600E mutation lost the ability to uptake iodine, and not all patients with negative *BRAF*V600E mutation reserved the ability to accumulate iodine. Therefore, a relationship between *BRAF*V600E mutation and prognosis was not found in our study.

The study has several limitations. First, the small number of PTC patients with LMs and *BRAF*V600E mutation results may influence the accuracy of this study. Second, *BRAF*V600E mutation testing results of primary PTC rather than LMs were used for evaluations due to limited sources. Third, selection bias may be caused by the retrospective nature of the study. Fourth, we only enrolled PTC patients with LMs and excluded patients with metastases in other sites that may not represent DMs. Fifth, the follow-up time is short for PTC patients. In addition, multiple pulmonary nodules were so small that the lesion measurements may be inaccurate.

Conclusion

In our study, we found that although the *BRAF*V600E mutation status of primary tumors was significantly associated with non-radioiodine-avid LMs in patients with PTC, *BRAF*V600E mutation status may not influence the prognosis of PTC patients with LMs. Radioiodine avidity of LMs was the only independent prognostic factor of clinical outcome. A longer follow-up needs to be undertaken to identify the predictors associated with OS of PTC patients with LMs.

Data availability statement

The original contributions presented in the study are included in the article/supplementary material. Further inquiries can be directed to the corresponding authors.

Ethics statement

The studies involving human participants were reviewed and approved by Ethics Institutional Review Board of West China hospital of Sichuan University. Written informed consent for participation was not required for this study in accordance with the national legislation and the institutional requirements.

Author contributions

SH and MQ collected clinical data and drafted the article. They are equally contributed to this article. TT and HD analyzed the data. RH and YT performed conception of the work, critical revision of the article and final approval of the version to be published. All authors contributed to the article and approved the submitted version.

Funding

This study was supported by the National Natural Science Foundation of China (No. 81972502).

Conflict of interest

The authors declare that the research was conducted in the absence of any commercial or financial relationships that could be construed as a potential conflict of interest.

Publisher's note

All claims expressed in this article are solely those of the authors and do not necessarily represent those of their affiliated organizations, or those of the publisher, the editors and the reviewers. Any product that may be evaluated in this article, or claim that may be made by its manufacturer, is not guaranteed or endorsed by the publisher.

References

1. Miranda-Filho A, Lortet-Tieulent J, Bray F, Cao B, Franceschi S, Vaccarella S, et al. Thyroid cancer incidence trends by histology in 25 countries: A population-based study. *Lancet Diabetes Endocrinol* (2021) 9(4):225–34. doi: 10.1016/s2213-8587(21)00027-9

2. Schlumberger M, Tubiana M, De Vathaire F, Hill C, Gardet P, Travagli JP, et al. Long-term results of treatment of 283 patients with lung and bone metastases from differentiated thyroid carcinoma. *J Clin Endocrinol Metab* (1986) 63(4):960–7. doi: 10.1210/jcem-63-4-960

3. Albano D, Panarotto MB, Durmo R, Rodella C, Bertagna F, Giubbini R. Clinical and prognostic role of detection timing of distant metastases in patients with differentiated thyroid cancer. *Endocrine* (2019) 63(1):79–86. doi: 10.1007/s12020-018-1713-2

4. Durante C, Haddy N, Baudin E, Leboulleux S, Hartl D, Travagli JP, et al. Long-term outcome of 444 patients with distant metastases from papillary and follicular thyroid carcinoma: Benefits and limits of radioiodine therapy. *J Clin Endocrinol Metab* (2006) 91(8):2892–9. doi: 10.1210/jc.2005-2838

5. Riesco-Eizaguirre G, Rodriguez I, de la Vieja A, Costamagna E, Carrasco N, Nistal M, et al. The Brafv600e oncogene induces transforming growth factor beta secretion leading to sodium iodide symporter repression and increased malignancy in thyroid cancer. *Cancer Res* (2009) 69(21):8317–25. doi: 10.1158/0008-5472.CAN-09-1248

6. Xing M. Braf mutation in thyroid cancer. *Endocr Relat Cancer* (2005) 12 (2):245–62. doi: 10.1677/erc.1.0978

7. Landa I, Knauf JA. Mouse models as a tool for understanding progression in Braf(V600e)-driven thyroid cancers. *Endocrinol Metab (Seoul)* (2019) 34(1):11–22. doi: 10.3803/EnM.2019.34.1.11

8. Dunn LA, Sherman EJ, Baxi SS, Tchekmedyian V, Grewal RK, Larson SM, et al. Vemurafenib redifferentiation of braf mutant, rai-refractory thyroid cancers. *J Clin Endocrinol Metab* (2019) 104(5):1417–28. doi: 10.1210/jc.2018-01478

9. Subbiah V, Kreitman RJ, Wainberg ZA, Cho JY, Schellens JHM, Soria JC, et al. Dabrafenib and trametinib treatment in patients with locally advanced or metastatic braf V600-mutant anaplastic thyroid cancer. *J Clin Oncol* (2018) 36 (1):7–13. doi: 10.1200/jco.2017.73.6785

10. Leboulleux S, Dupuy C, Lacroix L, Attard M, Grimaldi S, Corre R, et al. Redifferentiation of a Braf(K601e)-mutated poorly differentiated thyroid cancer patient with dabrafenib and trametinib treatment. *Thyroid* (2019) 29(5):735–42. doi: 10.1089/thy.2018.0457

11. Zhu G, Deng Y, Pan L, Ouyang W, Feng H, Wu J, et al. Clinical significance of the Brafv600e mutation in ptc and its effect on radioiodine therapy. *Endocr Connect* (2019) 8(6):754–63. doi: 10.1530/EC-19-0045

12. Makboul R, Mostafa NM, El-Deek HEM, Aboulhagag NA, Shehata MR, Abdelhafez YG. Do Brafv600e mutation and sodium-iodide symporter expression affect the response to radioactive iodine therapy in patients with papillary thyroid carcinoma? *Nucl Med Commun* (2020) 41(5):416–25. doi: 10.1097/MNM.0000000000001171

13. Xing M, Alzahrani AS, Carson KA, Viola D, Elisei R, Bendlova B, et al. Association between braf V600e mutation and mortality in patients with papillary thyroid cancer. *Jama* (2013) 309(14):1493–501. doi: 10.1001/jama.2013.3190

14. Shen G, Kou Y, Liu B, Huang R, Kuang A. Brafv600e mutation does not significantly affect the efficacy of radioiodine therapy in patients with papillary thyroid carcinoma without known distant metastases. *Clin Nucl Med* (2018) 43(7): e215–e9. doi: 10.1097/RLU.0000000000002142

15. Ho AL, Dedecjus M, Wirth LJ, Tuttle RM, Inabnet WB3rd, Tennvall J, et al. Selumetinib plus adjuvant radioactive iodine in patients with high-risk differentiated thyroid cancer: A phase iii, randomized, placebo-controlled trial (Astra). *J Clin Oncol* (2022) 40(17):1870–8. doi: 10.1200/jco.21.00714

16. Yang K, Wang H, Liang Z, Liang J, Li F, Lin Y. Brafv600e mutation associated with non-Radioiodine-Avid status in distant metastatic papillary thyroid carcinoma. *Clin Nucl Med* (2014) 39(8):675–9. doi: 10.1097/rlu.0000000000000498

17. Roman BR, Morris LG, Davies L. The thyroid cancer epidemic, 2017 perspective. *Curr Opin Endocrinol Diabetes Obes* (2017) 24(5):332–6. doi: 10.1097/med.0000000000000359

18. Haugen BR, Alexander EK, Bible KC, Doherty GM, Mandel SJ, Nikiforov YE, et al. 2015 American Thyroid association management guidelines for adult patients with thyroid nodules and differentiated thyroid cancer: The American thyroid association guidelines task force on thyroid nodules and differentiated thyroid cancer. *Thyroid* (2016) 26(1):1–133. doi: 10.1089/thy.2015.0020

19. Eisenhauer EA, Therasse P, Bogaerts J, Schwartz LH, Sargent D, Ford R, et al. New response evaluation criteria in solid tumours: Revised recist guideline (Version 1.1). *Eur J Cancer* (2009) 45(2):228–47. doi: 10.1016/j.ejca.2008.10.026

20. Sancisi V, Nicoli D, Ragazzi M, Piana S, Ciarrocchi A. Brafv600e mutation does not mean distant metastasis in thyroid papillary carcinomas. *J Clin Endocrinol Metab* (2012) 97(9):E1745–9. doi: 10.1210/jc.2012-1526

21. Costamagna E, García B, Santisteban P. The functional interaction between the paired domain transcription factor Pax8 and Smad3 is involved in transforming growth factor-beta repression of the Sodium/Iodide symporter gene. *J Biol Chem* (2004) 279(5):3439–46. doi: 10.1074/jbc.M307138200

22. Zhang Z, Liu D, Murugan AK, Liu Z, Xing M. Histone deacetylation of nis promoter underlies braf V600e-promoted nis silencing in thyroid cancer. *Endocr Relat Cancer* (2014) 21(2):161–73. doi: 10.1530/ERC-13-0399

23. Aashiq M, Silverman DA, Na'ara S, Takahashi H, Amit M. Radioiodine-refractory thyroid cancer: Molecular basis of redifferentiation therapies, management, and novel therapies. *Cancers (Basel)* (2019) 11(9):1382. doi: 10.3390/cancers11091382

24. Pu W, Shi X, Yu P, Zhang M, Liu Z, Tan L, et al. Single-cell transcriptomic analysis of the tumor ecosystems underlying initiation and progression of papillary thyroid carcinoma. *Nat Commun* (2021) 12(1):6058. doi: 10.1038/s41467-021-26343-3

25. Durante C, Puxeddu E, Ferretti E, Morisi R, Moretti S, Bruno R, et al. Braf mutations in papillary thyroid carcinomas inhibit genes involved in iodine

metabolism. *J Clin Endocrinol Metab* (2007) 92(7):2840–3. doi: 10.1210/jc.2006-2707

26. Ricarte-Filho JC, Ryder M, Chitale DA, Rivera M, Heguy A, Ladanyi M, et al. Mutational profile of advanced primary and metastatic radioactive iodine-refractory thyroid cancers reveals distinct pathogenetic roles for braf, Pik3ca, and Akt1. *Cancer Res* (2009) 69(11):4885–93. doi: 10.1158/0008-5472.Can-09-0727

27. Liu J, Liu R, Shen X, Zhu G, Li B, Xing M. The genetic duet of braf V600e and tert promoter mutations robustly predicts loss of radioiodine avidity in recurrent papillary thyroid cancer. *J Nucl Med* (2020) 61(2):177–82. doi: 10.2967/jnumed.119.227652

28. Cancer Genome Atlas Research Network. Integrated genomic characterization of papillary thyroid carcinoma. *Cell* (2014) 159(3):676–90. doi: 10.1016/j.cell.2014.09.050

29. Gandolfi G, Sancisi V, Piana S, Ciarrocchi A. Time to re-consider the meaning of braf V600e mutation in papillary thyroid carcinoma. *Int J Cancer* (2015) 137(5):1001–11. doi: 10.1002/ijc.28976

30. Guerra A, Sapio MR, Marotta V, Campanile E, Rossi S, Forno I, et al. The primary occurrence of Braf(V600e) is a rare clonal event in papillary thyroid carcinoma. *J Clin Endocrinol Metab* (2012) 97(2):517–24. doi: 10.1210/jc.2011-0618

31. Melo M, Gaspar da Rocha A, Batista R, Vinagre J, Martins MJ, Costa G, et al. Tert, braf, and nras in primary thyroid cancer and metastatic disease. *J Clin Endocrinol Metab* (2017) 102(6):1898–907. doi: 10.1210/jc.2016-2785

32. Oh JM, Ahn BC. Molecular mechanisms of radioactive iodine refractoriness in differentiated thyroid cancer: Impaired sodium iodide symporter (Nis) expression owing to altered signaling pathway activity and intracellular localization of nis. *Theranostics* (2021) 11(13):6251–77. doi: 10.7150/thno.57689

33. Masoodi T, Siraj AK, Siraj S, Azam S, Qadri Z, Albalawy WN, et al. Whole-exome sequencing of matched primary and metastatic papillary thyroid cancer. *Thyroid* (2020) 30(1):42–56. doi: 10.1089/thy.2019.0052

34. Elisei R, Ugolini C, Viola D, Lupi C, Biagini A, Giannini R, et al. Braf(V600e) mutation and outcome of patients with papillary thyroid carcinoma: A 15-year median follow-up study. *J Clin Endocrinol Metab* (2008) 93(10):3943–9. doi: 10.1210/jc.2008-0607

35. Xing M, Westra WH, Tufano RP, Cohen Y, Rosenbaum E, Rhoden KJ, et al. Braf mutation predicts a poorer clinical prognosis for papillary thyroid cancer. *J Clin Endocrinol Metab* (2005) 90(12):6373–9. doi: 10.1210/jc.2005-0987

36. Vuong HG, Duong UN, Altibi AM, Ngo HT, Pham TQ, Tran HM, et al. A meta-analysis of prognostic roles of molecular markers in papillary thyroid carcinoma. *Endocr Connect* (2017) 6(3):R8–r17. doi: 10.1530/ec-17-0010

frontiers | Frontiers in Endocrinology

TYPE Original Research
PUBLISHED 07 November 2022
DOI 10.3389/fendo.2022.991906

OPEN ACCESS

EDITED BY
Terry Francis Davies,
Icahn School of Medicine at Mount Sinai, United States

REVIEWED BY
María Belén Hapon,
CONICET Instituto de Medicina y Biologia Experimental de Cuyo (IMBECU), Argentina
Shahrun Niza Abdullah Suhaimi,
National University of Malaysia, Malaysia

*CORRESPONDENCE
Ping Liu
lpiuing@163.com

†These authors have contributed equally to this work

SPECIALTY SECTION
This article was submitted to Thyroid Endocrinology, a section of the journal Frontiers in Endocrinology

RECEIVED 12 July 2022
ACCEPTED 14 October 2022
PUBLISHED 07 November 2022

CITATION
Zhang Q, Li J, Shen H, Bai X, Zhang T and Liu P (2022) Screening and validation of lymph node metastasis risk-factor genes in papillary thyroid carcinoma.
Front. Endocrinol. 13:991906.
doi: 10.3389/fendo.2022.991906

Screening and validation of lymph node metastasis risk-factor genes in papillary thyroid carcinoma

Qiaoyue Zhang[1†], Jing Li[2†], Hengyan Shen[1], Xinyu Bai[1], Tao Zhang[3] and Ping Liu[1*]

[1]Department of Clinical Pharmacy, Key Laboratory of Basic Pharmacology of Guizhou Province and School of Pharmacy, Zunyi Medical University, Zunyi, China, [2]Liaoning Academy of Traditional Chinese Medicine, Liaoning University of Traditional Chinese Medicine, Shenyang, China, [3]Department of Laboratory Medicine, Affiliated Hospital of Zunyi Medical University, Zunyi, China

Background: Although most papillary thyroid carcinoma (PTC) cases have a good prognosis, some PTCs are more aggressive and are often accompanied by lymph node (LN) metastasis, a high recurrence rate, and poor prognosis. Distinguishing highly invasive metastatic PTC is an urgent problem that needs to be addressed clinically. We analyzed a microarray of metastasized PTC and validated it using quantitative reverse transcription PCR (RT-qPCR) and immunohistochemistry to identify biomarkers that can be used to assess the risk of PTC metastasis.

Methods: The microarray of metastasized PTC was screened using the Gene Expression Omnibus (GEO) database. The differences between cancer and normal tissues were analyzed using the official GEO tool: GEO2R. Gene expression profile data (GEPIA) were used to verify the expression of differential genes in large samples and to analyze their correlation. The Kaplan–Meier plotter (KM-plotter) database was used for the analysis of genes potentially related to survival. RT-qPCR was used to check the expression of risk factor genes in pathological sections from PTC patients with clinical LN metastasis. Immunohistochemistry was used to verify the expression of core risk-associated genes.

Results: Fourteen PTC metastasis-associated genes were identified. In metastasized PTC, *CLDN1*, *LRP4*, *LRRK2*, and *TENM1* were highly expressed, whereas *DIO1*, *DPP6*, *HGD*, *IPCEF1*, *MT1F*, *SLC26A4*, *SLC26A7*, *SPX*, *TFF3*, and *TPO* were expressed at low levels, compared to expression in normal tissues. *DIO1*, *HGD*, *SLC26A4*, and *TPO* were found to be the core risk genes in the PTC metastatic risk set. Results based on clinical samples showed that the expression differences for metastasis risk-associated genes were consistent with the bioinformatics analysis results.

Conclusions: Fourteen differentially expressed genes (*CLDN1*, *LRP4*, *LRRK2*, *TENM1*, *DIO1*, *DPP6*, *HGD*, *IPCEF1*, *MT1F*, *SLC26A4*, *SLC26A7*, *SPX*, *TFF3*, *TPO*)

are associated with an increased risk of PTC metastasis, and *DIO1*, *HGD*, *SLC26A4*, and *TPO* are the key risk-associated genes in this set that might affect the occurrence and development of PTC through iodine metabolism. These genes could provide a reference for clinical metastatic PTC risk evaluation and treatment.

KEYWORDS

papillary thyroid carcinoma, iodine, bioinformatics, clinical samples, transfer of risk genes

Introduction

The current incidence of thyroid cancer (TC) accounts for 3.4% of all cancers, making it the tenth most prevalent cancer globally and seventh most prevalent in China (1, 2). The reasons for the increased incidence of TC are complex. Overdiagnosis might be one of these, but an actual increase in TC cannot be ruled out (3–5). TC can be distinguished into medullary thyroid carcinoma, anaplastic thyroid carcinoma (ATC), and differentiated thyroid carcinoma (DTC), based on the histological type. DTC can be further distinguished into follicular thyroid cancer (FTC) and papillary thyroid carcinoma (PTC). PTC accounts for approximately 95% of TC cases (6). Patients with early PTC have a 5-year survival rate >90% after conventional treatment, and these are generally considered "indolent tumors" (7, 8). The recurrence rate of PTC is up to 30%, but the survival rate in patients with recurrence and metastasis is significantly reduced (9). Recurrence and metastasis are the key factors involved in PTC-associated mortality. Early detection and active intervention for PTC with a risk of metastasis is an effective strategy for improving prognosis. Unfortunately, a morphological evaluation of the primary tumor cannot be used to predict the likelihood of disease metastasis or recurrence.

Currently, fine-needle aspiration is the most reliable diagnostic tool for PTC; however, it cannot be used to cytologically distinguish between benign and malignant PTC and thus cannot be used to evaluate the risk of PTC metastasis (10, 11). Previous studies have found characteristic genetic changes in PTC, such as *RET-PTC*, *NTRK* rearrangements, *RAS* and *BRAF* mutations, and *PAX8*/*PPAR* translocation (12, 13), which have been used for the diagnosis of PTC; however, the genetic changes currently found in PTC cannot be used to characterize tumors with different clinical behaviors, such as LN metastasis (13, 14). Identifying genetic changes that can help diagnose PTC and assess the risk of metastasis is crucial for early clinical intervention in high-risk PTC patients. Therefore, screening for genetic metastatic PTC-specific changes in patients with LN metastasis can provide a reference to assess the risk of PTC metastasis.

The present study aimed to identify prognostic biomarkers for clinical diagnosis and risk assessment with respect to PTC metastasis by screening risk-associated genes exhibiting differential expression. The overall goal of the study was to reduce metastasis and recurrence rates in PTC patients and improve their prognosis.

Materials and methods

Microarray data acquisition

The GEO (https://www.ncbi.nlm.nih.gov/geo/) database was searched using the keywords "Thyroid cancer, Human." Samples comprising metastatic PTC and matching paracancerous tissue were screened from the retrieved results.

Data processing of DEGs

Using the GEO2R (https://www.ncbi.nlm.nih.gov/geo/info/geo2r.html) online tool, we used a $|\log FC| > 2$ to identify the DEGs between the metastatic PTC and normal thyroid gland tissue samples, and DEGs with $P < 0.05$ were screened. The raw data were then filtered online using the Venn diagram database to detect DEGs among the three datasets. DEGs with a $\log FC < -2$ and $\log FC > 2$ were considered downregulated and upregulated, respectively.

Verification of DEGs

GEPIA (http://gepia.cancer-pku.cn/) was used to verify the expression of DEGs with statistically significant differences based on a large sample size.

Analysis of DEGs associated with survival

The KM-plotter (https://kmplot.com/analysis/) was used to analyze the influence of genes on overall survival (OS) and relapse-free survival (RFS).

Correlation analysis of DEGs

The obtained DEGs were filtered through the GEPIA database for correlation analysis. The correlation between each DEG in TC was obtained, and the core risk-associated genes in the set of metastasis-associated genes were screened based on these correlations. The R software (version 4.0.3) was used to visualize correlations.

Validation of risk-associated gene sets

This study was reviewed by the Biomedical Research Ethics Committee of the Affiliated Hospital of Zunyi Medical University, batch no. KLL-2022-448. Preliminary data from major cancer databases represent a large sample size of real patient information. Therefore, in this study, eight clinical samples were collected for validation based on a small clinical sample set. The inclusion criteria were patients with confirmed PTC and metastatic lesions, between 18 and 70 years of age, who visited the Affiliated Hospital of Zunyi Medical University in 2020–2021. Patients with TC subtypes such as PTMC and ATC and other major diseases were excluded from the study. Pathological tissues of metastatic PTC patients meeting the inclusion criteria were collected and pathological sections and paraffin block were produced. The cancerous/paracancerous tissues were isolated from some sections under a microscope for RNA extraction. RT-qPCR was used to verify the 18 genes screened using bioinformatics associated with a risk of metastasis. Immunohistochemistry was performed to confirm the expression of the four core risk-associated genes that were highly associated with each risk gene.

RT-qPCR

RNA was extracted from tissues from patients with metastatic PTC using an RNeasy FFPE Kit (RNeasy FFPE Kit, QIAGEN, Hilden, Germany). cDNA was then synthesized using a reverse transcriptase system (SureScripTM First-Strand cDNA Synthesis Kit, GeneCopoeia, Guangzhou, China). RT-qPCR was used to validate gene expression in accordance with the manufacturer's instructions (BlazeTaq SYBR Green qPCR Mix 2.0, GeneCopoeia). The expression levels of all genes were normalized against *ATCB* gene expression, and relative gene expression was calculated using the $2^{-\Delta\Delta CT}$ method. Primers for RT-qPCR were purchased from Sangon Biotech (Shanghai, China).

Immunohistochemistry

The tissues from patients with metastasized PTC were fixed with formalin, included in paraffin, and sections were prepared. For the immunohistochemical (IHC) analysis of deiodinase, iodothyronine type I (DIO1, 1:100, Affinity Biosciences, OH, USA), homogentisate 1,2-dioxygenase (HGD, 1:100, Santa Cruz Biotechnology, Dallas, TX, USA), solute carrier family 26 member 4 (SLC26A4, 1:100, Santa Cruz Biotechnology), and thyroid peroxidase (TPO, 1:100, Servicebio, Wuhan, China). Pathological changes were observed under an optical microscope (NI-U, Nikon, Tokyo, Japan), and images were captured with a digital camera (DS-RI2, Nikon).

Institutional review board approval (or waiver) statement

In accordance with the Biosafety Law of the People's Republic of China and other laws, regulations, rules, normative documents, and international standards, this study was reviewed by the Biomedical Research Ethics Committee of Zunyi Medical University Hospital; the project was approved and the research conducted according to the scheduled plan (batch number, KLL-2022-448).

Statistical analysis

The SPSS 22.0 software was used for all statistical analyses. All data are presented as the standard error of the mean and compared using Student's *t*-test. Statistical significance was set at $P < 0.05$.

Results

Microarray data information

The NCBI GEO database included three gene expression profiles that met the requirements (including metastasized PTC and normal paracancerous tissues) as follows: GSE151181 (15) from the GPL23159 platform ([Clariom_S_Human] Affymetrix Clariom S Assay, Human; includes Pico Assay), GSE6004 (16) and GSE60542 (17) from the GPL570 platform [(HG-U133_Plus_2) Affymetrix Human Genome U133 Plus 2.0 Array]. In total, 100 samples met these requirements, consisting of 53 metastatic PTC and 47 normal thyroid tissue samples.

Identification of DEGs in metastasized PTC

The GEO2R online tool identified 462, 1392, and 2026 DEGs from GSE151181 (15), GSE6004 (16), and GSE60542 (17),

respectively. A |logFC| > 2 and $P < 0.05$ were used as the condition to filter significant DEGs, and subsequently, Venn diagram online tools were used to determine the intersection of the three datasets to obtain 23 DEGs, including 8 upregulated (Figure 1A) and 15 downregulated (Figure 1B) genes.

Verification of DEGs

The 23 identified DEGs were subjected to GEPIA for the verification of differential expression between TC and normal control samples, using a large sample size. Statistically significant differences in expression were obtained for 23 DEGs based on the large sample set ($P < 0.05$, Table 1); the 8 upregulated (Figure 1C) and 15 downregulated (Figure 1D) genes were confirmed.

Analysis of DEGs associated with overall survival

The KM-plotter was used to analyze the association between OS and the 23 DEGs. Eighteen DEGs were associated with reduced OS in patients with TC ($P < 0.05$, Table 2 and Figure 2), whereas for five the association was not significant ($P > 0.05$, Table 2).

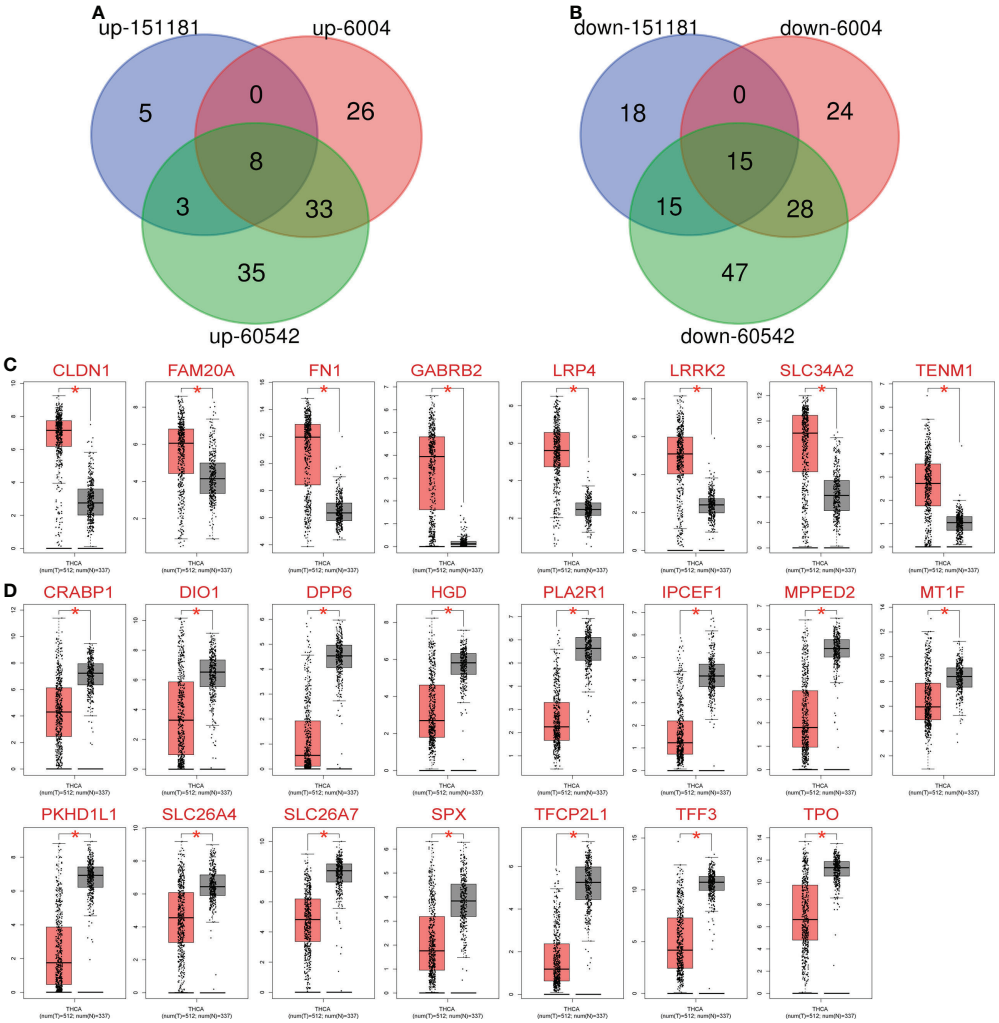

FIGURE 1
Expression of 23 differentially expressed genes (DEGs) in metastatic PTC and non-cancer tissues. **(A)** Common upregulated intersection DEGs obtained from Gene Expression Omnibus database: GSE15181, GSE6004 and GSE60542. **(B)** Common downregulated intersection DEGs obtained Gene Expression Omnibus database: GSE15181, GSE6004 and GSE60542. **(C)** Upregulated DEGs expression in thyroid cancer (TC) patients and normal controls. **(D)** Downregulated DEGs expression in TC patients and normal controls. Red: Cancer, black: Normal, *P< 0.05 vs. normal group.

10.3389/fendo.2022.991906

TABLE 1 Twenty-three differentially expressed genes between normal and thyroid cancer (TC) samples.

Expression	GENE
TC expression was lower than normal (P<0.05)	*CRABP1, DIO1, DPP6, HGD, IPCEF1, MPPED2, MT1F, PKHD1L1, PLA2R1, SLC26A4, SLC26A7, SPX, TFCP2L1, TFF3, TPO*
TC expression was more than normal (P<0.05)	*CLDN1, FAM20A, FN1, GABRB2, LRP4, LRRK2, SLC34A2, TENM1*

Correlation analysis of DEGs

The 18 DEGs that affected the prognosis of patients might be risk factors for PTC metastasis. Correlation analysis was performed for this risk-associated set using GEPIA, and the results were visualized using the R software (Figure 3A). A Pearson correlation coefficient absolute value < 0.4 (very weak correlation) was scored as 0, 0.4–0.6 (weak correlation) was scored as 1 point, 0.6–0.8 (strong correlation) was scored as 2 points, 0.8–1.0 (very strong correlation) was scored as 3 points, and the highest cumulative score was considered the core risk-associated gene. The Pearson correlation coefficient cumulative scores of the 18 DEGs are ranked as follows: *HGD* (21), *TPO* (21), *SLC26A4* (20), *DIO1* (19), *SLC26A7* (18), *SPX* (18), *TFCP2L1* (17), *IPCEF1* (16), *MT1F* (14), *DPP6* (13), *CLDN1* (11), *PKHD1L1* (10), *SLC34A2* (9), *GABRB2* (8), *LRP4* (2), *LRRK2* (2), *TENM1* (1), *TFF3* (1). The correlation between *HGD*, *TPO*, *SLC26A4* and *DIO1* is shown in Figure 3B.

RT-qPCR verification of risk gene set expression in clinical samples

Based on eight patients with metastatic PTC, cancerous and normal adjacent tissues were collected. Expression of the risk-associated gene set was verified using RT-qPCR, and expression of the top four core risk-associated genes was verified using immunohistochemistry. In the pathological tissues from patients, 14 genes were differentially expressed in metastatic PTC, with statistically significant differences (P < 0.05). Primer sequences are shown in Supplementary Table 1, and RT-qPCR results are shown in Figure 4.

Analysis of DEGs associated with relapse-free survival

Among the verified 14 genes with differential expression in the clinical samples, 9 DEGs significantly affected the RFS (P < 0.05, Figure 5) of patients with metastatic PTC, while the influence of 5 DEGs was not significant (P > 0.05).

IHC verification of core risk gene set expression in clinical samples

We analyzed *DIO1, HGD, SLC26A4* and *TPO* protein expression with IHC staining in metastatic PTC and its adjacent tissues. DIO1, HGD, SLC26A4 and TPO were significantly overexpressed in paracancerous tissues (Figure 6A). The judgment was based on the mean optical density (MOD) after Image-Pro Plus 6.0 analysis.

Discussion

Although the 5-year survival rate of patients with PTC is more than 90%, approximately 30% of patients have recurrent PTC (18). The prognosis of patients with recurrent PTC is poor and often accompanied by LN metastasis. Without early intervention, the 5-year survival rate of patients with distal metastatic PTC is only 53.3% (19). Unfortunately, there currently are no reliable biomarkers for PTC risk (20), and the risk in patients cannot be assessed (21). However, a high recurrence rate and aggressive PTC are usually accompanied by severe thyroid epitaxy, LN metastasis, or distant metastasis (21). To identify PTC patients at a high risk of metastasis and recurrence at an early stage, this study focused on patients with metastatic PTC. The gene expression differences between metastatic PTC and normal tissues were analyzed using bioinformatics methods, and expression verification based on a large sample size was conducted using GEPIA, The Cancer Genome Atlas (TCGA), and other databases. Survival analysis was conducted to identify the genes associated with a risk of PTC metastasis. Clinical samples were collected for secondary validation of the screening

TABLE 2 Kaplan–Meier-Plotter analysis of the association between prognosis and 23 differentially expressed genes.

Category	Genes
Significant impact on survival (P < 0.05)	*CLDN1, GABRB2, LRP4, LRRK2, SLC34A2, TENM1, DIO1, DPP6, HGD, IPCEF1, MT1F, PKHD1L1, SLC26A4, SLC26A7, SPX, TFCP2L1, TFF3, TPO*
Without significant impact on survival (P > 0.05)	*CRABP1, FAM20A, FN1, MPPED2, PLA2R1*

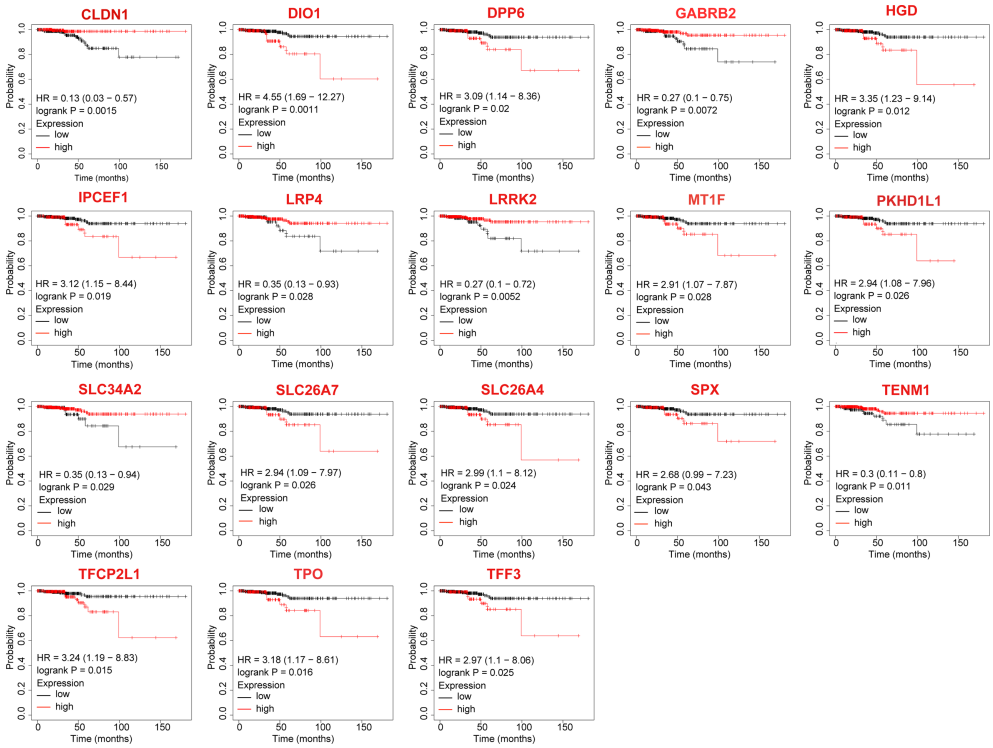

FIGURE 2
Differentially expressed genes that significantly affect overall survival in thyroid cancer patients.

results, to identify biomarkers that can be used to assess the risk of PTC metastasis.

In our study, 14 PTC metastasis risk-associated gene sets were screened, including four upregulated genes (*CLDN1*, *LRP4*, *LRRK2*, *TENM1*) and 10 downregulated genes (*DIO1*, *DPP6*, *HGD*, *IPCEF1*, *MT1F*, *SLC26A4*, *SLC26A7*, *SPX*, *TFF3*, *TPO*). Among all the risk-related genes, *DIO1*, *HGD*, *SLC26A4* and *TPO* have the highest correlation with each DEG and significantly affect the RFS of patients with metastatic PTC. Comprehensive multi-data analysis showed that these four genes

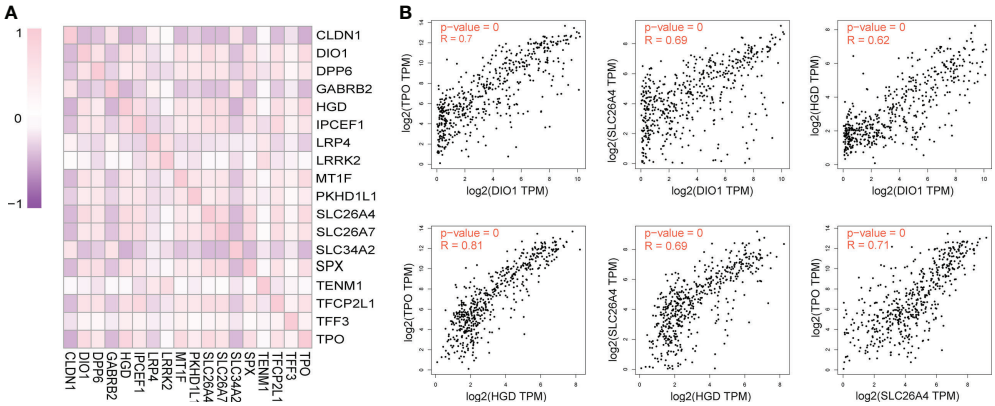

FIGURE 3
Pairwise correlation of differential expressed genes (DEGs) significantly affecting overall survival of TC patients in the context of TC disease. **(A)** R Software visualization of pairwise correlations of DEGs that significantly affected overall survival. **(B)** The correlation figure of *DIO1* and *TPO*, *DIO1* and *SLC26A4*, *DIO1* and *HGD*, *HGD* and *TPO*, *HGD* and *SLC26A4*, *TPO* and *SLC26A4*.

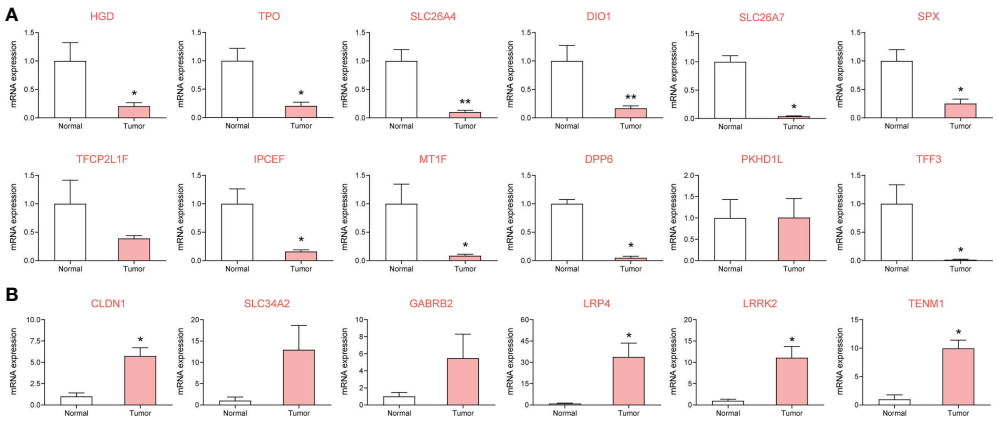

FIGURE 4
To investigate the expression of metastasis risk genes in papillary thyroid carcinoma (PTC) and adjacent clinical samples by RT-qPCR. 14 of which were significantly different. **(A)** DEGs downregulated in metastatic PTC compared with paracancellular tissues. **(B)** DEGs upregulated in metastatic PTC compared with paracancellular tissues. *$P< 0.05$, **$P< 0.01$ vs. normal group.

may be the key risk genes leading to PTC metastasis. Through further analysis of the core metastasis risk-associated genes, we found that the four DEGs (*DIO1*, *HGD*, *SLC26A4*, *TPO*) that highly correlate with each risk-associated gene are closely related to the transport and activation of iodine.

Further analysis of the relationship between iodine and PTC through literature search showed that abnormal iodine intake is a risk factor for PTC (22). However, existing studies have not fully clarified the relationship between iodine and PTC, though some studies have shown that PTC patients have higher iodine exposure (23–25) and that high iodine intake is a risk factor for PTC. Other studies (26, 27) have found that high iodine levels are not significantly correlated with the risk of PTC and only affect the growth and metastasis of PTC. Patients with PTC usually show high levels of urinary (25) and serum (28) iodine. Concomitantly, the level of thyroid-stimulating hormone (TSH) in PTC patients is higher than that in normal controls (29). Interestingly, iodine deficiency can lead to decreased thyroid hormone synthesis and secretion and thus increased TSH levels. This suggests that PTC patients have two seemingly contradictory pathological features occurring concomitantly, high iodine and high TSH levels, which might thus be predictors of poor prognosis for PTC (29–32).

To explore the causes of both high iodine and high TSH levels in patients with PTC, this study further analyzed the relationship between the identified core risk-associated genes for metastasis and PTC. A further analysis of the functions of downregulated core risk-associated genes in metastasized PTC revealed that DIO1 is a type 1 iodothyronine deiodinase that can convert T4 into T3, and T3 into T2. Notably, high free T4 is a

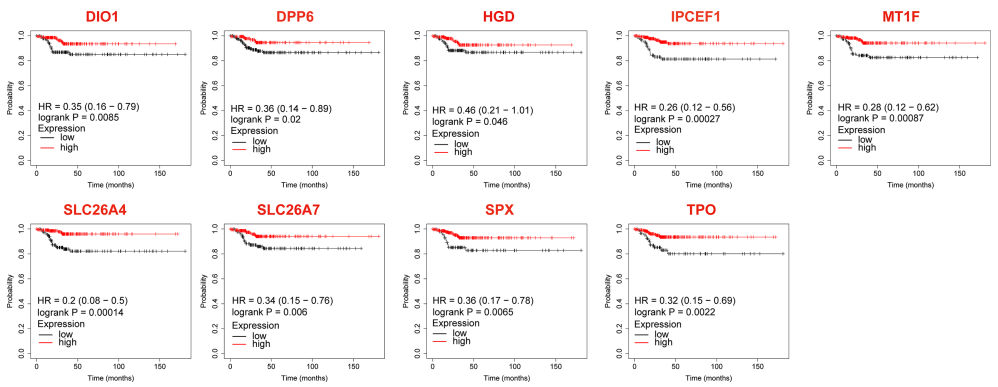

FIGURE 5
The Relapse-free survival of differentially expressed genes in thyroid cancer after validation by clinical samples.

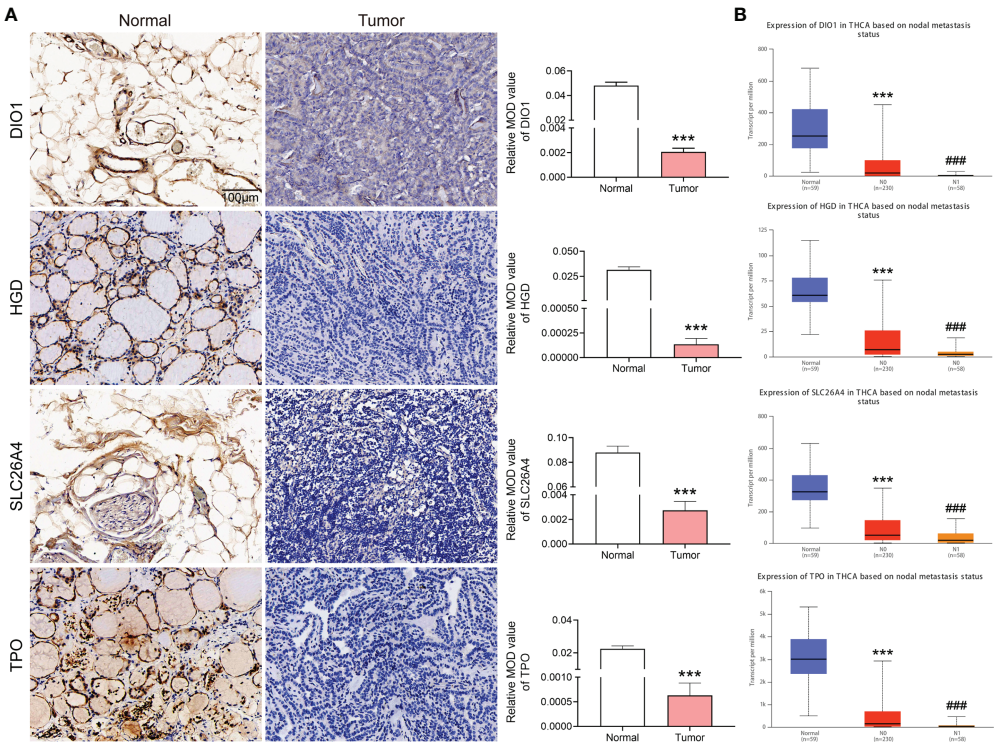

FIGURE 6
Expression of *DIO1*, *HGD*, *SLC26A4*, and *TPO* in metastatic papillary thyroid carcinoma (PTC) and adjacent normal tissues, and in different stages in the database. **(A)** Immunohistochemical staining of clinical samples, the expression of DIO1, HGD, SLC26A4 and TPO in normal and metastatic PTC. **(B)** *DIO1*, *HGD*, *SLC26A4*, and *TPO* expression in normal, PTC, and metastasized PTC based on TCGA database. N0: No regional Lymph node metastasis. N1: Metastases in 1–3 axillary Lymph nodes. ***$P < 0.001$ vs. normal group; ###$P < 0.001$ *vs.* N0 group.

risk factor for PTC (25). The possible mechanism through which low *DIO1* expression affects the occurrence and development of PTC is as follows: low *DIO1* expression leads to failed T4 de-iodization and a lack of free of T4 in the body. HGD participates in tyrosine metabolism. Tyrosine metabolism is related to thyroid hormone synthesis, and *HGD* expression in turn is highly correlated with *TPO*. The low expression of *HGD* might be involved in the occurrence and development of PTC by affecting *TPO* expression and thyroid hormone synthesis. *SLC26A4*, which encodes the pendrin protein located on the apical membrane of thyroid follicular cells, is a chloride/iodide ion transporter. SLC26A4 is a key protein that transports iodine into the follicle to synthesize thyroid hormones, and its low expression is an early event in thyroid tumorigenesis (33). *TPO* encodes thyroid peroxidase, which is synthesized by thyroid follicular cells and is present in the plasma membrane at the top of the follicular epithelial cells. Thyroid peroxidase can oxidize iodine in the follicular cells to activate it, providing activated iodine for thyroid hormone synthesis. *TPO* plays an important role in maintaining normal thyroid functions. With low expression of *TPO*, normal thyroid function cannot be maintained, and thyroid dysfunction is closely related to TC. In this study, we found that genes associated with iodine transport (*SLC26A4*), activated iodine (*TPO*), thyroid hormone synthesis (*HGD*), and disassembled free T4 (*DIO1*) are expressed at low levels in PTC, and their expression is further reduced in metastatic PTC (Figure 6B). The expression levels in normal, PTC, and metastatic PTC tissues are shown in Supplementary Table 2. In conclusion, iodine utilization in patients with metastatic PTC is blocked in many ways, including thyroid hormone synthesis. This indicates that patients with PTC are unable to utilize iodine in their body. Although serum iodine and urine iodine levels are elevated, thyroid hormone synthesis is still not possible, leading to elevated TSH levels. This study could explain the possible reasons for high serum iodine and TSH levels in PTC patients.

Previous studies have found that the level of iodine intake can affect thyroid function, but the relationship between iodine intake and TC is not clear (22); moreover, some studies (34) suggest that high iodine intake is an important risk factor for *BRAF* mutations and the subsequent development of PTC. Some studies (35) suggest that high iodine levels play a protective role

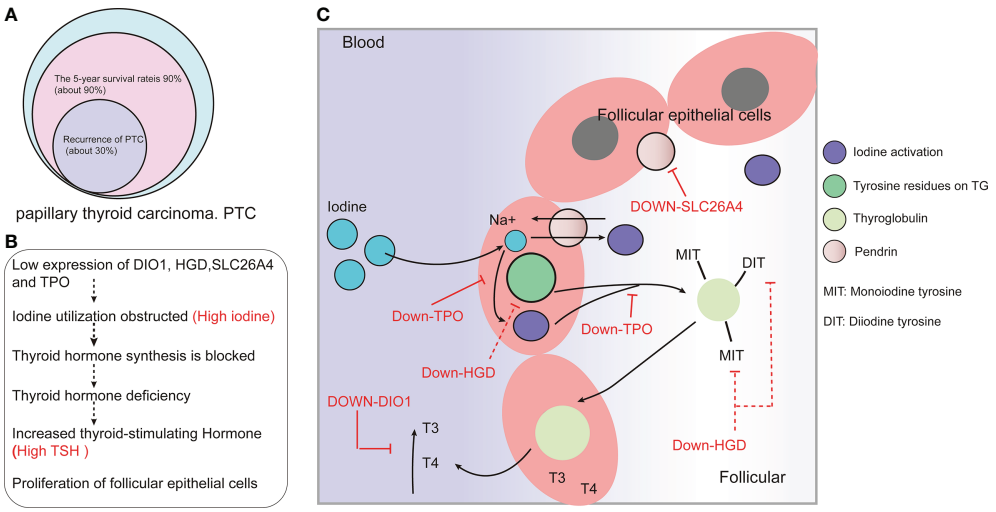

FIGURE 7
DIO1, *HGD*, *SLC26A4*, and *TPO* might be involved in the development of papillary thyroid carcinoma (PTC) by affects the absorption and utilization of iodine. **(A)** Prognosis of and recurrence rate in PTC patients. **(B)** Low expression of *DIO1, HGD, SLC26A4* and *TPO* may affect the synthesis and utilization of thyroid hormones. **(C)** The possible mechanism of iodine-resistant radiotherapy in patients with metastatic PTC: The low expression of *DIO1, HGD, SLC26A4*, and *TPO* leads to the inhibition of iodine recycling and thyroid hormone synthesis.

in thyroid cells and attenuate acute *BRAF* oncogene-mediated miRNA dysregulation. Of concern, one study (36) found that the 10, 15 and 20-year survival rate of patients receiving iodine-131 is 56%, 45% and 40%. However, the 10 and 15-year survival rate of patients without iodine-131 treatment was found to be 10% and 6%. Iodine intake is closely related to the prognosis of TC, and the expression of *SLC26A4* and *TPO* in iodine-resistant PTC is lower (15). This further supports our speculation that serum iodine content and level of iodine intake might not fully reflect the effect of iodine on PTC and that the ability of the body to use iodine could be important for the occurrence and development of PTC. The found providing a new treatment idea for patients with metastatic PTC who do not respond to iodine radiotherapy. For example, iodine absorption and utilization should be first improved for iodine-refractory PTC to ensure the efficacy of radiotherapy.

Although this study comprised a large-sample size analysis using GEO, GEPIA, TCGA, and other databases, in addition to utilizing pathological wax blocks from patients with metastatic PTC for RT-qPCR and immunohistochemistry verification, this was only a preliminary screen of a risk-associated gene set that might lead to PTC metastasis. As such, this set has not been quantitatively studied, and an evaluation of the risk of PTC metastasis based on the expression level of this gene set requires more clinical samples and quantitative studies based on each stage-based subgroup. A possible mechanism by which *DIO1*, *HGD*, *SLC26A4*, and *TPO* participate in the development of TC is shown in Figure 7.

Conclusions

CLDN1, *LRP4*, *LRRK2*, *TENM1*, *DIO1*, *DPP6*, *HGD*, *IPCEF1*, *MT1F*, *SLC26A4*, *SLC26A7*, *SPX*, *TFF3*, and *TPO* affect the prognosis of patients with PTC and are risk-associated genes for PTC metastasis. Further, *DIO1*, *HGD*, *SLC26A4*, and *TPO* are potential core risk-associated genes. Our study will help assess the risk of metastasis in patients with PTC, so that patients at high risk of metastasis can be followed up early and closely.

Data availability statement

The datasets presented in this study can be found in online repositories. The names of the repository/repositories and accession number(s) can be found in the article/Supplementary Material.

Ethics statement

The studies involving human participants were reviewed and approved by Biomedical Research Ethics Committee of Zunyi Medical University Hospital. Written informed consent for participation was not required for this study in accordance with the national legislation and the institutional requirements.

Author contributions

QZ designed the study and edited the manuscript. JL reviewed and revised the manuscript, HS proofread the manuscript. XB and TZ systemically revised the manuscript for important content. PL proposed the concept and designed the structure of the study. All authors contributed to the article and approved the submitted version.

Funding

This work was supported by the Program for Excellent Young Talents of Zunyi Medical University (No.18zy-006) and the Basic Research Program of Guizhou Provincial Department of Science and Technology (Natural Science) [Grant No. qiankehejichu-ZK [2022]yiban599].

Acknowledgments

We would like to thank Editage (https://www.editage.jp) for English language editing.

Conflict of interest

The authors declare that the research was conducted in the absence of any commercial or financial relationships that could be construed as a potential conflict of interest.

Publisher's note

Supplementary material

The Supplementary Material for this article can be found online at: https://www.frontiersin.org/articles/10.3389/fendo.2022.991906/full#supplementary-material

References

1. Cheng F, Xiao J, Shao C, Huang F, Wang L, Ju Y, Jia H. Burden of Thyroid Cancer From 1990 to 2019 and Projections of Incidence and Mortality Until 2039 in China: Findings From Global Burden of Disease Study. *Front Endocrinol (Lausanne)* (2021) 6, 38213. doi: 10.3389/fendo.2021.738213

2. Cao W, Chen HD, Yu YW, Li N, Chen WQ. Changing profiles of cancer burden worldwide and in China: a secondary analysis of the global cancer statistics 2020. *Chin Med J (Engl)* (2021) 134(7):783–91. doi: 10.1097/cm9.0000000000001474

3. Kitahara CM, Sosa JA. The changing incidence of thyroid cancer. *Nat Rev Endocrinol* (2016) 12(11):646–53. doi: 10.1038/nrendo.2016.110

4. Roman BR, Morris LG, Davies L. The thyroid cancer epidemic 2017 perspective. *Curr Opin Endocrinol Diabetes Obes* (2017) 24(5):332–6. doi: 10.1097/med.0000000000000359

5. Wirth S, Syleouni ME, Karavasiloglou N, Rinaldi S, Korol D, Wanner M. Incidence and mortality trends of thyroid cancer from 1980 to 2016. *Swiss Med Wkly* (2021) 151:w30029. doi: 10.4414/smw.2021.w30029

6. Laha D, Nilubol N, Boufraqech M. New therapies for advanced thyroid cancer. *Front Endocrinol (Lausanne)* (2020) 11:82. doi: 10.3389/fendo.2020.00082

7. Mazzaferri EL. An overview of the management of papillary and follicular thyroid carcinoma. *Thyroid* (1999) 9(5):421–7. doi: 10.1089/thy.1999.9.421

8. Ito Y, Miyauchi A, Kihara M, Fukushima M, Higashiyama T, Miya A. Overall survival of papillary thyroid carcinoma patients: A single-institution long-term follow-up of 5897 patients. *World J Surg* (2018) 42(3):615–22. doi: 10.1007/s00268-018-4479-z

9. Grogan RH, Kaplan SP, Cao H, Weiss RE, Degroot LJ, Simon CA, et al. A study of recurrence and death from papillary thyroid cancer with 27 years of median follow-up. *Surgery* (2013) 154(6):1436–1446; discussion 1446-1437. doi: 10.1016/j.surg.2013.07.008

10. Alexander EK, Kennedy GC, Baloch ZW, Cibas ES, Chudova D, Diggans J, et al. Preoperative diagnosis of benign thyroid nodules with indeterminate cytology. *N Engl J Med* (2012) 367(8):705–15. doi: 10.1056/NEJMoa1203208

11. Abooshahab R, Gholami M, Sanoie M, Azizi F, Hedayati M. Advances in metabolomics of thyroid cancer diagnosis and metabolic regulation. *Endocrine* (2019) 65(1):1–14. doi: 10.1007/s12020-019-01904-1

12. Prete A, Borges de Souza P, Censi S, Muzza M, Nucci N, Sponziello M. Update on fundamental mechanisms of thyroid cancer. *Front Endocrinol (Lausanne)* (2020) 11:102. doi: 10.3389/fendo.2020.00102

13. Zhang J, Wen X, Li Y, Zhang J, Li X, Qian C, et al. Diagnostic approach to thyroid cancer based on amino acid metabolomics in saliva by ultra-performance liquid chromatography with high resolution mass spectrometry. *Talanta* (2021) 235:122729. doi: 10.1016/j.talanta.2021.122729

14. Bergdorf K, Ferguson DC, Mehrad M, Ely K, Stricker T, Weiss VL. Papillary thyroid carcinoma behavior: clues in the tumor microenvironment. *Endocr Relat Cancer* (2019) 26(6):601–14. doi: 10.1530/erc-19-0074

15. Colombo C, Minna E, Gargiuli C, Muzza M, Dugo M, De Cecco L, et al. The molecular and gene/miRNA expression profiles of radioiodine resistant papillary thyroid cancer. *J Exp Clin Cancer Res* (2020) 39(1):245. doi: 10.1186/s13046-020-01757-x

16. Vasko V, Espinosa AV, Scouten W, He H, Auer H, Liyanarachchi S, et al. Gene expression and functional evidence of epithelial-to-mesenchymal transition in papillary thyroid carcinoma invasion. *Proc Natl Acad Sci U.S.A.* (2007) 104 (8):2803–8. doi: 10.1073/pnas.0610733104

17. Tarabichi M, Saiselet M, Trésallet C, Hoang C, Larsimont D, Andry G, et al. Revisiting the transcriptional analysis of primary tumours and associated nodal metastases with enhanced biological and statistical controls: Application to thyroid cancer. *Br J Cancer* (2015) 112(10):1665–74. doi: 10.1038/bjc.2014.665

18. Magarey MJ, Freeman JL. Recurrent well-differentiated thyroid carcinoma. *Oral Oncol* (2013) 49(7):689–94. doi: 10.1016/j.oraloncology.2013.03.434

19. Omry-Orbach G. Risk stratification in differentiated thyroid cancer: An ongoing process. *Rambam Maimonides Med J* (2016) 7(1):e003. doi: 10.5041/rmmj.10230

20. Yan T, Qiu W, Song J, Fan Y, Yang Z. ARHGAP36 regulates proliferation and migration in papillary thyroid carcinoma cells. *J Mol Endocrinol* (2021) 66 (1):1–10. doi: 10.1530/jme-20-0230

21. Coca-Pelaz A, Shah JP, Hernandez-Prera JC, Ghossein RA, Rodrigo JP, Hartl DM, et al. Papillary thyroid cancer-aggressive variants and impact on management: A narrative review. *Adv Ther* (2020) 37(7):3112–28. doi: 10.1007/s12325-020-01391-1

22. Liu Y, Su L, Xiao H. Review of factors related to the thyroid cancer epidemic. *Int J Endocrinol* (2017) 2017:5308635. doi: 10.1155/2017/5308635

23. Williams ED, Doniach I, Bjarnason O, Michie W. Thyroid cancer in an iodide rich area: A histopathological study. *Cancer* (1977) 39(1):215–22. doi: 10.1002/1097-0142(197701)39:1<215::aid-cncr2820390134>3.0.co;2-

24. Feldt-Rasmussen U. Iodine and cancer. *Thyroid* (2001) 11(5):483–6. doi: 10.1089/105072501300176435

25. Kim K, Cho SW, Park YJ, Lee KE, Lee DW, Park SK. Association between iodine intake, thyroid function, and papillary thyroid cancer: A case-control study. *Endocrinol Metab (Seoul)* (2021) 36(4):790–9. doi: 10.3803/EnM.2021.1034

26. Zhao H, Li H, Huang T. High urinary iodine, thyroid autoantibodies, and thyroid-stimulating hormone for papillary thyroid cancer risk. *Biol Trace Elem Res* (2018) 184(2):317–24. doi: 10.1007/s12011-017-1209-6

27. Zhao H, Li H, Huang T. High iodine intake and central LN metastasis risk of papillary thyroid cancer. *J Trace Elem Med Biol* (2019) 53:16–21. doi: 10.1016/j.jtemb.2019.01.015

28. Fan L, Tian Q, Xiu C, Wang F, Yuan Z, He Q, et al. High iodine nutrition may be a risk factor for cervical LN metastasis in papillary thyroid cancer patients. *Ann Nutr Metab* (2021) 77(2):90–9. doi: 10.1159/000513334

29. Kim HI, Jang HW, Ahn HS, Ahn S, Park SY, Oh YL, et al. High serum TSH level is associated with progression of papillary thyroid microcarcinoma during active surveillance. *J Clin Endocrinol Metab* (2018) 103(2):446–51. doi: 10.1210/jc.2017-01775

30. Zeng Q, Liu J, Zhu J, Hu G. [Association between preoperative serum thyroid-stimulating hormone level and nonfunctioning malignant nodule thyroid disease]. *Lin Chung Er Bi Yan Hou Tou Jing Wai Ke Za Zhi* (2014) 28(24):1931–3. doi: 10.13201/j.issn.1001-1781

31. Lee IS, Hsieh AT, Lee TW, Lee TI, Chien YM. The association of thyrotropin and autoimmune thyroid disease in developing papillary thyroid cancer. *Int J Endocrinol* (2017) 2017:5940367. doi: 10.1155/2017/5940367

32. Luo J, Hendryx M, Dinh P, He K. Association of iodine and iron with thyroid function. *Biol Trace Elem Res* (2017) 179(1):38–44. doi: 10.1007/s12011-017-0954-x

33. Yuan J, Song Y, Pan W, Li Y, Xu Y, Xie M, et al. LncRNA SLC26A4-AS1 suppresses the MRN complex-mediated DNA repair signaling and thyroid cancer metastasis by destabilizing DDX5. *Oncogene* (2020) 39(43):6664–76. doi: 10.1038/s41388-020-01460-3

34. Guan H, Ji M, Bao R, Yu H, Wang Y, Hou P, et al. Association of high iodine intake with the T1799A BRAF mutation in papillary thyroid cancer. *J Clin Endocrinol Metab* (2009) 94(5):1612–7. doi: 10.1210/jc.2008-2390

35. Fuziwara CS, Kimura ET. High iodine blocks a Notch/miR-19 loop activated by the BRAF(V600E) oncoprotein and restores the response to TGFβ in thyroid follicular cells. *Thyroid* (2014) 24(3):453–62. doi: 10.1089/thy.2013.0398

36. Durante C, Haddy N, Baudin E, Leboulleux S, Hartl D, Travagli JP, et al. Long-term outcome of 444 patients with distant metastases from papillary and follicular thyroid carcinoma: benefits and limits of radioiodine therapy. *J Clin Endocrinol Metab* (2006) 91(8):2892–9. doi: 10.1210/jc.2005-2838

frontiers | Frontiers in Endocrinology

TYPE Original Research
PUBLISHED 12 April 2023
DOI 10.3389/fendo.2023.1138100

OPEN ACCESS

EDITED BY
Francesca Mancuso,
University of Perugia, Italy

REVIEWED BY
Vicki E. Smith,
University of Birmingham, United Kingdom
Yuntao Song,
Beijing Cancer Hospital, Peking University, China

*CORRESPONDENCE
Xiao-Dong Teng
teng1102069@zju.edu.cn

†These authors have contributed equally to this work and share first authorship

SPECIALTY SECTION
This article was submitted to Cancer Endocrinology, a section of the journal Frontiers in Endocrinology

RECEIVED 05 January 2023
ACCEPTED 28 March 2023
PUBLISHED 12 April 2023

CITATION
Zhou J, Wang W-R, Zhang H-F, Gao Q-Q, Wang W-B, Zhu J-H, Han Y-S, Chen J, Ma T-H, Zhang X-Y and Teng X-D (2023) Molecular and clinical features of papillary thyroid cancer in adult patients with a non-classical phenotype.
Front. Endocrinol. 14:1138100.
doi: 10.3389/fendo.2023.1138100

Molecular and clinical features of papillary thyroid cancer in adult patients with a non-classical phenotype

Jie Zhou[1†], Wei-Ran Wang[2†], Hui-Fang Zhang[1], Qi-Qi Gao[1], Wei-Bin Wang[3], Jian-Hua Zhu[2], Yu-Shuai Han[2], Jing Chen[2], Tong-Hui Ma[2], Xiao-Yan Zhang[2] and Xiao-Dong Teng[1*]

[1]Department of Pathology, First Affiliated Hospital, Zhejiang University School of Medicine, Hangzhou, China, [2]Department of Translational Medicine, Genetron Health (Beijing) Technology, Co. Ltd., Beijing, China, [3]Cancer Center, First Affiliated Hospital, Zhejiang University School of Medicine, Hangzhou, China

Purpose: Genotyping is fundamental in papillary thyroid cancer (PTC) and helps to enhance diagnosis and prognosis and determine appropriate treatments. The phenotype-genotype association in PTC was previously studied, with *BRAF* V600E characterizing classic PTC and tall-cell PTC and *RAS* mutations characterizing follicular-variant PTC. In clinic, some non-classical histological subtypes of PTC were also identified, however, their genotype remains unclear. In this study, we collected samples of these non-classical PTC after the exclusion of classic phenotypes and examined their phenotypes, genotype and the relationship between phenotype and genotype.

Methods: We screened out non-classical PTC by excluding classical PTC from 1,059 different thyroid samples, and a total of 24 cases was obtained and described from the morphological features, which is rare in differentiated PTC. DNA/RNA sequencing was performed using 18 available samples to describe the genetic features.

Results: PTC with the non-classical phenotype were characterized cuboidal to low columnar tumor cells with subtle nuclear features of PTC and without discernible nuclear elongation, concurrently with dense microfollicles, delicate papillae or solid nodules with delicate fibrovascular cores. They were associated with lymphatic vessel invasion ($P<0.001$) but not with a worse prognosis ($P=0.791$). Gene fusions were identified in 14 of 18 (77.8%) cases, including eight fusions of *NTRK* and six fusions of *RET*. The high percentage of fusions in this papillary thyroid cancer subgroup suggested a correlation of gene fusions with the phenotype that does not belong to the *BRAF* V600E-mutant or *RAS*-mutant group.

Conclusions: Our study retrospectively screened a large cohort of different thyroid tissue samples, and presented the histopathological and genetic features

of a non-classical phenotype of PTC from 24 patients. It may contribute to diagnose in PTC, and patients of these non-classical phenotype may benefit from targeted therapy, compared to a natural patient cohort without selection.

KEYWORDS

papillary thyroid carcinoma, phenotype, gene fusion, ETV6-NTRK3, NCOA4-RET

1 Introduction

Globally, the incidence of thyroid cancer has markedly increased in the past 30 years (1, 2), and the prevalence of diverse histological and genetic characteristics has changed over time (3). With the exception of medullary thyroid cancer, all thyroid cancers are derived from follicular cells. About 80% to 85% of all thyroid cancers are papillary thyroid cancers (PTCs) (4–6), named for their papillary histological architecture. PTCs include several subtypes, such as classic PTC (CPTC), follicular-variant PTC (FVPTC), tall-cell PTC (TCPTC), and a few other rare variants (7, 8).

BRAF V600E and *RAS* mutations have been identified as the primary genetic drivers in thyroid carcinomas (9–11), followed by fusions involving *RET* (12) and other receptor tyrosine kinases (13). It is worthwhile pointing out that these mutations are almost always mutually exclusive (14). The *BRAF* V600E mutation is the most frequent genetic change in PTC, with a prevalence between 30 to 80% (15–17), and appears to be associated with a higher risk of cancer recurrence (18). The *RAS* oncogene family includes *HRAS*, *NRAS*, and *KRAS*. The prevalence of *RAS* mutations in thyroid cancer is approximately 20–40%, and the mutations are found in follicular lesions, including adenomas, carcinomas, and FVPTCs (19). Differentiated thyroid tumors harboring *RAS* mutations without co-alterations have an excellent prognosis (20). The Cancer Genome Atlas (TCGA) described a genomic landscape of 496 PTCs and confirmed the phenotype-genotype association in PTCs, with *BRAF* V600E characterizing CPTC and TCPTC and *RAS* mutations characterizing FVPTC (21).

RET fusion can result in oncogenic activation and occurs in about 5–35% of PTCs (22–24), whereas the rearrangements of other *RTKs* such as *NTRK1/3, ALK*, and *ROS1* translocations have been reported in a minor subset of PTCs (25–31). The associations of gene fusions with the outcome of the disease are not yet well understood. Yuri E Nikiforov's group described the morphological features of *ETV6-NTRK3*-positive PTC in adults without radiation exposure with the tumors exhibiting an admixture of papillary and follicular areas, clear cell or oncocytic foci with overt nuclear features of PTC, interspersed bland areas, glomeruloid follicles, reversed nuclear polarization and cytoplasmic vacuolization (32). However, this study did not propose a clear morphological standard for *NTRK* fusion-driven PTCs. At the same time, there are PTCs with histological characteristics that are non-classical from known pathological subtypes, and their genotypes are unclear. Thus, the relationship between morphological characteristics and genotypes still warrants further investigation.

Herein, 1,059 patients with thyroid cancer, who underwent surgery from 2008 to 2015, were retrospectively analyzed. A total of 24 PTC cases were identified according to morphological features that are different from the known subtypes. Molecular analyses were performed and revealed a high prevalence of gene fusion, while no mutations in *BRAF*, *RAS*, or *TERT* genes were detected. Identification of the relationship between these cytological morphologies and genomic fusions or clinical features will facilitate the rationalization of clinical treatment strategies.

2 Methods

2.1 Patients and samples

The study was conducted according to the guidelines of the Declaration of Helsinki, and approved by the Ethics Committee of the First Affiliated Hospital College of Medicine, Zhejiang University (NO. IIT20210692A). As a retrospective research, the data are anonymous, the requirement for informed consent was therefore waived.

A total of 1,059 thyroid cancer tissues were collected from patients who underwent thyroid surgery at The First Affiliated Hospital, Zhejiang University School of Medicine (Hangzhou, China) between 2008 and 2015. All available samples were fresh frozen thyroid tissues. Detailed clinical and pathological data were collected from patients harboring primary dominant PTCs with dimensions ≥1 cm.

2.2 PCR and sequencing of *BRAF* V600E

The genomic DNA was isolated using a commercial kit (QIAamp DNA Mini Kit; QIAGEN, Hilden, Germany). Exon 15 of the *BRAF* gene was amplified and then directly sequenced for *BRAF* V600E mutation as described previously (33).

2.3 Next-generation sequencing analysis

2.3.1 Thyroid NGS panel sequencing

The DNA and RNA extracted from PTC samples with the non-classical phenotype were analyzed with the Onco-Thyroid™ panel

(Genetron Health, Beijing, China, gene list is in Table S1) using one-step multiplex PCR targeted amplicons, as previously described (34).

2.3.2 RNA panel sequencing

Fusioncapture™ (GenetronHealth), which is a 395-gene RNA panel (gene list is in Table S2), was conducted to identify gene fusions in the PTC samples with the non-classical phenotype. The specific method is stated in the previous paper (35).

2.3.3 Whole-exome sequencing

Genomic DNA from PTC samples with the non-classical phenotype was fragmented for constructing a library using KAPA Hyper Prep kits (KAPA, KK8504) and captured using the Agilent SureSelect XT Human All Exon v5 kit (Agilent, Santa Clara, CA, USA). High-throughput sequencing was performed as previously described (36).

2.3.4 Statistical analyses

Comparisons of categorical variables were performed by Pearson's chi-squared test. The analyses and data presentation were carried out using GraphPad Prism (8.0.1).

3 Results

3.1 Sample selection

Figure 1 illustrates the study sample selection workflow. Of the 1,059 patients who underwent thyroid surgery at The First Affiliated Hospital, Zhejiang University School of Medicine (Hangzhou, China) between 2008 and 2015, 25 patients whose tumors were not primary differentiated PTC were first excluded, then 223 patients with papillary thyroid microcarcinoma were excluded. Finally, 787 PTC patients with common histopathologies, such as CPTC, FVPTC, TCPTC, oncocytic variant of PTC, the Warthin-like variant of PTC, and the diffuse sclerosing variant of PTC, were excluded. The final study sample consisted of 24 adult participants with no prior history of radiation exposure with a phenotype non-classical from common PTCs. The tumors were characterized as the following criteria: 1. Cuboidal to low-columnar tumor cells with subtle nuclear features of PTC and without discernible nuclear elongation. 2. Composed of dense microfollicles, delicate papillae or solid nodules with delicate fibrovascular cores.

3.2 Clinical characteristics

The clinical and pathologic features of PTC patients with the non-classical phenotype are summarized (Table 1, Table S3). The prevalence of PTC samples measuring at least 1 cm was 3.0% (24/811). There were 19 (79.2%) females and 5 (20.8%) males. The age at initial diagnosis ranged from 19 to 70 years (mean 42.1 years). The tumor size ranged from 1.0 cm to 7.0 cm (mean 1.8 cm). Moreover, the tumors were often described as solitary nodules (87.5%). Additionally, 416 PTC patients with normal phenotypes and clinical information were also included in the analysis (Table 1, Table S4). Overall, the non-classical phenotype was significantly associated with lymphatic vessel invasion, a strong prognostic factor for poor clinical outcomes in lymph node-negative patients with breast carcinoma, bladder cancer, non-small cell lung cancer, colorectal cancer and differentiated thyroid carcinoma (37–42). While tumor recurrence was 6.3% (26 of 416) in patients with a normal phenotype, it was 0% (0 of 24) in patients with the non-classical phenotype (P = 0.791).

3.3 Histopathological features of PTC with the non-classical phenotype

Microscopic examination revealed that all 24 tumors were lack of normal follicular structure of thyroid tissue and normal cell with small round-flat nucleus (Figure 2A). They were uniformly composed of small cuboidal to low columnar epithelial cells. The nucleus had subtle characteristics nuclear features of PTC and without significant elongation, in contrast, CPTC composed of columnar epithelial cells and the nucleus had classic characteristics nuclear features of PTC and with significant elongation (Figure 2B). Some nuclei were pushed by the cytoplasm and formed variable shapes such as rings and triangles. Furthermore, the cytoplasm was transparent or pale, and the borders of tumor cells were ill-defined. The tumors with non-classical phenotype showed three main patterns of growth. Firstly, it is the microfollicular pattern, which characterized by dense microfollicles (Figure 2C). The second one is papillary pattern,

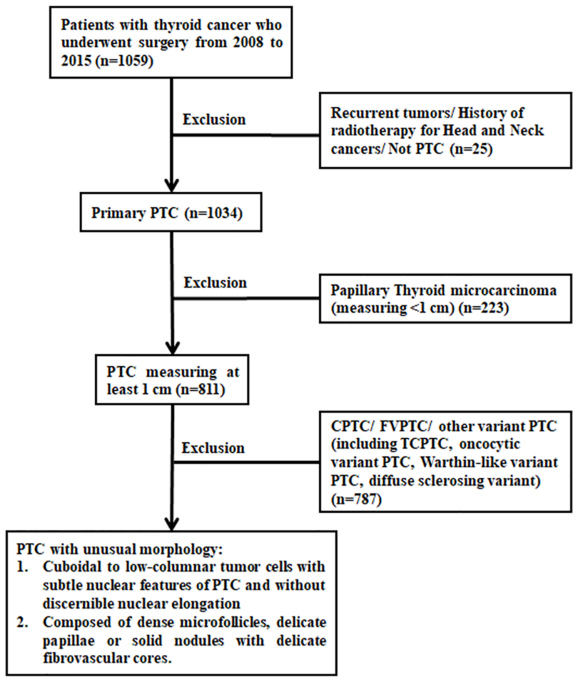

FIGURE 1
Workflow of the study sample selection.

which characterized by monotonous delicate papillae with a fine central fibrovascular stalk (Figure 2D), of which the delicate papillae are quite different from those in CPTC (Figure 2B). Occasionally, tumors presented glomeruloid bodies resembling abortive papillae (Figure 2E). The last pattern is solid growth, characterized by delicate fibrovascular cores within the solid nodules or islands (Figure 2F). Tumors with the non-classical phenotype were mostly poorly circumscribed and arranged in pushing, smooth-bordered nodules or islands of variable sizes, as separated by normal thyroid tissue (Figure 3A) or broad fibrous septa (jigsaw-like pattern) (Figure 3B). Often, there were small satellite nodules near or away from the dominant tumor (Figure 3C). Conventional aggressive features of PTC, including extrathyroidal extension, lymphatic vessel invasion, and lymph node metastases, were present in 6/24, 14/24, and 14/24 cases, respectively (Table 1, Table S3).

3.4 Molecular findings of PTC with the non-classical phenotype

BRAF V600E was analyzed using ARMS-PCR (AmoyDx, China) in all the tumors with the non-classical phenotype (n = 24), and molecular analyses revealed non-BRAF V600E. Meanwhile, the percentage of BRAF V600E positive patients in our control cohort was 72.6% (302/416). For the cases with remaining tumor samples (n = 18), Onco-thyroid panel (18/18), RNA panel (13/18), and whole-exome (15/18) sequencing were performed (Figures 4A–D, Tables S5–S7) to acquire additional genetic information. Fourteen tumors (77.8%, 14/18) harboring gene fusions were recognized by the Onco-thyroid panel and/or Fusioncapture sequencing, seven of which were ETV6-NTRK3, one was TPR-NTRK1, and the others were fusions of the RET gene (Figures S1, S2, Table S3). *RET* fusions were most frequent (33/484, 6.8%) in the TCGA study, and the most common partner gene was *CCDC6* (21/33, 63.6%) (21). Meanwhile, *NCOA4-RET* was recognized in four of cases (4/6, 66.7%) with the non-classical phenotype in this study and no *CCDC6-RET* was identified. More gene mutations, copy number variation (CNV), and tumor mutation burden (TMB) were detected and calculated by whole-exome sequencing, and the results showed that there were no other well-known driver mutations of PTC (Table S6). Notably, driver variations were not detected in 4 of the 13 patients, which indicates that the molecular mechanism of thyroid cancer still warrants further investigation. Extensive fibrosis was commonly encountered in our series, and cases with *RET* fusion (6/6) were more prone to severe fibrosis than those with the *NTRK* fusion (1/8). Besides, more patients with *NTRK* fusions (4/8) in the group appeared to have a high level of thyroid peroxidase antibody (TPO) compared to patients with *RET* fusions (1/6) (Table S3). However, the result of Fisher's exact test suggested no statistically difference in TPO levels (P=0.3007), which may due to small sample size.

3.5 Recurrence-free survival in patients with the non-classical phenotype

Follow-up data were available for 18 patients (median 86 months, range 18-127 months): all patients were alive and without recurrence (Table S3). The effects of non-classical and normal phenotypes on PTC recurrence were compared. Although non-classical phenotypic tumors were more likely to have lymphatic vessel invasion (Table 1), they did not show an elevated risk for recrudescence (Figure 4E).

4 Discussion

Key genetic alterations of PTC, co-occurring or mutually exclusive, are the basis of estimated prognosis. The phenotype-genotype association in PTCs was described as *BRAF* V600E characterizing CPTC, TCPTC and *RAS* mutations characterizing FVPTC (21). Numerous studies have demonstrated that co-

TABLE 1 Relationship of the non-classical phenotype group with clinicopathologic outcomes.

Clinicopathologic Outcomes	Normal Phenotype (n = 416)	Non-classical Phenotype (n = 24)	P
	No. (%)	No. (%)	
Age at diagnosis, years, Means ± SD	44.4 ± 12.6	42.1 ± 13.4	0.388
Sex, female	298 (71.6)	19 (79.1)	0.424
Size, cm, Means ± SD	1.7 ± 0.9	1.8 ± 1.2	0.483
Lymph node metastasis	195 (46.9)	14 (58.3)	0.274
Multifocality	126 (30.3)	3 (12.5)	0.063
Lymphatic vessel invasion	38 (9.1)	14 (58.3)	<0.001
Extrathyroidal Extension	83 (20.0)	6 (25)	0.736
Tumor recurrence	26 (6.3)	0 (0)	0.414
Total follow-up, months, Median (IQR)	69 (59-84)	86 (18-127)	0.791

IQR, interquartile range; SD, standard deviations.

10.3389/fendo.2023.1138100

occurrence of *BRAF* V600E and *TERT* promoter mutations defines an aggressive subgroup of PTCs (43–49). On the one hand, differentiated thyroid cancers harboring *RAS* mutations alone have an excellent prognosis (20). On the other hand, PTCs with a novel phenotype that do not belong to the *BRAF* V600E-mutant or *RAS*-mutant tumors should be better characterized, given that some of these tumors harbor gene fusions that can benefit from targeted therapy. As FDA approves larotrectinib and entrectinib for solid tumors with *NTRK* gene fusions, and pralsetinib and selpercatinib for thyroid cancers with *RET* gene mutations or fusions.

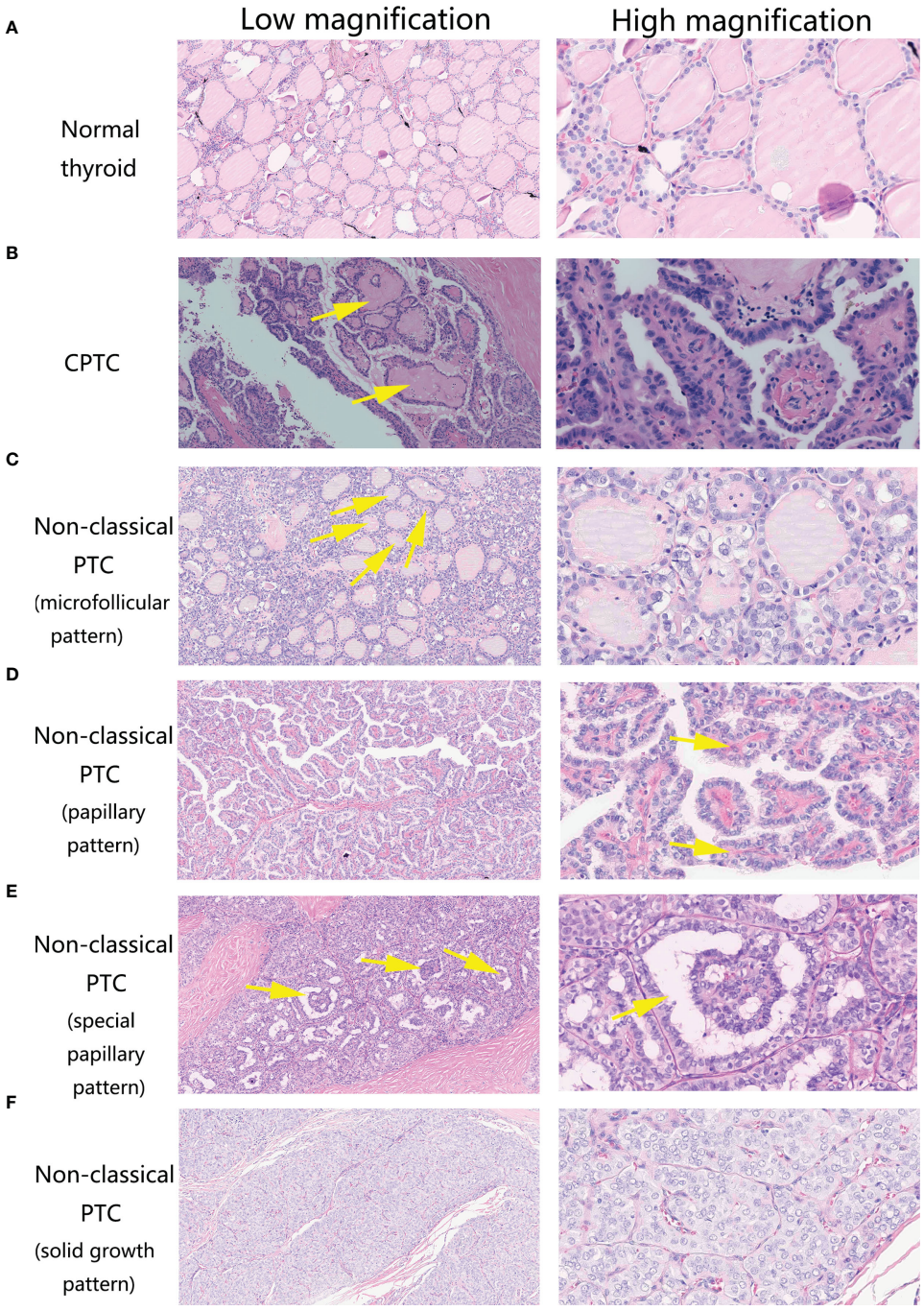

FIGURE 2
Growth patterns of Papillary Thyroid Carcinomas tumors with non-classical phenotype and controls in 100X and 400X magnification. **(A)** Normal thyroid. **(B)** Classic PTC: low magnification shows the papillae found in CPTC usually vary in size and shape and some have broader central stalks. The arrow shows the papillae with broader central stalks. High magnification shows that the papillae composed of columnar epithelial cells. The nucleus has classic characteristics nuclear features of PTC and with significant elongation. **(C)** Dense microfollicles are composed of small cuboidal epithelia with round nuclei intermixed with some variable shaped nuclei. The tumor cells have transparent or pale cytoplasm with ill-defined borders. Arrows show the microfollicles. **(D)** Tumor is dominantly composed of delicate papillae (arrow). **(E)** Occasionally tumors present glomeruloid bodies resembling abortive papillae. **(F)** Solid growth pattern, characterized by delicate fibrovascular cores within the solid nodules. The tumor cells have nucleus without significant elongation.

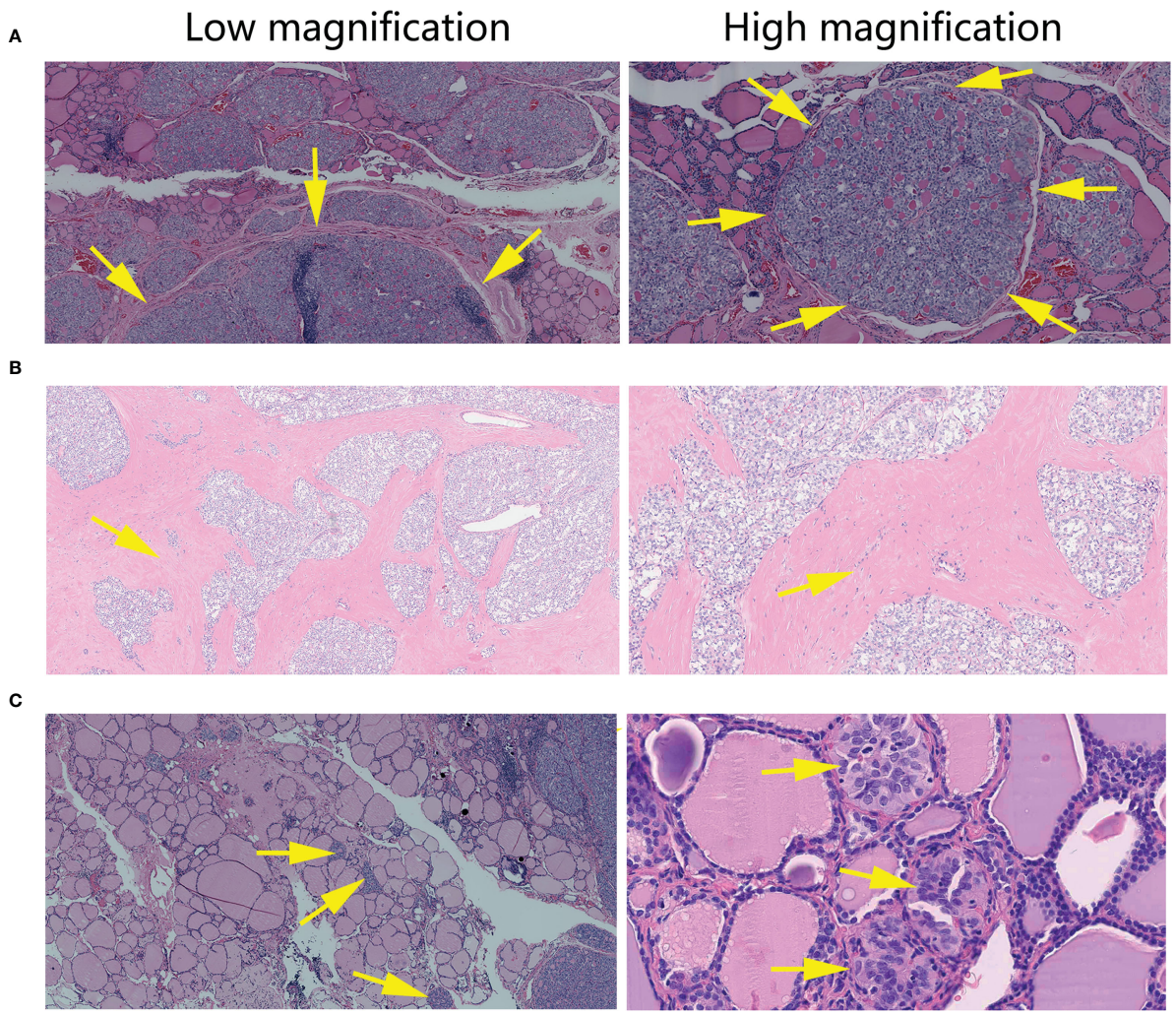

FIGURE 3
Histopathological features of Papillary Thyroid Carcinomas tumors with non-classical phenotype. **(A)** In 40X and 100X magnification, tumor tissue arranged in smooth-bordered nodules (arrow), as separated by normal thyroid tissue. **(B)** In 40X and 100X magnification, tumor tissue arranged in a geographic, jigsaw-like pattern within a broad fibrous background (arrow). **(C)** 40X and 400X magnification shows small satellite nodules (arrow) near or away from the dominant tumor.

Herein, we retrospectively analyzed a large cohort of thyroid tissue samples, screened out well-differentiated PTCs, and excluding PTMC, CPTC, FVPTC, TCPTC, oncocytic variants of PTC, the Warthin-like variant of PTC, and the diffuse sclerosing variant of PTC. A non-classical phenotype of PTC was summarized from 24 patients. The microfollicular architecture consisted of closely-packed small follicles with scanty colloids, different from the common FVPTC. The papillary structure could be predominant or even exclusive, but it was always monotonous, delicate. In comparison, the papillae found in CPTC usually vary in size and shape and generally have broader central stalks. We presumed that these delicate papillae were formed in the following ways: (1) originating from a solid structure with delicate fibrovascular cores by cellular dehiscence (Figure S3); or (2) originating from packed microfollicles by follicular-septum cracking, which may be different from the formation of the common papillae present in CPTC (Figure S4). Meanwhile, considering that the solid growth pattern was predominant (> 50%) in our cases, a diagnosis of a solid variant of PTC (SVPTC) may also be established (50, 51), which is most commonly seen in children after the Chernobyl nuclear accident (52, 53) or in few adults without a history of radiation exposure (51), accounting for 1-3% of all PTCs (54). Different from the most common encapsulated type (65%) (54) in reported SVPTC, our general solid growth cases were almost non-encapsulated and invasive (87.5%, 7/8), and showed a lower proportion (0.76%, 8/1059) in Chinese, suggest it may be clinically rare. Furthermore, extensive fibrosis was quite common in our series. Although sometimes seen in CPTC, the tumor nests were more irregular and infiltrative. Other features, including clear or pale cytoplasm, no elongated nuclei, and smaller and shorter cells, are also of tremendous significance in these subtypes of PTC.

We selected 416 patients with a common PTC phenotype who underwent surgery in the hospital from 2008 to 2015 as a real-world data control to explore whether PTC patients with a non-classical phenotype have significant differences in clinical characteristics. The median age of PTC patients with the non-classical phenotype

10.3389/fendo.2023.1138100

(42 years old) was similar to that of PTC patients with a common phenotype (44 years old) (P = 0.388). The female to male ratios were 2.5:1 and 3.8:1 in the common and non-classical phenotype of PTC groups (P = 0.424), respectively. For aggressive features such as invasive border, extrathyroidal extension, lymphatic vessel invasion, and lymph node metastases, PTCs with the non-classical phenotype showed a significant difference in lymphatic vessel invasion (P < 0.001), whereas there was no difference in tumor recurrence (P = 0.414). The results suggest that although there are differences in histopathological features between common and non-classical phenotypes of PTC, clinical characteristics and recurrence are relatively similar. Among the 24 cases of PTC with a non-classical phenotype, 18 had fresh frozen tissues stored. After Onco-Thyroid and/or RNA panel sequencing, 14 gene fusions were recognized, including 8 fusions in *NTRK* and 6 fusions in *RET*. In the thyroid, *NTRK*-driven malignancies are rare, and their frequency ranges from 2 to 3% in adult patients without radiation exposure (21, 55–57). However, the frequency of *NTRK* fusion-positive PTCs was 44.4% (8/18) in this group. *RET* fusions occur in 5%–10% of sporadic PTCs (58, 59). In the TCGA study, 6.8% of cases harbored a *RET* fusion (21). In contrast, *RET* fusions were observed in 33.3% (6/18) of PTCs with the non-classical phenotype in this study. The results indicate that the fusions of *NTRK* and *RET* are associated with the non-classical phenotype of

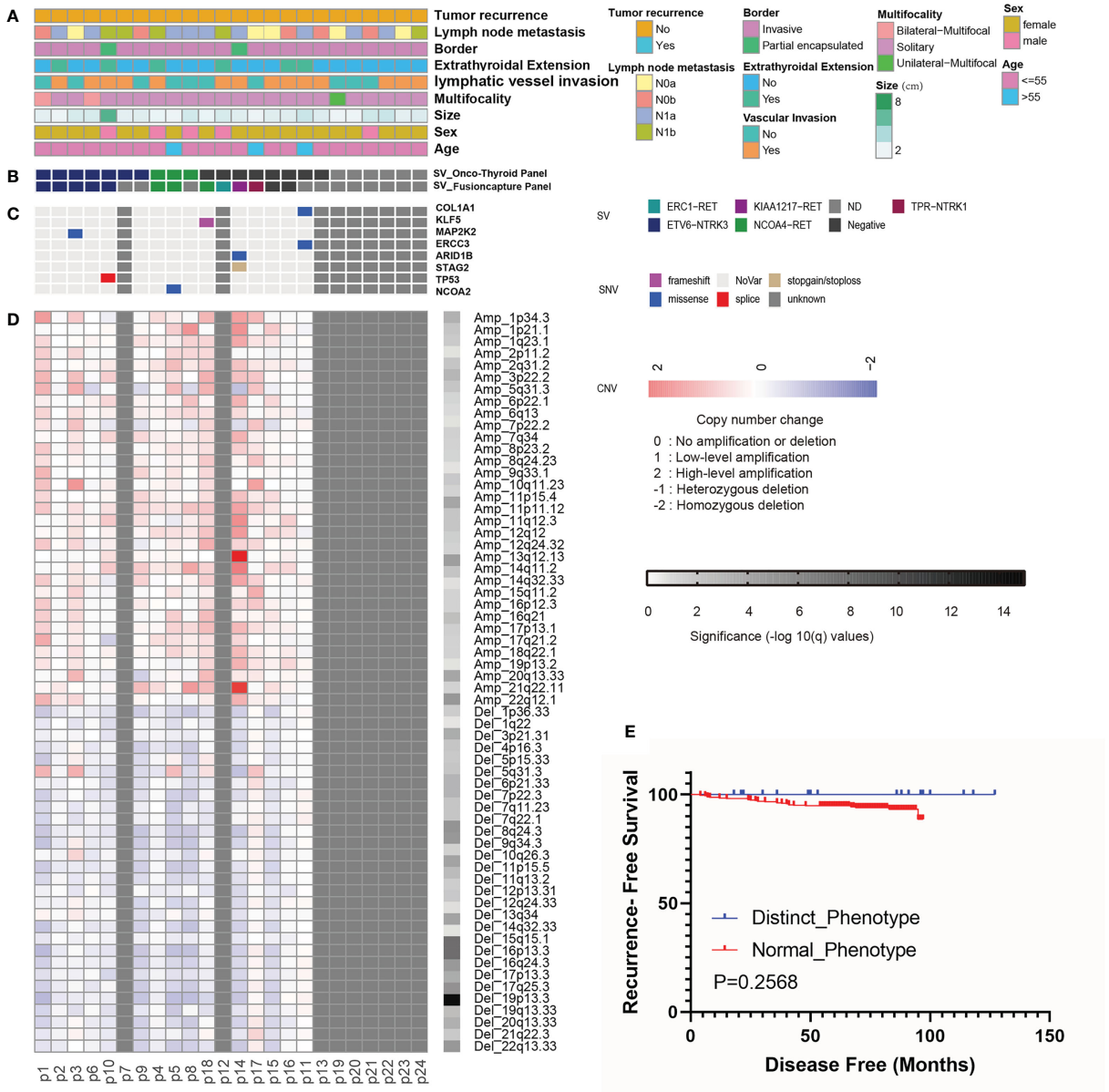

FIGURE 4
Landscape of genomic alterations and Kaplan-Meier analyses in Papillary Thyroid Carcinomas with non-classical phenotype. **(A-D)** Landscape of genomic alterations (n=24). **(A)** Tumor recurrence, lymph node metastasis, border, extrathyroidal extension, lymphatic vessel invasion, multifocality, tumor size, patient gender and age. **(B)** Fusion events detected by Onco-Thyroid Panel and Fusioncapture Panel sequencing. **(C)** Mutations of driver genes detected by WES. **(D)** Copy number changes detected by WES. **(E)** Kaplan-Meier analyses of the impacts of phenotype on recurrence-free survival of PTC patients (n=18).

PTC. Meanwhile, in this phenotype of PTC, cases with *RET* fusion are more prone to fibrosis than those with *NTRK* fusion. Various *RET* and *NTRK* fusions have been reported in PTC. The two most prevalent *RET* fusions are *CCDC6-RET* and *NCOA4-RET*, which account for more than 90% of all *RET* rearrangements (60–62). *NTRK* fusions discovered in thyroid tumors so far include *EML4-NTRK3* (57), *ETV6-NTRK3* (26, 27, 63), *SQSTM1-NTRK3* (57), *IRF2BP2-NTRK1* (57), *TPR-NTRK1* (26, 27), *TPM3-NTRK1* (25, 64), *TFG-NTRK1* (64, 65), and *TRIM33-NTRK1* (65). Interestingly, the common fusions of *RET/NTRK3* discovered in this study are *NCOA4-RET* (4/6) and *ETV6-NTRK3* (7/7), showing selectivity of fusion partners. Meanwhile, except for one mutation in *TP53*, no mutations leading to the occurrence of PTC were found in other common genes (such as *AKT1, BRAF, CTNNB1, EIF1AX, EZH1, GNAS, HRAS, KRAS, NRAS, PIK3CA, RET, SPOP, TERT, TSHR, ZNF148*, and so on), signaling the pivotal role of gene fusion in this group of PTC. Recently, there has been a growing interest in testing and characterizing *NTRK* and *RET* fusion genes because they are therapeutically targetable. For instance, *NTRK* and *RET* fusion-positive tumors are sensitive to inhibitors, such as larotrectinib and selpercatinib, which appear to be well tolerated and effective (58, 66, 67). Due to the limited sample size in current research, it is not yet possible to have an impact on clinical treatment options for those patients. However, our study provides a possibility that this type of non-classical PTC may be classified together to spare these patients unnecessary aggressive therapy, as they shared similar molecular and clinical features and had a relatively good prognosis.

5 Conclusion

In conclusion, our study retrospectively screened a large cohort of different thyroid tissue samples, and a non-classical phenotype of PTC was summarized from 24 patients. Herein, the histopathological and genetic features of this subgroup of PTC were presented. Our findings may facilitate diagnostic approaches in PTC, and patients of this peculiar subgroup may benefit from targeted therapy compared to a natural patient cohort without selection. However, this study was based on a small population, and genetic testing were not performed on all tissue samples. In the future, further analyses are warranted to corroborate the results.

Data availability statement

The raw datasets presented in this study can be found in the National Omics Data Encyclopedia (NODE) database (https://www.biosino.org/node/index), accession number OEP003392.

Ethics statement

The studies involving human participants were reviewed and approved by the Ethics Committee of the First Affiliated Hospital College of Medicine, Zhejiang University (NO. IIT20210692A). Written informed consent for participation was not required for this study in accordance with the national legislation and the institutional requirements.

Author contributions

Conceptualization, JZ and X-DT. Methodology, JZ, W-RW, T-HM and X-YZ. Software, H-FZ, Q-QG, and X-YZ. Validation, JZ, W-RW, W-BW, J-HZ and Y-SH. Formal Analysis, JZ, W-RW, H-FZ, Q-QG, W-BW, Y-SH, T-HM, X-YZ and X-DT. Investigation, JZ and W-RW. Resources, X-DT. Data Curation, JZ and W-RW. Writing – Original Draft Preparation, JZ, W-RW. Writing – Review & Editing, JC, T-HM and XDT. Visualization, JZ and W-RW. Funding – T-HM. Supervision, X-DT. Project Administration, X-DT. All authors contributed to the article and approved the submitted version.

Funding

This work was supported by grants from the Zhejiang Province medical and health research projects (Grant No. 2016KYB027 and Grant No. 2017KY010).

Acknowledgments

We gratefully acknowledge the participation of all patients in this study.

Conflict of interest

W-RW, J-HZ, Y-SH, JC, T-HM, X-YZ are the employees of Genetron Health Beijing Technology, Co. Ltd., Beijing, China.

The remaining authors declare that the research was conducted in the absence of any commercial or financial relationships that could be constructed as a potential conflict of interest.

Publisher's note

Supplementary material

The Supplementary Material for this article can be found online at: https://www.frontiersin.org/articles/10.3389/fendo.2023.1138100/full#supplementary-material

SUPPLEMENTARY FIGURE 1
The Integrative Genomics Viewer (IGV) screenshots display the reads from next-generation sequencing by Onco-Thyroid panel and reveal harbouring of gene fusions. The reference is fusion gene sequences.

SUPPLEMENTARY FIGURE 2
The IGV screenshots display the reads from next-generation sequencing by Fusioncapture panel and reveal harbouring of gene fusions. The reference is GRCh37/hg19.

SUPPLEMENTARY FIGURE 3
The delicate papillae result from cellular dehiscence, with rugged surface and adhesion.

SUPPLEMENTARY FIGURE 4
Putative scheme of papillae formations. **(A)** The delicate papillae originate from packed microfollicles. **(B)** The common papillae originate from irregular follicles.

References

1. Li M, Dal Maso L, Vaccarella S. Global trends in thyroid cancer incidence and the impact of overdiagnosis. *Lancet Diabetes Endocrinol* (2020) 8:468–70. doi: 10.1016/S2213-8587(20)30115-7

2. Chen AY, Jemal A, Ward EM. Increasing incidence of differentiated thyroid cancer in the united states, 1988-2005. *Cancer* (2009) 115:3801–7. doi: 10.1002/cncr.24416

3. Jung CK, Little MP, Lubin JH, Brenner AV, Wells SA Jr., Sigurdson AJ, et al. The increase in thyroid cancer incidence during the last four decades is accompanied by a high frequency of BRAF mutations and a sharp increase in RAS mutations. *J Clin Endocrinol Metab* (2014) 99:E276–285. doi: 10.1210/jc.2013-2503

4. Jemal A, Bray F, Center MM, Ferlay J, Ward E, Forman D. Global cancer statistics. *CA Cancer J Clin* (2011) 61:69–90. doi: 10.3322/caac.20107

5. Gansler T, Ganz PA, Grant M, Greene FL, Johnstone P, Mahoney M, et al. Sixty years of CA: a cancer journal for clinicians. *CA Cancer J Clin* (2010) 60:345–50. doi: 10.3322/caac.20088

6. Pacini F, Schlumberger M, Dralle H, Elisei R, Smit JW, Wiersinga W, et al. European Consensus for the management of patients with differentiated thyroid carcinoma of the follicular epithelium. *Eur J Endocrinol* (2006) 154:787–803. doi: 10.1530/eje.1.02158

7. Lam AK, Lo CY, Lam KS. Papillary carcinoma of thyroid: A 30-yr clinicopathological review of the histological variants. *Endocr Pathol* (2005) 16:323–30. doi: 10.1385/ep:16:4:323

8. Shi X, Liu R, Basolo F, Giannini R, Shen X, Teng D, et al. Differential clinicopathological risk and prognosis of major papillary thyroid cancer variants. *J Clin Endocrinol Metab* (2016) 101:264–74. doi: 10.1210/jc.2015-2917

9. Garcia-Rostan G, Zhao H, Camp RL, Pollan M, Herrero A, Pardo J, et al. Tallini, g. ras mutations are associated with aggressive tumor phenotypes and poor prognosis in thyroid cancer. *J Clin Oncol* (2003) 21:3226–35. doi: 10.1200/JCO.2003.10.130

10. Xing M. Molecular pathogenesis and mechanisms of thyroid cancer. *Nat Rev Cancer* (2013) 13:184–99. doi: 10.1038/nrc3431

11. Xing M, Alzahrani AS, Carson KA, Viola D, Elisei R, Bendlova B, et al. Association between BRAF V600E mutation and mortality in patients with papillary thyroid cancer. *JAMA* (2013) 309:1493–501. doi: 10.1001/jama.2013.3190

12. Grieco M, Santoro M, Berlingieri MT, Melillo RM, Donghi R, Bongarzone I, et al. PTC is a novel rearranged form of the ret proto-oncogene and is frequently detected *in vivo* in human thyroid papillary carcinomas. *Cell* (1990) 60:557–63. doi: 10.1016/0092-8674(90)90659-3

13. Pierotti MA, Bongarzone I, Borrello MG, Mariani C, Miranda C, Sozzi G, et al. Rearrangements of TRK proto-oncogene in papillary thyroid carcinomas. *J Endocrinol Invest* (1995) 18:130–3. doi: 10.1007/BF03349721

14. Soares P, Trovisco V, Rocha AS, Lima J, Castro P, Preto A, et al. BRAF mutations and RET/PTC rearrangements are alternative events in the etiopathogenesis of PTC. *Oncogene* (2003) 22:4578–80. doi: 10.1038/sj.onc.1206706

15. Xing M. BRAF mutation in thyroid cancer. *Endocr Relat Cancer* (2005) 12:245–62. doi: 10.1677/erc.1.0978

16. Tanaka A, Matsuse M, Saenko V, Nakao T, Yamanouchi K, Sakimura C, et al. TERT mRNA expression as a novel prognostic marker in papillary thyroid carcinomas. *Thyroid* (2019) 29:1105–14. doi: 10.1089/thy.2018.0695

17. Sun J, Zhang J, Lu J, Gao J, Ren X, Teng L, et al. BRAF V600E and TERT promoter mutations in papillary thyroid carcinoma in Chinese patients. *PloS One* (2016) 11:e0153319. doi: 10.1371/journal.pone.0153319

18. Enumah S, Fingeret A, Parangi S, Dias-Santagata D, Sadow PM, Lubitz CC. BRAF(V600E) mutation is associated with an increased risk of papillary thyroid cancer recurrence. *World J Surg* (2020) 44:2685–91. doi: 10.1007/s00268-020-05521-2

19. An JH, Song KH, Kim SK, Park KS, Yoo YB, Yang JH, et al. RAS mutations in indeterminate thyroid nodules are predictive of the follicular variant of papillary thyroid carcinoma. *Clin Endocrinol (Oxf)* (2015) 82:760–6. doi: 10.1111/cen.12579

20. Xing M. Clinical utility of RAS mutations in thyroid cancer: a blurred picture now emerging clearer. *BMC Med* (2016) 14:12. doi: 10.1186/s12916-016-0559-9

21. Cancer Genome Atlas Research, N. Integrated genomic characterization of papillary thyroid carcinoma. *Cell* (2014) 159:676–90. doi: 10.1016/j.cell.2014.09.050

22. Santoro M, Moccia M, Federico G, Carlomagno F. RET gene fusions in malignancies of the thyroid and other tissues. *Genes (Basel)* (2020) 11(4):424. doi: 10.3390/genes11040424

23. Kim P, Jia P, Zhao Z. Kinase impact assessment in the landscape of fusion genes that retain kinase domains: a pan-cancer study. *Brief Bioinform* (2018) 19:450–60. doi: 10.1093/bib/bbw127

24. Nikiforov YE. Molecular analysis of thyroid tumors. *Mod Pathol* (2011) 24 Suppl 2:S34–43. doi: 10.1038/modpathol.2010.167

25. Rabes HM, Demidchik EP, Sidorow JD, Lengfelder E, Beimfohr C, Hoelzel D, et al. Pattern of radiation-induced RET and NTRK1 rearrangements in 191 post-chernobyl papillary thyroid carcinomas: biological, phenotypic, and clinical implications. *Clin Cancer Res* (2000) 6:1093–103.

26. Prasad ML, Vyas M, Horne MJ, Virk RK, Morotti R, Liu Z, et al. NTRK fusion oncogenes in pediatric papillary thyroid carcinoma in northeast united states. *Cancer* (2016) 122:1097–107. doi: 10.1002/cncr.29887

27. Ricarte-Filho JC, Li S, Garcia-Rendueles ME, Montero-Conde C, Voza F, Knauf JA, et al. Identification of kinase fusion oncogenes in post-Chernobyl radiation-induced thyroid cancers. *J Clin Invest* (2013) 123:4935–44. doi: 10.1172/JCI69766

28. Chu YH, Dias-Santagata D, Farahani AA, Boyraz B, Faquin WC, Nose V, et al. Clinicopathologic and molecular characterization of NTRK-rearranged thyroid carcinoma (NRTC). *Mod Pathol* (2020) 33:2186–97. doi: 10.1038/s41379-020-0574-4

29. Hamatani K, Mukai M, Takahashi K, Hayashi Y, Nakachi K, Kusunoki Y. Rearranged anaplastic lymphoma kinase (ALK) gene in adult-onset papillary thyroid cancer amongst atomic bomb survivors. *Thyroid* (2012) 22:1153–9. doi: 10.1089/thy.2011.0511

30. Ritterhouse LL, Wirth LJ, Randolph GW, Sadow PM, Ross DS, Liddy W, et al. ROS1 rearrangement in thyroid cancer. *Thyroid* (2016) 26:794–7. doi: 10.1089/thy.2016.0101

31. Yakushina VD, Lerner LV, Lavrov AV. Gene fusions in thyroid cancer. *Thyroid* (2018) 28:158–67. doi: 10.1089/thy.2017.0318

32. Seethala RR, Chiosea SI, Liu CZ, Nikiforova M, Nikiforov YE. Clinical and morphologic features of ETV6-NTRK3 translocated papillary thyroid carcinoma in an adult population without radiation exposure. *Am J Surg Pathol* (2017) 41:446–57. doi: 10.1097/PAS.0000000000000814

33. Wang W, Zhao W, Wang H, Teng X, Wang H, Chen X, et al. 3rd; teng, l. poorer prognosis and higher prevalence of BRAF (V600E) mutation in synchronous bilateral papillary thyroid carcinoma. *Ann Surg Oncol* (2012) 19:31–6. doi: 10.1245/s10434-011-2096-2

34. Song Y, Xu G, Ma T, Zhu Y, Yu H, Yu W, et al. Utility of a multigene testing for preoperative evaluation of indeterminate thyroid nodules: A prospective blinded single center study in China. *Cancer Med* (2020) 9:8397–405. doi: 10.1002/cam4.3450

35. Shi M, Wang W, Zhang J, Li B, Lv D, Wang D, et al. Identification of RET fusions in a Chinese multicancer retrospective analysis by next-generation sequencing. *Cancer Sci* (2022) 113:308–18. doi: 10.1111/cas.15181

36. Xie L, Yang Y, Guo W, Che D, Xu J, Sun X, et al. The clinical implications of tumor mutational burden in osteosarcoma. *Front Oncol* (2020) 10:595527. doi: 10.3389/fonc.2020.595527

37. Lee AH, Pinder SE, Macmillan RD, Mitchell M, Ellis IO, Elston CW, et al. Prognostic value of lymphovascular invasion in women with lymph node negative invasive breast carcinoma. *Eur J Cancer* (2006) 42:357–62. doi: 10.1016/j.ejca.2005.10.021

38. Bolenz C, Herrmann E, Bastian PJ, Michel MS, Wulfing C, Tiemann A, et al. Lymphovascular invasion is an independent predictor of oncological outcomes in patients with lymph node-negative urothelial bladder cancer treated by radical cystectomy: a multicentre validation trial. *BJU Int* (2010) 106:493–9. doi: 10.1111/j.1464-410X.2009.09166.x

39. Naito Y, Goto K, Nagai K, Ishii G, Nishimura M, Yoshida J, et al. Vascular invasion is a strong prognostic factor after complete resection of node-negative non-small cell lung cancer. *Chest* (2010) 138:1411–7. doi: 10.1378/chest.10-0185

40. Zlobec I, Baker K, Minoo P, Jass JR, Terracciano L, Lugli A. Node-negative colorectal cancer at high risk of distant metastasis identified by combined analysis of lymph node status, vascular invasion, and raf-1 kinase inhibitor protein expression. *Clin Cancer Res* (2008) 14:143–8. doi: 10.1158/1078-0432.CCR-07-1380

41. Vuong HG, Kondo T, Duong UNP, Pham TQ, Oishi N, Mochizuki K, et al. Prognostic impact of vascular invasion in differentiated thyroid carcinoma: a systematic review and meta-analysis. *Eur J Endocrinol* (2017) 177:207–16. doi: 10.1530/EJE-17-0260

42. Wreesmann VB, Nixon IJ, Rivera M, Katabi N, Palmer F, Ganly I, et al. Prognostic value of vascular invasion in well-differentiated papillary thyroid carcinoma. *Thyroid* (2015) 25:503–8. doi: 10.1089/thy.2015.0052

43. Bae JS, Kim Y, Jeon S, Kim SH, Kim TJ, Lee S, et al. Clinical utility of TERT promoter mutations and ALK rearrangement in thyroid cancer patients with a high prevalence of the BRAF V600E mutation. *Diagn Pathol* (2016) 11:21. doi: 10.1186/s13000-016-0458-6

44. Insilla AC, Proietti A, Borrelli N, Macerola E, Niccoli C, Vitti P, et al. TERT promoter mutations and their correlation with BRAF and RAS mutations in a consecutive cohort of 145 thyroid cancer cases. *Oncol Lett* (2018) 15:2763–70. doi: 10.3892/ol.2017.7675

45. Liu R, Bishop J, Zhu G, Zhang T, Ladenson PW, Xing M. Mortality risk stratification by combining BRAF V600E and TERT promoter mutations in papillary thyroid cancer: Genetic duet of BRAF and TERT promoter mutations in thyroid cancer mortality. *JAMA Oncol* (2017) 3:202–8. doi: 10.1001/jamaoncol.2016.3288

46. Liu X, Qu S, Liu R, Sheng C, Shi X, Zhu G, et al. TERT promoter mutations and their association with BRAF V600E mutation and aggressive clinicopathological characteristics of thyroid cancer. *J Clin Endocrinol Metab* (2014) 99:E1130–1136. doi: 10.1210/jc.2013-4048

47. Song YS, Lim JA, Choi H, Won JK, Moon JH, Cho SW, et al. Prognostic effects of TERT promoter mutations are enhanced by coexistence with BRAF or RAS mutations and strengthen the risk prediction by the ATA or TNM staging system in differentiated thyroid cancer patients. *Cancer* (2016) 122:1370–9. doi: 10.1002/cncr.29934

48. Xing M, Liu R, Liu X, Murugan AK, Zhu G, Zeiger MA, et al. BRAF V600E and TERT promoter mutations cooperatively identify the most aggressive papillary thyroid cancer with highest recurrence. *J Clin Oncol* (2014) 32:2718–26. doi: 10.1200/JCO.2014.55.5094

49. Matsuse M, Yabuta T, Saenko V, Hirokawa M, Nishihara E, Suzuki K, et al. TERT promoter mutations and ki-67 labeling index as a prognostic marker of papillary thyroid carcinomas: combination of two independent factors. *Sci Rep* (2017) 7:41752. doi: 10.1038/srep41752

50. Carcangiu ML, Zampi G, Pupi A, Castagnoli A, Rosai J. Papillary carcinoma of the thyroid. a clinicopathologic study of 241 cases treated at the university of Florence, Italy. *Cancer* (1985) 55:805–28. doi: 10.1002/1097-0142(19850215)55:4<805::aid-cncr2820550419>3.0.co;2-z

51. Nikiforov YE, Erickson LA, Nikiforova MN, Caudill CM, Lloyd RV. Solid variant of papillary thyroid carcinoma: incidence, clinical-pathologic characteristics, molecular analysis, and biologic behavior. *Am J Surg Pathol* (2001) 25:1478–84. doi: 10.1097/00000478-200112000-00002

52. Furmanchuk AW, Averkin JI, Egloff B, Ruchti C, Abelin T, Schappi W, et al. Pathomorphological findings in thyroid cancers of children from the republic of Belarus: a study of 86 cases occurring between 1986 ('post-chernobyl') and 1991. *Histopathology* (1992) 21:401–8. doi: 10.1111/j.1365-2559.1992.tb00423.x

53. Nikiforov Y, Gnepp DR, Fagin JA. Thyroid lesions in children and adolescents after the Chernobyl disaster: implications for the study of radiation tumorigenesis. *J Clin Endocrinol Metab* (1996) 81:9–14. doi: 10.1210/jcem.81.1.8550800

54. Xu B, Viswanathan K, Zhang L, Edmund LN, Ganly O, Tuttle RM, et al. The solid variant of papillary thyroid carcinoma: a multi-institutional retrospective study. *Histopathology* (2022) 81(2):171–82. doi: 10.1111/his.14668

55. Solomon JP, Linkov I, Rosado A, Mullaney K, Rosen EY, Frosina D, et al. NTRK fusion detection across multiple assays and 33,997 cases: diagnostic implications and pitfalls. *Mod Pathol* (2020) 33:38–46. doi: 10.1038/s41379-019-0324-7

56. Okamura R, Boichard A, Kato S, Sicklick JK, Bazhenova L, Kurzrock R. Analysis of NTRK alterations in pan-cancer adult and pediatric malignancies: implications for NTRK-targeted therapeutics. *JCO Precis Oncol* (2018) 2018. doi: 10.1200/PO.18.00183

57. Liang J, Cai W, Feng D, Teng H, Mao F, Jiang Y, et al. Genetic landscape of papillary thyroid carcinoma in the Chinese population. *J Pathol* (2018) 244:215–26. doi: 10.1002/path.5005

58. Subbiah V, Yang D, Velcheti V, Drilon A, Meric-Bernstam F. State-of-the-Art strategies for targeting RET-dependent cancers. *J Clin Oncol* (2020) 38:1209–21. doi: 10.1200/JCO.19.02551

59. Kohno T, Tabata J, Nakaoku T. REToma: a cancer subtype with a shared driver oncogene. *Carcinogenesis* (2020) 41:123–9. doi: 10.1093/carcin/bgz184

60. Elisei R, Romei C, Vorontsova T, Cosci B, Veremeychik V, Kuchinskaya E, et al. RET/PTC rearrangements in thyroid nodules: studies in irradiated and not irradiated, malignant and benign thyroid lesions in children and adults. *J Clin Endocrinol Metab* (2001) 86:3211–6. doi: 10.1210/jcem.86.7.7678

61. Fenton CL, Lukes Y, Nicholson D, Dinauer CA, Francis GL, Tuttle RM. The ret/PTC mutations are common in sporadic papillary thyroid carcinoma of children and young adults. *J Clin Endocrinol Metab* (2000) 85:1170–5. doi: 10.1210/jcem.85.3.6472

62. Romei C, Fugazzola L, Puxeddu E, Frasca F, Viola D, Muzza M, et al. Modifications in the papillary thyroid cancer gene profile over the last 15 years. *J Clin Endocrinol Metab* (2012) 97:E1758–1765. doi: 10.1210/jc.2012-1269

63. Leeman-Neill RJ, Kelly LM, Liu P, Brenner AV, Little MP, Bogdanova TI, et al. ETV6-NTRK3 is a common chromosomal rearrangement in radiation-associated thyroid cancer. *Cancer* (2014) 120:799–807. doi: 10.1002/cncr.28484

64. Musholt TJ, Musholt PB, Khaladj N, Schulz D, Scheumann GF, Klempnauer J. Prognostic significance of RET and NTRK1 rearrangements in sporadic papillary thyroid carcinoma. *Surgery* (2000) 128:984–93. doi: 10.1067/msy.2000.110845

65. Pfeifer A, Rusinek D, Zebracka-Gala J, Czarniecka A, Chmielik E, Zembala-Nozynska E, et al. Novel TG-FGFR1 and TRIM33-NTRK1 transcript fusions in papillary thyroid carcinoma. *Genes Chromosomes Cancer* (2019) 58:558–66. doi: 10.1002/gcc.22737

66. Hong DS, DuBois SG, Kummar S, Farago AF, Albert CM, Rohrberg KS, et al. Larotrectinib in patients with TRK fusion-positive solid tumours: a pooled analysis of three phase 1/2 clinical trials. *Lancet Oncol* (2020) 21:531–40. doi: 10.1016/S1470-2045(19)30856-3

67. Wirth LJ, Sherman E, Robinson B, Solomon B, Kang H, Lorch J, et al. Efficacy of selpercatinib in RET-altered thyroid cancers. *N Engl J Med* (2020) 383:825–35. doi: 10.1056/NEJMoa2005651

frontiers | Frontiers in Endocrinology

TYPE Original Research
PUBLISHED 04 October 2023
DOI 10.3389/fendo.2023.1270796

OPEN ACCESS

EDITED BY
Juan Pablo Nicola,
National University of Cordoba, Argentina

REVIEWED BY
Ines Califano,
Instituto de Oncología Ángel H. Roffo, Argentina
Alicia Gauna,
Hospital Ramos Mejía, Argentina

*CORRESPONDENCE
Ali S. Alzahrani
aliz@kfshrc.edu.sa

RECEIVED 01 August 2023
ACCEPTED 14 September 2023
PUBLISHED 04 October 2023

CITATION
Mukhtar N, Alhamoudi K, Alswailem M, Alhindi H, Murugan AK, Alghamdi B and Alzahrani AS (2023) How do *BRAF*^{V600E} and *TERT* promoter mutations interact with the ATA and TNM staging systems in thyroid cancer? *Front. Endocrinol.* 14:1270796. doi: 10.3389/fendo.2023.1270796

How do *BRAF*^{V600E} and *TERT* promoter mutations interact with the ATA and TNM staging systems in thyroid cancer?

Noha Mukhtar[1], Kheloud Alhamoudi[2], Meshael Alswailem[2], Hindi Alhindi[3], Avaniyapuram Kannan Murugan[2], Balgees Alghamdi[2] and Ali S. Alzahrani[1,2*]

[1]Department of Medicine, King Faisal Specialist Hospital & Research Centre, Riyadh, Saudi Arabia, [2]Department of Molecular Oncology, King Faisal Specialist Hospital & Research Centre, Riyadh, Saudi Arabia, [3]Department of Pathology and Laboratory Medicine, King Faisal Specialist Hospital & Research Centre, Riyadh, Saudi Arabia

Context: The American Thyroid Association risk stratification (ATA) and the American Joint Committee on Cancer Tumor Node Metastases (TNM) predict recurrence and mortality of differentiated thyroid cancer (DTC). *BRAF*^{V600E} and *TERT* promoter mutations have been shown to correlate with the histopathological features and outcome of DTC. Our objectives were to study the correlation of these molecular markers with these clinicopathological-staging systems.

Patients and methods: We studied 296 unselected patients, 214 females and 82 males with a median age of 36 years (IQR 23.3-49.0). *BRAF*^{V600E} and *TERT* promoter mutations were tested by PCR-based Sanger sequencing. Data were extracted from medical records and analysed using Chi-Square and Fisher Exact tests and Kaplan Meier analysis.

Results: Of 296 patients tested, 137 (46.3%) had *BRAF*^{V600E}-positive tumors and 72 (24.3%) were positive for *TERT* promoter mutations. The *BRAF*^{V600E} mutation did not correlate with the ATA and TNM staging, being non-significantly different in various stages of these systems and did not predict the development of persistent disease (PD) (*P* 0.12). Unlike *BRAF*^{V600E}, *TERT* promoter mutations were more frequent in the ATA high-risk than in intermediate- or low-risk tumors (P 0.006) and in TNM stages III and IV than lower stages (*P* <0.0001). *TERT* promoter mutations also predicted the outcome, being present in 37.2% of patients with PD compared to only 15.4% in those without evidence of disease (*P* <0.0001). The same pattern was also seen when *BRAF*^{V600E} and *TERT* promoter mutations were combined.

Conclusion: *TERT* promoter mutations alone or in combination with *BRAF*^{V600E} mutation, but not *BRAF*^{V600E} mutation alone, correlated well with the ATA and TNM staging and predicted development of PD, especially in higher stages of these systems.

KEYWORDS

thyroid cancer, differentiated thyroid cancer, *BRAF*^{V600E}, *TERT* promoter mutations, risk stratifications

1 Introduction

Differentiated thyroid cancer (DTC) has been increasingly diagnosed over the past four decades (1). This increase in incidence is largely attributable to improved diagnostic tools, particularly the widespread use of neck ultrasonography (1, 2). As a result, many small tumors with low risk of metastasis, recurrence, and mortality have been detected (3). This fact led to a more conservative approach to the management of DTC based on risk stratification (4, 5). Currently, several risk stratification systems are available for risk-based management planning (6–9). Two of the most widely used systems are the American Thyroid Association (ATA) and the American Joint Committee on Cancer Tumor Node and Metastasis (AJCC TNM) risk stratification systems (7, 8). The ATA system predicts risk of DTC recurrence, while the TNM system predicts risk of DTC-related mortality (6, 7, 9). Both systems have been well validated and are routinely used in clinical practice and research communications (9–11).

Advances in understanding the molecular pathogenesis of DTC have paralleled better understanding of its clinical behavior and outcome and the development of risk stratification systems (12–17). These advances in molecular genetics led to development of diagnostic tests and therapeutic agents for patients with thyroid nodules and advanced thyroid cancer, respectively (14, 18–20). The use of molecular markers for prognostication of DTC has also been studied but remains controversial and less mature than diagnostic and therapeutic advances (7, 21, 22). One of the earliest discoveries is the *BRAF*^{V600E} mutation as a major oncogenic driver in papillary thyroid cancer (PTC) and to a lesser extent in poorly differentiated (PDTC) and anaplastic thyroid cancer (ATC) (15, 23, 24). Several studies have shown a strong association between *BRAF*^{V600E} mutation and aggressive histopathological features of DTC (25–28). However, others questioned its prognostic value (29, 30). More recently, *TERT* promoter mutations (C250T and C228T) were discovered as strong oncogenic drivers in many types of thyroid cancer (31–33). They occur in approximately 10% of well-differentiated PTC but are increasingly commoner in the more aggressive types such as PDTC and ATC (13). Although these mutations are associated with aggressive histopathological features and worse outcome of DTC, especially when they co-occur with *BRAF*^{V600E} or *RAS* mutations (34, 35), their use as prognostic markers is not yet widely accepted (7). The 2015 ATA guidelines acknowledge the potential prognostic value of *BRAF*^{V600E} and *TERT* promoter mutations but do not fully endorse it or routinely recommend it (7). To further study the potential relationship between the clinicopathological staging systems and the driver mutations of DTC, we hypothesized that these mutations are more prevalent in higher ATA and TNM stages than the low-risk stages and that they may contribute further to risk stratification in different stages of these systems. For these reasons, we studied a cohort of patients with DTC in whom *BRAF*^{V600E} and *TERT* promoter mutations have been tested and assessed their relationships with the ATA and TNM risk stratification systems. Specifically, we assessed the prevalence of *BRAF*^{V600E} and *TERT* promoter mutations in different ATA and TNM stages and analysed their potential incremental prognostic value over these risk stratification systems.

2 Patients and methods

An Institutional Review Board (IRB) approval was obtained from the Office of Research Affairs, King Faisal Specialist Hospital and Research Centre, Riyadh Saudi Arabia (ORA # 2020-1514) with a waiver of consent to use archived Formalin Fixed Paraffin Embedded (FFPE) samples for mutation testing. We isolated tumor DNA, performed PCR and directly sequenced exon 15 of *BRAF* gene and the *TERT* promoter using the Dideoxy Chain Termination method. The DNA isolation, PCR primers and conditions, and the Sanger sequencing methods for *BRAF*^{V600E} and *TERT* promoter mutations have been previously described (36–38). A total of 296 unselected DTC patients in whom *BRAF*^{V600E} and *TERT* promoter mutations were available have been included in this study. Data on their demographics, histopathological data, ATA and TNM staging, management and outcome were obtained from their medical records. The outcome was assessed based on definitions included in the 2015 ATA guidelines (7). An excellent response (175 patients) was defined as absence of any evidence of disease with suppressed serum thyroglobulin (Tg) < 0.2 ng/dl and/or stimulated Tg < 1 ng/dl in the absence of Tg antibodies and negative imaging studies. Persistent disease included patients with structurally incomplete, biochemically incomplete and indeterminate response to therapy statuses as defined in the ATA guidelines for DTC (7).

2.1 Statistical methods

We expressed continuous variables as medians and interquartile ranges and categorical variables as rates, proportions and percentages. Fisher Exact and X^2- tests were used for analysis of categorical variables and T test for continuous variables. Kaplan Meier survival analysis was used to analyse outcome over time stratified by ATA or TNM stages or presence or absence of *BRAF*^{V600E} mutation and/or *TERT* promoter mutations. Disease-free survival is the time between the initial thyroid surgery and diagnosis of indeterminate, biochemically or structurally incomplete response (evidence of disease). A P value < 0.05 was considered significant.

3 Results

3.1 Clinicopathological characteristics

We studied 296 patients, 214 (73.3%) females, 82 (27.7%) males (F:M ratio 2.6:1) with a median age of 36 years (IQR 23.25-49 years). *BRAF*^{V600E} mutation was significantly more prevalent in patients ≥ 55 years (29/45, 62%) than in those less than 55 years of

10.3389/fendo.2023.1270796

age (109/251, 43.3%), *P* 0.03. Similarly, *TERT* promoter mutations were more prevalent in patients ≥ 55 years (28/45, 64.4%) than in those less than 55 years of age (43/251, 17%), *P* <0.0001. The histopathological characteristics, management and outcome are summarized in Table 1. The median follow up was 7.6 years (Interquartile range 5.25-10.1)

3.2 ATA and TNM risk stratification systems predict outcome of DTC

As demonstrated in many previous studies, in this study, the ATA and TNM risk stratification systems predict the outcome (Table 2 and Figure 1). Persistent disease increases from 19.8% in ATA low-risk to 72% in the high-risk classes (P<0.0001). Similarly, persistent disease increases from 31.3% in TNM stage I to 95% in stage IV (p <0.0001), (Table 2). Kaplan Meier analysis shows significant differences in the disease-free survival between different ATA and TNM stages (Figure 1). Of six patients who died due to DTC, five were ATA high grade and one ATA intermediate grade. Two were in TNM stage 2, two in stage 3 and two in stage 4.

TABLE 1 The clinical and pathological features, staging and outcome of 296 DTC patients.

Characteristic	Median and IQR or No. (%)
Median age (IQR), years	36 (23.25-49)
Sex F:M	214:82
Tumor type Classic papillary thyroid cancer (PTC) Follicular variant PTC Tall cell variant PTC Diffuse sclerosing PTC Follicular thyroid cancer Oncocytic (Hurthle) cell cancer	 181 (61) 62 (21) 34 (11.5) 8 (2.7) 7 (2.4) 4 (1.4)
Median Tumor size (range) cm	2.5 (1.65-4.5)
Tumor multifocality	188 (63.5)
Extra-thyroidal extension	152 (51.4)
Lymphovascular invasion	97 (32.8)
Lymph node metastases	192 (64.9)
Distant metastases	47 (15.9)
ATA risk stratification Low risk Intermediate Risk High risk	 96 (32.4) 125 (42.2) 75 (25.3
TNM stages I II III IV	 99 (33.4) 150 (50.7) 27 (9.1) 20 (6.8)
Received radioactive iodine-131	259 (87.5%)
Median administered activity	123 mCi (100-150)
Received additional therapies	95 (32%)
Outcome No evidence of disease (Excellent response) Persistent disease (Indeterminate response, biochemically and structurally incomplete)	 175 (59) 121 (41)

3.3 *BRAF*^{V600E} mutation does not correlate with ATA and TNM staging

Of 296 patients tested, 137 (46.3%) had *BRAF*^{V600E}-positive tumors while 159 patients (53.7%) had wild-*BRAF* tumors. *BRAF*^{V600E} was positive in 92 of 181 (50.8%) conventional PTC, 18 of 62 (29%) follicular variant PTC (FVPTC), 25 of 34 (73.5%) tall cell varia PTC (TCPTC) and 2 of 8 (25%) diffuse sclerosing PTC (DSPTC). *BRAF*^{V600E} mutation did not correlate with the ATA and TNM staging. As seen in Table 3, the rates of the mutation were not significantly different between low and higher stages. *BRAF*^{V600E} also did not predict the outcome (Table 4 and Figure 1) with no difference in the rates of *BRAF*^{V600E} mutation between those who achieved an excellent response (42.3%) and those who had a persistent disease (52.1%) (*P* 0.12), (Table 4). Six patients died of DTC in this cohort, four of them were *BRAF*^{V600E} mutation-positive.

3.4 *TERT* promoter mutations correlate with the ATA and TNM staging and predict outcome

TERT promoter mutations, C250T (9 tumors) and C228T (63 tumors) were found in tumors of 72 patients (24.3%). *TERT* promoter mutations were positive in 40/181 (22.1%) conventional PTC, 17/62 (27.4%) FVPTC, 9/34 (26.5%) TCPTC, 2/8 (25%) DSPTC, 3/7 (43%) follicular thyroid cancer (FTC) and ¼ (25%) Oncocytic thyroid cancer. Unlike *BRAF*^{V600E} mutations, *TERT* promoter mutations were more frequent in the ATA high-risk (37.3%) than in intermediate- (17.6%) or low-risk tumors (22.9%) (*P* 0.007) (Table 3). More clearly is the higher prevalence of *TERT* promoter mutations in TNM stage IV (75%) than lower stages (Table 3). *TERT* promoter mutations also predicted the outcome, being present in 37.2% of patients with persistent disease compared to only 15.4% in those without evidence of disease (*P* <0.0001) (Table 4 and Figure 1). *TERT* promoter mutations were significantly more frequent in patients with structurally incomplete disease than other response to therapy status groups, being positive in only 19/175 (10.9%) in excellent response, 3/54 (5.6%) of indeterminate response, 3/14 (21.4%) of biochemically incomplete and 13/53 (24.5%) of structurally incomplete response (P <0.0001) (Table 5). Of six patients who died due to DTC, five (83%) were positive for *TERT* promoter mutations.

In a multivariate logistic regression model that included *BRAF*^{V600E} mutation, *TERT* promoter mutations, age at diagnosis, tumor size, ATA stage and TNM stage, *TERT* promoter mutations remain a significant predictor of persistent disease (*P* 0.01, odds ratio 2.7, 95% CI 1.2-5.9).

TABLE 2 Outcome of DTC in different ATA and TNM stages showing more persistent thyroid cancer in higher stages.

ATA risk group	NED No. (%)	PD No. (%)	*P* value
Low risk	77 (80.2)	19 (19.8)	<0.0001
Intermediate risk	77 (64)	48 (38.4)	
High risk	21 (28.0)	54 (72.0)	
TNM stages			
I	68 (68.7)	31 (31.3)	<0.001
II	97 (64.7)	53 (35.3)	
III	9 (33.3)	18 (66.7)	
IV	1 (5)	19 (95)	
Total	**175 (59)**	**121 (41)**	

NED, no evidence of disease; PD, persistent disease.

3.5 Combination of *BRAF*^{V600E} and TERT promoter mutations correlate with the ATA and TNM staging and predict outcome of DTC

The combination of *BRAF*^{V600E} mutation and a *TERT* promoter mutation occurred in 34 cases (11.5%) and correlated well with high-risk ATA and higher TNM stages (Table 6). This combination occurred in 21.3% in high-risk ATA class compared to 8.8% and 7.3% in intermediate and low-risk stages, respectively (*P* 0.006, Table 6). It also occurred in 45% of TNM stage IV compared to 7.4%, 14.7% and 1% in stages III, II, and I, respectively ($P < 0.0001$) (Table 6). Of 34 cases that had this combination of *BRAF*^{V600E}/mutated *TERT*, 26 (76.5%) continued to have persistent disease compared to only 8 (23.5%) in excellent response (P <0.0001) (Table 4). The percentages of patients with persistent disease increased progressively from 12.8% in patients with ATA low-risk and no mutations to 100% in patients with ATA high-risk with positive *BRAF*^{V600E}/*TERT* promoter mutations (Table 7). Similarly, persistent disease increased progressively from 26.4% in stage I without *BRAF*^{V600E} or *TERT* promoter mutations to 100% in stage IV disease with positive *BRAF*^{V600E}/*TERT* promoter mutations

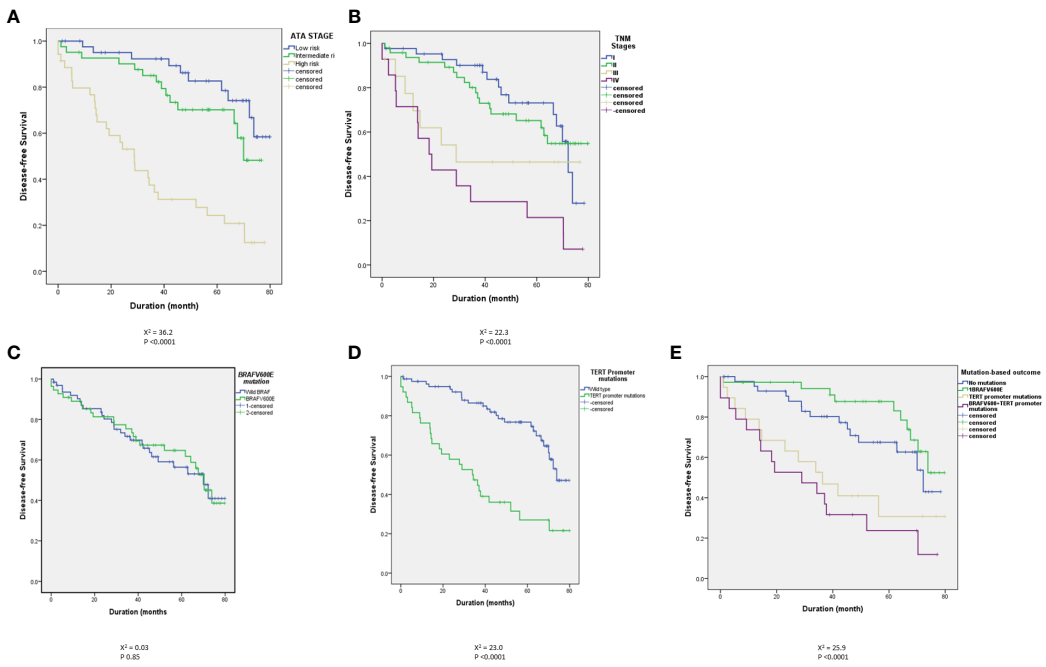

FIGURE 1
Kaplan Meier curves showing a clear and significant separation of disease-free survival (DFS) between different ATA stages **(A)** and different TNM stages **(B)**. There was no statistically significant difference between *BRAF*^{V600E}-positive and wild *BRAF* tumors **(C)** but there are statistically significant differences between *TERT* promoter mutation-positive tumors and tumors with wild type *TERT* promoter in the absence **(D)** or presence **(E)** of concomitant *BRAF*^{V600E} mutation.

10.3389/fendo.2023.1270796

TABLE 3 The prevalence of *BRAF*^{V600E} and *TERT* promoter mutations in different ATA and TNM stages.

	Wild *BRAF* No. (%)	*BRAF*^{V600E} No. (%)	P value	Wild *TERT* No. (%)	*TERT* promoter No. (%)	P value
ATA staging						
Low risk	54 (56.2)	42 (43.8)	0.33	74 (77.1)	22 (22.9)	0.007
Intermediate risk	61 (48.8)	64 (51.2)		103 (82.4)	22 (17.6)	
High risk	44 (58.7)	31 (41.3)		47 (62.7)	28 (37.3)	
TNM staging						
I	55 (55.6)	44 (44.4)	0.41	96 (97.0)	3 (3.0)	<0.001
II	77 (51.3)	73 (48.7)		104 (69.3)	46 (30.7)	
III	18 (66.7)	9 (33.3)		19 (70.4)	8 (29.6)	
IV	9 (45)	11 (55)		5 (25)	15 (75)	

(Table 7). In fact, all patients (100%) with *BRAF*^{V600E} and *TERT* promoter mutation combination who are in ATA high-risk or TNM stage IV groups continued to have persistent disease (Table 7). The combination of *TERT* promoter/*BRAF*^{V600E} mutations were significantly more frequent in patients with biochemically and structurally incomplete disease than other response to therapy status groups being positive in only 8/175 (4.6%) in excellent response, 5/54 (9.3%) of indeterminate response, 6/14 (42.9%) of biochemically incomplete and 15/53 (28.3%) of structurally incomplete response (P <0.0001).

4 Discussion

The ATA and TNM staging systems predict risk of recurrence and mortality, respectively (7–9). *BRAF*^{V600E} and *TERT* promoter mutations have also been shown to predict risk of recurrence and mortality (26, 33, 39, 40). However, the relationship between these histopathological systems and molecular markers is not clear. In this study, we tried to analyse this potential relationship. Our findings confirm the previously shown high accuracy of the ATA and TNM staging systems in predicting the outcome (persistent disease) (7, 9) and lack of an association between *BRAF*^{V600E} and these staging systems and the DTC outcome. However, the main finding of this study is the strong association between *TERT* promoter mutations and the ATA and TNM staging systems, and the high prognostic value of these mutations in isolation or in combination with *BRAF*^{V600E} mutation in predicting the outcome of DTC, especially in the high ATA and TNM stages. The occurrence of these mutations in ATA high-risk or TNM stage IV tumors was associated with 100% chance of persistent disease. This suggests that *TERT* promoter mutations± *BRAF*^{V600E} mutation identify a subgroup of patients in the high-risk ATA or TNM who have an extremely high risk of persistent disease. This group may need more proactive management and follow up approaches.

The association between *TERT* promoter mutations and aggressive histopathological features and outcome of DTC has been reported in several studies from different parts of the World. Similar to our study, a meta-analysis that included 11 studies and 3911 patients showed a graded risk of DTC based on the presence or absence of *TERT* promoter mutations and *BRAF*^{V600E} mutation with the highest risk in DTC harboring both types of mutations followed by DTC with *TERT* mutation alone, *BRAF*^{V600E} mutation and no mutation (41). In a more recent meta-analysis that included 51 studies with 11,382 patients from different populations, *TERT* promoter mutations were found in 10.9% of DTC in general and in 10.6% of PTC and 15.1% of FTC. In PTC, *TERT* promoter mutations were significantly associated with sex, age, tumor size, vascular invasion, extrathyroidal extension, lymph node and distant metastases, persistence/recurrence, and disease-specific mortality. Similarly, in FTC, *TERT* promoter mutations were significantly associated with age, distant metastases, advanced TNM stage, persistence/recurrence, and disease-specific mortality (42).

In another recent meta-analysis that looked at risk factors for development of radioiodine refractory thyroid cancer (RAIR), Luo Y. et al. included 13 studies with 1431 patients, of whom 603 were patients with RAIR. *TERT* and *BRAF*^{V600E} mutations, extrathyroidal extensions and high-grade histopathological

TABLE 4 Outcome of DTC with respect to *BRAF*^{V600E}, *TERT* promoter mutations or both.

	Total No. (%)	NED No. (%)	PD No. (%)	P value
BRAF^{V600E} mutation	137 (46.3)	74/175 (42.3)	63/121 (52.1)	0.12
TERT promoter mutations	72 (24.3)	27/175 (15.4)	45/121 (37.2)	<0.0001
BRAF^{V600E}+*TERT* promoter mutations	34 (11.5)	8/175 (4.9)	26/121 (21.5)	<0.0001

NED, no evidence of disease; PD, persistent disease.

10.3389/fendo.2023.1270796

TABLE 5 The outcome of 296 patients with DTC and its relationship to *BRAF*^{V600} and *TERT* promoter mutations.

	Excellent response No. (%)	Indeterminate response No. (%)	Biochemically incomplete No. (%)	Structurally incomplete No. (%)	P value
BRAF Wild type	101 (57.7)	23 (42.6)	5 (35.7)	30 (56.6)	0.12
***BRAF*^{V600E}**	74 (42.3)	31 (57.4)	9 (64.3)	23 (43.4)	
***TERT* wild type**	148 (84.6)	46 (85.2)	5 (35.7)	25 (47.2)	<0.0001
***TERT* promoter mutated**	27 (15.4)	8 (14.8)	9 (64.3)	28 (52.8)	
Total	**175**	**54**	**14**	**53**	**296**

thyroid cancer subtypes were associated with increased risk of development of RAIR (43).

Over the past 3 decades, several staging systems have been proposed and validated (6, 8, 9). Although most of the old systems were designed to predict mortality of DTC, mortality is very low in DTC (2). On the other hand, persistent/recurrent DTC is common occurring in approximately 20-30% of patients (7, 44). Currently, the ATA risk stratification system, which encompasses several histopathological tumor features, is the most widely used system for predicting recurrence of DTC (7). It considers risk of DTC recurrence as a continuum but also classifies DTC into low-, intermediate- and high risk for recurrence (7, 45). Several studies have shown the robustness of this system for predicting recurrence and it is currently the most widely used system in clinical practice

TABLE 6 Rates of different combinations of *BRAF*^{V600E} and *TERT* promoter mutations in different ATA and TNM stages.

Stage (Number of patients)	Wild *BRAF*/ wild *TERT* No. (%)	*BRAF*^{V600E}/ wild *TERT* No. (%)	Wild *BRAF*/ Mutated *TERT* No. (%)	*BRAF*^{V600E}/ mutated *TERT* No. (%)	P value
ATA staging					
Low-risk (96)	39 (40.6)	35 (36.5)	15 (15.6)	7 (7.3)	0.006
Intermediate risk (125)	50 (40.0)	53 (42.4)	11 (8.8)	11 (8.8)	
High-risk (75)	32 (42.7)	15 (20.0)	12 (16)	16 (21.3)	
TNM staging					
I (99)	53 (53.5)	43 (43.4)	2 (2.0)	1 (1.0)	<0.0001
II (150)	53 (35.3)	51 (34.0)	24 (16.0)	22 (14.7)	
III (27)	12 (44.4)	7 (25.9)	6 (22.2)	2 (7.4)	
IV (20)	3 (15.0)	2 (10.0)	6 (30)	9 (45.0)	

TABLE 7 Number of cases with persistent disease/total number (%) in each ATA and TNM stage categorized by the presence and type of mutation.

Stage	No mutations No. (%)	*BRAF only* No. (%)	*TERT only* No. (%)	*BRAF/TERT* No. (%)	Total
ATA stages					P <0.0001
Low	5/39 (12.8)	9/35 (25.7)	3/15 (20)	2/7 (28.6)	19/96 (19.8)
Intermediate	16/50 (32.0)	20/53 (37.7)	4/11 (36.4)	8/11 (72.7)	48/125 (38.4)
High	18/32 (56.2)	8/15 (53.3)	12/12 (100)	16/16 (100)	54/75 (72.0)
TNM stage					P <0.0001
I	14/39 (26.4)	16/43 (37.0)	1/2 (50.0)	0/1 (0)	31/99 (31.3)
II	15/53 (28.5)	16/35 (31.4)	7/24 (29.2)	15/22 (68.5)	53/150 (35.3)
III	7/12 (58.3)	4/7 (57.1)	5/6 (83.3)	2/2 (100)	18/27 (66.7)
IV	3/3 (100)	1/2 (50.0)	6/6 (100)	9/9 (100)	19/20 (95)

and research communication (10, 11, 46, 47). The AJCC TNM system is one of the mortality-predicting staging systems and is based on age and several histopathological features including tumor size, extrathyroidal invasion, lymph node and distant metastasis (8, 48). It has also been shown to be highly reliable in predicting cancer-specific mortality (8, 48).

The significant progress that took place in the field of molecular genetics of DTC was also translated in clinical practice to diagnostic tests for indeterminate thyroid nodules and therapeutic agents for progressive radioactive iodine refractory thyroid cancer (49–51). Due to conflicting studies and variable behavior of DTC carrying *BRAF*^{V600E} or *TERT* promoter mutations, the use of these genetic markers in predicting the course and outcome of DTC remain controversial (7, 22, 52). In fact, the 2015 ATA thyroid cancer guidelines acknowledged the potential roles of these genetic markers for prognostication but did not fully endorse them as a basis for intensity of the management and follow up of patients with DTC (7).

Since the ATA and TNM staging systems are clinicopathological systems for predicting the outcome and *BRAF*^{V600E} and *TERT* promoter mutations are potential predictors of outcome, we undertook this study to assess any potential relationship between these clinicopathological and molecular predictors of prognosis. Specifically, we aimed to study whether *BRAF*^{V600E} and/or *TERT* promoter mutations may add incremental prognostic value to the ATA and TNM staging systems. Our results suggest that *BRAF*^{V600E} does not correlate with the ATA or TNM staging systems and does not predict the outcome alone. However, *TERT* promoter mutations alone or in combination with *BRAF*^{V600E} mutation have significant correlation with the ATA and TNM risk stratification systems and are predictive of disease-free survival and persistent/recurrent disease, especially in high-stage DTC. In patients with ATA high-risk group and TNM stage IV, the presence of *TERT* promoter alone or in combination with *BRAF*^{V600E} predicts a very high probability of persistent disease. These results are in agreement with several studies that have shown a strong impact of *TERT* promoter mutations on the DTC behavior and outcome, especially when they co-occur with *BRAF*^{V600E} mutation (33–36). However, our study also joins several previous studies that casted doubts on the prognostic role of *BRAF*^{V600E} mutation alone (21, 29, 30, 39, 53). While there is no doubt about the strong oncogenic role of *BRAF*^{V600E}, its final impact on the DTC behavior is probably influenced by other histopathological features and the stage of the disease (39, 53). The strong synergistic effect of *TERT* promoter mutations on tumors that also harbor *BRAF*^{V600E} mutation is clear (34, 35) and it is possible that old studies that showed a strong prognostic impact of *BRAF*^{V600E} mutation were enriched by then the unknown *TERT* promoter mutations. In other words, it is possible that studies that showed a strong prognostic role of *BRAF*^{V600E} had high rates of *TERT* promoter mutations, which were not known to occur in DTC at the time of these old studies before 2013.

Our study has strengths and weaknesses. It included a good sample size from a single institution with uniform practice. However, the sample size is still relatively small for the study of an association. Reassuring in this study about the sample representation of DTC is the fact that the patients' characteristics, the histopathological features, the rates of *BRAF*^{V600E} and *TERT* promoter mutations and the distribution of patients between different ATA and TNM risk classes are the usual spectrum of DTC seen in most centers. The clinic pathological features are similar to a previous descriptive study in which we characterized DTC in Saudi population (54). Notably, the median age in our population (36 years) is younger than the median age of the SEER data (51 years) and the rate of distant metastases is high. These are similar in this study to our previous publication (54) and a more comprehensive recent study that looked at thyroid cancer in Saudi Arabia over the last 30 years (55). The rate of *TERT* promoter mutations is also relatively higher in our study than The Cancer Genome Atlas (TCGA) database but this latter contained only well differentiated PTC and our study contained a significant number of patients with tall cell subtype of PTC and other DTC types accounting for the relatively high *TERT* promoter mutation.

In summary, we have shown that *BRAF*^{V600E} alone does not correlate with the widely used ATA and TNM staging systems while *TERT* promoter mutations alone or in combination with *BRAF*^{V600E} do correlate with these systems and predict DTC outcome. Their presence in higher stages of these risk stratification systems is associated with a very high risk of persistent disease and probably worse outcome. Further studies with larger sample size, preferably multi institutional, are needed to assess the incremental prognostic value of these molecular markers over the current ATA and TNM risk stratification systems.

Data availability statement

The original contributions presented in the study are included in the article/supplementary material. Further inquiries can be directed to the corresponding author.

Ethics statement

The studies involving humans were approved by Office of Research Affairs, King Faisal Specialist Hospital & Research Centre, Riyadh, Saudi Arabia. The studies were conducted in accordance with the local legislation and institutional requirements. The ethics committee/institutional review board waived the requirement of written informed consent for participation from the participants or the participants' legal guardians/next of kin because we only used archived paraffin block without any direct contact with the patients and the data were kept anonymous.

Author contributions

NM: Data curation, Writing – review & editing. KA: Data curation, Writing – review & editing. MA: Data curation, Methodology, Writing – review & editing. HA-H: Methodology, Writing – review & editing, Resources. AM: Data curation, Writing – review & editing. BA: Data curation, Methodology, Writing –

review & editing. AA: Methodology, Conceptualization, Formal Analysis, Writing – original draft.

Funding

The authors declare that no financial support was received for the research, authorship, and/or publication of this article.

Acknowledgments

We would like to thank our colleagues in the Section of Endocrinology and Department of Molecular Oncology for their support.

Conflict of interest

The authors declare that the research was conducted in the absence of any commercial or financial relationships that could be construed as a potential conflict of interest.

Publisher's note

References

1. Miranda-Filho A, Lortet-Tieulent J, Bray F, Cao B, Franceschi S, Vaccarella S, et al. Thyroid cancer incidence trends by histology in 25 countries: a population-based study. *Lancet Diabetes Endocrinol* (2021) 9:225–34. doi: 10.1016/S2213-8587(21)00027-9

2. Pizzato M, Li M, Vignat J, Laversanne M, Singh D, La Vecchia C, et al. The epidemiological landscape of thyroid cancer worldwide: GLOBOCAN estimates for incidence and mortality rates in 2020. *Lancet Diabetes Endocrinol* (2022) 10:264–72. doi: 10.1016/S2213-8587(22)00035-3

3. Shih P, Nickel B, Degeling C, Thomas R, Brito JP, Mcleod DSA, et al. Terminology change for small low-risk papillary thyroid cancer as a response to overtreatment: Results from three Australian community juries. *Thyroid* (2021) 31:1067–75. doi: 10.1089/thy.2020.0694

4. Ito Y, Miyauchi A, Oda H. Low-risk papillary microcarcinoma of the thyroid: A review of active surveillance trials. *Eur J Surg Oncol* (2018) 44:307–15. doi: 10.1016/j.ejso.2017.03.004

5. Smulever A, Pitoia F. Conservative management of low-risk papillary thyroid carcinoma: a review of the active surveillance experience. *Thyroid Res* (2023) 16:6. doi: 10.1186/s13044-023-00148-6

6. Lang BH, Lo CY, Chan WF, Lam KY, Wan KY. Staging systems for papillary thyroid carcinoma: a review and comparison. *Ann Surg* (2007) 245:366–78. doi: 10.1097/01.sla.0000250445.92336.2a

7. Haugen BR, Alexander EK, Bible KC, Doherty GM, Mandel SJ, Nikiforov YE, et al. 2015 American thyroid association management guidelines for adult patients with thyroid nodules and differentiated thyroid cancer: The American thyroid association guidelines task force on thyroid nodules and differentiated thyroid cancer. *Thyroid* (2016) 26:1–133. doi: 10.1089/thy.2015.0020

8. Tuttle RM, Haugen B, Perrier ND. *Updated American Joint Committee on cancer/tumor-node-metastasis staging system for differentiated and anaplastic thyroid cancer: what changed and why?* 140 Huguenot Street, 3rd Floor New Rochelle, NY 10801 USA: Mary Ann Liebert, Inc (2017).

9. Tuttle RM, Alzahrani AS. Risk stratification in differentiated thyroid cancer: From detection to final follow-up. *J Clin Endocrinol Metab* (2019) 104:4087–100. doi: 10.1210/jc.2019-00177

10. Wijewardene A, Gill AJ, Gild M, Learoyd DL, Glover AR, Sywak M, et al. A retrospective cohort study with validation of predictors of differentiated thyroid cancer outcomes. *Thyroid* (2022) 32:1201–10. doi: 10.1089/thy.2021.0563

11. Wu J, Hu XY, Ghaznavi S, Kinnear S, Symonds CJ, Grundy P, et al. The prospective implementation of the 2015 ATA guidelines and modified ATA recurrence risk stratification system for treatment of differentiated thyroid cancer in a canadian tertiary care referral setting. *Thyroid* (2022) 32:1509–18. doi: 10.1089/thy.2022.0055

12. Xing M. Molecular pathogenesis and mechanisms of thyroid cancer. *Nat Rev Cancer* (2013) 13:184–99. doi: 10.1038/nrc3431

13. Cancer Genome Atlas Research, N. Integrated genomic characterization of papillary thyroid carcinoma. *Cell* (2014) 159:676–90. doi: 10.1016/j.cell.2014.09.050

14. Fagin JA, Wells SA Jr. Biologic and clinical perspectives on thyroid cancer. *N Engl J Med* (2016) 375:1054–67. doi: 10.1056/NEJMra1501993

15. Landa I, Ibrahimpasic T, Boucai L, Sinha R, Knauf JA, Shah RH, et al. Genomic and transcriptomic hallmarks of poorly differentiated and anaplastic thyroid cancers. *J Clin Invest* (2016) 126:1052–66. doi: 10.1172/JCI85271

16. Riesco-Eizaguirre G, Santisteban P. ENDOCRINE TUMOURS: Advances in the molecular pathogenesis of thyroid cancer: lessons from the cancer genome. *Eur J Endocrinol* (2016) 175:R203–217. doi: 10.1530/EJE-16-0202

17. Volante M, Lam AK, Papotti M, Tallini G. Molecular pathology of poorly differentiated and anaplastic thyroid cancer: What do pathologists need to know? *Endocr Pathol* (2021) 32:63–76. doi: 10.1007/s12022-021-09665-2

18. Nishino M. Molecular cytopathology for thyroid nodules: A review of methodology and test performance. *Cancer Cytopathol* (2016) 124:14–27. doi: 10.1002/cncy.21612

19. Cabanillas ME, Ryder M, Jimenez C. Targeted therapy for advanced thyroid cancer: Kinase inhibitors and beyond. *Endocr Rev* (2019) 40:1573–604. doi: 10.1210/er.2019-00007

20. Hernando J, Ros J, Arroyo A, Capdevila J. Clinical and translational challenges in thyroid cancer. *Curr Med Chem* (2020) 27:4806–22. doi: 10.2174/0929867327666200214125712

21. Tallini G, De Biase D, Durante C, Acquaviva G, Bisceglia M, Bruno R, et al. BRAF V600E and risk stratification of thyroid microcarcinoma: a multicenter pathological and clinical study. *Mod Pathol* (2015) 28:1343–59. doi: 10.1038/modpathol.2015.92

22. Censi S, Barollo S, Grespan E, Watutantrige-Fernando S, Manso J, Iacobone M, et al. Prognostic significance of TERT promoter and BRAF mutations in TIR-4 and TIR-5 thyroid cytology. *Eur J Endocrinol* (2019) 181:1–11. doi: 10.1530/EJE-19-0073

23. Cohen Y, Xing M, Mambo E, Guo Z, Wu G, Trink B, et al. BRAF mutation in papillary thyroid carcinoma. *J Natl Cancer Inst* (2003) 95:625–7. doi: 10.1093/jnci/95.8.625

24. Pozdeyev N, Gay LM, Sokol ES, Hartmaier R, Deaver KE, Davis S, et al. Genetic analysis of 779 advanced differentiated and anaplastic thyroid cancers. *Clin Cancer Res* (2018) 24:3059–68. doi: 10.1158/1078-0432.CCR-18-0373

25. Xing M. BRAF mutation in thyroid cancer. *Endocr Relat Cancer* (2005) 12:245–62. doi: 10.1677/erc.1.0978

26. Xing M. BRAF mutation in papillary thyroid cancer: pathogenic role, molecular bases, and clinical implications. *Endocr Rev* (2007) 28:742–62. doi: 10.1210/er.2007-0007

27. Tufano RP, Teixeira GV, Bishop J, Carson KA, Xing M. BRAF mutation in papillary thyroid cancer and its value in tailoring initial treatment: a systematic review and meta-analysis. *Med (Baltimore)* (2012) 91:274–86. doi: 10.1097/MD.0b013e31826a9c71

28. Pak K, Suh S, Kim SJ, Kim IJ. Prognostic value of genetic mutations in thyroid cancer: a meta-analysis. *Thyroid* (2015) 25:63–70. doi: 10.1089/thy.2014.0241

29. Soares P, Sobrinho-Simoes M. Cancer: Small papillary thyroid cancers–is BRAF of prognostic value? *Nat Rev Endocrinol* (2011) 7:9–10. doi: 10.1038/nrendo.2010.213

30. Zurnadzhy L, Bogdanova T, Rogounovitch TI, Ito M, Tronko M, Yamashita S, et al. The BRAF(V600E) mutation is not a risk factor for more aggressive tumor behavior in radiogenic and sporadic papillary thyroid carcinoma at a young age. *Cancers (Basel)* (2021) 13:6038. doi: 10.3389/fmed.2022.882727

31. Landa I, Ganly I, Chan TA, Mitsutake N, Matsuse M, Ibrahimpasic T, et al. Frequent somatic TERT promoter mutations in thyroid cancer: higher prevalence in advanced forms of the disease. *J Clin Endocrinol Metab* (2013) 98:E1562–1566. doi: 10.1210/jc.2013-2383

32. Liu X, Bishop J, Shan Y, Pai S, Liu D, Murugan AK, et al. Highly prevalent TERT promoter mutations in aggressive thyroid cancers. *Endocr Relat Cancer* (2013) 20:603–10. doi: 10.1530/ERC-13-0210

33. Liu R, Xing M. TERT promoter mutations in thyroid cancer. *Endocr Relat Cancer* (2016) 23:R143–155. doi: 10.1530/ERC-15-0533

34. Xing M, Liu R, Liu X, Murugan AK, Zhu G, Zeiger MA, et al. BRAF V600E and TERT promoter mutations cooperatively identify the most aggressive papillary thyroid cancer with highest recurrence. *J Clin Oncol* (2014) 32:2718–26. doi: 10.1200/JCO.2014.55.5094

35. Song YS, Lim JA, Choi H, Won JK, Moon JH, Cho SW, et al. Prognostic effects of TERT promoter mutations are enhanced by coexistence with BRAF or RAS mutations and strengthen the risk prediction by the ATA or TNM staging system in differentiated thyroid cancer patients. *Cancer* (2016) 122:1370–9. doi: 10.1002/cncr.29934

36. Qasem E, Murugan AK, Al-Hindi H, Xing M, Almohanna M, Alswailem M, et al. TERT promoter mutations in thyroid cancer: a report from a Middle Eastern population. *Endocr Relat Cancer* (2015) 22:901–8. doi: 10.1530/ERC-15-0396

37. Murugan AK, Qasem E, Al-Hindi H, Shi Y, Alzahrani AS. Classical V600E and other non-hotspot BRAF mutations in adult differentiated thyroid cancer. *J Transl Med* (2016) 14:204. doi: 10.1186/s12967-016-0958-x

38. Alzahrani AS, Murugan AK, Qasem E, Alswailem M, Al-Hindi H, Shi Y. Single point mutations in pediatric differentiated thyroid cancer. *Thyroid* (2017) 27:189–96. doi: 10.1089/thy.2016.0339

39. Xing M, Alzahrani AS, Carson KA, Viola D, Elisei R, Bendlova B, et al. Association between BRAF V600E mutation and mortality in patients with papillary thyroid cancer. *JAMA* (2013) 309:1493–501. doi: 10.1001/jama.2013.3190

40. Xing M, Alzahrani AS, Carson KA, Shong YK, Kim TY, Viola D, et al. Association between BRAF V600E mutation and recurrence of papillary thyroid cancer. *J Clin Oncol* (2015) 33:42–50. doi: 10.1200/JCO.2014.56.8253

41. Vuong HG, Altibi AMA, Duong UNP, Hassell L. Prognostic implication of BRAF and TERT promoter mutation combination in papillary thyroid carcinoma-A meta-analysis. *Clin Endocrinol (Oxf)* (2017) 87:411–7. doi: 10.1111/cen.13413

42. Yang J, Gong Y, Yan S, Chen H, Qin S, Gong R. Association between TERT promoter mutations and clinical behaviors in differentiated thyroid carcinoma: a systematic review and meta-analysis. *Endocrine* (2020) 67:44–57. doi: 10.1007/s12020-019-02117-2

43. Luo Y, Jiang H, Xu W, Wang X, Ma B, Liao T, et al. Clinical, pathological, and molecular characteristics correlating to the occurrence of radioiodine refractory differentiated thyroid carcinoma: A systematic review and meta-analysis. *Front Oncol* (2020) 10:549882. doi: 10.3389/fonc.2020.549882

44. Kim HJ, Sohn SY, Jang HW, Kim SW, Chung JH. Multifocality, but not bilaterality, is a predictor of disease recurrence/persistence of papillary thyroid carcinoma. *World J Surg* (2013) 37:376–84. doi: 10.1007/s00268-012-1835-2

45. American Thyroid Association Guidelines Taskforce on Thyroid, N., Differentiated Thyroid, C, Cooper DS, Doherty GM, Haugen BR, Kloos RT, Lee SL, et al. Revised American Thyroid Association management guidelines for patients with thyroid nodules and differentiated thyroid cancer. *Thyroid* (2009) 19:1167–214. doi: 10.1089/thy.2009.0110

46. Van Velsen EFS, Stegenga MT, Van Kemenade FJ, Kam BLR, Van Ginhoven TM, Visser WE, et al. Evaluating the 2015 American thyroid association risk stratification system in high-risk papillary and follicular thyroid cancer patients. *Thyroid* (2019) 29:1073–9. doi: 10.1089/thy.2019.0053

47. Grani G, Zatelli MC, Alfo M, Montesano T, Torlontano M, Morelli S, et al. Real-world performance of the American thyroid association risk estimates in predicting 1-year differentiated thyroid cancer outcomes: A prospective multicenter study of 2000 patients. *Thyroid* (2021) 31:264–71. doi: 10.1089/thy.2020.0272

48. Amin MB, Edge SB, Greene FL, Byrd DR, Brookland RK, Washington MK, et al. *AJCC cancer staging manual*. Springer (2017).

49. Xing M, Haugen BR, Schlumberger M. Progress in molecular-based management of differentiated thyroid cancer. *Lancet* (2013) 381:1058–69. doi: 10.1016/S0140-6736(13)60109-9

50. Boufraqech M, Nilubol N. Multi-omics signatures and translational potential to improve thyroid cancer patient outcome. *Cancers (Basel)* (2019) 11:1988. doi: 10.3390/cancers11121988

51. Tirro E, Martorana F, Romano C, Vitale SR, Motta G, Di Gregorio S, et al. Molecular alterations in thyroid cancer: From bench to clinical practice. *Genes (Basel)* (2019) 10:709. doi: 10.3390/genes10090709

52. Kim D. Thyroid cancer: are molecular studies making any difference? *J Laryngology Otology* (2007) 121:917–26. doi: 10.1017/S0022215107009279

53. Li X, Kwon H. The impact of BRAF mutation on the recurrence of papillary thyroid carcinoma: A meta-analysis. *Cancers (Basel)* (2020) 12:2056. doi: 10.3390/cancers12082056

54. Alzahrani AS, Alomar H, Alzahrani N. Thyroid cancer in Saudi Arabia: A histopathological and outcome study. *Int J Endocrinol* (2017) 2017:8423147. doi: 10.1155/2017/8423147

55. Flemban AF, Kabrah S, Alahmadi H, Alqurashi RK, Turaes AS, Almaghrabi R, et al. Patterns of thyroid cancer mortality and incidence in Saudi Arabia: A 30-year study. *Diagnostics (Basel)* (2022) 12:2716. doi: 10.3390/diagnostics12112716

frontiers | Frontiers in Endocrinology

TYPE Original Research
PUBLISHED 05 October 2023
DOI 10.3389/fendo.2023.1267499

OPEN ACCESS

EDITED BY
Juan Pablo Nicola,
National University of Cordoba, Argentina

REVIEWED BY
Julio Ricarte-Filho,
Children's Hospital of Philadelphia, United States
Frederique Savagner,
INSERM U1048 Institut des Maladies Métaboliques et Cardiovasculaires, France

*CORRESPONDENCE
Angela Greco
Angela.Greco@istitutotumori.mi.it
Emanuela Minna
Emanuela.Minna@istitutotumori.mi.it

†PRESENT ADDRESS
Giuseppe Mauro,
Eurofins Biolab, Milan, Italy

‡These authors share last authorship

RECEIVED 26 July 2023
ACCEPTED 12 September 2023
PUBLISHED 05 October 2023

CITATION
Minna E, Devecchi A, Pistore F, Paolini B, Mauro G, Penso DA, Pagliardini S, Busico A, Pruneri G, De Cecco L, Borrello MG, Sensi M and Greco A (2023) Genomic and transcriptomic analyses of thyroid cancers identify DICER1 somatic mutations in adult follicular-patterned RAS-like tumors. *Front. Endocrinol.* 14:1267499. doi: 10.3389/fendo.2023.1267499

Genomic and transcriptomic analyses of thyroid cancers identify DICER1 somatic mutations in adult follicular-patterned RAS-like tumors

Emanuela Minna[1,2*], Andrea Devecchi[1], Federico Pistore[2], Biagio Paolini[3], Giuseppe Mauro[2†], Donata Alda Penso[1], Sonia Pagliardini[2], Adele Busico[1], Giancarlo Pruneri[4,5], Loris De Cecco[2], Maria Grazia Borrello[2], Marialuisa Sensi[6‡] and Angela Greco[2*‡]

[1]Pathology Unit 2, Department of Diagnostic Innovation, Fondazione IRCCS Istituto Nazionale dei Tumori, Milan, Italy, [2]Integrated Biology of Rare Tumors, Department of Experimental Oncology, Fondazione IRCCS Istituto Nazionale dei Tumori, Milan, Italy, [3]Pathology Unit 1, Fondazione IRCCS Istituto Nazionale dei Tumori, Milan, Italy, [4]Department of Oncology and Hemato-Oncology, University of Milan, Milan, Italy, [5]Department of Diagnostic Innovation, Fondazione IRCCS Istituto Nazionale dei Tumori, Milan, Italy, [6]Platform of Integrated Biology, Department of Applied Research and Technology Development, Fondazione IRCCS Istituto Nazionale dei Tumori, Milan, Italy

Background: Papillary thyroid carcinoma (PTC) is the most common type of thyroid cancer (TC). Several genomic and transcriptomic studies explored the molecular landscape of follicular cell-derived TCs, and *BRAF*V600E, *RAS* mutations, and gene fusions are well-established drivers. *DICER1* mutations were described in specific sets of TC patients but represent a rare event in adult TC patients.

Methods: Here, we report the molecular characterization of 30 retrospective follicular cell-derived thyroid tumors, comprising PTCs (90%) and poorly differentiated TCs (10%), collected at our Institute. We performed DNA whole-exome sequencing using patient-matched control for somatic mutation calling, and targeted RNA-seq for gene fusion detection. Transcriptional profiles established in the same cohort by microarray were investigated using three signaling-related gene signatures derived from The Cancer Genome Atlas (TCGA).

Results: The occurrence of *BRAF*V600E (44%), *RAS* mutations (13%), and gene fusions (13%) was confirmed in our cohort. In addition, in two patients lacking known drivers, mutations of the *DICER1* gene (p.D1709N and p.D1810V) were identified. *DICER1* mutations occur in two adult patients with follicular-pattern lesions, and in one of them a second concurrent *DICER1* mutation (p.R459*) is also observed. Additional putative drivers include *ROS1* gene (p.P2130A mutation), identified in a patient with a rare solid-trabecular subtype of PTC. Transcriptomics indicates that *DICER1* tumors are RAS-like, whereas the *ROS1*-mutated tumor displays a borderline RAS-/BRAF-like subtype. We also provide an

overview of *DICER1* and *ROS1* mutations in thyroid lesions by investigating the COSMIC database.

Conclusion: Even though small, our series recapitulates the genetic background of PTC. Furthermore, we identified *DICER1* mutations, one of which is previously unreported in thyroid lesions. For these less common alterations and for patients with unknown drivers, we provide signaling information applying TCGA-derived classification.

KEYWORDS

thyroid cancer, whole exome sequencing, transcriptomics, mutations, *DICER1*

Introduction

Follicular cell-derived tumors represent the majority of thyroid cancers (TCs) and encompass various histological types and subtypes. Based on histological features, they are classified as well-differentiated tumors, comprising papillary thyroid carcinoma (PTC) and follicular thyroid carcinoma (FTC), and poorly differentiated and undifferentiated thyroid carcinomas (PDTCs and ATCs, respectively). It is recognized that these less-differentiated tumors can develop from preexisting PTC or FTC according to a model of sequential dedifferentiation process and accumulation of multiple genetic abnormalities (1, 2).

PTC is the most common type in both adult and pediatric thyroid malignancies (3) and represents a heterogeneous disease with several subtypes that differ in terms of histological and clinical features, as well as molecular alterations. The most frequent and studied subtypes are the classical, follicular, and tall cells (4, 5), whereas other subtypes with solid and/or trabecular growth patterns exist (6) but are less characterized due to their rarity.

PTC and FTC display distinctive characteristics; PTC (especially the classical subtype) displays papillary architecture, specific nuclear morphological changes, and preferential metastatic dissemination *via* lymphatic vessels. FTC instead displays follicular architecture and can retain thyroid cell differentiation but lacks the PTC nuclear features and metastasizes preferentially *via* blood vessels (7). Thyroid lesions can be thus papillary- or follicular-patterned based on tumor origin and on these features. Follicular-patterned lesions include benign, low-risk, and malignant neoplasms, such as the follicular adenoma (FA), the PTC follicular subtype, FTC, FTC-derived PDTC, and other less common entities (8).

Along with the histopathological classification, molecular studies have then demonstrated that specific genetic alterations occur in given TC types, driving carcinogenesis according to a genotype/phenotype correlation (1, 4). In well-differentiated TCs in general, a very low mutational burden is observed compared with other cancers (9) and few somatic mutations or mutually exclusive gene fusions involving effectors of the mitogen-activated protein kinase (MAPK) and phosphatidylinositol 3-kinase (PI3K) signaling cascades are identified. In PTC, the *BRAF*V600E mutation is the most common genetic alteration followed by *RET* and *NTRK1/3* tyrosine kinase receptor gene fusions (4, 10). These drivers are particularly enriched in the PTC tall cell and classical subtypes, whereas somatic mutations of *RAS* gene family members *NRAS*, *HRAS*, and *KRAS* (mostly affected at codon 61, and less often at codon 12/13) are more frequent in the PTC follicular subtype and in FTC (5, 11, 12). The same alterations can be found in PDTC and ATC along with additional mutations in PI3K-AKT pathway genes and other well-established cancer-associated genes (such as *TP53*, *TERT* promoter, chromatin remodeling, and DNA damage response genes (12, 13)), in agreement with the sequential accumulation of gene alterations promoting tumor progression.

In addition to the well-known gene drivers, in more recent years with the advancement of sequencing technologies, several other genes have emerged as altered in TC. For instance, mutations in the *DICER1* gene, coding for an RNase III endoribonuclease involved in microRNA biogenesis, were identified as a rare event in adult TCs (5, 11–16), whereas they were more frequently reported in pediatric TC patients (8, 17–20) and in carriers of the DICER1 syndrome (21–27), an inherited cancer-predisposing disorder caused by germline *DICER1* mutations. DICER1 syndrome patients display a wide spectrum of neoplasias with early onset, including thyroid nodular goiter, follicular adenoma, and differentiated TC (28). The occurrence of thyroid manifestations, as multi-nodular goiter in children and young adults and in a familial context, has been even proposed as an early event to identify DICER1 syndrome families (29, 30). In the lesions of DICER1 syndrome patients, the co-occurrence of a germline *DICER1* variant, often loss-of-function, with a second missense somatic mutation was observed, and tumorigenesis induced by double-hit mutations has been proposed (31).

Subsequent TC omics studies have demonstrated that the identified mutations in the MAPK pathway stimulate specific transcriptional programs, affecting the downstream extracellular signal–regulated kinases (ERK) signaling, the expression of thyroid differentiation and function genes, and the activation of proliferative and immune-inflammatory programs. In particular, based on the expression of gene signatures, The Cancer Genome Atlas (TCGA) consortium defined in PTC three transcriptional signatures, related to the presence of *BRAF*V600E *vs. RAS*

mutations, to the degree of retained thyroid differentiation and to MAPK pathway output (5). These transcriptional signatures have been subsequently validated in various TC types and cohorts (11, 13, 32–34), also from our laboratory (35–37). It is now established indeed that *BRAF*V600E- and *RAS*-mutated PTCs display a signaling defined BRAF-like and RAS-like, respectively, and that tumors with other drivers can display BRAF-like, RAS-like, or intermediate/borderline signaling. Tumors with *RET/PTC1*, for instance, are BRAF-like, whereas other gene fusions can be RAS-like (5, 11). PDTCs are frequently RAS-like, even though BRAF-like subtypes can be also identified (13). Similarly, different transcriptional subtypes referred to thyroid differentiation (TD) and to MAPK pathway output have been established, with *BRAF*V600E and BRAF-like tumor displaying loss of TD and higher activation of the MAPK pathway, which could explain the worse prognosis in *BRAF*V600E- compared with *RAS*-mutated patients (4).

In this study, we profiled by DNA whole-exome sequencing, targeted RNA-sequencing, and transcriptomics 30 follicular cell-derived thyroid tumors, comprising both PTCs and PDTCs, collected at our Institute, to classify them according to known and novel genomic driver alterations and to TCGA-defined thyroid cancer-related transcriptional subtypes.

Materials and methods

Caselist collection

A retrospective caselist of thyroid cancer patients collected at our Institute was selected based on (i) confirmed diagnosis of follicular cell-derived thyroid tumor and (ii) availability of residual archive material from both tumor and matched non-neoplastic thyroid (NT), included as patient-specific control for DNA sequencing. The obtained cohort included both various PTC histological subtypes and PDTCs. PTCs were classified according to the WHO classification of endocrine tumors (38) and PDTCs according to the Turin proposal (39). Formalin-fixed paraffin-embedded (FFPE) tissue blocks were obtained, and hematoxylin and eosin (H&E)-stained slides were reviewed by an experienced pathologist (PB); when necessary, the areas of interest were manually microdissected. Primary tumor and patient-matched NT were obtained from 57 patients and subjected to nucleic acid extraction and quality control, for a total of 126 processed samples.

The study was approved by the Independent Ethics Committee of Fondazione IRCCS Istituto Nazionale dei Tumori (protocol INT DI-20/12/13-0006020), and informed consent was obtained from patients.

Nucleic acid extraction

Nucleic acids were extracted from unstained FFPE tissue serial sections consecutive to the pathologically revised H&E. Genomic DNA and total RNA were extracted by GeneRead DNA FFPE kit and by miRNeasy FFPE kit (Qiagen, Hilden, Germany), respectively, using the QIAcube-automated purification system. Extracted nucleic acids were quantified by Qubit 4 Fluorometer using Qubit Assay Kits (Thermo Fisher Scientific, Waltham, MA, USA), and quality was assessed by TapeStation 4200 (Agilent Technologies, Santa Clara, CA, USA) using Agilent ScreenTape Assays. Only patients with adequate DNA quantity (total extracted DNA >200 ng) from both tumor and matched NT were processed for DNA sequencing.

Whole exome sequencing and data processing

Tumor/NT pairs derived from 32 patients underwent library construction. DNA was fragmented by a Covaris M220 sonicator, and libraries were prepared using Illumina TruSeq Exome Library Prep Kit (Illumina, San Diego, CA, USA) according to the manufacturer's instructions. A total of 60 samples, corresponding to 30 patient-matched tumor/NT pairs, passed library quality control on TapeStation 4200 (Agilent Technologies) and were submitted to library pooling and sequencing on Illumina NextSeq500 System according to the manufacturer's standard protocol.

DNA sequencing data were processed as previously reported (40). Briefly, raw fastq files were quality-controlled with FastQC (41) and paired-end reads were aligned to the reference human genome (hg19) using a Burrows–Wheeler Aligner (BWAMEM, v0.7.12) (42). Duplicate and unmapped reads were identified and removed with Picard software (http://broadinstitute.github.io/picard/) and SAMtools v1.3.1.31. Reads were then post-processed according to Genome Analysis Toolkit (GATK) Best Practices 3.7 which include left alignment of small insertions and deletions, indel realignment, and base quality score recalibration.

Somatic single-nucleotide variants (SNVs) and small indels were called by two different variant callers: MuTect2 (v3.7) and Strelka (v.29.10). To create a high-confidence variant list, only the variants called by both algorithms were considered. Somatic variants (substitutions and indels) were annotated with Oncotator (v1.9.9.0). To remove false positives and polymorphisms, variants were then excluded based on at least one of the following additional filters: (i) read depth <30 in both tumor and NT; (ii) unidirectional call; (iii) alternative allele present in matched NT if the variant was not listed in the Catalogue Of Somatic Mutations In Cancer (COSMIC) database; (iv) C>A/G>T variants with a frequency <0.1 (oxoG artifacts); and (v) variants annotated in polymorphism databases (ExAC (43), NCBI dbSNP (44), and 1000 Genome Project (45)) without a COSMIC annotation. COSMIC Cancer Gene Census (https://cancer.sanger.ac.uk/census) was interrogated to explore the impact of somatic mutations in selected genes.

Targeted RNA sequencing for gene fusion detection

Gene fusions were assessed on total RNA by Oncomine™ Comprehensive Assay Plus RNA panel (OCA Plus RNA, Thermo

Fisher Scientific) that covers more than 1,300 isoforms across 49 known cancer-related fusion drivers. Libraries were prepared using the Ion AmpliSeq Library Kit plus with OCA RNA plus pools and sequenced on an Ion GeneStudio S5 Prime sequencer using Ion 530 chips, Ion 510 & Ion 520 & Ion 530 Kit-Chef, and Ion Chef System (Thermo Fisher Scientific), according to the manufacturer's instructions. Data were processed by Torrent Suite™ and analyzed by Ion Reporter™ software (5.18 version) with the "Oncomine Comprehensive Plus - w2.2 - Fusions - Single Sample" workflow.

Transcriptomics

Gene expression profiles were established by microarrays using Clariom S Pico Assay (Thermo Fisher Scientific). Total RNA was reverse transcribed, amplified, fragmented, biotin-labeled, and hybridized to Affymetrix GeneChip Human Clariom S (CLS) Arrays according to the manufacturer's standard protocols. Washing and staining procedures were performed using the GeneChip Hybridization, Wash and Stain Kit (Thermo Fisher Scientific) on Affymetrix GeneChip Fluidics Station 450. Microarrays were scanned with the GeneChip Scanner 3000 7G system (Thermo Fisher Scientific), and data were obtained using Affymetrix GeneChip Command Console (AGCC) software.

Data were processed using the robust multi-array average (RMA) algorithm on paraffin samples (46); raw Affymetrix CEL file data were background-noise-adjusted, normalized, and log2-transformed using the oligo package and RMA function. Probes were annotated with Bioconductor annotation package clariomshumantranscriptcluster.db, whereas probes not associated with gene symbols and control probes were filtered out. Multiple probes mapping to the same gene were collapsed using the collapseRows function with the "MaxMean" method of the WGCNA package (47). All analyses were performed using RStudio version 4.0.3. Microarray data were deposited in the ArrayExpress repository with the accession number E-MTAB-13222.

Transcriptional subtypes were defined using three gene signatures derived from TCGA (5); the complete gene lists are published (5, 33), and the corresponding expression scores were calculated as previously reported (37). Briefly, the BRAF-/RAS-like signaling gene set comprises 71 genes; 69 out of 71 genes were available on the used CLS array and assessed for score computation. The BRAF-RAS score (BRS) was calculated as reported (48). Negative BRS values were defined as BRAF-like subtype, whereas positive BRS values were defined as RAS-like subtype as reported (5); close-to-zero BRS values were considered as borderline subtype. Thyroid differentiation (TD) and MAPK output gene sets comprise 16 and 52 genes, respectively. TD and MAPK output scores were calculated as mean of log2-transformed and median-centered expression across samples as previously reported (5, 33). Positive and negative TD score values were defined as high and low expressions of thyroid function genes, respectively. Positive and negative MAPK output score values were defined high and low MAPK pathway transcriptional activation, respectively.

Meta-analysis of DICER1 and ROS1 mutations in thyroid tissues from COSMIC

The COSMIC database (https://cancer.sanger.ac.uk/cosmic, accessed on 30 January 2023) was interrogated to explore *DICER1* (COSMIC gene COSG526495; transcript ENST00000526495.5) and *ROS1* (COSMIC gene COSG418; transcript ENST00000368508.7) gene mutations. Thyroid tissue was specifically investigated, and the linked data for each gene were downloaded.

DICER1 and *ROS1* mutations were reported in 24 and 8 different studies, respectively. We focused on the 19 and 6 studies reporting at least one mutated sample, respectively. For *DICER1*, an additional study derived from literature (11), and not included in COSMIC, was also considered.

Data derived from published studies were checked on the original publication to confirm mutation type, tissue histology, and patient-matched samples. Data derived from CGP (Cancer Genome Project) studies were manually curated: (i) samples from CGP study_542 were assigned to TCGA study (5) based on ID matching; (ii) one sample from CGP study_542 (COSMIC ID 2122053) with *ROS1* synonymous mutation was excluded; and (iii) duplicated samples from CGP study_676 were excluded.

Results

Caselist description

We investigated a retrospective series of TC patients collected at Fondazione IRCCS Istituto Nazionale dei Tumori of Milan. Caselist selection and processing are described in Material and Methods, Figure 1A and Supplementary Figure 1. Starting from 126 FFPE tissues derived from 57 patients, and comprising TCs and patient-matched non-neoplastic thyroids (NTs), a final set of 30 tumor/NT pairs (collectively 60 tissues) passed quality control standards and were profiled first by DNA whole-exome sequencing (WES) and then by targeted RNA sequencing and transcriptomics (Figure 1A). Clinicopathological features are reported in Table 1 and Supplementary Table 1. This series includes PTCs (90%) and PDTCs (10%). PTC histological types comprise classical and follicular subtypes, the less frequent tall cell and solid-trabecular subtypes, and two cases with mixed components (Figure 1B, Table 1 and Supplementary Table 1), thus being representative of the histological heterogeneity observed in this tumor type.

Somatic mutations

DNA WES was established using patient-matched NT as filtering control for somatic mutation calling. We specifically focused on non-synonymous mutations, causing amino acid (aa) changing, and comprising missense, nonsense, and splice-site mutations with aa changing. The identified mutations for each tumor are in Supplementary Table 2.

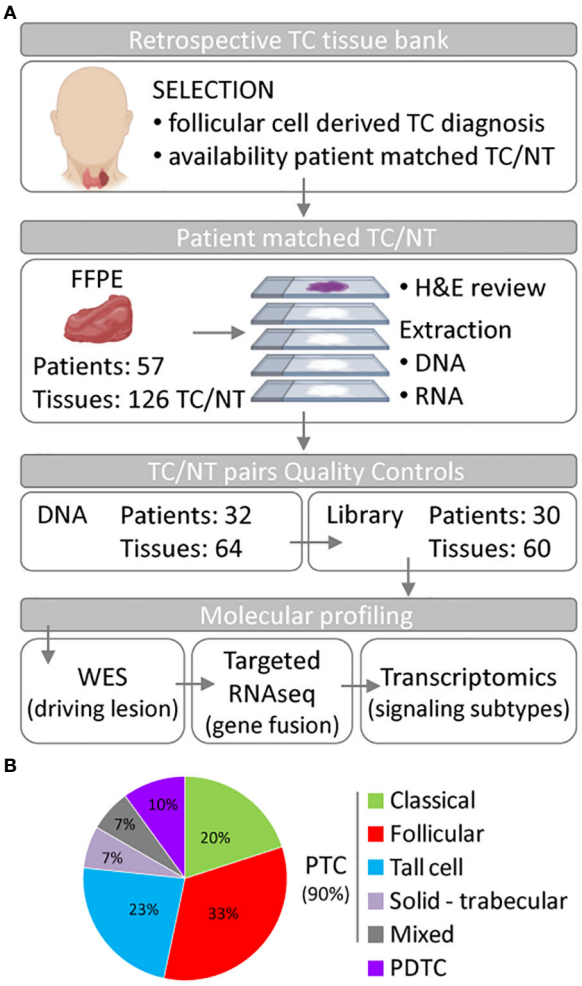

FIGURE 1
Summary of the thyroid cancer caselist processing and features. **(A)** Flowchart of thyroid tissue selection and processing to obtain the set of 30 thyroid cancer (TC) patients who undergone genomic and transcriptomic molecular profiling. Part of this Figure has been created using Biorender under institutional account. **(B)** Pie chart of the histological subtype distribution in the 30 TC patients. Abbreviations: NT, non-neoplastic thyroid; FFPE, formalin-fixed paraffin-embedded tissue; H&E, hematoxylin and eosin; WES, whole-exome sequencing; PTC, papillary thyroid carcinoma; PDTC, poorly differentiated thyroid carcinoma.

The mutation load of our set (Figure 2A and Supplementary Figure 2) was low in agreement with that of thyroid cancers from TCGA (Supplementary Figure 2A) and from other TC series (5, 12, 13). The median number of mutations was 6.5 (range 1–28), with the majority of samples (19/30, 63%) harboring less than 10 mutations (Supplementary Figure 2B). The top mutated samples (number of mutations ≥15) included all the three tumors with PDTC component/histology (Supplementary Figure 2B), in agreement with the higher mutational burden reported in advanced and less differentiated TCs (12, 13). A significant correlation between patient age and mutation load was also observed (Supplementary Figure 2C), confirming a lower mutation load in younger patients (Supplementary Figure 2D) as previously reported (12).

TABLE 1 Feature of the 30 TC patients.

Gender: female/male		24/6
Age (years): median (Range)		42 (13–74)
Tumor size (cm): median (range)		2 (1.2-6.5)
ETE	Yes; n (%)	17 (57%)
	No; n (%)	11 (37%)
	NA; n (%)	2 (7%)
LNM	Yes; n (%)	11 (37%)
	No; n (%)	19 (63%)
Histological subtype; n (%)		
PTC	Classical	6 (20%)
	Follicular	10 (33%)
	Tall cell	7 (23%)
	Solid—trabecular	2 (7%)
	Mixed	2 (7%)
PDTC		3 (10%)

ETE, extra thyroid extension; LNM, lymph node metastases; PTC; papillary thyroid carcinoma; PDTC poorly differentiated thyroid carcinoma; NA, not available.

Driver/putative driver alterations

The most frequently altered genes were related to the MAPK pathway and included well-established gene drivers (Figures 2A, E). *BRAF*V600E was the most frequent mutation (13/30 samples, 44%), followed by *RAS* mutations (4/30 samples, 13%), with *NRAS*_Q61R identified in three patients and *KRAS*_G12V, co-occurring with a beta-catenin (*CTNNB1*) mutation, in another patient.

In samples lacking the abovementioned alterations (Figure 2A), mutations in the *DICER1* gene were detected. A meta-analysis of *DICER1* mutation in TC is presented hereafter.

The identified mutations were mutually exclusive (Figure 2A) and displayed a genotype/histological subtype distribution (Supplementary Table 1), as already observed in other TC series. Most *BRAF*V600E were found in PTC classical and tall cell subtypes (10/13, 77%), whereas *RAS* mutations were found in the PTC follicular subtype (3/4, 75%) and in a PDTC with the PTC component where *KRAS* and *CTNNB1* mutations were co-occurring. *DICER1* mutations were found in a follicular subtype PTC and in a PDTC with solid-insular histology. This agrees with the increasing body of evidence describing *DICER1* mutations in TCs with a follicular pattern rather than a papillary pattern (49).

Collectively, we identified these somatic mutations in known/putative drivers in 19/30 cases (64%) (Figure 2A).

Meta-analysis of DICER1 mutations in TC

We used as primary information source the COSMIC database. Mutations in *DICER1* are reported by 20 independent studies (collectively 1669 samples, Table 2), describing 61 *DICER1* mutations (3.6%) in 53 patients. It should be noted that for some patients multiple specimens were tested (Table 2 and Figure 3) and that some pedigrees of DICER1 syndrome carriers are included, thus possibly representing

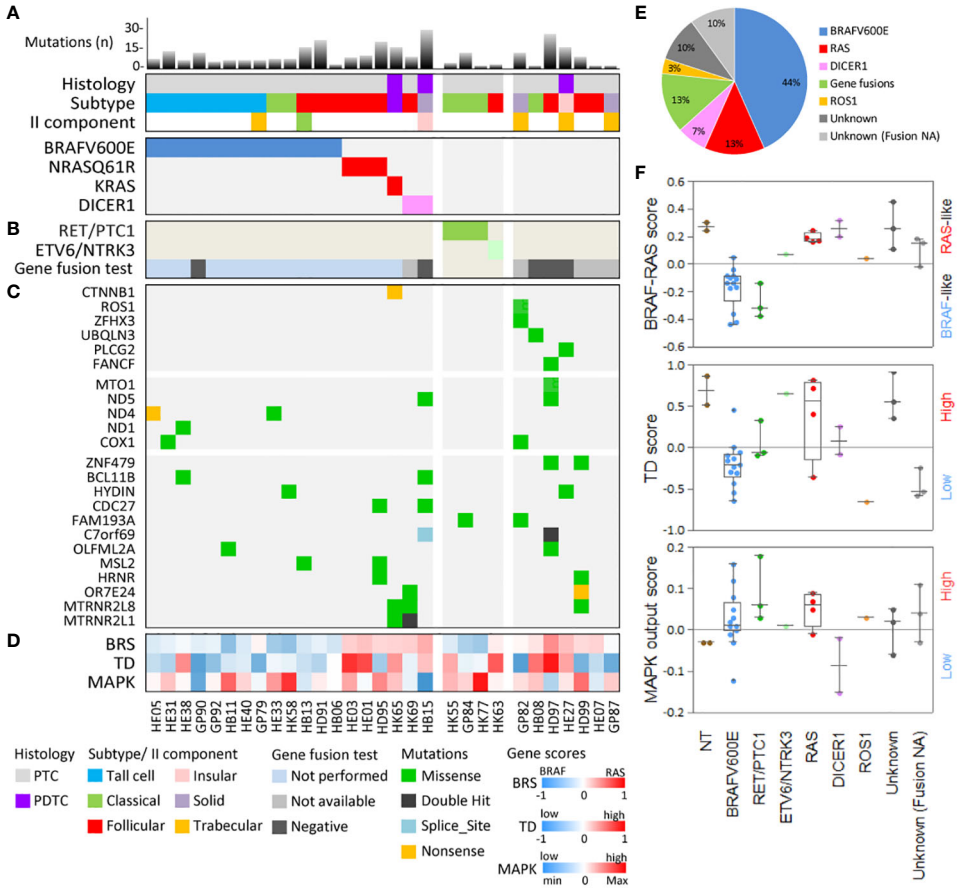

FIGURE 2
Genomic and transcriptomic characterization of the 30 thyroid cancer patients. **(A)** The mutational load (bar chart, top panel), histology features (middle panel), and driver/putative driver mutations (lower panel) are shown for each patient. Mutational load represents the number of somatic non-synonymous mutations (missense, nonsense, and splice-site mutations with amino acid changing). **(B)** Gene fusion detected by targeted RNA-seq. **(C)** Selected genes mutated in our cohort, including mitochondrial function-related genes (middle panel) and commonly mutated genes (lower panel). **(D)** Signaling subtypes defined by gene expression score based on TCGA gene signatures related to BRAF-RAS signaling (BRAF-/RAS-like score, BRS), thyroid differentiation (TD score), and activation status of the MAPK pathway (MAPK output score). Patient identifiers and color-code legends are shown at the bottom. **(E)** Pie chart showing the distribution of driver/putative driver alterations in the 30 TC patients. **(F)** Boxplot with scatter plot showing signaling subtypes in the 30 TC patients stratified for alteration. Two non-neoplastic thyroids (NTs) are included as controls. Tumors with unknown driver and gene fusion data not available (NA) are shown as a separate group.

a slight overestimation of *DICER1* mutation frequency in TC. Specific hotspots are frequently identified and include the functionally relevant codons E1705, D1709, D1810, and E1813, all representing metal ion-binding sites localized within the DICER1 RNase IIIb domain and affecting its enzymatic activity (21). In our cohort, *DICER1* alterations (i.e., D1709N VAF 0.94 and D1810V VAF 0.37, highlighted in Figure 3) are found in two of these hotspots, thus falling into the same functional category, and display amino acid substitutions previously reported (12, 19, 25).

In addition, in HK69 patient, *DICER1*_D1810V co-occurs with *DICER1*_R459* mutation (VAF 0.43, splice-site mutations with stop codon introduction; Supplementary Table 2), localized into the DICER1 helicase C domain. To our knowledge, this mutation has not been previously reported in other thyroid patients but is listed in the *DICER1* mutation panel (50). Notably, a frame-shift loss-of-function mutation at the N458 residue concurring with *DICER1*_D1810Y, both somatic, has been recently reported in an adult TC patient (51). In addition, co-occurring *DICER1* mutations have been similarly identified in TC patients not related to DICER1 syndrome (28, 51–53) and also in COSMIC patients (Figure 3C) where RNase IIIb domain mutations (at codons E1705 and D1709) co-occur with a second nonsense/frameshift_nonsense mutation.

Focusing on the histology (Figure 3D), our meta-analysis confirms that *DICER1* mutations can frequently occur in follicular-pattern lesions, as PTC follicular subtype (either alone or with the PDTC component), PTC solid subtype, FTC, and Hurtle cell carcinoma (collectively 20%), as well as in benign/premalignant lesions (adenoma, nodular goiter, and follicular adenoma, collectively computed as unique class, 19%), and also in less differentiated TCs (PDTC+ATC 19%).

Gene fusions

As reported in the previous section, 11/30 cases did not display mutations in the abovementioned known/putative drivers. We

TABLE 2 COSMIC-derived thyroid studies reporting *DICER1* mutation.

	Study ID	Mutations (n)	Patients (n)	Total reported samples (n)	Reference
1	de Kock _JCEM2014	3	3	3	(21)
2	TCGA_Cell2014*	4	4	402	(5)
3	Costa_Oncotarget2015	1	1	18	(14)
4	de Kock _JTO2016	1	1	1	(22)
5	Durieux_VirchArchiv2016	2	2	2	(17)
6	Landa_JCI2016	2	2	117	(13)
7	Rutter _JCEM2016	4[1]	3	5	(23)
8	Wu_ERC2016	1	1	1	(24)
9	Yoo_PlosGen2016 **	4	4	180	(11)
10	Apellaniz-Ruiz_EJE2017	4[1]	3	6	(25)
11	Zehir_NatMed2017	7[1,2]	5	233	(15)
12	Chen_JCO2018	1	1	1	(26)
13	Gullo_AJCP2018	3[1]	1	5	(27)
14	Pozdeyev_CCR2018	4[2]	3	631	(12)
15	Ravella_AnnPathologie2018	1	1	1	(18)
16	Chernock _ModernPath2020	6[2]	5	7	(19)
17	Lee_JCI2021	5	5	37	(20)
18	Kim_InVivo2022	1	1	12	(16)
19	CGP Study_589	3	3	3	NA
20	CGP Study_676*	4	4	4	NA
	Total	61	53	1669	

* Manually curated (see Material and methods). ** Not included in COSMIC-derived studies.
[1]Multiple samples from the same patient. [2] DICER1 double mutation. NA, not available.

therefore investigated these samples for the presence of gene fusions, well-established drivers in PTC, by a targeted RNA sequencing panel covering 49 cancer-related chromosomal rearrangements (see Material and Methods). In the analysis, we also included *DICER1*-mutated samples, as the co-occurrence of a *DICER1* mutation with a rare gene fusion has been reported (14); and one *BRAF*V600E sample, included as negative control.

RET and *NTRK3* fusions were found in four cases, all lacking mutations in *BRAF*, *RAS*, and *DICER1* genes, thus confirming to be mutually exclusive with each other and with other known/putative drivers (Figure 2B). The identified fusions were *RET/PTC1* (fusion partner *CCDC6* gene) in three cases and *ETV6/NTRK3* in one case, both representing the oncogenic fusions more frequently identified in PTC. *RET/PTC1* fusions were found in the PTC classical subtype, whereas *ETV6/NTRK3* was found in the follicular subtype; this agrees with the genotype/histological subtype distribution observed in other TC series (5, 11) and with the described association of *NTRK* fusions with the follicular growth pattern (54). Negative samples were one *DICER1*-mutated sample, the negative control (*BRAF*V600E), and three samples, which thus remained with the unknown gene driver. Five samples did not pass assay quality control due to low-quality RNA, thus displaying not available data for this analysis.

Collectively, considering also gene fusions, we identified gene alterations in 23/30 samples (77%), whereas 7 samples remained with unknown driver (Figure 2E).

Samples with unknown drivers

To identify additional potential drivers in our cohort, we then revised somatic mutation data (Supplementary Table 2).

In one patient, a *ROS1* gene mutation was detected (Figure 2C). *ROS1* codes for a receptor tyrosine kinase and is included in Cosmic Cancer Gene Census as containing mutations causally implicated in cancer. While its rearrangement has been found in various tumor types (55), including recent TC case reports (56, 57), its mutation seems a quite rare event in thyroid tumors. In the COSMIC database, 25 *ROS1* mutations (2%) are described across 1,215 samples (Supplementary Table 3). No common mutations are reported, and the *ROS1*_P2130A mutation detected in our patient (VAF 0.18, Supplementary Table 2) represents a new alteration for

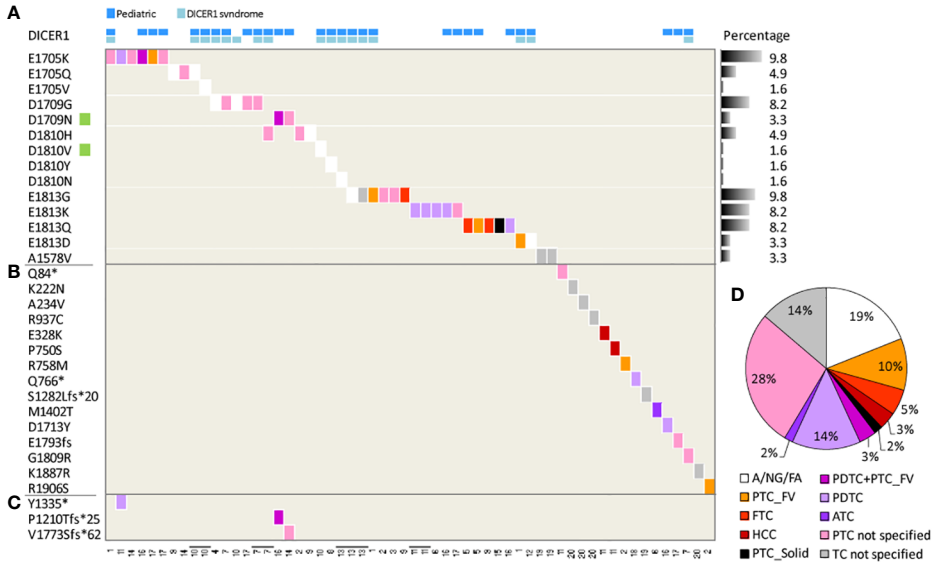

FIGURE 3
DICER1 mutations in thyroid lesions derived from COSMIC. Heatmap of *DICER1* mutations in 53 patients across 20 studies. The tissue histology is shown, when available, according to the color-code legend on the right; the study identifier (see Table 2) is at the bottom. Each column represents a patient; four patients with multiple tissues tested are displayed as adjacent lanes, highlighted by bolt lines on study identifier. *DICER1* mutations (row) are listed based on **(A)** most frequently mutated codons, the percentage across samples (n = 61) reported; **(B)** patient-specific mutations; **(C)** second-hit somatic mutations. Green squares on the mutation list highlight the two mutations identified also in the present study. **(D)** Pie chart of histological subtypes distribution; all the specimens (n = 58) were considered. Abbreviation: A, adenoma; NG, nodular goiter, FA, follicular adenoma; TC, thyroid carcinoma; PTC, papillary TC; FV, follicular variant/subtype; FTC, follicular TC; HCC, hurtle cell carcinoma; solid, solid subtype; PDTC, poorly differentiated TC; ATC, anaplastic TC. A/NG/FA were computed as a single class of benign lesions. PTC and TC non-specified classes include samples with a non-specified histological subtype.

this gene in thyroid lesions. Other drivers (as *BRAF*V600E or *HRAS*, Supplementary Table 3) co-occur with *ROS1* mutations, thus raising the possibility that this gene may not represent a standalone driver in TC. However, in our patient, mutations in known drivers are absent, thus suggesting that other alterations may be involved; due to unavailable data, we cannot confirm the absence of gene fusion (see previous section). Interestingly, in our patient *ROS1* mutation co-occurs with *ZFHX3*_A472E (Supplementary Table 2), and the same co-occurrence is observed in COSMIC (Supplementary Table 3; COSMIC ID 2121935). The meaning and impact of these data remain to be established. Notably, *ZFHX3* mutations co-occur with other gene drivers in 1.7% of PTC from TCGA (5).

In our cohort, the *ROS1* mutation was found in a PTC with the rare solid-trabecular histology, whereas the few available COSMIC data (Supplementary Table 3) describe *ROS1* mutations in both follicular-pattern tumors (as FTC and FTA), as well as in ATC and *BRAF*V600E PTCs, thus suggesting that the current data are sparse and insufficient to address a genotype/phenotype association for *ROS1* mutations in TC.

Revising the other samples with unknown drivers, especially the three with confirmed absence of gene fusions (i.e. sample ID HB08, HD97, HE27; Figures 2B, C), we found a variable number of somatic mutations (range 1–25, Figure 2A); mostly were missense mutations (Supplementary Table 2) and affected genes previously reported in other cancer types, such as *UBQLN3*, *PLCG2*, and *FANCF* genes (Figure 2C).

In addition, in the HD97 patient, mutations in two genes encoding mitochondrial proteins were identified: the mitochondrial gene *ND5* (NADH dehydrogenase subunit 5, p.F429L mutation) and the nuclear gene *MTO1* (mitochondrial tRNA translation optimization 1, p.M386L mutation) (Figure 2C and Supplementary Table 2). Of note, mutations in other mitochondrial genes were identified in six other patients of our caselist, and affecting *ND4* and *ND1* genes (NADH dehydrogenase subunit 4 and subunit 1), involved in the activity of the mitochondrial membrane NADH dehydrogenase (complex I), which catalyzes the electron transfer from NADH through the respiratory chain, and the *COX1* gene (cytochrome c oxidase I) involved in the electron transport in mitochondrial respiratory chain complex III and IV (Figure 2C). Mutations in mitochondrial genes have been previously identified in thyroid cancer. Nonsense disruptive mitochondrial DNA mutations in complex I subunits have been reported in the oncocytic variant of thyroid carcinoma (58), and more recently in other TC subtypes (59–61). Interestingly, the *ND4* gene mutation here identified (*ND4*_W24*, Supplementary Table 2) is nonsense, possibly affecting complex I formation. Furthermore, four of the patients with mitochondrial gene mutations are *BRAF*V600E positive, in agreement with a previously suggested correlation between *BRAF* mutation and mitochondrial alterations in TC (62).

Along with mitochondrial genes, other genes were found commonly mutated in both samples with unknown and known/putative driver (Figure 2C). These genes belong to different

functional categories and cellular processes, such as cell proliferation (*CDC27* gene), ERK signaling (*HYDIN* gene), transcription regulation by DNA binding (*BCL11B* and *ZNF479* genes), extracellular matrix organization (*OLFML2A* gene), chromatin organization (*MSL2* gene), calcium ion binding (*HRNR* gene), and apoptosis regulation (*MTRNR2L8* and *MTRNR2L1*), or are less characterized genes (Figure 2C and Supplementary Table 2).

To get more information about the pathways affected by the identified mutated genes, we performed a pathway-level analysis (Supplementary Figure 3). The somatic mutations found in our cohort (Supplementary Table 2) were tested on the Hallmark collection derived from Molecular Signature Database (63). We found that several mutated genes fall into biological processes related to (i) cell proliferation; (ii) p53 and apoptosis; (iii) stress responses as hypoxia and DNA damage; (iv) signaling pathways associated with KRAS, MTOR, TNFA, and estrogen receptor; (v) metabolic functions; and (vi) inflammation, consistently with the biological alterations and features typically observed in cancer (64). The vast majority of the genes identified in these pathways, however, are altered in samples with a known/putative driver, whereas very limited information is obtained for the unknown samples.

Transcriptional subtypes

In our cohort, we then established transcriptional profiles by RNA microarray; two normal thyroids were included as control. We tested our samples with the three TCGA-derived gene signatures related to BRAF/RAS signaling (BRAF-/RAS-like subtypes), thyroid differentiation (TD score), and activation status of the MAPK pathway (MAPK output) (5). This was aimed not only to validate these transcriptional subtypes in samples with recognized drivers, but also, and more importantly, to obtain signaling information for the samples with putative and unknown drivers.

For NT controls and samples with established drivers, we confirmed literature findings. Normal thyroids displayed, as expected, a high TD score (5), low MAPK output, and RAS-like subtype as previously reported (34, 36) (Figure 2F). *BRAF*V600E samples were BRAF-like, with a low TD score and high MAPK output (4) (Figures 2D, F). Samples with *RET/PTC1* fusion showed results similar to *BRAF*V600E samples, except for the higher TD score (Figure 2F) indicative of a partial preservation of thyroid function, as already reported (5, 35). On the contrary, *RAS*-mutated samples were confirmed as RAS-like, with higher TD score and intermediate MAPK output. Also, *DICER1*-mutated samples were RAS-like, consistently with previous reports (5, 14), and with the histological subtypes (follicular and PDTC solid-insular) in which these alterations were found. Of note, they displayed on average TD scores lower than those of *RAS* and higher than those of *BRAF*V600E samples, and reduced MAPK output, consistently with previous data (65). The *ETV6/NTRK3* sample displayed a borderline RAS-/BRAF-like signaling subtypes, as already reported (5, 11).

Regarding the samples with unknown driver, the one with *ROS1* mutation displayed a borderline RAS-/BRAF-like subtype, whereas the remaining samples were RAS-like, consistently with their histology (mostly follicular and solid/insular/trabecular) and displayed intermediate MAPK output and a heterogeneous degree of thyroid differentiation.

Discussion

In this study, we report the molecular characterization of 30 TCs collected at our Institute. We applied DNA WES on tumor/normal thyroid patient-matched tissues, targeted RNA sequencing for gene fusion testing in samples negative for known driving mutations, and transcriptomics to assess TCGA-derived signaling subtypes.

Even though small, our cohort includes both the most frequent and less common histological subtypes of PTC, as well as a minor fraction of PDTCs, thus being representative of various histological types observed in follicular cell-derived thyroid tumors.

We confirmed literature data about the low mutational burden in well-differentiated TC and younger patients, the occurrence and distribution of well-established gene drivers, and their genotype/phenotype association.

In samples lacking *BRAF*V600E, *RAS* mutations, and *RET* and *NTRK* gene fusions, we found mutations in the *DICER1* gene. Alterations in this gene have been identified by various independent studies, as also highlighted by our COSMIC meta-analysis, raising the possibility of its involvement in TC tumorigenesis.

We described three different *DICER1* mutations; the two affecting the functionally relevant and frequently altered hotspots in the RNase IIIb domain have been already reported in thyroid lesions, whereas the *DICER1*_R459* has been previously identified only in pleuropulmonary blastoma (66). Mutations of *DICER1* in thyroid tumors are quite rare (3.6% from COSMIC). Notably, in our small cohort, we detected a higher alteration frequency (two mutation-positive patients out of 30, 6.6%). This increased detection could be explained by the composition of our cohort, comprising a high fraction of follicular-pattern/RAS-like tumors.

Although numerous studies have identified *DICER1* mutations in thyroid lesions, particularly in pediatric TC patients and DICER1 syndrome carriers, the functional meaning of these alterations still remains poorly understood. DICER1 operates in mature miRNA synthesis, and recently it has been confirmed that actually thyroid lesions with *DICER1* mutations in the RNase IIIb domain display an altered mature miRNA transcriptome compared with *DICER1* wild-type tumors and non-neoplastic thyroids (67, 68). Unfortunately, we are not able to test mature miRNA expression in transcriptomic data from our cohort as the exploited microarray platform is not designed for short RNA assessment, and mature miRNA data are not available.

In our cohort, somatic *DICER1* mutations were identified in two adult patients: a follicular subtype PTC (with missense *DICER1*_D1810V and nonsense *DICER1*_R459*) and a PDTC with solid-insular histology (with missense *DICER1*_D1709N), respectively, in agreement with the enrichment of follicular-pattern TCs observed in *DICER1*-mutated patients (49). Other more recent studies, not included in the COSMIC-derived dataset, have reported *DICER1* mutations in thyroid neoplasms.

They confirmed not only hotspot mutations in the *DICER1* RNAse IIIb domain, including the D1810V and D1709N mutations identified in our samples, but also the co-occurrence of second loss-of-function mutations (28, 51–53), as well as the enrichment of *DICER1* mutations in follicular pattern thyroid tumors. A revision of these studies is available at reference (28).

Given the increasing number of studies reporting *DICER1* mutations, this gene has been recognized among relevant molecular markers for TC (6) and its testing has been included in thyroid-specific NGS panels, such as the gene test ThyroSeq v3 (69). In addition, as previously reported, in the presence of two somatic *DICER1* mutations in the same tumor tissue, germline *DICER1* testing should be taken into account to confirm the not inherited nature of the case, and to exclude a DICER1 syndrome-related manifestation for which specific management, surveillance strategies, and follow-up have been recommended (70).

In one sample with an unknown driver, we identified the *ROS1*_P2130A mutation. To our knowledge, this alteration has not been previously reported in thyroid lesions but has been detected in a lung adenocarcinoma patient (71). Although this mutation affects a conserved amino acid in the kinase domain of the protein, its potential role as genetic driver in thyroid cancer remains to be established.

Interestingly, the *ROS1*-mutated sample displayed a borderline RAS-/BRAF-like subtype that could be explained by the co-occurrence of other drivers (including gene fusions, undetermined in this sample) that may affect the transcriptional signaling. Indeed, PTCs carrying both *ROS1* and *BRAF*V600E mutations are BRAF-like (5), whereas an ATC with co-occurring *ROS1* and PI3K pathway mutations is RAS-like (13). Further studies are required to define the impact and role of *ROS1* mutations in TC.

In the other samples with an unknown driver, we identified missense mutations in *UBQLN3*, *PLCG2*, and *FANCF*, among other genes (Supplementary Table 2).

The mutation in the *UBQLN3* gene (*UBQLN3*_R624Q), encoding a ubiquitin-like protein, is detected in a classical subtype PTC (HB08 patient). Of note, this represents the only somatic mutation identified in this patient. UBQLN3 belongs to the ubiquilins protein family, essential factors for the maintenance of cell proteostasis and found involved in cancer progression. *UBQLN3* missense mutations have been reported in lung, breast, central nervous system, and pancreatic cancer, although their functional role in cancer remains unexplored (72).

The mutation in *PLCG2* genes (*PLCG2*_R653C), encoding the Phospholipase Cgamma 2 enzyme, is identified in a follicular subtype PTC (HE27 patient). *PLCG2* missense and nonsense mutations are reported in 2% of all cancers (https://www.mycancergenome.org/content/gene/plcg2) as in colon cancer, lung cancer, prostate cancer, endometrial carcinoma, and cutaneous melanoma, as well as in ibrutinib-resistant chronic lymphocytic leukemia patients (73). Of note, a *PLCG2* mutation of unknown significance has been found in an ATC with *BRAF*V600E mutation (74).

The mutation in the *FANCF* gene (*FANCF*_A81V), encoding the DNA repair protein Fanconi Anemia Complementation group F, is identified in a PDTC (HD97 patient). FANCF is an adaptor protein of the Fanconi Anemia core complex and plays a key role in DNA post-replication repair and in cell-cycle checkpoints. Mutations in *FANCF* are frequently observed in human tumors as breast, lung, kidney, and ovary (75). Moreover, *FANCF* promoter methylation has been found in cancer and a *FANCF*-deficient mouse model was prone to ovarian cancers (76). The mutation of other elements of the Fanconi Anemia core complex and of genes involved in DNA damage response has been already observed in TC, especially in advanced and less differentiated tumors (12, 13). The significance of the here identified mutation remains to be investigated.

In the same patient (HD97), we also identified missense mutations in mitochondrial genes. Multiple mutations of genes related to mitochondrial function were found in our cohort, in agreement with the body of evidence showing aberrant mitochondrial function in cancer.

In addition, we found several genes commonly mutated across our samples; they are still poorly characterized both at the functional level and for a possible involvement in cancer, and further studies are mandatory to assess the impact of the here identified mutations.

To decipher the possible pathways and biological processes affected by the mutations identified in our cohort, we performed a pathway-level analysis. We found that several of the identified mutations converge on relevant biological processes already recognized as altered in cancer. However, the vast majority of the genes identified in these pathways were altered in samples with known/putative drivers, whereas very limited information was obtained for the unknown samples, which still remain largely uncharacterized. In this sense, the availability of matched transcriptomic data for these patients may be further explored in future to dissect downstream changes in gene expression and obtain more information about the altered functions and pathways in driver unknown patients.

In conclusion, here we described genomic and transcriptomic data for a proprietary cohort of thyroid cancer patients. Even though small, our cohort, mostly consisting of PTC, recapitulates the well-established genetic background for this tumor type. Moreover, in adult patients with follicular-pattern tumors, we described *DICER1* mutations, one of which is previously unreported in TC. In addition, our study suggested several putative driver alterations, including a ROS1 mutation, whose role in TC remains to be investigated. We also provided signaling subtype information applying the well-established TCGA-derived classification, thus unveiling the molecular features of TCs carrying less common and poorly characterized gene mutations.

Data availability statement

The gene expression data presented in this study can be found in the online repository ArrayExpress (https://www.ebi.ac.uk/biostudies/arrayexpress) with the accession number E-MTAB-13222. The raw WES data presented in the study are not publicly available since they contain information that could compromise research participant privacy. Pre-processed somatic mutation data are included in the article/Supplementary Material (Supplementary Table 2). Further inquiries can be directed to the corresponding author/s.

Ethics statement

The studies involving humans were approved by Independent Ethics Committee of Fondazione IRCCS Istituto Nazionale dei Tumori (protocol INT DI-20/12/13-0006020). The studies were conducted in accordance with the local legislation and institutional requirements. The participants provided their written informed consent to participate in this study.

Author contributions

EM: Data curation, Formal Analysis, Investigation, Validation, Visualization, Writing – original draft, Writing – review & editing. AD: Data curation, Formal Analysis, Methodology, Software, Validation, Writing – review & editing. FP: Data curation, Formal Analysis, Software, Validation, Writing – review & editing. BP: Validation, Writing – review & editing, Investigation. GM: Data curation, Investigation, Writing – review & editing. DAP: Investigation, Validation, Writing – review & editing. SP: Investigation, Writing – review & editing. AB: Formal Analysis, Investigation, Validation, Writing – review & editing. GP: Resources, Writing – review & editing. LDC: Methodology, Supervision, Writing – review & editing. MGB: Conceptualization, Investigation, Writing – review & editing. MS: Conceptualization, Formal Analysis, Supervision, Writing – review & editing. AG: Conceptualization, Funding acquisition, Project administration, Resources, Supervision, Writing – review & editing.

Funding

The authors declare financial support was received for the research, authorship, and/or publication of this article. This research was funded by institutional "Fondi 5 x 1000 - Ministero della salute 2010".

Acknowledgments

The authors thank Dr Canevari Silvana for important advice in the initial study design, Dr Dugo Matteo for scientific support in WES data analysis, Marchesi Edoardo for contributing in RNA extraction, Ventura Lorena for contributing in FFPE tissue slice preparation, and Dr Disciglio Vittoria for participating in the initial phases of the study. This paper is dedicated to the memory of Prof Carcangiu Maria Luisa who contributed to the initial caselist selection.

Conflict of interest

GP received honoraria from Lilly, AstraZeneca, Novartis, Illumina, and Roche and is part of the advisory board of ADS Biotec.

The remaining authors declare that the research was conducted in the absence of any commercial or financial relationships that could be construed as a potential conflict of interest.

Publisher's note

Supplementary material

The Supplementary Material for this article can be found online at: https://www.frontiersin.org/articles/10.3389/fendo.2023.1267499/full#supplementary-material

References

1. Xing M. Molecular pathogenesis and mechanisms of thyroid cancer. *Nat Rev Cancer* (2013) 13:184–99. doi: 10.1038/nrc3431

2. Cabanillas ME, McFadden DG, Durante C. Thyroid cancer. *Lancet* (2016) 388:2783–95. doi: 10.1016/S0140-6736(16)30172-6

3. Kitahara CM, Sosa JA. Understanding the ever-changing incidence of thyroid cancer. *Nat Rev Endocrinol* (2020) 16:617–8. doi: 10.1038/s41574-020-00414-9

4. Fagin JA, Wells SA. Biologic and clinical perspectives on thyroid cancer. *N Engl J Med* (2016) 375:1054–67. doi: 10.1056/NEJMra1501993

5. Agrawal N, Akbani R, Aksoy BA, Ally A, Arachchi H, Asa SL, et al. Integrated genomic characterization of papillary thyroid carcinoma. *Cell* (2014) 159:676–90. doi: 10.1016/j.cell.2014.09.050

6. Baloch ZW, Asa SL, Barletta JA, Ghossein RA, Juhlin CC, Jung CK, et al. Overview of the 2022 WHO classification of thyroid neoplasms. *Endocr Pathol* (2022) 33:27–63. doi: 10.1007/s12022-022-09707-3

7. Haugen BR, Alexander EK, Bible KC, Doherty GM, Mandel SJ, Nikiforov YE, et al. 2015 American thyroid association management guidelines for adult patients with thyroid nodules and differentiated thyroid cancer: the american thyroid association guidelines task force on thyroid nodules and differentiated thyroid cancer. *Thyroid* (2016) 26:1–133. doi: 10.1089/thy.2015.0020

8. Bae JS, Jung SH, Hirokawa M, Bychkov A, Miyauchi A, Lee S, et al. High prevalence of DICER1 mutations and low frequency of gene fusions in pediatric follicular-patterned tumors of the thyroid. *Endocr Pathol* (2021) 32:336–46. doi: 10.1007/s12022-021-09688-9

9. Lawrence MS, Stojanov P, Polak P, Kryukov GV, Cibulskis K, Sivachenko A, et al. Mutational heterogeneity in cancer and the search for new cancer-associated genes. *Nature* (2013) 499:214–8. doi: 10.1038/nature12213

10. Kondo T, Ezzat S, Asa SL. Pathogenetic mechanisms in thyroid follicular-cell neoplasia. *Nat Rev Cancer* (2006) 6:292–306. doi: 10.1038/nrc1836

11. Yoo SK, Lee S, Kim Sj, Jee HG, Kim BA, Cho H, et al. Comprehensive analysis of the transcriptional and mutational landscape of follicular and papillary thyroid cancers. *PloS Genet* (2016) 12:e1006239. doi: 10.1371/journal.pgen.1006239

12. Pozdeyev N, Gay LM, Sokol ES, Hartmaier R, Deaver KE, Davis S, et al. Genetic analysis of 779 advanced differentiated and anaplastic thyroid cancers. *Clin Cancer Res* (2018) 24:3059–68. doi: 10.1158/1078-0432.CCR-18-0373

13. Landa I, Ibrahimpasic T, Boucai L, Sinha R, Knauf JA, Shah RH, et al. Genomic and transcriptomic hallmarks of poorly differentiated and anaplastic thyroid cancers. *J Clin Invest* (2016) 126:1052–66. doi: 10.1172/JCI85271

14. Costa V, Esposito R, Ziviello C, Sepe R, Bim LV, Cacciola NA, et al. New somatic mutations and WNK1-B4GALNT3 gene fusion in papillary thyroid carcinoma. *Oncotarget* (2015) 6:11242–51. doi: 10.18632/oncotarget.3593

15. Zehir A, Benayed R, Shah RH, Syed A, Middha S, Kim HR, et al. Mutational landscape of metastatic cancer revealed from prospective clinical sequencing of 10,000 patients. *Nat Med* (2017) 23:703–13. doi: 10.1038/nm.4333

16. Kim JH, Jeong JY, Seo AN, Park NJY, Kim M, Park JY. Genomic profiling of aggressive thyroid cancer in association with its clinicopathological characteristics. *In Vivo* (2022) 36:111–20. doi: 10.21873/invivo.12682

17. Durieux E, Descotes F, Mauduit C, Decaussin M, Guyetant S, Devouassoux-Shisheboran M. The co-occurrence of an ovarian Sertoli-Leydig cell tumor with a thyroid carcinoma is highly suggestive of a DICER1 syndrome. *Virchows Arch Int J Pathol* (2016) 468:631–6. doi: 10.1007/s00428-016-1922-0

18. Ravella L, Lopez J, Descotes F, Lifante JC, David C, Decaussin-Petrucci M. [DICER1 mutated, solid/trabecular thyroid papillary carcinoma in an 11-year-old child]. *Ann Pathol* (2018) 38:316–20. doi: 10.1016/j.annpat.2018.04.003

19. Chernock RD, Rivera B, Borrelli N, Hill DA, Fahiminiya S, Shah T, et al. Poorly differentiated thyroid carcinoma of childhood and adolescence: a distinct entity characterized by DICER1 mutations. *Mod Pathol* (2020) 33:1264–74. doi: 10.1038/s41379-020-0458-7

20. Lee YA, Lee H, Im SW, Song YS, Oh DY, Kang HJ, et al. *NTRK* and *RET* fusion–directed therapy in pediatric thyroid cancer yields a tumor response and radioiodine uptake. *J Clin Invest* (2021) 131:e144847. doi: 10.1172/JCI144847

21. de Kock L, Sabbaghian N, Soglio DBD, Guillerman RP, Park BK, Chami R, et al. Exploring the association Between DICER1 mutations and differentiated thyroid carcinoma. *J Clin Endocrinol Metab* (2014) 99:E1072–1077. doi: 10.1210/jc.2013-4206

22. de Kock L, Bah I, Wu Y, Xie M, Priest JR, Foulkes WD. Germline and somatic DICER1 mutations in a well-differentiated fetal adenocarcinoma of the lung. *J Thorac Oncol* (2016) 11:e31–33. doi: 10.1016/j.jtho.2015.09.012

23. Rutter MM, Jha P, Schultz KAP, Sheil A, Harris AK, Bauer AJ, et al. DICER1 mutations and differentiated thyroid carcinoma: evidence of a direct association. *J Clin Endocrinol Metab* (2016) 101:1–5. doi: 10.1210/jc.2015-2169

24. Wu MK, de Kock L, Conwell LS, Stewart CJR, King BR, Choong CS, et al. Functional characterization of multiple DICER1 mutations in an adolescent. *Endocr Relat Cancer* (2016) 23:L1–5. doi: 10.1530/ERC-15-0460

25. Apellaniz-Ruiz M, de Kock L, Sabbaghian N, Guaraldi F, Ghizzoni L, Beccuti G, et al. Familial multinodular goiter and Sertoli-Leydig cell tumors associated with a large intragenic in-frame DICER1 deletion. *Eur J Endocrinol* (2018) 178:K11–9. doi: 10.1530/EJE-17-0904

26. Chen KS, Stuart SH, Stroup EK, Shukla AS, Wang J, Rajaram V, et al. Distinct DICER1 hotspot mutations identify bilateral tumors as separate events. *JCO Precis Oncol* (2018) 2. doi: 10.1200/PO.17.00113

27. Gullo I, Batista R, Rodrigues-Pereira P, Soares P, Barroca H, do Bom-Sucesso M, et al. Multinodular goiter progression toward Malignancy in a case of DICER1 syndrome: histologic and molecular alterations. *Am J Clin Pathol* (2018) 149:379–86. doi: 10.1093/ajcp/aqy004

28. Ghossein CA, Dogan S, Farhat N, Landa I, Xu B. Expanding the spectrum of thyroid carcinoma with somatic DICER1 mutation: a survey of 829 thyroid carcinomas using MSK-IMPACT next generation sequencing platform. *Virchows Arch Int J Pathol* (2022) 480:293–302. doi: 10.1007/s00428-021-03212-4

29. Khan NE, Bauer AJ, Schultz KAP, Doros L, Decastro RM, Ling A, et al. Quantification of thyroid cancer and multinodular goiter risk in the DICER1 syndrome: A family-based cohort study. *J Clin Endocrinol Metab* (2017) 102:1614–22. doi: 10.1210/jc.2016-2954

30. Oliver-Petit I, Bertozzi AI, Grunenwald S, Gambart M, Pigeon-Kerchiche P, Sadoul JL, et al. Multinodular goitre is a gateway for molecular testing of DICER1 syndrome. *Clin Endocrinol* (2019) 91:669–75. doi: 10.1111/cen.14074

31. Thunders M, Delahunt B. Gene of the month: DICER1: ruler and controller. *J Clin Pathol* (2021) 74:69–72. doi: 10.1136/jclinpath-2020-207203

32. Yoo SK, Song YS, Lee EK, Hwang J, Kim HH, Jung G, et al. Integrative analysis of genomic and transcriptomic characteristics associated with progression of aggressive thyroid cancer. *Nat Commun* (2019) 10:2764. doi: 10.1038/s41467-019-10680-5

33. Dunn LA, Sherman EJ, Baxi SS, Tchekmedyian V, Grewal RK, Larson SM, et al. Vemurafenib redifferentiation of BRAF mutant, RAI-refractory thyroid cancers. *J Clin Endocrinol Metab* (2018) 104:1417–28. doi: 10.1210/jc.2018-01478

34. Kim K, Jeon S, Kim TM, Jung CK. Immune gene signature delineates a subclass of papillary thyroid cancer with unfavorable clinical outcomes. *Cancers* (2018) 10:494. doi: 10.3390/cancers10120494

35. Colombo C, Minna E, Gargiuli C, Muzza M, Dugo M, De Cecco L, et al. The molecular and gene/miRNA expression profiles of radioiodine resistant papillary thyroid cancer. *J Exp Clin Cancer Res* (2020) 39:245. doi: 10.1186/s13046-020-01757-x

36. Minna E, Brich S, Todoerti K, Pilotti S, Collini P, Bonaldi E, et al. Cancer associated fibroblasts and senescent thyroid cells in the invasive front of thyroid carcinoma. *Cancers* (2020) 12:112. doi: 10.3390/cancers12010112

37. Bonaldi E, Gargiuli C, De Cecco L, Micali A, Rizzetti MG, Greco A, et al. BRAF inhibitors induce feedback activation of RAS pathway in thyroid cancer cells. *Int J Mol Sci* (2021) 22:5744. doi: 10.3390/ijms22115744

38. Lloyd RV, Osamura RY, Klöppel G, Rosai J. WHO classification of tumours of endocrine organs. In: WHO Clasification of Tumors, *4th edition*. Lyon, France: International Agency for Research on Cancer (IARC (2017). p. 355.

39. Volante M, Collini P, Nikiforov YE, Sakamoto A, Kakudo K, Katoh R, et al. Poorly differentiated thyroid carcinoma: the Turin proposal for the use of uniform diagnostic criteria and an algorithmic diagnostic approach. *Am J Surg Pathol* (2007) 31:1256–64. doi: 10.1097/PAS.0b013e3180309e6a

40. Zicchedda B, Biancon G, Bagnoli F, De Philippis C, Maura F, Rustad EH, et al. Integrative analysis of the genomic and transcriptomic landscape of double-refractory multiple myeloma. *Blood Adv* (2020) 4:830–44. doi: 10.1182/bloodadvances.2019000779

41. *Babraham Bioinformatics - FastQC A Quality Control tool for High Throughput Sequence Data*. Available at: https://www.bioinformatics.babraham.ac.uk/projects/fastqc/.

42. Li H, Durbin R. Fast and accurate long-read alignment with Burrows-Wheeler transform. *Bioinforma Oxf Engl* (2010) 26:589–95. doi: 10.1093/bioinformatics/btp698

43. Lek M, Karczewski KJ, Minikel EV, Samocha KE, Banks E, Fennell T, et al. Analysis of protein-coding genetic variation in 60,706 humans. *Nature* (2016) 536:285–91. doi: 10.1038/nature19057

44. Sherry ST, Ward MH, Kholodov M, Baker J, Phan L, Smigielski EM, et al. dbSNP: the NCBI database of genetic variation. *Nucleic Acids Res* (2001) 29:308–11. doi: 10.1093/nar/29.1.308

45. 1000 Genomes Project Consortium, Abecasis GR, Auton A, Brooks LD, DePristo MA, Durbin RM, et al. An integrated map of genetic variation from 1,092 human genomes. *Nature* (2012) 491:56–65. doi: 10.1038/nature11632

46. Irizarry RA, Hobbs B, Collin F, Beazer-Barclay YD, Antonellis KJ, Scherf U, et al. Exploration, normalization, and summaries of high density oligonucleotide array probe level data. *Biostat Oxf Engl* (2003) 4:249–64. doi: 10.1093/biostatistics/4.2.249

47. Zhang B, Horvath S. A general framework for weighted gene co-expression network analysis. *Stat Appl Genet Mol Biol* (2005) 4. doi: 10.2202/1544-6115.1128

48. Rusinek D, Pfeifer A, Cieslicka M, Kowalska M, Pawlaczek A, Krajewska J, et al. TERT promoter mutations and their impact on gene expression profile in papillary thyroid carcinoma. *Cancers* (2020) 12:1597. doi: 10.3390/cancers12061597

49. Sauer M, Barletta JA. Proceedings of the north american society of head and neck pathology, los angeles, CA, March 20, 2022: DICER1-related thyroid tumors. *Head Neck Pathol* (2022) 16:190–9. doi: 10.1007/s12105-022-01417-w

50. Hata A, Kashima R. Dysregulation of microRNA biogenesis machinery in cancer. *Crit Rev Biochem Mol Biol* (2016) 51:121–34. doi: 10.3109/10409238.2015.1117054

51. Chong AS, Nikiforov YE, Condello V, Wald AI, Nikiforova MN, Foulkes WD, et al. Prevalence and spectrum of DICER1 mutations in adult-onset thyroid nodules with indeterminate cytology. *J Clin Endocrinol Metab* (2021) 106:968–77. doi: 10.1210/clinem/dgab025

52. Wasserman JD, Sabbaghian N, Fahiminiya S, Chami R, Mete O, Acker M, et al. DICER1 mutations are frequent in adolescent-onset papillary thyroid carcinoma. *J Clin Endocrinol Metab* (2018) 103:2009–15. doi: 10.1210/jc.2017-02698

53. Lee YA, Im SW, Jung KC, Chung EJ, Shin CH, Kim JI, et al. Predominant DICER1 pathogenic variants in pediatric follicular thyroid carcinomas. *Thyroid* (2020) 30:1120–31. doi: 10.1089/thy.2019.0233

54. Pekova B, Sykorova V, Mastnikova K, Vaclavikova E, Moravcova J, Vlcek P, et al. NTRK fusion genes in thyroid carcinomas: clinicopathological characteristics and their impacts on prognosis. *Cancers* (2021) 13:1932. doi: 10.3390/cancers13081932

55. Drilon A, Jenkins C, Iyer S, Schoenfeld A, Keddy C, Davare MA. ROS1-dependent cancers — biology, diagnostics and therapeutics. *Nat Rev Clin Oncol* (2021) 18:35–55. doi: 10.1038/s41571-020-0408-9

56. Ritterhouse LL, Wirth LJ, Randolph GW, Sadow PM, Ross DS, Liddy W, et al. ROS1 rearrangement in thyroid cancer. *Thyroid* (2016) 26:794–7. doi: 10.1089/thy.2016.0101

57. Liu SV, Macke LA, Colton BS, Imran SS, Christiansen J, Chow-Maneval E, et al. Response to entrectinib in differentiated thyroid cancer with a ROS1 fusion. *JCO Precis Oncol* (2017) 1. doi: 10.1200/PO.17.00105

58. Gasparre G, Porcelli AM, Bonora E, Pennisi LF, Toller M, Iommarini L, et al. Disruptive mitochondrial DNA mutations in complex I subunits are markers of oncocytic phenotype in thyroid tumors. *Proc Natl Acad Sci USA* (2007) 104:9001–6. doi: 10.1073/pnas.0703056104

59. Gopal RK, Kübler K, Calvo SE, Polak P, Livitz D, Rosebrock D, et al. Widespread chromosomal losses and mitochondrial DNA alterations as genetic drivers in hürthle cell carcinoma. *Cancer Cell* (2018) 34:242–255.e5. doi: 10.1016/j.ccell.2018.06.013

60. Ganly I, Makarov V, Deraje S, Dong Y, Reznik E, Seshan V, et al. Integrated genomic analysis of hürthle cell cancer reveals oncogenic drivers, recurrent mitochondrial mutations, and unique chromosomal landscapes. *Cancer Cell* (2018) 34:256–270.e5. doi: 10.1016/j.ccell.2018.07.002

61. Dabravolski SA, Nikiforov NG, Zhuravlev AD, Orekhov NA, Mikhaleva LM, Orekhov AN. The role of altered mitochondrial metabolism in thyroid cancer development and mitochondria-targeted thyroid cancer treatment. *Int J Mol Sci* (2021) 23:460. doi: 10.3390/ijms23010460

62. Tsybrovskyy O, De Luise M, de Biase D, Caporali L, Fiorini C, Gasparre G, et al. Papillary thyroid carcinoma tall cell variant shares accumulation of mitochondria, mitochondrial DNA mutations, and loss of oxidative phosphorylation complex I integrity with oncocytic tumors. *J Pathol Clin Res* (2022) 8:155–68. doi: 10.1002/cjp2.247

63. Liberzon A, Birger C, Thorvaldsdóttir H, Ghandi M, Mesirov JP, Tamayo P. The Molecular Signatures Database (MSigDB) hallmark gene set collection. *Cell Syst* (2015) 1:417–25. doi: 10.1016/j.cels.2015.12.004

64. Hanahan D, Weinberg RA. Hallmarks of cancer: the next generation. *Cell* (2011) 144:646–74. doi: 10.1016/j.cell.2011.02.013

65. Stosic A, Fuligni F, Anderson ND, Davidson S, de Borja R, Acker M, et al. Diverse oncogenic fusions and distinct gene expression patterns define the genomic landscape of pediatric papillary thyroid carcinoma. *Cancer Res* (2021) 81:5625–37. doi: 10.1158/0008-5472.CAN-21-0761

66. Pugh TJ, Yu W, Yang J, Field AL, Ambrogio L, Carter SL, et al. Exome sequencing of pleuropulmonary blastoma reveals frequent biallelic loss of TP53 and two hits in DICER1 resulting in retention of 5p-derived miRNA hairpin loop sequences. *Oncogene* (2014) 33:5295–302. doi: 10.1038/onc.2014.150

67. Poma AM, Condello V, Denaro M, Torregrossa L, Elisei R, Vitti P, et al. DICER1 somatic mutations strongly impair miRNA processing even in benign thyroid lesions. *Oncotarget* (2019) 10:1785–97. doi: 10.18632/oncotarget.26639

68. Ricarte-Filho JC, Casado-Medrano V, Reichenberger E, Spangler Z, Scheerer M, Isaza A, et al. DICER1 RNase IIIb domain mutations trigger widespread miRNA dysregulation and MAPK activation in pediatric thyroid cancer. *Front Endocrinol* (2023) 14:1083382. doi: 10.3389/fendo.2023.1083382

69. Nikiforova MN, Mercurio S, Wald AI, Barbi de Moura M, Callenberg K, Santana-Santos L, et al. Analytical performance of the ThyroSeq v3 genomic classifier for cancer diagnosis in thyroid nodules. *Cancer* (2018) 124:1682–90. doi: 10.1002/cncr.31245

70. Schultz KAP, Williams GM, Kamihara J, Stewart DR, Harris AK, Bauer AJ, et al. DICER1 and associated conditions: identification of at-risk individuals and recommended surveillance strategies. *Clin Cancer Res* (2018) 24:2251–61. doi: 10.1158/1078-0432.CCR-17-3089

71. Chen J, Yang H, Teo ASM, Amer LB, Sherbaf FG, Tan CQ, et al. Genomic landscape of lung adenocarcinoma in East Asians. *Nat Genet* (2020) 52:177–86. doi: 10.1038/s41588-019-0569-6

72. Jantrapirom S, Piccolo LL, Pruksakorn D, Potikanond S, Nimlamool W. Ubiquilin networking in cancers. *Cancers* (2020) 12:1586. doi: 10.3390/cancers12061586

73. Jackson JT, Mulazzani E, Nutt SL, Masters SL. The role of PLCγ2 in immunological disorders, cancer, and neurodegeneration. *J Biol Chem* (2021) 297:100905. doi: 10.1016/j.jbc.2021.100905

74. Moore A, Bar Y, Maurice-Dror C, Finkel I, Goldvaser H, Dudnik E, et al. Next-generation sequencing in thyroid cancers: do targetable alterations lead to a therapeutic advantage?: A multicenter experience. *Medicine* (2021) 100:e26388. doi: 10.1097/MD.0000000000026388

75. Nalepa G, Clapp DW. Fanconi anaemia and cancer: an intricate relationship. *Nat Rev Cancer* (2018) 18:168–85. doi: 10.1038/nrc.2017.116

76. Bakker ST, van de Vrugt HJ, Visser JA, Delzenne-Goette E, van der Wal A, Berns MAD, et al. Fancf-deficient mice are prone to develop ovarian tumours. *J Pathol* (2012) 226:28–39. doi: 10.1002/path.2992

frontiers | Frontiers in Endocrinology

TYPE Original Research
PUBLISHED 26 October 2023
DOI 10.3389/fendo.2023.1247542

OPEN ACCESS

EDITED BY
Cesar Seigi Fuziwara,
University of São Paulo, Brazil

REVIEWED BY
Da Huang,
Second Affiliated Hospital of Nanchang University, China
Adrián Acuña-Ruiz,
Memorial Sloan Kettering Cancer Center, United States
Saad Khan,
Stanford University, United States

*CORRESPONDENCE
Jaime M. Pita
jmpita8@gmail.com;
Jaime.Miguel.Pita@ulb.be
Pierre P. Roger
Pierre.Roger@ulb.be

†Deceased

RECEIVED 26 June 2023
ACCEPTED 26 September 2023
PUBLISHED 26 October 2023

CITATION
Pita JM, Raspé E, Coulonval K, Decaussin-Petrucci M, Tarabichi M, Dom G, Libert F, Craciun L, Andry G, Wicquart L, Leteurtre E, Trésallet C, Marlow LA, Copland JA, Durante C, Maenhaut C, Cavaco BM, Dumont JE, Costante G and Roger PP (2023) CDK4 phosphorylation status and rational use for combining CDK4/6 and BRAF/MEK inhibition in advanced thyroid carcinomas. *Front. Endocrinol.* 14:1247542. doi: 10.3389/fendo.2023.1247542

CDK4 phosphorylation status and rational use for combining CDK4/6 and BRAF/MEK inhibition in advanced thyroid carcinomas

Jaime M. Pita[1*], Eric Raspé[1], Katia Coulonval[1], Myriam Decaussin-Petrucci[2], Maxime Tarabichi[1], Geneviève Dom[1], Frederick Libert[1,3], Ligia Craciun[4], Guy Andry[5], Laurence Wicquart[6], Emmanuelle Leteurtre[7], Christophe Trésallet[8,9], Laura A. Marlow[10], John A. Copland[10], Cosimo Durante[11], Carine Maenhaut[1], Branca M. Cavaco[12], Jacques E. Dumont[1†], Giuseppe Costante[13] and Pierre P. Roger[1*]

[1]Institut de Recherche Interdisciplinaire en Biologie Humaine et Moléculaire (IRIBHM) and Université Libre de Bruxelles (ULB)-Cancer Research Center (U-CRC), Université Libre de Bruxelles (ULB), Brussels, Belgium, [2]Department of Pathology, Lyon Sud Hospital, Claude Bernard Lyon 1 University, Lyon, France, [3]BRIGHTCore, Université Libre de Bruxelles (ULB), Brussels, Belgium, [4]Tumor Bank of the Institut Jules Bordet Comprehensive Cancer Center – Hôpital Universitaire de Bruxelles, Université Libre de Bruxelles (ULB), Brussels, Belgium, [5]Department of Head & Neck and Thoracic Surgery, Institut Jules Bordet Comprehensive Cancer Center – Hôpital Universitaire de Bruxelles, Université Libre de Bruxelles (ULB), Brussels, Belgium, [6]Tumorothèque du Groupement de Coopération Sanitaire-Centre Régional de Référence en Cancérologie (C2RC) de Lille, Lille, France, [7]Department of Pathology, Univ. Lille, Centre National de la Recherche Scientifique (CNRS), Inserm, Centre Hospitalo-Universitaire (CHU) Lille, UMR9020-U1277-CANTHER-Cancer Heterogeneity, Plasticity and Resistance to Therapies, Lille, France, [8]Department of General and Endocrine Surgery - Pitié-Salpêtrière Hospital, Sorbonne University, Assistance Publique des Hôpitaux de Paris, Paris, France, [9]Department of Digestive, Bariatric and Endocrine Surgery - Avicenne University Hospital, Paris Nord - Sorbonne University, Assistance Publique des Hôpitaux de Paris, Paris, France, [10]Department of Cancer Biology, Mayo Clinic, Jacksonville, FL, United States, [11]Department of Translational and Precision Medicine, Sapienza University of Rome, Rome, Italy, [12]Molecular Endocrinology Group, Unidade de Investigação em Patobiologia Molecular (UIPM), Instituto Português de Oncologia de Lisboa Francisco Gentil (IPOLFG), Lisbon, Portugal, [13]Departments of Endocrinology and Medical Oncology, Institut Jules Bordet Comprehensive Cancer Center – Hôpital Universitaire de Bruxelles, Université Libre de Bruxelles (ULB), Brussels, Belgium

Background: CDK4/6 inhibitors (CDK4/6i) have been established as standard treatment against advanced Estrogen Receptor-positive breast cancers. These drugs are being tested against several cancers, including in combinations with other therapies. We identified the T172-phosphorylation of CDK4 as the step determining its activity, retinoblastoma protein (RB) inactivation, cell cycle commitment and sensitivity to CDK4/6i. Poorly differentiated (PDTC) and anaplastic (ATC) thyroid carcinomas, the latter considered one of the most lethal human malignancies, represent major clinical challenges. Several molecular evidence suggest that CDK4/6i could be considered for treating these advanced thyroid cancers.

Methods: We analyzed by two-dimensional gel electrophoresis the CDK4 modification profile and the presence of T172-phosphorylated CDK4 in a

collection of 98 fresh-frozen tissues and in 21 cell lines. A sub-cohort of samples was characterized by RNA sequencing and immunohistochemistry. Sensitivity to CDK4/6i (palbociclib and abemaciclib) was assessed by BrdU incorporation/viability assays. Treatment of cell lines with CDK4/6i and combination with BRAF/MEK inhibitors (dabrafenib/trametinib) was comprehensively evaluated by western blot, characterization of immunoprecipitated CDK4 and CDK2 complexes and clonogenic assays.

Results: CDK4 phosphorylation was detected in all well-differentiated thyroid carcinomas (n=29), 19/20 PDTC, 16/23 ATC and 18/21 thyroid cancer cell lines, including 11 ATC-derived ones. Tumors and cell lines without phosphorylated CDK4 presented very high $p16^{CDKN2A}$ levels, which were associated with proliferative activity. Absence of CDK4 phosphorylation in cell lines was associated with CDK4/6i insensitivity. *RB1* defects (the primary cause of intrinsic CDK4/6i resistance) were not found in 5/7 tumors without detectable phosphorylated CDK4. A previously developed 11-gene expression signature identified the likely unresponsive tumors, lacking CDK4 phosphorylation. In cell lines, palbociclib synergized with dabrafenib/trametinib by completely and permanently arresting proliferation. These combinations prevented resistance mechanisms induced by palbociclib, most notably Cyclin E1-CDK2 activation and a paradoxical stabilization of phosphorylated CDK4 complexes.

Conclusion: Our study supports further clinical evaluation of CDK4/6i and their combination with anti-BRAF/MEK therapies as a novel effective treatment against advanced thyroid tumors. Moreover, the complementary use of our 11 genes predictor with p16/KI67 evaluation could represent a prompt tool for recognizing the intrinsically CDK4/6i insensitive patients, who are potentially better candidates to immediate chemotherapy.

KEYWORDS

ATC, PDTC, CDK4 Thr172-phosphorylation, palbociclib, trametinib, dabrafenib, biomarkers

1 Introduction

Despite overall good prognosis associated to thyroid cancer, the management of patients with advanced thyroid tumors represents a major clinical challenge. Indeed, up to 10% of well-differentiated thyroid carcinomas (WDTC), initially cured with surgery followed by radioactive iodine treatment (RAI), may develop locally advanced or metastatic disease. Sixty to seventy percent of these tumors eventually become RAI-refractory (1), with a dramatic impact on survival. On the other hand, poorly differentiated carcinomas (PDTC) and anaplastic carcinomas (ATC), composed by dedifferentiated cells, primarily present as highly aggressive tumors. ATC has been claimed as one of the most lethal tumor types, contributing up to 50% of the deaths attributable to thyroid cancer, with patients displaying a median survival of 3 to 5 months (2, 3). In the majority of cases, tumor resection is not possible and response to chemo- or radio-therapy is poor (2, 4, 5). PDTC and differentiated high grade carcinomas exhibit intermediate behavior and prognosis between WDTC and ATC (6, 7).

In the last decade, targeted therapies have improved the management of RAI-refractory recurrent/metastatic WDTC and PDTC, but the toxicity associated to these treatments greatly impairs their clinical use (8). Moreover, the new therapeutic strategies, including targeted therapy and immunotherapy, did not produce major improvement in terms of survival for most ATC patients (5, 9, 10).

Aberrant cell proliferation due to dysregulated cell division is a peculiar trait of cancer. The complexes between cyclins and cyclin-dependent kinases (CDK) play a pivotal role in the control of cell division and modulation of transcription in response to mitogenic factors. Particularly, CDK4 and CDK6 represent the master node of regulation for the G1 phase restriction point (11), by phosphorylating and initiating the inactivation of the retinoblastoma tumor-suppressor protein (RB). This process is subsequently maintained by a positive feedback loop linking RB to E2F-dependent transcription of *CCNE1* (cyclin E1), which activates CDK2. CDK4/6 assembly with a D-type cyclin is required for its activity and this binding can be counteracted by proteins of the INK4 family (such as p16 and p15), or can be

facilitated by CIP/KIP family members (p21 and p27) (12, 13). Due to its deregulation, many cancer cells are addicted to CDK4/6 activity (14). Selective inhibitors of CDK4/6 are being tested in numerous clinical trials against various types of cancers (15, 16). The CDK4/6 inhibitors (CDK4/6i) palbociclib, ribociclib and abemaciclib have become the standard of care for the treatment of Estrogen Receptor-positive advanced or metastatic breast tumors in combination with endocrine therapy, providing major improvements in progression-free and overall survival (17–20). Still, indication for these drugs is limited by the lack of suitable biomarker of potential sensitivity. We have extensively demonstrated that phosphorylation on amino acid T172 is an absolute requirement for the activation of CDK4 and is finely regulated, determining the cell cycle commitment (11, 13, 21–24). By contrast, the homologous T177 phosphorylation on CDK6 is not regulated and is generally absent or weak (13, 25). In our previous studies in breast tumors (26) and pleural mesotheliomas (27), we observed a variable presence of CDK4 T172-phosphorylation in most tumors. Its absence however, was also observed in some highly proliferative tumors, in association with the main mechanisms of resistance to CDK4/6i, including RB defects or inactivation, and high expressions of *CDKN2A* (p16), *CCNE1* (cyclin E1) and *E2F1* (26–29). Hence, CDK4 T172-phosphorylation might be the most relevant biomarker of potential tumor sensitivity to CDK4/6i, by identifying or predicting the presence of active CDK4, which is the actual target of inhibitory drugs. Furthermore, we showed that the CDK4 modification profile of breast tumors and cell lines can be predicted using the expression values of 11 genes (26).

PDTC and ATC are highly proliferative cancers associated with increased cell cycle progression and chromosomal instability (30–34). Several studies from our group indicated CDK4 as a critical regulator of physiological and cancerous thyrocyte proliferation (13, 21, 35, 36). Moreover, MAPK/ERK, EGFR/ERBB and PI3K/AKT, widely recognized as the main deregulated signaling pathways in thyroid tumors (37, 38), have CDK4/6 as major integrating node. It could therefore be speculated that inhibition of CDK4/6 might effectively represent a therapeutic approach for advanced thyroid tumors.

The aims of this work were to define if the CDK4 phosphorylation can be detected in thyroid cancer, whether it is variable and indicative of sensitivity to CDK4/6i and predictable on a biomarker based upon protein and/or mRNA expression. Furthermore, we aimed to identify drug combinations including CDK4/6i, which actively block the growth of advanced thyroid cancers, providing the rationale for testing in clinical trials.

2 Materials and methods

2.1 Human thyroid tissue samples

Thyroid tumors and normal thyroid tissues from flash-frozen samples or optimal cutting temperature (OCT) compound-embedded samples were obtained from different institutions. This study was performed in accordance with the Declaration of Helsinki and collection of patient tissues and associated data was done in agreement with the Ethics Committees of Jules Bordet Institute (CE1978, CE2970) with informed consent of patients, Sapienza University of Rome, Pitié-Salpêtrière Hospital and with the Mayo Clinic Institutional Review Board protocol. Samples and associated data from the Institute – Instituto Português de Oncologia de Lisboa Francisco Gentil (IPOLFG) – were obtained in compliance with all applicable laws, including a written consent, and the study was approved by the institute's Ethics Committee. Written informed consent was obtained from all patients of the tumor tissue bank – Tumorothèque Centre de Ressources Biologiques des Hospices Civil de Lyon. Samples and associated data were obtained from the tumor tissue bank – Tumorothèque ALLIANCE CANCER de Lille – that operates under the authorization AC-2018-3110 granted by the French ministry of research. Prior to scientific use, patients were appropriately informed and asked to consent in compliance with the French regulations.

All ATC and PDTC diagnoses were histologically re-evaluated and confirmed by an expert thyroid pathologist (MD), by examination of corresponding FFPE slides or, whenever possible, of serial sections of OCT slides. PDTC were defined following the Turin proposal (39).

A total of 140 samples were collected for two-dimensional gel (2D-gel) electrophoresis analysis (42 ATC, 30 PDTC, 8 follicular thyroid carcinoma (FTC), 9 oncocytic FTC, 23 papillary thyroid carcinoma (PTC) (1 metastasis), 7 lymph node metastases (LNM) and 21 normal thyroid tissues). Twenty-one samples were discarded due to signs of wide necrotic tissue (more than 80% of tissue area; 2 ATC), misclassification (1 ATC and 1 oncocytic FTC), bad RNA quality (RNA integrity number lower than 3)/protein quality (3 PTC, 8 ATC, 1 normal and 3 oncocytic FTC) or insufficient protein quantity (1 PTC and 1 PDTC). Eighty-four of 119 samples were selected for RNA-seq, and following an exploratory analysis, 27 cases were further excluded from analysis due to: gross contamination/misclassification (3 normal with neoplastic cells, 1 PDTC with no neoplastic signs, 2 ATC with more than 70% of PTC cells, 1 ATC with 60% of stroma area); sample duplicate (1 normal); low RNA quality (RNA integrity number lower than 4.5; 1 ATC and 2 PDTC); high proportion of PCR duplicates (more than 0.5% of the library; 1 FTC and 2 oncocytic FTC); or very low/undetectable 2D-gel signal (4 ATC, 6 PDTC and 2 PTC). In summary, 98 samples were included in the 2D-gel proteomic analysis and 57 samples were included in the transcriptomic analysis.

2.2 Thyroid cancer cell lines

2.2.1 Cell culture and inhibitors

Human thyroid carcinoma cell lines were maintained in a humidified atmosphere (5% CO_2) at 37°C and cultured as described in Supplementary Table S1. The origin, authentication, and main features of each cell line are also provided (40). Cells were passaged for fewer than 2 months or within 20 passages. Cell culture reagents were obtained from Gibco (Carlsbad, CA, USA). Palbociclib (PD0332991; S1116), abemaciclib (LY2835219; S7158),

trametinib (GSK1120212; S2673) and dabrafenib (GSK118436; S2807) were purchased from SelleckChem (Houston, TX, USA) and dissolved in DMSO. Controls were treated with the same concentration of DMSO.

2.2.2 DNA synthesis and cell growth assays

For DNA synthesis assay, cells seeded in triplicates in 96-well plates were incubated for at least 16 h before being challenged with the indicated serial dilutions of inhibitors for 24 h. One hour before fixation with methanol, 100 µM 5-bromo-2′-deoxyuridine (BrdU, Sigma-Aldrich, St Louis, MO, USA) and 4 µM 5-fluoro-2′-deoxyuridine (FldU, Sigma-Aldrich) were added to the cells. Immunodetection of DNA-incorporated BrdU was done as described (26, 41), imaged and analyzed semi-automatically with a custom-made ImageJ macro as described previously (26).

The effect of inhibitory drugs on cellular growth was also evaluated using the SRB assay and MTT assay, as described previously (26). Cells seeded in triplicates in 96-well plates were allowed to attach for at least 16 h before being incubated with serial dilutions of CDK4/6i for 144 h (SRB) or 48 h (MTT). Serial dilutions of puromycin were used as positive controls.

2.2.3 Long-term cell treatments

To evaluate the effect of a prolonged treatment on DNA synthesis, cells seeded in duplicates in 3-cm dishes were incubated for at least 16 h before being treated with 1 µM palbociclib for 2 d or 10 d. After 10 d, cells were either fixed or washed twice with phosphate-buffered saline (PBS) and allowed to grow without drug for 1 d. Media and drugs were replenished every 3 d. One hour before fixation with methanol and permeabilization with 0.1% Triton X-100 (Sigma-Aldrich), 40 µM 5-ethynyl-2'-deoxyuridine (EdU, Invitrogen, Waltham, MA, USA) was added to the cells. DNA-incorporated EdU was detected following the Click-iT assay protocol (Invitrogen). Briefly, fixed and permeabilized cells were incubated for 30 min with a Tris-buffered saline buffer supplemented in the following order, with 1 mM copper(II) sulfate (Sigma-Aldrich), 100 mM L-ascorbic acid (Sigma-Aldrich) and 5 µM Alexa Fluor 594 Azide (Thermo Fischer Scientific). DAPI (1 µg/ml) was used as nuclear counterstain and round coverslips were mounted in each dish with ProLong Gold Antifade mountant. Cells were observed under a microscope and, for each condition, a total of at least 500 cells was manually counted.

2.2.4 Clonogenic assays

Equal amounts of cells (5×10^2 to 2×10^3/well depending on the cell line) were seeded in 6-well plates and allowed to attach for at least 16 h, before being treated with the indicated drugs. After 10 d, cells were either stopped or washed twice with PBS and allowed to grow without drugs for the same amount of time. Media and drugs were replenished every 3 d. Cells were then fixed with 4% paraformaldehyde (Sigma-Aldrich) and stained with 0.05% crystal violet solution (in distilled water, Sigma-Aldrich) for 30 min. After washing and air-drying, the plates were photographed.

2.2.5 Senescence-associated β-galactosidase activity staining

Cells seeded in 6-well plates, at densities adapted for each condition (5×10^2 to 2×10^4/well), were incubated for at least 16 h before being treated with drugs. After 6 or 8 d (media and drugs replenished every 3 d), β-galactosidase activity in cells was detected using the Senescence β-galactosidase staining kit (Cell Signaling Technology, Danvers, MA, USA) at pH 6.0, following the manufacturer's protocol. After incubation with the staining solution for 16-18 h at 37°C without CO_2, the proportion of cells with developed blue color was quantified. For each condition, a total of at least 500 cells was counted manually using a light-field microscope.

2.2.6 Combination index calculation

Analysis of drug synergy was done using the CompuSyn software (www.combosyn.com) which is based on Chou-Talalay's combination index theorem (42). The software uses a median-effect method that determines if the drug combination produces greater effects together than expected from the summation of their individual effects. The combination index (CI) values were calculated for the different concentration-effect plots (for each of the serial dilutions) based on the parameters derived from the median-effect plots of the individual drugs or drug combinations at the fixed ratios. The CI was calculated based on the assumption of mutually nonexclusive drug interactions. Definition of the degree of synergism in accordance to the CI value was based as described (43).

2.3 Protein analyses

The antibodies used in this work are listed in Supplementary Table S2. Equal amounts of whole-cell extract proteins or immunoprecipitates were separated by SDS-PAGE and immunodetected. For 2D-gel electrophoresis, cells were lysed in a buffer containing 7 M urea and 2 M thiourea. Ground tissues obtained from cryogrinding of flash-frozen tumor tissues and frozen tumor slides embedded in OCT (at least, 10 sections of 10 µm per sample) were solubilized as described (26). Proteins were separated by isoelectric focusing on immobilized linear pH gradient strips (pH 5 to 8, Bio-Rad, Hercules, CA, USA) before separation by SDS-PAGE. Chemiluminescence images of the samples were acquired on films or with a Vilber-Lourmat Solo7S camera and quantified using the Bio1D software (Vilber-Lourmat, Marne-la-Vallée, France). The profile of CDK4 separated by 2D-gel electrophoresis has been characterized previously (13, 26). Quantification of the spot 2 and spot 3 volumes (corresponding to the two main modified forms of CDK4) were done from 16-bit scans of the 2D-gel immunoblots, with unsaturated signals. After linear correction of the background, the volume ratio (spot3/spot2) was used to define three types of CDK4 modification profiles: a profile A (for absent) was attributed when the ratio was below 0.02; a profile L (for low) was attributed when the ratio lied between 0.02

and 0.50; and a profile H (for high) was given when the ratio was equal or above 0.50.

Co-immunoprecipitations were performed as described (13, 21). RB-kinase activity of immunoprecipitated CDK complexes was measured by *in vitro* incubation with ATP and a fragment of RB, as described (21, 36).

2.4 RNA-sequencing

2.4.1 Library preparation and sequencing

Total RNA was isolated from cell lines using the RNeasy Mini Kit (Qiagen, Hilden, Germany). Total RNA from ground tissues (obtained from cryogrinding of flash-frozen tumor pieces) and from OCT-embedded frozen tissue slides (at least, 10 sections of 10 µm per sample) were first extracted with TRI Reagent Solution (Invitrogen) using a Potter-Elvehjem homogenizer with a motorized PTFE pestle, and then were purified with the RNeasy Mini kit (Qiagen) and on-column DNase digestion (RNase-free DNase Set, Qiagen) according to the manufacturer's protocol. Alternatively, RNA and DNA were extracted with Buffer RLT Plus using the AllPrep DNA/RNA mini kit (Qiagen) according to the manufacturer's protocol. RNA yield and purity were assessed using a Fragment Analyzer 5200 (Agilent Technologies, Massy, France). 10ng to 100 ng of RNA was used for cDNA libraries and sequences production, as previously described (27). Homo_sapiens.GRCh38.90.gtf annotations and Homo_sapiens.GRCh38.90.dna.primary-assembly.fa sequence files downloaded from ftp.Ensembl.org were used for reads alignments. Transcript level counts were calculated with HTSeq and normalized to library size to obtain counts per 20 million reads (CP20M). Integrative Genomics Viewer software (44) (IGV version 2.12.3) was used for visualization and screening of mutations.

2.4.2 Analysis of RNA-sequencing data

Principal component analysis (PCA) was performed in R (version 4.2.3) using the libraries FactoMineR (45) and factoextra. The gene expression profiles of all samples tested in the study were used. Genes were first filtered by removing those with a null mean expression. Next, gene expression values were scaled by dividing each expression value by the standard deviation of the expression values of the considered gene with the sweep function. The PCA function was used to compute the principal components explaining decreasing proportions of the variance. The two first recorded principal components were plotted with symbols corresponding to CDK4 profiles and colors to types using the ggplot2 package. As in the exploratory plot, several samples were not clustering with others of the same group, the outlier samples were removed prior to define 95% confidence ellipses. These include two normal samples clustering with PDTC or ATC, one ATC clustering with PTC and two PDTC clustering with ATC. Finally, exclusion from the selection was extended to the samples with bad quality proteomic profiles or RNA (as detailed in section 2.1). The final sample selection used to define the confidence ellipses included 52 tumors out of the 84 tumors analyzed. A new plot was drawn with the excluded samples and the ellipses described above.

The thyroid differentiation score (TDS) was defined as the mean z-score of the 16 genes previously described (46). An epithelial-mesenchymal transition (EMT) score was obtained as previously described (47) (with the minor difference of including *OCLN* gene), by subtracting the mean z-score of 4 epithelial marker genes from the mean z-score of 13 mesenchymal marker genes. To obtain a gene z-score in each sample, gene expression in CP20M was first mean-centered and then divided by the corresponding standard deviation of the gene expression across all samples.

2.4.3 Calculation of *CDKN2A* exon 1α expression

The pileup function of the R package Rsamtools was used to extract the coverage values at each position of the *CDKN2A* locus from each sample BAM file. Genomic coordinates of the whole locus and all introns and exons coding for p14 and p16 were extracted from ftp.Ensembl.org. A linear regression between the coverage at each intronic position and their gene coordinates was used to correct the coverage at each exon positions for background. When background estimates were higher than the observed coverage, the value was set to zero. As the best fitting between exon 2 coverage and the sum of the exons 1α and 1β coverage was obtained using maximum coverage values, this parameter was used. To be able to compare *CDKN2A* gene and exon 1α expression levels in each sample, exon 1α expression was calculated as a fraction of *CDKN2A* gene expression. This fraction was defined by the ratio of maximum coverage values between exon 1α and the sum of exons 1α and 1β in each of the samples.

2.4.4 Prediction of the CDK4 modification profile

As previously detailed and characterized (26), a centroid method was used to predict the CDK4 profile whereby the expression profile of 11 genes (including *CDKN2A*) of an unknown sample was compared to three references built by computing, for each 11 genes, the average of their expression among prototype tumors with A, H or L CDK4 profiles. The predicted profile was the one corresponding to the A, H or L centroid with the highest correlation coefficient. As they were initially profiled with the Affymetrix platform (26), the breast tumor references used to predict the CDK4 modification profile were first adapted by using the RNA-seq expression data acquired with RNA extracted from the same samples. Raw thyroid RNA-seq CP20M expression values were compared to these adapted references by Spearman correlation. For the *CDKN2A* gene, these values were also corrected, as detailed in section 2.4.3, by calculating the contribution of the p16-specific exon 1α to the expression of the whole *CDKN2A* locus expression. In this case, all samples were scaled by the same factor such as the average expression *CDKN2A* exon 1α of profile A thyroid tumors was equal to the *CDKN2A* value of the reference for profile A breast tumors.

2.5 Targeted DNA-sequencing

2.5.1 Preparation and sequencing

Genomic DNA was extracted with Buffer RLT Plus using the AllPrep DNA/RNA mini kit (Qiagen) or was purified from the

remaining interphase/organic phase left from RNA extraction by performing an alkaline phenol-chloroform extraction. Briefly, back extraction buffer (4M guanidine-thiocyanate; 50 mM sodium citrate; 1 M Tris, pH 8.0) and 200 µl of chloroform were added, the mixture was agitated vigorously and was let to sit for 10 min. After centrifugation at 12000 g for 15 min at 4°C, the upper phase was kept, and an equal volume of chloroform was added. After vigorously agitation and incubation for 3 min, samples were centrifuged as before. After precipitation by addition of equal volume of chilled isopropanol to the upper phase and washing 3 times with 70% ethanol, the pelleted DNA was dried at 55°C for 15 min and was resuspended in EB buffer (10 mM Tris-HCl, pH 8.5) with agitation at 60°C. DNA was quantified, and quality checked with the Quant-iT PicoGreen dsDNA Assay Kit (Thermo Fisher Scientific). Massive parallel sequencing was performed using targeted-capturing of the 165 genes included in the 'Solid and Haematological tumors' panel (BRIGHTCore, Brussels, Belgium). 150 ng of genomic DNA was fragmented and processed to construct libraries with barcodes, which were hybridized with the DNA panel. The libraries were sequenced on Illumina NovaSeq 6000 with a coverage of 1500×.

2.5.2 DNA-sequencing analyses

We derived genome-wide copy number profiles using the off-target reads from our targeted panel by running ASCAT.sc (https://github.com/VanLoo-lab/ASCAT.sc). Briefly, ASCAT.sc first removes the on-target regions from the bed definition of the target with padding of 1000 bp upstream and downstream. Then it bins the rest of the genome in 30 kb bins and count the number of reads with MAPQ > 30 falling in each bin to obtain a read-count track genome-wide. We used a normal diploid sample (L2), previously profiled with the same panel (27), to normalize the read counts. The number of reads in each bin is divided by the average number to get a ratio r, which can be expressed as a function of the purity ρ, the average number of copies (or average ploidy ψ) and the local number of DNA copies nT: $r = (n_T \rho + 2(1-\rho))/\psi$. We take the log of this track and segment it with circular binary segmentation (48). Then for each value of the ploidy $\psi \in [1.5,5]$ by 0.01 and purity $\rho \in [.2,1]$ by 0.01 we fit n_T of each segment from the first equation $n_T = (\psi r - 2(1-\rho))/\rho$. We calculate the sum of Euclidean distances between n_T and the closest integer values, that is, round (n_T), and then select the combination of values of ψ and ρ that minimizes this distance.

2.6 Immunohistochemical analysis

Hematoxylin/eosin (HE), KI67 and p16 immunohistochemistry (IHC) was performed with FFPE tissue sections on a fully automated BenchMark Ultra IHC system (Ventana, Roche Diagnostics, Basel, Switzerland) with the UltraView Universal DAB Detection Kit (Roche Diagnostics), using standard routine protocols. Otherwise, FFPE sections from Mayo Clinic center were processed as described (49) and probed with a different set of antibodies (Supplementary Table S2). Pictures were acquired with a NanoZoomer digital scanner (Hamamatsu Photonics, Hamamatsu, Japan) at 40× magnification or in an Aperio AT2 scanner (Leica Biosystems, Wetzlar, Germany) at 40x magnification (samples from IPOLFG institute).

The QuPath software (50) (version 0.4.0) was used for immunohistochemistry scoring analysis. For each section, the most appropriate tumor areas (without necrosis or fibrosis) were delimited and the positive cell detection command was applied using the sum of optical density, and the nuclear minimum area for detection was set between 10-25 μm^2. A 0.2 intensity threshold for the nuclear mean DAB optical density was applied for KI67 positive detection. Three intensity thresholds were set for the cellular mean DAB optical density of p16 staining, categorizing cells into weak ($0.2 \leq$ threshold < 0.4), moderate ($0.4 \leq$ threshold < 0.6) and strong (threshold ≥ 0.6) positive detection. The H-score was calculated by the software, which is a weighted sum (1 for weak, 2 for moderate and 3 for strong) of the percentage of cells in each intensity class, ranging from 0 to 300.

2.7 Response curves and statistical analysis

Response curves and statistical analyses were performed using GraphPad Prism version 6.0 (GraphPad Software, La Jolla, CA, USA). Half-maximal inhibitory concentrations of the cell proliferation (GI50) and 95% confidence intervals were estimated by fitting the data to the logarithm of concentration vs. normalized response model, with standard slope (Hill slope of -1.0) and using a least-squares fitting method. The two-sided unpaired Student's t-test was used for comparison between two groups. Multiple group comparisons were done using the Kruskal–Wallis test followed by Dunn's multiple comparison tests. Correlations were evaluated with the Pearson correlation (two-sided). Comparison of Kaplan–Meier survival curves was performed using the Mantel–Cox log-rank test. The Fisher's exact test (two-sided) was used for the analysis of contingency tables. A p-value ≤ 0.05 was considered statistically significant.

3 Results

3.1 CDK4 phosphorylation is detected in most thyroid tumors and its absence is associated to higher expressions of *CCNE1*, *E2F1* and $p16^{CDKN2A}$ together with lower *RB1* levels

To evaluate the proportion of patient thyroid tumors that would be potentially responsive or intrinsically resistant to CDK4/6 inhibition, we determined the CDK4 modification profile and the presence of activated T172-phosphorylated CDK4 from a cohort of fresh-frozen samples (n=98) representative of the different subtypes of thyroid tumors (Figure 1A, Supplementary Figure S1 and Table S3). CDK4 was detected by immunoblotting from whole protein extracts separated by 2D-gel electrophoresis. CDK4 was thus resolved by its charge into three main forms as first characterized in thyroid primary cultures (13, 21, 51) and in other tumor types (26, 27). The most basic form (spot 1) is the native CDK4. The most acidic form (spot 3) increases in response to *in vitro* proliferation stimulus of various cells including thyrocytes (13, 21, 24, 35, 51–53) and has been identified as the highly regulated T172-

phosphorylated CDK4 form, using several approaches including T172-phosphospecific antibodies (11, 22, 26, 54). To evaluate the relative level of CDK4 activation, we compared the presence of this T172-phosphorylated form to another modified CDK4 form (spot 2). This latter form does not incorporate [32P] phosphate and binds to p16 but only weakly to cyclins D (13). The abundance ratio of the T172-phosphorylated form (spot 3) over the form separated in spot 2 allowed us to define three types of profiles (L for low, H for high and A for absent phosphorylated CDK4), as previously reported (26, 27). All WDTC exhibited the T172-phosphorylated form of CDK4 (n=29). This form was also present in all LNM (n=7) and in one available PTC distant metastasis, with higher proportion of profiles H in these groups of samples (50%), than in primary WDTC (25%). In advanced dedifferentiated tumors, phosphorylated CDK4 was present in 95% of PDTC (n=20) but only in 70% of ATC (n=23). On the other hand, as expected with quiescent tissue, normal thyroid samples (n=18) predominantly lacked CDK4 phosphorylation.

In order to evaluate the molecular features associated with the different CDK4 profiles, we analyzed a sub-cohort of 84 cases by RNA-seq (complete gene expression data provided in Data Set 1). An exploratory classification of the gene expression profiles by PCA revealed misclassified outliers (Supplementary Figure S2A). After excluding the samples with major technical issues and/or clear misclassification (as detailed in section 2.1), further analysis was done for 57 selected cases (Supplementary Table S4). As expected (37, 55–57), we observed that samples were mainly separated according to their tumor sub-types (Figure 1B). No clear segregation of samples according to the CDK4 modification profile was observed; nevertheless, most PTC samples with CDK4 profile H were closer to ATC samples (Figure 1B). Evaluation of the proliferation with the *MKI67* gene expression (Figure 1C), of the thyroid differentiation (TDS, Supplementary Figure S2B) and of the epithelial-mesenchymal transition scores (EMT, Supplementary Figure S2C) validated the identity of ATC cases. As expected, these were the most proliferative samples and had lost thyroid identity with acquisition of mesenchymal features. PDTC and PTC samples although being very heterogeneous, showed higher *MKI67* expressions and lower differentiation than normal tissues. Paradoxically, PDTC tended to have a higher differentiation score than PTC, as reported by others (37). Also, worth mentioning is that the only PDTC case with CDK4 profile A (sample JPI25) had the highest *MKI67* expression (Figure 1C) and the second lowest thyroid differentiation score of PDTC group (Supplementary Figure S2B). Still, its EMT score (Supplementary Figure S2C) was similar to other PDTC [in contrast to sample JPI73 that is probably a misclassified ATC (Supplementary Figure S2A)].

Search for mutations (synonymous mutations excluded) in the main genes involved in thyroid cancer and in cell cycle, revealed *TP53* mutations as the major oncogenic driver for ATC, being present in 65% of cases (Supplementary Table S5). For PDTC, *NRAS* and *TP53* mutations were present in 21% and 37% of the tumors, respectively. As previously observed (32), these mutations were mutually exclusive and together affected more than half of the PDTC. *PTEN* mutations were also present in 21% of PDTC. Interestingly, these appeared to co-occur with *TP53* mutations (in 3 of 4 *PTEN* mutated cases). Mutations in other genes were involved in less than 20% of the ATC and PDTC. *BRAFV600E* was the only driver mutation identified in PTC, lymph node or PTC metastases, being present in 88% of samples. Among the five tumor samples with no phosphorylated CDK4 (profile A), we identified two samples with mutated *RB1* (a nonsense and a frameshift mutation). Three of these profile A samples had *TP53* mutations.

As in our previous studies in breast tumors (26) and pleural mesotheliomas (27), we observed the lack of CDK4 T172-phosphorylation in some thyroid tumors to be associated with high expressions of *CDKN2A* (p16), *CCNE1* (cyclin E1) and *E2F1*. Transcript levels of *CDKN2A*, *E2F1* and *CCNE1* were indeed elevated in ATC and PDTC samples with profile A of CDK4 (Figures 1D-F). High p16 cellular levels are expected to prevent the activating phosphorylation of CDK4 by impairing its binding to cyclins D. By contrast, in normal quiescent thyroid tissue, lack of CDK4 phosphorylation was likely due to the absence of mitogenic stimulation (13, 21) because it was associated to a particularly low p16/*CDKN2A* expression, an intriguing feature already reported by others (35, 58–61). Overexpression of p16/*CDKN2A* in cancer cells has been generally related to *RB1* loss of function (28, 62, 63). However, three of these profile A samples (with high *CDKN2A* expression) were ATC without any detectable *RB1* mutation (samples JPI21, JPI27 and JPI74). Lack of *RB1* mutation was confirmed with targeted DNA-sequencing (Supplementary Figure S3) in two samples (JPI21 and JPI27, although the latter showed *RB1* hemizygous loss). Two other cases of profile A ATC, which could not be RNA-sequenced, also revealed an absence of *RB1* mutations or loss. The copy number profile of the profile A PDTC (JPI25) was very complex (Supplementary Figure S3) and we could not evaluate if the very low *RB1* variant allelic fraction of 7% (compared to the *TP53* variant allelic fraction of 25%) suffice to explain the high expression of *CDKN2A* and lack of CDK4 phosphorylation. Indeed, the RB alteration might be a subclonal event in this sample. Nevertheless, samples with profile A had a reduced *RB1* expression, comparable to the one observed in normal tissue samples (Figure 1G).

Due to an alternative open reading frame (ORF), *CDKN2A* translates into two different proteins (p16 and p14). In contrast to breast tumors (26), high *CDKN2A* expression measured by RNA-seq analysis in thyroid tumors, did not entirely correlate with elevated p16 expression and lack of CDK4 phosphorylation. Among PDTC and ATC, eleven samples had elevated *CDKN2A* mRNA expression levels, but displayed CDK4 profiles H or L. In most of these cases, over-expressed *CDKN2A* mRNA seemed to mainly encode the p14 protein (only reads covering exon 1β, specific for p14 isoform, were observed in IGV) or would encode a truncated p16 protein (p.Q50* mutation). If we account for this by correcting *CDKN2A* transcription (as detailed in Materials and Methods), elevated expression of p16/*CDKN2A* was exclusively found in samples lacking phosphorylated CDK4 (Figure 1H). Immunohistochemical staining corroborated the absence of p16 protein in samples with p14-driven *CDKN2A* transcription (Figure 1I). By contrast, profile A samples with similar *CDKN2A* expression levels had strong p16 staining. Importantly, in all such cases, KI67 staining was similarly elevated in the p16-high tumor

10.3389/fendo.2023.1247542

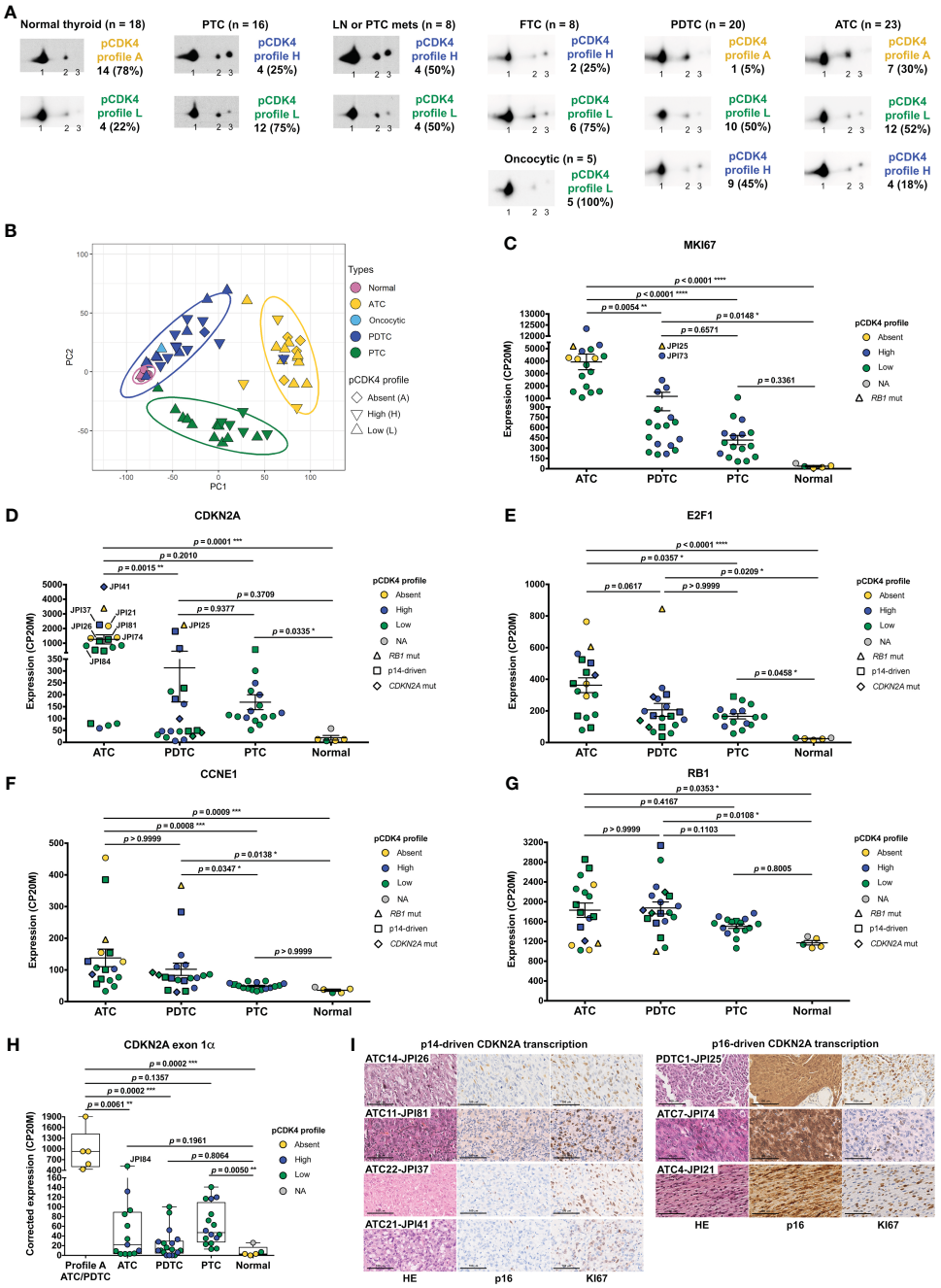

FIGURE 1
CDK4 phosphorylation is detected in most thyroid tumors and its absence is associated to higher expressions of *CCNE1*, *E2F1* and p16^{CDKN2A} together with lower *RB1* levels. **(A)** Representative immunodetections of CDK4 after 2D-gel electrophoresis separation of whole protein extracts from fresh-frozen samples of normal thyroid tissues and different thyroid tumors subtypes. CDK4 modification profiles (number of cases and fraction in each subtype of tissue shown on the right side of immunoblots) were defined based on the ratio of T172-phosphorylated form of CDK4 (spot 3) over another modified form (spot 2), quantified from the immunoblots. H for high CDK4 phosphorylation: ratio ≥ 0.5; L for low CDK4 phosphorylation: 0.02 ≤ ratio < 0.5; A for absent CDK4 phosphorylation: ratio < 0.02. Unmodified native form of CDK4 is labelled as spot 1. **(B)** Representation of the gene expression variance between RNA-seq analyzed samples by principal component (PC) analysis (lymph node metastasis assigned as PTC). Computed 95% confidence ellipses for each sample subtype are plotted. **(C-G)** Expression levels of *MKI67*, *CDKN2A*, *E2F1*, *CCNE1* (cyclin E1) and *RB1* in the samples grouped into normal tissues and the different subtypes of tumors (lymph node metastasis assigned to PTC). Expression levels calculated from the RNA-seq data and expressed as counts per 20 million reads (CP20M). Samples defined as presenting p14-driven *CDKN2A* transcription were checked in Integrative Genomics Viewer (IGV) to have exclusive expression of the exon 1β of *CDKN2A* gene. Error bars: mean +/- SEM. Statistical significance was calculated with the Kruskal-Wallis test corrected by Dunn's multiple comparison tests. **(H)** Expression level of *CDKN2A* exon 1α in each group of samples, calculated from the RNA-seq data and expressed as the contribution of the exon 1α to the expression of the locus (in CP20M). Statistical significance between profile A group or normal tissues and other groups was calculated with the Kruskal-Wallis test corrected by Dunn's multiple comparison tests. **(I)** Representative immunohistochemistry images of hematoxylin/eosin (HE), p16 and KI67 staining in 7 tumors with comparably high *CDKN2A* mRNA levels, as highlighted in **(D)**. Scale bars = 100 µm. *p<0.05, **p<0.01, ***p<0.001, ****p<0.0001; NA, not applicable.

area, further demonstrating that p16 accumulation did not preclude tumor cell proliferation in these tumors.

3.2 Evaluation of p16/KI67 staining and a 11-gene signature as predictive biomarkers

To validate the high levels of p16 protein as a useful biomarker to identify tumors with no phosphorylated CDK4 (profile A), we performed immunohistochemistry staining in FFPE samples from 13 ATC, 17 PDTC, 12 PTC including 2 LNM, and 3 normal thyroid tissues (Supplementary Table S6 and Figure S4). No p16 staining was observed in the normal thyroid samples. All six profile A tumors (5 ATC and 1 PDTC) were p16-positive, 3 of which with very strong staining. However, 9 out of 19 profile L and 7 out of 15 profile H, including most PTC, were also p16-positive in a significant proportion (more than 15%) of cells. The remaining cases (mostly profile L and H ATC and PDTC) had no or very faint staining, and positivity appeared rather in the stroma. Staining of serial cuts for the proliferation marker KI67 revealed that profile A tumors had a higher proportion of KI67-stained cells and, more importantly, that p16-positive areas were co-stained for KI67. By contrast, no such co-expression of p16 and KI67 was observed in most profile H and L tumors, including PTC samples in which the p16-positivity was also particularly heterogeneous (Supplementary Table S6 and Figure S4). Only one profile L ATC case (JPI84, L* in Supplementary Table S6) exhibited areas with co-expression of both proteins, indicating that it could be a heterogeneous sample with profile A areas, which could also explain its very low ratio of CDK4 spot 3/spot 2.

We previously reported that the CDK4 modification profile of breast tumors and cell lines can be predicted using the expression values of 11 genes (26). The tool was initially developed with Affymetrix microarrays. Our ongoing work (manuscript in preparation) indicates that the prediction tool can be run with gene expression profiles quantified with other technologies (RNA-seq, AmpliSeq) and adapted to RNA extracted from FFPE tumor samples. Therefore, we first tested whether the tool based on the genes (Supplementary Table S7) selected for the CDK4 profile prediction in breast tumors and the corresponding RNA-seq breast references could correctly predict the profiles of thyroid tumors, using raw CP20M gene expression values. The accuracy (proportion of predictions matching the observations) reached only 57.4% when applied to the prediction of the three CDK4 modification profile in thyroid tumors (Supplementary Table S8). Five samples were erroneously predicted as A profiles. Four of them were samples with exclusive contribution of exon1β (coding for p14) to the expression of the locus. In addition, profiles H or L were confounded in 19 tumor samples (7 L profiles predicted as H and 12 H profiles predicted as L). Upon use of the *CDKN2A* CP20M gene expression values corrected by the contribution of the exon1α to the expression of the locus, the overall accuracy raised to 68.5% for the prediction of the three profiles. As risk evaluation by distinguishing H from L profiles may not be practically useful in advanced thyroid cancer, we next checked whether a binary prediction of tumors as A or non-A (L or H) profiles might be more accurate. When a tumor was predicted to have A profile by a highest correlation with the A profile reference compared to the H or L profile references, the accuracy of the prediction, based on the exon1α *CDKN2A* contribution, raised to 98.2% (Supplementary Table S8). All observed A profile tumors were correctly predicted and only one sample (the PTC lymph node metastasis JPI38) was falsely predicted as A profile.

3.3 Higher levels of CDK4 phosphorylation are associated to higher proliferative potential and worse clinical outcomes

ATC with CDK4 profile H were significantly more proliferative than profile L cases ($p = 0.0063$), as judged by the higher expression of *MKI67* (Figure 2A, Supplementary Figure S5A). A similar tendency could be seen for PDTC ($p = 0.0854$). However, we noticed that only a subset of profile H PDTC samples had higher *MKI67* expression levels than profile L samples (Figure 2A, Supplementary Figure S5B). By contrast in PTC, several tumors displayed a H profile, but none was observed to be more proliferative than L profile ones (Figure 2A, Supplementary Figure S5C). Expression of *MKI67* was indeed significantly correlated with phosphorylated CDK4 levels in ATC ($p = 0.0462$) and PDTC ($p = 0.0490$) but not in PTC ($p = 0.4329$) (Supplementary Figures S5A-C). Nevertheless, PTC with profile H had significantly lower thyroid differentiation than profile L ($p = 0.0266$), a tendency that was not clearly associated to BRAF mutations (Figure 2B). In each of the ATC and PDTC groups, samples with profile H showed significantly higher expression of *E2F1* than samples with profile L ($p = 0.0288$ and $p = 0.001$, respectively; Figure 2C). *CCNE1* and *RB1* expressions did not differ significantly between the two profiles (Supplementary Figures S5D, E).

PDTC patients, for which tumors exhibited a CDK4 profile H, had significantly shorter overall survival than those with profile L tumors ($p = 0.0407$; Figure 2D). In ATC, the median survival tended to be lower for profile H (2 months vs 7.5 months for profile L), but more cases are needed to prove a true association ($p = 0.1590$; Figure 2E). Similarly, PDTC and WDTC patients associated to profile H were more likely to have distant metastases (89% vs 50%; Figure 2F) and nodal metastases (83% vs 33%; Figure 2G), respectively. Therefore, even if it was not associated with a higher proliferation in WDTC, a higher CDK4 activation appeared associated to features of higher aggressiveness.

Unfortunately, complete clinical data could not be retrieved for several profile A tumor patients and several ATC patients were lost to follow-up. Remarkably, one of these profile A-ATC patients (JPI21) is still alive more than 8 years after diagnosis and chemotherapy.

3.4 Most thyroid cancer cell lines are sensitive to CDK4/6 inhibitors, which correlates with presence of phosphorylated CDK4 and can be predicted by the signature tool

Both commercial (n=17) and patient-derived cell lines (64) (n=4) from different subtypes of tumors were analyzed in order to

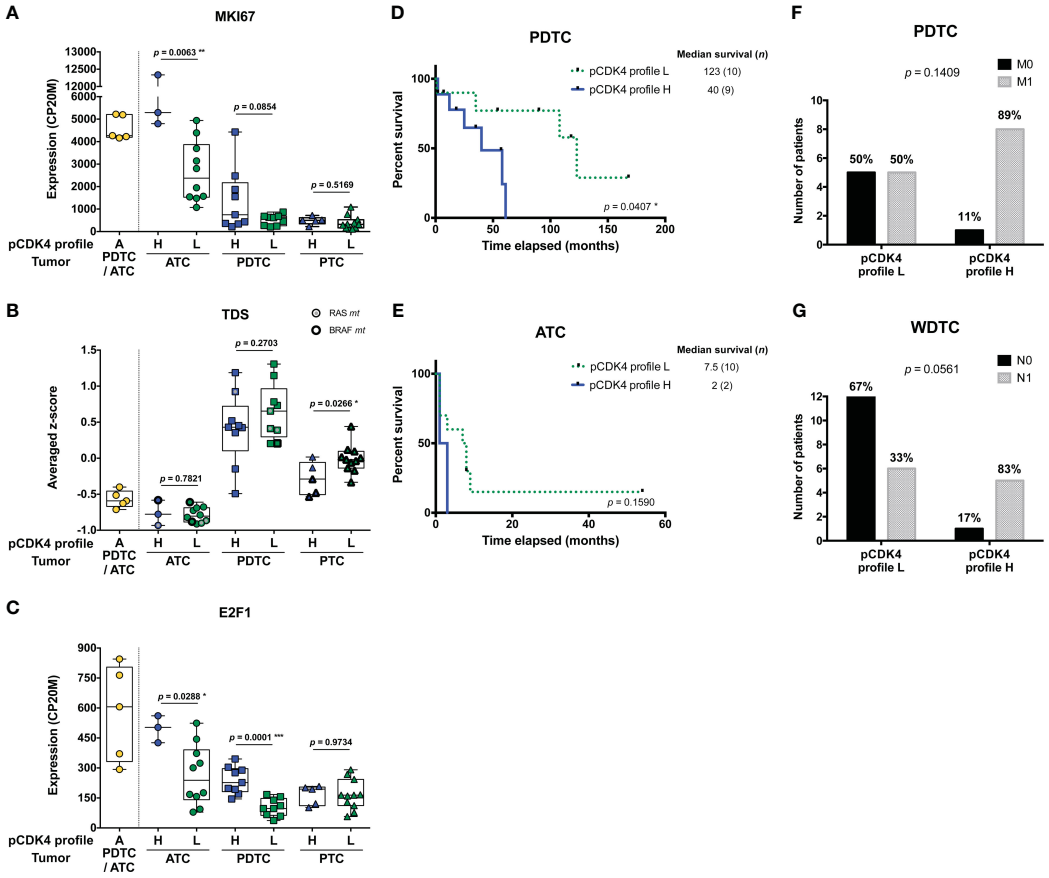

FIGURE 2
Higher levels of CDK4 phosphorylation are associated to higher proliferative potential and worse clinical outcomes. **(A-C)** Expression levels of *MKI67*, thyroid differentiation score (TDS) and *E2F1* in the samples grouped according to their CDK4 modification profiles in each subtype of tumors (lymph node metastasis assigned to PTC). CDK4 modification profiles were defined based on the ratio of T172-phosphorylated form of CDK4 (spot 3) over another modified form (spot 2), quantified from the immunoblots. H for high CDK4 phosphorylation: ratio ≥ 0.5; L for low CDK4 phosphorylation: 0.02 ≤ ratio < 0.5; A for absent CDK4 phosphorylation: ratio < 0.02. Expression levels calculated from the RNA-seq data and expressed as counts per 20 million reads (CP20M) or as averaged Z-score of CP20M. Statistical significance between profile H and profile L groups in each type of tumors were calculated with unpaired t-test. **(D, E)** Kaplan–Meier curves comparing overall survival of ATC and PDTC patients with profile L or profile H of CDK4. Statistical significance was calculated using a log-rank test. **(F, G)** Proportion of PDTC or WDTC patients (patients with oncocytic FTC included), grouped according to their tumor's CDK4 modification profile, for which distant (M) or regional nodal (N) metastases were assessed (0, not found; 1, found). Statistical significance was calculated with Fisher's exact test. *p<0.05, **p<0.01, ***p<0.001.

characterize their response to two CDK4/6i - palbociclib and abemaciclib. Only three cell lines were intrinsically resistant to the drugs (Figure 3A). For the remaining cells, including all ATC-derived lines, both inhibitors reduced S-phase entry (as measured by BrdU incorporation into DNA), in a dose-dependent way. Palbociclib's half-maximal inhibitory concentrations of the cell proliferation (GI50) were similar to the ones reported in other types of cancer cells and had no apparent correlation with the cell line subtype or driver mutations (Figure 3B). Nevertheless, six cell lines had a significant residual proliferation (defined by more than 20% of cells in S-phase, relatively to the control) at the maximum dose of 1μM of palbociclib (Figure 3A). Assessment of cell viability by other methods, dependent on mitochondrial dehydrogenases activity (MTT) or on the cellular protein content (SRB), showed less pronounced effect (Supplementary Figure S6), stressing the mainly cytostatic properties of CDK4/6i. CDK4 immunoblotting from 2D-gel electrophoresis revealed that T172 phosphorylation of CDK4 was present in all the sensitive cell lines (Figures 3C, D). By contrast, the three completely resistant cells lacked the (active) phosphorylated CDK4 form (Figure 3C). Further analysis by western blotting showed that these resistant cell lines had no RB or no phosphorylated RB expression, in accordance with the mutations previously reported (65) (a frameshift mutation in T243, a nonsense mutation in FTC-238 and two amino acids deletion in FTC-133) and confirmed by our RNA-seq data (Figure 3D; Supplementary Table S2). The absence of functional RB in these cells probably accounted for the elevated expressions of p16 and Cyclin E1 observed in Figure 3D. In almost all sensitive cell lines, p16 was affected either by mutation, deletion or promoter methylation of the p16-coding transcript and thus was not expressed (Figures 3D, E). Nevertheless, *CDKN2A* transcripts were detected in most sensitive cell lines without reported *CDKN2A* gene deletion. Analogously to what we observed in profile L and H tumors with high *CDKN2A* transcript levels, *CDKN2A* expression was exclusively due to the alternative ORF p14 expression in these cell lines (Figure 3E). Exon 1β, which is

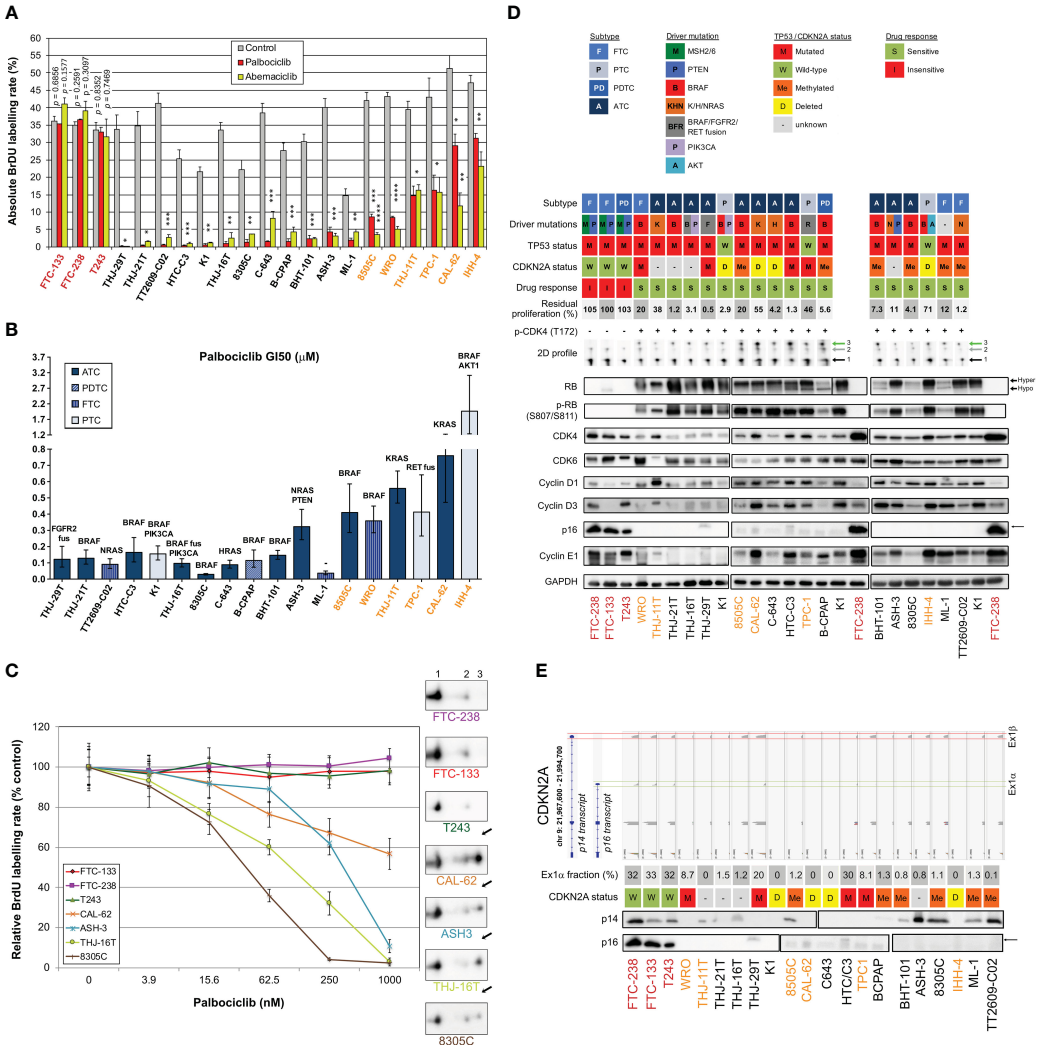

FIGURE 3
Most thyroid cancer cell lines are sensitive to CDK4/6 inhibitors, which correlates with presence of phosphorylated CDK4. **(A)** BrdU incorporation rate (during a 1 h pulse) following 24 h treatment with vehicle or with CDK4/6 inhibitors (1 μM). Pooled data from at least two independent experiments (error bars: mean ± SEM). Statistical significances were calculated by unpaired t-test. *p<0.05, **p<0.01, ***p<0.001, ****p<0.0001. **(B)** Half-maximal inhibitory concentration of the cell proliferation (GI50) determined from palbociclib's response curves with serial dilutions of the drug. The main known driver oncogenes in each cell line are shown (gene fusions denoted as 'fus'). Pooled data from at least two independent experiments were fitted by nonlinear regression model (error bars: best-fit value ± 95% confidence intervals). **(C)** Palbociclib's response curves and relationship with T172 phosphorylation of CDK4. The illustrated cell lines are representative of the analyses performed in the 21 thyroid cancer cell lines. The 2D-gel electrophoresis and CDK4 immunodetection for each cell line is presented in the same font color as the correspondent response curve. BrdU incorporation was determined as in panel A with serial dilutions of the drug. T172-phosphorylated form (spot 3) is indicated by a black arrow. Native unmodified form of CDK4 and another modified form are labelled as spot 1 and spot 2, respectively. Pooled data from at least two independent experiments (error bars: mean ± SEM). **(D)** Western blot analyses of the indicated proteins extracted from cells cultured in control conditions. The vertical solid line in RB detection separate parts of the same blot detection that were re-assembled. K1 and FTC-238 were loaded on each gel to compare protein expression between the different gels. Relevant genomic features [from the analysis of the RNA-seq data and/or in accordance with Landa and colleagues (65)] and the 2D-gel electrophoresis profile of CDK4 (native form – spot 1, another modified form – spot 2, T172-phosphorylated form – green arrowed spot 3) are shown for each cell line. *CDKN2A* status refers to p16 protein and CpG methylated status at exon 1α (exclusive for p16 protein) was retrieved from the Cancer Cell Line Encyclopedia (CCLE) project. *CDKN2A* status was considered unknown for cell lines with no expression of p16 protein, with unknown methylation status and with no genomic aberration detected. Residual proliferation corresponds to the average relative BrdU labelling rate after 24 h treatment with palbociclib (1μM). Hyper- and hypo-phosphorylated forms of RB are indicated. Correct p16 band is indicated by a black arrow. **(E)** Illustration of the genomic organization of *CDKN2A* locus (not on scale) adapted from Integrative Genomics Viewer (IGV) visualization of each cell line's BAM file. Coverage track of the transcripts from p14 and p16 proteins, and respective protein immunodetection by western blot are presented for each cell line (the western blot detections are from the same cell extracts also shown in **(D)**. The loading control (GAPDH) detection is shown in panel D and p16 detection is the same as in **(D)**. Exon 1α fraction calculated from the exon 1α coverage over the sum of exon 1α and 1β coverages. *CDKN2A* status defined as in **(D)**. Cell lines with residual proliferation ≥ 90% (resistant), ≥ 20% (sensitive with residual proliferation) or < 20% (sensitive) are indicated by red, orange or black font colors, respectively.

unique to p14 transcript, was expressed in more than half of the cell lines and, consistently, p14 was detected by western blotting (Figure 3E). On the other hand, *CDKN2A* exon 1α, which is exclusively present in p16 transcript, was only expressed in 5 cell lines. In two of them (the sensitive HTC-C3 and THJ-29T cells), *CDKN2A* is mutated (H66R+D108N and G55Afs*91, respectively) and p16 protein was not detected. Cyclin E1 and CDK4 expressions were elevated in all the resistant cell lines and were more variable in sensitive ones (Figure 3D). High residual proliferation was seen in cell lines with higher expression of Cyclin E1 (WRO, CAL-62 and IHH-4) or CDK4 (THJ-11T). At the transcript level, *CDK4* expression showed a significant negative correlation with the sensitivity of the cell lines and the expression of both *CDK4* and *CCNE1* were significantly correlated with the residual proliferation of the cell lines (Supplementary Figure S7). The basal proliferation of the cell lines was also significantly correlated with the residual proliferation. By contrast, the transcript levels of *CDK6*, *RB1* or *CCND1* (cyclin D1) were not correlated with the residual proliferation (Supplementary Figure S7).

We next explored the impact of palbociclib treatment for 4 d (tested at 1 μM), on selected cell cycle related protein expressions (Figure 4A). At this drug concentration, no alteration was seen in the resistant cells upon palbociclib treatment. This suggests that any effect observed in responsive cells was specific. In sensitive cells, we observed diminished RB expression/hyper-phosphorylation and decreased levels of Cyclin A2 and E2F1 (Figure 4A). Palbociclib-treated cells exhibited elevated levels of CDK4, Cyclins D and E1. These observations are consistent with a cell cycle arrest at G1 phase. Drug-exposed cells observed at the microscope were flat, enlarged and seemed to have increased cellular complexity (not shown), suggestive of cells undergoing senescence. Palbociclib treatment induced higher senescence-associated β-galactosidase (SA-β-gal) activity in all the sensitive cell lines (Figure 4B). However, this increase was detected in more than 30% of cells only in three cell lines (THJ-29T, HTC-C3 and BHT-101). Aside from decreased levels of PARP1 [E2F target already described as down regulated by CDK4/6 inhibition (16)], treated cells showed no appreciable evidence for increased apoptosis (no cleaved PARP1 nor cleaved caspase 3) or autophagy (minimally changed p62 and LC3B levels) (Supplementary Figure S8). This is in agreement with previous studies, where no or minimal induction of apoptosis was seen in thyroid cancer cell lines (66–68). Permanent arrest in the three cell lines with elevated SA-β-gal activity was further evidenced by reduced S-phase entry during prolonged palbociclib treatment (up to 10 d), which was maintained even after drug washout (Figure 4C). However, in most of the other sensitive cell lines, palbociclib did not induce a durable cell cycle arrest. Indeed, the proportion of cells entering into S-phase raised when the treatment was prolonged, or rapidly increased once the compound was withdrawn (Figure 4C).

The 11-gene expression signature used to predict the CDK4 profile in tumors was further evaluated in these 21 thyroid cell lines (Supplementary Table S9), as performed for the tumors in section 3.2. Upon use of the *CDKN2A* gene expression values corrected by the contribution of the exon1α to the expression of the locus, the accuracy of the prediction of A or non-A CDK4 profiles raised to 90.5% (Supplementary Table S10). The three profile A cell lines were correctly predicted and only two cell lines were falsely predicted to have a profile A. These two cell lines (HTC-C3 and THJ-29T) have mutated *CDKN2A* with high expression of the locus. These data further validate the use of the gene expression signature to predict the presence of CDK4 phosphorylation and hence the potential sensitivity to CDK4/6 inhibition. Nevertheless, in case of high expression of *CDKN2A*, potential mutations of the locus will have to be identified to exclude this confounding factor.

3.5 Combination of CDK4/6 inhibitors with MEK/BRAF inhibition potentiates the growth-inhibitory effects and prevents the clonogenic ability of thyroid cancer cells

We have observed that MAPK/ERK activity was increased upon palbociclib treatment, as judged by the elevated phosphorylation levels of ERK in most sensitive cell lines, and this mirrored the effect seen for Cyclin D1 (Figure 5A). In 12 of 18 sensitive cell lines, palbociclib also induced increased phosphorylation of p70S6 kinase and an electrophoretic mobility shift of this protein to a slower-migrating form, suggestive of hyperphosphorylation (69). By contrast, a palbociclib effect on 4EB-P1 and ribosomal protein S6 (RPS6) was less apparent (Figure 5A). We have thus investigated the possible synergism between CDK4/6 inhibition and BRAF and/or MEK inhibition using a combination of dabrafenib (BRAF inhibitor) and trametinib (MEK inhibitor). This dabrafenib/trametinib combination is the only targeted therapy approved by the FDA for the treatment of patients with locally advanced or metastatic ATC harboring *BRAF* V600E mutation (70). In a subset of seven ATC-derived cell lines carrying different oncogenic drivers and having distinct responses to palbociclib (Supplementary Table S11), triple combined treatment potentiated drugs action, leading to complete suppression of proliferation (Figure 5B). A strong synergistic effect was obtained, as judged by the calculated combination indexes (CI below one) (Figure 5C). Double combination of trametinib and palbociclib was equally effective against cell lines possessing mutated oncogenes other than BRAF. The synergism was reached even in cells displaying partial response to palbociclib alone (8505C and CAL-62 lines). Identical drug cooperation was observed using either palbociclib or abemaciclib (Supplementary Figure S9).

To evaluate the long-term effect of the combinations, we performed clonogenic assays at two different concentration schemes, in two RAS- and in two BRAF-mutated cell lines (Figure 6A). Tested concentrations were chosen in accordance to the concentration-response curves for each of the drugs and to known pharmacodynamics data [100-200 nM dabrafenib (71); 15-30 nM trametinib (72, 73); 200-260 nM palbociclib (74)]. Hence, higher palbociclib concentration was tested (1μM instead of 500 nM) for the most palbociclib-partially resistant line CAL-62, and trametinib concentration was unchanged between the two treatment schemes for cell lines with BRAF V600E mutation (highly effective at 5 nM). Cell lines treated for 10 d had their ability to form colonies reduced by each of the drugs alone (for cell

10.3389/fendo.2023.1247542

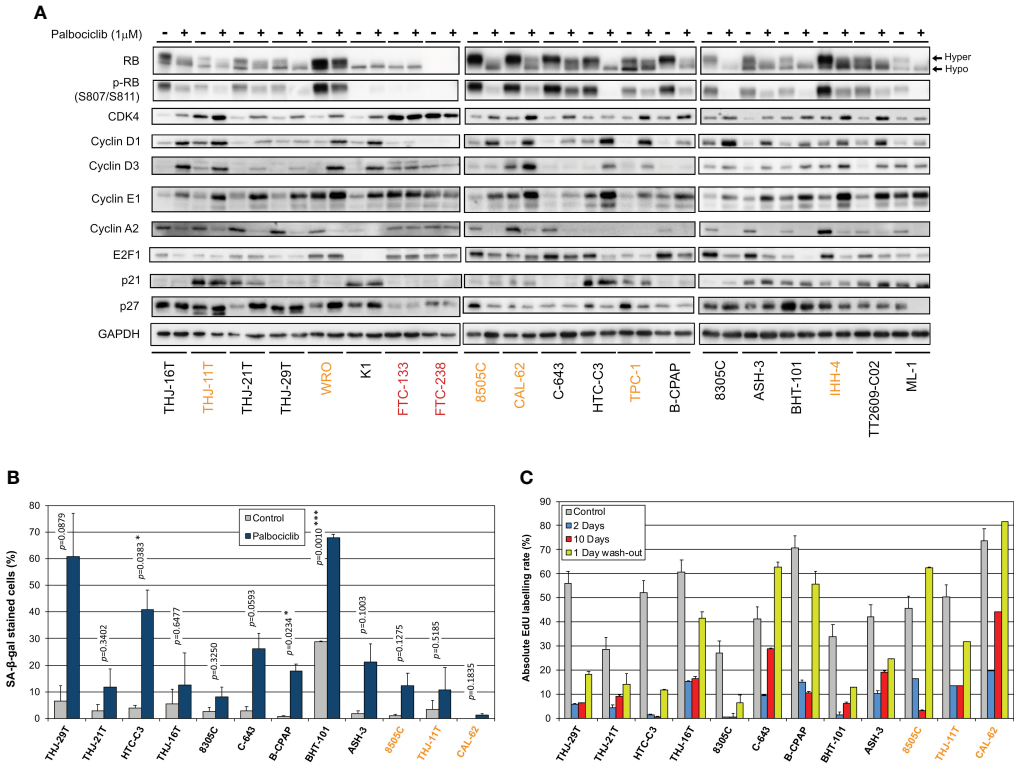

FIGURE 4
Thyroid cancer cell lines are responsive to palbociclib, but the induced cell cycle arrest is transient. **(A)** Indicated proteins were immunodetected after SDS-PAGE of total protein extracts from cells treated for 4 d with vehicle or with 1 μM palbociclib. Hyper- and hypo-phosphorylated forms of RB are indicated. **(B)** Cells stained for senescence-associated β-galactosidase (SA-β-gal) activity in ATC- and PDTC-derived cell lines were quantified following treatment for 6 d with vehicle or with 1 μM palbociclib. Pooled data from two independent experiments (error bars: mean ± SEM). Statistical significance was calculated by unpaired t-test. *p<0.05, ***p<0.001. **(C)** EdU incorporation rate (during a 1 h pulse) in ATC- and PDTC-derived cell lines, treated with vehicle for 11 d or treated with 1 μM palbociclib for 2 d, for 10 d or for 10 d followed by 1 d without drug. Error bars: mean ± SD (of duplicates; n = 1). Cell lines with residual proliferation ≥ 90% (resistant), ≥ 20% (sensitive with residual proliferation) or < 20% (sensitive) are indicated by red, orange or black font colors, respectively.

lines with mutant RAS, this was seen only with higher concentrations). However, when the compounds were removed, there was a complete or almost complete regrowth (except for HTC-C3 line, which was more sensitive to palbociclib and trametinib than other cell lines). In combined treatments (either trametinib with dabrafenib, trametinib with palbociclib or the three drugs), clonogenic potentials of the cell lines were drastically reduced during the continuous presence of drugs (Figure 6A). Importantly, following drugs withdrawal, only regimens combining palbociclib to BRAF and/or MEK inhibitors showed the most efficient and durable responses, completely abolishing the regrowth of most cell lines. For RAS mutant lines, this effect was observed only with higher concentration of drugs, while the triple combination was already effective at lower concentrations in BRAF mutant lines. The same effects were also seen for cell lines possessing other oncogenes (Supplementary Figure S10). We observed that SA-β-gal activity was higher following combined treatment than with each of the drugs alone (Figure 6B), whereas neither cleaved caspase 3 nor cleaved PARP1 were changed (data not shown). Thus, inhibition of ERK pathway synergizes with CDK4/6i, potentiating the proliferation-suppressive properties of each of the drugs and strongly impairing the long-term growth of thyroid cancer cells and the development of resistance.

3.6 Palbociclib treatment induces a paradoxical stabilization of activated Cyclin D-CDK4 complexes, which can be prevented by MEK/BRAF inhibitors

We next explored the molecular mechanisms behind the synergistic inhibition of cell cycle progression and cell proliferation in response to combined targeting of CDK4/6 and MEK/ERK pathways. We observed that a 3 d treatment with the combination of the drugs at low concentrations, similar to the ones used for clonogenic assays (Figure 6A), already allowed to efficiently arrest the cell proliferation by repressing RB phosphorylation and Cyclin A2 expression (Figure 7A). In addition, the combination with trametinib and dabrafenib prevented the upregulation of both Cyclins D and Cyclin E1, as well as the activation of ERK and mTOR pathways (as inferred by the decreased phosphorylation levels of ERK, p70S6K1, RPS6 and 4EB-P1), that were observed upon palbociclib treatment (Figure 7A). These effects were also maintained or further enhanced when 250 nM of palbociclib was used instead of 62.5 nM (Supplementary Figure S11).

We then evaluated the effect of the combined treatments on the formation and specific kinase activities of CDK4 complexes, by performing co-immunoprecipitation assays from cells treated for 6

10.3389/fendo.2023.1247542

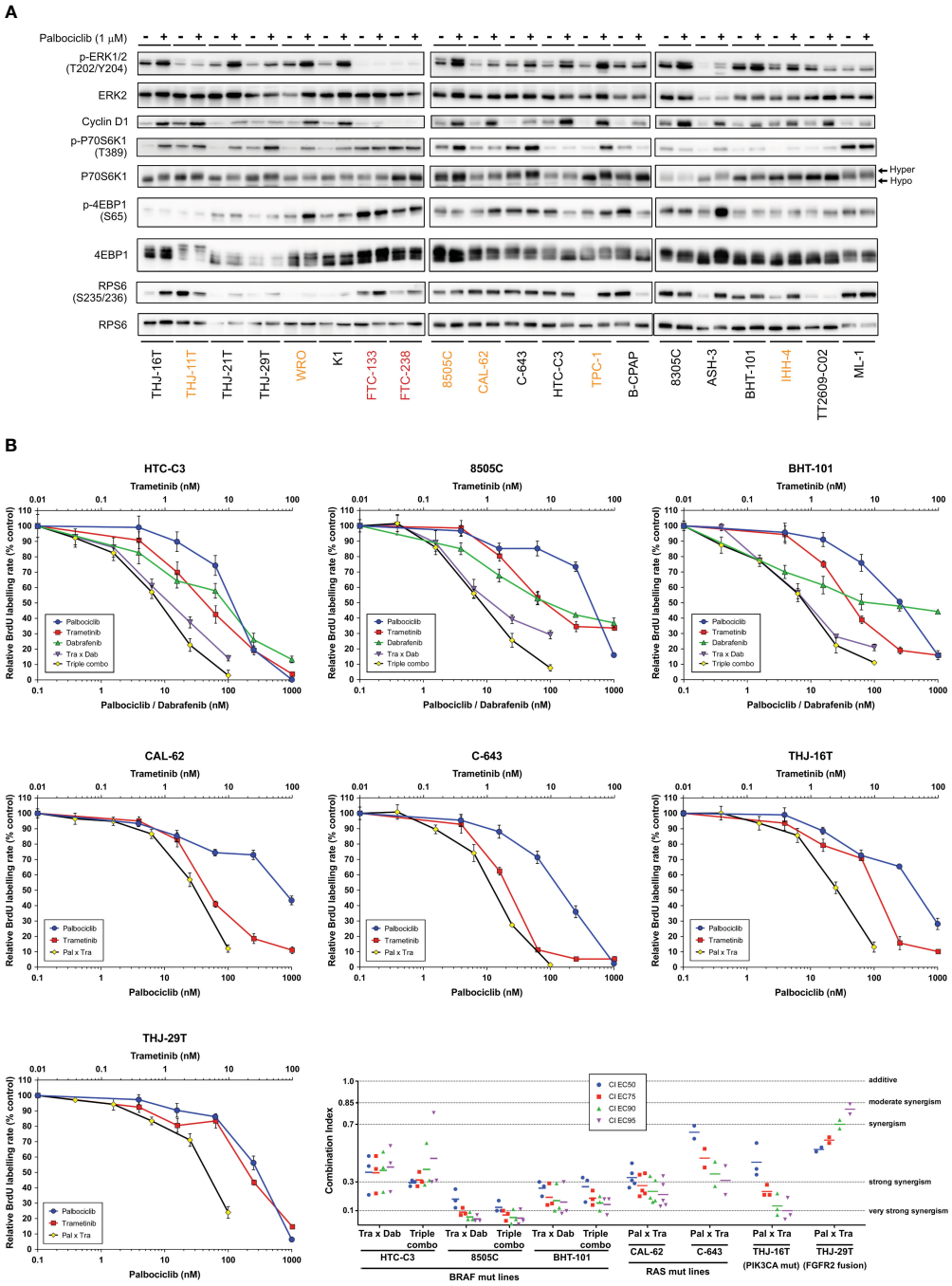

FIGURE 5
Combination of CDK4/6 inhibitors with MEK/BRAF inhibition potentiates the growth-inhibitory effects. **(A)** Indicated proteins were immunodetected after SDS-PAGE of total protein extracts from cells treated for 4 d with vehicle or with 1 μM palbociclib. The western blot detections are from the same cell extracts also shown in Figure 4A. The loading control (GAPDH) detection is shown in Figure 4A and Cyclin D1 detection is the same as in Figure 4A. Hyper- and hypo-phosphorylated forms of p70S6K1 are indicated. Cell lines with residual proliferation ≥ 90% (resistant), ≥ 20% (sensitive with residual proliferation) or < 20% (sensitive) are indicated by red, orange or black font colors, respectively. **(B)** Response curves (measured as BrdU incorporation during a 1 h pulse) in ATC-derived cell lines, following 24 h treatment with serial dilutions of dabrafenib (BRAF inhibitor), trametinib (MEK inhibitor) or palbociclib either alone, in combination of two (Tra x Dab; Pal x Tra) or in combination of three drugs (triple combo). Representative data of two or more independent experiments as shown in panel C (error bars: mean ± SD of triplicates). **(C)** Drug combination indexes (CI) calculated at different effective concentrations (EC) in the tested ATC-derived cell lines. Values obtained in each independent experiment are presented (line at mean).

10.3389/fendo.2023.1247542

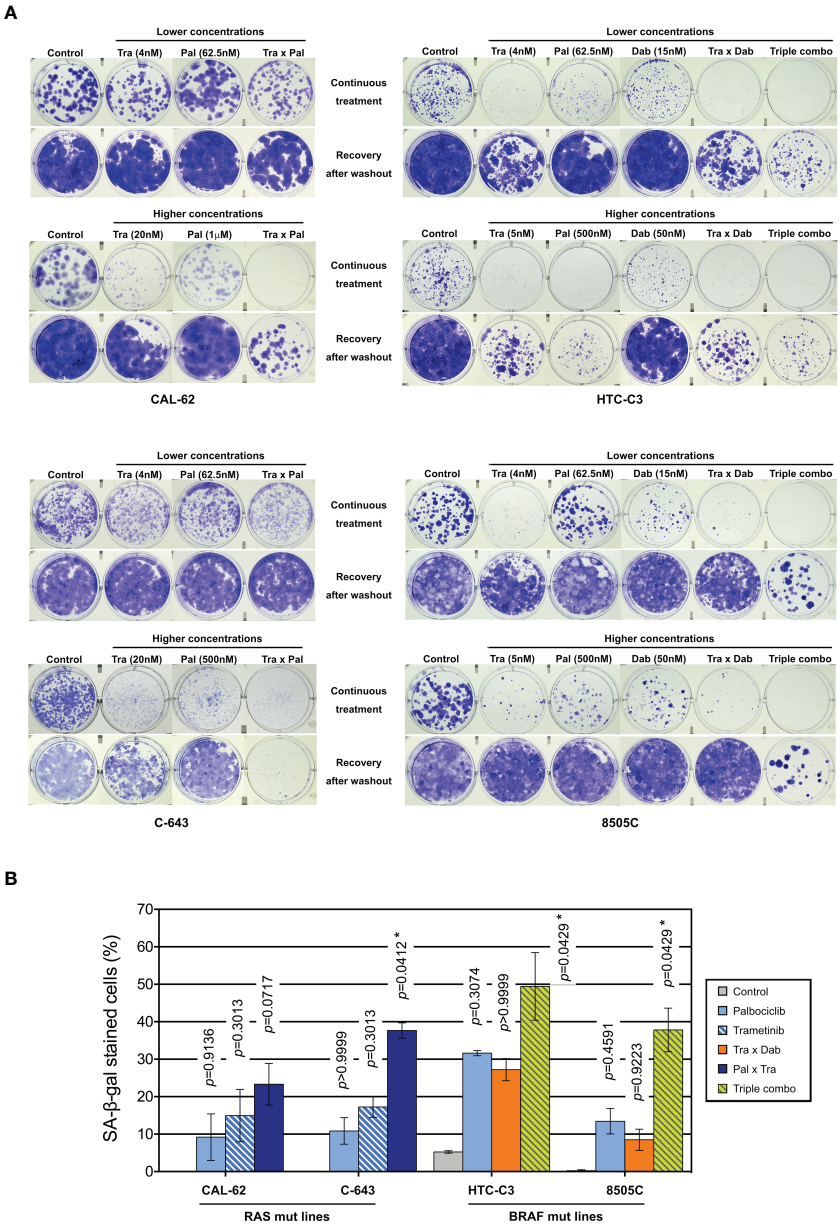

FIGURE 6
Combination of CDK4/6 inhibitors with MEK/BRAF inhibition prevents the clonogenic ability of thyroid cancer cells. **(A)** Clonogenic potentials of ATC-derived cell lines treated for 10 d at indicated concentrations with vehicle, dabrafenib (dab, BRAF inhibitor), trametinib (tra, MEK inhibitor) or palbociclib (pal) either alone, in combination of two or in combination of three drugs (triple combo), followed or not by a 10 d recovery period (drugs withdrawal). Representative photographic images of two independent experiments. **(B)** Cells stained for SA-β-gal activity in ATC-derived cell lines were quantified following treatment for 8 d (higher concentrations of drugs were used as indicated in panel A). Pooled data from two independent experiments (error bars: mean ± SEM). Statistical significance between control and each treatment was calculated with the Kruskal-Wallis test corrected by Dunn's multiple comparison tests. *p < 0.05.

d (Figure 7B, upper panel), with the high concentration scheme of drugs tested in the clonogenic assays (Figure 6A). The *in vitro* RB-kinase activity of CDK4 complexes (assayed in the absence of palbociclib, hence reflecting the presence of activated CDK4) was increased by palbociclib mostly in CAL-62 cells (the more palbociclib-resistant cell line) and to a lesser extend in HTC-C3, 8505C and C-643 cell lines. This increase was prevented by the co-treatment with trametinib in CAL-62 cells or by the dabrafenib/trametinib combination in the BRAF-mutated cells (Figure 7B, upper panel). In CAL-62 (and more weakly in 8505C cells), the dramatic increase of RB-kinase activity of CDK4 induced by palbociclib was associated with a similarly increased formation of cyclin D3-CDK4 complexes, which were devoid of p21 and thus did not require the p21 assembly activity. This observation exactly corresponds to our previous description of a paradoxical effect of palbociclib that specifically stabilized activated cyclin D3-CDK4/6 complexes, which could become hyperactive upon drug removal, because their activity was not restricted by binding to CIP/KIP inhibitory proteins (52). Similar to what we observed in Figure 4A, palbociclib-treated cells exhibited increased levels of either CDK4,

10.3389/fendo.2023.1247542

Cyclin D3 and/or Cyclin D1, and reduced levels of p27 (Figure 7B, lower panel). Conversely, trametinib and the dabrafenib/trametinib combination reduced the protein concentrations of CDK4, Cyclin D1 and Cyclin D3, while increasing p27 accumulation (Figure 7B, lower panel). The p27 modulation is in agreement with the already described reduction of p27 levels upon expression of RAS, BRAF or RET/PTC mutants in thyroid cancer cells, which would be reversed by MEK inhibition (75). These effects, which were variably observed in the different cell lines, might also concur (respectively) to increase the formation of activated CDK4 complexes in response to palbociclib, and to explain the inhibition of this formation by BRAF/MEK inhibitors (Figure 7B, upper panel). To further

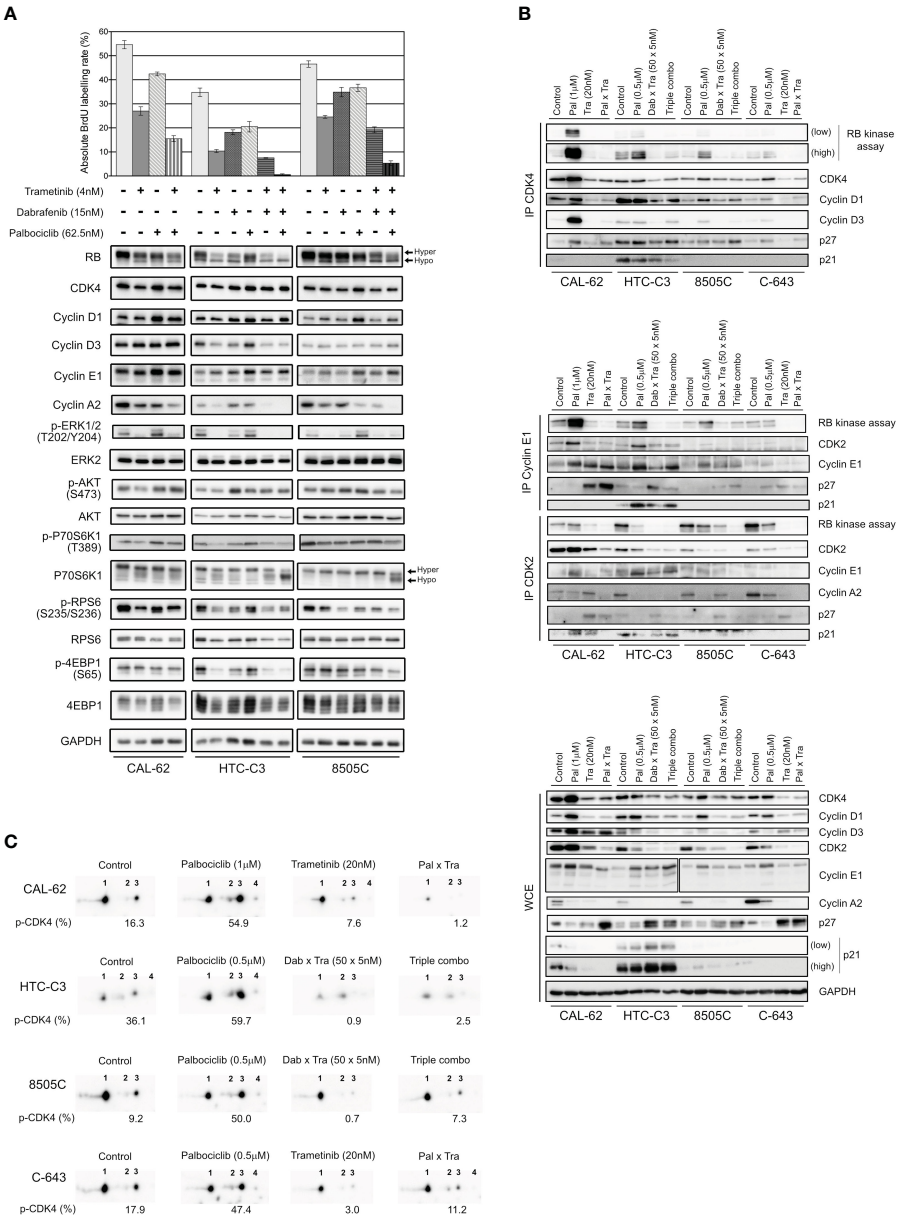

FIGURE 7
Palbociclib treatment induces a paradoxical stabilization of active Cyclin D-CDK4 complexes, which can be prevented by MEK/BRAF inhibitors. **(A)** BrdU incorporation rate (during a 1 h pulse) following 24 h treatment with vehicle or with indicated drugs. Error bars: mean ± SD (of triplicates; n = 1). Indicated proteins were immunodetected after SDS-PAGE of total protein extracts from cells treated for 3 d with vehicle or with indicated drugs. Hyper- and hypo-phosphorylated forms of RB and p70S6K1 are indicated. **(B)** Co-immunoprecipitation assays (IP) with an anti-CDK4 (upper panel), anti-Cyclin E1 or anti-CDK2 antibody (middle panel) followed by *in vitro* RB-kinase assay and immunodetection of indicated proteins, from cells treated for 6 d with vehicle, dabrafenib (dab, BRAF inhibitor), trametinib (tra, MEK inhibitor) or palbociclib (pal) either alone, in combination of two or of three drugs (triple combo). RB-kinase activity was evaluated by the immunodetection of the *in vitro* phosphorylated RB fragment. Immunodetection of the indicated proteins were also done after SDS-PAGE of whole-cell extracts (WCE) from cells treated in the same conditions (lower panel). Low: low exposure time; high: high exposure time. **(C)** Immunodetection of CDK4 after 2D-gel electrophoresis separation of whole protein extracts from cells treated as in **(B)**. Below each detection is shown the ratio of T172-phosphorylated form of CDK4 (spot 3) over the total of detected CDK4 forms (native form, another modified form, T172-phosphorylated form and double modified form labelled as spot 1, spot 2, spot 3 and spot 4, respectively), quantified from the immunoblots.

characterize the effect of the drugs on CDK4 activity, whole protein extracts from treated cell lines were resolved by 2D-gel electrophoresis (Figure 7C). Treatment with palbociclib increased the presence of all the CDK4 forms, and even more the proportion of the activated T172-phosphorylated form. Again, combination with MEK/BRAF inhibitors was able to counteract these effects, consistently with our previous observation that CDK4 phosphorylation depends on MEK activity (24).

In the same experiments, we similarly evaluated the effects of the combined treatments on the formation and RB-kinase activity of CDK2 complexes that were (co-) immunoprecipitated using either CDK2 or Cyclin E1 antibodies (Figure 7B, middle panel). Intriguingly, the RB-kinase activity associated with Cyclin E1 complexes also increased in response to palbociclib treatment in CAL-62, HTC-C3 and 8505C cells, mirroring the situation observed in CDK4 complexes. Again, this paradoxical effect of palbociclib was prevented by BRAF/MEK inhibitors (Figure 7B, middle panel). These effects were (respectively) associated with an increased abundance of Cyclin E1 and Cyclin E1-CDK2 complex in palbociclib-treated cells, and a reduction of the binding of CDK2 to Cyclin E1 together with an increased association of p27, in cells treated with MEK or MEK/BRAF inhibitors.

At variance with the situation observed in Cyclin E1 co-immunoprecipitates, the total RB-kinase activity associated with CDK2 complexes (immunoprecipitated using a CDK2 antibody, and thus comprising both Cyclin E1 and Cyclin A2 complexes) was not increased by palbociclib in CAL-62 cells and was reduced in the three other cell lines with the most complete inhibition in HTC-C3 (the most palbociclib-sensitive cells) (Figure 7B, middle panel). In all the cell lines, accumulation of Cyclin A2 and its association with CDK2 were reduced in palbociclib-treated cells, compensating for the increased presence and activity of Cyclin E1-CDK2 complexes. Intriguingly, treatments with trametinib and with dabrafenib/trametinib used alone (respectively in CAL-62 and in 8505C), reduced Cyclin A2 expression (Figure 7B, lower panel) but not its presence in CDK2 complexes (Figure 7B, middle panel). Nevertheless, the most complete inhibitions of both CDK2 activity and CDK2-Cyclin A2 association were observed in cells treated with the combination of palbociclib and MEK/BRAF inhibitors (Figure 7B, middle panel).

To summarize, the upregulation of Cyclins D with stabilization of activated (T172-phosphorylated) CDK4 complexes and the upregulation of Cyclin E1 with increase of its kinase activity are most probably the mechanisms that bypass CDK4/6 inhibition in thyroid cancer cells. Nonetheless, this can be prevented through combined MAPK/ERK inhibition, which reduces the accumulation of Cyclins D and Cyclin E1, the phosphorylation of CDK4, and increases p27 to further inhibit CDK2 activity.

4 Discussion

CDK4/6 inhibitors have been proposed as an important tumor therapy for which there should be the fewest bypass mechanisms (76). It is generally considered to be reserved to RB-proficient tumors, because intrinsic resistance to CDK4/6i is mostly associated to RB loss. However, aberrant activation of E2F factors, Cyclin E or CDK2 can also circumvent CDK4/6 inhibition and may be involved in either intrinsic or adaptive resistance. One of the novelties of our work comes from our ability to detect in tumors the presence of the main target of CDK4/6i, i.e. T172-phosphorylated active CDK4. This phosphorylation, which is required for the opening of the catalytic site of CDK4 (77, 78), actually represents the rate-limiting step of CDK4 activation because, contrary to other CDKs, like CDK2 and CDK1 (79, 80), CDK4 activity is not limited by inhibitory phosphorylations (13, 81, 82); and because the T172 phosphorylation is finely regulated, while depending on all the preceding steps, including binding to a cyclin D (11). Here, we interrogated, for the first time, the presence of T172-phosphorylated CDK4 in the different sub-types of thyroid cancer. Our results extend our demonstration in breast tumors and for pleural mesotheliomas: CDK4 phosphorylation was absent or very weak in normal quiescent thyroid tissue, but detectable in most thyroid tumors and derived cell lines. Nevertheless, its absence in tumors (despite active proliferation) was also observed, which correlated with insensitivity to CDK4/6i in cell lines and with known resistance markers to these drugs. In our transcriptome analyses, in one of the biggest cohorts of ATC and PDTC samples studied by RNA-seq so far, we showed that the absence of phosphorylated CDK4 (profile A) is mainly found in ATC (30%, n=7) and in one exceptional PDTC case (5%). This is associated with lower *RB1* expression and higher *CCNE1* and *E2F1* expressions. Still, *RB1* loss or mutation was not observed in several profile A cases and aberrations of *E2F1* or *CCNE1* were not found. In one ATC (JPI21) with no detectable *RB1* alteration, *CCNE1* was highly expressed, possibly as a result of *E2F1* amplification (Supplementary Figure S3). Therefore, although relatively minor, the prevalence of ATC that should be intrinsically resistant to CDK4/6i might well exceed the low mutation rate of *RB1* gene reported in ATC (5), indicating that the presence or absence of phosphorylated CDK4 could be the most relevant biomarker to predict CDK4/6i sensitivity.

The biochemical detection of T172-phosphorylated CDK4 was dependent upon the availability of fresh-frozen tissue samples. Moreover, detection of CDK4 phosphorylation by IHC in FFPE samples may be precluded by the low abundance of the phosphorylated CDK4 form (54) and the likely loss of phosphorylation before and/or during formalin fixation. Surrogate biomarkers including signatures constructed from gene expression analysis like RNA-seq, may instead be used to predict the CDK4 phosphorylation status (26). Moreover, like most profile A cases in breast cancers and mesotheliomas, the ATC and PDTC cases lacking CDK4 phosphorylation were associated with over-expression of p16 mRNA and protein. Nevertheless, high *CDKN2A* mRNA levels were also found in some profiles H and L thyroid tumors (associated with CDK4 phosphorylation). In depth analyses of these cases revealed that the *CDKN2A* expression was restricted to exons encoding the alternative protein p14 (instead of p16) or was encoding a mutated (truncated) p16 protein. An immunohistochemistry assessment showed that most profile A tumors exhibited strong p16 expression. Still the elevation of p16 staining should be carefully appreciated. Intriguingly, the

expression of p16 is very low in normal thyroid tissues but often moderately elevated in different thyroid tumors, including PTC and FTC (58, 60, 61, 83–85), which we also confirmed here. Possibly, this reflects a p16-dependent senescence mechanism limiting oncogene-driven proliferation (86–88) and thus, it would be important to characterize the proliferative state of these p16-positive cells (28). In contrast, in profile A ATC and PDTC cases, the expression and immunostaining of p16 were much higher and were associated with a proliferation marker such as KI67. Therefore, appropriately scored p16 IHC (especially regarding intensity and homogeneity of expression) associated with positive KI67 detection might identify most of the profile A cases. Worth mentioning is that in one case, p16 elevated expression seemed to be a subclonal event - the protein was highly expressed but not present in all tumor regions. Our results show that the CDK4 modification profile of thyroid tumors and cell lines can also be predicted using the expression values of the same 11 genes used to predict the CDK4 modification profiles of breast tumors (26), reaching accuracies of 98.2% in tumors and 90.5% in cell lines, with a binary A/nonA classification. Such a binary classification of thyroid tumors, which distinguishes tumors with intrinsic resistance to CDK4/6i from tumors expressing the drug target, would meet the clinical need. Once adapted to the use of RNA extracted from FFPE tissue (manuscript in preparation for the breast scenario), our prediction tool may directly help to guide the treatment of advanced thyroid cancer. It will complement the IHC evaluation of the p16 and KI67 expression by identifying the potential false positives defined above. On the other hand, the IHC evaluation of the p16 and KI67 expression will identify tumors with exclusive p14 contribution to the expression of the locus and tumors with high *CDKN2A* expression due to frameshift or stop mutation, which are the main sources of false positives in the prediction test.

Predicting the intrinsic insensitivity of some ATC to CDK4/6i might be important because, like RB-deficient tumors in other cancers such as small cell lung cancers (SCLC), they might respond particularly well to genotoxic chemotherapy (89, 90). A larger number of cases and longer follow-up should indeed determine whether the remission of an ATC patient (JPI21), who is still alive more than 8 years after diagnosis and chemotherapy, is really exceptional or holds hope for similar cases. Among two other patients with profile A and/or high p16 detection who also received chemotherapy, one was still alive at last follow-up (PDTC JPI25), and the other is still followed currently (ATC JPI84), more than 8 months after diagnosis (Supplementary Table S3). Interestingly, two exceptional cases of advanced ATC with complete pathological response after radio/chemotherapy have been molecularly characterized and one of them was associated to a *RB1* frameshift mutation (91). More clinical cases are needed to conclude whether the mechanisms underlying p16 over-expression and lack of active CDK4 might promote a better response to chemotherapy. In addition, transient administration of CDK4/6i in tumors predicted to be insensitive could be used to temporarily arrest proliferation of normal cells and prevent chemotherapy-induced side-effects (such as myelosuppression), hence allowing increase of the dose of genotoxic drugs (92). This has been validated for SCLC (93), which led to the recent approval of trilaciclib for this indication by the FDA.

On the other hand, p16 deficiency (either by mutation, promoter methylation or deletion) has been associated with more aggressive cases of thyroid cancer (55, 59, 94–96). This includes a lower thyroid differentiation in ATC and significant association with increased mortality in patients with metastatic PTC, PDTC and ATC (55). Analogously, despite the limited number of cases, we observed in our study that tumors with higher CDK4 activation (CDK4 profiles H versus profiles L) tend to have lower differentiation in PTC, higher proliferative potential in PDTC and ATC, higher incidence of metastases in PTC and PDTC and a shorter overall survival for PDTC and ATC patients. Nevertheless, in PTC and in a subset of PDTC, the H profile of CDK4 was not associated with a higher proliferative activity, in a similar manner as reported for the over-expression of Cyclin D1 in PTC (97, 98). Likely, in more differentiated tumors, inhibitory mechanisms involving p53 and higher expression of p21 (*CDKN1A*) or p27 (*CDKN1B*), which also can restrict the activity of CDK4 complexes without impeding T172 phosphorylation (13, 22, 36, 53), and also impair CDK2 activity, might still limit the cell cycle progression.

Overall, these observations support the potentially favorable clinical impact of inhibiting CDK4 activation in some thyroid tumors. In cases presenting T172-phosphorylated CDK4 (excluding the rare possibility of p16 loss co-occurring with RB deficiency), tumors are expected to depend on the CDK4 activity and CDK4/6i might represent a relevant therapy when required. We indeed observed that palbociclib and abemaciclib strongly inhibit cell cycle progression and proliferation in most thyroid cancer cell lines, including all ATC and PDTC-derived ones. Our large collection of cell lines from different tumor histotypes further completes previous works on the evaluation of CDK4/6i (66–68, 99). The inhibitory concentrations calculated in the present study were in agreement with the ones analyzed in the collection of ATC cell lines from Wong et al. (66), although we did not observe any tendency for differential sensitivity according to mutational status. Nevertheless, we confirmed that sensitivity to palbociclib was negatively correlated with *CDK4* mRNA levels (but not with the levels of *CCND1* nor *CDK6*) and we also evidenced a similar negative correlation with *CCNE1* expression.

Despite initial response, the cell cycle blockade by palbociclib was bypassed over time in several thyroid tumor cell lines, as also reported by Wong et al. (66) and in other cancers, including pancreatic ductal carcinomas (100). As in these other cancer models, this adaptation to CDK4/6 inhibition was associated to the induction of Cyclins -D1, -D3 and -E1 (66, 100). Particularly, the upregulation of Cyclin E1 resulted in much augmented interaction of Cyclin E1 with CDK2 and associated RB-kinase activity (Figure 7B). In addition, we identified here a novel mechanism that involves a strong increase of CDK4 T172 phosphorylation and the stabilization of activated CDK4 complexes in response to palbociclib (Figures 7B, C). Therefore, the direct inhibition of CDK4/6 could be compensated by various adaptive responses involving both a dramatic augmentation of activated CDK4 complexes and the distal activation of Cyclin E1-CDK2. Irrespective of the mechanism, the bypass or adaptation to CDK4/6 pharmacological blockade imposes the use of combinatorial therapy (101). In breast cancer, the combination of

CDK4/6i with endocrine therapy became standard procedure and is certainly essential to restrict adaptive events, via reduction of Cyclin D1 levels and Cyclin E1 activity (102). A PI3K/mTOR dual inhibitor was previously used to potentiate the palbociclib action in an ATC xenograft model (66) but due to lethality, doses had to be reduced. In the present study we combined CDK4/6i with anti-MEK/BRAF agents. Indeed, we observed here that the upregulation of cyclins D and T172-phosphorylated CDK4 during palbociclib treatment, for the most part, paralleled an increased activity of MAPK/ERK pathway (101). This ERK pathway activation was critical because all the adverse responses associated with the adaptation to CDK4/6 inhibition (including upregulation of cyclins D and E and accumulation of activated CDK4 and cyclin E1 complexes) were prevented by the combination of palbociclib with dabrafenib and trametinib in BRAF-mutated cell lines and with trametinib in the BRAF-wild type cell lines. This allowed a sustained, and largely irreversible, control of cell proliferation in response to the combined treatments, with lower concentrations of palbociclib and of the BRAF and/or MEK inhibitors, compared to single agent therapy. The combination therapy of dabrafenib with trametinib was beneficial in a relevant proportion of locally advanced or metastatic ATC with *BRAF* V600E mutation (70, 103), becoming the first ever regimen approved for ATC patients by the FDA. While recommended (104) and showing clear benefits over standard care also in a European real-world setting (105), this targeted therapy is not yet approved by European Medical Association (EMA). Treatment with dabrafenib plus trametinib or in combination with immunotherapy (pembrolizumab) is presently considered a useful strategy for pursuing ATC patient stabilization or slowing disease progression, as well as in the neo-adjuvant setting, with complete surgical resection achieved in some cases (9, 105–108). Indeed, the clinical benefit of these options may still be impacted by the frequent high-grade adverse events and by the emergence of acquired resistance. In *BRAF* V600E-mutated patient-derived melanoma xenografts, addition of palbociclib to dabrafenib and trametinib combination was shown to drastically increase tumor regression, in both naïve and dabrafenib/trametinib-resistant tumors (109). Interestingly, p16 loss appears to be positively selected following treatment with anti-BRAF agents (110). We have not verified the synergistic effect between CDK4/6i and BRAF inhibitors (dabrafenib monotherapy or other BRAF-targeting drugs, like vemurafenib). The described synergism in our work is most likely between CDK4/6 and the MEK inhibitions. Nevertheless, there could be a strong rationale for combining anti-BRAF therapy with CDK4/6 inhibition, especially in neo-adjuvant settings, to improve the probability of effective tumor surgical resection.

According to NGS analysis, *BRAF* V600E mutation are found in only 13 to 44% of ATC cases (5). Here, we provided evidence that the combination of trametinib with CDK4/6i could potentially represent a therapeutic option in the relevant proportion of wild type BRAF-ATC. Anti-CDK4/6 drugs have been shown to impact different cell types in the tumor microenvironment and enhance tumor immunogenicity (111–115). Combination with trametinib was also shown to be effective in different cancer types and to be able to boost immune anti-tumoral activity (101, 116, 117). RAS mutations are known to confer greater sensitivity to CDK4/6i and CDK4 was found to be critical for oncogenic NRAS and KRAS signaling (118–120). Thus, the use of this drug combination most likely will be beneficial for the treatment of both PDTC and RAI-refractory differentiated thyroid cancers. Currently, only three multi-targeted tyrosine kinase inhibitors (sorafenib, lenvatinib and cabozantinib) are approved with this indication and are restricted to patients presenting symptomatic, multi-metastatic, rapidly progressive disease (8, 121). Unfortunately, the impact of these drugs on patient survival is rather limited, with resistance and disease progression occurring after a few months (8, 121, 122). Moreover, the patients are exposed to numerous serious side effects, often requiring dose reduction or discontinuation of the treatment (122). Thus, the association trametinib-CDK4/6i could actually represent a therapeutic option also as second/third line therapy in such patients.

To conclude, our study supports the potentially favorable clinical impact of CDK4/6i for the treatment of aggressive dedifferentiated thyroid tumors including in combinations with anti-BRAF/MEK and, likely, anti-ERK therapies. Most ATC and PDTC patients could at least initially respond to CDK4/6i, which may arrest tumor growth, facilitating surgery in the neo-adjuvant setting or improving the efficacy of other treatment option. Future clinical trials are warranted to determine dose limiting toxicities, maximum tolerated dose and efficacy. Eventually, the prompt identification of tumors lacking CDK4 phosphorylation could represent a useful tool for recognizing the intrinsically CDK4/6i insensitive patients as potentially better candidates to immediate chemotherapy. This can be achieved by the complementary use of the 11 genes expression-based tool with p16 and KI67 IHC evaluation.

Data availability statement

The targeted DNA sequencing data and the RNA-sequencing data from patient-derived cell lines and from the 57 selected thyroid tumor samples have been deposited at the European Genome-phenome Archive (EGA), which is hosted by the EBI and the CRG, under accession number EGAS00001007577. The RNA-sequencing data from the remaining cell lines have been deposited in the Gene Expression Omnibus with accession number GSE235468.

Ethics statement

The studies involving humans were approved by Ethics Committees of Jules Bordet Institute (CE1978, CE2970) with informed consent of patients, Sapienza University of Rome, Pitié-Salpêtrière Hospital and with the Mayo Clinic Institutional Review Board protocol. Samples and associated data from the Institute – Instituto Português de Oncologia de Lisboa Francisco Gentil (IPOLFG) – were obtained in compliance with all applicable laws, including a written consent, and the study was approved by the institute's Ethics Committee. Written informed consent was obtained from all patients of the tumor tissue bank – Tumorothèque Centre de Ressources Biologiques des Hospices

Civil de Lyon. Samples and associated data were obtained from the tumor tissue bank – Tumorothèque ALLIANCE CANCER de Lille – that operates under the authorization AC-2018-3110 granted by the French ministry of research. Prior to scientific use, patients were appropriately informed and asked to consent in compliance with the French regulations. The studies were conducted in accordance with the local legislation and institutional requirements. The participants provided their written informed consent to participate in this study.

Author contributions

PR and ER conceived the project; JP, KC and PR designed and performed experiments; JP, ER, KC, JD, GC and PR analyzed and discussed the data; ER, MT and FL performed bioinformatics analyses; MD-P and EL performed the histopathological analyses; LM and JC provided patient-derived cell lines; MD-P, GD, LC, GA, LW, EL, CT, LM, JC, CD, CM and BC provided samples and related data; JP, ER, GC and PR wrote the original draft. All authors contributed to the article and approved the submitted version.

Funding

This study was supported by the Belgian Foundation against Cancer (grants 2014-130 and 2018-138); the Fonds de la Recherche Scientifique-FNRS (FRS-FNRS) under Grants J.0002.16, J.0141.19 and J.0169.22; Télévie (grant 7.4514.17); WALInnov 2017.2 (CICLIBTEST 1710166); the Fund Doctor J.P. Naets managed by the King Baudouin Foundation; and the Academic Medical Interdisciplinary Research (AMIR) Foundation (ASBL). The financial support (to GC) of the Association Jules Bordet Asbl (ex Les Amis de L'Institut Bordet) is gratefully acknowledged. MT and PR are (respectively) Postdoctoral Researcher and Senior Research Associate of the FRS-FNRS. This work was funded by Fundação para a Ciência e Tecnologia/Ministério da Ciência, Tecnologia e Ensino Superior (FCT/MCTES, Portugal) through national funds to iNOVA4Health (UIDB/04462/2020 and UIDP/04462/2020) and the Associated Laboratory LS4FUTURE (LA/P/0087/2020).

Acknowledgments

We thank Sabine Paternot for support, discussion and critical reading of the manuscript; Vincent Vercruysse for technical assistance; The Pathology Department from Institut Jules Bordet, particularly Alex Spinette and Dr. Nicolas de Saint Aubain for the assistance; Margarida M. Moura and Carolina Pires from Unidade de Investigação em Patobiologia Molecular from IPOLFG for tumor sample selection and preparation; Teresa Pereira, Marta Mesquita and Rafael Cabrera, from the Pathology Department from IPOLFG, for immunohistochemical and histopathological analysis; Dr. Valeriano Leite, from IPOLFG, for support and revision on patients' clinical data; Tumor banks from Centre de Ressources Biologiques (CRB) des Hospices Civils de Lyon (HCL) and Groupement de Coopération Sanitaire-Centre Régional de Référence en Cancérologie (C2RC) de Lille for the contribution and technical support on the samples; Annick Brandenburger, Laure Twyffels and Véronique Kruys for assistance on microscopic images acquisition; Manuel Saiselet and Adrien Tourneur for continued interest and support on samples collection/analysis; We also thank the Brussels Interuniversity Genomics High Throughput Core (www.brightcore.be) and Dr Anne Lefort for RNA handling and sequencing.

In memoriam

Jacques E. Dumont closely followed and supported this work. The authors dedicate this study to his memory.

Conflict of interest

The authors declare that the research was conducted in the absence of any commercial or financial relationships that could be construed as a potential conflict of interest.

Publisher's note

Supplementary material

The Supplementary Material for this article can be found online at: https://www.frontiersin.org/articles/10.3389/fendo.2023.1247542/full#supplementary-material

Supplementary materials are also available on FigShare: 10.6084/m9.figshare.24278626.

SUPPLEMENTARY DATA SHEET 1
Complete list of gene expressions obtained from RNA-seq analysis of thyroid tissue samples **(A)** and thyroid cell lines **(B)**.

References

1. Durante C, Haddy N, Baudin E, Leboulleux S, Hartl D, Travagli JP, et al. Long-term outcome of 444 patients with distant metastases from papillary and follicular thyroid carcinoma: Benefits and limits of radioiodine therapy. *J Clin Endocrinol Metab* (2006) 91:2892–9. doi: 10.1210/jc.2005-2838

2. Nagaiah G, Hossain A, Mooney CJ, Parmentier J, Remick SC. Anaplastic thyroid cancer: A review of epidemiology, pathogenesis, and treatment. *J Oncol* (2011) 2011:542358. doi: 10.1155/2011/542358

3. Lin B, Ma H, Ma M, Zhang Z, Sun Z, Hsieh I-Y, et al. The incidence and survival analysis for anaplastic thyroid cancer: a SEER database analysis. *Am J Transl Res* (2019) 11:5888–96.

4. Smallridge RC, Marlow LA, Copland JA. Anaplastic thyroid cancer: Molecular pathogenesis and emerging therapies. *Endocr Relat Cancer* (2009) 16:17–44. doi: 10.1677/ERC-08-0154

5. Jungels C, Pita JM, Costante G. Anaplastic thyroid carcinoma: advances in molecular profiling and targeted therapy. *Curr Opin Oncol* (2023) 35:1–9. doi: 10.1097/CCO.0000000000000918

6. Sanders EM, LiVolsi VA, Brierley J, Shin J, Randolph GW. An evidence-based review of poorly differentiated thyroid cancer. *World J Surg* (2007) 31:934–45. doi: 10.1007/s00268-007-9033-3

7. Baloch ZW, Asa SL, Barletta JA, Ghossein RA, Juhlin CC, Jung CK, et al. Overview of the 2022 WHO classification of thyroid neoplasms. *Endocr Pathol* (2022) 33:27–63. doi: 10.1007/s12022-022-09707-3

8. Fugazzola L, Elisei R, Fuhrer D, Jarzab B, Leboulleux S, Newbold K, et al. European thyroid association guidelines for the treatment and follow-up of advanced radioiodine-refractory thyroid cancer. *Eur Thyroid J* (2019) 8:227–45. doi: 10.1159/000502229

9. Iyer PC, Dadu R, Ferrarotto R, Busaidy NL, Habra MA, Zafereo M, et al. Real-world experience with targeted therapy for the treatment of anaplastic thyroid carcinoma. *Thyroid* (2018) 28:79–87. doi: 10.1089/thy.2017.0285

10. Molinaro E, Romei C, Biagini A, Sabini E, Agate L, Mazzeo S, et al. Anaplastic thyroid carcinoma: From clinicopathology to genetics and advanced therapies. *Nat Rev Endocrinol* (2017) 13:644–60. doi: 10.1038/nrendo.2017.76

11. Bockstaele L, Coulonval K, Kooken H, Paternot S, Roger PP. Regulation of CDK4. *Cell Div* (2006) 1:25. doi: 10.1186/1747-1028-1-25

12. Sherr CJ, Roberts JM. CDK inhibitors: positive and negative regulators of G1-phase progression. *Genes Dev* (1999) 13:1501–12. doi: 10.1101/gad.13.12.1501

13. Bockstaele L, Kooken H, Libert F, Paternot S, Dumont JE, de Launoit Y, et al. Regulated activating Thr172 phosphorylation of cyclin-dependent kinase 4(CDK4): its relationship with cyclins and CDK "inhibitors." *Mol Cell Biol* (2006) 26:5070–85. doi: 10.1128/mcb.02006-05

14. Musgrove EA, Caldon CE, Barraclough J, Stone A, Sutherland RL. Cyclin D as a therapeutic target in cancer. *Nat Rev Cancer* (2011) 11:558–72. doi: 10.1038/nrc3090

15. Di Sante G, Pagé J, Jiao X, Nawab O, Cristofanilli M, Skordalakes E, et al. Recent advances with cyclin-dependent kinase inhibitors: therapeutic agents for breast cancer and their role in immuno-oncology. *Expert Rev Anticancer Ther* (2019) 19:569–87. doi: 10.1080/14737140.2019.1615889

16. Fassl A, Geng Y, Sicinski P. CDK4 and CDK6 kinases: From basic science to cancer therapy. *Science* (2022). doi: 10.1126/science.abc1495

17. Finn RS, Martin M, Rugo HS, Jones S, Im S-A, Gelmon K, et al. Palbociclib and letrozole in advanced breast cancer. *N Engl J Med* (2016) 375:1925–36. doi: 10.1056/NEJMoa1607303

18. Hortobagyi GN, Stemmer SM, Burris HA, Yap Y-S, Sonke GS, Paluch-Shimon S, et al. Ribociclib as first-line therapy for HR-positive, advanced breast cancer. *N Engl J Med* (2016) 375:1738–48. doi: 10.1056/NEJMoa1609709

19. Sledge GW, Toi M, Neven P, Sohn J, Inoue K, Pivot X, et al. MONARCH 2: abemaciclib in combination with fulvestrant in women with HR+/HER2– advanced breast cancer who had progressed while receiving endocrine therapy. *J Clin Oncol* (2017) 35:2875–84. doi: 10.1200/JCO.2017.73.7585

20. Goyal RK, Chen H, Abughosh SM, Holmes HM, Candrilli SD, Johnson ML. Overall survival associated with CDK4/6 inhibitors in patients with HR+/HER2– metastatic breast cancer in the United States: A SEER-Medicare population-based study. *Cancer* (2023) 129:1051–63. doi: 10.1002/cncr.34675

21. Paternot S, Coulonval K, Dumont JE, Roger PP. Cyclic AMP-dependent phosphorylation of cyclin D3-bound CDK4 determines the passage through the cell cycle restriction point in thyroid epithelial cells. *J Biol Chem* (2003) 278:26533–40. doi: 10.1074/jbc.M302492200

22. Bisteau X, Paternot S, Colleoni B, Ecker K, Coulonval K, De Groote P, et al. CDK4 T172 phosphorylation is central in a CDK7-dependent bidirectional CDK4/CDK2 interplay mediated by p21 phosphorylation at the restriction point. *PloS Genet* (2013) 9:e1003546. doi: 10.1371/journal.pgen.1003546

23. Rocha AS, Paternot S, Coulonval K, Dumont JE, Soares P, Roger PP. Cyclic AMP inhibits the proliferation of thyroid carcinoma cell lines through regulation of CDK4 phosphorylation. *Mol Biol Cell* (2008) 19:4814–25. doi: 10.1091/mbc.E08-06-0617

24. Paternot S, Roger PP. Combined inhibition of MEK and mammalian target of rapamycin abolishes phosphorylation of cyclin-dependent kinase 4 in glioblastoma cell lines and prevents their proliferation. *Cancer Res* (2009) 69:4577–81. doi: 10.1158/0008-5472.CAN-08-3260

25. Bockstaele L, Bisteau X, Paternot S, Roger PP. Differential regulation of cyclin-dependent kinase 4 (CDK4) and CDK6, evidence that CDK4 might not be activated by CDK7, and design of a CDK6 activating mutation. *Mol Cell Biol* (2009) 29:4188–200. doi: 10.1128/mcb.01823-08

26. Raspe E, Coulonval K, Pita JM, Paternot S, Rothe F, Twyffels L, et al. CDK 4 phosphorylation status and a linked gene expression profile predict sensitivity to palbociclib. *EMBO Mol Med* (2017) 9:1052–66. doi: 10.15252/emmm.201607084

27. Paternot S, Raspé E, Meiller C, Tarabichi M, Assié J-BB, Libert F, et al. Preclinical evaluation of CDK4 phosphorylation predicts high sensitivity of pleural mesotheliomas to CDK4/6 inhibition. *Mol Oncol* (2022). doi: 10.1002/1878-0261.13351

28. Witkiewicz AK, Knudsen KE, Dicker AP, Knudsen ES. The meaning of p16 (ink4a) expression in tumors: functional significance, clinical associations and future developments. *Cell Cycle* (2011) 10:2497–503. doi: 10.4161/cc.10.15.16776

29. Dean JL, Thangavel C, McClendon AK, Reed CA, Knudsen ES. Therapeutic CDK4/6 inhibition in breast cancer: key mechanisms of response and failure. *Oncogene* (2010) 29:4018–32. doi: 10.1038/onc.2010.154

30. Salvatore G, Nappi TC, Salerno P, Jiang Y, Garbi C, Ugolini C, et al. A cell proliferation and chromosomal instability signature in anaplastic thyroid carcinoma. *Cancer Res* (2007) 67:10148–58. doi: 10.1158/0008-5472.CAN-07-1887

31. Pita JM, Banito A, Cavaco BM, Leite V. Gene expression profiling associated with the progression to poorly differentiated thyroid carcinomas. *Br J Cancer* (2009) 101:1782–91. doi: 10.1038/sj.bjc.6605340

32. Pita JM, Figueiredo IF, Moura MM, Leite V, Cavaco BM. Cell cycle deregulation and TP53 and RAS mutations are major events in poorly differentiated and undifferentiated thyroid carcinomas. *J Clin Endocrinol Metab* (2014) 99:E497–507. doi: 10.1210/jc.2013-1512

33. Hébrant A, Dom G, Dewaele M, Andry G, Trésallet C, Leteurtre E, et al. mRNA expression in papillary and anaplastic thyroid carcinoma: molecular anatomy of a killing switch. *PloS One* (2012) 7:e37807. doi: 10.1371/journal.pone.0037807

34. Montero-Conde C, Martín-Campos JM, Lerma E, Gimenez G, Martínez-Guitarte JL, Combalía N, et al. Molecular profiling related to poor prognosis in thyroid carcinoma. Combining gene expression data and biological information. *Oncogene* (2008) 27:1554–61. doi: 10.1038/sj.onc.1210792

35. Paternot S, Dumont JE, Roger PP. Differential utilization of cyclin D1 and cyclin D3 in the distinct mitogenic stimulations by growth factors and TSH of human thyrocytes in primary culture. *Mol Endocrinol* (2006) 20:3279–92. doi: 10.1210/me.2005-0515

36. Paternot S, Arsenijevic T, Coulonval K, Bockstaele L, Dumont JE, Roger PP. Distinct specificities of pRb phosphorylation by CDK4 activated by cyclin D1 or cyclin D3: Differential involvement in the distinct mitogenic modes of thyroid epithelial cells. *Cell Cycle* (2006) 5:61–70. doi: 10.4161/cc.5.1.2265

37. Landa I, Ibrahimpasic T, Boucai L, Sinha R, Knauf JA, Shah RH, et al. Genomic and transcriptomic hallmarks of poorly differentiated and anaplastic thyroid cancers. *J Clin Invest* (2016) 126:1052–66. doi: 10.1172/JCI85271

38. Kunstman JW, Christofer Juhlin C, Goh G, Brown TC, Stenman A, Healy JM, et al. Characterization of the mutational landscape of anaplastic thyroid cancer via whole-exome sequencing. *Hum Mol Genet* (2015) 24:2318–29. doi: 10.1093/hmg/ddu749

39. Volante M, Collini P, Nikiforov YE, Sakamoto A, Kakudo K, Katoh R, et al. Poorly differentiated thyroid carcinoma: the Turin proposal for the use of uniform diagnostic criteria and an algorithmic diagnostic approach. *Am J Surg Pathol* (2007) 31:1256–64. doi: 10.1097/PAS.0b013e3180309e6a

40. Schweppe RE, Klopper JP, Korch C, Pugazhenthi U, Benezra M, Knauf JA, et al. Deoxyribonucleic acid profiling analysis of 40 human thyroid cancer cell lines reveals cross-contamination resulting in cell line redundancy and misidentification. *J Clin Endocrinol Metab* (2008) 93:4331–41. doi: 10.1210/jc.2008-1102

41. Roger PP, Baptist M, Dumont JE. A mechanism generating heterogeneity in thyroid epithelial cells: suppression of the thyrotropin/cAMP-dependent mitogenic pathway after cell division induced by cAMP-independent factors. *J Cell Biol* (1992) 117:383–93. doi: 10.1083/jcb.117.2.383

42. Chou TC, Talalay P. Quantitative analysis of dose-effect relationships: the combined effects of multiple drugs or enzyme inhibitors. *Adv Enzyme Regul* (1984) 22:27–55. doi: 10.1016/0065-2571(84)90007-4

43. Chou TC. Theoretical basis, experimental design, and computerized simulation of synergism and antagonism in drug combination studies. *Pharmacol Rev* (2006) 58:621–81. doi: 10.1124/pr.58.3.10

44. Robinson JT, Thorvaldsdóttir H, Winckler W, Guttman M, Lander ES, Getz G, et al. Integrative genomics viewer. *Nat Biotechnol* (2011) 29:24–6. doi: 10.1038/nbt.1754

45. Lê S, Josse J, Husson F. FactoMineR: an R package for multivariate analysis. *J Stat Softw* (2008) 25:1–18. doi: 10.18637/jss.v025.i01

46. Agrawal N, Akbani R, Aksoy BA, Ally A, Arachchi H, Asa SL, et al. Integrated genomic characterization of papillary thyroid carcinoma. *Cell* (2014) 159:676–90. doi: 10.1016/j.cell.2014.09.050

47. Chae YK, Chang S, Ko T, Anker J, Agte S, Iams W, et al. Epithelial-mesenchymal transition (EMT) signature is inversely associated with T-cell infiltration in non-small cell lung cancer (NSCLC). *Sci Rep* (2018) 8:2918. doi: 10.1038/s41598-018-21061-1

48. Olshen AB, Venkatraman ES, Lucito R, Wigler M. Circular binary segmentation for the analysis of array-based DNA copy number data. *Biostatistics* (2004) 5:557–72. doi: 10.1093/biostatistics/kxh008

49. Marlow LA, von Roemeling CA, Cooper SJ, Zhang Y, Rohl SD, Arora S, et al. Foxo3a drives proliferation in anaplastic thyroid carcinoma through transcriptional regulation of cyclin A1: A paradigm shift that impacts current therapeutic strategies. *J Cell Sci* (2012) 125:4253–63. doi: 10.1242/jcs.097428

50. Bankhead P, Loughrey MB, Fernández JA, Dombrowski Y, McArt DG, Dunne PD, et al. QuPath: Open source software for digital pathology image analysis. *Sci Rep* (2017) 7:16878. doi: 10.1038/s41598-017-17204-5

51. Coulonval K, Bockstaele L, Paternot S, Dumont JE, Roger PP. The cyclin D3-CDK4-p27kip1 holoenzyme in thyroid epithelial cells: activation by TSH, inhibition by TGFbeta, and phosphorylations of its subunits demonstrated by two-dimensional gel electrophoresis. *Exp Cell Res* (2003) 291:135–49. doi: 10.1016/S0014-4827(03)00392-6

52. Paternot S, Colleoni B, Bisteau X, Roger PP. The CDK4/CDK6 inhibitor PD0332991 paradoxically stabilizes activated cyclin D3-CDK4/6 complexes. *Cell Cycle* (2014) 13:2879–88. doi: 10.4161/15384101.2014.946841

53. Colleoni B, Paternot S, Pita JM, Bisteau X, Coulonval K, Davis RJ, et al. JNKs function as CDK4-activating kinases by phosphorylating CDK4 and p21. *Oncogene* (2017) 36:4349–61. doi: 10.1038/onc.2017.7

54. Coulonval K, Vercruysse V, Paternot S, Pita JM, Corman R, Raspe E, et al. Monoclonal antibodies to activated CDK4: use to investigate normal and cancerous cell cycle regulation and involvement of phosphorylations of p21 and p27. *Cell Cycle* (2022) 21:12–32. doi: 10.1080/15384101.2021.1984663

55. Yoo S-K, Song YS, Lee EK, Hwang J, Kim HH, Jung G, et al. Integrative analysis of genomic and transcriptomic characteristics associated with progression of aggressive thyroid cancer. *Nat Commun* (2019) 10:2764. doi: 10.1038/s41467-019-10680-5

56. Yoo SK, Lee S, Kim SJ, Jee HG, Kim BA, Cho H, et al. Comprehensive analysis of the transcriptional and mutational landscape of follicular and papillary thyroid cancers. *PloS Genet* (2016) 12:e1006239. doi: 10.1371/journal.pgen.1006239

57. Haase J, Misiak D, Bauer M, Pazaitis N, Braun J, Pötschke R, et al. IGF2BP1 is the first positive marker for anaplastic thyroid carcinoma diagnosis. *Mod Pathol an Off J United States Can Acad Pathol Inc* (2021) 34:32–41. doi: 10.1038/s41379-020-0630-0

58. Lam AKY, Lo CY, Leung P, Lang BHH, Chan WF, Luk JM. Clinicopathological roles of alterations of tumor suppressor gene p16 in papillary thyroid carcinoma. *Ann Surg Oncol* (2007) 14:1772–9. doi: 10.1245/s10434-006-9280-9

59. Boltze C, Zack S, Quednow C, Bettge S, Roessner A, Schneider-Stock R. Hypermethylation of the CDKN2/p16INK4A promotor in thyroid carcinogenesis. *Pathol - Res Pract* (2003) 199:399–404. doi: 10.1078/0344-0338-00436

60. Ball E, Bond J, Franc B, DeMicco C, Wynford-Thomas D. An immunohistochemical study of p16INK4a expression in multistep thyroid tumourigenesis. *Eur J Cancer* (2007) 43:194–201. doi: 10.1016/j.ejca.2006.08.025

61. Ferru A, Fromont G, Gibelin H, Guilhot J, Savagner F, Tourani JM, et al. The status of CDKN2A alpha (p16INK4A) and beta (p14 ARF) transcripts in thyroid tumour progression. *Br J Cancer* (2006) 95:1670–7. doi: 10.1038/sj.bjc.6603479

62. Gil J, Peters G. Regulation of the INK4b–ARF–INK4a tumour suppressor locus: all for one or one for all. *Nat Rev Mol Cell Biol* (2006) 7:667–77. doi: 10.1038/nrm1987

63. Palafox M, Monserrat L, Bellet M, Villacampa G, Gonzalez-Perez A, Oliveira M, et al. High p16 expression and heterozygous RB1 loss are biomarkers for CDK4/6 inhibitor resistance in ER+ breast cancer. *Nat Commun* (2022) 13:5258. doi: 10.1038/s41467-022-32828-6

64. Marlow LA, D'Innocenzi J, Zhang Y, Rohl SD, Cooper SJ, Sebo T, et al. Detailed molecular fingerprinting of four new anaplastic thyroid carcinoma cell lines and their use for verification of RhoB as a molecular therapeutic target. *J Clin Endocrinol Metab* (2010) 95:5338–47. doi: 10.1210/jc.2010-1421

65. Landa I, Pozdeyev N, Korch C, Marlow LA, Smallridge RC, Copland JA, et al. Comprehensive genetic characterization of human thyroid cancer cell lines: A validated panel for preclinical studies. *Clin Cancer Res* (2019) 25:3141–51. doi: 10.1158/1078-0432.CCR-18-2953

66. Wong K, Di Cristofano F, Ranieri M, De Martino D, Di Cristofano A. PI3K/mTOR inhibition potentiates and extends palbociclib activity in anaplastic thyroid cancer. *Endocr Relat Cancer* (2018) 26:425–36. doi: 10.1530/ERC-19-0011

67. Lee HJ, Lee WK, Kang CW, Ku CR, Cho YH, Lee EJ. A selective cyclin-dependent kinase 4, 6 dual inhibitor, Ribociclib (LEE011) inhibits cell proliferation and induces apoptosis in aggressive thyroid cancer. *Cancer Lett* (2018) 417:131–40. doi: 10.1016/j.canlet.2017.12.037

68. Lopes-Ventura S, Pojo M, Matias AT, Moura MM, Marques IJ, Leite V, et al. The efficacy of HRAS and CDK4/6 inhibitors in anaplastic thyroid cancer cell lines. *J Endocrinol Invest* (2019) 42:527–40. doi: 10.1007/s40618-018-0947-4

69. Dibble CC, Asara JM, Manning BD. Characterization of rictor phosphorylation sites reveals direct regulation of mTOR complex 2 by S6K1. *Mol Cell Biol* (2009) 29:5657–70. doi: 10.1128/mcb.00735-09

70. Subbiah V, Cabanillas ME, Kreitman RJ, Wainberg ZA, Cho JY, Keam B, et al. Dabrafenib and trametinib treatment in patients with locally advanced or metastatic BRAF V600–mutant anaplastic thyroid cancer. *J Clin Oncol* (2018) 36:7–13. doi: 10.1200/JCO.2017.73.6785

71. Falchook GS, Long GV, Kurzrock R, Kim KB, Arkenau HT, Brown MP, et al. Dose selection, pharmacokinetics, and pharmacodynamics of BRAF inhibitor dabrafenib (GSK2118436). *Clin Cancer Res* (2014) 20:4449–58. doi: 10.1158/1078-0432.CCR-14-0887

72. Infante JR, Fecher LA, Falchook GS, Nallapareddy S, Gordon MS, Becerra C, et al. Safety, pharmacokinetic, pharmacodynamic, and efficacy data for the oral MEK inhibitor trametinib: A phase 1 dose-escalation trial. *Lancet Oncol* (2012) 13:773–81. doi: 10.1016/S1470-2045(12)70270-X

73. Leonowens C, Pendry C, Bauman J, Young GC, Ho M, Henriquez F, et al. Concomitant oral and intravenous pharmacokinetics of trametinib, a MEK inhibitor, in subjects with solid tumours. *Br J Clin Pharmacol* (2014) 78:524–32. doi: 10.1111/bcp.12373

74. Klein ME, Kovatcheva M, Davis LE, Tap WD, Koff A. CDK4/6 inhibitors: the mechanism of action may not be as simple as once thought. *Cancer Cell* (2018) 34:9–20. doi: 10.1016/j.ccell.2018.03.023

75. Motti ML, De Marco C, Califano D, De Gisi S, Malanga D, Troncone G, et al. Loss of p27 expression through RAS→BRAF→MAP kinase-dependent pathway in human thyroid carcinomas. *Cell Cycle* (2007) 6:2817–25. doi: 10.4161/cc.6.22.4883

76. Knudsen ES, Witkiewicz AK. The strange case of CDK4/6 inhibitors: mechanisms, resistance, and combination strategies. *Trends Cancer* (2017) 3:39–55. doi: 10.1016/j.trecan.2016.11.006

77. Day PJ, Cleasby A, Tickle IJ, O'Reilly M, Coyle JE, Holding FP, et al. Crystal structure of human CDK4 in complex with a D-type cyclin. *Proc Natl Acad Sci U.S.A.* (2009) 106:4166–70. doi: 10.1073/pnas.0809645106

78. Takaki T, Echalier A, Brown NR, Hunt T, Endicott JA, Noble MEM. The structure of CDK4/cyclin D3 has implications for models of CDK activation. *Proc Natl Acad Sci U.S.A.* (2009) 106:4171–6. doi: 10.1073/pnas.0809674106

79. Coulonval K, Bockstaele L, Paternot S, Roger PP. Phosphorylations of cyclin-dependent kinase 2 revisited using two-dimensional gel electrophoresis. *J Biol Chem* (2003) 278:52052–60. doi: 10.1074/jbc.M307012200

80. Coulonval K, Kooken H, Roger PP. Coupling of T161 and T14 phosphorylations protects cyclin B-CDK1 from premature activation. *Mol Biol Cell* (2011) 22:3971–85. doi: 10.1091/mbc.E11-02-0136

81. Paternot S, Bockstaele L, Bisteau X, Kooken H, Coulonval K, Roger PP. Rb inactivation in cell cycle and cancer: The puzzle of highly regulated activating phosphorylation of CDK4 versus constitutively active CDK-activating kinase. *Cell Cycle* (2010) 9:689–99. doi: 10.4161/cc.9.4.10611

82. Kato JY, Matsuoka M, Strom DK, Sherr CJ. Regulation of cyclin D-dependent kinase 4 (cdk4) by cdk4-activating kinase. *Mol Cell Biol* (1994) 14:2713–21. doi: 10.1128/mcb.14.4.2713

83. Wiseman SM, Melck A, Masoudi H, Ghaidi F, Goldstein L, Gown A, et al. Molecular phenotyping of thyroid tumors identifies a marker panel for differentiated thyroid cancer diagnosis. *Ann Surg Oncol* (2008) 15:2811–26. doi: 10.1245/s10434-008-0034-8

84. Zafon C, Obiols G, Castellví J, Ramon Y Cajal S, Baena JA, Mesa J. Expression of p21cip1, p27kip1, and p16 INk4a cyclin-dependent kinase inhibitors in papillary thyroid carcinoma: Correlation with clinicopathological factors. *Endocr Pathol* (2008) 19:184–9. doi: 10.1007/s12022-008-9037-z

85. Do SI, Kim DH, Yang JH, Pyo JS, Kim K, Lee H, et al. Decreased expression of p27 is associated with Malignant transformation and extrathyroidal extension in papillary thyroid carcinoma. *Tumor Biol* (2016) 37:3359–64. doi: 10.1007/s13277-015-4163-y

86. Vizioli MG, Possik PA, Tarantino E, Meissl K, Borrello MG, Miranda C, et al. Evidence of oncogene-induced senescence in thyroid carcinogenesis. *Endocr Relat Cancer* (2011) 18:743–57. doi: 10.1530/ERC-11-0240

87. Jones CJ, Kipling D, Morris M, Hepburn P, Skinner J, Bounacer A, et al. Evidence for a telomere-independent "clock" limiting RAS oncogene-driven proliferation of human thyroid epithelial cells. *Mol Cell Biol* (2000) 20:5690–9. doi: 10.1128/mcb.20.15.5690-5699.2000

88. Bellelli R, Vitagliano D, Federico G, Marotta P, Tamburrino A, Salerno P, et al. Oncogene-induced senescence and its evasion in a mouse model of thyroid neoplasia. *Mol Cell Endocrinol* (2018) 460:24–35. doi: 10.1016/j.mce.2017.06.023

89. Knudsen ES, Zacksenhaus E. The vulnerability of RB loss in breast cancer: Targeting a void in cell cycle control. *Oncotarget* (2018) 9:30940–1. doi: 10.18632/oncotarget.25797

90. Bosco EE, Wang Y, Xu H, Zilfou JT, Knudsen KE, Aronow BJ, et al. The retinoblastoma tumor suppressor modifies the therapeutic response of breast cancer. *J Clin Invest* (2007) 117:218–28. doi: 10.1172/JCI28803

91. Chevalier B, Karleskind O, Jannin A, Farchi O, Vermaut C, Escande A, et al. Complete pathological response following chemotherapy and radiotherapy in two cases of advanced anaplastic thyroid carcinoma. *Eur Thyroid J* (2022) 12:e220111. doi: 10.1530/etj-22-0111

92. He S, Roberts PJ, Sorrentino JA, Bisi JE, Storrie-White H, Tiessen RG, et al. *Transient CDK4/6 inhibition protects hematopoietic stem cells from chemotherapy-induced exhaustion*. Sci Transl Med (2017) 9:eaal3986. doi: 10.1126/scitranslmed.aal3986

93. Ferrarotto R, Anderson I, Medgyasszay B, Garcia-Campelo MR, Edenfield W, Feinstein TM, et al. Trilaciclib prior to chemotherapy reduces the usage of supportive care interventions for chemotherapy-induced myelosuppression in patients with small cell lung cancer: Pooled analysis of three randomized phase 2 trials. *Cancer Med* (2021) 10:5748–56. doi: 10.1002/cam4.4089

94. Pozdeyev N, Gay LM, Sokol ES, Hartmaier R, Deaver KE, Davis S, et al. Genetic analysis of 779 advanced differentiated and anaplastic thyroid cancers. *Clin Cancer Res* (2018) 24:3059–68. doi: 10.1158/1078-0432.CCR-18-0373

95. Lee JJ, Au AYM, Foukakis T, Barbaro M, Kiss N, Clifton-Bligh R, et al. Array-CGH identifies cyclin D1 and UBCH10 amplicons in anaplastic thyroid carcinoma. *Endocr Relat Cancer* (2008) 15:801–15. doi: 10.1677/ERC-08-0018

96. Evans JJ, Crist HS, Durvesh S, Bruggeman RD, Goldenberg D. A comparative study of cell cycle mediator protein expression patterns in anaplastic and papillary thyroid carcinoma. *Cancer Biol Ther* (2012) 13:776–81. doi: 10.4161/cbt.20560

97. Lazzereschi D, Sambuco L, Carnuvale Scalzo C, Raniri A, Mincione G, Nardi F, et al. Cyclin D1 and Cyclin E expression in Malignant thyroid cells and in human thyroid carcinomas. *Int J Cancer* (1998) 76:806–11. doi: 10.1002/(SICI)1097-0215(19980610)76:6<806::AID-IJC7>3.0.CO;2-1

98. Basolo F, Caligo MA, Pinchera A, Fedeli F, Baldanzi A, Miccoli P, et al. Cyclin D1 overexpression in thyroid carcinomas: relation with clinico-pathological parameters, retinoblastoma gene product, and Ki67 labeling index. *Thyroid* (2000) 10:741–6. doi: 10.1089/thy.2000.10.741

99. Anania MC, Gasparri F, Cetti E, Fraietta I, Todoerti K, Miranda C, et al. Identification of thyroid tumor cell vulnerabilities through a siRNA-based functional screening. *Oncotarget* (2015) 6:34629–48. doi: 10.18632/oncotarget.5282

100. Knudsen ES, Kumarasamy V, Ruiz A, Sivinski J, Chung S, Grant A, et al. Cell cycle plasticity driven by MTOR signaling: integral resistance to CDK4/6 inhibition in patient-derived models of pancreatic cancer. *Oncogene* (2019) 38:3355–70. doi: 10.1038/s41388-018-0650-0

101. Wagner V, Gil J. Senescence as a therapeutically relevant response to CDK4/6 inhibitors. *Oncogene* (2020) 39:5165–76. doi: 10.1038/s41388-020-1354-9

102. Doisneau-Sixou SF, Sergio CM, Carroll JS, Hui R, Musgrove EA, Sutherland RL. Estrogen and antiestrogen regulation of cell cycle progression in breast cancer cells. *Endocr Relat Cancer* (2003) 10:179–86. doi: 10.1677/erc.0.0100179

103. Bible KC, Kebebew E, Brierley J, Brito JP, Cabanillas ME, Clark TJ, et al. 2021 American thyroid association guidelines for management of patients with anaplastic thyroid cancer. *Thyroid* (2021) 31:337–86. doi: 10.1089/thy.2020.0944

104. Filetti S, Durante C, Hartl DM, Leboulleux S, Locati LD, Newbold K, et al. ESMO Clinical Practice Guideline update on the use of systemic therapy in advanced thyroid cancer. *Ann Oncol Off J Eur Soc Med Oncol* (2022) 33:674–84. doi: 10.1016/j.annonc.2022.04.009

105. da Silva TN, Rodrigues R, Saramago A, Pires C, Rito M, Horta M, et al. Target therapy for BRAF mutated anaplastic thyroid cancer: a clinical and molecular study. *Eur J Endocrinol* (2023) 188:1–8. doi: 10.1093/ejendo/lvac011

106. Cabanillas ME, Ferrarotto R, Garden AS, Ahmed S, Busaidy NL, Dadu R, et al. Neoadjuvant BRAF-and immune-directed therapy for anaplastic thyroid carcinoma. *Thyroid* (2018) 28:945–51. doi: 10.1089/thy.2018.0060

107. Iyer PC, Dadu R, Gule-Monroe M, Busaidy NL, Ferrarotto R, Habra MA, et al. Salvage pembrolizumab added to kinase inhibitor therapy for the treatment of anaplastic thyroid carcinoma. *J Immunother Cancer* (2018) 6:68. doi: 10.1186/s40425-018-0378-y

108. Wang JR, Zafereo ME, Dadu R, Ferrarotto R, Busaidy NL, Lu C, et al. Complete surgical resection following neoadjuvant dabrafenib plus trametinib in BRAFV600E-mutated anaplastic thyroid carcinoma. *Thyroid* (2019) 29:1036–43. doi: 10.1089/thy.2019.0133

109. Harris AL, Lee SE, Dawson LK, Marlow LA, Edenfield BH, Durham WF, et al. Targeting the cyclin dependent kinase and retinoblastoma axis overcomes standard of care resistance in BRAFV600E-mutant melanoma. *Oncotarget* (2018) 9:10905–19. doi: 10.18632/oncotarget.23649

110. Duquette M, Sadow PM, Husain A, Sims JN, Antonello ZA, Fischer AH, et al. Metastasis-associated MCL1 and P16 copy number alterations dictate resistance to vemurafenib in a BRAFV600E patient-derived papillary thyroid carcinoma preclinical model. *Oncotarget* (2015) 6:42445–67. doi: 10.18632/oncotarget.6442

111. Goel S, Bergholz JS, Zhao JJ. Targeting CDK4 and CDK6 in cancer. *Nat Rev Cancer* (2022) 22:356–72. doi: 10.1038/s41568-022-00456-3

112. Deng J, Wang ES, Jenkins RW, Li S, Dries R, Yates K, et al. CDK4/6 inhibition augments anti-tumor immunity by enhancing T cell activation. *Cancer Discovery* (2018) 8:216–33. doi: 10.1158/2159-8290.CD-17-0915

113. Lelliott EJ, Kong IY, Zethoven M, Ramsbottom KM, Martelotto LG, Meyran D, et al. CDK4/6 inhibition promotes antitumor immunity through the induction of T-cell memory. *Cancer Discovery* (2021) 11:2582–601. doi: 10.1158/2159-8290.CD-20-1554

114. Schaer DA, Beckmann RP, Dempsey JA, Huber L, Forest A, Amaladas N, et al. The CDK4/6 inhibitor abemaciclib induces a T cell inflamed tumor microenvironment and enhances the efficacy of PD-L1 checkpoint blockade. *Cell Rep* (2018) 22:2978–94. doi: 10.1016/j.celrep.2018.02.053

115. Uzhachenko RV, Bharti V, Ouyang Z, Blevins A, Mont S, Saleh N, et al. Metabolic modulation by CDK4/6 inhibitor promotes chemokine-mediated recruitment of T cells into mammary tumors. *Cell Rep* (2021) 35:108944. doi: 10.1016/j.celrep.2021.108944

116. Ruscetti M, Leibold J, Bott MJ, Fennell M, Kulick A, Salgado NR, et al. NK cell–mediated cytotoxicity contributes to tumor control by a cytostatic drug combination. *Science* (2018) 362:1416–22. doi: 10.1126/science.aas9090

117. Ruscetti M, Morris JP, Mezzadra R, Russell J, Leibold J, Romesser PB, et al. Senescence-induced vascular remodeling creates therapeutic vulnerabilities in pancreas cancer. *Cell* (2020) 181:424–41. doi: 10.1016/j.cell.2020.03.008

118. Kwong LN, Costello JC, Liu H, Jiang S, Helms TL, Langsdorf AE, et al. Oncogenic NRAS signaling differentially regulates survival and proliferation in melanoma. *Nat Med* (2012) 18:1503–10. doi: 10.1038/nm.2941

119. Patnaik A, Rosen LS, Tolaney SM, Tolcher AW, Goldman JW, Gandhi L, et al. Efficacy and safety of Abemaciclib, an inhibitor of CDK4 and CDK6, for patients with breast cancer, non–small cell lung cancer, and other solid tumors. *Cancer Discovery* (2016) 6:740–53. doi: 10.1158/2159-8290.CD-16-0095

120. Puyol M, Martin A, Dubus P, Mulero F, Pizcueta P, Khan G, et al. A synthetic lethal interaction between K-Ras oncogenes and Cdk4 unveils a therapeutic strategy for non-small cell lung carcinoma. *Cancer Cell* (2010) 18:63–73. doi: 10.1016/j.ccr.2010.05.025

121. Haugen BR, Alexander EK, Bible KC, Doherty GM, Mandel SJ, Nikiforov YE, et al. 2015 American thyroid association management guidelines for adult patients with thyroid nodules and differentiated thyroid cancer: the american thyroid association guidelines task force on thyroid nodules and differentiated thyroid cancer. *Thyroid* (2016) 26:1–133. doi: 10.1089/thy.2015.0020

122. Costante G. Multikinase inhibitors for the treatment of radioiodine refractory thyroid cancer: What have we learned from the "real-world" experience? *Curr Opin Oncol* (2021) 33:3–8. doi: 10.1097/CCO.0000000000000693

10.3389/fendo.2023.1247542

Glossary

2D-gel	two-dimensional gel
ATC	anaplastic thyroid carcinoma
BrdU	5-bromo-2'-deoxyuridine
CDK	cyclin-dependent kinase
CDK4/6i	CDK4/CDK6 inhibitors
CI	combination index
CIP/KIP	CDK interacting protein/kinase inhibitory protein
CP20M	counts per 20 million reads
CpG	cytosines followed by guanine residues
DMSO	dimethyl sulfoxide
EdU	5-ethynyl-2'-deoxyuridine
EMT	epithelial-mesenchymal transition
FFPE	formalin-fixed, paraffin-embedded
FTC	follicular thyroid carcinoma
GI50	half-maximal inhibitory concentration of the cell proliferation
HE	hematoxylin/eosin
IGV	Integrative Genomics Viewer
IHC	immunohistochemistry
INK4	inhibitor of CDK4
LNM	lymph node metastasis
MEK	MAP/ERK kinase
MTT	3-[4,5-dimethylthiazol-2-yl]-2,5 diphenyl tetrazolium bromide
mTOR	mammalian target of rapamycin
OCT	optimal cutting temperature
ORF	open reading frame
pCDK4	phosphorylated CDK4
PDTC	poorly differentiated thyroid carcinoma
PTC	papillary thyroid carcinoma
PI3K	Phosphoinositide 3-kinase
Profile A	absent phosphorylated CDK4
Profile H	high phosphorylated CDK4
Profile L	Low phosphorylated CDK4
RAI	radioactive iodine treatment
RNA-seq	RNA-sequencing
SDS-PAGE	sodium dodecylsulfate polyacrylamide gel electrophoresis
SA-β-gal	senescence-associated β-galactosidase
SRB	sulforhodamine B
TDS	thyroid differentiation score
WDTC	well-differentiated thyroid carcinoma

frontiers | Frontiers in Endocrinology

TYPE Original Research
PUBLISHED 27 October 2023
DOI 10.3389/fendo.2023.1286747

OPEN ACCESS

EDITED BY
Cesar Seigi Fuziwara,
University of São Paulo, Brazil

REVIEWED BY
Ileana G. Rubio,
Federal University of São Paulo, Brazil
Mirian Romitti,
Université libre de Bruxelles, Belgium

*CORRESPONDENCE
Aurore Carré
aurore.carre@inserm.fr
Michel Polak
michel.polak@aphp.fr

†These authors share first authorship

RECEIVED 31 August 2023
ACCEPTED 05 October 2023
PUBLISHED 27 October 2023

CITATION
Didier-Mathon H, Stoupa A, Kariyawasam D, Yde S, Cochant-Priollet B, Groussin L, Sébag F, Cagnard N, Nitschke P, Luton D, Polak M and Carré A (2023) Borealin/CDCA8 deficiency alters thyroid development and results in papillary tumor-like structures. *Front. Endocrinol.* 14:1286747. doi: 10.3389/fendo.2023.1286747

Borealin/CDCA8 deficiency alters thyroid development and results in papillary tumor-like structures

Hortense Didier-Mathon[1†], Athanasia Stoupa[1,2,3†], Dulanjalee Kariyawasam[1,2,3], Sonny Yde[1], Beatrix Cochant-Priollet[4,5], Lionel Groussin[6], Frédéric Sébag[7], Nicolas Cagnard[8], Patrick Nitschke[8], Dominique Luton[9], Michel Polak[1,2,3,10,11*] and Aurore Carré[1,2*]

[1]Université Paris Cité, Centre National de la Recherche Scientifique (CNRS), Institut National de la Santé et de la Recherche Médicale (INSERM), Institut Cochin, Paris, France, [2]IMAGINE Institute Affiliate, Paris, France, [3]Pediatric Endocrinology, Gynecology and Diabetology Department, Hôpital Universitaire Necker-Enfants Malades, Assistance Publique Hopitaux de Paris (AP-HP), Paris, France, [4]Université Paris Cité, Faculté de Médecine, Paris, France, [5]Department of Pathology, Cochin Hospital, Assistance Publique Hopitaux de Paris (AP-HP) Centre, Paris, France, [6]Department of Endocrinology, Université Paris Cité, Cochin Hospital, Assistance Publique Hopitaux de Paris (AP-HP) Centre, Paris, France, [7]Endocrine Surgery, Conception University Hospital, Aix-Marseille University, Marseille, France, [8]Bioinformatics Platform, Institut Imagine, Institut National de la Santé et de la Recherche Médicale (INSERM) UMR 1163, Paris, France, [9]Département de Gynécologie Obstétrique, Hôpital Bicêtre, Assistance Publique Hopitaux de Paris (AP-HP) Le Kremlin Bicêtre France, Université Paris Saclay, Le Kremlin Bicêtre, France, [10]Centre de référence des maladies endocriniennes rares de la croissance et du développement, Necker-Enfants Malades University Hospital, Paris, France, [11]Centre régional de dépistage néonatal (CRDN) Ile de France, Paris, France

Background: *BOREALIN/CDCA8* mutations are associated with congenital hypothyroidism and thyroid dysgenesis. Borealin is involved in mitosis as part of the Chromosomal Passenger Complex. Although *BOREALIN* mutations decrease thyrocyte adhesion and migration, little is known about the specific role of Borealin in the thyroid.

Methods: We characterized thyroid development and function in Borealin-deficient (*Borealin*$^{+/-}$) mice using histology, transcriptomic analysis, and quantitative PCR.

Results: Thyroid development was impaired with a hyperplastic anlage on embryonic day E9.5 followed by thyroid hypoplasia from E11.5 onward. Adult *Borealin*$^{+/-}$ mice exhibited euthyroid goiter and defect in thyroid hormone synthesis. *Borealin*$^{+/-}$ aged mice had disorganized follicles and papillary-like structures in thyroids due to ERK pathway activation and a strong increase of *Braf*-like genes described by The Cancer Genome Atlas (TCGA) network of papillary thyroid carcinoma. Moreover, *Borealin*$^{+/-}$ thyroids exhibited structural and transcriptomic similarities with papillary thyroid carcinoma tissue from a human patient harboring a *BOREALIN* mutation, suggesting a role in thyroid tumor susceptibility.

Conclusion: These findings demonstrate Borealin involvement in critical steps of thyroid structural development and function throughout life. They support a role for Borealin in thyroid dysgenesis with congenital hypothyroidism. Close

monitoring for thyroid cancer seems warranted in patients carrying *BOREALIN* mutations.

KEYWORDS

Borealin, congenital hypothyroidism, thyroid cancer, thyroid dysgenesis, thyroid function

Introduction

Congenital hypothyroidism (CH) is among the most common preventable causes of intellectual disability, reflecting the critical role of the thyroid hormones thyroxine (T4) and triiodothyronine (T3) in brain development. In France, where routine neonatal screening was started in 1978, CH is found in 1/3,000 neonates, with an increase in recent decades (1). Thyroid dysgenesis (TD) accounts for approximately 65% of CH cases and hormone-synthesis abnormalities for the remaining 35%. TD may be initiated at any step during thyroid development and, therefore, has widely variable manifestations including athyreosis (21%), ectopic thyroid (41%), and thyroid hypoplasia or hemithyroid (3%) (2, 3). In humans, the thyroid anlage on the midline starts to invaginate from the floor of the foregut at about embryonic day (E) 22 and expresses NKX2-1, PAX8, and FOXE1 from E32–33 (E8.5–9.5 in mice) onward (4, 5). Starting on E26, the ultimobranchial bodies (lateral anlage) develop from the fourth pharyngeal pouch on each side (6). The midline and lateral anlages migrate actively and then fuse in the definitive pretracheal position on E44 (E13.5 in mice) (7). The cells differentiate into thyrocytes, which produce thyroglobulin (TG) and T4 starting at 8 and 11 gestational weeks, respectively, (E16.5 for T4 production in mice) (8). Thyrocytes also express thyroid peroxidase (TPO), which contributes to T4 synthesis, and the sodium/iodide symporter NIS, with iodide being the limiting factor in T4 synthesis.

Thyroid cancers, except medullary carcinoma, are derived from thyrocytes, and 80% are papillary thyroid carcinoma (PTC) (9). Genetic studies report high frequency (70%) of somatic alterations of genes coding for effectors in the mitogen-activated protein kinase (MAPK) signaling pathway, including point mutations of *BRAF*. BRAF is a serine- or threonine-specific protein kinase activated by RAS, which results in a phosphorylation cascade leading to MAPK activation, which regulates cell division and survival. All *BRAF* genetic alterations lead to constitutive activation of the kinase with stimulation of the MAPK pathway including ERK phosphorylation and cause oncogenic transformation. $BRAF^{V600E}$ is the most frequent genetic alteration found in PTC (40%–60%) (10). ERK is negatively feedback-regulated by Dual Specificity Phosphatases (DUSPs), especially two ERK-specific DUSPs, DUSP5 and DUSP6. DUSP5 and DUSP6 mRNA levels are markers of activation of the MAPK signaling pathway in PTC (11).

We have reported three missense *BOREALIN/CDCA8* mutations in patients with CH and TD (c.443C>T, p.S148F; c.341G>A, p.R114Q; and c.530T> G, p.L177W) (12). Another *BOREALIN* mutation, a splice site mutation:c.585-1G>C in intron 7, was also identified in a patient with CH and TD (13). Borealin/CDCA8 is a component of the Chromosomal Passenger Complex (CPC), which is involved in various steps of mitosis and makes a major contribution to cytokinesis coordination (14, 15),. We have demonstrated that Borealin is also involved in thyrocyte adhesion and migration (12).

BOREALIN mutations are mono- or biallelic and have incomplete penetrance, thus producing TD with or without CH (12). *In vitro* studies of functional effects found no differences in severity across *BOREALIN* mutations and lead to loss of function of BOREALIN with decrease of thyrocyte adhesion and migration (12). Accordingly, homozygous and heterozygous mutations produce similar phenotypes in humans. In addition, a link to carcinogenesis is suggested by a report of the mother of a CHTD patient harboring a heterozygous mutation, c.341G>A, p.R114Q, having asymmetric thyroid lobes and who has developed PTC later during adulthood (12).

The objective of this experimental study was to shed light on the role of Borealin in thyroid development and function. We used mice deficient in Borealin. Homozygous Borealin knockout mice die during early embryogenesis, on E5.5, in keeping with the crucial role of Borealin in development (16). We therefore studied heterozygous $Borealin^{+/-}$ mice throughout intrauterine development and postnatal life. As patients carried heterozygous *BOREALIN* mutation, analyzing $Borealin^{+/-}$ mice was legitimate. We also investigated thyroid samples from a patient with a heterozygous c.341G>A, p.R114Q mutation, and papillary thyroid carcinoma (12). Our findings support a role for Borealin in thyroid development, function, and abnormal architecture.

Material and methods

Animals

Borealin-deficient mice generated as previously described were donated by the RIKEN Center for Genomic Medicine (Yokohama, Kanagawa 230-0045, Japan) (16). Briefly, a lacZ cDNA reading frame and a neomycin resistance cassette were inserted into the first exon of *Borealin/Cdca8* to disrupt the ATG codon and null allele of the *Borealin* gene.

Experiments using mice were certified by the Direction Departementale de la Protection des Populations for the French Ministry of Research, Health and Agriculture (Paris) under

agreement number A75-13–19 in accordance with approved guidelines of French and European legislation. The animals were housed in a temperature-controlled room on a 12:12-h light–dark cycle and given free access to food and water. *Borealin*$^{+/-}$ mice were obtained from wild-type (WT) and *Borealin*$^{+/-}$ mice. Embryos at each studied stage and male adults at 4 and 18 months of age were genotyped. Thyroids at embryonic stages from E13.5 to E17.5 and thyroids from adults aged 4 and 18 months were microdissected as described previously (17). At 18 months old, thyroid tissue of *Borealin*$^{+/-}$ mice had no Braf^{V637E} corresponding to BRAF^{V600E} in humans (three mice were investigated).

Induction of hypothyroidism in adult mice

We used a well-validated model to induce hypothyroidism in 13 WT and 19 *Borealin*$^{+/-}$ male mice aged 4 months (18). The drinking water was supplemented with 0.02% methimazole (MMI; Sigma-Aldrich, St. Louis, MI, USA) and 0.5% sodium perchlorate (ClO_4^-) (Sigma-Aldrich) for 3 weeks.

Assays on mouse serum samples

The serum was separated from blood samples collected from 4- and 18-month-old WT and *Borealin*$^{+/-}$ mice. Thyroid-stimulating hormone (TSH) was assayed using the Mouse Thyroid Stimulating Hormone (TSH) ELISA Kit (Abbexa, Cambridge, UK). Serum T4 was measured using an immunochemiluminescent assay using the Elecsys T4 assay on a cobas E801 (Roche Diagnostics, Basel, Switzerland). The assay was based on the recognition of the T4 by a sheep-origin antibody, in competition with a Ru2+-marked exogen T4. The assay measuring range was 5.4 to 320 nmol/L. Internal quality controls during the study indicated acceptable target values associated with a low coefficient of variation (CV < 5%).

RNA extraction and quantitative real-time PCR

The thyroids were microdissected, snap-frozen immediately, and then stored at −80°C. Total RNA of sorted cells or thyroid tissue was isolated using the Qiagen RNeasy MicroKit or MiniKit (Qiagen, Valencia, CA, USA). The Maxima First Strand cDNA Synthesis Kit (Thermo Fisher Scientific, Waltham, MA, USA) was used for reverse transcription of 250 ng of each RNA sample. Each PCR was performed on 5 µL of synthesized cDNA diluted to 1/20 using the SybrGreen PCR Master Mix (Thermo Fisher Scientific) and primers. Peptidylprolyl isomerase A served as an endogenous control. Real-time PCR (RT-PCR) was performed using the QuantStudio 3 Real-Time PCR System (Thermo Fisher Scientific). The data were analyzed using the comparative cycle threshold method and reported as the fold change in gene expression, normalized for a calibrator of value 1. Primer sequences are listed in Supplemental Figure G.

Immunohistochemistry and quantification

Mouse tissues were fixed by immersion in 3.7% buffered formalin and then embedded in paraffin. Subsequently, 4-µm-thick sections were mounted on StarFrost adhesive slides (Knittel Glaser, Braunschweig, Germany) and processed for immunohistochemistry, as previously described (17). The primary antibodies were used at the following dilutions: rabbit anti-BOREALIN (1:1,000, donated by William Taylor), rabbit anti-Nkx2-1 (1:2,500, #PA0100, BioPAT, Caserta, Italy), mouse anti-Ki67 (1:20, #550609, Becton Dickinson, Franklin Lakes, NJ, USA), mouse anti-BrdU (1/4, Amersham, Fairfield, CT, USA), mouse anti-TG (1:100, Dako-Cytomation, Glostrup, Denmark), mouse anti-I-Tg (1:500, donated by Carrie Ris-Stalpers), and rabbit anti-T4 (1:5,000, BioRad, Hercules, CA, USA). The fluorescent secondary antibodies were Alexa Fluor 594 goat anti-rabbit and Alexa Fluor 488 goat anti-mouse antibodies (1:400, Thermo Fisher Scientific). The nuclei were stained using the Hoechst 33,342 fluorescent stain (0.3 mg/ml; Thermo Fisher Scientific). Photographs were taken using a fluorescence microscope (Leitz DMRB; Leica, Wetzlar, Germany) and digitized using a chilled 3CCD camera (C5810; Hamamatsu Photonics, Hamamatsu City, Japan). The sections were then analyzed using ImageJ 1.32s (freeware, www.rsbweb.nih.gov/ij) as previously described (17, 19). The Nkx2-1-positive surface areas per section served to estimate the total thyroid surface area in µm^2. For stained surface area quantification, we used alternate sections at E9.5 and E11.5, one of every three sections at E13.5 and E15.5, one of every four sections at E17.5, and one of every five sections in adults. The surface area values then served to estimate the total stained surface area for each thyroid and each marker: the average of all sections counted was compared to the total number of sections containing thyroid tissue. The proliferation of Nkx2-1-positive cells (at E9.5, E11.5, E13.5, and E17.5) was estimated by counting Ki67-positive nuclei among Nkx2-1-positive cells on alternate sections throughout the entire tissue sample. The surface areas positive for T4, a marker of advanced thyroid differentiation, were normalized for total thyroid surface area. At least five thyroids were analyzed per genotype. The results are reported as mean ± SEM.

For Nkx2-1 staining of adult mouse thyroid glands, the first immunohistochemistry steps were as described above. After application of the primary antibody, the sections were incubated with biotinylated secondary antibody for 1 h. Immunostaining was then performed using the Vectastain ABC Kit (Vector Laboratories, Burlingame, CA, USA) according to the manufacturer's instructions. The sections were then incubated in 3,3′-diaminobenzidine tetrahydrochloride and counterstained with hematoxylin and eosin.

The surface area of follicles was estimated from serial transverse sections of thyroids from adult WT and *Borealin*$^{+/-}$ mice. The sections were deparaffinized and then stained with hematoxylin and eosin for quantification of follicles. Hematoxylin stains cell nuclei purple–blue, and eosin stains extracellular matrix and cytoplasm pink. Automated follicle size measurement was achieved using ImageJ 1.32s software. Follicles were classified by size as <1,000,

1,000–3,000, and >3,000 μm^2 as previously described (20), and follicle size distribution was determined.

TUNEL experiments were performed using an *in situ* cell death detection kit (Roche, Neuilly-sur-Seine, France) according to the manufacturer's instructions. Nkx2-1 immunostaining was then performed. To determine the percentage of apoptotic thyroid cells, the frequency of TUNEL-positive cells was counted among 300 Nkx2-1-positive cells.

Microarray and analysis

After validation of the RNA quality with Bioanalyzer 2100 (using Agilent (Santa Clara, CA, USA) RNA 6000 nano chip kit),75 ng of total RNA was reverse transcribed following the GeneChip® WT Plus Reagent Kit (Affymetrix, Santa Clara, CA, USA). Briefly, the resulting double-strand cDNA was used for *in vitro* transcription with T7 RNA polymerase. After purification according to Affymetrix protocol, 5.5 µg of Sens Target DNA was fragmented and biotin labeled. After control of fragmentation using Bioanalyzer 2100, cDNA was then hybridized to GeneChip® Clariom S Mouse (Affymetrix) at 45°C for 17 h. After overnight hybridization, chips were washed on the fluidic station FS450 following specific protocols (Affymetrix) and scanned using the GCS3000 7G. The scanned images were then analyzed with Expression Console software (Affymetrix) to obtain raw data (cel files) and metrics for Quality Controls. Gene expression levels were calculated using the RMA (Robust Multichip Algorithm algorithm), and flags were computed using a custom algorithm within R (R Project for Statistical Computing http://www.r-project.org/). Assuming that a maximum of 80% of genes were expressed, the 20% lowest values were selected for each microarray as background. A threshold was fixed at two standard deviations over the mean of the background. All probes whose normalized intensity measures were lower than the computed threshold were flagged 0 instead of 1. Three probe lists were used for each comparison according to flagged measurements in the relevant chips. The "P50" list had been created filtering probes flagged as "Present" for at least half of the chips. The group comparisons were performed using Student's t-test. To estimate the false discovery rate, the resulting *p*-values at 5% were filtered, and the Benjamini and Hochberg, Bonferroni, or without correction was used. Cluster analysis was performed by hierarchical clustering using Spearman's correlation similarity measure and average linkage algorithm.

Data were submitted to Ingenuity Pathway Analysis (IPA http://www.ingenuity.com) and Gene Set Enrichment Analysis (GSEA https://www.gsea-msigdb.org/gsea/index.jsp) to model networks and unveil relevant pathways and biological processes.

Western blotting studies of mouse thyroid tissue

Proteins from mouse thyroid tissue collected in radioimmunoprecipitation assay (RIPA) buffer and sonicated were quantified using the bicinchoninic acid (BCA) protein assay (Thermo Fisher Scientific). Then, 20 µg of total protein was separated on Bis–Tris polyacrylamide gel with a 4%–12% gradient (Thermo Fisher Scientific) and transferred onto polyvinylidene difluoride (PVDF) membranes (Thermo Fisher Scientific). The membranes were incubated with the primary antibodies rabbit anti-P-ERK, ERK, (1:1,000, #4370S, 9102S, Cell Signaling Technology, Danvers, MA, USA) or rabbit anti-Vinculin (1:1,000, #4650, Cell Signaling) and then with horseradish peroxidase-conjugated goat anti-rabbit antibody. The binding of secondary antibodies was revealed using the Amersham ECL Prime Detection Reagent Kit (GE Healthcare, Chicago, IL, USA). The protein bands on the membranes were scanned with the ImageQuant LAS 4000 Station (GE Healthcare) and then analyzed using ImageJ 1.32s to determine the protein levels.

Statistics

The sample size was estimated based on previous experience with similar studies (17, 21). Results are reported as mean ± SEM for the number of experiments indicated in the figure legends. Statistical analyses were performed using GraphPad Prism4 (GraphPad, La Jolla, CA, USA). Comparisons were with the unpaired Mann–Whitney test or Fisher's test, as indicated in the figure legends. Differences were considered significant when $p < 0.05$.

Results

Borealin expression in mouse thyroid

We found intense Borealin expression during development and lower expression levels in adulthood using quantitative PCR (qPCR) on WT thyroids (Figure 1A). In mouse embryos, Borealin protein was detectable by immunohistofluorescence in the nuclei of a few thyroid anlage cells at E9.5 and the midline anlage and ultimobranchial bodies on E11.5 (Figure 1B). Interestingly, in ultimobranchial bodies at E11.5, Borealin was observed in progenitor cells during mitosis. Borealin was found at E13.5 in the nuclei of Nkx2-1-expressing cells, i.e., chiefly thyrocyte progenitors and, on E17.5, in the thyrocytes (Figure 1B and Supplemental Figure A). During development, Borealin was co-expressed in some bromodeoxyuridine (BrdU)-positive (proliferating) cells. In adults, Borealin was very scantly expressed in the thyrocyte nuclei of thyroid tissue except in some regions (Figure 1B).

Thyroid phenotype of *Borealin*$^{+/-}$ mice

Thyroid development was abnormal from E9.5 onward

We used immunohistochemistry to detect Nkx2-1, a marker for progenitor cells and thyrocytes. At E9.5, the midline anlage appeared thicker, and the thyroid-anlage surface area was 25%

larger ($p < 0.05$) in the *Borealin*$^{+/-}$ *vs.* WT mice (Figures 2A, B). Indeed, the number of cells in the median anlage at E9.5 was increased by 32% in *Borealin*$^{+/-}$ *vs.* WT mice (Supplemental Figure B). This size increase was ascribable to increased proliferation of Nkx2-1-expressing progenitors: the proliferation ratio evaluated using a nuclear proliferation marker Ki67 was 46% higher in *Borealin*$^{+/-}$ mice than in WT mice ($p < 0.05$) (Figure 2C). Nkx2-1 staining showed thyroid anlage fragmentation in two of nine *Borealin*$^{+/-}$ embryos *vs.* none of eight WT embryos (Supplemental Figure C).

Between E11.5 and E17.5, thyroid surface area was significantly smaller in *Borealin*$^{+/-}$ *vs.* WT mice, with decreases of 30% on E11.5, 15% on E13.5, 25% on E15.5, and 25% on E17.5 ($p < 0.05$ for all four comparisons) (Figures 2A, D). On E11.5, the midline anlage and ultimobranchial bodies exhibited similar decreases in surface area. Cell proliferation as assessed using Ki67 did not differ significantly between groups on E11.5, E13.5, or E17.5 (Supplemental Figure D), whereas on E13.5 and E17.5, the proliferation ratio tended to be higher in the *Borealin*$^{+/-}$ group than in the WT group. Apoptosis on E11.5 and E13.5 was not significantly different between the two groups. The transcriptomic analysis of E13.5 thyroids from *Borealin*$^{+/-}$ and WT thyroids evidenced negative enrichment of genes involved in engulfment, endocytosis, and development of the abdomen and body trunk (Figure 2F). The qPCR assays performed on E15.5 and E17.5 samples to assess the thyroid markers Nkx2-1, Pax8, and Foxe1 (transcription factors) and differentiation markers such as Tg, Tpo, and Nis showed no significant differences between *Borealin*$^{+/-}$ and WT thyroids (Supplemental Figure E).

T4 staining showed a significant increase in the ratio of T4-positive over total thyroid surface area and embryo weight in *Borealin*$^{+/-}$ compared to WT mice at E17.5 (Figure 2E). The amount of I-Tg stored in the follicles was greater in the *Borealin*$^{+/-}$ mice than in the WT mice at E17.5 (Figure 2G).

Thus, *Borealin* invalidation led to abnormal thyroid size during development from thyroid budding to maturation.

At 4 months old, the Borealin$^{+/-}$ mice developed a goiter with large follicles

At 4 months of age, *Borealin*$^{+/-}$ mice had normal thyroid function as assessed by plasma TSH and T4 levels (Figures 3A, B). The thyroids were 38% larger in the *Borealin*$^{+/-}$ group *vs.* the WT group ($p < 0.01$) (Figure 3C). The follicles were also significantly larger in the *Borealin*$^{+/-}$ group ($p < 0.01$) (Figures 3D, E).

For further investigation of thyroid function, we induced hypothyroidism using a validated methodology by administering an antithyroid drug (methimazole) and sodium perchlorate for 3 weeks to male *Borealin*$^{+/-}$ and WT mice. We assayed serum T4 and TSH at treatment initiation and then at treatment discontinuation (D0) and 3 days later (D3). Features of hypothyroidism including patchy alopecia and dry skin developed in both groups but were more marked in the *Borealin*$^{+/-}$ mice. T4 on D0 *vs.* before treatment was 68% and 45% lower in the *Borealin*$^{+/-}$ and WT groups ($p < 0.01$), while TSH was 172% and 134% higher, respectively. On D3, T4 was higher and TSH was lower than those on D0.

Transcriptomic analysis of thyroids from both groups showed decreases in genes involved in endocytosis and engulfment in the *Borealin*$^{+/-}$ group (Figure 3F), as well as an increase in genes involved in cancer function.

Thus, 4-month-old *Borealin*$^{+/-}$ mice had normal thyroid function, enlarged thyroids and follicles, increased sensitivity to antithyroid drugs, and transcriptome abnormalities.

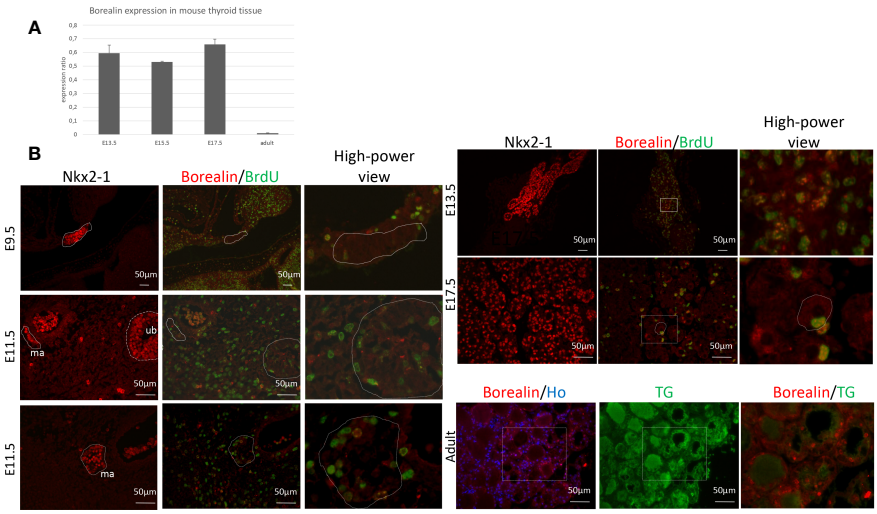

FIGURE 1
Borealin expression in mouse thyroid tissue: high in embryos and low in adults. **(A)** Quantitative PCR assessment of *Borealin* expression by thyroid tissue on embryonic days E13.5, E15.5, and E17.5, and, in adulthood, normalized for thyroid tissue on E13.5 and peptidylprolyl isomerase **(A)** Two tissue samples (pool of three to five thyroids) were studied at each developmental stage. **(B)** Immunohistofluorescence staining for Nkx2-1 (in red) and co-staining for Borealin (in red) and BrdU (in green) in whole embryos on E9.5 and E11.5 and in thyroid tissue on E13.5 and E17.5; on E11.5, the median anlage (ma) and ultimobranchial bodies (ub) can be identified. In adults, thyroid samples were co-stained for Borealin (in red) and thyroglobulin (TG, in green). Hoechst stained nuclei in blue. High-power views of the surrounding regions are provided in the right-hand columns. E, embryonic day; Nkx2-1, Nkx2 Homeobox 1; BrdU, bromodeoxyuridine; TG, thyroglobulin; ma, midline anlage; ub, ultimobranchial body; Ho, Hoechst.

At 18 months old, the Borealin$^{+/-}$ mice developed a goiter with abnormal structures

Based on the role of Borealin during mitosis and for thyroid physiology (12, 14), we followed the evolution of the thyroid during old age.

Plasma T4 and TSH levels were 27% higher and 65% lower, respectively, in *Borealin*$^{+/-}$ mice *vs.* WT mice ($p < 0.01$ and $p < 0.05$, respectively) (Figures 4A, B). Thyroid weight normalized for body weight was 47% higher in the *Borealin*$^{+/-}$ mice *vs.* the WT mice ($p < 0.01$) (Figures 4C, D). The T4 and TSH values in the *Borealin*$^{+/-}$ group were within the normal range (euthyroid goiter), whereas the WT mice had hypothyroidism. In the *Borealin*$^{+/-}$ group, follicle size distribution was significantly more heterogeneous (Fisher's test, $p < 0.01$) (Figure 4E), and the thyroids contained very large follicles and nodular structures (Figure 4C). Hematoxylin and eosin staining, a common method for viewing cellular and tissue structure, revealed modified follicles and microfoci with papillary structures in the *Borealin*$^{+/-}$ mice but not in the WT mice (Figures 5A–H). Thyrocytes had a normal aspect, but there was a large increase in follicle size and a loss of colloid in *Borealin*$^{+/-}$ thyroids (Figures 5C, D). We also observed foci of hyperplastic cells with abundant cytoplasm (Figures 5C, D, G, H) and microfoci of cells displaying a characteristic papillary structure (Figures 5C–F). However, we did not find nuclear inclusions and cleared nuclei, which are characteristic features of human PTC. The transcriptomic analysis showed marked differences in genes involved in follicle organization between thyroids of *Borealin*$^{+/-}$ and WT mice (Figure 4F). This gene set was inspired by Koumarianou et al. as genes involved in apical–basal thyroid cell polarization, lumen formation, and follicle maturation (22).

Borealin, thyroid cancer in mice and in a subject with a BOREALIN mutation

We performed transcriptomic analyses of thyroid tissue samples from 18-month-old *Borealin*$^{+/-}$ and WT mice. Compared to the WT mice, the *Borealin*$^{+/-}$ mice exhibited positive enrichment in expressed genes involved in malignancy function (extracranial solid tumor and cancer), cytoskeletal and/or cytoplasmic functions (microtubule dynamics and organization of the cytoskeleton, filaments, and cytoplasm), viability (increased cell viability and

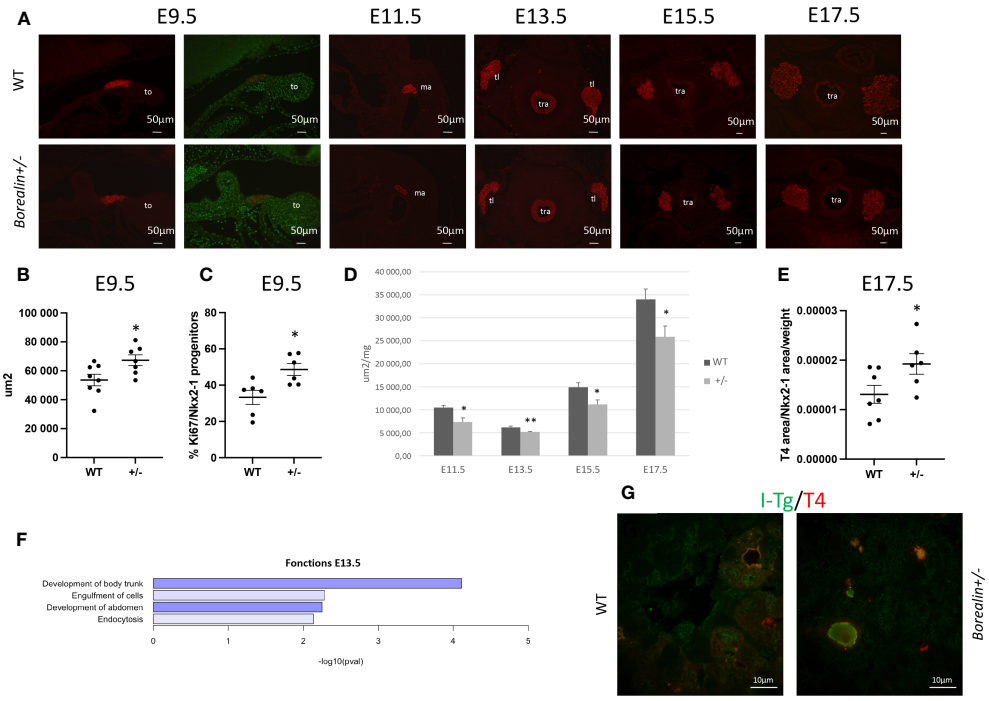

FIGURE 2
Abnormal thyroid development in *Borealin*$^{+/-}$ *mice*. **(A)** Thyroid morphology was investigated using Nkx2-1 staining on E9.5 and E11.5 (sagittal sections) and E13.5, E15.5, and E17.5 (transverse sections) in wild-type (WT) and *Borealin*$^{+/-}$ littermates. Nkx2-1 is a marker of early thyrocyte progenitors and differentiated thyrocytes. Nkx2-1 is stained in red, and the proliferation marker Ki67 is in green. Note an increase of thyroid anlage at E9.5 in the *Borealin*$^{+/-}$ mice than in the WT mice. WT, wild type; to, tongue; ma, median anlage; tl, thyroid lobe; tr, trachea. **(B)** Total thyroid surface area (µm^2) quantified by Nkx2-1 staining on E9.5 was larger in the *Borealin*$^{+/-}$ mice than in the WT mice. Seven to eight mice with each genotype were investigated. **(C)** Proliferation ratio calculated as the proportion of Nkx2-1-positive cells labeled with Ki67 on E9.5 (as described in Material and Methods): thyroid anlage hyperplasia in Borealin$^{+/-}$ *vs.* WT mice. Six mice with each genotype were investigated. **(D)** Total thyroid surface area (µm^2) was quantified using Nkx2-1 staining on E11.5, E13.5, E15.5, and E17.5, with normalization for the weight of each embryo. At each of the four stages and for each genotype, five to seven mice were studied. Note that from E11.5 onward, the *Borealin*$^{+/-}$ thyroids were smaller (black bars) compared to the WT thyroids (gray bars). **(E)** Ratio of T4-positive surface area over Nkx2-1-positive surface area normalized for embryo weight at E17.5. Six to seven mice with each genotype were investigated. Note the larger amount of T4 in the *Borealin*$^{+/-}$ *vs.* the WT thyroids. **(F)** Transcriptomic analysis of thyroid tissue on E13.5. The genes with lower expression levels in the *Borealin*$^{+/-}$ mice *vs.* the WT mice were involved in body trunk development, cell engulfment, abdomen development, and endocytosis. Genes with lower expression were in blue. **(G)** Co-staining for I-Tg and T4 in the *Borealin*$^{+/-}$ *vs.* the WT thyroids at E17.5. Note the increased staining of Tg-I surface area in the *Borealin*$^{+/-}$ *vs.* the WT thyroids. The data are mean ± SEM. *$p < 0.05$ and **$p < 0.01$, Mann–Whitney test. E, embryonic day; WT, wild type; Tg, thyroglobulin; I-Tg, iodinated thyroglobulin.

decreased organismal death), and angiogenesis (Figure 5I). Then, we deciphered the thyroid abnormalities observed in *Borealin*$^{+/-}$ mice. Strong activation of *Braf*-like genes described by The Cancer Genome Atlas (TCGA) network of PTC (9) was found in the *Borealin*$^{+/-}$ thyroids (Figure 6A). ERK/MAPK signaling was also activated (Figure 6C), and P-ERK protein expression increased (Figure 6D) in the *Borealin*$^{+/-}$ *vs.* WT thyroids. DUSP5 and DUSP6 expression levels were higher in the *Borealin*$^{+/-}$ thyroids than in the WT thyroids (Figure 6E). These data showed overexpression of tumorigenesis genes and MAPK pathway activation in *Borealin*$^{+/-}$ thyroids.

We previously reported that the mother of a girl with TD and CH had normal thyroid function, asymmetrical thyroid lobes, and PTC (12). She and her daughter were heterozygous for the c.341G>A, p.R114Q *BOREALIN* mutation. The tumor cells carried the *BRAF*^{V600E} mutation. By whole exome sequencing, no additional *BOREALIN* variant was observed in the thyroid tumor part, and *BOREALIN* expression was equivalent between thyroid tumor and tumor-free thyroid by transcriptomic analysis. In the patient, gene sets of the cytoskeleton and cytoplasmic functions were increased in the thyroid tumor (Figure 5J) as in *Borealin*$^{+/-}$ thyroids and decreased in the tumor-free thyroid (Figure 5K). Angiogenesis genes and cell viability were increased and organismal death decreased in two thyroid regions with and without tumor (Figures 5J, K) as in *Borealin*$^{+/-}$ thyroids. The tumor signaling pathways (extracranial solid tumor and cancer pathway) were activated in the *Borealin*$^{+/-}$ mouse thyroids (Figure 5I) and the tumoral and tumor-free thyroid samples from the patient, with a very high ratio in the tumoral human tissue. Strong activation of *Braf*-like genes was found in the tumor as in *Borealin*$^{+/-}$ thyroids, but not the tumor-free tissue, from the human patient (Figure 6B). DUSP5 and DUSP6 expression levels were higher in human thyroid tumors than in the tumor-free tissue and controls (Figure 6E).

The Braf-like signature observed in *Borealin*$^{+/-}$ mice's thyroid tissue, structures, and transcriptomic analysis was in line with the patient's tumor.

Discussion

Borealin-deficient mice had abnormal thyroid development, thyroid goiter with follicle disorganization at 4 months of age, and further structural thyroid abnormalities as papillary tumor-like structures at 18 months. Transcriptome abnormalities were evidenced both in the *Borealin*$^{+/-}$ mice and in PTC tissue from a

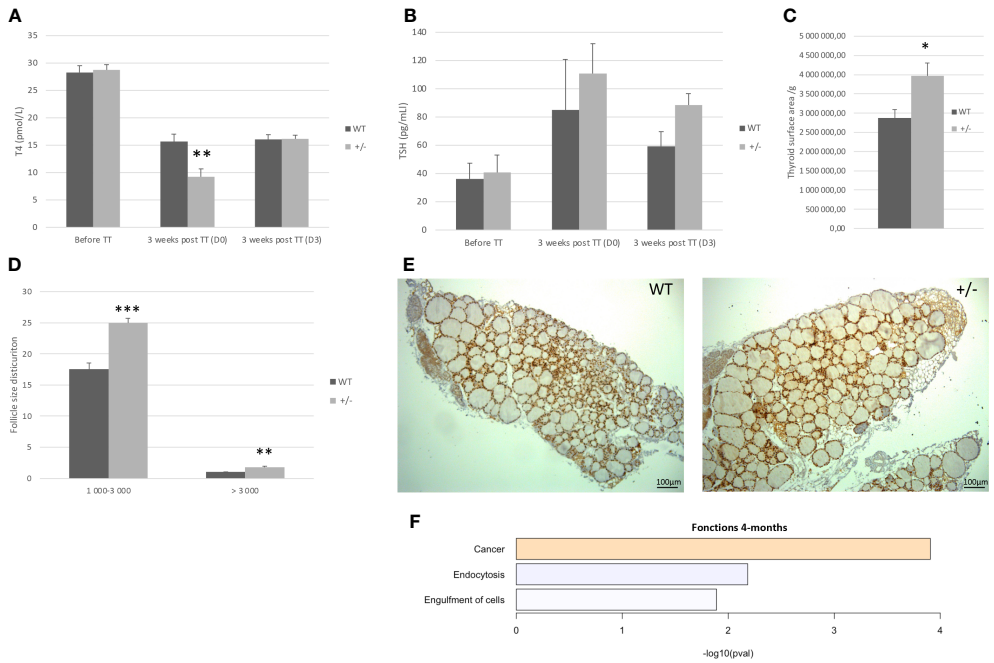

FIGURE 3
Four-month-old mice: *Borealin*$^{+/-}$ thyroids are hypertrophic, with large follicles. **(A, B)** Serum T4 **(A)** and thyroid-stimulating hormone (TSH) **(B)** levels in male mice given antithyroid drugs for 3 weeks; 19 *Borealin*$^{+/-}$ and 13 wild-type (WT) mice were investigated for T4 assay and three to 13 mice for TSH assay. Assays were performed before treatment and then at treatment discontinuation (D0) and 3 days later (D3). Note the increased sensitivity of the *Borealin*$^{+/-}$ mice to the treatment, with 45% and 68% less T4 on D0 ($p < 0.01$) and 134% and 172% more TSH on D0 compared to the WT (black bars) and *Borealin*$^{+/-}$ (gray bars) mice. **(C)** Thyroid surface area estimated by Nkx2-1 staining normalized for body weight. Note the significantly larger thyroids in *Borealin*$^{+/-}$ mice *vs.* WT mice ($p < 0.05$). Five mice with each genotype were investigated. **(D)** Follicles were divided into two size categories based on whether the lumen surface area was 1,000–3,000 µm^2 or >3,000 µm^2. Four to six animals per genotype were investigated. **(E)** Nkx2-1 staining (in brown) of thyroid tissue from 4-month-old mice. Note the larger thyroids and larger follicles in *Borealin*$^{+/-}$ mice *vs.* WT mice. **(F)** Transcriptomic analysis of thyroid tissue from 4-month-old mice (three per genotype). The genes with lower expression levels in the *Borealin*$^{+/-}$ mice *vs.* the WT mice were involved in endocytosis and cell engulfment (in blue). The genes with higher expression levels in the *Borealin*$^{+/-}$ mice *vs.* the WT mice were involved in tumorigenesis (in orange). The data are mean ± SEM. *$p < 0.05$, **$p < 0.01$, and ***$p < 0.001$, Mann–Whitney test. E, embryonic day; WT, wild type; TT, treatment.

human patient carrying a *BOREALIN* mutation. These findings establish a role for Borealin in thyroid development, function, and tumorigenesis.

The thyroid anlage was hyperplastic in *Borealin*$^{+/-}$ mice on E9.5. Normally, progenitor cells show very little proliferation on E9.5, as shown in our WT mice. The proliferation ratio was accurately regulated in thyroid anlage, and any abnormality disturbs thyroid development afterward. Disrupted thyroid development after the demonstration of an increased proliferation ratio on E9.5 has been reported (21). Defects of endocytosis observed at E13.5 by transcriptomic analysis could lead to defects of TG-colloid engulfment at E17.5 with high thyroid T4 content seen in the *Borealin*$^{+/-}$ mice. Consequently, *Borealin*$^{+/-}$ mice displayed hypoplastic thyroid from E11.5 and more intra-thyroid T4 later in development.

At 4 months old, *Borealin*$^{+/-}$ thyroids were hyperplastic with large disorganized follicles. One hypothesis is gland enlargement to compensate for insufficient T4 release from the gland, possibly related to impaired TG endocytosis. The transcriptomic analysis showing decreases in genes involved in endocytosis and engulfment supports this hypothesis at 4 months old. Endocytosis and engulfment are processes involved in TG internalization via vesicle-mediated endocytosis at the apical membrane of thyrocytes for TH secretion at the basal membrane (23, 24). Decreased TG endocytosis would also explain the follicle enlargement seen in the *Borealin*$^{+/-}$ mice (25). The consequence of follicle defects would be an unadapted response to antithyroid drugs leading to more profound hypothyroidism at 4 months old. Due to their deficiency in releasing T4, *Borealin*$^{+/-}$ thyroids may not adapt to stress and respond to a specific increased need for TH. Thus, Borealin plays a role in proper thyroid hormone synthesis and release and also in homeostasis. The thyroid hyperplasia with large disorganized follicles persisted from adulthood to older age. At 18 months old, *Borealin*$^{+/-}$ mice had structural follicular defects of thyroid tissue with an increase of follicular polarization gene sets (22). In addition to that, most of these genes are linked to cytoskeleton organization. *Borealin*$^{+/-}$ thyroids were enriched in cytoskeleton gene sets compared to WT thyroids. Borealin binds to the microtubules, and Borealin deficiency may therefore alter the thyrocyte cytoskeleton, explaining the abnormal follicle shapes in the *Borealin*$^{+/-}$ mice (26). Thus, Borealin is involved not only in the CPC, which controls mitosis, but also in cell and tissue structure.

In addition, despite heterogeneous and disorganized follicles, *Borealin*$^{+/-}$ mice still have normal thyroid function at this advanced age. In contrast, thyroid function is decreased in the 18-month-old WT mice with larger surface area and larger follicles in comparison with 4-month-old mice (Supplemental Figure F). Similarly, in a study of healthy mice, the thyroid follicles at 23 months old were larger, plasma TSH levels were higher, and plasma T4 levels were lower than at 3 months old, consistent with the development of

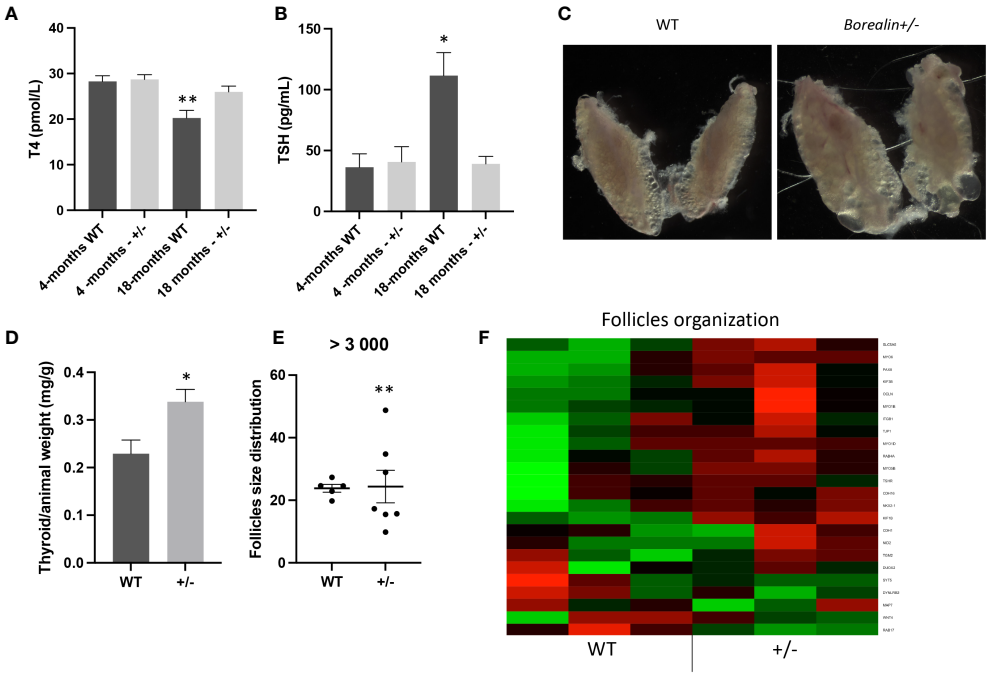

FIGURE 4
Eighteen-month-old mice: *Borealin*$^{+/-}$ thyroids are hypertrophic, with abnormal follicles. **(A, B)** Serum T4 levels were higher **(A)** and serum thyroid-stimulating hormone (TSH) levels lower **(B)** in *Borealin*$^{+/-}$ *vs.* wild-type (WT) mice (six to 10 with each genotype); the Borealin-deficient mice had normal thyroid function, whereas the WT mice developed hypothyroidism. Assays at 4 months and 18 months were added for better understanding. **(C)** Abnormal thyroid morphology with variable follicle size in *Borealin*$^{+/-}$ mice. **(D)** Thyroid weight normalized for body weight (10 WT and eight *Borealin*$^{+/-}$ mice). Note the significant hyperplasia of the *Borealin*$^{+/-}$ thyroids. **(E)** Follicle size distribution among follicles >3,000 µm^2 (five to seven mice with each genotype). Note the significantly greater size heterogeneity in the *Borealin*$^{+/-}$ group. **(F)** Heatmap of genes involved in thyroid follicle organization (three mice with each genotype). Note the marked overexpression of these genes in the *Borealin*$^{+/-}$ group compared to the WT group. The genes with low expression are in green, and the genes with high expression are in red. The data are mean ± SEM. *$p < 0.05$, **$p < 0.01$, and ***$p < 0.001$, Mann–Whitney test, Fisher's test. WT, wild type.

aging-related hypothyroidism (27). At 18 months old, due to their old age, WT and *Borealin*$^{+/-}$ mice had larger follicles and larger thyroid than at 4 months old, but only WT mice had hypothyroidism. The WT mice had a decrease in thyroid activity due to their age, whereas *Borealin*$^{+/-}$ mice had persistent thyroid activity leading to an undeclined normal thyroid function. This is probably why we observed by thyroid transcriptomic analysis an enrichment in angiogenesis, cellular viability gene sets, and a decrease in organismal death when compared to WT thyroids. We hypothesize that to maintain thyroid homeostasis, the activity of the gland should be stimulated. This regulatory mechanism encouraged in a sustained manner can lead to tissue changes favoring tumorigenesis. Thus, Borealin plays a role in thyroid homeostasis.

At an older age, *Borealin*$^{+/-}$ thyroids were enriched in cancer gene sets compared to WT thyroids, which may be due to defects of homeostasis with hyperactivity of the gland. Older *Borealin*$^{+/-}$ mice exhibited activation of *Braf*-associated genes when compared to WT mice, further supporting a link between genes for Borealin and BRAF pathway. Moreover, the microfoci seen in aged *Borealin*$^{+/-}$ mice had a papillary and vesicular structure consistent with *Braf*-driven tumorigenesis (28). Also, ERK/MAPK signaling activation, a known effect of the oncogenic *BRAF* mutation, was found in *Borealin*$^{+/-}$ thyroids (10). Thus, the *Borealin* deficiency in thyroids activated the ERK/MAPK signaling leading to disorganization of tissue with papillary-like structures. Indeed, we previously described data from an adult with thyroid dysgenesis and a heterozygous *BOREALIN* mutation (c.341G>A, p.R114Q) who developed PTC (12). The tumor cells harbored the *BRAF*^{V600E} mutation known to be associated with PTC (10) and presented enrichment of genes involved in cancer and BRAF signature like the thyroid of *Borealin*$^{+/-}$ mice. Borealin has been reported to be involved in the development of several types of cancer in humans, including breast cancer, cutaneous melanoma, and lung cancer (29). A study of human lung cancer samples demonstrated that overexpression of the Borealin was associated with a poor prognosis (29). In TCGA database of human PTC, *BOREALIN* expression correlated with tumor dedifferentiation (Supplemental Figure H). As we observed papillary tumor-like structure in thyroid mice with Borealin deficiency, we supposed that Borealin is tightly regulated with a narrow frame of gene expression level. At 18 months old, *Borealin*$^{+/-}$ mice have normal TSH but developed

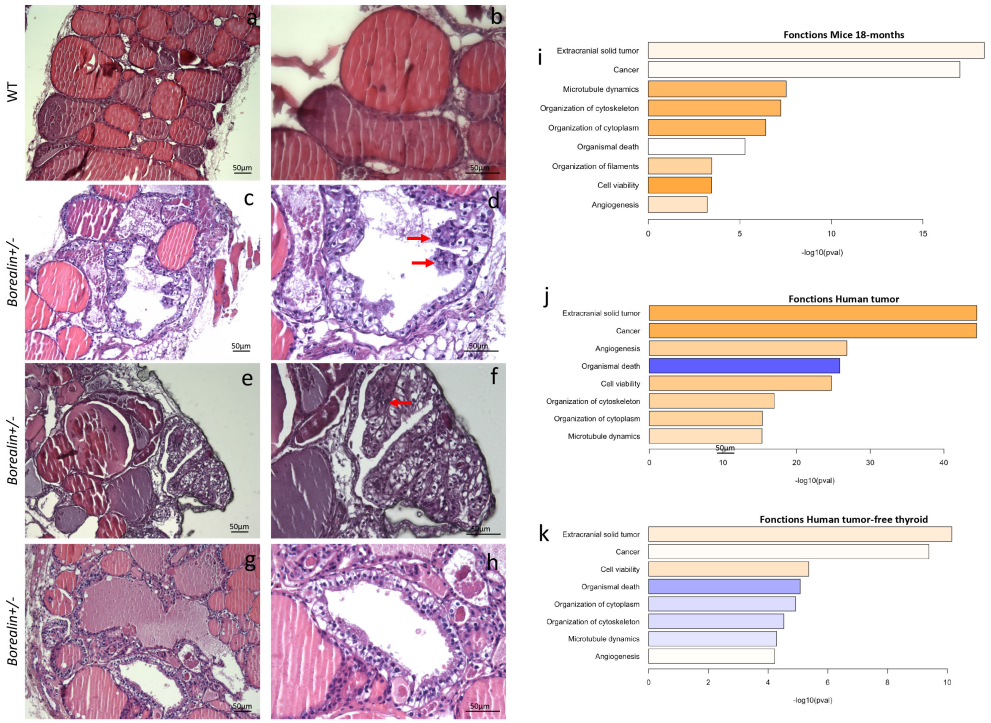

FIGURE 5
Abnormal papillary-like structures and cytoskeleton defects in the *Borealin*$^{+/-}$ thyroids at 18 months; comparison with thyroid tissue from a human with a heterozygous *BOREALIN* mutation. **(A–H)** Hemalum-eosin-stained thyroid tissue from *Borealin*$^{+/-}$ **(C–H)** and wild-type (WT) **(A, B)** mice. **(A, B)** Normal thyroid architecture with colloid in follicles. **(C, D)** Large increase in follicle size and a loss of colloid with some papillary structure (see arrow). **(E, F)** Enlarged follicles containing some papillary structures (see arrow). **(G, H)** Enlarged follicles without colloid with higher cells without nuclear atypia. Note the thyroid tissue changes in the *Borealin*$^{+/-}$ sample, which contains papillary-like structures and cells with abundant cytoplasm surrounding empty follicles. On the right panel, high-power view of specific regions. **(I)** Transcriptomic analysis of mouse thyroid tissue at 18 months. The genes with higher expression levels in the *Borealin*$^{+/-}$ mice *vs.* the WT mice are involved in extracranial tumor, cancer, microtubule dynamics, cytoskeleton organization, and filament organization. **(J)** Transcriptomic analysis of the papillary thyroid carcinoma from the patient with a heterozygous *BOREALIN*$^{+/-}$ mutation and *BRAF*-mutated thyroid tumor. The genes with high expression levels include those highly expressed in the *Borealin*$^{+/-}$ mice. **(K)** Transcriptomic analysis of tumor-free thyroid tissue from the patient with a heterozygous *BOREALIN*$^{+/-}$ mutation and papillary thyroid carcinoma. The genes involved in cytoskeleton are decreased in the tumor-free thyroid tissue of the patient.

10.3389/fendo.2023.1286747

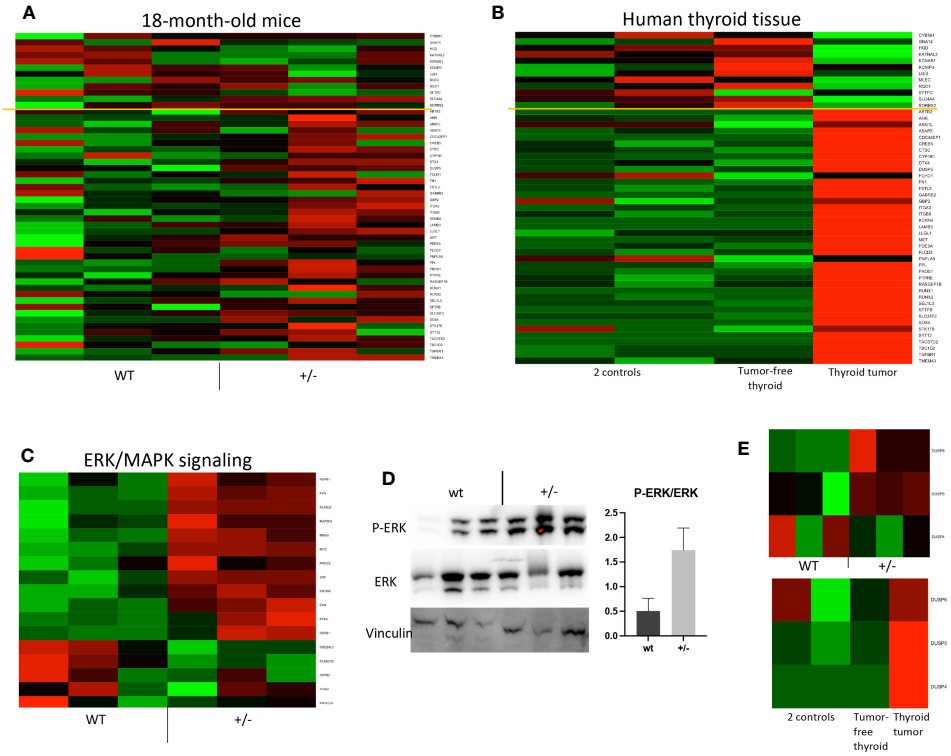

FIGURE 6
Braf-associated gene expression and ERK pathway activation in *Borealin*$^{+/-}$ thyroids. **(A)** Transcriptome of 71 genes in *Borealin*$^{+/-}$ and wild-type (WT) thyroid tissue. The Cancer Genome Atlas Research network used 391 human papillary thyroid cancer samples to identify 71 genes, which then served to derive a score differentiating *BRAF*^{V600E}-driven from *RAS*-driven tumors limited by the yellow line (9). The transcriptome results support Braf^{V600E}-associated gene expression in the *Borealin*$^{+/-}$ thyroids. The genes with low expression at the top are in green, and all the genes with high expression at the bottom are in red. **(B)** Same analysis on samples from the patient with a heterozygous *BOREALIN*$^{+/-}$ mutation and papillary thyroid carcinoma. The tumor is clearly *BRAF*-driven. Note the marked differences between the tumor-free thyroid tissue from this patient and thyroid tissue from two controls. **(C)** Heatmap of ERK/MAPK signaling in thyroid tissue from *Borealin*$^{+/-}$ and WT mice. Note the increased expression of genes involved in ERK/MAPK signaling in the *Borealin*$^{+/-}$ thyroids. **(D)** Western blotting of P-ERK, ERK, and vinculin, with quantification of the P-ERK/ERK ratio for *Borealin*$^{+/-}$ and WT thyroids. Note the P-ERK increase in the *Borealin*$^{+/-}$ thyroids. **(E)** DUSP6, DUSP5, and DUSP4 mRNAs in thyroid tissue. Top: *Borealin*$^{+/-}$ and WT mice; note the increased expression of DUPS6 and DUPS5 in the *Borealin*$^{+/-}$ thyroids. Bottom: DUSP6, DUSP5, and DUSP4 mRNAs in thyroid tissue from two controls and in tumor-free thyroid tissue and thyroid tumor from the patient with a heterozygous *BOREALIN*$^{+/-}$ mutation; note the high DUSP expression in the tumor.

thyroid tumor-like, suggesting that the lack of Borealin under normal TSH stimulation at the late stage induces larger and later tumor-like development such as in other thyroid mouse models (22, 30). In addition, this may be in relation to what has been reported in humans harboring variants in genes implicated in TH synthesis (*NIS*, *TG*, *TPO*, and *SLC26A4*); thyroid goiter with dyshormonogenesis may develop thyroid cancer later in life (31). Thus, impairment in the expression or function of any protein involved in thyroid development or hormonogenesis can lead to thyroid tumor predisposition.

The thyroid phenotype differed between the *Borealin*$^{+/-}$ mice and the patients carrying *BOREALIN* mutations in our previous study (12). These last exhibited ectopic thyroid, athyreosis, hemiagenesis, or thyroid asymmetry, all of which were absent in the Borealin-deficient mice but also difficult to observe in mice. However, identical phenotypes between humans and mice were very rare (32, 33). Thyroid function in the patients was normal or deficient (12). Mutations carried by patients are localized in a domain with no known function between two crucial domains for mitosis. In transgenic mice, *Borealin*$^{+/-}$, all the domains are deleted in a heterozygous manner. Our Borealin-deficient mice had large thyroids with large, disorganized follicles, a high T4 content, and normal thyroid function but increased susceptibility to antithyroid drugs. The patient whose thyroid tumor we studied here had normal thyroid function, whereas her daughter, who carried the same Borealin mutation, had CH, suggesting incomplete penetrance in humans. A major similarity between the Borealin-deficient mice and the human patient is the presence in thyroid cancer tissue of a *BRAF*-associated signature. The respective contributions of the *BOREALIN* and *BRAF* mutations to tumor development in the patient cannot be determined from our data. Nonetheless, close monitoring for thyroid cancer of patients carrying *BOREALIN* mutations seems warranted.

In conclusion, our results demonstrate a key role for Borealin in thyroid development and function. Despite being expressed at high levels only during early development, Borealin may have a role throughout life for thyroid tissue architecture and homeostasis. Borealin deficiency may increase the risk of thyroid tumorigenesis.

Data availability statement

The raw data supporting the conclusions of this article will be made available by the authors, upon reasonable request. Requests to access the datasets should be directed to AC (aurore.carre@inserm.fr) or MP (michel.polak@aphp.fr).

Ethics statement

The studies involving humans were approved by the French institutional review board. The studies were conducted in accordance with the local legislation and institutional requirements. The participants provided their written informed consent to participate in this study. The animal study was approved by Direction Departementale de la Protection des Populations for the French Ministry of Research, Health and Agriculture (Paris) under agreement number A75-13–19 in accordance with approved guidelines of French and European legislation. The study was conducted in accordance with the local legislation and institutional requirements. Written informed consent was obtained from the individual(s) for the publication of any potentially identifiable images or data included in this article.

Author contributions

HD-M: Formal Analysis, Investigation, Writing – original draft. AS: Investigation, Writing – review & editing. DK: Writing – review & editing. SY: Investigation, Writing – original draft. BC-P: Formal Analysis, Writing – review & editing. LG: Writing – review & editing. FS: Writing – review & editing, Resources. NC: Formal Analysis, Software, Writing – review & editing. PN: Formal Analysis, Software, Writing – review & editing. DL: Writing – review & editing. MP: Writing – review & editing, Conceptualization, Funding acquisition, Supervision. AC: Conceptualization, Funding acquisition, Supervision, Writing – review & editing, Data curation, Formal Analysis, Investigation, Methodology, Writing – original draft.

Funding

The author(s) declare financial support was received for the research, authorship, and/or publication of this article. HD-M was supported by the non-profit *Fonds d'Etudes et de Recherche du Corps Médical* (FERCM) and *Assistance Publique-Hôpitaux de Paris* (AP-HP). AC and MP received financial support from three corporations (EDF, Sandoz SAS, and Merck Serono France). The funders were not involved in the study design, analysis, interpretation of data, the writing of this article or the decision to submit it for publication. AS was supported by a European Society for Paediatric Endocrinology Research Fellowship Grant and by the Alexander S. Onassis Foundation.

Acknowledgments

We thank the patients and families for their kind participation. We are grateful to Corinne Dupuy for her helpful discussion, Raphaël Scharfmann for his support, Camille Gobeaux for T4 assays, and Pierre Chérel, DVM, and his team at the animal facility for technical assistance with the animal studies.

Conflict of interest

The authors declare that the research was conducted in the absence of any commercial or financial relationships that could be construed as a potential conflict of interest.

Publisher's note

Supplementary material

The Supplementary Material for this article can be found online at: https://www.frontiersin.org/articles/10.3389/fendo.2023.1286747/full#supplementary-material

SUPPLEMENTARY FIGURE

(A) Immunohistofluorescence staining for Borealin (in red) and BrdU (in green) in thyroid tissue on E13.5 and E17.5. Hoechst stained nuclei in blue. Note the Borealin expression in nuclei of thyrocytes progenitors and thyrocytes (co-staining Borealin/Hoescht/BrdU). **(B)** Number of cells Nkx2-1-positive in median anlage at E9.5. Note the increase of number of progenitors in *Borealin*$^{+/-}$ compared to WT. $P<0.05$. **(C)** Thyroid morphology using Nkx2-1 staining on E9.5 (sagittal sections) of *Borealin*$^{+/-}$ littermate. Note thyroid anlage fragmentation at E9.5 in this *Borealin*$^{+/-}$ embryo. to: tongue. **(D)**. Proliferation ratio calculated as the proportion of Nkx2-1-positive cells labelled with Ki67 on E11.5, E13.5 and E17.5: no significant difference. Three to four tissue samples were studied at each developmental stage. **(E)** Quantitative PCR assessment of thyroid markers expression by thyroid tissue on embryonic days E15.5 and E17.5 normalized for peptidylpropyl isomerase A and WT. Thyroid markers: Foxe1, Nkx2-1, Pax8, Tg, Tpo and Nis. Three to eight tissue samples were studied at each developmental stage. **(F)** Follicle size distribution among follicles >3000 µm^2 and thyroid surface area reported to animal weight at 4-months and 18 months-old (five to eight mice with each genotype). Note the increase in the number of large follicles and thyroid surface area at 18-months compared to 4-months in WT and *Borealin*$^{+/-}$ groups. Note the significantly greater size heterogeneity in the *Borealin*$^{+/-}$ group at 18-months. **(G)** List of primers sequence used for quantitative real-time PCR. **(H)** Expression of *BOREALIN/CDCA8* according to the thyroid differentiation score. Data retrieved from TCGA (9). Note that the expression of *BOREALIN* increased when the score is higher.

References

1. Barry Y, Bonaldi C, Goulet V, Coutant R, Léger J, Paty AC, et al. Increased incidence of congenital hypothyroidism in France from 1982 to 2012: a nationwide multicenter analysis. *Ann Epidemiol* (2016) 26:100–5. doi: 10.1016/j.annepidem.2015.11.005

2. Van Vliet G. Development of the thyroid gland: lessons from congenitally hypothyroid mice and men. *Clin Genet* (2003) 63:445–55. doi: 10.1034/j.1399-0004.2003.00107.x

3. Parlato R, Rosica A, Rodriguez-Mallon A, Affuso A, Postiglione MP, Arra C, et al. An integrated regulatory network controlling survival and migration in thyroid organogenesis. *Dev Biol* (2004) 276:464–75. doi: 10.1016/j.ydbio.2004.08.048

4. Trueba SS, Augé J, Mattei G, Etchevers H, Martinovic J, Czernichow P, et al. PAX8, TITF1, and FOXE1 gene expression patterns during human development: new insights into human thyroid development and thyroid dysgenesis-associated malformations. *J Clin Endocrinol Metab* (2005) 90:455–62. doi: 10.1210/jc.2004-1358

5. Nilsson M, Fagman H. Mechanisms of thyroid development and dysgenesis: an analysis based on developmental stages and concurrent embryonic anatomy. *Curr Top Dev Biol* (2013) 106:123–70. doi: 10.1016/B978-0-12-416021-7.00004-3

6. Johansson E, Andersson L, Örnros J, Carlsson T, Ingeson-Carlsson C, Liang S, et al. Revising the embryonic origin of thyroid C cells in mice and humans. *Development* (2015) 142:3519–28. doi: 10.1242/dev.126581

7. Fagman H, Andersson L, Nilsson M. The developing mouse thyroid: embryonic vessel contacts and parenchymal growth pattern during specification, budding, migration, and lobulation. *Dev Dyn* (2006) 235:444–55. doi: 10.1002/dvdy.20653

8. Szinnai G, Lacroix L, Carré A, Guimiot F, Talbot M, Martinovic J, et al. Sodium/iodide symporter (NIS) gene expression is the limiting step for the onset of thyroid function in the human fetus. *J Clin Endocrinol Metab* (2007) 92:70–6. doi: 10.1210/jc.2006-1450

9. Cancer Genome Atlas Research Network. Integrated genomic characterization of papillary thyroid carcinoma. *Cell* (2014) 159:676–90. doi: 10.1016/j.cell.2014.09.05

10. Buffet C, Groussin L. Molecular perspectives in differentiated thyroid cancer. *Ann Endocrinol Paris* (2015) 76(1 Suppl 1). doi: 10.1016/S0003-4266(16)30009-9

11. Buffet C, Hecale-Perlemoine K, Bricaire L, Dumont F, Baudry C, Tissier F, et al. DUSP5 and DUSP6, two ERK specific phosphatases, are markers of a higher MAPK signaling activation in BRAF mutated thyroid cancers. *PloS One* (2017) 12:e0184861. doi: 10.1371/journal.pone.0184861

12. Carré A, Stoupa A, Kariyawasam D, Gueriouz M, Ramond C, Monus T, et al. Mutations in BOREALIN cause thyroid dysgenesis. *Hom Mol Genet* (2017) 26:599–610. doi: 10.1093/hmg/ddw419

13. Zou M, Alzahrani AS, Al-Odaib A, Alqahtani MA, Babiker O, Al-Rijjal RA, et al. Molecular analysis of congenital hypothyroidism in Saudi Arabia: SLC26A7 mutation is a novel defect in thyroid dyshormonogenesis. *J Clin Endocrinol Metab* (2018) 103:1889–98. doi: 10.1210/jc.2017-02202

14. Gassmann R, Carvalho A, Henzing AJ, Ruchaud S, Hudson DF, Honda R, et al. Borealin: a novel chromosomal passenger required for stability of the bipolar mitotic spindle. *J Cell Biol* (2004) 166:179–91. doi: 10.1083/jcb.200404001

15. Ruchaud S, Carmena M, Earnshaw WC. Chromosomal passengers: conducting cell division. *Nat Rev Mol Cell Biol* (2007) 8:798–812. doi: 10.1038/nrm2257

16. Yamanaka Y, Heike T, Kumada T, Shibata M, Takaoka Y, Kitano A, et al. Loss of Borealin/DasraB leads to defective cell proliferation, p53 accumulation and early embryonic lethality. *Mech Dev* (2008) 125:441–50. doi: 10.1016/j.mod.2008.01.011

17. Carré A, Rachdi L, Tron E, Richard B, Castanet M, Schlumberger M, et al. Hes1 is required for appropriate morphogenesis and differentiation during mouse thyroid gland development. *PloS One* (2011) 6. doi: 10.1371/journal.pone.0016752

18. Di Cosmo C, Liao XH, Dumitrescu AM, Philp NJ, Weiss RE, Refetoff S. Mice deficient in MCT8 reveal a mechanism regulating thyroid hormone secretion. *J Clin Invest* (2010) 120:3377–88. doi: 10.1172/JCI42113

19. Kariyawasam D, Rachdi L, Carré A, Martin M, Houlier M, Janel N, et al. DYRK1A BAC transgenic mouse: a new model of thyroid dysgenesis in Down syndrome. *Endocrinology* (2015) 156:171–80. doi: 10.1210/en.2014-1329

20. Andersson L, Westerlund J, Liang S, Carlsson T, Amendola E, Fagman H, et al. Role of EphA4 receptor signaling in thyroid development: regulation of folliculogenesis and propagation of the C-cell lineage. *Endocrinology* (2011) 152:1154–64. doi: 10.1210/en.2010-0232

21. Stoupa A, Adam F, Kariyawasam D, Strassel C, Gawade S, Szinnai G, et al. TUBB1 mutations cause thyroid dysgenesis associated with abnormal platelet physiology. *EMBO Mol Med* (2018) 10:e9569. doi: 10.15252/emmm.201809569

22. Koumarianou P, Goméz-López G, Santisteban P. Pax8 controls thyroid follicular polarity through cadherin-16. *J Cell Sci* (2017) 130:219–31. doi: 10.1242/jcs.184291

23. Maenhaut C, Christophe D, Vassart G, Dumont J, Roger PP, Opitz R. Ontogeny, anatomy, metabolism and physiology of the thyroid. *Feingold KR Anawalt B Boyce Chrousos G Herder WW Dhatariya K Dungan K Hershman JM Hofland J Kalra Kaltsas G Koch C Kopp P Korbonits M Kovacs CS Kuohung W Laferrère B Levy M McGee EA McLachlan R Morley JE New M Purnell J Sahay R Sing F Sperling MA Strat CA Trence DL Wilson DP Ed Endotext* (2015).

24. Saito T, Lamy F, Roger PP, Lecocq R, Dumont JE. Characterization and identification as cofilin and destrin of two thyrotropin- and phorbol ester-regulated phosphoproteins in thyroid cells. *Exp Cell Res* (1994) 212:49–61. doi: 10.1006/excr.1994

25. Lee J, Yi S, Kang YE, Kim HW, Joung KH, Sul HJ, et al. Morphological and functional changes in the thyroid follicles of the aged murine and humans. *J Pathol Transl Med* (2016) 50:426–35. doi: 10.4132/jptm.2016.07.19

26. Trivedi P, Zaytsev AV, Godzi M, Ataullakhanov FI, Grishchuk EL, Stukenberg PT. The binding of Borealin to microtubules underlies a tension independent kinetochore-microtubule error correction pathway. *Nat Comm* (2019) 10:682. doi: 10.1038/s41467-019-08418-4

27. Rakov H, De Angelis M, Renko K, Hönes GS, Zwanziger D, Moeller LC, et al. Aging is associated with low thyroid state and organ-specific sensitivity to thyroxine. *Thyroid* (2019) 29:1723–33. doi: 10.1089/thy.2018.0377

28. Shimamura M, Shibusawa N, Kurashige T, Mussazhanova Z, Matsuzaki H, Nakashima M, et al. Mouse models of sporadic thyroid cancer derived from BRAFV600E alone or in combination with PTEN haploinsufficiency under physiologic TSH levels. *PloS One* (2018) 13:e0201365v. doi: 10.1371/journal.pone.0201365

29. Hayama S, Daigo Y, Yamabuki T, Hirata D, Kato T, Miyamoto M, et al. Phosphorylation and activation of cell division cycle associated 8 by aurora kinase B plays a significant role in human lung carcinogenesis. *Cancer Res* (2007) 67:4113–22. doi: 10.1158/0008-5472.CAN-06-4705

30. Charles RP, Iezza G, Amendola E, Dankort D, McMahon M. Mutationally activated BRAF(V600E) elicits papillary thyroid cancer in the adult mouse. *Cancer Res* (2011) 71:3863–71. doi: 10.1158/0008-5472.CAN-10-4463

31. van Trotsenburg P, Stoupa A, Léger J, Rohrer T, Peters C, Fugazzola L, et al. Congenital hypothyroidism: A 2020-2021 consensus guidelines update-an ENDO-european reference network initiative endorsed by the european society for pediatric endocrinology and the european society for endocrinology. *Thyroid* (2021) 31:387–419. doi: 10.1089/thy.2020.0333

32. Kimura S, Hara Y, Pineau T, Fernandez-Salguero P, Fox CH, Ward JM, et al. The T/ebp null mouse: thyroid-specific enhancer-binding protein is essential for the organogenesis of the thyroid, lung, ventral forebrain, and pituitary. *Genes Dev* (1996) 10:60–9. doi: 10.1101/gad.10.1.60

33. Rurale G, Persani L, Marelli F. GLIS3 and thyroid: A pleiotropic candidate gene for congenital hypothyroidism. *Front Endocrinol* (2018) 9:730. doi: 10.3389/fendo.2018.00730

frontiers | Frontiers in Endocrinology

TYPE Original Research
PUBLISHED 08 December 2023
DOI 10.3389/fendo.2023.1247709

OPEN ACCESS

EDITED BY
Murilo Vieira Geraldo,
State University of Campinas, Brazil

REVIEWED BY
Chandra Sekhar Bhol,
National University of Singapore, Singapore
Qiuxia Cui,
Wuhan University, China

*CORRESPONDENCE
Haohao Chen
HaohaoChen@tom.com

RECEIVED 26 June 2023
ACCEPTED 17 November 2023
PUBLISHED 08 December 2023

CITATION
Liu Y, Yin Z, Wang Y and Chen H (2023) Exploration and validation of key genes associated with early lymph node metastasis in thyroid carcinoma using weighted gene co-expression network analysis and machine learning. *Front. Endocrinol.* 14:1247709. doi: 10.3389/fendo.2023.1247709

Exploration and validation of key genes associated with early lymph node metastasis in thyroid carcinoma using weighted gene co-expression network analysis and machine learning

Yanyan Liu[1], Zhenglang Yin[1], Yao Wang[2] and Haohao Chen[1*]

[1]Department of General Surgery, The Third Affiliated Hospital of Anhui Medical University (The First People's Hospital of Hefei), Hefei, Anhui, China, [2]Digestive Endoscopy Department, Jiangsu Province Hospital, The First Affiliated Hospital with Nanjing Medical University, Nanjing, Jiangsu, China

Background: Thyroid carcinoma (THCA), the most common endocrine neoplasm, typically exhibits an indolent behavior. However, in some instances, lymph node metastasis (LNM) may occur in the early stages, with the underlying mechanisms not yet fully understood.

Materials and methods: LNM potential was defined as the tumor's capability to metastasize to lymph nodes at an early stage, even when the tumor volume is small. We performed differential expression analysis using the 'Limma' R package and conducted enrichment analyses using the Metascape tool. Co-expression networks were established using the 'WGCNA' R package, with the soft threshold power determined by the 'pickSoftThreshold' algorithm. For unsupervised clustering, we utilized the 'ConsensusCluster Plus' R package. To determine the topological features and degree centralities of each node (protein) within the Protein-Protein Interaction (PPI) network, we used the CytoNCA plugin integrated with the Cytoscape tool. Immune cell infiltration was assessed using the Immune Cell Abundance Identifier (ImmuCellAI) database. We applied the Least Absolute Shrinkage and Selection Operator (LASSO), Support Vector Machine (SVM), and Random Forest (RF) algorithms individually, with the 'glmnet,' 'e1071,' and 'randomForest' R packages, respectively. Ridge regression was performed using the 'oncoPredict' algorithm, and all the predictions were based on data from the Genomics of Drug Sensitivity in Cancer (GDSC) database. To ascertain the protein expression levels and subcellular localization of genes, we consulted the Human Protein Atlas (HPA) database. Molecular docking was carried out using the mcule 1-click Docking server online. Experimental validation of gene and protein expression levels was conducted through Real-Time Quantitative PCR (RT-qPCR) and immunohistochemistry (IHC) assays.

Results: Through WGCNA and PPI network analysis, we identified twelve hub genes as the most relevant to LNM potential from these two modules. These 12 hub genes displayed differential expression in THCA and exhibited significant correlations with the downregulation of neutrophil infiltration, as well as the

upregulation of dendritic cell and macrophage infiltration, along with activation of the EMT pathway in THCA. We propose a novel molecular classification approach and provide an online web-based nomogram for evaluating the LNM potential of THCA (http://www.empowerstats.net/pmodel/?m=17617_LNM). Machine learning algorithms have identified ERBB3 as the most critical gene associated with LNM potential in THCA. ERBB3 exhibits high expression in patients with THCA who have experienced LNM or have advanced-stage disease. The differential methylation levels partially explain this differential expression of ERBB3. ROC analysis has identified ERBB3 as a diagnostic marker for THCA (AUC=0.89), THCA with high LNM potential (AUC=0.75), and lymph nodes with tumor metastasis (AUC=0.86). We have presented a comprehensive review of endocrine disruptor chemical (EDC) exposures, environmental toxins, and pharmacological agents that may potentially impact LNM potential. Molecular docking revealed a docking score of -10.1 kcal/mol for Lapatinib and ERBB3, indicating a strong binding affinity.

Conclusion: In conclusion, our study, utilizing bioinformatics analysis techniques, identified gene modules and hub genes influencing LNM potential in THCA patients. ERBB3 was identified as a key gene with therapeutic implications. We have also developed a novel molecular classification approach and a user-friendly web-based nomogram tool for assessing LNM potential. These findings pave the way for investigations into the mechanisms underlying differences in LNM potential and provide guidance for personalized clinical treatment plans.

KEYWORDS

thyroid cancer, bioinformatics analysis, The Cancer Genome Atlas, nomogram, machine learning

Introduction

The continuous advancement in detection technology has resulted in an ongoing rise in the rate of thyroid carcinoma (THCA) detection. Compared to other types of endocrine malignancies, THCA holds the highest prevalence, experiencing an annual increase in its incidence (1). Surgical resection is the primary treatment modality for THCA. Post-surgery, the decision to perform neck lymph node dissection or radioactive iodine therapy should be based on the patient's condition and pathological type. Additional treatment modalities include radioisotope therapy, endocrine inhibition therapy, and external beam radiation therapy (mainly used for anaplastic thyroid cancer), among others. Despite typically displaying an indolent nature and promising overall prognosis, THCA has a significant potential to exhibit an invasive phenotype and in some cases may metastasize (2). Recent reports indicate an approximate 38.5%~58.8% rate of lymph node metastasis (LNM) in THCA (3). Moreover, cervical LNM may occur at the early stages of disease progression (4). The presence of LNM serves as a key indicator for prognosis and treatment options in individuals afflicted with THCA (5). In cases where LNM is detected, a comprehensive approach incorporating radical surgery with lymph node dissection is deemed necessary (6). Furthermore, the implementation of iodine-131 treatment may also be considered based on specific indications (7). LNM constitutes an important prognostic determinant, exhibiting a close association with both tumor recurrence and unfavorable prognostic outcomes among individuals afflicted with THCA (8). Additionally, performing neck lymph node dissection due to suspected cervical lymph node metastasis can potentially lead to damage to glands and nerves, such as the internal jugular vein, submandibular gland, brachial plexus, and accessory nerve. This can also result in adverse postoperative outcomes for the patients (9). Hence, gaining clarity regarding the occurrence or inclination towards lymph node metastasis in instances of THCA would facilitate the development of a more scientifically-informed treatment plan, enable regular assessment of patient prognosis, prompt timely treatment adjustments, and ultimately enhance patient prognosis.

In the case of THCA, several known risk factors have been linked to LNM, such as patient age, sex, multifocality, calcification, and extrathyroidal extension (ETE) (5, 10–12). In addition to established clinical factors, there has been a burgeoning interest in exploring genetic variations associated with LNM in recent years (13, 14). For example, experimental evidence from both *in vitro* and *in vivo* studies has demonstrated that the upregulation of lnc-MPEG1-1:1 in papillary thyroid cancer (PTC) cell lines can

elevate cell proliferation and migration (15). Moreover, this long non-coding RNA (lncRNA) is observed to be overexpressed in the cytoplasm of PTC cells and has been shown to exert its function by acting as a competitive endogenous RNA (ceRNA), competitively sequestering the shared binding sequences of miR-766-5p (15). In addition, researchers have reported that primary patients with positive lymph node status tend to exhibit relatively advanced TI-RADS levels and higher prevalence of the RET genetic alteration (16). Therefore, a comprehensive understanding and analysis of genomic alterations in THCA with LNM are necessary to advance the current knowledge of the underlying pathophysiology involved in the development and predisposition to LNM. Such enhanced understanding could potentially pave the way for the development of improved resources and novel strategies for the prevention and treatment of LNM (17, 18).

Endocrine-disrupting chemicals (EDCs) are exogenous compounds found in the environment that can emulate or impair the functioning of endogenous hormones (19, 20). EDCs have the ability to interfere with reproductive, neuroendocrine, cardiovascular, and metabolic function, resulting in compromised health outcomes (20). The extensive impact of EDCs on the progression and metastasis of tumors of endocrine organs has been widely documented. According to a recent study report, bisphenol A (BPA), a kind of EDCs, has a promotional effect on breast ductal carcinoma *in situ* (DCIS) cell proliferation and migration, as well as macrophage migration (21). When exposed to an orally-administered, environmentally human-relevant low dose of 2.5 μg/l BPA for 70 days through drinking water in a DCIS xenograft model, primary tumor growth rate was promoted approximately 2-fold and lymph node metastasis was significantly increased, along with a notable enhancement of CD206+ M2 macrophage polarization, indicating a protumorigenic response. These findings reveal the role of BPA as an accelerator in advancing DCIS progression into invasive breast cancer by influencing DCIS cellular activity and macrophage polarization toward a cancer-supporting phenotype (21). Moreover, Tamoxifen, being an EDC, is widely used as a hormone therapy in postmenopausal women with breast cancer who are ER+ and is regarded as one of the most effective adjuvant breast cancer treatments available (22). Its effectiveness in controlling breast cancer recurrence and metastasis has been extensively reported. Previous studies have revealed the potential role of EDCs in THCA. Existing literature has revealed that exposure to certain congeners of flame retardants, polychlorinated biphenyls (PCBs), phthalates, and specific isomers of pesticides can lead to an increased risk of thyroid cancer (23). Exposure to Bisphenol A (BPA) has been associated with an increased risk of thyroid nodules in Chinese women (24). Additionally, animal experiments have demonstrated a correlation between BPA exposure and the risk of thyroid cancer (25). Despite THCA being the most frequent type of endocrine tumor, there has not been widespread research into the impact of EDCs on the LNM of THCA. Therefore, utilizing bioinformatics to investigate EDCs relevant to LNM in THCA is advantageous for further screening of potential therapeutic drugs and improving patient prognosis.

In light of the recent progress in high-throughput sequencing technology, the integration of multiple omics analysis has gained widespread utilization in tumor research (26–28). The high-throughput sequencing technology is capable of exploring tumor biomarkers, evaluating therapeutic responsiveness, and providing convenience for the development of clinical management plans among tumor patients (29–32). Therefore, the aim of this study is to comprehensively investigate the key genetic variations and EDCs relevant to LNM in THCA using multiple bioinformatics techniques. Additionally, we aim to screen for potential therapeutic drugs and corresponding treatment targets capable of inhibiting the incidence of LNM in THCA.

Materials and methods

Data acquisition

The clinical data, RNA-seq data, 450K methylation data, and copy number variation (CNV) data pertaining to the THCA (THCA) cohort were extracted from the GDC database (https://portal.gdc.cancer.gov/projects/TCGA-THCA) (33). A total of 510 THCA specimens, along with 58 normal specimens, were identified in the TCGA-THCA cohort. After obtaining the RNA-seq FPKM dataset, we proceeded to transform the expression profile into transcripts per kilobase million (TPM). The GSE60542 cohort, comprising 33 primary thyroid tumor samples, 23 metastatic lymph nodes, 30 normal thyroid samples, and 4 normal lymph node samples, was extracted from the Gene Expression Omnibus (GEO) database (http://www.ncbi.nlm.nih.gov/geo/), and it served as the validation cohort (34).

Gene Expression Profiling Interactive Analysis (GEPIA) database was used to obtain the differentially expressed genes (DEGs) between THCA and normal tissues (35). The criterion for screening DEGs is that the $|Log_2FC|>1$ and q-value<0.05. The DEGs were also plotted as chromosomal distribution via GEPIA database.

Identification of the potential for tumors to undergo lymph node metastasis

Our study introduces a novel concept called 'LNM potential. ' In cases where a thyroid cancer patient experiences LNM with a small primary tumor volume, they are considered to have a high LNM potential. Conversely, if a thyroid cancer patient does not experience LNM despite having a larger primary tumor volume, they are considered to have a low LNM potential. In the TCGA-THCA cohort, patients with a tumor size exceeding the median but without LNM were classified as having low LNM potential (LNM Low), while patients with a tumor size below the median but with LNM were classified as having high LNM potential (LNM High).

Weighted correlation network analysis

The transcriptional profiles of the DEGs obtained from GEPIA database were used as the input file for the R package "WGCNA" to establish the co-expression networks (36). WGCNA was performed

with the default-recommended parameters. To distinguish modules with different expression patterns, a soft threshold power obtained from "pickSoftThreshold" algorithm was used for creating co-expression networks. The minimum module size was set to 30, and the dissimilarity threshold for module merging was set to 0.25. Pearsons correlation analysis were carried out to estimate correlation between Module eigengenes (MEs) and clinical traits and then the module with the highest and lowest pearsons coefficient was identified as the module most relevant to clinical traits.

Identification of the hub genes

The online database STRING was employed to formulate the Protein-Protein Interaction (PPI) Network for all the genes in the module most relevant to clinical traits (37). Default setting was used in STRING database. The visual representation of the PPI network was accomplished through the Cytoscape tool (Version 3.7.2). The CytoNCA plugin, integrated with the Cytoscape tool, was utilized for determining the topological features and degree centralities of each node (protein) within the PPI network (38). Subsequently, the hub genes was singled out and delineated as the prominent node of the PPI network, crucial for mediating protein-protein interactions.

The hub gene-miRNA, Transcription factor (TF)-hub gene and TF-miRNA interactions was established using NetworkAnalyst online tool based on ENCODE database (http://www.encodeproject.org/ENCODE/), miRTarBase (v8.0; http://mirtarbase.mbc.nctu.edu/) and Regulatory Network Repository (https://regnetworkweb.org/) (39–42).

Pathway enrichment analysis and immune infiltration analysis

Conducting pathway and process enrichment analyses was accomplished through employment of the Metascape platform (43) (Metascape, http://metascape.org). By following the default settings, the Metascape tool facilitated hierarchical clustering to segregate enrichment terms into unique clusters, with the representative term being selected based on minimal p-value criteria.

In order to ascertain the relative enrichment of a gene set in the given sample population, gene set variance analysis (GSVA) was implemented (44). The higher scores indicate a relatively greater activation of the gene set in the given sample. In this study, 10 cancer-associated pathways' activity scores were computed for 7876 samples collected from 32 cancer types using the Reverse Phase Protein Array (RPPA) data derived from the TCPA database and the TCGA database (45). The pathways examined in this study are TSC/mTOR, RTK (receptor tyrosine kinase), RAS/MAPK, PI3K/AKT, Hormone ER, Hormone AR, EMT (epithelial-mesenchymal transition), DNA Damage Response, Cell Cycle, and Apoptosis pathways, all of which are well-known pathways associated with cancer. RPPA is a high-throughput antibody-based technology that involves procedures analogous to those of Western blots (46). In this technique, the proteins are extracted from cancerous tissue or cultured cells, denatured with SDS, and then immobilized on nitrocellulose-coated slides. Next, an antibody probe is used for analysis. Utilizing the Gene Set Cancer Analysis (GSCA) tool, the aforementioned analytical process was carried out to compute a pathway activity score (PAS) that effectively represents activation levels of the respective signaling pathway (47).

Immune Cell Abundance Identifier (ImmuCellAI) database was utilized to evaluate immune cell infiltration in each sample of TCGA-THCA cohort (48). The aforementioned tool was developed to assess the abundance of 24 immune cells within a given gene expression dataset, including RNA-Seq and microarray data. The 24 immune cells encompass 18 T-cell subtypes, as well as an additional six immune cells, specifically, B cells, NK cells, monocytes, macrophages, neutrophils, and DC cells.

Recognition of molecular subtypes

Unsupervised hierarchical clustering of the hub genes was established by R package "ConsensusClusterPlus" to identify the different molecular subtypes in TCGA-THCA cohort (49). ConsensusClusterPlus was executed with default settings for all parameters, with the maximum evaluated 'k' (max K) restricted to 10. The optimal number of clusters ('k') was determined using the Consensus Cumulative Distribution Function (CDF) Plot. Visualization of the expression patterns of hub genes across different molecular subtypes was performed using the R package 'pheatmap,' with a heatmap-type display.

Machine learning framework

In the TCGA-THCA cohort, a comprehensive analysis was conducted to identify key gene from the hub genes of PPI network utilizing the Least Absolute Shrinkage and Selection Operator (LASSO), Support Vector Machine (SVM), and the Random Forest (RF) algorithms available in the "glmnet", "e1071", and "randomForest" R packages, respectively (50–55). The application of these machine learning techniques enabled the effective screening of genes with potential diagnostic significance in the context of the studied cohort.

In order to perform LASSO algorithmic analysis, a set of specific parameters were established, including the family parameter, set to "binomial", alpha parameter which was set to 1, type measure parameter defined as "deviance", as well as the nfolds parameter set to 10 (31). For the construction of a forest of 500 trees, the "randomForest" package within R was effectively utilized through standard settings (29). Additionally, feature importance scores were calculated through the application of the "importance" function, which was performed through the utilization of the "randomForest" package in R. Following the implementation of randomForest algorithms, genes exhibiting an importance value exceeding the median were selected and subjected to downstream analysis. The SVM method ran using the default parameters. Through cross-referencing the results generated by the three methodologies, an intersectional subset was identified as the key gene set (30).

Comparative toxicogenomics database

The publicly accessible CTD database (http://ctdbase.org/) is a comprehensive repository of toxicogenomic data, offering reliable and meticulously scrutinized information regarding gene/protein interactions with chemicals across an extensive range of peer-reviewed scientific literature (56). This trustworthy and vigorous database serves as a valuable platform for researchers seeking to access critical toxicogenomic information. Against the backdrop of default parameters, the CTD database is utilized to explore the potency of EDCs, antineoplastic drugs, and environmental toxins in their ability to incite changes in key gene expression within all species. Dependable EDCs were sourced from previously published literature (19).

Discovery of potential drugs by computational methods

Drug sensitivity of anticancer drugs was estimated in each tumor specimen of TCGA-THCA by R package "oncoPredict" (57). Ridge regression was performed by "oncoPredict" algorithm and all above prediction was performed based on the Genomics of Drug Sensitivity in Cancer (GDSC) database (58).

Molecular docking procedure

To obtain the crystal structures of proteins encoded by the hub gene, the RCSB Protein Data Bank (PDB) (www.rcsb.org/pdb/home/home.do) was accessed, while the 3D structures of the drugs were downloaded from PubChem (https://www.ncbi.nlm.nih.gov/pccompound) (59, 60). The molecular docking process was conducted using mcule 1-click Docking server online (https://mcule.com/apps/1-click-docking/) (61). The best pose was selected based on the docking score and the rationality of the molecular conformation.

Exploration of protein expression level and subcellular localization of the key gene

The Human Protein Atlas (HPA) database (https://www.proteinatlas.org/), a comprehensive collection of human proteins in normal and tumor cells and tissues, integrates multiple cutting-edge omics technologies, including immunohistochemistry (IHC) and immunofluorescence (IF) (62). We employed the HPA online tool to investigate protein expression profiles of specific genes in both normal and tumor tissues, utilizing the immunohistochemistry data available in the HPA database.

Using the subcellular domain of the HPA database, we gained a high-resolution understanding of the spatiotemporal distribution and expression of proteins. Subcellular protein localization was investigated through immunofluorescence (ICC-IF) and confocal microscopy, involving up to three distinct cell lines. Based on image analysis, protein subcellular localization was systematically categorized into distinct organelles and intricately detailed subcellular structures.

Real time quantitative PCR and IHC

Total RNA extraction was performed utilizing TRIzol reagent (Ambion, USA), followed by conversion of the extracted mRNA to cDNA using PrimeScript™ RT Master Mix (Takara, Japan). The gene transcripts were quantified through RT-qPCR assay utilizing ChamQ SYBR qPCR Master Mix (Vazyme, China). The 2-ΔΔCT method was used to evaluate the relative expression levels of the genes, with GAPDH serving as the internal reference. To detect ERBB3 and GAPDH expression levels, the forward primer of ERBB3 was 5′-GCAGATCAGTGTGTAGCGTG-3′, and the reverse primer of ERBB3 was 5′-CGTGTGCAGTTGAA GTGACA-3′; while the forward primer of GAPDH was 5′-TGTTCGTCATGGGTGTGAAC-3′ and the reverse primer of GAPDH was 5′-ATGGCATGGACTGTGGTCAT-3′. The experiment was repeated thrice for establishing the average. Gene expression was detected utilizing the RT-qPCR method.

The tumors were fixed in 4% paraformaldehyde and embedded in paraffin. Subsequently, 4 μm sections were obtained from the paraffin-embedded samples and fixed on glass slides. Epitope retrieval of the sections was performed in 10 mmol/L citric acid buffer at pH7.2, heated in a microwave. Following epitope retrieval, the slides were incubated at 4°C overnight with the primary antibody (rabbit anti-ERBB3, dilution 1:100, K113334P, Solarbio; Beijing, CN), followed by HRP-conjugated secondary antibody for 1 h at room temperature. The detection of antibodies was done using the substrate diaminobenzidine (DAB, Beyotime), and slides were counterstained with hematoxylin (Beyotime). For statistical analysis, Average Optical Density (AOD) was used as a scoring method. AOD measurements were executed by professional pathologists using the ImageJ software, and at least three measurements were taken per IHC sample to establish the mean AOD values.

The study utilized samples from 9 THCA patients without LNM and 11 patients with LNM from The Third Affiliated Hospital of Anhui Medical University. The samples were employed for RT-qPCR and IHC analyses. All patients involved in the study provided informed consent prior to their inclusion in the study.

Statistical analyses

For statistical analysis, we employed R software (version 4.2.1). To compare continuous variables, the Wilcoxon/Kruskal-Wallis Test was utilized, whereas differences in proportion were assessed by the Chi-Square test. A p-value of less than 0.05 was regarded as statistically significant. For evaluation of diagnostic performance, the Receiver Operating Characteristic (ROC) curve was employed. Correlations were analyzed using Spearman's correlation. T-Distribution Stochastic Neighbor Embedding (t-SNE), uniform manifold approximation and projection (UMAP), and principal component analysis (PCA) were employed for dimensionality reduction (63–65).

Results

Alterations in biological processes and immune cell infiltration associated with LNM in thyroid cancer

The median tumor diameter in the TCGA-THCA cohort was 2.5cm. There were 99 cases of patients (LMN Low) with tumor diameter exceeding 2.5cm but no LNM, and 88 cases of patients (LMN High) with tumor diameter below 2.5cm but with LNM. The Table 1 presented patient clinical characteristics.

Differential gene analysis of the LMN High and LMN Low groups was performed using the limma R package, with a screening criterion of |Log2FC| > 1 and p-value < 0.05. A total of 1038 upregulated genes and 332 downregulated genes were identified in the LMN High group of patients (Supplementary Table 1). Pathway enrichment analysis was performed on upregulated and downregulated genes separately, revealing that the upregulated genes were mainly enriched in adaptive immune response, NABA MATRISOME ASSOCIATED, and positive regulation of immune response. Meanwhile, the downregulated genes were mainly enriched in positive regulation of CoA-transferase activity, Metallothioneins bind metals, and monoatomic ion transmembrane transport (Supplementary Figures 1A, B).

Moreover, there were significant differences in immune infiltration status between the LMN High and LMN Low groups (Supplementary Table 2). Specifically, nTreg, iTreg, Th1, and CD8T cells exhibited relatively higher infiltration levels in the LMN High group, while neutrophils exhibited relatively higher infiltration levels in the LMN Low group (Supplementary Figure 1C). Out of the 10 cancer-related pathways obtained using RPPA technology, only the PI3K/AKT, TSC/mTOR, and RTK pathways were found to have significantly lower activation levels in the LMN High group compared to the LMN Low group (Supplementary Figure 1D).

LNM potential-related gene module revealed by WGCNA

To achieve a signed scale-free co-expression gene network, a power of β=4 and a scale-free R2 = 0.93 were chosen as the soft-threshold parameters (Figures 1A, B). Within the context of WGCNA analysis, sample clustering was conducted utilizing gene expression patterns in order to identify outliers (Figure 1C). Consequently, 9 gene modules were successfully delineated in the TCGA-THCA cohort (Figure 1D; Supplementary Table 3). The "grey" module was created to encompass genes that could not be sorted into any other discernible genetic module. The module with

TABLE 1 The clinical data from enrolled patients into the study.

Characteristics	LNM High(N=88)	LNM Low(N=99)	Total(N=187)	pvalue	FDR
Age				0.1	0.58
<=46	39(20.86%)	57(30.48%)	96(51.34%)		
>46	49(26.20%)	42(22.46%)	91(48.66%)		
Sex				1	1
FEMALE	63(33.69%)	71(37.97%)	134(71.66%)		
MALE	25(13.37%)	28(14.97%)	53(28.34%)		
Primary neoplasm				3.20E-03	0.02
Multifocal	52(27.81%)	34(18.18%)	86(45.99%)		
Unifocal	35(18.72%)	63(33.69%)	98(52.41%)		
unknow	1(0.53%)	2(1.07%)	3(1.60%)		
T				3.00E-09	2.70E-08
T1	40(21.39%)	7(3.74%)	47(25.13%)		
T2	17(9.09%)	53(28.34%)	70(37.43%)		
T3	27(14.44%)	36(19.25%)	63(33.69%)		
T4	4(2.14%)	3(1.60%)	7(3.74%)		
N				1.10E-41	1.10E-40
N0	0(0.0e+0%)	99(52.94%)	99(52.94%)		
N1	88(47.06%)	0(0.0e+0%)	88(47.06%)		
M				0.67	1
M0	51(27.27%)	57(30.48%)	108(57.75%)		

(Continued)

10.3389/fendo.2023.1247709

TABLE 1 Continued

Characteristics	LNM High(N=88)	LNM Low(N=99)	Total(N=187)	pvalue	FDR
M1	1(0.53%)	3(1.60%)	4(2.14%)		
unknow	36(19.25%)	39(20.86%)	75(40.11%)		
Stage				2.00E-07	1.60E-06
Stage I	45(24.06%)	43(22.99%)	88(47.06%)		
Stage II	1(0.53%)	30(16.04%)	31(16.58%)		
Stage III	24(12.83%)	21(11.23%)	45(24.06%)		
Stage IV	18(9.63%)	4(2.14%)	22(11.76%)		
unknow	0(0.0e+0%)	1(0.53%)	1(0.53%)		
Location				0.28	1
Bilateral	19(10.16%)	14(7.49%)	33(17.65%)		
Isthmus	6(3.21%)	4(2.14%)	10(5.35%)		
Left lobe	27(14.44%)	25(13.37%)	52(27.81%)		
Right lobe	35(18.72%)	55(29.41%)	90(48.13%)		
unknow	1(0.53%)	1(0.53%)	2(1.07%)		
Residual tumor				0.17	0.87
R0	65(34.76%)	79(42.25%)	144(77.01%)		
R1	12(6.42%)	5(2.67%)	17(9.09%)		
R2	0(0.0e+0%)	1(0.53%)	1(0.53%)		
unknow	11(5.88%)	14(7.49%)	25(13.37%)		
Thyroid gland disorder history				0.43	1
No	50(26.74%)	47(25.13%)	97(51.87%)		
Yes	27(14.44%)	38(20.32%)	65(34.76%)		
unknow	11(5.88%)	14(7.49%)	25(13.37%)		

the greatest number of included genes was the "blue" module (n=585), while the "grey" module (n=2) contained the fewest number of included genes (Figure 1E). The calculation of correlation between module eigengenes (MEs) and clinical features was conducted using the Pearson's correlation analysis. Through this analytical process, it was discovered that the "brown" module displayed the highest positive correlation with LMN High, while conversely, the "yellow" module showed the highest negative correlation with LMN High (Figure 1F). The significant correlation observed between GS and MM within both the "brown" and "yellow" modules suggests a strong association between these modules and the potential for LNM (Figures 1G, H). The biological processes primarily enriched by genes within the "yellow" module included organic hydroxy compound metabolic process, homeostasis, and monocarboxylic acid metabolic process, among others (Figure 2A). The "brown" module was primarily enriched in genes associated with biological processes such as cell junction organization, cell-cell adhesion, skin development, and positive regulation of cell motility (Figure 2B).

Identification of hub genes in the LNM potential-related gene modules

PPI network analysis of all genes within the 'yellow' and 'brown' modules was performed using the STRING tool (Figure 3A). A key cluster (Cluster 1) of the PPI network was extracted using the CytoNCA plugin within the Cytoscape software, and ERBB3 served as the seed of this cluster (Supplementary Table 4). The identified cluster consisted of 12 hub genes related to LNM potential, with 4 of them originating from the 'yellow' gene module and the rest from the 'brown' module (Figure 3B).

Expression levels of ALDH1A1 and NCAM1 were observed to be upregulated in the LNM Low group, whereas PLAU, KRT19, FN1, ITGA3, ERBB3, PLAUR, and ANPEP were found to be overexpressed in the LNM High group (Figure 3C; Supplementary Table 5). Using the 12 hub genes as the central framework, we constructed gene-miRNA, TF-gene, and TF-miRNA interaction networks to investigate the key regulatory mechanisms underlying gene expression (Figure 3D; Supplementary Table 6).

10.3389/fendo.2023.1247709

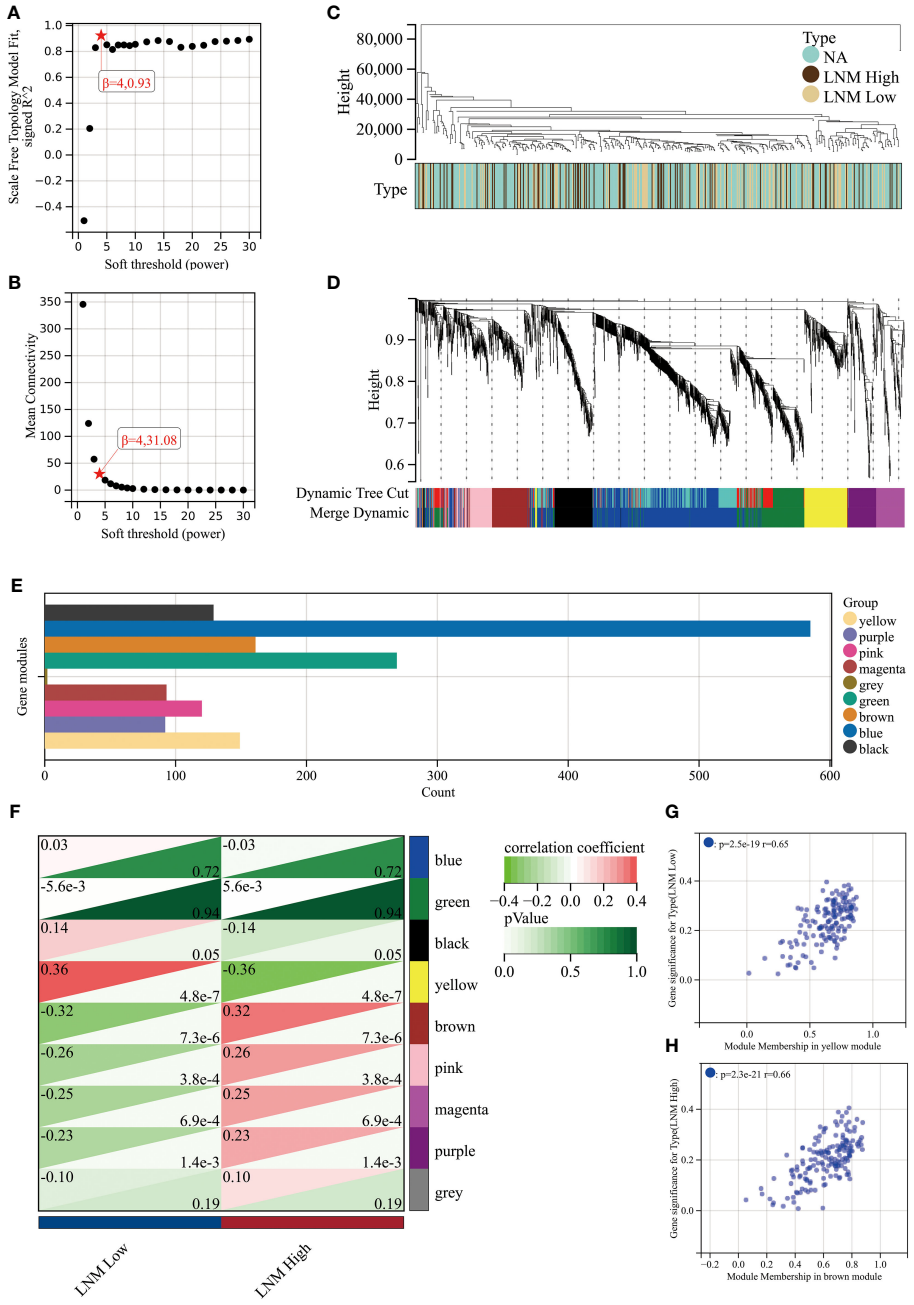

FIGURE 1
An investigation into the determination of soft-thresholding power used in WGCNA. **(A)** An examination of the scale-free fit index for different soft-thresholding powers (β). **(B)** Investigation into the mean connectivity for different soft-thresholding powers. **(C)** Illustration of the sample dendrogram and clustering dendrogram via WGCNA. **(D)** Hierarchical cluster tree depicting the co-expression modules discovered through WGCNA. **(E)** The number of genes in different gene modules. **(F)** The correlation between different gene modules and the LNM potential. The correlation between module membership (MM) and gene significance (GS) in the yellow **(G)** and brown **(H)** modules.

The diagnostic ability of hub genes in THCA

All 12 hub genes related to LNM potential exhibited significant differential expression between THCA and normal thyroid tissues (Figure 4A). Specifically, the gene expressions of ALDH1A1, NCAM1, and SNAI1 were downregulated in THCA, while the expressions of the remaining nine genes were upregulated.

Subsequently, we conducted dimensional reduction analysis based on hub gene expression using PCA, UMAP, and t-SNE. These analyses effectively distinguished THCA from normal tissues (Figure 4B). ROC analysis demonstrated that PCA1/2, UMAP1/2, t-

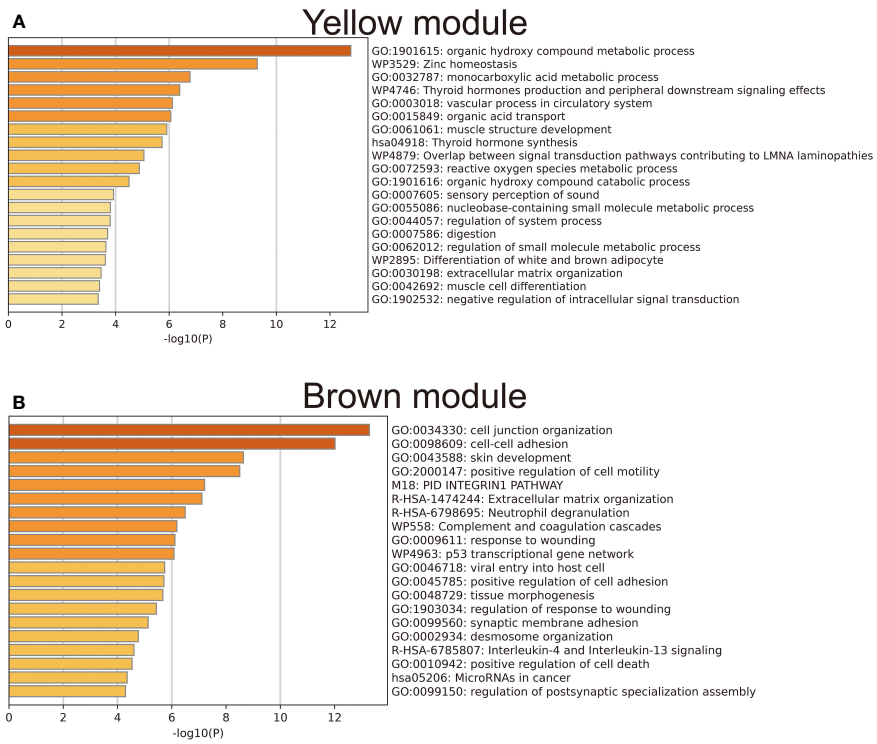

FIGURE 2
Results of gene enrichment analysis for the yellow **(A)** and brown **(B)** gene modules.

SNE1/2, and their combination can serve as outstanding diagnostic biomarkers for THCA (Figures 4B, C).

The variations in immune infiltration and pathway activation associated to LNM potential-related hub genes

A Spearman correlation analysis was performed to investigate the correlation between the gene expression levels of all 12 LNM potential-related hub genes and the infiltration scores of different immune cells (Figure 5A; Supplementary Table 7). With the exceptions of SNAI1, NCAM1, and ALDH1A1, the infiltration levels of DC cells showed significant positive correlations with other hub genes, with R>0.5 and p<0.0001. Of particular note was the strongest positive correlation observed between the infiltration levels of DC cells and the gene expression levels of FN1 (R=0.77; p<0.001). Furthermore, there was a significant negative correlation between the gene expression levels of DC cells and ALDH1A1 (R=-0.58; p<0.0001). Neutrophil infiltration levels did not show a significant correlation with SNAI1 and CCND1. The correlation observed between Neutrophil infiltration levels and NCAM1 was weakly positive (R=0.17; p <0.0001). In addition, there were significant negative correlations observed between Neutrophil infiltration levels and the other nine identified hub genes, with ANPEP exhibiting the strongest negative correlation (R=-0.69; p <0.0001).

Subsequently, we investigated the influence of CNV and SNV status of hub genes on immune cell infiltration in tumors. A sample was classified as either CNV-Amplification (Amp), CNV-Deletion (Del), or SNV-Mutant based on the occurrence of a CNV or SNV alteration in at least one of the identified hub genes. Using a significance level of P<0.05 as a filtering criterion, it was observed that the occurrence of CNV Amplification in hub genes was associated with a relatively higher degree of variability in immune cell infiltration, compared to CNV Deletion and SNV-Mutant (Supplementary Figures 3A, B). Furthermore, we conducted an evaluation of the influence of the activation levels of identified hub genes (GSVA scores) on immune cell infiltration in various cancer types using pan-cancer analysis based on the GSVA algorithm. This analysis encompassed assessments across 33 cancer types (Supplementary Figure 3C; Supplementary Table 8). A positive correlation was observed between the activation levels of identified hub genes and the levels of DC and macrophage infiltration in the majority of the analyzed tumor types. In contrast, a negative correlation was noted between hub gene activation levels and the level of neutrophil infiltration.Similar results were observed in the TCGA-THCA cohort, where a strong positive correlation was found between the GSVA scores of identified hub genes and the level of DC infiltration. Simultaneously, a robust negative correlation was identified between hub gene GSVA scores and the level of neutrophil infiltration (Supplementary Figure 3D).

Based on the median gene expression of hub genes, the samples were segregated into two groups – High and Low. To determine the

10.3389/fendo.2023.1247709

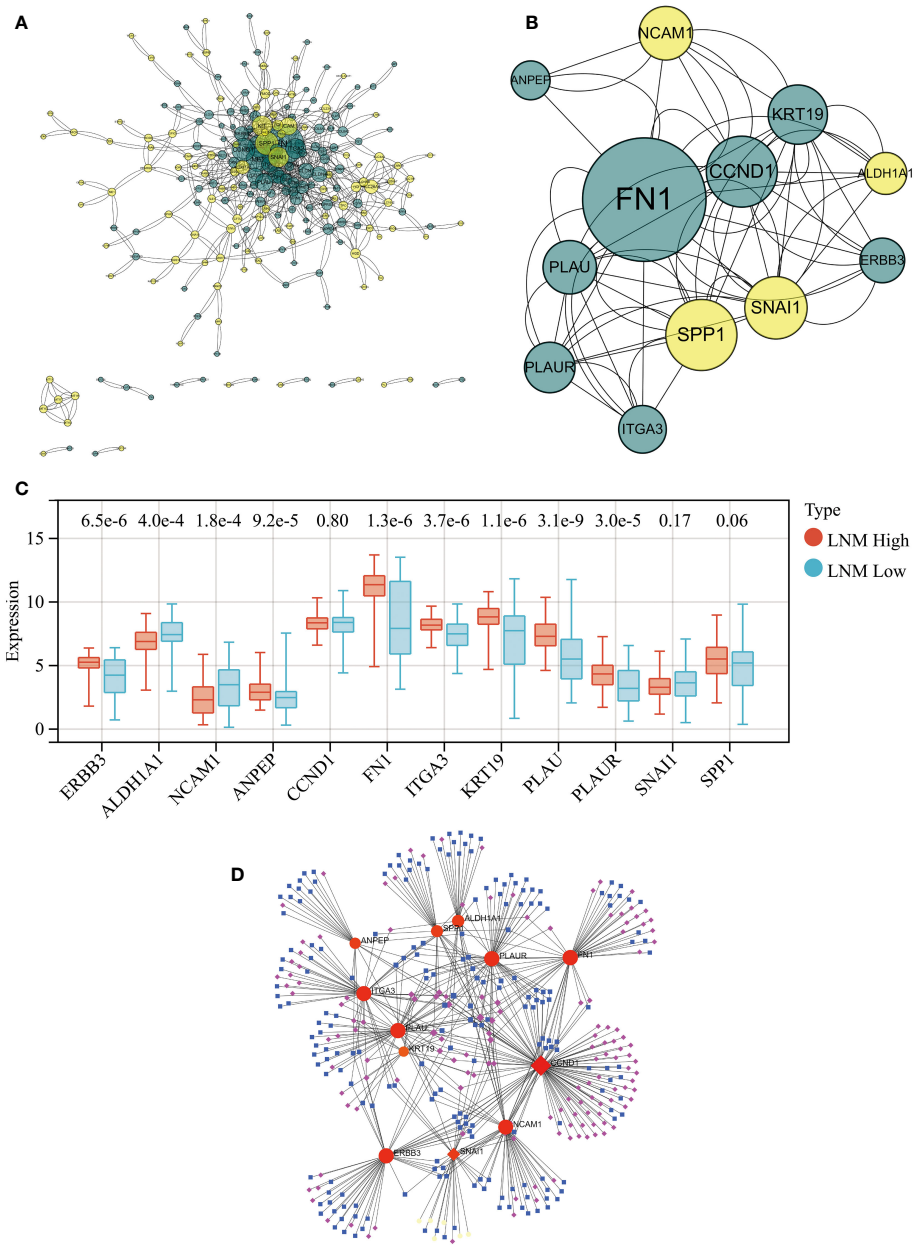

FIGURE 3
(A) PPI network for all genes within the yellow and brown gene modules. **(B)** The PPI network's hub genes were screened through the use of CytoNCA, with the top 12 hub genes being further selected via CytoNCA. **(C)** Expression levels of these 12 hub genes in THCA patients with high and low LNM potential. **(D)** Gene-miRNA, TF-gene, and TF-miRNA interaction networks centered around these 12 hub genes.

difference in PAS score between the groups, the student T test was performed and the *p*-value was adjusted by false discovery rate (FDR). We considered a gene to have an activating effect on a pathway if the FDR PAS (gene A Low expression) value suggested so (FDR<0.05), and conversely, we classified it as having an inhibitory effect. A similar methodology was employed by Y. Ye et al. (66). The results of the TCGA-THCA cohort highlighted a pronounced regulatory impact of hub genes on the EMT, PI3K-AKT, and RTK signaling pathways. The overexpression of NCAM1 and ALDH1A1 signifies a more inhibitory effect on the EMT pathway and an enhanced activation of the RTK and PI3K-AKT pathways. The activation of the EMT, RTK, and PI3K-AKT pathways are not significantly influenced by SNAI1, whereas CCND1 activates the EMT pathway while suppressing the RTK pathway. Elevated expression levels of the remaining hub genes indicate the activation of the EMT pathway and inhibition of the RTK and PI3K-AKT pathways (Figure 5B; Supplementary Table 9). Furthermore, a pancancer analysis was conducted to investigate the regulatory effects of different hub genes on cancer-associated pathways in various types of cancer, as demonstrated in Supplementary Figure 3E. The pancancer analysis revealed that these hub genes exhibit the highest advantage in activating the EMT pathway.

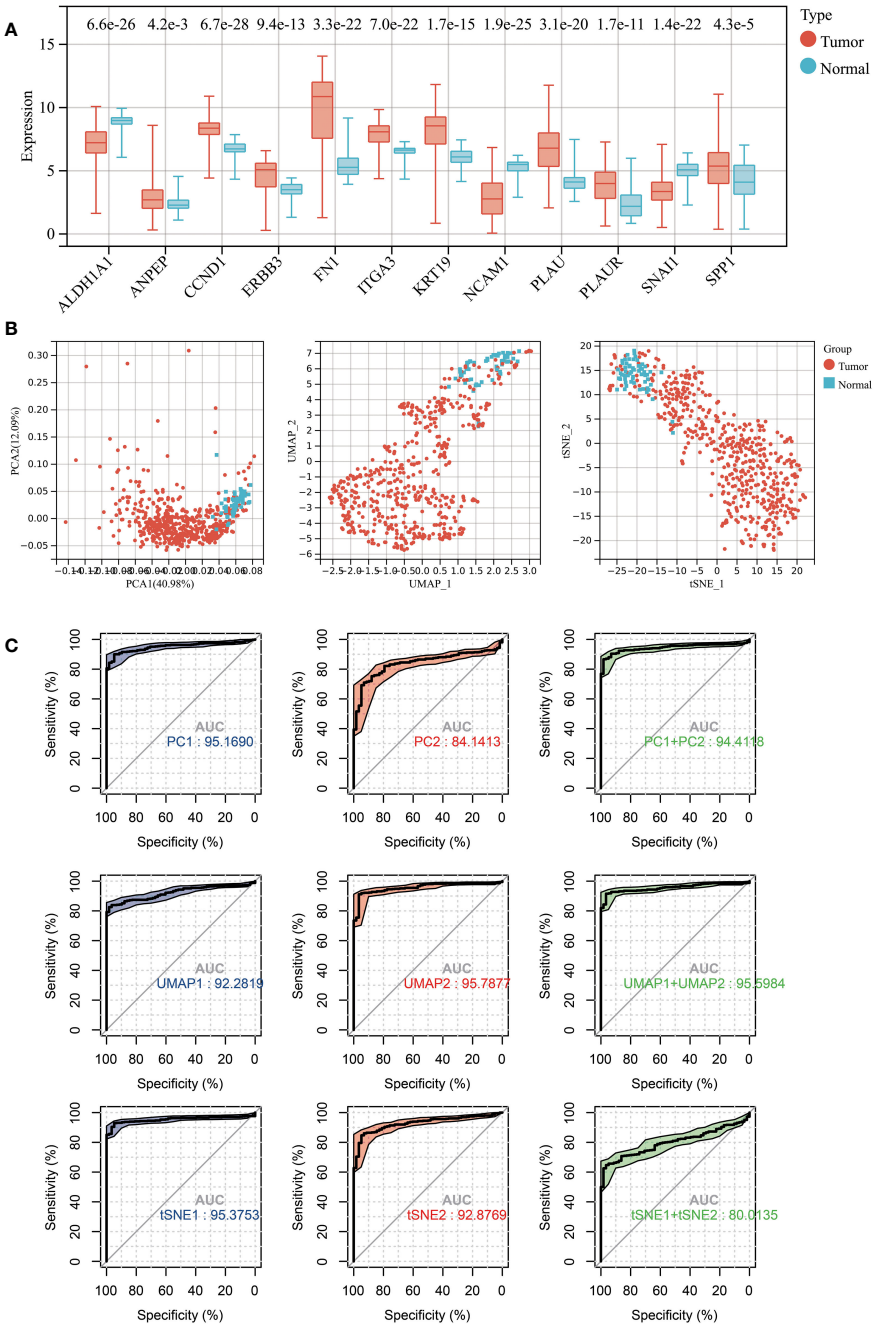

FIGURE 4
(A) Expression levels of 12 LNM potential-related hub genes between THCA and normal thyroid tissue. **(B)** The PCA (left), UMAP (middle), and TSNE (right) dimensionality reduction algorithms were utilized to generate data visualization. **(C)** The diagnostic capability of various dimensionality reduction algorithms on THCA was evaluated via ROC plot, utilizing the first two principal components and the sum of the first and second principal components.

The establishment of a molecular classification scheme

To further integrate the features of the 12 identified hub genes for predicting LNM potential in THCA patients, we performed unsupervised clustering using "ConsensusClusterPlus". Based on the consensus CDF and relative changes in the area beneath the CDF curve, it was determined that all patients could be effectively clustered into two distinct groups (cluster 1 and cluster 2; Figures 6A–D). The heatmap revealed distinct gene expression patterns across different patient clusters (Figure 6E). Subsequently, we conducted further investigations into the relationship between the molecular classification scheme and LNM in THCA patients. In the TCGA-THCA cohort, patients with low LNM potential were found to be predominantly composed of individuals within cluster 2 (65%; chi-square test, chi-square

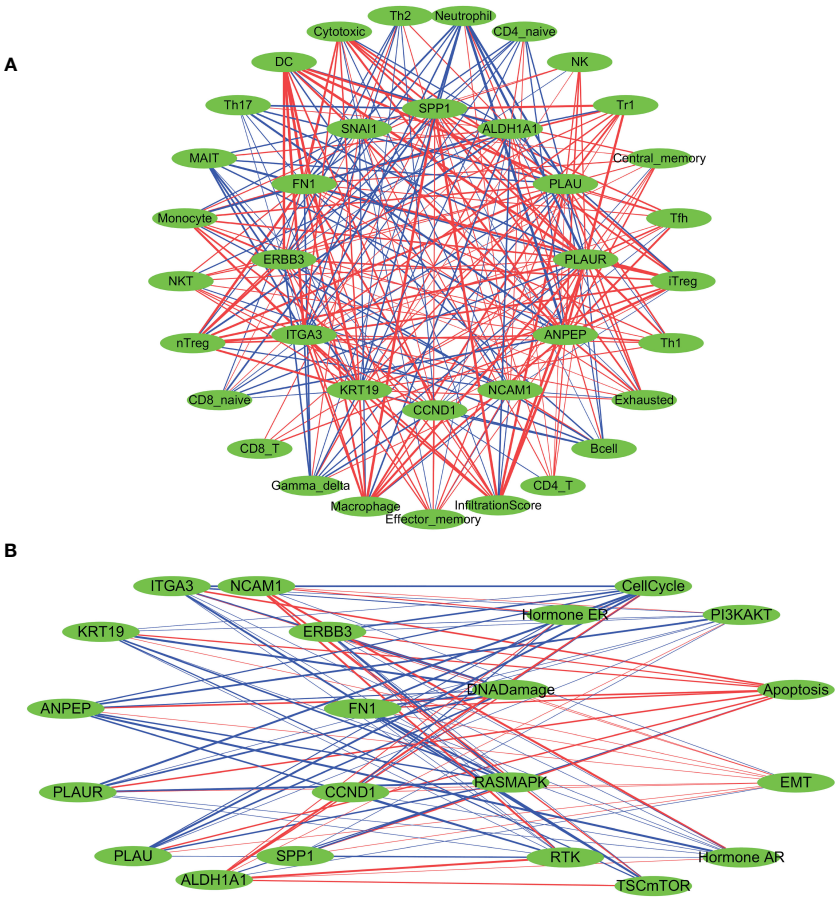

FIGURE 5
Spearman's correlation analysis was performed to evaluate the correlation between the expression levels of LNM potential-related hub genes and tumor immune cell infiltration **(A)**, as well as the ten cancer-related pathways **(B)**. The red lines indicate positive correlation, the blue lines indicate negative correlation, and the thickness of the lines represents the correlation coefficient.

value= 14.92, *p*-value<0.001; Figure 6F), whereas those within cluster 1 demonstrated a higher incidence of LNM (64%; chi-square test, chi-square value= 41.03, *p*-value<0.0001, Figure 6G).

Establishment of an online nomogram tool for improved clinical decision making

We constructed a nomogram based on the gene expression levels of 12 hub genes that serves to assess the LNM potential of THCA patients (Figure 7A). Establishment of the nomogram was executed using the rms R package. Performance assessment of the nomogram was conducted using decision curve analysis (DCA) (Figure 7B), receiver operating characteristic curve (ROC) (Figure 7C), and calibration curve (Figure 7D). Clinical utility of the nomogram was confirmed by DCA. Figure 7C demonstrated that the area under the ROC curve (AUC) of the nomogram incorporating all predictors for high-LNM potential patients was 0.816. The calibration curve's proximity to the ideal diagonal line was indicative of the good predictive performance of the nomogram. Furthermore, in order to further promote the accessibility and clinical utilization of our nomogram, it is noteworthy that an online web tool named "LNM potential" has been devised. The web address for this online tool is located at http://www.empowerstats.net/pmodel/?m=17617_LNM. By means of this online tool, the application of our research findings to the clinical setting may be further actualized. This tool contributes to the identification of THCA patients with a high LNM potential, providing a foundation for the development of individualized clinical treatment regimens.

Further exploration based on machine learning to identify key genes associated with LNM potential

Three machine learning methods (Lasso, Random forest, SVM) were employed to further screen key genes that could influence the LNM potential in patients with THCA from 12 hub genes (Figures 8A–C). ERBB3 was identified as being important for LNM potential in all three machine learning algorithms (Figure 8D). ERBB3 expression was upregulated in patients with high lymph node metastatic potential (LNM High) and ROC analysis indicated ERBB3 as a promising diagnostic biomarker for LNM High patients (Figures 8E, F).

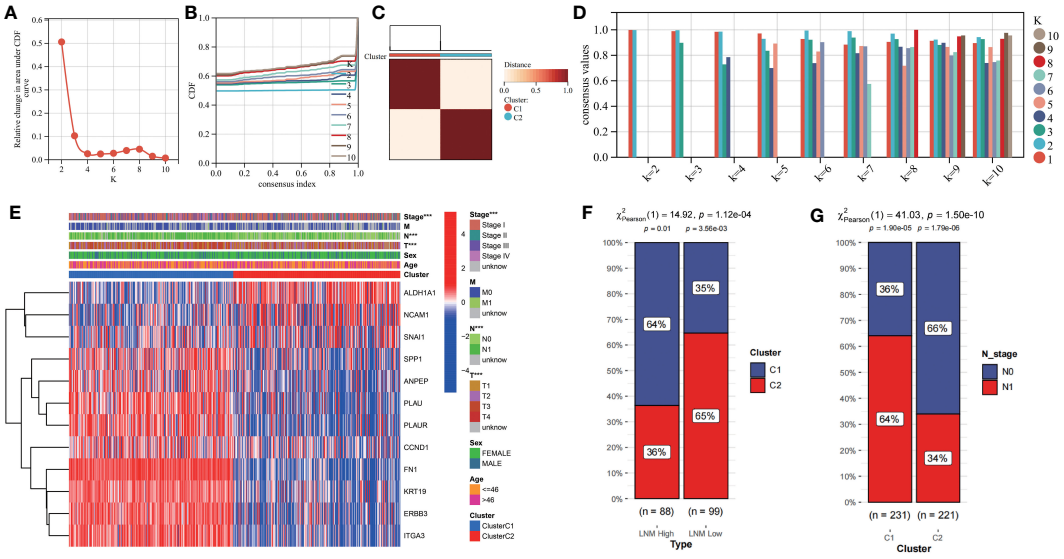

FIGURE 6
Constructing a novel molecular subtyping scheme using unsupervised clustering. **(A)** relative change in area under cumulative distribution function (CDF) curve. **(B)** Consensus clustering CDF for k=2-10. **(C)** Consensus matrix of THCA samples co-occurrence proportion for k = 2. **(D)** Cluster consensus values when K=1 to 10. **(E)** The expression levels of LNM potential-related hub genes between different clusters are shown in a heatmap. **(F)** The proportions ofpatients with high and low LNM potential in Cluster 1 and Cluster 2. **(G)** The proportions of patients with N0 and N1 staging in Cluster 1 and Cluster 2. ***: p<0.001.

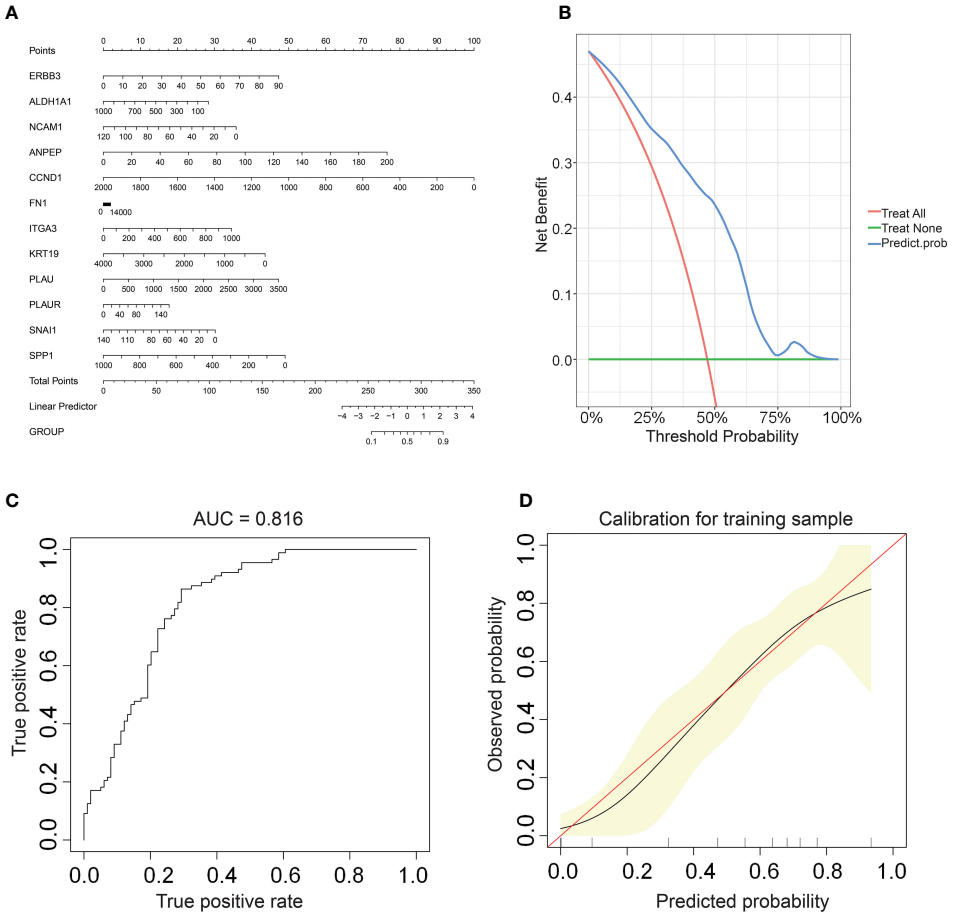

FIGURE 7
(A) A nomogram for predicting LNM potential in THCA. The DCA curve **(B)**, ROC curve **(C)**, and calibration curve **(D)** for the predictive nomogram.

10.3389/fendo.2023.1247709

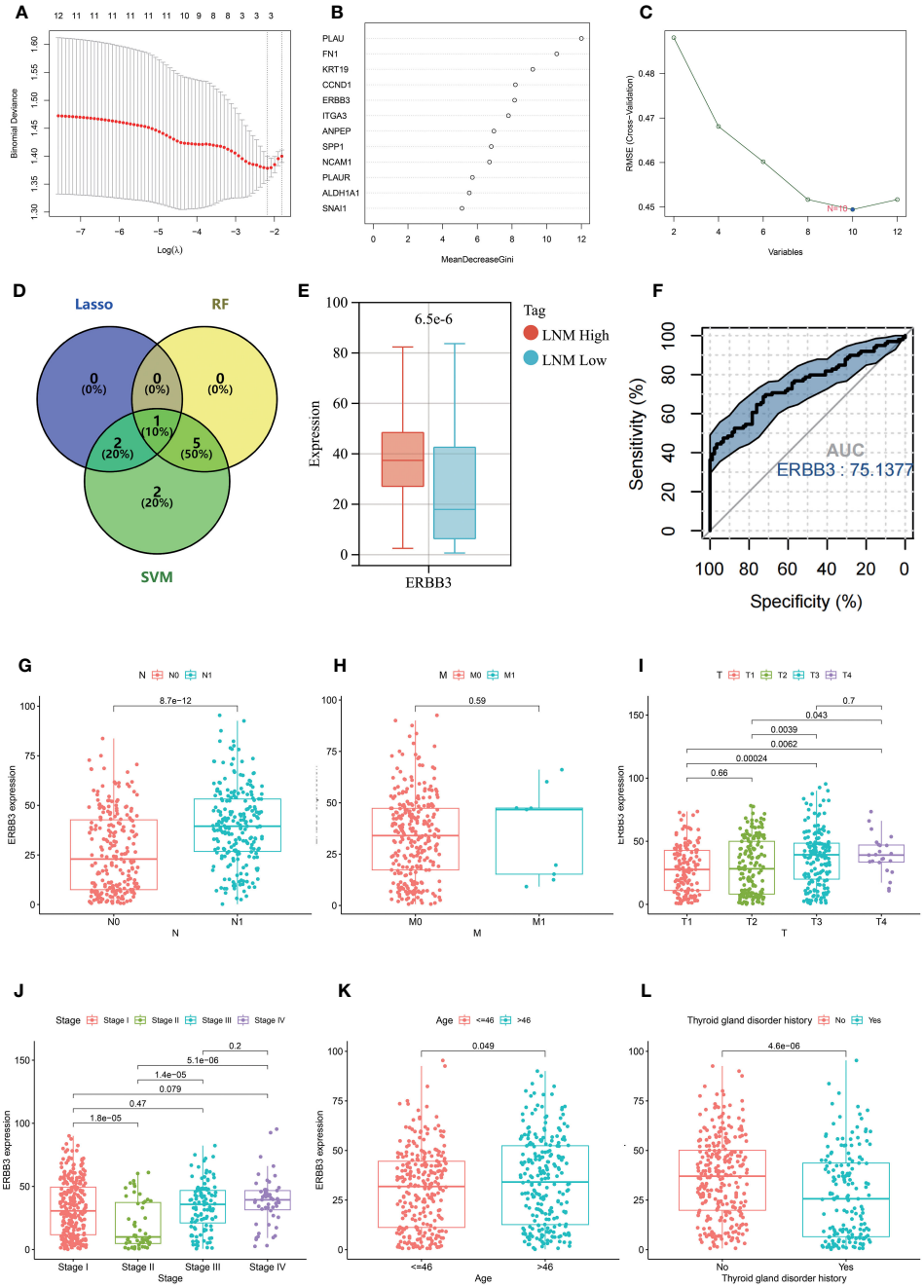

FIGURE 8
Results of selection by LASSO **(A)**, random forest **(B)**, and SVM **(C)**. **(D)** Venn diagram depicting the overlapping genes selected by LASSO, random forest, and SVM models. **(E)** The expression level of ERBB3 in individuals with different LNM potentials of THCA. **(F)** ROC analysis for the ability of ERBB3 to diagnose individuals with high LNM potentials of THCA. The expression level of ERBB3 has been examined in relation to different N stages **(G)**, M stages **(H)**, T stages **(I)**, tumor stages **(J)**, and ages **(K)**. **(L)** The gene expression levels of ERBB3 in patients with and without a history of Thyroid gland disorder.

The relationship between ERBB3 mRNA expression and DNA methylation levels with different clinical features

Further investigation was conducted to explore the association between ERBB3 and various clinical characteristics (Table 2). ERBB3 was significantly upregulated in THCA patients with lymph node metastasis as well as those with higher T stage, but there was no significant difference in ERBB3 expression between M0 and M1 patients (Figures 8G–I). Patients in Stage II had the lowest level of ERBB3 expression (Figure 8J). It is noteworthy that patients of older age or with a medical history of thyroid gland disorder exhibited a significant upregulation of ERBB3 mRNA levels (Figures 8K, L). In the TCGA-THCA cohort, the variables of Sex, primary neoplasm location, and number did not significantly perturb the expression level of ERBB3 (Supplementary Figures 4A–

C). ERBB3 has no impact on the complete surgical resection rate of THCA (Supplementary Figure 4D).

A pan-cancer analysis was conducted to investigate the DNA methylation levels of ERBB across various types of cancer (Supplementary Figure 5A). It was observed that the methylation levels of ERBB3 in the THCA samples were significantly lower than those in normal tissue, which partially explains the high expression of ERBB3 mRNA in THCA. The Shiny Methylation Analysis Resource Tool (SMART) was employed to annotate the methylation sites of ERBB3 (Supplementary Figures 5B, C). As anticipated, the methylation level of ERBB3 was notably higher in patients with low LNM potential, which could be a significant contributing factor impeding the expression level of ERBB3 mRNA in patients with low LNM potential (Supplementary Figure 5D; Table 3). Age and gender did not exhibit a significant effect on the degree of ERBB3 methylation (Supplementary Figure 5E). Patients who experienced LNM or were classified as T4 exhibited a diminished level of ERBB3 methylation, whereas stage II patients experienced an elevated amount of methylation. The occurrence of tumor metastasis, however, did not impact the degree of ERBB3 methylation (Supplementary Figures 5G–J). Furthermore, a tumor that develops in the isthmus or a patient with a history of thyroid gland disorder results in lower levels of ERBB3 methylation. The degree of ERBB3 methylation shows no significant correlation with the number of tumors or postoperative residual tumors (Supplementary Figures 5K–N).

Exploring EDCs, antineoplastic drugs, and environmental toxins that potentially influence the LNM potential

The thyroid gland is regarded as one of the most crucial endocrine organs. The endocrine system has been demonstrated to impact the metastasis and prognosis of various endocrine organ tumors. Hence, we aspire to investigate whether certain EDCs can

TABLE 2 Clinical information of patients with high and low ERBB3 mRNA expression levels.

Covariates	Type	Total	mRNA-High	mRNA-Low	Pvalue
Age	<=46	266(52.99%)	128(51%)	138(54.98%)	0.4209
	>46	236(47.01%)	123(49%)	113(45.02%)	
Sex	FEMALE	367(73.11%)	180(71.71%)	187(74.5%)	0.5459
	MALE	135(26.89%)	71(28.29%)	64(25.5%)	
Primary neoplasm	Multifocal	226(45.02%)	119(47.41%)	107(42.63%)	0.3618
	Unifocal	266(52.99%)	128(51%)	138(54.98%)	
	unknow	10(1.99%)	4(1.59%)	6(2.39%)	
T	T1	143(28.49%)	57(22.71%)	86(34.26%)	0
	T2	164(32.67%)	73(29.08%)	91(36.25%)	
	T3	170(33.86%)	103(41.04%)	67(26.69%)	
	T4	23(4.58%)	18(7.17%)	5(1.99%)	
	unknow	2(0.4%)	0(0%)	2(0.8%)	
N	N0	229(45.62%)	90(35.86%)	139(55.38%)	0
	N1	223(44.42%)	141(56.18%)	82(32.67%)	
	unknow	50(9.96%)	20(7.97%)	30(11.95%)	
M	M0	282(56.18%)	148(58.96%)	134(53.39%)	1
	M1	9(1.79%)	5(1.99%)	4(1.59%)	
	unknow	211(42.03%)	98(39.04%)	113(45.02%)	
Stage	Stage I	281(55.98%)	135(53.78%)	146(58.17%)	2.00E-04
	Stage II	52(10.36%)	16(6.37%)	36(14.34%)	
	Stage III	112(22.31%)	59(23.51%)	53(21.12%)	
	Stage IV	55(10.96%)	40(15.94%)	15(5.98%)	
	unknow	2(0.4%)	1(0.4%)	1(0.4%)	
Location	Bilateral	86(17.13%)	50(19.92%)	36(14.34%)	0.012

(Continued)

TABLE 2 Continued

Covariates	Type	Total	mRNA-High	mRNA-Low	Pvalue
	Isthmus	22(4.38%)	14(5.58%)	8(3.19%)	
	Left lobe	175(34.86%)	95(37.85%)	80(31.87%)	
	Right lobe	213(42.43%)	89(35.46%)	124(49.4%)	
	unknow	6(1.2%)	3(1.2%)	3(1.2%)	
Residual tumor	R0	384(76.49%)	185(73.71%)	199(79.28%)	0.1177
	R1	52(10.36%)	32(12.75%)	20(7.97%)	
	R2	4(0.8%)	3(1.2%)	1(0.4%)	
	unknow	62(12.35%)	31(12.35%)	31(12.35%)	
Thyroid gland disorder history	Yes	165(32.87%)	69(27.49%)	96(38.25%)	0.0069
	No	279(55.58%)	155(61.75%)	124(49.4%)	
	unknow	58(11.55%)	27(10.76%)	31(12.35%)	

TABLE 3 Clinical information of patients with high and low ERBB3 methylation levels.

Covariates	Type	Total	Methy-High	Methy-Low	Pvalue
Age	<=46	266(52.99%)	139(55.38%)	127(50.6%)	0.3253
	>46	236(47.01%)	112(44.62%)	124(49.4%)	
Sex	FEMALE	367(73.11%)	188(74.9%)	179(71.31%)	0.4207
	MALE	135(26.89%)	63(25.1%)	72(28.69%)	
Primary neoplasm	Multifocal	226(45.02%)	112(44.62%)	114(45.42%)	1
	Unifocal	266(52.99%)	132(52.59%)	134(53.39%)	
	unknow	10(1.99%)	7(2.79%)	3(1.2%)	
T	T1	143(28.49%)	80(31.87%)	63(25.1%)	0.0032
	T2	164(32.67%)	90(35.86%)	74(29.48%)	
	T3	170(33.86%)	74(29.48%)	96(38.25%)	
	T4	23(4.58%)	5(1.99%)	18(7.17%)	
	unknow	2(0.4%)	2(0.8%)	0(0%)	
N	N0	229(45.62%)	136(54.18%)	93(37.05%)	0
	N1	223(44.42%)	87(34.66%)	136(54.18%)	
	unknow	50(9.96%)	28(11.16%)	22(8.76%)	
M	M0	282(56.18%)	140(55.78%)	142(56.57%)	1
	M1	9(1.79%)	4(1.59%)	5(1.99%)	
	unknow	211(42.03%)	107(42.63%)	104(41.43%)	
Stage	Stage I	281(55.98%)	138(54.98%)	143(56.97%)	0.0011
	Stage II	52(10.36%)	37(14.74%)	15(5.98%)	
	Stage III	112(22.31%)	57(22.71%)	55(21.91%)	
	Stage IV	55(10.96%)	18(7.17%)	37(14.74%)	
	unknow	2(0.4%)	1(0.4%)	1(0.4%)	

(Continued)

TABLE 3 Continued

Covariates	Type	Total	Methy-High	Methy-Low	Pvalue
Location	Bilateral	86(17.13%)	44(17.53%)	42(16.73%)	0.2743
	Isthmus	22(4.38%)	7(2.79%)	15(5.98%)	
	Left lobe	175(34.86%)	85(33.86%)	90(35.86%)	
	Right lobe	213(42.43%)	113(45.02%)	100(39.84%)	
	unknow	6(1.2%)	2(0.8%)	4(1.59%)	
Residual tumor	R0	384(76.49%)	185(73.71%)	199(79.28%)	0.5754
	R1	52(10.36%)	23(9.16%)	29(11.55%)	
	R2	4(0.8%)	1(0.4%)	3(1.2%)	
	unknow	62(12.35%)	42(16.73%)	20(7.97%)	
Thyroid gland disorder history	Yes	165(32.87%)	100(39.84%)	65(25.9%)	0
	No	279(55.58%)	110(43.82%)	169(67.33%)	
	unknow	58(11.55%)	41(16.33%)	17(6.77%)	

impact the LNM potential of THCA. Our analysis of the CTD database revealed a potential interaction between 14 types of EDCs and the key gene ERBB3 that can affect ERBB3 mRNA expression, implying their indirect impact on the LNM potential of THCA. The 14 types of EDCs identified consist of Benzo(a)pyrene, bisphenol A, Estradiol, Genistein, Progesterone, Copper, Tamoxifen, Ethinyl Estradiol, Arsenic, Diethylstilbestrol, Androgen Antagonists, Cadmium, Raloxifene Hydrochloride, and Androgens (Supplementary Table 10).

Moreover, we have identified several antineoplastic drugs that are already in clinical use that can disturb the gene expression level of ERBB3. These drugs include Capecitabine, Doxorubicin, Epirubicin, Erlotinib Hydrochloride, Etoposide, Fluorouracil, Lapatinib, Mitomycin, and Paclitaxel (Supplementary Table 10). Therefore, we can speculate that these anticancer drugs may have the potential to reduce the LNM potential of THCA and could represent a potential therapeutic option for patients with thyroid cancer who have already undergone LNM. These findings will be further validated in the next chapter of this study.

Additionally, there are other drugs and environmental toxins that have been found to interact with ERBB3. Therefore, our study suggests that it would be beneficial for patients with THCA to avoid exposure to these toxins or use these drugs with caution, thereby contributing to the refinement of clinical care protocols (Supplementary Table 10).

Validation of the diagnostic capability of ERBB3 for THCA and LNM potential

In an independent validation set (GSE60542), we noted significant differential expression of 11 of the 12 previously identified hub genes, with the exception of ANPEP, between normal thyroid tissue and thyroid tumors (Supplementary Figure 6A). We noted a significant upregulation of ERBB3 expression in thyroid tumors in both the validation set and TCGA-THCA cohort. Furthermore, the immunohistochemical analysis revealed a significant elevation in protein expression levels of ERBB3 in thyroid tumors compared to normal thyroid tissue (Supplementary Figure 6B). In the GSE60542 cohort, our ROC analysis demonstrated that ERBB3 exhibits excellent discriminatory power for thyroid tumors (AUC=0.89; Supplementary Figure 6C). Notably, our results indicate a significant upregulation in ERBB3 expression levels in metastatic lymph nodes compared to normal lymphoid tissue (Supplementary Figure 6D). ERBB3 also exhibited excellent diagnostic efficacy for metastatic lymph nodes (Supplementary Figure 6E).

Exploration and validation of the therapeutic potential of ERBB3 in THCA

The subcellular localization of ERBB3 in tumor cells was investigated using ICC-IF and confocal microscopy techniques. ERBB3 was detected in the plasma membrane and actin filaments, and it is predicted to be secreted (Supplementary Figures 7A, B). The increased expression of ERBB3 in THCA, combined with its membrane localization, makes this protein an attractive target for cancer therapy.

Using the "oncoPredict" algorithm and the GDSC database, we evaluated the sensitivity of all tumor samples in TCGA-THCA to the anti-tumor drugs identified as potentially impacting LNM potential. Patients with high LNM potential and high expression of ERBB3 have lower half-maximal inhibitory concentrations (IC50) for Capecitabine, Doxorubicin, Epirubicin, Erlotinib Hydrochloride, Etoposide, Fluorouracil, Lapatinib, Mitomycin, and Paclitaxel, indicating increased sensitivity (Figures 9A, B).

To further verify the strong correlation between ERBB3 and these potential therapeutic drugs, we performed molecular docking of these drugs with ERBB3. The three-dimensional and two-dimensional conformations of the molecular docking between Capecitabine, Doxorubicin, Epirubicin, Erlotinib Hydrochloride,

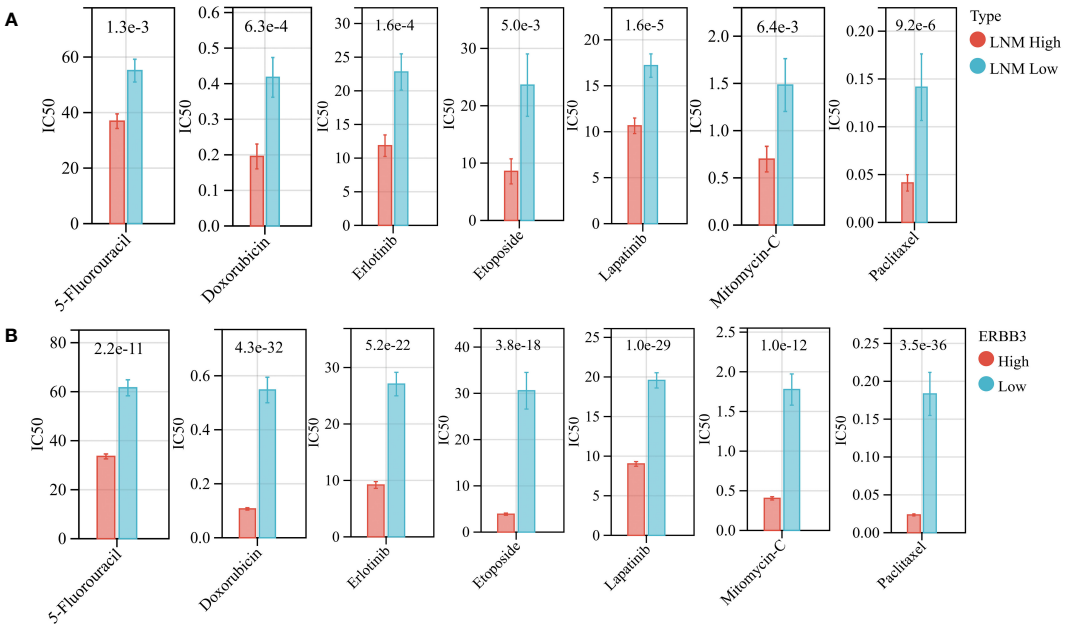

FIGURE 9
(A) The drug sensitivity of various anti-tumor drugs in patients with high and low LNM potential. **(B)** The drug sensitivity of various anti-tumor drugs in patients with high and low ERBB3 expression level.

Etoposide, Fluorouracil, Lapatinib, Mitomycin, and Paclitaxel with ERBB3 are shown in Figures 10A–G. The docking scores of Lapatinib, Etoposide, and Doxorubicin with ERBB3 are the most favorable, with values of -10.1 kcal/mol, -9.3 kcal/mol, and -8.8 kcal/mol, respectively.

We further conducted a meta-analysis to validate the therapeutic potential of Lapatinib in tumor patients with LNM. Since there is a scarcity of research studies on the therapeutic effects of Lapatinib in the treatment of thyroid cancer, we focused our investigation on endocrine-related tumors instead. A total of five clinical studies were collected (Supplementary Figure 8A) (67–70). The heterogeneity test result of the rates of achieving PCR between lapatinib combination therapy and monotherapy group was (Q=23.4, P=0.0001, I2 = 83%) and the combined value of the estimated effect was [RR=1.48, 95% CI (1.19, 1.86); P=0.0005]. The funnel plot presented is not suggestive of publication bias (Supplementary Figure 8B). Our meta-analysis indicates that the treatment regimen incorporating Lapatinib is more effective in achieving pathological complete response (PCR) in patients with LNM.

Experimental validation of expression levels of ERBB3 in THCA cases with and without LNM

Primarily, we observed a significant upregulation in the gene expression levels of ERBB3 in THCA samples that had experienced LNM through RT-qPCR experimental analysis (Supplementary Figure 9). Subsequently, our IHC results revealed that while ERBB3 protein was expressed in the cytoplasm of THCA cases without LNM, a significant increase in the expression levels of the ERBB3 protein was evident in THCA cases with LNM (Figure 11A). This was also quantified by the AOD values measured for different pathological slides, thus corroborating the findings (Figure 11B). Moreover, the ROC analysis indicated that the AOD values of ERBB3 protein immunohistochemical positive staining could serve as a promising diagnostic biomarker for determining the occurrence of lymph node metastasis in THCA cases (AUC=0.89, 95%CI 0.73-1.00; Figure 11C).

Discussion

LNM, particularly in the cervical region, is a common pathological feature encountered in THCA and may manifest in the early stages of the disease. In this study, we introduce a novel concept - LNM potential - aimed at elucidating the genetic basis of this phenomenon. Additionally, we employ a diverse range of bioinformatics analysis techniques, including WGCNA, machine learning, and molecular docking, to pinpoint the key gene underlying LNM potential and explore potentially therapeutic drugs targeting this gene.

Our study identified 12 hub genes as a potential high-risk biomarker for LNM in THCA. Simultaneously, we explored the association between the 12 hub genes and the biological processes and immune infiltration in THCA. Regardless of whether in THCA or pan-cancer, hub genes were significantly associated with the decrease of neutrophils and the increase of DC and macrophages in tumors. Considerable research has demonstrated the utility of neutrophil-to-lymphocyte ratio (NLR) in predicting lymph node metastasis in multiple types of cancer (71–74). The study conducted

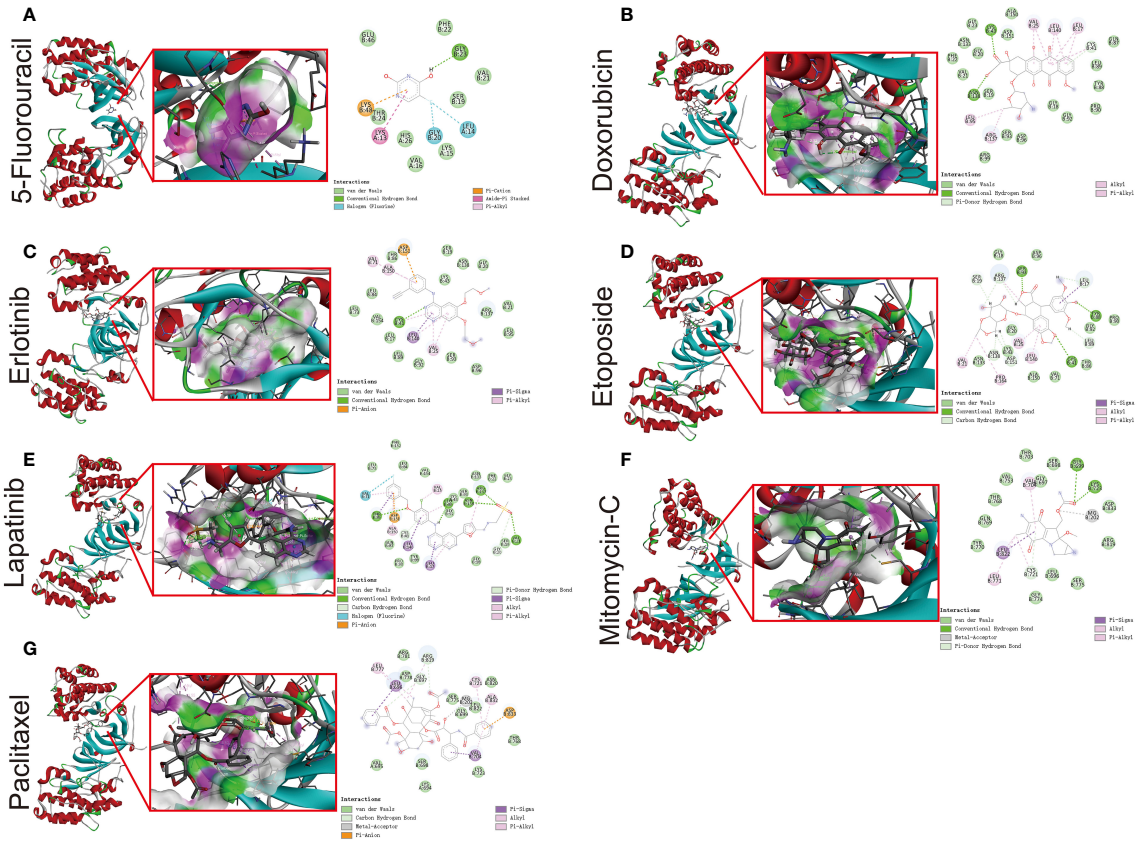

FIGURE 10
Molecular docking simulation between ERBB3 and 5-Fluorouracil **(A)**, Doxorubicin **(B)**, Erlotinib **(C)**, Etoposide **(D)**, Lapatinib **(E)**, Mitomycin-C **(F)**, and Paclitaxel **(G)**.

by Hiromu Fujita et al. revealed that the accumulation of neutrophils, especially CD16b-positive neutrophils, in the peritumoral region is an independent factor contributing to lymph node metastasis (75). Notably, the authors' research was centered on thoracic esophageal squamous cell carcinoma (75). The investigations undertaken by Yuandong Liao et al. demonstrate that STC1-dependent immune escape from macrophage phagocytosis can be suppressed by the inhibition of competitive interaction between LNMAS and HMGB1, resulting in the abrogation of TWIST1 and STC1 chromatin accessibility, thereby suppressing cervical cancer lymph node metastasis (76). DC cells, as professional antigen-presenting cells, are responsible for presenting cancer-associated antigens to the adaptive immune system in the sentinel lymph nodes (77, 78). It has been observed that sentinel lymph nodes with macrometastases in cancer patients exhibit arrested maturation of dendritic cells, fewer interactions between mature dendritic cells and cytotoxic T cells, and an increased population of regulatory T cells, as opposed to sentinel lymph nodes without metastasis. However, these observations were not made when compared to healthy controls (79). Therefore, the physiological basis for the influence of hub genes on the lymph node metastatic potential of THCA lies in the observed differences in immune cell infiltration associated with these hub genes, particularly in neutrophils, DC cells, and macrophages. However, it is important to note that this study is based on bioinformatics techniques for estimating immune cell infiltration within tumors. Further in-depth experiments, such as flow cytometry and immunofluorescence, are required for the validation of clinical samples. Additionally, it's worth mentioning that ITGA3, one of the 12 Hub genes we identified, has been found to serve as a biomarker of progression and recurrence in THCA (80). The results of the CCK-8 experiment conducted by Jizong Zhang et al. indicate that overexpression of ITGA3 significantly enhances the proliferation capability of thyroid cancer cell lines. Additionally, it markedly augments their invasive and migratory abilities (81).

It is worth noting that our pan-cancer analysis indicates a close correlation between the activation of these 12 hub genes and the oncological feature of EMT, a critical step in tumor invasion and metastasis (82). In particular, SNAI1 and FN1 were found to be positively correlated with EMT activation in more than half of the tumor types analyzed. Consistent with previous research, SNAI1 was identified as the first and most extensively studied transcription repressor of CDH1, a hallmark of EMT encoded by the epithelial gene encoding E-cadherin. Direct binding of SNAI1 to the E-boxes present in the CDH1 promoter leads to transcriptional repression of CDH1 expression (83). SNAI1 is an EMT regulatory factor that has been widely reported, which is consistent with our research findings. In cancer-associated EMT, SNAI1 serves as an imperative factor in driving the transition by strongly repressing E-cadherin and tight junction components (claudins), while also

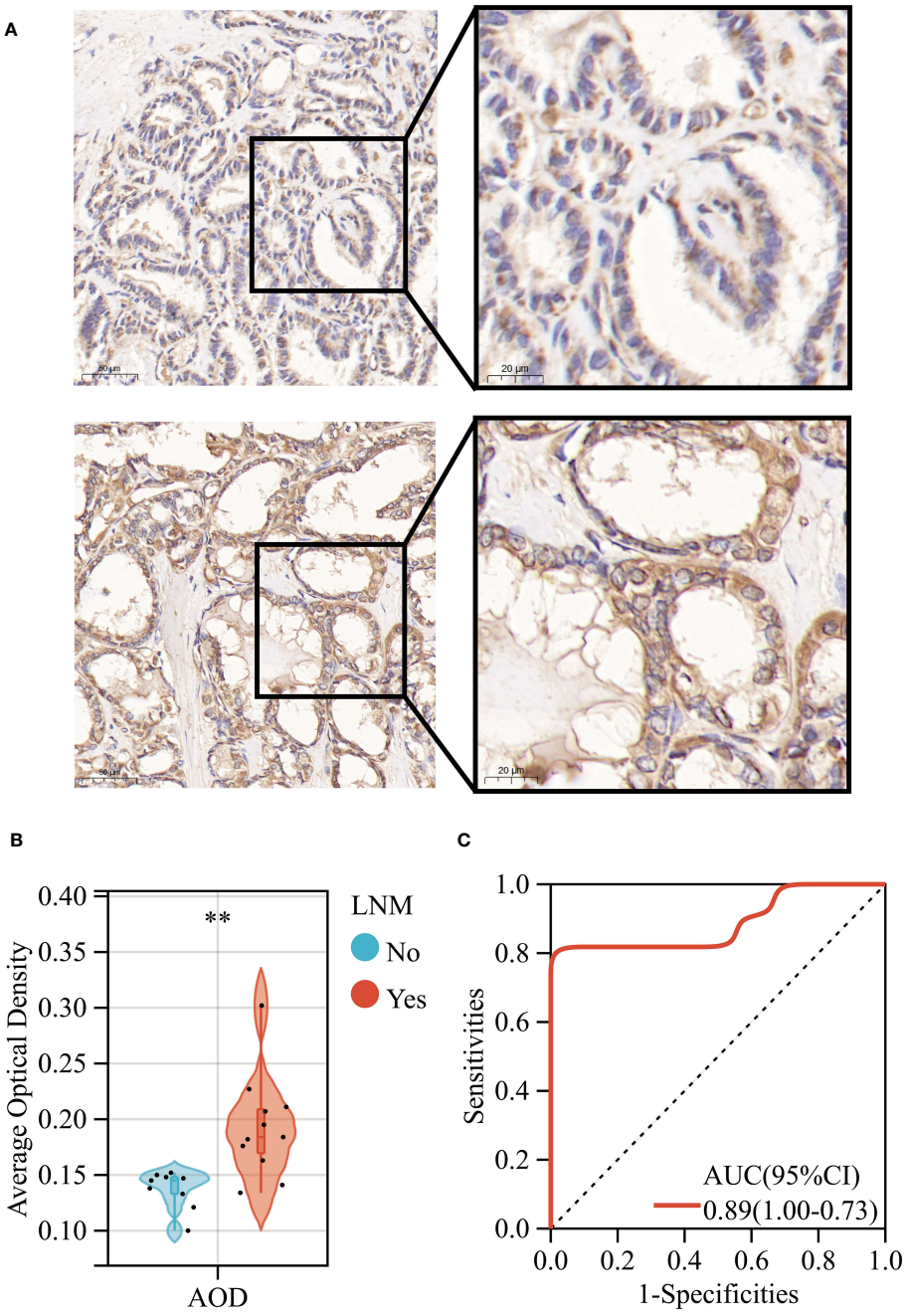

FIGURE 11
(A) Immunohistochemical expression levels of ERBB3 in THCA with (Lower) and without (Upper) lymph node metastasis. **(B)** AOD of ERBB3 protein immunohistochemical positive staining. **(C)** ROC curves of the AOD of ERBB3 protein for predicting LNM in THCA. **: $p<0.01$.

upregulating mesenchymal marker proteins, including vimentin and fibronectin (84). The study by Haihai Liang et al. revealed that knockdown of PTAL resulted in increased expression of miR-101 and consequent inhibition of FN1 expression, ultimately leading to upregulation of EMT, which in turn promoted the migration of OvCa cells (85). Thus, EMT represents another potential biological basis for the hub genes we have identified that can affect the LNM potential of THCA (86). In general, the identification of these hub genes provides a valuable and significant resource for further understanding and exploring the phenomenon of early LNM in THCA.

Furthermore, we have developed a nomogram capable of accurately predicting the likelihood of LNM in THCA patients. Additionally, we have established a web-based tool to access this nomogram's prediction model. The nomogram presented in this study can be easily utilized in clinical practice through our web-based tool, offering valuable resources and guidance for the formulation of clinical treatment and care strategies for THCA patients (87, 88).

Subsequently, employing an integrative analysis of three machine learning techniques, we identify ERBB3 as the key gene influencing LNM potential. ErbB/HER receptor tyrosine kinases (RTKs) occupy a crucial position in animal development, and their dysfunctional operation may catalyze the pathophysiological progression of certain tumor types (89, 90). In mammals, the existence of four ErbB/HER receptors is expounded: the epidermal growth factor receptor (EGFR/HER1), HER2/ErbB2/neu, HER3/ErbB3, and HER4/ErbB4 (91). Physiological expression of these receptors has been reported in epithelial, mesenchymal, cardiac, and neuronal tissues. The gene ERBB3 codes for HER3, a discovery credited to Kraus et al. in 1989 (92). Located on human chromosome 12q13, HER3 exhibits a wide expression across adult human tissues, including cells from the reproductive, endocrine, urinary, gastrointestinal, respiratory, skin, and nervous systems (93–96). Structurally, HER3 comprises an extensive extracellular domain (ECD), an individual hydrophobic transmembrane segment, and an intracellular domain, which comprises a tyrosine-rich carboxyterminal tail, a juxtamembrane region, and a tyrosine kinase segment (97–99). Featuring four subdomains, the HER3 extracellular domain is known as subdomains I-IV. ERBB3 expression has been discovered to be upregulated in numerous types of tumors, including but not limited to breast, ovarian, lung, colon, pancreatic, melanoma, gastric, head and neck, and prostate cancers (100–105). In additional reports, targeting ERBB3, such as gene knockdown and knockout, has also been shown to impact the proliferation and migration of thyroid cancer. This implies that targeting ERBB3 may become one of the potential therapeutic targets for thyroid cancer (106). Notably, there exists limited research on ERBB3 in THCA, and at present, no studies have reported the potential biological functions of ERBB3 in THCA lymph node metastasis.

The gene expression level of ERBB3 has been found to be associated with distinct clinical characteristics of THCA, particularly the occurrence of LNM. Aberrant methylation of the gene promoter is a significant cause of deactivation (107–109). To further investigate the underlying mechanisms of ERBB3 gene expression alterations, our attention was directed towards the variation in methylation levels of ERBB3. Notably, clinical traits associated with upregulation of ERBB3 mRNA expression were always accompanied by decreased levels of ERBB3 methylation, and vice versa. Hence, the downregulation of ERBB3 gene expression is partly attributed to CpG island hypermethylation in its promoter region (104, 110).

THCA belongs to endocrine tumors which arise from specialized cells responsible for hormone secretion. The migration of tumor cells, which is a prerequisite for the development of metastasis, has been demonstrated to be controlled by signaling molecules in the environment, including neuroendocrine hormones (111–113). Therefore, our study investigated some potential EDCs that may impact the LNM potential of THCA in an ERBB3-dependent manner. Some of the discovered EDCs are substances that individuals may come into contact with in their daily lives, including Benzo(a)pyrene, bisphenol A, and copper; while others are drugs that may be used in the clinic, such as Estradiol, Tamoxifen, and Raloxifene Hydrochloride (114–119). Therefore, it may be necessary for THCA patients to avoid exposure to these substances or drugs in their daily lives.

We further discovered, via the CTD database, that 7 anti-tumor drugs have the potential to interact with ERBB3 and impact its gene expression levels (56). Subsequently, we utilized multiple techniques to validate these findings. Initially, the GDSC database indicated that ERBB3 serves as a biomarker for the sensitivity of these anti-tumor drugs (58). Further molecular docking validation revealed the binding affinity between these drugs and ERBB3 (120). Among these drugs, Lapatinib, Etoposide, and Doxorubicin displayed the strongest binding affinity with ERBB3, especially Lapatinib. Furthermore, our study suggests that THCA patients with high LNM potential may benefit more from Lapatinib, a finding that has not been previously documented in the literature. Additionally, we conducted a meta-analysis that demonstrated combination regimens containing Lapatinib to have better therapeutic efficacy for late-stage endocrine tumors with lymph node metastasis. Certainly, the physiological basis for targeting the ERBB3 protein is supported by its significant upregulation in THCA tumors and lymph nodes with metastasis (121). Additionally, subcellular structural analysis using immunofluorescence indicates that ERBB3 is primarily enriched on the cell membrane. It is well-known that more than 60% of all drug targets are membrane proteins, which is also one of the bases for ERBB3 to become a therapeutic target (122). Although no studies have been conducted in THCA, a randomized controlled study by Alexandra Leary et al. suggests that Lapatinib has antiproliferative effects in a subgroup of nonamplified breast tumors characterized by high HER3 expression. It is worth investigating the potential role of high HER2:HER3 heterodimers in predicting response to lapatinib (123). Very few studies have explored the role of lapatinib in thyroid cancer treatment. Koichi Ohno's research discovered that the combined use of lapatinib and lenvatinib significantly inhibits the growth of TPC-1/LR (a drug-resistant thyroid cancer cell line) *in vitro* and in a xenograft mouse model (124). Lingxiao Cheng's study suggests that the addition of lapatinib results in more pronounced changes in iodine and glucose regulation gene expression, sodium-iodine symporter membrane localization, radioactive iodine uptake, and cytotoxicity in thyroid cancer cells, indicating a more significant redifferentiation effect on thyroid cancer cells (125). Furthermore, due to the scarcity of reports about the role of lapatinib in thyroid cancer treatment, our investigation into lapatinib is also one of the novelty of this study. Therefore, our study proposes a potential therapeutic agent and target for THCA treatment, which requires further mechanism research to corroborate.

To validate the gene and protein expression levels of ERBB3 in THCA cases with or without LNM, we conducted RT-qPCR and IHC experiments. Encouragingly, our findings were consistent with the bioinformatic analysis we previously performed. Concurrently, we identified a quantitative index of IHC staining, AOD, which could serve as a diagnostic biomarker for determining the occurrence of lymph node metastasis in THCA cases. Remarkably, the AOD value exhibited satisfactory performance in the ROC analysis. Therefore, our IHC findings for ERBB3 in THCA cases indicate that it could serve as a useful auxiliary diagnostic tool.

Furthermore, ERBB3 is significantly upregulated in lymph nodes that have undergone tumor metastasis compared to normal lymph nodes. Therefore, ERBB3 has the potential to assist pathologists in discriminating lymph nodes invaded by tumors. For LNM to occur, tumor cells must flow or settle in the marginal sinus of the lymph nodes (126–128). To detect cancer metastasis in the lymph nodes, pathologists need to search for tumor cells in the marginal sinus through multiple sections and tissue samples (129). However, confirming micro-metastases in some lymph nodes can be challenging (130). Therefore, determining whether lymph nodes have been invaded by tumors using ERBB3 as a marker could aid in the precise clinical staging of cancer.

This study has constructed several tools that can be further optimized and utilized in future clinical practice. Firstly, we have developed a novel molecular subtyping scheme that can preliminarily assess the tumor's ability to develop LNM at the genetic level. Furthermore, we have built an online nomogram tool that can conveniently calculate the probability of LNM occurrence in different THCA patients based on our research. This tool can be used alongside the development of clinical treatment plans, taking into consideration the scores obtained from the online nomogram tool. In addition, our research has provided new evidence for future pathological precision diagnosis. Specifically, it suggests that ERBB3 positivity has the potential to assist in diagnosing lymph nodes that have already experienced THCA metastasis. This also presents a novel approach to confirming micro-metastases in some lymph nodes at the early stages of the disease.

In summary, we performed comprehensive analysis of THCA patients with different LNM potentials using multiple bioinformatic techniques. We explored the activities of different pathways and identified key genes that affect LNM potential. Additionally, we also screened potential therapeutic drugs and targets for THCA. Our study provides useful resources and new perspectives for the development and optimization of clinical treatment plans for THCA patients in the future. However, there are also limitations to our study. Firstly, although we utilized multiple datasets for exploration and validation, the lack of *in vivo* and *in vitro* experiments restricts the understanding of underlying mechanisms. Additionally, our study is akin to a retrospective analysis, and the conclusions drawn require further validation from prospective studies with larger sample sizes.

Conclusion

Utilizing multiple bioinformatics analysis techniques, we have investigated differences in pathway activation and immune infiltration among THCA patients with varying LNM potential. Our analysis using WGCNA has revealed two gene modules that influence LNM potential, with a total of 12 genes identified as hub genes significantly impacting LNM potential. These hub genes primarily affect the infiltration levels of neutrophils, DC cells, and macrophages, as well as the activation of the EMT pathway in THCA. Employing multiple machine learning algorithms, we have identified ERBB3 as a key gene associated with LNM potential. We have observed that ERBB3 is upregulated in THCA patients with LNM and advanced THCA, and this upregulation may be attributed to changes in the methylation status of ERBB3. The interaction between ERBB3 and Lapatinib may present a potential therapeutic target for thyroid carcinoma patients who develop lymph node metastasis. Furthermore, we have developed a novel and user-friendly web-based tool (http://www.empowerstats.net/pmodel/?m=17617_LNM) that utilizes a nomogram to assess the potential for LNM in THCA patients. Our study lays the foundation for future investigations into the underlying mechanisms driving differences in lymph node metastatic potential among cases of thyroid carcinoma. Therefore, our findings provide valuable resources and guidance for the development of personalized clinical treatment plans for patients with this disease.

Data availability statement

Publicly available datasets were analyzed in this study. This data can be found here: TCGA (https://portal.gdc.cancer.gov/projects/TCGA-THCA) and GEO database (https://www.ncbi.nlm.nih.gov/geo/).

Ethics statement

The studies involving human participants were reviewed and approved by the Ethics Committees of the Third Affiliated Hospital of Anhui Medical University. The patients/participants provided their written informed consent to participate in this study. Written informed consent was obtained from the individual(s) for the publication of any potentially identifiable images or data included in this article.

Author contributions

Conceptualization, YL. Data curation, ZY. Formal analysis, YL. Investigation, YL, WY and HC. Methodology, YL. Resources, ZY. Supervision, HC. Validation, WY and HC. Writing – original draft, YL and WY. Writing – review & editing, HC. All authors contributed to the article and approved the submitted version.

Acknowledgments

The authors thank the Department of Pathology, The Third Affiliated Hospital of Anhui Medical University, for the technical advice on RT-qPCR and IHC.

Conflict of interest

The authors declare that the research was conducted in the absence of any commercial or financial relationships that could be construed as a potential conflict of interest.

Publisher's note

Supplementary material

The Supplementary Material for this article can be found online at: https://www.frontiersin.org/articles/10.3389/fendo.2023.1247709/full#supplementary-material

SUPPLEMENTARY FIGURE 1
Enrichment analysis results for up- **(A)** and down-regulated **(B)** genes in THCA. Distinctive patterns in immune infiltration **(C)** and cancer-related pathway activation **(D)** in THCA patients, stratified by high or low LNM potentials.

SUPPLEMENTARY FIGURE 2
(A) Chromosomal locations of DEGs in normal thyroid and THCA. **(B)** A heatmap of inter-module distances between different gene modules. Correlation between module membership (MM) and gene significance (GS) for blue **(C)**, pink **(D)**, black **(E)**, purple **(F)**, magenta **(G)**, and green **(H)** gene modules.

SUPPLEMENTARY FIGURE 3
Sample was classified as either CNV-Amp, CNV-Del, or SNV-Mutant based on the occurrence of a CNV or SNV alteration in at least one of the identified LNM potential-related hub genes. A volcano plot reveals significant differences in immune cell infiltration between THCA patients with CNV **(A)** and SNV alterations **(B)** relative to the wild-type group. **(C)** Assessing the correlation between the GSVA scores of LNM potential-related hub genes and immune cell infiltrate levels in types of cancer, including THCA **(D)**, using Spearman's correlation analysis. **(E)** Summary of the correlations between GSVA score and cancer-related pathway activity among 33 cancer types. (*: *p* value <= 0.05; #: FDR <= 0.05).

SUPPLEMENTARY FIGURE 4
Expression of ERBB3 in THCA patients differentiated by gender **(A)**, site of occurrence **(B)**, number of primary tumors **(C)**, and extent of surgical resection **(D)**.

SUPPLEMENTARY FIGURE 5
(A) Methylation levels of ERBB3 in tumor specimens compared to their corresponding normal tissues among 33 cancer types. The position of CpG islands **(B)** and CpG sites **(C)** of ERBB3 used for DNA methylation analyses. Methylation levels of ERBB3 in THCA patients with different LNM potential **(D)**, age **(E)**, gender **(F)**, N **(G)**/M **(H)**/T **(I)** staging, tumor stage **(J)**, tumor location **(K)**, number of primary tumors (L), extent of surgical resection **(M)**, and history of thyroid gland disorder **(N)**.

SUPPLEMENTARY FIGURE 6
(A) Expression levels of LNM potential related-hub genes in primary THCA and normal thyroid tissues in the GSE60542 cohort. **(B)** Protein expression levels of ERBB3 in primary THCA and normal thyroid tissues. **(C)** ROC analysis of ERBB3 for diagnosis in primary THCA and normal thyroid tissues in the GSE60542 cohort. **(D)** Gene expression levels of ERBB3 in normal lymph nodes and lymph nodes with metastatic tumors. **(E)** ROC analysis of ERBB3 for diagnosis in lymph nodes with metastatic tumors.

SUPPLEMENTARY FIGURE 7
(A) Subcellular localization of ERBB3 protein in various tumor cells. **(B)** Schematic representation of subcellular localization of ERBB3 protein in tumor cells.

SUPPLEMENTARY FIGURE 8
(A) Meta-analysis validates the efficacy of combined treatment regimen with Lapatinib in advanced endocrine organ tumors with lymph node metastasis. **(B)** Assessment of publication bias via funnel plot analysis.

SUPPLEMENTARY FIGURE 9
qRT-PCR verification of expression of ERBB3 in THCA with (Yes) and without (No) lymph node metastasis (***: $p<0.001$).

References

1. Sanabria A, Kowalski LP, Shah JP, Nixon IJ, Angelos P, Williams MD, et al. Growing incidence of thyroid carcinoma in recent years: Factors underlying overdiagnosis. *Head Neck* (2018) 40(4):855–66. doi: 10.1002/hed.25029

2. LiVolsi VA. Papillary thyroid carcinoma: an update. *Mod Pathol* (2011) 24 Suppl 2:S1–9. doi: 10.1038/modpathol.2010.129

3. Jensen K, Patel A, Hoperia V, Larin A, Bauer A, Vasko V. Dynamic changes in E-cadherin gene promoter methylation during metastatic progression in papillary thyroid cancer. *Exp Ther Med* (2010) 1(3):457–62. doi: 10.3892/etm_00000071

4. Zhang LY, Chen Y, Ao YZ. Value of thyroglobulin combined with ultrasound-guided fine-needle aspiration cytology for diagnosis of lymph node metastasis of thyroid carcinoma. *World J Clin Cases* (2022) 10(2):492–501. doi: 10.12998/wjcc.v10.i2.492

5. Mao J, Zhang Q, Zhang H, Zheng K, Wang R, Wang G. Risk factors for lymph node metastasis in papillary thyroid carcinoma: A systematic review and meta-analysis. *Front Endocrinol (Lausanne)* (2020) 11:265. doi: 10.3389/fendo.2020.00265

6. Lo CY. Lymph node dissection for papillary thyroid carcinoma. *Methods Mol Biol* (2022) 2534:57–78. doi: 10.1007/978-1-0716-2505-7_5

7. He Y, Pan MZ, Huang JM, Xie P, Zhang F, Wei LG. Iodine-131: an effective method for treating lymph node metastases of differentiated thyroid cancer. *Med Sci Monit* (2016) 22:4924–8. doi: 10.12659/MSM.899028

8. Czarniecka A, Jarzab M, Krajewska J, Chmielik E, Szcześniak-Klusek B, Stobiecka E, et al. Prognostic value of lymph node metastases of differentiated thyroid cancer (DTC) according to the local advancement and range of surgical excision. *Thyroid Res* (2010) 3:8. doi: 10.1186/1756-6614-3-8

9. Pino A, Mazzeo C, Frattini F, Zhang D, Wu CW, Zanghì G, et al. Lymph node dissection morbidity in thyroid cancer: an integrative review. *Sisli Etfal Hastan Tip Bul* (2021) 55:433–7. doi: 10.14744/SEMB.2021.33401

10. Liu C, Xiao C, Chen J, Li X, Feng Z, Gao Q, et al. Risk factor analysis for predicting cervical lymph node metastasis in papillary thyroid carcinoma: a study of 966 patients. *BMC Cancer* (2019) 19(1):622. doi: 10.1186/s12885-019-5835-6

11. Wang Y, Deng C, Shu X, Yu P, Wang H, Su X, et al. Risk factors and a prediction model of lateral lymph node metastasis in CN0 papillary thyroid carcinoma patients with 1-2 central lymph node metastases. *Front Endocrinol (Lausanne)* (2021) 12:716728. doi: 10.3389/fendo.2021.716728

12. Guang Y, He W, Zhang W, Zhang H, Zhang Y, Wan F. Clinical study of ultrasonographic risk factors for central lymph node metastasis of papillary thyroid carcinoma. *Front Endocrinol (Lausanne)* (2021) 12:791970. doi: 10.3389/fendo.2021.791970

13. Ruiz EML, Niu T, Zerfaoui M, Kunnimalaiyaan M, Friedlander PL, Abdel-Mageed AB, et al. A novel gene panel for prediction of lymph-node metastasis and recurrence in patients with thyroid cancer. *Surgery* (2020) 167(1):73–9. doi: 10.1016/j.surg.2019.06.058

14. Zhang Q, Li J, Shen H, Bai X, Zhang T, Liu P. Screening and validation of lymph node metastasis risk-factor genes in papillary thyroid carcinoma. *Front Endocrinol (Lausanne)* (2022) 13:991906. doi: 10.3389/fendo.2022.991906

15. Huang C, Su X, Zhou DL, Xu BH, Liu Q, Zhang X, et al. A diagnostic and predictive lncRNA lnc-MPEG1-1 promotes the proliferation and metastasis of papillary thyroid cancer cells by occupying miR-766-5p. *Mol Ther Nucleic Acids* (2022) 28:408–22. doi: 10.1016/j.omtn.2022.03.023

16. Wei M, Wang R, Zhang W, Zhang J, Fang Q, Fang Z, et al. Landscape of gene mutation in Chinese thyroid cancer patients: Construction and validation of lymph node metastasis prediction model based on clinical features and gene mutation marker. *Cancer Med* (2023) 12(11):12929–42. doi: 10.1002/cam4.5945

17. Feng Y, Min Y, Chen H, Xiang K, Wang X, Yin G. Construction and validation of a nomogram for predicting cervical lymph node metastasis in classic papillary thyroid

carcinoma. *J Endocrinol Invest* (2021) 44(10):2203–11. doi: 10.1007/s40618-021-01524-5

18. Gao L, Li X, Xia Y, Liu R, Liu C, Shi X, et al. Large-volume lateral lymph node metastasis predicts worse prognosis in papillary thyroid carcinoma patients with N1b. *Front Endocrinol (Lausanne)* (2021) 12:815207. doi: 10.3389/fendo.2021.815207

19. Alwadi D, Felty Q, Yoo C, Roy D, Deoraj A. Endocrine disrupting chemicals influence hub genes associated with aggressive prostate cancer. *Int J Mol Sci* (2023) 24 (4):3191. doi: 10.3390/ijms24043191

20. Yilmaz B, Terekeci H, Sandal S, Kelestimur F. Endocrine disrupting chemicals: exposure, effects on human health, mechanism of action, models for testing and strategies for prevention. *Rev Endocr Metab Disord* (2020) 21(1):127–47. doi: 10.1007/s11154-019-09521-z

21. Kim H, Kim HS, Piao YJ, Moon WK. Bisphenol A promotes the invasive and metastatic potential of ductal carcinoma *in situ* and protumorigenic polarization of macrophages. *Toxicol Sci* (2019) 170(2):283–95. doi: 10.1093/toxsci/kfz119

22. Jordan VC. Fourteenth Gaddum Memorial Lecture. A current view of tamoxifen for the treatment and prevention of breast cancer. *Br J Pharmacol* (1993) 110 (2):507–17.

23. Alsen M, Sinclair C, Cooke P, Ziadkhanpour K, Genden E, van Gerwen M. Endocrine disrupting chemicals and thyroid cancer: an overview. *Toxics* (2021) 9:14. doi: 10.3390/toxics9010014

24. Li L, Ying Y, Zhang C, Wang W, Li Y, Feng Y, et al. Bisphenol A exposure and risk of thyroid nodules in Chinese women: A case-control study. *Environ Int* (2019) 126:321–8. doi: 10.1016/j.envint.2019.02.026

25. Boas M, Feldt-Rasmussen U, Main KM. Thyroid effects of endocrine disrupting chemicals. *Mol Cell Endocrinol* (2012) 355:240–8. doi: 10.1016/j.mce.2011.09.005

26. Reuter JA, Spacek DV, Snyder MP. High-throughput sequencing technologies. *Mol Cell* (2015) 58(4):586–97. doi: 10.1016/j.molcel.2015.05.004

27. Wajnberg G, Passetti F. Using high-throughput sequencing transcriptome data for INDEL detection: challenges for cancer drug discovery. *Expert Opin Drug Discov* (2016) 11(3):257–68. doi: 10.1517/17460441.2016.1143813

28. Xu J, Liao K, Yang X, Wu C, Wu W. Using single-cell sequencing technology to detect circulating tumor cells in solid tumors. *Mol Cancer* (2021) 20(1):104. doi: 10.1186/s12943-021-01392-w

29. Chen H, Liu Y, Yin Z, Chen H, Wang Y, Qian Y. Homologous repair deficiency-associated genes in invasive breast cancer revealed by WGCNA co-expression network analysis and genetic perturbation similarity analysis. *Cell Cycle* (2023) 22(9):1077–100. doi: 10.1080/15384101.2023.2174339

30. Chen H, Zhang J, Sun X, Wang Y, Qian Y. Mitophagy-mediated molecular subtypes depict the hallmarks of the tumor metabolism and guide precision chemotherapy in pancreatic adenocarcinoma. *Front Cell Dev Biol* (2022) 10:901207. doi: 10.3389/fcell.2022.901207

31. Wang Y, Sun J, Yang Y, Zebaze Dongmo S, Qian Y, Wang Z. Identification and development of subtypes with poor prognosis in gastric cancer based on both hypoxia and immune cell infiltration. *Int J Gen Med* (2021) 14:9379–99. doi: 10.2147/IJGM.S326647

32. Wang Y, Wang Z, Sun J, Qian Y. Identification of HCC subtypes with different prognosis and metabolic patterns based on mitophagy. *Front Cell Dev Biol* (2021) 9:799507. doi: 10.3389/fcell.2021.799507

33. Tomczak K, Czerwińska P, Wiznerowicz M. The Cancer Genome Atlas (TCGA): an immeasurable source of knowledge. *Contemp Oncol (Pozn)* (2015) 19(1A):A68–77. doi: 10.5114/wo.2014.47136

34. Clough E, Barrett T. The gene expression omnibus database. *Methods Mol Biol* (2016) 1418:93–110. doi: 10.1007/978-1-4939-3578-9_5

35. Tang Z, Li C, Kang B, Gao G, Li C, Zhang Z. GEPIA: a web server for cancer and normal gene expression profiling and interactive analyses. *Nucleic Acids Res* (2017) 45 (W1):W98–W102. doi: 10.1093/nar/gkx247

36. Langfelder P, Horvath S. WGCNA: an R package for weighted correlation network analysis. *BMC Bioinf* (2008) 9:559. doi: 10.1186/1471-2105-9-559

37. Szklarczyk D, Gable AL, Nastou KC, Lyon D, Kirsch R, Pyysalo S, et al. The STRING database in 2021: customizable protein-protein networks, and functional characterization of user-uploaded gene/measurement sets. *Nucleic Acids Res* (2021) 49 (D1):D605–12. doi: 10.1093/nar/gkaa1074

38. Tang Y, Li M, Wang J, Pan Y, Wu FX. CytoNCA: a cytoscape plugin for centrality analysis and evaluation of protein interaction networks. *Biosystems* (2015) 127:67–72. doi: 10.1016/j.biosystems.2014.11.005

39. Zhou G, Soufan O, Ewald J, Hancock R, Basu N, Xia J. NetworkAnalyst 3.0: a visual analytics platform for comprehensive gene expression profiling and meta-analysis. *Nucleic Acids Res* (2019) 47(W1):W234–41. doi: 10.1093/nar/gkz240

40. Jou J, Gabdank I, Luo Y, Lin K, Sud P, Myers Z, et al. The ENCODE portal as an epigenomics resource. *Curr Protoc Bioinf* (2019) 68(1):e89. doi: 10.1002/cpbi.89

41. Huang HY, Lin YC, Li J, Huang KY, Shrestha S, Hong HC, et al. miRTarBase 2020: updates to the experimentally validated microRNA-target interaction database. *Nucleic Acids Res* (2020) 48(D1):D148–54. doi: 10.1093/nar/gkz896

42. Liu ZP, Wu C, Miao H, Wu H. RegNetwork: an integrated database of transcriptional and post-transcriptional regulatory networks in human and mouse. *Database (Oxford)* (2015) 2015:bav095. doi: 10.1093/database/bav095

43. Zhou Y, Zhou B, Pache L, Chang M, Khodabakhshi AH, Tanaseichuk O, et al. Metascape provides a biologist-oriented resource for the analysis of systems-level datasets. *Nat Commun* (2019) 10(1):1523. doi: 10.1038/s41467-019-09234-6

44. Hänzelmann S, Castelo R, Guinney J. GSVA: gene set variation analysis for microarray and RNA-seq data. *BMC Bioinf* (2013) 14:7. doi: 10.1186/1471-2105-14-7

45. Chen MM, Li J, Wang Y, Akbani R, Lu Y, Mills GB, et al. TCPA v3.0: an integrative platform to explore the pan-cancer analysis of functional proteomic data. *Mol Cell Proteomics* (2019) 18(8 suppl 1):S15–25. doi: 10.1074/mcp.RA118.001260

46. Labrie M, Fang Y, Kendsersky ND, Li J, Liang H, Westin SN, et al. Using reverse phase protein array (RPPA) to identify and target adaptive resistance. *Adv Exp Med Biol* (2019) 1188:251–66. doi: 10.1007/978-981-32-9755-5_14

47. Liu CJ, Hu FF, Xie GY, Miao YR, Li XW, Zeng Y, et al. GSCA: an integrated platform for gene set cancer analysis at genomic, pharmacogenomic and immunogenomic levels. *Brief Bioinform* (2023) 24(1):bbac558. doi: 10.1093/bib/bbac558

48. Miao YR, Zhang Q, Lei Q, Luo M, Xie GY, Wang H, et al. ImmuCellAI: A unique method for comprehensive T-cell subsets abundance prediction and its application in cancer immunotherapy. *Adv Sci (Weinh)* (2020) 7(7):1902880. doi: 10.1002/advs.201902880

49. Wilkerson MD, Hayes DN. ConsensusClusterPlus: a class discovery tool with confidence assessments and item tracking. *Bioinformatics* (2010) 26(12):1572–3. doi: 10.1093/bioinformatics/btq170

50. Kang J, Choi YJ, Kim IK, Lee HS, Kim H, Baik SH, et al. LASSO-based machine learning algorithm for prediction of lymph node metastasis in T1 colorectal cancer. *Cancer Res Treat* (2021) 53(3):773–83. doi: 10.4143/crt.2020.974

51. Feng Y, Yan X. Support vector machine based lane-changing behavior recognition and lateral trajectory prediction. *Comput Intell Neurosci* (2022) 2022:3632333. doi: 10.1155/2022/3632333

52. Rigatti SJ. Random forest. *J Insur Med* (2017) 47(1):31–9. doi: 10.17849/insm-47-01-31-39.1

53. Engebretsen S, Bohlin J. Statistical predictions with glmnet. *Clin Epigenetics* (2019) 11(1):123. doi: 10.1186/s13148-019-0730-1

54. Xu N, Guo H, Li X, Zhao Q, Li J. A five-genes based diagnostic signature for sepsis-induced ARDS. *Pathol Oncol Res* (2021) 27:580801. doi: 10.3389/pore.2021.580801

55. Li S, Que Y, Yang R, He P, Xu S, Hu Y. Construction of osteosarcoma diagnosis model by random forest and artificial neural network. *J Pers Med* (2023) 13(3):447. doi: 10.3390/jpm13030447

56. Davis AP, Grondin CJ, Johnson RJ, Sciaky D, Wiegers J, Wiegers TC, et al. Comparative toxicogenomics database (CTD): update 2021. *Nucleic Acids Res* (2021) 49(D1):D1138–43. doi: 10.1093/nar/gkaa891

57. Maeser D, Gruener RF, Huang RS. oncoPredict: an R package for predicting *in vivo* or cancer patient drug response and biomarkers from cell line screening data. *Brief Bioinform* (2021) 22(6):bbab260. doi: 10.1093/bib/bbab260

58. Yang W, Soares J, Greninger P, Edelman EJ, Lightfoot H, Forbes S, et al. Genomics of Drug Sensitivity in Cancer (GDSC): a resource for therapeutic biomarker discovery in cancer cells. *Nucleic Acids Res* (2013) 41(Database issue):D955–61. doi: 10.1093/nar/gks1111

59. Burley SK, Berman HM, Kleywegt GJ, Markley JL, Nakamura H, Velankar S. Protein data bank (PDB): the single global macromolecular structure archive. *Methods Mol Biol* (2017) 1607:627–41. doi: 10.1007/978-1-4939-7000-1_26

60. Kim S, Chen J, Cheng T, Gindulyte A, He J, He S, et al. PubChem in 2021: new data content and improved web interfaces. *Nucleic Acids Res* (2021) 49(D1):D1388–95. doi: 10.1093/nar/gkaa971

61. Odhar HA, Rayshan AM, Ahjel SW, Hashim AA, Albeer A. Molecular docking enabled updated screening of the matrix protein VP40 from Ebola virus with millions of compounds in the MCULE database for potential inhibitors. *Bioinformation* (2019) 15(9):627–32. doi: 10.6026/97320630015627

62. Zheng Q, Min S, Zhou Q. Identification of potential diagnostic and prognostic biomarkers for LUAD based on TCGA and GEO databases. *Biosci Rep* (2021) 41(6): BSR20204370. doi: 10.1042/BSR20204370

63. Hu Y, Li X, Wang L, Han B, Nie S. T-distribution stochastic neighbor embedding for fine brain functional parcellation on rs-fMRI. *Brain Res Bull* (2020) 162:199–207. doi: 10.1016/j.brainresbull.2020.06.007

64. Lopes AM, Tenreiro MaChado JA. Uniform manifold approximation and projection analysis of soccer players. *Entropy (Basel)* (2021) 23(7):793. doi: 10.3390/e23070793

65. Ben Salem K, Ben Abdelaziz A. Principal component analysis (PCA). *Tunis Med* (2021) 99(4):383–9.

66. Ye Y, Xiang Y, Ozguc FM, Kim Y, Liu CJ, Park PK, et al. The genomic landscape and pharmacogenomic interactions of clock genes in cancer chronotherapy. *Cell Syst* (2018) 6:314–28.e2. doi: 10.1016/j.cels.2018.01.013

67. Baselga J, Bradbury I, Eidtmann H, Di Cosimo S, de Azambuja E, Aura C, et al. Lapatinib with trastuzumab for HER2-positive early breast cancer (NeoALTTO): a randomized, open-label, multicenter, phase 3 trial. *Lancet* (2012) 379(9816):633–40. doi: 10.1016/S0140-6736(11)61847-3

68. Guarneri V, Frassoldati A, Bottini A, Cagossi K, Bisagni G, Sarti S, et al. Preoperative chemotherapy plus trastuzumab, lapatinib, or both in human epidermal

growth factor receptor 2-positive operable breast cancer: results of the randomized phase II CHER-LOB study. *J Clin Oncol* (2012) 30(16):1989–95. doi: 10.1200/JCO.2011.39.0823

69. Robidoux A, Tang G, Rastogi P, Geyer CE Jr, Azar CA, Atkins JN, et al. Lapatinib as a component of neoadjuvant therapy for HER2-positive operable breast cancer (NSABP protocol B-41): an open-label, randomised phase 3 trial. *Lancet Oncol* (2013) 14(12):1183–92. doi: 10.1016/S1470-2045(13)70411-X

70. Carey LA, Berry DA, Cirrincione CT, Barry WT, Pitcher BN, Harris LN, et al. Molecular heterogeneity and response to neoadjuvant human epidermal growth factor receptor 2 targeting in CALGB 40601, a randomized phase III trial of paclitaxel plus trastuzumab with or without lapatinib. *J Clin Oncol* (2016) 34(6):542–9. doi: 10.1200/JCO.2015.62.1268

71. Wang B, Liu J, Zhong Z. Prediction of lymph node metastasis in oral tongue squamous cell carcinoma using the neutrophil-to-lymphocyte ratio and platelet-to-neutrophil ratio. *J Clin Lab Anal* (2021) 35(6):e23684. doi: 10.1002/jcla.23684

72. Urs AB, Augustine J, Khurana N, Uniyal A, Passey JC, Meher R. Preoperative platelet-lymphocyte ratio and neutrophil-lymphocyte ratio as predictors of occult lymph node metastasis detected using Desmoglein 3 and Cytokeratin in Indian population. *J Oral Maxillofac Pathol* (2022) 26(4):596. doi: 10.4103/jomfp.jomfp_49_21

73. Xia X, Li K, Wu R, Lv Q, Deng X, Fei Z, et al. Predictive value of neuron-specific enolase, neutrophil-to-lymphocyte-ratio and lymph node metastasis for distant metastasis in small cell lung cancer. *Clin Respir J* (2020) 14(11):1060–6. doi: 10.1111/crj.13242

74. Song CY, Meng YL, Liu B, Yan L, Shang PZ, Jia ZF, et al. [Correlation analysis of neutrophil-to-lymphocyte ratio and platelet-to-lymphocyte ratio and central cervical lymph node metastasis of papillary thyroid microcarcinoma]. *Zhonghua Zhong Liu Za Zhi* (2021) 43(9):944–8. doi: 10.3760/cma.j.cn112152-20200509-00434

75. Fujita H, Motoyama S, An J, Nagakai Y, Yamaguchi T, Koyota S, et al. Peritumoral CD16b positive-neutrophil accumulation strongly correlates with regional lymph node metastasis in thoracic esophageal squamous cell cancer. *Surgery* (2022) 171(6):1535–42. doi: 10.1016/j.surg.2021.11.022

76. Liao Y, Huang J, Liu P, Zhang C, Liu J, Xia M, et al. Downregulation of LNMAS orchestrates partial EMT and immune escape from macrophage phagocytosis to promote lymph node metastasis of cervical cancer. *Oncogene* (2022) 41(13):1931–43. doi: 10.1038/s41388-022-02202-3

77. Yin X, Chen S, Eisenbarth SC. Dendritic cell regulation of T helper cells. *Annu Rev Immunol* (2021) 39:759–90. doi: 10.1146/annurev-immunol-101819-025146

78. Waisman A, Lukas D, Clausen BE, Yogev N. Dendritic cells as gatekeepers of tolerance. *Semin Immunopathol* (2017) 39(2):153–63. doi: 10.1007/s00281-016-0583-z

79. Mansfield AS, Heikkila P, von Smitten K, Vakkila J, Leidenius M. Metastasis to sentinel lymph nodes in breast cancer is associated with maturation arrest of dendritic cells and poor co-localization of dendritic cells and CD8+ T cells. *Virchows Arch* (2011) 459(4):391–8. doi: 10.1007/s00428-011-1145-3

80. Zhang G, Li B, Lin Y. Evaluation of ITGA3 as a biomarker of progression and recurrence in papillary thyroid carcinoma. *Front Oncol* (2021) 11:614955. doi: 10.3389/fonc.2021.614955

81. Zhang J, Zhong Y, Sang Y, Ren G. miRNA-144-5p/ITGA3 suppressed the tumor-promoting behaviors of thyroid cancer cells by downregulating ITGA3. *Comput Math Methods Med* (2021) 2021:9181941. doi: 10.1155/2021/9181941

82. Bakir B, Chiarella AM, Pitarresi JR, Rustgi AK. EMT. MET, plasticity, and tumor metastasis. *Trends Cell Biol* (2020) 30(10):764–76. doi: 10.1016/j.tcb.2020.07.003

83. Dong B, Wu Y. Epigenetic regulation and post-translational modifications of SNAI1 in cancer metastasis. *Int J Mol Sci* (2021) 22(20):11062. doi: 10.3390/ijms222011062

84. Sundararajan V, Tan M, Zea Tan T, Pang QY, Ye J, Chung VY, et al. SNAI1-driven sequential EMT changes attributed by selective chromatin enrichment of RAD21 and GRHL2. *Cancers (Basel)* (2020) 12:1140. doi: 10.3390/cancers12051140

85. Liang H, Yu M, Yang R, Zhang L, Zhang L, Zhu D, et al. A PTAL-miR-101-FN1 axis promotes EMT and invasion-metastasis in serous ovarian cancer. *Mol Ther Oncolytics* (2020) 16:53–62. doi: 10.1016/j.omto.2019.12.002

86. Aiello NM, Kang Y. Context-dependent EMT programs in cancer metastasis. *J Exp Med* (2019) 216(5):1016–26. doi: 10.1084/jem.20181827

87. Wu Z, Zou Y, Fu R, Jin P, Yuan H. A nomogram for predicting sclerotherapy response for treatment of lymphatic malformations in children. *Eur J Med Res* (2022) 27(1):209. doi: 10.1186/s40001-022-00844-3

88. Zhu H, Gao Y, Wang C, Chen Z, Yu X, Qi X, et al. A nomogram for decision-making assistance on surgical treatment of chronic osteomyelitis in long bones: Establishment and validation based on a retrospective multicenter cohort. *Int J Surg* (2022) 99:106267. doi: 10.1016/j.ijsu.2022.106267

89. Wang Z. ErbB receptors and cancer. *Methods Mol Biol* (2017) 1652:3–35. doi: 10.1007/978-1-4939-7219-7_1

90. Arndt- Jovin DJ, Botelho MG, Jovin TM. Structure-function relationships of ErbB RTKs in the plasma membrane of living cells. *Cold Spring Harb Perspect Biol* (2014) 6(4):a008961. doi: 10.1101/cshperspect.a008961

91. Patnaik SK, Chandrasekar M, Nagarjuna P, Ramamurthi D, Swaroop AK. Targeting of erbB1, erbB2, and their dual targeting using small molecules and natural peptides: blocking EGFR cell signaling pathways in cancer: A mini-review. *Mini Rev Med Chem* (2022) 22(22):2831–46. doi: 10.2174/1389557522666220512152448

92. Kraus MH, Issing W, Miki T, Popescu NC, Aaronson SA. Isolation and characterization of ERBB3, a third member of the ERBB/epidermal growth factor receptor family: evidence for overexpression in a subset of human mammary tumors. *Proc Natl Acad Sci USA* (1989) 86(23):9193–7. doi: 10.1073/pnas.86.23.9193

93. Gandullo- Sánchez L, Ocaña A, Pandiella A. HER3 in cancer: from the bench to the bedside. *J Exp Clin Cancer Res* (2022) 41(1):310. doi: 10.1186/s13046-022-02515-x

94. Haikala HM, Jänne PA. Thirty years of HER3: from basic biology to therapeutic interventions. *Clin Cancer Res* (2021) 27(13):3528–39. doi: 10.1158/1078-0432.CCR-20-4465

95. Gil V, Miranda S, Riisnaes R, Gurel B, D'Ambrosio M, Vasciaveo A, et al. HER3 is an actionable target in advanced prostate cancer. *Cancer Res* (2021) 81(24):6207–18. doi: 10.1158/0008-5472.CAN-21-3360

96. Yonesaka K, Tanizaki J, Maenishi O, Haratani K, Kawakami H, Tanaka K, et al. HER3 augmentation via blockade of EGFR/AKT signaling enhances anticancer activity of HER3-targeting patritumab deruxtecan in EGFR-mutated non-small cell lung cancer. *Clin Cancer Res* (2022) 28(2):390–403. doi: 10.1158/1078-0432.CCR-21-3359

97. Diwanji D, Trenker R, Thaker TM, Wang F, Agard DA, Verba KA, et al. Structures of the HER2-HER3-NRG1β complex reveal a dynamic dimer interface. *Nature* (2021) 600(7888):339–43. doi: 10.1038/s41586-021-04084-z

98. Littlefield P, Liu L, Mysore V, Shan Y, Shaw DE, Jura N. Structural analysis of the EGFR/HER3 heterodimer reveals the molecular basis for activating HER3 mutations. *Sci Signal* (2014) 7(354):ra114. doi: 10.1126/scisignal.2005786

99. Hashimoto Y, Koyama K, Kamai Y, Hirotani K, Ogitani Y, Zembutsu A, et al. A novel HER3-targeting antibody-drug conjugate, U3-1402, exhibits potent therapeutic efficacy through the delivery of cytotoxic payload by efficient internalization. *Clin Cancer Res* (2019) 25(23):7151–61. doi: 10.1158/1078-0432.CCR-19-1745

100. Kiavue N, Cabel L, Melaabi S, Bataillon G, Callens C, Lerebours F, et al. ERBB3 mutations in cancer: biological aspects, prevalence and therapeutics. *Oncogene* (2020) 39(3):487–502. doi: 10.1038/s41388-019-1001-5

101. Hafeez U, Parslow AC, Gan HK, Scott AM. New insights into ErbB3 function and therapeutic targeting in cancer. *Expert Rev Anticancer Ther* (2020) 20(12):1057–74. doi: 10.1080/14737140.2020.1829485

102. Ross JS, Fakih M, Ali SM, Elvin JA, Schrock AB, Suh J, et al. Targeting HER2 in colorectal cancer: The landscape of amplification and short variant mutations in ERBB2 and ERBB3. *Cancer* (2018) 124(7):1358–73. doi: 10.1002/cncr.31125

103. Engelman JA, Zejnullahu K, Mitsudomi T, Song Y, Hyland C, Park JO, et al. MET amplification leads to gefitinib resistance in lung cancer by activating ERBB3 signaling. *Science* (2007) 316(5827):1039–43. doi: 10.1126/science.1141478

104. Yang X, Chen Y, Li M, Zhu W. ERBB3 methylation and immune infiltration in tumor microenvironment of cervical cancer. *Sci Rep* (2022) 12(1):8112. doi: 10.1038/s41598-022-11415-1

105. Weickhardt AJ, Lau DK, Hodgson-Garms M, Lavis A, Jenkins LJ, Vukelic N, et al. Dual targeting of FGFR3 and ERBB3 enhances the efficacy of FGFR inhibitors in FGFR3 fusion-driven bladder cancer. *BMC Cancer* (2022) 22(1):478. doi: 10.1186/s12885-022-09478-4

106. Kang YY, Liu Y, Wang ML, Guo M, Wang Y, Cheng ZF. Construction and analyses of the microRNA-target gene differential regulatory network in thyroid carcinoma. *PloS One* (2017) 12:e0178331. doi: 10.1371/journal.pone.0178331

107. Moore LD, Le T, Fan G. DNA methylation and its basic function. *Neuropsychopharmacology* (2013) 38(1):23–38. doi: 10.1038/npp.2012.112

108. Mattei AL, Bailly N, Meissner A. DNA methylation: a historical perspective. *Trends Genet* (2022) 38(7):676–707. doi: 10.1016/j.tig.2022.03.010

109. Saghafinia S, Mina M, Riggi N, Hanahan D, Ciriello G. Pan-cancer landscape of aberrant DNA methylation across human tumors. *Cell Rep* (2018) 25(4):1066–80.e8. doi: 10.1016/j.celrep.2018.09.082

110. He J, Xu Q, Jing Y, Agani F, Qian X, Carpenter R, et al. Reactive oxygen species regulate ERBB2 and ERBB3 expression via miR-199a/125b and DNA methylation. *EMBO Rep* (2012) 13(12):1116–22. doi: 10.1038/embor.2012.162

111. Zhong J, Shan W, Zuo Z. Norepinephrine inhibits migration and invasion of human glioblastoma cell cultures possibly via MMP-11 inhibition. *Brain Res* (2021) 1756:147280. doi: 10.1016/j.brainres.2021.147280

112. Evangelou AI, Winter SF, Huss WJ, Bok RA, Greenberg NM. Steroid hormones, polypeptide growth factors, hormone refractory prostate cancer, and the neuroendocrine phenotype. *J Cell Biochem* (2004) 91(4):671–83. doi: 10.1002/jcb.10771

113. Slominski RM, Raman C, Chen JY, Slominski AT. How cancer hijacks the body's homeostasis through the neuroendocrine system. *Trends Neurosci* (2023) 46(4):263–75. doi: 10.1016/j.tins.2023.01.003

114. Kosińska I, Nitsch- Osuch A. [Benzo(a)pyrene in atmospheric and indoor air, health hazards and possibilities of limitation]. *Pol Merkur Lekarski* (2020) 49(286):282–8.

115. Michałowicz J. Bisphenol A–sources, toxicity and biotransformation. *Environ Toxicol Pharmacol* (2014) 37(2):738–58. doi: 10.1016/j.etap.2014.02.003

116. Scheiber I, Dringen R, Mercer JF. Copper: effects of deficiency and overload. *Met Ions Life Sci* (2013) 13:359–87. doi: 10.1007/978-94-007-7500-8_11

117. Luine VN. Estradiol and cognitive function: past, present and future. *Horm Behav* (2014) 66(4):602–18. doi: 10.1016/j.yhbeh.2014.08.011

118. Shagufta, Ahmad I. Tamoxifen a pioneering drug: An update on the therapeutic potential of tamoxifen derivatives. *Eur J Med Chem* (2018) 143:515–31. doi: 10.1016/j.ejmech.2017.11.056

119. Snyder KR, Sparano N, Malinowski JM. Raloxifene hydrochloride. *Am J Health Syst Pharm* (2000) 57(18):1669–75; quiz 1676-8. doi: 10.1093/ajhp/57.18.1669

120. Kaur T, Madgulkar A, Bhalekar M, Asgaonkar K. Molecular docking in formulation and development. *Curr Drug Discov Technol* (2019) 16(1):30–9. doi: 10.2174/1570163815666180219112421

121. Lee YT, Tan YJ, Oon CE. Molecular targeted therapy: Treating cancer with specificity. *Eur J Pharmacol* (2018) 834:188–96. doi: 10.1016/j.ejphar.2018.07.034

122. Overington JP, Al- Lazikani B, Hopkins AL. How many drug targets are there. *Nat Rev Drug Discov* (2006) 5(12):993–6. doi: 10.1038/nrd2199

123. Leary A, Evans A, Johnston SR, A'Hern R, Bliss JM, Sahoo R, et al. Antiproliferative effect of lapatinib in HER2-positive and HER2-negative/HER3-high breast cancer: results of the presurgical randomized MAPLE trial (CRUK E/06/039). *Clin Cancer Res* (2015) 21(13):2932–40. doi: 10.1158/1078-0432.CCR-14-1428

124. Ohno K, Shibata T, Ito KI. Epidermal growth factor receptor activation confers resistance to lenvatinib in thyroid cancer cells. *Cancer Sci* (2022) 113:3193–210. doi: 10.1111/cas.15465

125. Cheng L, Jin Y, Liu M, Ruan M, Chen L. HER inhibitor promotes BRAF/MEK inhibitor-induced redifferentiation in papillary thyroid cancer harboring BRAFV600E. *Oncotarget* (2017) 8:19843–54. doi: 10.18632/oncotarget.15773

126. Lin S, Lv Y, Xu J, Mao X, Chen Z, Lu W. Over-expression of Nav1.6 channels is associated with lymph node metastases in colorectal cancer. *World J Surg Oncol* (2019) 17(1):175. doi: 10.1186/s12957-019-1715-4

127. Hu J, Xu J, Li M, Zhang Y, Yi H, Chen J, et al. Targeting lymph node sinus macrophages to inhibit lymph node metastasis. *Mol Ther Nucleic Acids* (2019) 16:650–62. doi: 10.1016/j.omtn.2019.04.016

128. Chung EJ, Lee SH, Baek SH, Park IS, Cho SJ, Rho YS. Pattern of cervical lymph node metastasis in medial wall pyriform sinus carcinoma. *Laryngoscope* (2014) 124 (4):882–7. doi: 10.1002/lary.24299

129. Lee SK, Lee KW, Kim S, Choi MY, Kim J, Lee J, et al. Lymph node metastasis in patients with frozen section analyses that are negative for tumors. *Oncology* (2012) 83 (1):31–7. doi: 10.1159/000336486

130. Holtkamp LH, Wang S, Wilmott JS, Madore J, Vilain R, Thompson JF, et al. Detailed pathological examination of completion node dissection specimens and outcome in melanoma patients with minimal (<0.1 mm) sentinel lymph node metastases. *Ann Surg Oncol* (2015) 22(9):2972–7. doi: 10.1245/s10434-015-4615-z

frontiers | Frontiers in Endocrinology

TYPE Original Research
PUBLISHED 08 January 2024
DOI 10.3389/fendo.2023.1343848

OPEN ACCESS

EDITED BY
Juan Pablo Nicola,
National University of Cordoba, Argentina

REVIEWED BY
Ines Califano,
Instituto de Oncología Ángel H. Roffo, Argentina
Alexandra Chera,
Victor Babes National Institute of Pathology (INCDVB), Romania

*CORRESPONDENCE
Vladimir A. Saenko
saenko@nagasaki-u.ac.jp

†These authors have contributed equally to this work

RECEIVED 24 November 2023
ACCEPTED 18 December 2023
PUBLISHED 08 January 2024

CITATION
Bogdanova T, Rogounovitch TI, Zurnadzhy L, Mitsutake N, Tronko M, Ito M, Bolgov M, Chernyshov S, Gulevatyi S, Masiuk S, Yamashita S and Saenko VA (2024) Characteristics and immune checkpoint status of radioiodine-refractory recurrent papillary thyroid carcinomas from Ukrainian Chornobyl Tissue Bank donors. *Front. Endocrinol.* 14:1343848. doi: 10.3389/fendo.2023.1343848

Characteristics and immune checkpoint status of radioiodine-refractory recurrent papillary thyroid carcinomas from Ukrainian Chornobyl Tissue Bank donors

Tetiana Bogdanova[1,2†], Tatiana I. Rogounovitch[3†], Liudmyla Zurnadzhy[1,2], Norisato Mitsutake[2,3], Mykola Tronko[4], Masahiro Ito[5], Michael Bolgov[6], Serhii Chernyshov[6], Serhii Gulevatyi[7], Sergii Masiuk[8], Shunichi Yamashita[3,9] and Vladimir A. Saenko[2*]

[1]Laboratory of Morphology of Endocrine System, State Institution "VP Komisarenko Institute of Endocrinology and Metabolism of the National Academy of Medical Sciences of Ukraine", Kyiv, Ukraine, [2]Department of Radiation Molecular Epidemiology, Atomic Bomb Disease Institute, Nagasaki University, Nagasaki, Japan, [3]Department of Radiation Medical Sciences, Atomic Bomb Disease Institute, Nagasaki University, Nagasaki, Japan, [4]Department of Fundamental and Applied Problems of Endocrinology, State Institution "VP Komisarenko Institute of Endocrinology and Metabolism of the National Academy of Medical Sciences of Ukraine", Kyiv, Ukraine, [5]Department of Diagnostic Pathology, National Hospital Organization Nagasaki Medical Center, Omura, Japan, [6]Department of Surgery of Endocrine Glands, State Institution "VP Komisarenko Institute of Endocrinology and Metabolism of the National Academy of Medical Sciences of Ukraine", Kyiv, Ukraine, [7]Laboratory of Radiology and Radiobiology, State Institution "VP Komisarenko Institute of Endocrinology and Metabolism of the National Academy of Medical Sciences of Ukraine", Kyiv, Ukraine, [8]Radiation Protection Laboratory, State Institution "National Research Center of Radiation Medicine of the National Academy of Medical Science of Ukraine", Kyiv, Ukraine, [9]Global Exchange Center, Fukushima Medical University, Fukushima, Japan

Introduction: The radioiodine-refractory (RAI-R) recurrent papillary thyroid carcinomas (PTCs) are more frequent in elderly patients and have an unfavorable prognosis. Data on the prevalence and characteristics of RAI-R recurrent PTCs in patients of young and middle age with or without a history of radiation exposure in childhood are poorly described. The aim of the current study was: i) to determine the frequency of RAI-R recurrent PTCs among donors of the Chornobyl Tissue Bank (CTB) and analyze the clinicopathological features of primary tumors (PTs), primary metastases (PMTSs), recurrent metastases (RMTSs) and risk factors for RMTS, and ii) to determine the immune checkpoint status (ICS) of the RAI-R recurrent PTCs and to assess the factors associated with ICS positivity.

Methods: Sixty RAI-R recurrent PTCs (46 exposed to radiation and 14 non-exposed, 2.5% of all cases registered with the CTB) from the Ukrainian patients aged up to 48 years were identified.

Results: The clinicopathological characteristics of the PTs moderately to weakly resembled those of the PMTS and RMTS from the same patients while the metastatic tissues were highly similar. The multivariate model of RMTS

included the dominant solid-trabecular growth pattern of the PT, cystic changes, N1b metastases, and the probability of a causation (POC) of PTC by radiation as risk factors. Among these factors, the lateral PMTS (N1b) had the strongest effect. The longer period of latency (a POC component) was the second statistically significant characteristic. ICS percent agreement between the PT and RAI-R RMTS was 91.5%; 23.7% of PTs and 28.8% of RMTSs had positive ICS (positive PD-L1 tumor epithelial cells (TECs) and positive PD-L1/PD1 tumor-associated immune cells). ICS positivity of PTs was associated with pronounced oncocytic changes and high density of the $p16^{INK4A}$-positive TECs in the invasive areas of PTs. In RMTSs, ICS positivity was associated with pronounced oncocytic changes and Ki-67 labeling index ≥ 4.5% of PTs, and the dominant solid-trabecular growth pattern, Ki-67 labeling index ≥ 7.6% and $p16^{INK4A}$-positivity of RMTS.

Discussion: The findings are of clinical relevance and may be useful for developing individual treatment approaches for patients with RAI-R recurrent PTCs possibly involving immunotherapy.

KEYWORDS

radioiodine-refractory recurrent papillary thyroid carcinoma, Chornobyl tissue bank, radiation exposure, pathology, immune checkpoint status, PD-L1, PD-1, p16 INK4a

Introduction

Papillary thyroid carcinoma (PTC) accounts for more than 90% of differentiated thyroid cancer cases (1–3). Depending on the initial risk stratification, treatment of PTC may include thyroid surgery of various extent, radioiodine (RAI) therapy, and hormone suppression/replacement therapy resulting generally in a very good prognosis with a 5-year relative patient survival of 94-98% (2), and a > 90% 10-year overall survival (4–7). However, 5-20% of patients may experience a local, regional or distant recurrence (2, 4). Furthermore, 5-15% of differentiated thyroid carcinomas may be insensitive to RAI therapy (8–10). The RAI-refractory (RAI-R) tumors may be a life-threatening condition reducing a 5-year disease-specific survival rate to 60-70% (11, 12), and a 10-year survival rate to as low as 10-20% for patients with RAI-R metastatic malignancies (6, 13–16).

The RAI-R recurrent PTCs occur more often in elderly patients who have the most unfavorable prognosis (16–19). Young and middle-aged patients (< 45 years old) have a better overall survival (19), but data on the frequency of RAI-R recurrent PTC in patients of this age with a history of radiation exposure in childhood, and clinicopathological characteristics of primary tumors, primary metastases and recurrent metastases are poorly described. In this regard, the international Chornobyl Tissue Bank (CTB), which consists of > 80% tumor samples from the Ukrainian donors with demographic, clinical and histopathological data, individual radiation thyroid doses and a consensus CTB diagnosis, provides a unique opportunity to address these questions (20, 21).

In view of unfavorable prognosis, management of RAI-R recurrent PTC is a difficult and important clinical problem. Current modalities may include surgery, external beam radiotherapy and targeted multi-kinase inhibitor treatment (22). In recent years, the immune checkpoint inhibitor therapy started to gain increasing attention (23–27). Possible effectiveness of the immunotherapy of RAI-R recurrent PTC was hypothesized because the microenvironment of differentiated thyroid cancer is enriched with different types of immune cells (28). However, some tumors can evade the immune response by expressing the programmed cell death ligand PD-L1, which binds the PD-1 receptor on T-lymphocytes and disrupts cytotoxic activity of the latter, leading to higher tumor aggressiveness and progression (23, 25, 28). The PD-1/PD-L1 immune checkpoint is the principal target of immunotherapy for various malignant tumors, including the RAI-R recurrent PTC (24, 27, 29, 30). Again, our knowledge of the immune checkpoint status of the RAI-R recurrent PTCs in young and middle-aged patients exposed or non-exposed to radiation is insufficient.

This study set out i) to determine the frequency of RAI-R recurrent PTCs among the Chornobyl Tissue Bank (CTB) donors, to analyze clinicopathological characteristics of the primary tumors (PT), primary metastases (PMTS) and recurrent metastases (RMTS), to ascertain risk factors for RMTS development, and ii) to determine the frequency of a positive immune checkpoint status

(ICS) among the RAI-R recurrent PTCs and to identify the clinicopathological characteristics of PT, PMTS and RAI-R RMTS associated with positive ICS.

Materials and methods

Patients

Clinical records and follow-up data on 3,595 Ukrainian patients operated on for benign or malignant thyroid tumors at the State Institution "V.P. Komisarenko Institute of Endocrinology and Metabolism of the National Academy of Medical Sciences of Ukraine" (IEM, Kyiv, Ukraine) during the period from 1998 to 2017 were reviewed. A total of 2,411 patients with PTCs, including micro-PTCs, all registered with the CTB, were identified, among whom 60 patients were re-operated for the RAI-R recurrences. Recurrence was defined as a regional metastasis newly detected not earlier than six months after the initial treatment. Follow-up period ranged from 1 to 21 years, median 8.4; no fatal outcomes were documented. The RAI-R status was determined according to the existing guidelines (4, 5, 7). All patients underwent two-projection whole-body scintigraphy (RAI-activity from 2,000 to 5,500 MBq) at different times after the first surgery (Table 1) and displayed no

TABLE 1 Descriptive characteristics of the RAI-R recurrent PTC cases: primary tumors, primary metastases and recurrent RAI-R metastases.

Parameters	Primary tumors, n=60	Primary LN metastases, n=39	Recurrent metastases, n=60
	n (%) or median (range; IQR)	n (%) or median (range; IQR)	n (%) or median (range; IQR)
Exposed/nonexposed (% exposed)	46/14 (76.7%)	27/12 (69.2%)	PT[1]
Radiation dose to the thyroid, mGy	n=46; 32.1 (2.3-825.1; 20.9-64.4)	n=27; 34.7 (3.1-801.6; 21.1-88.5)	NA[2]
Probability of causation (POC), %	n=46; 12.4 (0.8-86.5; 6.5-31.2)	n=27; 13.5 (0.8-79.5; 8.2-39.9)	NA
≤ 25%	32 (69.6%)	16 (59.3%)	NA
> 25 – 50%	6 (13.0%)	6 (22.2%)	NA
> 50 – 75%	6 (13.0%)	4 (14.8%)	NA
> 75 – 100%	2 (4.4%)	1 (3.7%)	NA
Age at operation, years	28.4 (8.7-48.4; 22.5-35.5)	27.6 (8.7-46.4; 21.8-35.1)	32.6 (9.9-49.0; 24.8-37.9)
Age at exposure, years	n=46; 9.6 (0-18.3; 4.2-13.0)	n=27; 9.3 (0-18.1; 4.0-13.1)	PT
Period of latency, years	n=46; 22.9 (12.6-31.0; 19.4-26.9)	n=27; 23.9 (12.6-30.4; 21.6-27.2)	NA
Sex F/M (%M, F:M ratio)	44/16 (26.7%; 2.7:1)	31/8 (20.5%; 3.9:1)	PT
Tumor size, mm	20.0 (6-105; 14-35)	16 (3-100; 9-32)	13.0 (6-25; 10-15)
≤ 10 mm (microcarcinoma)	7 (11.7%)	NA	NA
11 – 20 mm	25 (41.7%)	NA	NA
21 – 40 mm	20 (33.3%)	NA	NA
> 40 mm	8 (13.3%)	NA	NA
Dominant growth pattern			
papillary	40 (66.7%)	18 (46.2%)	29 (48.3%)
follicular	5 (8.3%)	5 (12.8%)	4 (6.7%)
solid-trabecular	15 (25.0%)	16 (41.0%)	27 (45.0%)
Histological subtype			
papillary	14 (23.3%)	9 (23.1%)	16 (26.7%)
follicular	2 (3.3%)	3 (7.7%)	2 (3.3%)
solid-trabecular	5 (8.3%)	12 (30.8%)	23 (38.3%)
conventional	29 (48.3%)	11 (28.2%)	15 (25.0%)
rare	10 (16.7%)[3]	4 (10.3%)[4]	4 (6.7%)[5]

(Continued)

10.3389/fendo.2023.1343848

TABLE 1 Continued

Parameters	Primary tumors, n=60	Primary LN metastases, n=39	Recurrent metastases, n=60
	n (%) or median (range; IQR)	n (%) or median (range; IQR)	n (%) or median (range; IQR)
Tall cell features	27 (45.0%)	14 (35.9%)	26 (43.3%)
Hobnail features	4 (6.7%)	3 (7.7%)	10 (16.7%)
Full tumor capsule	4 (6.7%)	NA	NA
Multifocality	19 (31.7%)	NA	NA
Lymphatic/vascular invasion	45 (75.0%)	NA	NA
Extrathyroidal extension (any)	35 (58.3%)	13 (33.3%)	23 (38.3%)
microscopic	26 (43.3%)	NA	NA
macroscopic	9 (15.0%)	NA	NA
Extranodal extension	NA	13 (33.3%)	23 (38.3%)
pT category			
pT1	32 (53.3%)	NA	NA
pT1a	7 (11.7%)	NA	NA
pT1b	25 (41.6%)	NA	NA
pT2	12 (20.0%)	NA	NA
pT3	16 (26.7%)	NA	NA
pT3a	4 (6.7%)	NA	NA
pT3b	12 (20.0%)	NA	NA
pN category (N1)	39 (65.0%)	NA	NA
pN1a	15 (25.0%)	NA	NA
pN1b	24 (40.0%)	NA	NA
M category (M1)	1 (1.7%)	NA	NA
Oncocytic changes	49 (81.7%)	31 (79.5%)	48 (80.0%)
≤ 25% focal	9 (15.0%)	7 (17.9%)	7 (11.7%)
> 25 – 50% moderate	24 (40.0%)	10 (25.7%)	16 (26.7%)
> 50 – 75% severe	13 (21.7%)	9 (23.1%)	11 (18.3%)
> 75 – 100% oncocytic tumor	3 (5.0%)	5 (12.8%)	14 (28.3%)
Cystic changes	15 (25.0%)	14 (35.9%)	29 (48.3%)
≤ 25% focal	14 (23.3%)	8 (20.5%)	9 (15.0%)
> 25 – 50% moderate	1 (1.7%)	3 (7.7%)	10 (16.7%)
> 50 – 75% severe	0	1 (2.6%)	2 (3.3%)
> 75 – 100% cystic tumor	0	2 (5.1%)	8 (13.3%)
$BRAF^{V600E}$-positive	n=59; 41 (69.5%)	n=35; 24 (68.6%)	n=59; 41 (69.5%)
$NRAS^{Q61R}$-positive	n=59; 1 (1.7%)	n=35; 1 (2.9%)	1 (1.7%)
Ki-67 labeling index, %	n=59; 5.1 (1.0-14.3; 3.7-7.3)	n=34; 4.6 (1.2-12.2; 3.3-7.1)	n=59; 5.4 (1.6-14.6; 3.5-7.3)
0 – 5%	29 (49.2%)	18 (52.9%)	27 (45.8%)
> 5 – 10%	24 (40.7%)	13 (38.2%)	30 (50.8%)
> 10%	6 (10.1%)	3 (8.9%)	2 (3.4%)

(Continued)

10.3389/fendo.2023.1343848

TABLE 1 Continued

Parameters	Primary tumors, n=60	Primary LN metastases, n=39	Recurrent metastases, n=60
	n (%) or median (range; IQR)	n (%) or median (range; IQR)	n (%) or median (range; IQR)
p16-positive TEC[6], invasive areas	n=59; 58 (98.3%)	n=35; 33 (94.3%)	n=59; 59 (100%)
≤ 25%	18 (30.5%)	7 (20.0%)	12 (20.3%)
> 25 – 50%	14 (23.7%)	7 (20.0%)	12 (20.3%)
> 50 – 75%	20 (33.9%)	7 (20.0%)	16 (27.1%)
> 75 – 100%	6 (10.2%)	12 (34.3%)	19 (32.3%)
Coexisting thyroid cancer	0	NA	NA
Concomitant benign nodules	14 (23.3%)	NA	NA
Concomitant Graves' disease	1 (1.7%)	NA	NA
Chronic thyroiditis	15 (25.0%)	NA	NA
Total thyroidectomy	60 (100%)	NA	NA
Lymph node dissection performed	47 (78.3%)	39 (100%)	60 (100%)
level ≥ 6	16 (26.6%)	12 (30.8%)	27 (45.0%)
level 1 – 5	31 (51.7%)	27 (69.2%)	33 (55.0%)
Lymph nodes removed	NA	10 (1-29; 5-14)	4.5 (1-22; 2-6)
Metastatic lymph nodes	NA	7 (1-17; 3-10)	2.5 (1-18; 1-4)
Greatest metastatic lymph node size, mm	NA	16 (3-100; 9-33)	13 (6-25; 10-15)
RIT performed	60 (100%)	NA	NA
RIT cycles	2 (1-10; 1-2)	NA	NA
Cumulative RI activity, MBq	5455 (1425-54036; 3787-8338)	NA	NA
Follow-up, years	8.4 (1-21; 4.8-13.9)	NA	NA
Time to recurrence, yrs	NA	NA	1.6 (0.5-19.5; 0.9-3.9)

[1] Identical to the primary tumor data.
[2] Not applicable.
[3] Seven tall cell and three Warthin-like subtypes.
[4] Three tall cell and one hobnail subtypes.
[5] Four tall cell subtypes.
[6] Tumor epithelial cells.

abnormal RAI uptake. On ultrasound, however, enlarged hypoechoic lymph nodes measuring from 7 to 15 mm were detected in the neck, which according to fine-needle aspiration biopsy/cytology and postoperative histopathology were classified as recurrent PTC metastases. Formalin-fixed paraffin-embedded tissues samples of the primary tumor, primary (where existed) and recurrent metastases were retrieved from the pathological archive and analyzed as described below.

The study was conducted according to the guidelines of the Declaration of Helsinki and was approved by the IEM Bioethics Committee (protocols N 22-KE of April 26, 2018, and N 31-KE of February 27, 2020), the Chornobyl Tissue Bank (CTB, project N001-2020), and the Ethics Committee of Nagasaki University (protocol 20130401–7 of July 1, 2021, the latest update). Informed consent was obtained from all patients enrolled in the study or their guardians (for minors).

Histopathology

Pathological examination of paraffin sections stained with hematoxylin and eosin was performed by two experienced IEM pathologists (TB and LZ). Pathological diagnosis was based on the 4th edition of the WHO histological classification (31). All tumors had been also reviewed by the international pathology panel of the CTB project (32), and PTC diagnosis was confirmed in all cases. pTNM categories were determined according to the 8th edition of the TNM Classification (33). Tumors were classified by size, the presence of a capsule, dominant histological growth pattern (papillary, follicular or solid-trabecular) and histological subtype. The presence of tall cell and of hobnail areas, and the frequency of oncocytic changes were recorded. In case of multifocal PTs or multiple primary or recurrent lymph node involvement, characteristics of the largest were considered.

Immunohistochemistry

Immunohistochemical (IHC) staining for PD-L1, PD-1, $p16^{INK4A}$ and $BRAF^{V600E}$ were performed according to the Department of Radiation Molecular Epidemiology of the Atomic Bomb Diseases Institute's (Nagasaki, Japan) laboratory-developed tests (TIR).

PD-L1, PD-1 and p16

Heat-induced epitope retrieval was performed for 15 min in VENTANA Cell Conditioning Solution (CC1) (950-124, Roche Diagnostics, Mannheim, Germany) at 120°C followed by slow cooling down during 2 h after a closed autoclave has reached 60°C upon the heating cycle completion. Endogenous peroxidase neutralization was done for 5 min with Leica Peroxidase Block (component of the Novolink Polymer Detection System (250T), RE7140-K, Leica Biosystems); non-specific blocking was performed for 5 min with Leica Protein Block (component of the Novolink Polymer Detection System (250T), RE7140-K, Leica Biosystems).

Incubation with the primary antibody: prediluted VENTANA PD-L1 (SP263) (790-4905, Roche Diagnostics) rabbit monoclonal antibody (~ 1.61 µg/ml) for 1 h at 37°C; prediluted CELL MARQUE PD-1 (NAT105) (760-4895, Roche Diagnostics) mouse monoclonal antibody (4 µg/ml) for 20 min at 37°C; prediluted VENTANA CINtec p16 Histology (705-4713, Roche Diagnostics) mouse monoclonal antibody (~ 1.0 µg/ml) for 15 min at 37°C in a wet chamber.

The Novolink Polymer Detection System (250T) (RE7140-K, Leica Biosystems) was used to detect the IHC reaction product, which included 30 min treatment with the secondary rabbit anti-mouse IgG antibody (for PD-1 and p16, omitted for PD-L1), attachment of the Novolink Polymer for 30 min and visualization with DAB diluted in the Novolink DAB Substrate Buffer according to the manufacturer's recommendations. Cell nuclei were stained with Mayer's hematoxylin. Placenta and tonsil tissue sections were used as positive controls for PD-L1; tonsil tissue sections were used as positive controls for PD-1 and p16 staining.

PD-L1 expression in tumor epithelial cells (TECs) was determined as the percentage of TECs with membrane and cytoplasmic staining. PD-L1 expression in tumor-associated immune cells (TAIC) was determined as the percentage of TAIC with membrane and cytoplasmic staining. PD-1 expression was determined as the percentage of TAICs with cytoplasmic staining. $p16^{INK4A}$ expression was determined in the tumor invasive areas in TECs with nuclear and cytoplasmic staining. PD-L1 expression in TEC and TAIC, PD-1 expression in TAIC and $p16^{INK4A}$ expression in TEC were scored as: 0:0; 1: ≤ 25%; 2: > 25% – ≤ 50%; 3: > 50% – ≤ 75%; 4: > 75% –100%.

For analysis, the immune checkpoint status (ICS) of each individual PT, PMTS or RMTS was evaluated as positive if PD-L1 expression was observed in > 25% of the TECs (i.e., score 2 or higher), and that of PD-L1 and PD-1 in any percentage of the TAICs above 0 (i.e., score > 0). The high density of PD-L1 and PD-1 positive TAICs in the germinal centers of lymph nodes with PTC metastases was not considered.

NRAS (mutated p.Q61R)

Heat-induced epitope retrieval was performed for 15 min in BOND Epitope Retrieval Solution 2 (AR9640, Leica Biosystems) at 120°C following by cool down to 60°C in a closed autoclave (without further incubation). Endogenous peroxidase neutralization was done for 5 min with Leica Peroxidase Block (component of the Novolink Polymer Detection System (250T), RE7140-K, Leica Biosystems); non-specific blocking was performed for 5 min with Leica Protein Block (component of the Novolink Polymer Detection System (250T), RE7140-K, Leica Biosystems).

Incubation with the Anti-NRAS (mutated Q61R) rabbit monoclonal antibody (SP174) (ab227658, Abcam) at a 1:25 dilution in freshly prepared 1% BSA in PBS was performed for 45 min at 37°C in a wet chamber.

The Novolink Polymer Detection System (250T) (RE7140-K, Leica Biosystems) was used to detect the IHC reaction product according to the manufacturer's recommendations. Cell nuclei were stained with Mayer's hematoxylin. Sections of a formalin-fixed paraffin-embedded PTC tissue from a patient not related to this study with the confirmed by Sanger sequencing *NRAS* c.182A>G mutation (resulting in the p.Q61R substitution) were used as a positive control. The IHC reaction was considered positive (expression of the $NRAS^{Q61R}$ mutant protein) when a membrane and cytoplasmic staining of TECs was observed.

$BRAF^{V600E}$

IHC using the anti-BRAF (mutated V600E) antibody (VE1) (ab228461, Abcam, Tokyo, Japan) was performed as described before (34). Sections of a formalin-fixed paraffin-embedded tumor tissue from a patient not related to this study with the confirmed by Sanger sequencing $BRAF^{V600E}$ mutation-positive PTC (35) were used as a positive control.

Ki-67 labeling index

The proliferative activity of TECs was evaluated by IHC using Ki-67 antibody (clone MIB-1; DAKO, Glostrup, Denmark, 1:100 dilution) in a Ventana BenchMark ULTRA instrument. Stained slides were digitally scanned with a NanoZoomer-XR (Hamamatsu, Japan) device and visualized using the NDP.view 2 software (Hamamatsu). The Ki-67 labeling index (Ki-67 LI) was determined with the image-analyzing software (CountσCell, Ki-67 antigen Semi-Auto Counter, Seiko Tec LTD, Fukuoka, Japan) in ~1,000 cells per case (TB, LZ). Image analysis was performed in a blind for the PD-L1, PD-1, $p16^{INK4A}$, $BRAF^{V600E}$ or $NRAS^{Q61R}$ status manner.

Thyroid dosimetry

^{131}I thyroid radiation doses (the absorbed doses in mGy) were calculated for each patient in the Radiation Protection Laboratory of the State Institution "National Research Center for Radiation Medicine of the National Academy of Medical Sciences of Ukraine", Kyiv using an ecological dosimetry model, which includes the

system of ecological iodine transport and biokinetic models of iodine ("TD-CTB") (36).

Probability of causation due to radiation

The probability of causation (POC) of a tumor by exposure to a known dose of radiation of a certain quality of a subject of a given sex and age after a definite period of latency was determined using the US NIH/NCI Division of Cancer Epidemiology and Genetics' Interactive RadioEpidemiological Program - Probability of Cancer Causation from Radiation Version 5.7.1 software [https://radiationcalculators.cancer.gov/irep, (37)] as described in our previous works (38, 39). In this study, the assigned share associated with the expected value of the excess relative risk was used as a POC estimate. The higher POC value reflects the higher likelihood of cancer development due to radiation exposure.

Statistical analysis

Univariate analyses were performed using Fisher's exact test for categorical data, and the Mann–Whitney test for continuous data comparison between two groups. Different coefficients of agreement and of correlation were calculated, and correspondence analysis was performed to assess the resemblance of various characteristics of the PTs, PMTSs and RMTSs (statistical tests are indicated in corresponding table footnotes or figure legends). The conditional logistic regression to analyze associations or stratified Cox proportional hazard models to analyze recurrences were run. Optimized models were created by non-automatic selection of variables using the minimization of the Akaike information criterion method. Models with small numbers of outcomes (< 5) or those with a quasi-complete separation of data points were conducted using Firth's approach to bias-reducing penalized maximum likelihood fit or exact logistic regression. Calculations were performed using SAS 9.4 (SAS Institute, Cary, NC, USA), IBM SPSS Statistics Version 24 software (International Business Machines Corp., Armonk, NY, USA) or R (R Core Team). All tests were two-sided; $p < 0.05$ was considered indicative of statistical significance.

Results

Clinicopathological characteristics

Subjects and groups

From 1998 to 2017, a total of 2,411 PTC tissues from the Ukrainian patients were collected and registered with the CTB. Among those, 2,018 PTCs were from patients aged from 18.0 to 48.4 years (32.7 (25.4-36.5) years, median and IQR) who were less than 18 [9.6 (4.2-13.0)] years at the time of the Chornobyl accident. These subjects belong to the high-risk group for developing radiogenic thyroid cancer as a result of internal exposure to ^{131}I (40–42). In addition, 393 sporadic PTCs were removed from patients aged from 8.7 to 25.3 [17.1 (13.7-23.3)] years born from January 1987 who were not exposed to radioactive fallout.

The RAI-R recurrent metastases reoperated at least 6 months after the primary surgery were detected in 60/2,411 (2.5%) patients of whom 46/2,018 (2.3%) were exposed and 14/393 (3.6%) were not exposed to radiation (p=0.155 for the difference in frequencies). On exploratory analysis, no statistical difference in the distribution of clinicopathological characteristics were detected between the radiogenic and sporadic PTC subgroups for the PTs, PMTSs and RMTSs except for the higher frequency of patients of older age at operation in the radiation-exposed subgroup, (Supplementary Tables 1–3). Therefore, all cases were pooled into the PT, PMTS and RMTS groups for further analysis. Data collected or generated in the course of this work are shown in Supplementary Figures 1–3, and descriptive characteristics of the pooled groups are presented in Table 1.

The PTs were characterized by a low frequency of microcarcinomas, 11.7%; 66.7% of tumors had a dominant papillary growth pattern, 45.0% had tall cell, and 6.7% hobnail features, more than 90% of PTs were non-encapsulated. Multifocality was seen in 31.7% of PTs; lymphovascular invasion was frequent, 75%, and so was extrathyroidal extension, 58.3%. Approximately a half of tumors were pT1, 53.3%; lymph node involvement, according to the pathological reports, was registered in 65% of patients (and in 83.0% in whom lymph node dissection was performed). Distant metastasis was detected in 1.7% of patients (1 case). Oncocytic and cystic changes were observed in 81.7% and 25%, respectively. The frequency of $BRAF^{V600E}$ was high, 69.5%, while that of $NRAS^{Q61R}$ was low, 1.7%, (1 case). The median Ki-67 LI was 5.1%, and tumors with Ki-67 LI exceeding 5% accounted for about a half of all cases, 50.8%. Expression of the p16 protein in tumor invasive areas was found in the vast majority of PTs, 98.3%.

Resemblance of clinicopathological characteristics between PT, PMTS and RMTS

Availability of the three types of malignant thyroid tissues from the same patient enabled the analysis of clinicopathological similarities between them. To assess the resemblance, we calculated various measures of association, including the odds ratios (ORs, Table 2), the agreement coefficients, correlation coefficients, and performed pairwise comparisons (Supplementary Figure 4, Supplementary Tables 4, 5) and correspondence analysis (Supplementary Figure 5) of tumor characteristics. Overall, different statistics aligned well to each other: the lack of association in the conditional logistic regression models were accompanied by the high agreement and correlation coefficients, and statistically insignificant estimate of the difference. Oppositely, statistically significant ORs were likely to be coupled with poor agreement and correlation coefficients, and statistically significant difference.

The PTs displayed very weak similarities of their dominant growth patterns and histological subtypes to those of the PMTSs and RMTSs. However, the presence of tall cell and hobnail features in the PTs was rather preserved in the PMTSs and RMTSs. Extrathyroidal tumor extension of the PTs was in a poor correspondence with extranodal

TABLE 2 Pairwise associations between clinicopathological characteristics of the PTs, PMTSs and RMTSs.

Parameters	OR (95% CI)[a]	p-value[a]	OR (95% CI)	p-value	OR (95% CI)	p-value
	PTs (ref) and PMTSs		*PTs (ref) and RMTSs*		*PMTSs (ref) and RMTSs*	
Dominant growth pattern	2.299 (1.073-4.926)	**0.032**	1.738 (1.085-2.784)	**0.021**	1.385 (0.540-3.550)	0.498
papillary	0.250 (0.071-0.886)	**0.032**	0.389 (0.162-0.931)	**0.034**	1.000 (0.202-4.955)	1.000
follicular	2.000 (0.366-10.919)	0.423	0.750 (0.168-3.351)	0.706	0.260 (0.000-1.714)	0.125
solid-trabecular	4.500 (0.972-20.827)	0.054	3.000 ((1.191-7.558)	**0.020**	4.000 (0.396-196.990)	0.375
Histological subtype	0.747 (0.537-1.040)	0.084	0.785 (0.620-0.993)	**0.043**	1.029 (0.723-1.474)	0.935
papillary	1.667 (0.324-10.732)	0.727	1.200 (0.518-2.777)	0.670	1.250 (0.336-4.655)	0.739
follicular variant	1.500 (0.251-8.977)	0.657	1.000 (0.141-7.099)	1.000	0.414 (0.000-3.472)	0.250
solid-trabecular	13.933 (2.863-inf [b])	**9.77E-04**	10.000 (2.429-88.241)	**1.21E-04**	3.000 (0.536-30.393)	0.289
conventional	0.286 (0.094-0.868)	**0.027**	0.364 (0.162-0.817)	**0.014**	0.857 (0.238-2.979)	1.000
rare (tall cell and Warthin-like)	0.400 (0.078-2.062)	0.273	0.250 (0.053-1.177)	0.080	1.000 (0.072-13.796)	1.000
Tall cell features	0.500 (0.125-1.999)	0.327	0.900 (0.366-2.215)	0.819	2.000 (0.287-22.110)	0.688
Hobnail features	1.000 (0.141-7.099)	1.000	3.000 (0.812-11.081)	0.099	5.000 (0.559-236.488)	0.219
Extrathyroidal and extranodal extension	0.059 (0.008-0.442)	**0.006**	0.368 (0.155-0.876)	**0.024**	1.500 (0.356-7.227)	0.754
Oncocytic changes	0.260 (0.000-1.714)	0.125	0.857 (0.238-2.979)	1.000	0.750 (0.110-4.433)	1.000
Cystic changes	3.333 (0.858-18.849)	0.092	3.332 (1.291-10.143)	**0.009**	3.000 (0.536-30.393)	0.289
$BRAF^{V600E}$-positive	NA[c]	NA	NA	NA	NA	NA
$NRAS^{Q61R}$-positive	NA	NA	NA	NA	NA	NA
Ki-67 labeling index, % group	0.731 (0.331-1.612)	0.437	0.909 (0.496-1.667)	0.758	0.691 (0.293-1.628)	0.398
p16-positive TEC, invasive areas	0.414 (0.000-3.472)	0.250	1.000 (0.053-inf)	0.500	2.414 (0.288-inf)	0.250

[a]exact conditional logistic regression.
[b]infinity.
[c]not available (due to the lack of variability).
Numbers in bold indicate statistical significance.

extension in the PMTSs and RMTSs. Oncocytic changes were quite consistent between the three tumor tissue types. Cystic changes in the PTs corresponded weakly with the presence of those in the PMTSs and RMTSs. Mutational statuses of the three tumor tissue types were fully concordant. The distributions of Ki-67 LI groups and p16-positivity in the PT TECs corresponded rather weakly to those of the PMTSs and RMTSs.

The clinicopathological characteristics of the PMTSs and RMTSs, in contrast to those of the PTs, were markedly consistent between each other. Except for the Ki-67 LI distribution, whose resemblance in PMTSs and RMTSs was rather weak, all other parameters moderately to nearly perfectly corresponded to each other in the two metastatic tissues.

Changes of clinicopathological characteristics from PT to PMTS and RMTS

Comparison of changes from the PT to PMTS and to RMTS (Table 2; Supplementary Figure 4 for pairwise comparisons) demonstrated that the papillary dominant growth pattern was statistically significantly less frequently observed in the PMTSs and RMTSs (OR = 0.250 (0.071-0.886) and 0.389 (0.162-0.931), respectively) than in the PTs. Accordingly, the frequencies of the conventional histological subtype (which has the papillary dominant growth pattern more commonly) was lower in the metastatic (OR = 0.286 (0.094-0.868) and 0.364 (0.162-0.817) for PMTS and RMTSs, respectively) than in the primary tumors. In contrast, the frequencies of the solid-trabecular dominant growth pattern in the PMTSs and RMTSs (OR = 4.500 (0.972-20.827), marginally, and 3.000 (1.191-7.558), respectively) and of the solid-trabecular subtype (OR = 13.933 (2.863-infinity) and 10.000 (2.429-88.241), respectively) were higher than in the PTs. Cystic changes were also more frequent in the metastatic tumors [OR = 3.333 (0.858-18.849), marginally) and 3.332 (1.291-10.143)]. Frequencies of the tall cell and hobnail features which are commonly associated with the aggressive tumor phenotype did not statistically significantly differ between the three tumor tissue types, although the frequency of the latter tended to increase from PMTS to RMTS. Extranodal extension in the metastatic tumors was less frequent than in the PTs (OR = 0.059 (0.008-0.442) for PMTSs and 0.368 (0.155-0.876) for RMTSs). The distributions of Ki-67 LI and p16-positivity did not shift towards the increase in the metastatic tumors as compared to the PTs (all ORs ≤ 1).

Of note, in contrast to comparisons to PTs, there were no statistically significant changes in the clinicopathological

parameters between the PMTSs and RMTSs (Table 2; Supplementary Figure 4), which is consistent with their highly concordant characteristics described above.

Risk factors for RAI-R recurrent metastases

Univariate regression analysis revealed a few risk factors for the RAI-R recurrent metastases (Supplementary Table 6). Interestingly, a history of radiation exposure [HR = 0.526 (0.283-0.980)] and the higher POC level [HR = 0.987 (0.975-0.999)] reduced the risk, while the longer period of latency of radiogenic PTCs elevated it [HR = 1.117 (1.047-1.192)]. At the same time, radiation dose to the thyroid was not a risk factor [HR = 0.999 (0.997-1.000)]. Among the clinicopathological characteristics, the presence of N1b primary metastases was a risk factor for RAI-R RMTS [HR = 1.777 (1.034-3.053)]; naturally, since N1b could only be pathologically confirmed after the lateral lymph node dissection, this surgical option was a "technical" risk factor [HR = 1.932 (1.141-3.272)]. The greater number of RAI therapy cycles [HR = 1.220 (1.023-1.456)] and, correspondingly, the higher cumulative activity of RAI (HR = 1.000 (1.000-1.000), p = 0.006) were the treatment options associating with elevated risk for RAI-R that are explainable by the continuous attempts to eradicate a recurrent tumor.

The optimized stratified multivariate regression model of risk for RAI-R RMTS included four variables: the POC level, N1b primary metastases, dominant solid-trabecular growth pattern, and cystic changes in the PT (Table 3). The model had a moderate predictive performance as judged by the area under the curve [0.736 (0.595-0.797)], the Brier score (0.325), and Harrell's concordance index (0.658). In agreement with univariate assessment, the N1b primary metastases was the strongest risk factor (HR = 2.430 (1.308-4.666), and POC level, on the contrary, had a protective impact [HR = 0.983 (0.930-0.996)]. Of note, POC level had an independent effect seen as a negligible change in effect size between the univariate and multivariate models (see Table 3). When POC was decomposed into its components (thyroid dose, sex, latency period and age at the time of the Chornobyl accident), it appeared that its "protective" effect was not related to radiation exposure *per se* [i.e., the thyroid dose, HR = 0.897 (0.686-1.172)], but to a longer latency period (i.e., time between irradiation and PT development (HR = 1.116 (1.043-1.194), see Table 3). POC is inversely associated with the latency period (the longer the latency, the lower POC), again pointing at the validity of POC association with the risk for RMTS due to the period of latency, which was also seen on univariate analysis.

Despite the effects of two other variables in the multivariate model, i.e. the solid-trabecular growth pattern and cystic changes did not reach statistical significance, the presence of those in pathological report would be advisable to be taken into account as factors potentially suggestive of the risk for developing RAI-R RMTS.

TABLE 3 Risk factors for recurrent RAI-R metastases.

Parameters	HR (95% CI)	p-value
Optimized multivariate model		
Probability of causation (POC), %	0.983 (0.970-0.996)	**0.011**
N1b	2.470 (1.308-4.666)	**0.005**
Solid-trabecular growth pattern	1.899 (0.922-3.910)	0.063
Cystic changes	1.483 (0.757-2.906)	0.251
Model performance: AIC[1] = 372.098; MITD AUC[2] = 0.736 (0.595-0.797); BS[3] = 0.325; HC[4] = 0.658		
Independent effect of the Probability of causation (POC)		
Probability of causation (POC), %	0.987 (0.975-0.999)	**0.036**
Model performance: AIC=374.200; MITD AUC=0.652 (0.641-0.661); BS=0.328; HC=0.604		
POC decomposed to the components		
Thyroid dose, mGy (log)	0.897 (0.686-1.172)	0.426
Sex (ref=F)	0.788 (0.382-1.625)	0.519
Period of latency, years	1.116 (1.043-1.194)	**0.001**
Age at accident, years	1.007 (0.937-1.082)	0.857
Model performance: AIC=260.989; MITD AUC=0.779 (0.670-0.868); BS=0.326; HC=0.683		

[1] Akaike information criterion.
[2] Median integrated time-dependent area under curve (5-95% distribution-free CI).
[3] Brier score (a metric of the accuracy of probabilistic prediction; the closer to 0, the better).
[4] Harrell's concordance index (predictive power of a model; the closer to 1, the better).
Numbers in bold indicate statistical significance.

TABLE 4 Immune checkpoint (ICS) status of the primary tumors, primary metastases and recurrent metastases of the RAI-R recurrent PTCs.

Parameters	Primary tumors n=59 (%)	Primary LN metastases n=35 (%)	Recurrent metastases n=59 (%)
PD-L1-positive TEC[1]	30 (50.8%)	19 (54.2%)	29 (49.1%)
≤ 25%	14 (23.7%)	7 (20.0%)	12 (20.3%)
> 25 – 50%	13 (22.0%)	6 (17.1%)	7 (11.9%)
> 50 – 75%	3 (5.1%)	6 (17.1%)	10 (16.9%)
> 75 – 100%	0	0	0
PD-L1-positive TAIC[2]	44 (74.6%)	30 (85.7%)	48 (81.4%)
≤ 25%	35 (59.3%)	17 (48.6%)	28 (47.5%)
> 25 – 50%	9 (15.3%)	13 (37.1%)	20 (33.9%)
> 50 – 75%	0	0	0
> 75 – 100%	0	0	0
PD-1-positive TAIC	35 (59.3%)	26 (74.3%)	37 (62.7%)
≤ 25%	31 (52.5%)	16 (45.7%)	29 (49.2%)
> 25 – 50%	4 (6.8%)	10 (28.6%)	8 (13.5%)
> 50 – 75%	0	0	0
> 75 – 100%	0	0	0
Positive ICS	14 (23.7%)	12 (34.3%)	17 (28.8%)

[1] Tumor epithelial cells.
[2] Tumor-associated immune cells.

Immune checkpoint status

Positive ICS *versus* negative ICS

About 50% of TECs and 75-85% of TAICs were positive for PD-L1, and 60-70% of TAICs also expressed PD-1 in the PT, PMTS and RMTS (Table 4). Based on the definition (see Methods), positive ICS for each individual tumor tissue was found in 23.7% (14/59) of PTs, 34.3% (12/35) of PMTS, and 28.8% (17/59) of RMTS.

Comparisons of baseline and clinicopathological characteristics of ICS-positive and ICs-negative tumor tissues of the PTs, PMTSs and RMTSs are presented in Supplementary Tables 7–9, respectively. In general, in all three forms of tumors, most of characteristics did not differ, including a radiation history, yet some were at variance.

In the subgroup of ICS-positive PTs (Figures 1A-D), there were only female patients (p = 0.013), more frequent rare histological variants (p = 0.047, the Warthin-like and tall cell variants), more frequent pronounced oncocytic changes (in > 50% TECs, p = 0.013), higher Ki-67 LI (p = 0.003), and higher frequencies of p16-positivity (in > 50% TECs, p = 0.030) and of chronic thyroiditis (p = 4.41E-04).

In the ICS-positive PMTSs (Figures 1E-H), the differences included more frequent solid-trabecular dominant growth pattern and subtype (p = 0.011 and 0.022, respectively), higher frequency of oncocytic metastatic tumors (p = 0.038) and of p16-positivity (in > 75% TECs, p = 0.007). Ki-67 LI was somewhat higher, but the difference did not reach statistical significance (p = 0.087).

The ICS-positive RMTSs (Figures 1I-L) were characterized by the female patient prevalence (p = 0.045), less frequent papillary growth pattern and subtype (p = 3.10E-05 and 0.003, respectively) and, in contrast, more frequent solid-trabecular growth pattern and subtype (p = 2.00E-06 and 2.96E-04, respectively), more frequent pronounced oncocytic changes (in > 50% TECs, p = 1.11E-04), higher Ki-67 LI (p = 0.041), and higher frequency of p16-positivity (in > 50% TECs, p = 0.007).

Note that, while the ICS-positive PTs had comparable proportions of the dominant papillary and solid-trabecular architecture, the PMTSs and especially RMTSs had a solid-trabecular dominant growth pattern with increasing frequencies (Figures 1A, E, I). A similar tendency was observed for the p16-positivity in tumor invasive areas (Figures 1D, H, L). Also of interest, despite the ICS-positive tumors generally had a higher Ki-67 LI and p16-positivity than the ICS-negative ones, even in the areas with high density of the p16-positive TECs, the Ki67-positive TECs were absent or isolated and did not colocalize with the $p16^{INK4A}$-positive cells (Figure 2). No statistically significant correlation between Ki-67 and $p16^{INK4A}$ levels was detected in the primary or metastatic tumors (p > 0.05 for any comparison). No

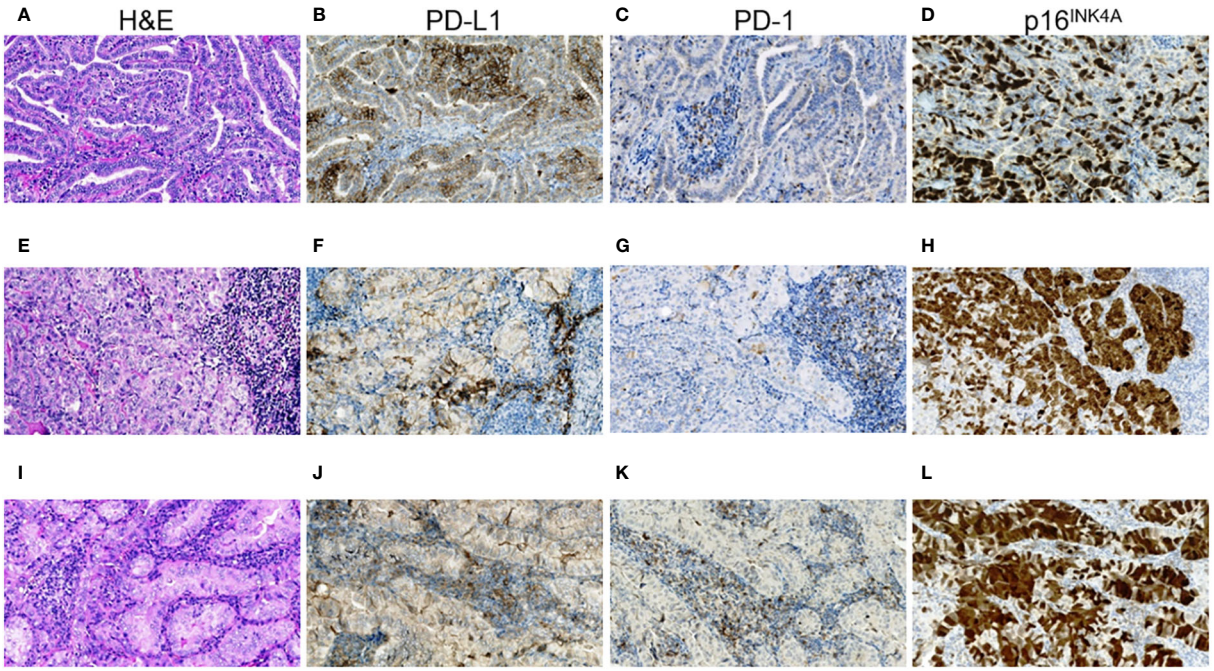

FIGURE 1
RAI-R recurrent papillary thyroid carcinoma with positive immune checkpoint status and $p16^{INK4A}$ staining. **(A–D)** Primary tumor: **(A)** papillary-trabecular growth pattern, tall cell features, oncocytic changes, H&E, ×200; **(B)** positive membrane-cytoplasmic IHC staining for PD-L1 in > 50% of TECs, some positive TAICs can be seen, ×200; **(C)** negative IHC staining for PD-1 in TECs and positive reaction in up to 25% TAICs, ×200; **(D)** positive nucleo-cytoplasmic IHC staining for $p16^{INK4A}$ in > 50% TECs, ×200. **(E–H)** Primary oncocytic cell metastasis of the tumor: **(E)** solid growth pattern, H&E, ×200; **(F)** positive membrane-cytoplasmic IHC staining for PD-L1 in > 50% of TECs and in > 25% TAICs, ×200; **(G)** negative IHC staining for PD-1 in TECs and positive reaction in > 25% TAICs, ×200; **(H)** positive nucleo-cytoplasmic IHC staining for $p16^{INK4A}$ in > 75% TECs, ×200; **(I–L)** RAI-R recurrent oncocytic cell metastasis removed 2.8 years after the 1st surgery: **(I)** solid-trabecular growth pattern, H&E, ×200; **(J)** positive membrane-cytoplasmic IHC staining for PD-L1 in > 50% of TECs and in > 25% TAICs, ×200; **(K)** negative IHC staining for PD-1 in TECs and positive reaction in > 25% TAICs, ×200; **(L)** positive nucleo-cytoplasmic IHC staining for $p16^{INK4A}$ in > 75% TECs, ×200. H&E, hematoxylin-eosin staining; TECs, tumor epithelial cells; TAICs, tumor-associated immune cells.

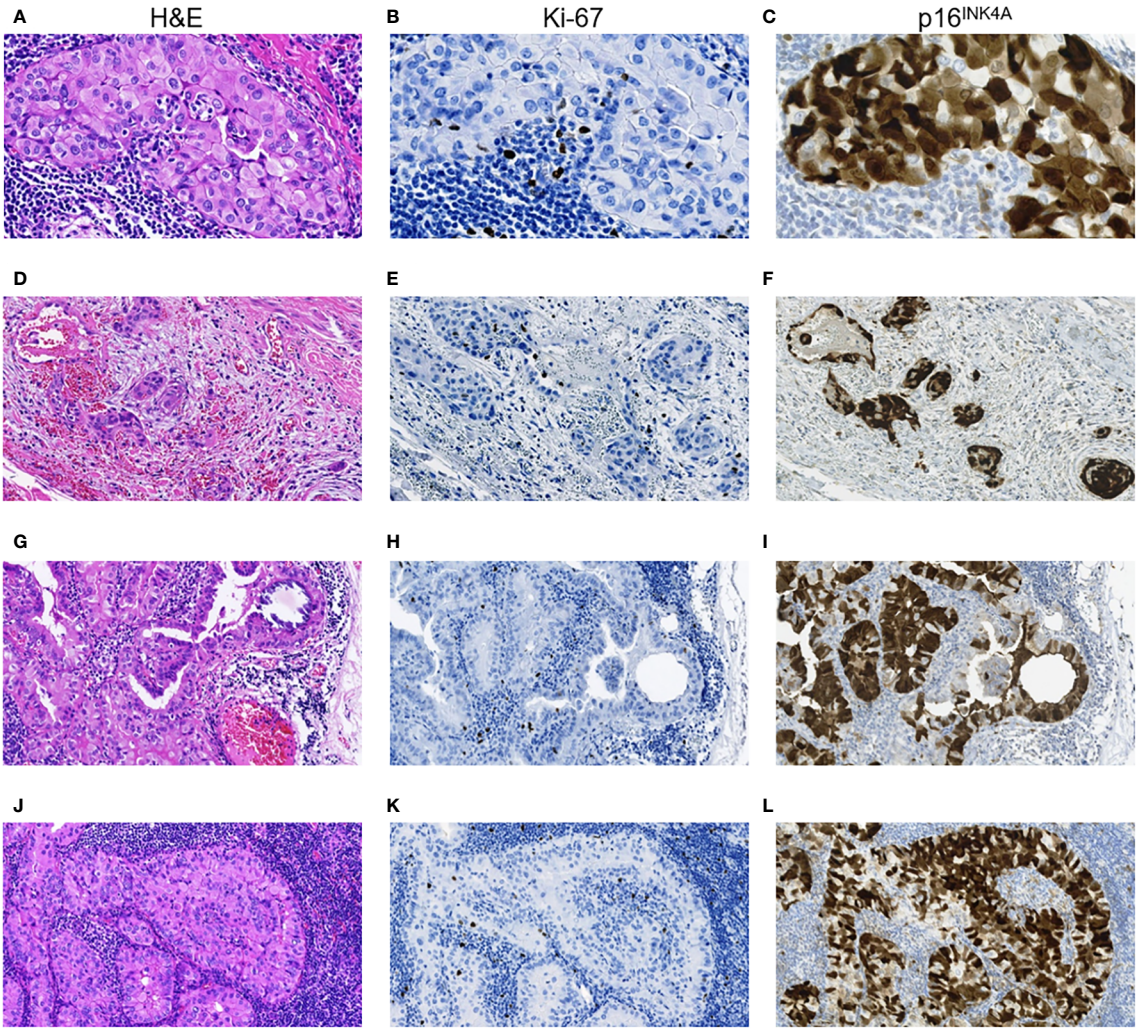

FIGURE 2
RAI-R recurrent papillary thyroid carcinoma with positive immune checkpoint status: particularities of Ki-67 and p16^{INK4A} expression. **(A–C)** Primary tumor: **(A)** intrathyroid spread, oncocytic solid TEC locus, H&E, ×400; **(B)** same locus, isolated Ki-67 positive TECs, IHC reaction with anti-Ki67 antibody, ×400; **(C)** same locus, positive nucleo-cytoplasmic IHC staining for p16^{INK4A} in > 75% TECs, ×400. **(D–F)** Primary tumor: **(D)** extrathyroidal extension of TEC loci, H&E, ×200; **(E)** same area, isolated Ki-67 positive TECs, IHC reaction with anti-Ki67 antibody, ×200; **(F)** positive nucleo-cytoplasmic IHC staining for p16^{INK4A} in > 75% TECs, ×200. **(G–I)** Primary lymph node metastasis of the tumor: **(G)** peripheral area with solid-papillary structure, H&E, ×400; **(H)** same area, isolated Ki-67 positive TECs, IHC reaction with anti-Ki67 antibody, ×400; **(I)** same area, positive nucleo-cytoplasmic IHC staining for p16^{INK4A} in > 75% TECs, ×400; **(J–L)** RAI-R recurrent lymph node metastasis of the tumor: **(J)** oncocytic solid tumor loci spread, H&E, ×400; **(K)** same area, isolated Ki-67 positive TECs, IHC reaction with anti-Ki67 antibody, ×400; **(L)** same area, positive nucleo-cytoplasmic IHC staining for p16^{INK4A} in > 75% TECs, ×400. H&E, hematoxylin-eosin staining; TEC, tumor epithelial cell.

indications pointing at the association between the mutational status and ICS was found in a given group of RAI-R PTCs (Supplementary Tables 7–9; Figure 3).

Predictors of the ICS positivity

First, we assessed the consistency of ICSs of the PTs, PMTSs and RMTSs. As shown in Table 5, for the vast majority of cases, there was an excellent agreement, correlation and no statistical difference between ICSs in the three corresponding tumors. There was only one patient in whom the positive ICS of the PT was lost in the PMTS and RMTS (Figure 4). In contrast, in four patients with ICS-negative PTs, ICS-positivity was observed in the RMTSs, of whom in two patients ICS-positivity was gained in PMTSs and persisted in RMTSs, and in one patient with ICS-negative PT and PMTS, ICS positivity was found in RMTS. These data strongly suggest that there is no reason to expect frequent decline of ICS in RMTS as compared to that of PT and/or PMTS.

A highly consistent ICS between the tumors from the same patient also suggested that ICS of the PT may be a good predictor of ICS of the RMTS. Indeed, a multivariate regression model adjusted for age and sex returned the following parameter estimates for the ICS of the PT: OR = 76.488 (8.201-713.404), p = 1.407E-07, AUC = 0.920 (0.840-1.000), crossvalidated AUC = 0.861 (0.729-0.994), Brier score = 0.075.

Finally, we attempted to determine clinicopathological parameters that could be associated with the positive ICS of the PT, PMTS and RMTS. The optimized multivariate models (Table 6) showed that for the PTs these were the pronounced oncocytic

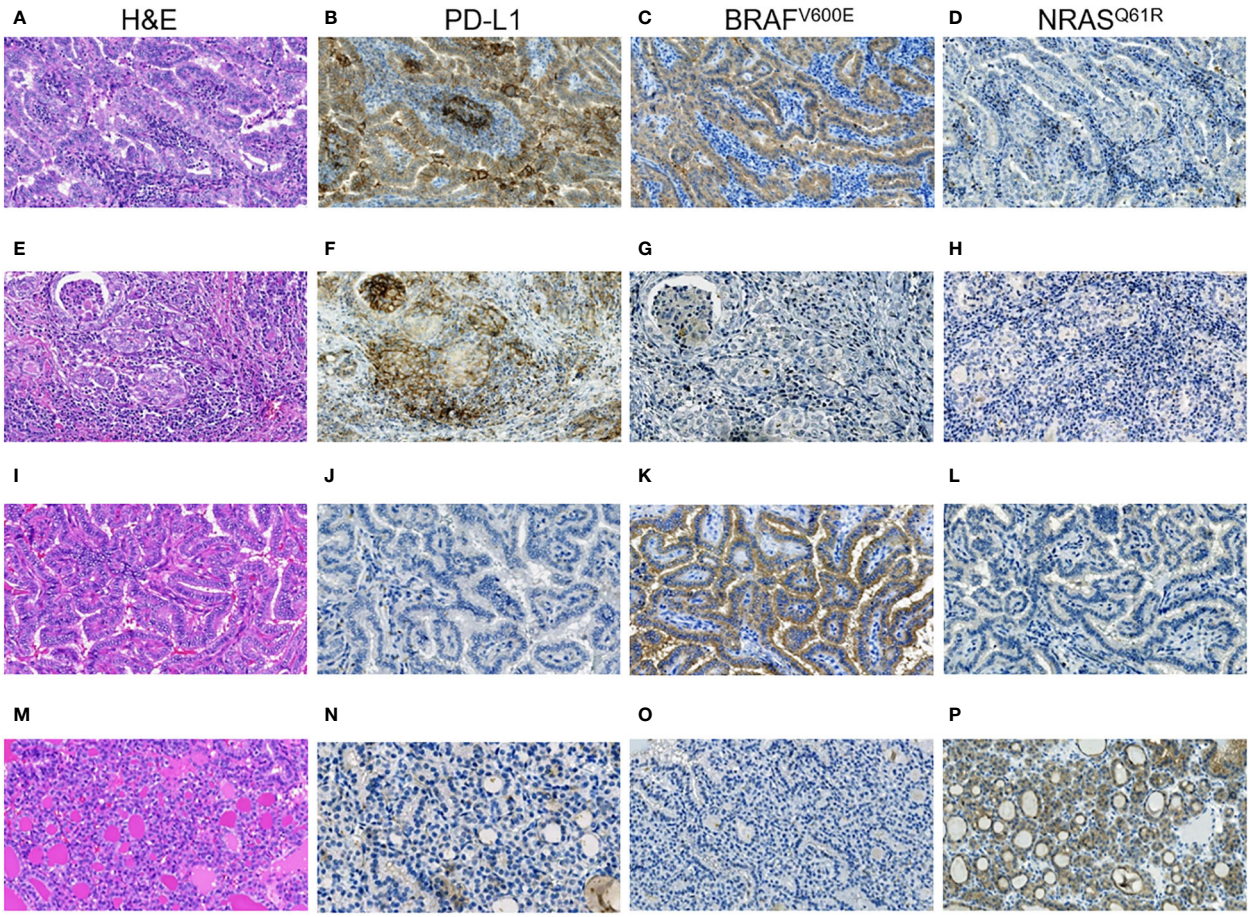

FIGURE 3
RAI-R recurrent papillary thyroid carcinomas with different immune checkpoint status and driver oncogenes. **(A–D)** Primary tumor: **(A)** Warthin-like growth pattern, oncocytic changes, H&E, ×200; **(B)** positive membrane-cytoplasmic IHC staining for PD-L1 in > 50% of TECs, and in > 25% TAICs, ×200; **(C)** positive diffuse cytoplasmic IHC staining for $BRAF^{V600E}$ in TECs, ×200; **(D)** negative IHC staining for $NRAS^{Q61R}$ in TECs, ×200. **(E-H)** Primary tumor: **(E)** solid growth pattern, oncocytic changes, H&E, ×200; **(F)** positive membrane-cytoplasmic IHC staining for PD-L1 in > 50% of TECs, and in > 25% TAICs, ×200; **(G)** negative IHC staining for $BRAF^{V600E}$ in TECs, ×200; **(H)** negative IHC staining for $NRAS^{Q61R}$ in TECs, ×200. **(I–L)** Primary tumor: **(I)** papillary growth pattern, oncocytic changes, focal tall cell features, H&E, ×200; **(J)** negative IHC staining for PD-L1 in TECs, ×200; **(K)** positive diffuse cytoplasmic IHC staining for $BRAF^{V600E}$ in TECs, ×200; **(L)** negative IHC staining for $NRAS^{Q61R}$ in TECs, ×200. **(M–P)** Primary tumor: **(M)** fully encapsulated, follicular growth pattern, H&E, ×200; **(N)** negative IHC staining for PD-L1 in TECs, ×200; **(O)** negative IHC staining for $BRAF^{V600E}$ in TECs, ×200; **(P)** positive membrane-cytoplasmic staining for $NRAS^{Q61R}$ in TECs, ×200. H&E, hematoxylin-eosin staining; TECs, tumor epithelial cells; TAICs, tumor-associated immune cells.

changes [OR = 2.235 (1.120-4.460)] and a high density of $p16^{INK4A}$-positive TECs in the invasive tumor areas [OR = 2.582 (1.259-5.292)]. For PMTSs these were the dominant solid-trabecular growth pattern (OR = 48.596 (2.972-794.494)) and Ki-67 LI > 4.3% [OR = 1.676 (1.072-2.621)] of the PMTS. For RMTSs, the pronounced oncocytic changes [OR = 2.921 (1.405-6.074)] and Ki-67 LI > 4.5% [OR = 1.290 (1.033-1.610)] of the PT, and the solid-trabecular growth pattern [OR = 48.596 (2.972-794.494)] and Ki-67 LI > 7.6% [OR = 1.594 (1.095- 2.321)] and a high density of $p16^{INK4A}$-positive TECs in the invasive metastatic areas [OR=3.374 (1.169-9.739)] of the RMTS were the predictors. Note that the formal risk scores (i.e., the odds ratios of ICS positivity of a given tumor tissue depending on the number of the identified by the model predictors) were consistently increasing with increasing number of such predictors (see Table 6). These findings may be useful for tentative or preliminary determination of candidate patients with RAI-R PTC for ICS testing if deemed necessary.

Discussion

The first major purpose of this study was to determine the prevalence of the RAI-R recurrent metastases in young and middle-aged PTC patients, and whether radiation exposure in childhood and/or other clinicopathological characteristics affect the chance of such recurrences.

We found that in young and middle-aged patients the RAI-R RMTSs of PTC are rather rare (~2-4%). This frequency is somewhat lower than that reported in the literature (8–10), and it is explainable by a relatively young age of patients in the CTB. The frequency of RAI-R RMTSs was low among both exposed to radiation in childhood and non-exposed individuals. The difference between the frequency of RAI-R RMTSs in the two etiological groups was negligible despite the exposed patients being significantly older at first surgery. The unlikeliness that

TABLE 5 The immune checkpoint status resemblance in the primary tumors, primary metastases and recurrent metastases.

Parameters	Agreement[a]	Correlation[b]	Comparison[c]
Primary tumor and primary metastasis			
Percent agreement	91.40%		
Coefficient (95% CI)	0.829 (0.564-1.000)	0.808 (0.738-0.860)	
p-value	**4.45E-08**	**2.49E-06**	1.000
Primary tumor and recurrent metastasis			
Percent agreement	91.5%		
Coefficient (95% CI)	0.831 (0.681-0.980)	0.789 (0.713-0.846)	
p-value	**4.44E-16**	**1.89E-09**	0.688
Primary metastasis and recurrent metastasis			
Percent agreement	97.10%		
Coefficient (95% CI)	0.943 (0.706-1.000)	0.940 (0.906-0.962)	
p-value	**6.10E-11**	**4.28E-08**	1.000

[a]weighted Brennan-Prediger kappa (ordinal).
[b]Kendall's tau-b.
[c]Wilcoxon signed rank test using the Pratt method, exact p-value.
Numbers in bold indicate statistical significance.

radiation exposure may specifically affect the risk of developing RAI-R RMTS was further confirmed by regression models which demonstrated statistically insignificant impact of thyroid radiation dose.

Our analysis of histopathological resemblance of PT and metastatic tissues from the same patient clearly showed that PTs were quite different from metastases, whereas PMTSs and RMTSs displayed a high degree of similarity. Structural differences between primary PTC and their PMTS are well described, and usually a classical papillary structure is more often observed in PMTS than in PT (43), that is, metastatic lesions more often have a more differentiated phenotype than the PT. In our study, in contrast, both PMTS and RAI-R RMTS differed from PT by a more frequent less differentiated phenotype, namely a solid-trabecular structure, suggestive of a higher metastatic potential of TECs from such areas of PTs than that of cells from tumor areas of other structure. The current study was focused on RAI-R cases, however, which are the minority of PTCs that may demonstrate difference from PTCs totality.

In line with the latter observation, the dominant solid-trabecular growth pattern of PT was a parameter remaining (although with the borderline statistical significance) in the optimized risk model (see Table 3), and therefore it can be considered as a warning histopathological characteristic suggestive of the possibility of further development of RAI-R RMTS. While radiation dose to the thyroid did not appear to be a risk factor for recurrence, the longer latency period did associate with the RAI-R RMTSs risk, demonstrating that the chance of RMTS development is proportional to the time factor. A statistically significant parameter in our study that increased the risk of RAI-R was the lateral primary metastasis (N1b), which was also reported among risk factors for older patients (18).

The $BRAF^{V600E}$ mutation has been claimed to be a risk factor for recurrent RAI-R metastases of PTC in a number of studies (12, 16, 44, 45). In our previous work, we also obtained similar results in subjects exposed to radiation in childhood who lived in the northern regions of Ukraine most affected by the Chornobyl accident (38). The presence of the $BRAF^{V600E}$ mutation was associated with the decreased POC level and longer latency. We noted that among the 8 PTC cases with RAI-R RMTSs in the mentioned paper, 6 (75%) were $BRAF^{V600E}$-positive. In the current study, we analyzed the RAI-R RMTSs among all CTB donors with radiogenic and sporadic PTC and obtained almost the same frequency of $BRAF^{V600E}$-positive cases (41/59, 69.5%, p = 1.000

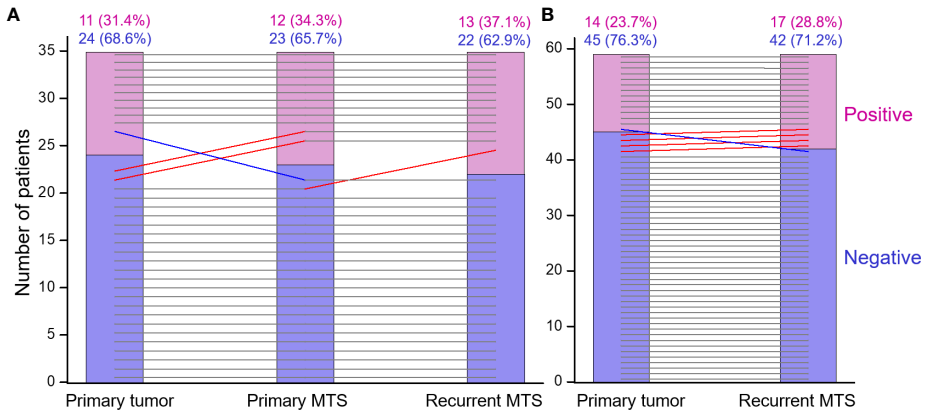

FIGURE 4
The immune checkpoint statuses of the primary tumor, primary metastasis and recurrent RAI-R metastasis are highly concordant. **(A)** Primary tumor, primary metastasis and recurrent RAI-R metastasis (n=35). **(B)** Primary tumor and recurrent RAI-R metastasis (n=59). The grey horizontal lines indicate no change in the statuses of tumors from the same patient. The red and blue lines indicate status elevation or decline, respectively; the slopes do not reflect the degree of change and serve for depiction only.

TABLE 6 Factors associated with the positive immune checkpoint status of the primary tumors, primary metastases and recurrent metastases.

Parameters	OR (95% CI)	p-value	Cut-off[1]
Primary tumors (primary tumor parameters)			
Oncocytic changes	2.235 (1.120-4.460)	**0.022**	Severe/oncocytic tumor
p16 positivity in invasive areas	2.582 (1.259-5.292)	**0.010**	≥ 50% p16-positive cells
Model performance: AIC[2] = 56.583; AUC[2] = 0.797 (0.647-0.947); AUC-CV[4] = 0.716 (0.538-0.894); BS[5] = 0.132			
Parameters present[6]			
0	1.000	ref	
1	4.000 (0.721-22.183)	0.113	
2	24.000 (3.247-177.404)	**0.002**	
Primary metastases (primary metastasis parameters)			
Solid-trabecular growth pattern	48.596 (2.972-794.494)	**0.006**	Sol-Trab structures ≥ 50%
Ki-67 labeling index	1.676 (1.072-2.621)	**0.024**	Ki-67 LI ≥ 4.3%
Model performance: AIC=33.183; AUC=0.881 (0.769-0.993); AUC-CV=0.818 (0.675-0.962); BS=0.134			
Parameters present			
0	1.000	ref	
1	9.881 (0.423-231.015)	0.154	
2	82.347 (2.370-inf)	**0.015**	
Recurrent RAI-R metastases (primary tumor parameters)			
Oncocytic changes	2.921 (1.405-6.074)	**0.004**	Severe/oncocytic tumor
Ki-67 labeling index	1.290 (1.033-1.610)	**0.024**	KI-67 LI ≥ 4.5%
Model performance: AIC=60.355; AUC=0.807 (0.680-0.934); AUC-CV=0.754 (0.613-0.894); BS=0.150			
Parameters present			
0	1.000	ref	
1	6.856 (0.781-60.159)	0.082	
2	47.990 (4.304-535.055)	**0.002**	
Recurrent RAI-R metastases (recurrent RAI-R metastasis parameters)			
Solid-trabecular growth pattern	43.635 (5.075-375.185)	**0.001**	Sol-Trab structures ≥ 50%
Ki-67 labeling index	1.594 (1.095-2.321)	**0.014**	KI-67 LI ≥ 7.6%
p16 positivity in invasive areas	3.374 (1.169-9.739)	**0.025**	≥ 75% p16-positive cells
Model performance: AIC=28.527; AUC=0.969 (0.931-1.000); AUC-CV=0.931 (0.855-1.000); BS=0.067			
Parameters present			
0	1.000	ref	
1	6.067 (0.273-134.747)	0.254	
2	246.999 (8.247-inf)	**0.001**	
3	428.949 (5.915-inf)	**0.006**	

[1] Cut-off values were determined using ROC analysis.
[2] Akaike information criterion.
[3] Area under the curve.
[4] Leave-one-out cross-validated area under the curve.
[5] Brier score.
[6] Tumors were categorized by the unweighted number of parameters from the corresponding regression model.
Numbers in bold indicate statistical significance.

compared to the previous work). From analytical point of view, the current study included RAI-R RMTS-only cases, which makes statistical models in it principally different from previous works which included both RAI-R RMTS and non-RAI-R RMTS cases. The difference in data sets and study design are the likeliest reasons for the presence or absence of certain other parameters in the presented multivariate models, which need to be interpreted appropriately. Despite the fact that *BRAF*^{V600E} mutation was not in the optimized risk model in the current study, it still should be considered as a factor affecting the chance of RAI-R RMTS. In practice, oncocytic changes in TECs are strongly predictive of the BRAF^{V600E} mutation, and therefore can be used as a morphological indicator suggestive of the presence of this oncogenic driver both in radiation-related and sporadic PTC (34, 38).

Our second purpose was to determine how often the positive immune checkpoint status can be expected in the primary tumors and metastatic tissues, and which clinicopathological characteristics are associated with it.

ICS positivity was found in about one-quarter of primary or metastatic tumors. This is not an exceedingly small proportion, and may thus deserve attention from clinicians. Note that ICS percent agreement between the PTs and metastatic tissues was 91%, and that between metastatic tissues was as high as 97%. This finding strongly suggests that ICS is rather consistent between a given PT and its metastases in most cases, and that ICS of a PT may be a strong predictor of ICS of a RMTS. In the current tumor series only one ICS-positive PT gave rise to ICS-negative PMTS and RMTS. On the contrary, ICS elevation from PT to RMTS was noted in 4 cases, demonstrating that the loss of ICS positivity in metastatic tissues is highly unlikely.

Positive ICS of primary and metastatic tumors was not associated with radiation exposure or radiation dose to the thyroid. Statistically significant factors associating with positive ICS of the PTs were more frequent pronounced oncocytic changes and a high density of p16^{INK4A} positive TECs in invasive tumor areas. The p16^{INK4A}-positive TECs constitute the so-called senescent tumor cells, which have received considerable attention in PTC during recent years (46–50). Due to their particular senescence-associated secretory phenotype, senescent tumor cells may potentiate tumor invasiveness, cell migration and metastatic spread contributing to PTC progression. Our study found that the high density of p16^{INK4A}-positive TECs in invasive areas was associated with the positive ICS both in the primary tumor and in RAI-R recurrent metastases. The mechanism by which tumor senescent cells modulate ICS in PTC is unknown, and remains to be established. Nevertheless, the high p16^{INK4A}-positivity of TECs along with pronounced oncocytic changes may serve as useful characteristics of a positive ICS of PT. In addition to pronounced oncocytic changes, Ki-67 LI ≥ 4.5% of PT can also be considered a factor associating with ICS positivity of the RMTS.

It should be noted that in contrast to other studies (51, 52), we did not find an association between positive ICS and the *BRAF*^{V600E} mutation. A high frequency of BRAF^{V600E}-positive RAI-R recurrent PTCs (approximately 70%) was found regardless of their ICS. This difference can probably be due to specific characteristics of a focused group of PTCs in our study restricted to RAI-R recurrent cases in patents of relatively young age. In fact, our study does not disprove the possibility of a link between *BRAF*^{V600E} and PD-L1 expression in PTC described by other groups.

In summary, we report that in young and middle-aged patients, the RAI-R recurrent PTCs are rather rare (2.5% of cases). Radiation dose to the thyroid does not appear to elevate the chance for recurrence after the first surgery, although in patients exposed to radiation the longer period of latency does. The presence of lateral primary metastases (N1b) is a risk factor for recurrence, and the solid-trabecular growth pattern and cystic changes in PTs are suggestive risk factors. Histopathological resemblance between PTs and metastatic tumors is rather weak, except for the solid-trabecular structures which tend to be preserved from PTs to metastatic tissues, implying their possibly higher metastatic potential. In contrast, histopathological characteristics of PMTSs and RMTSs are largely concordant, suggesting that only some PT cells may be associated with the development of RAI-R recurrent metastases, at least in the age group studied. About one-fourth of the PTs, PMTSs and RMTSs from young and middle-aged patients with RAI-R recurrent PTCs have positive ICS, which is highly concordant between the primary and metastatic tumors in most cases. ICS positivity is associated with pronounced oncocytic changes and high density of p16^{INK4A} positive TECs in invasive areas of the PTs and RMTSs. Pronounced oncocytic changes in TECs and a high Ki-67 LI of the PTs, and the solid-trabecular growth pattern and a high Ki-67 LI of the RMTSs are also associated with the positive ICS of RMTSs. These data may be useful for the development of individual treatment approaches to a subset of patients with RAI-R recurrent PTC for whom immunotherapy may be considered as an option from which the patients may benefit.

Data availability statement

The original contributions presented in the study are included in the article/Supplementary Material. Further inquiries can be directed to the corresponding author.

Ethics statement

The studies involving humans were approved by IEM Bioethics Committee and Ethics Committee of Nagasaki University. The studies were conducted in accordance with the local legislation and institutional requirements. The human samples used in this study were acquired from the pathological archive of IEM. Written informed consent for participation was not required from the participants or the participants' legal guardians/next of kin in accordance with the national legislation and institutional requirements.

Author contributions

TB: Conceptualization, Data curation, Formal analysis, Funding acquisition, Investigation, Methodology, Visualization, Writing –

original draft, Writing – review & editing. TIR: Conceptualization, Data curation, Formal analysis, Funding acquisition, Investigation, Methodology, Resources, Visualization, Writing – original draft, Writing – review & editing. LZ: Conceptualization, Data curation, Formal analysis, Funding acquisition, Investigation, Methodology, Visualization, Writing – review & editing. NM: Conceptualization, Funding acquisition, Methodology, Project administration, Resources, Supervision, Writing – review & editing. MT: Conceptualization, Methodology, Project administration, Supervision, Writing – review & editing. MI: Data curation, Formal analysis, Investigation, Methodology, Writing – review & editing. MB: Data curation, Formal analysis, Methodology, Writing – review & editing. SC: Data curation, Methodology, Writing – review & editing. SG: Data curation, Methodology, Writing – review & editing. SM: Data curation, Writing – review & editing. SY: Conceptualization, Methodology, Writing – review & editing. VAS: Conceptualization, Data curation, Formal analysis, Funding acquisition, Investigation, Methodology, Project administration, Resources, Supervision, Visualization, Writing – original draft, Writing – review & editing.

Funding

The author(s) declare financial support was received for the research, authorship, and/or publication of this article. This research was supported in part by the Program of the Network-Type Joint Usage/Research Center for Radiation Disaster Medical Science, intramurally by the Atomic Bomb Disease Institute, Nagasaki University, and the Japan Society for the Promotion of Science (JSPS), KAKENHI Grant Numbers 19K07471, 19KK02670001, and 20KK0217.

Acknowledgments

We gratefully acknowledge the commitment of the staff of the Laboratory of Morphology of Endocrine System and of the Department of Surgery of Endocrine Glands of IEM, who prepared all pathological material and operated on the patients, respectively. The authors gratefully acknowledge the confirmation of Ukrainian diagnoses by the International Pathology Panel of the Chornobyl Tissue Bank, which was supported by NCI grant number U24CA082102: A. Abrosimov, TB, G. Fadda, J. Hunt, MI, V. Livolsi, J. Rosai, E. D. Williams, N. Dvinskyh, and LZ.

Conflict of interest

The authors declare that the research was conducted in the absence of any commercial or financial relationships that could be construed as a potential conflict of interest.

Publisher's note

Supplementary material

The Supplementary Material for this article can be found online at: https://www.frontiersin.org/articles/10.3389/fendo.2023.1343848/full#supplementary-material

References

1. Aschebrook-Kilfoy B, Ward MH, Sabra MM, Devesa SS. Thyroid cancer incidence patterns in the United States by histologic type, 1992-2006. *Thyroid* (2011) 21(2):125–34. doi: 10.1089/thy.2010.0021

2. Dal Maso L, Tavilla A, Pacini F, Serraino D, van Dijk BAC, Chirlaque MD, et al. Survival of 86,690 patients with thyroid cancer: A population-based study in 29 European countries from Eurocare-5. *Eur J Cancer* (2017) 77:140–52. doi: 10.1016/j.ejca.2017.02.023

3. Baloch ZW, Asa SL, Barletta JA, Ghossein RA, Juhlin CC, Jung CK, et al. Overview of the 2022 who classification of thyroid neoplasms. *Endocr Pathol* (2022) 33(1):27–63. doi: 10.1007/s12022-022-09707-3

4. Haugen BR, Alexander EK, Bible KC, Doherty GM, Mandel SJ, Nikiforov YE, et al. 2015 American thyroid association management guidelines for adult patients with thyroid nodules and differentiated thyroid cancer: the american thyroid association guidelines task force on thyroid nodules and differentiated thyroid cancer. *Thyroid* (2016) 26(1):1–133. doi: 10.1089/thy.2015.0020

5. Luster M, Aktolun C, Amendoeira I, Barczynski M, Bible KC, Duntas LH, et al. European perspective on 2015 american thyroid association management guidelines for adult patients with thyroid nodules and differentiated thyroid cancer: proceedings of an interactive international symposium. *Thyroid* (2019) 29(1):7–26. doi: 10.1089/thy.2017.0129

6. Tuttle RM, Ahuja S, Avram AM, Bernet VJ, Bourguet P, Daniels GH, et al. Controversies, consensus, and collaboration in the use of (131)I therapy in differentiated thyroid cancer: A joint statement from the American Thyroid Association, the European Association of Nuclear Medicine, the Society of Nuclear Medicine and Molecular Imaging, and the European Thyroid Association. *Thyroid* (2019) 29(4):461–70. doi: 10.1089/thy.2018.0597

7. Gulec SA, Ahuja S, Avram AM, Bernet VJ, Bourguet P, Draganescu C, et al. A joint statement from the American thyroid association, the European association of nuclear medicine, the European thyroid association, the society of nuclear medicine and molecular imaging on current diagnostic and theranostic approaches in the management of thyroid cancer. *Thyroid* (2021) 31(7):1009–19. doi: 10.1089/thy.2020.0826

8. Xing M, Haugen BR, Schlumberger M. Progress in molecular-based management of differentiated thyroid cancer. *Lancet* (2013) 381(9871):1058–69. doi: 10.1016/S0140-6736(13)60109-9

9. Worden F. Treatment strategies for radioactive iodine-refractory differentiated thyroid cancer. *Ther Adv Med Oncol* (2014) 6(6):267–79. doi: 10.1177/1758834014548188

10. Capdevila J, Galofre JC, Grande E, Zafon Llopis C, Ramon YCAT, Navarro Gonzalez E, et al. Consensus on the management of advanced radioactive iodine-refractory differentiated thyroid cancer on behalf of the Spanish society of endocrinology thyroid cancer working group (Gtseen) and Spanish rare cancer working group (Gethi). *Clin Transl Oncol* (2017) 19(3):279–87. doi: 10.1007/s12094-016-1554-5

11. Nixon IJ, Whitcher MM, Palmer FL, Tuttle RM, Shaha AR, Shah JP, et al. The impact of distant metastases at presentation on prognosis in patients with differentiated carcinoma of the thyroid gland. *Thyroid* (2012) 22(9):884–9. doi: 10.1089/thy.2011.0535

12. Aashiq M, Silverman DA, Na'ara S, Takahashi H, Amit M. Radioiodine-refractory thyroid cancer: molecular basis of redifferentiation therapies, management, and novel therapies. *Cancers (Basel)* (2019) 11(9):1382. doi: 10.3390/cancers11091382

13. Durante C, Haddy N, Baudin E, Leboulleux S, Hartl D, Travagli JP, et al. Long-term outcome of 444 patients with distant metastases from papillary and follicular thyroid carcinoma: benefits and limits of radioiodine therapy. *J Clin Endocrinol Metab* (2006) 91(8):2892–9. doi: 10.1210/jc.2005-2838

14. Schlumberger M, Brose M, Elisei R, Leboulleux S, Luster M, Pitoia F, et al. Definition and management of radioactive iodine-refractory differentiated thyroid cancer. *Lancet Diabetes Endocrinol* (2014) 2(5):356–8. doi: 10.1016/S2213-8587(13)70215-8

15. Schmidt A, Iglesias L, Klain M, Pitoia F, Schlumberger MJ. Radioactive iodine-refractory differentiated thyroid cancer: an uncommon but challenging situation. *Arch Endocrinol Metab* (2017) 61(1):81–9. doi: 10.1590/2359-3997000000245

16. Liu H, Yang D, Li L, Tu Y, Chen C, Sun S. Appraisal of radioiodine refractory thyroid cancer: advances and challenges. *Am J Cancer Res* (2020) 10(7):1923–36.

17. Nakanishi K, Kikumori T, Miyajima N, Takano Y, Noda S, Takeuchi D, et al. Impact of patient age and histological type on radioactive iodine avidity of recurrent lesions of differentiated thyroid carcinoma. *Clin Nucl Med* (2018) 43(7):482–5. doi: 10.1097/RLU.0000000000002078

18. Shi LY, Liu J, Yu LJ, Lei YM, Leng SX, Zhang HY. Clinic-pathologic features and prognostic analysis of thyroid cancer in the older adult: A seer based study. *J Cancer* (2018) 9(15):2744–50. doi: 10.7150/jca.24625

19. Saie C, Wassermann J, Mathy E, Chereau N, Leenhardt L, Tezenas du Montcel S, et al. Impact of age on survival in radioiodine refractory differentiated thyroid cancer patients. *Eur J Endocrinol* (2021) 184(5):667–76. doi: 10.1530/EJE-20-1073

20. Thomas GA, Williams ED, Becker DV, Bogdanova TI, Demidchik EP, Lushnikov E, et al. Chernobyl tumor bank. *Thyroid* (2000) 10(12):1126–7. doi: 10.1089/thy.2000.10.1126a

21. Thomas GA. The chernobyl tissue bank: integrating research on radiation-induced thyroid cancer. *J Radiol Prot* (2012) 32(1):N77–80. doi: 10.1088/0952-4746/32/1/N77

22. Nervo A, Retta F, Ragni A, Piovesan A, Gallo M, Arvat E. Management of progressive radioiodine-refractory thyroid carcinoma: current perspective. *Cancer Manag Res* (2022) 14:3047–62. doi: 10.2147/CMAR.S340967

23. Shi RL, Qu N, Luo TX, Xiang J, Liao T, Sun GH, et al. Programmed death-ligand 1 expression in papillary thyroid cancer and its correlation with clinicopathologic factors and recurrence. *Thyroid* (2017) 27(4):537–45. doi: 10.1089/thy.2016.0228

24. Ulisse S, Tuccilli C, Sorrenti S, Antonelli A, Fallahi P, D'Armiento E, et al. Pd-1 ligand expression in epithelial thyroid cancers: potential clinical implications. *Int J Mol Sci* (2019) 20(6):1405. doi: 10.3390/ijms20061405

25. D'Andrea G, Lassalle S, Guevara N, Mograbi B, Hofman P. From biomarkers to therapeutic targets: the promise of pd-L1 in thyroid autoimmunity and cancer. *Theranostics* (2021) 11(3):1310–25. doi: 10.7150/thno.50333

26. Kovacevic B, Vucevic D, Cerovic S, Eloy C. Peripheral versus intraparenchymal papillary thyroid microcarcinoma: different morphologies and pd-L1 expression. *Head Neck Pathol* (2022) 16(1):200–12. doi: 10.1007/s12105-021-01337-1

27. Oh DY, Algazi A, Capdevila J, Longo F, Miller W Jr., Chun Bing JT, et al. Efficacy and safety of pembrolizumab monotherapy in patients with advanced thyroid cancer in the phase 2 keynote-158 study. *Cancer* (2023) 129(8):1195–204. doi: 10.1002/cncr.34657

28. Varricchi G, Loffredo S, Marone G, Modestino L, Fallahi P, Ferrari SM, et al. The immune landscape of thyroid cancer in the context of immune checkpoint inhibition. *Int J Mol Sci* (2019) 20(16):3934. doi: 10.3390/ijms20163934

29. Girolami I, Pantanowitz L, Mete O, Brunelli M, Marletta S, Colato C, et al. Programmed death-ligand 1 (Pd-L1) is a potential biomarker of disease-free survival in papillary thyroid carcinoma: A systematic review and meta-analysis of pd-L1 immunoexpression in follicular epithelial derived thyroid carcinoma. *Endocr Pathol* (2020) 31(3):291–300. doi: 10.1007/s12022-020-09630-5

30. Fullmer T, Cabanillas ME, Zafereo M. Novel therapeutics in radioactive iodine-resistant thyroid cancer. *Front Endocrinol (Lausanne)* (2021) 12:720723. doi: 10.3389/fendo.2021.720723

31. Lloyd RV, Osamura RY, Kloppel G, Rosai J. *Who Classification of Tumours of Endocrine Organs. 4 ed*. Lyon: IARC Press (2017).

32. Williams ED. Guest editorial: two proposals regarding the terminology of thyroid tumors. *Int J Surg Pathol* (2000) 8(3):181–3. doi: 10.1177/106689690000800304

33. Brierley JD, Gospodarowich MK, Wittekind C. *TNM Classification of Malignant Tumours. 8 ed*. Oxford: Wiley-Blackwell (2017).

34. Zurnadzhy L, Bogdanova T, Rogounovitch TI, Ito M, Tronko M, Yamashita S, et al. The Braf(V600e) mutation is not a risk factor for more aggressive tumor behavior in radiogenic and sporadic papillary thyroid carcinoma at a young age. *Cancers (Basel)* (2021) 13(23):6038. doi: 10.3390/cancers13236038

35. Nakao T, Matsuse M, Saenko V, Rogounovitch T, Tanaka A, Suzuki K, et al. Preoperative detection of the tert promoter mutations in papillary thyroid carcinomas. *Clin Endocrinol (Oxf)* (2021) 95(5):790–9. doi: 10.1111/cen.14567

36. Likhtarov I, Thomas G, Kovgan L, Masiuk S, Chepurny M, Ivanova O, et al. Reconstruction of individual thyroid doses to the Ukrainian subjects enrolled in the chernobyl tissue bank. *Radiat Prot Dosimetry* (2013) 156(4):407–23. doi: 10.1093/rpd/nct096

37. Kocher DC, Apostoaei AI, Henshaw RW, Hoffman FO, Schubauer-Berigan MK, Stancescu DO, et al. Interactive radioepidemiological program (Irep): A web-based tool for estimating probability of causation/assigned share of radiogenic cancers. *Health Phys* (2008) 95(1):119–47. doi: 10.1097/01.HP.0000291191.49583.f7

38. Zurnadzhy L, Bogdanova T, Rogounovitch TI, Ito M, Tronko M, Yamashita S, et al. Clinicopathological implications of the braf (V600e) mutation in papillary thyroid carcinoma of ukrainian patients exposed to the chernobyl radiation in childhood: A study for 30 years after the accident. *Front Med (Lausanne)* (2022) 9:882727. doi: 10.3389/fmed.2022.882727

39. Bogdanova T, Chernyshov S, Zurnadzhy L, Rogounovitch TI, Mitsutake N, Tronko M, et al. The relationship of the clinicopathological characteristics and treatment results of post-chornobyl papillary thyroid microcarcinomas with the latency period and radiation exposure. *Front Endocrinol (Lausanne)* (2022) 13:1078258. doi: 10.3389/fendo.2022.1078258

40. Likhtarev IA, Sobolev BG, Kairo IA, Tronko ND, Bogdanova TI, Oleinic VA, et al. Thyroid cancer in the Ukraine. *Nature* (1995) 375(6530):365. doi: 10.1038/375365a0

41. Saenko V, Ivanov V, Tsyb A, Bogdanova T, Tronko M, Demidchik Y, et al. The chernobyl accident and its consequences. *Clin Oncol (R Coll Radiol)* (2011) 23(4):234–43. doi: 10.1016/j.clon.2011.01.502

42. Tronko M, Bogdanova T, Saenko V, Thomas GA, Likhtaterv, Yamashita S. *Thyroid Cancer in Ukraine after Chernobyl: Dosimetry, Epidemiology, Pathology, Molecular Biology*. Nagasaki: IN-TEX (2014).

43. Nikiforov YE, Biddinger PW, Thompson LDR. *Diagnostic Pathology and Molecular Genetics of the Thyroid: A Comprehensive Guide for Practicing Thyroid Pathology. 3 ed*. Philadelphia: Wolters Kluwer (2020).

44. Luo Y, Jiang H, Xu W, Wang X, Ma B, Liao T, et al. Clinical, pathological, and molecular characteristics correlating to the occurrence of radioiodine refractory differentiated thyroid carcinoma: A systematic review and meta-analysis. *Front Oncol* (2020) 10:549882. doi: 10.3389/fonc.2020.549882

45. Jafri S, Yaqub A. Redifferentiation of braf V600e-mutated radioiodine refractory metastatic papillary thyroid cancer after treatment with Dabrafenib and Trametinib. *Cureus* (2021) 13(8):e17488. doi: 10.7759/cureus.17488

46. Zafon C, Obiols G, Castellvi J, Ramon y Cajal S, Baena JA, Mesa J. Expression of P21cip1, P27kip1, and P16ink4a cyclin-dependent kinase inhibitors in papillary thyroid carcinoma: correlation with clinicopathological factors. *Endocr Pathol* (2008) 19(3):184–9. doi: 10.1007/s12022-008-9037-z

47. Wang P, Pei R, Lu Z, Rao X, Liu B. Methylation of P16 cpg islands correlated with metastasis and aggressiveness in papillary thyroid carcinoma. *J Chin Med Assoc* (2013) 76(3):135–9. doi: 10.1016/j.jcma.2012.11.007

48. Kim YH, Choi YW, Lee J, Soh EY, Kim JH, Park TJ. Senescent tumor cells lead the collective invasion in thyroid cancer. *Nat Commun* (2017) 8:15208. doi: 10.1038/ncomms15208

49. Yoo SK, Song YS, Lee EK, Hwang J, Kim HH, Jung G, et al. Integrative analysis of genomic and transcriptomic characteristics associated with progression of aggressive thyroid cancer. *Nat Commun* (2019) 10(1):2764. doi: 10.1038/s41467-019-10680-5

50. Hong K, Cen K, Chen Q, Dai Y, Mai Y, Guo Y. Identification and validation of a novel senescence-related biomarker for thyroid cancer to predict the prognosis and immunotherapy. *Front Immunol* (2023) 14:1128390. doi: 10.3389/fimmu.2023.1128390

51. Siraj AK, Parvathareddy SK, Pratheeshkumar P, Divya SP, Al-Sobhi SS, Al-Dayel F, et al. Pd-L1 is an independent prognostic marker in middle eastern Ptc and its expression is upregulated by brafv600e mutation. *Cancers (Basel)* (2021) 13(3):555. doi: 10.3390/cancers13030555

52. Zhang M, Gu J, Wang W, Wang K, Zheng L, Feng J, et al. Combined expression of the braf(V600e) mutation and Pd-L1 in early papillary thyroid carcinoma and its relationship with clinicopathological features and recurrence-a retrospective cohort study. *Gland Surg* (2022) 11(12):1908–23. doi: 10.21037/gs-22-701

frontiers | Frontiers in Oncology

TYPE Original Research
PUBLISHED 06 February 2024
DOI 10.3389/fonc.2024.1323313

OPEN ACCESS

EDITED BY
Daekyu Sun,
University of Arizona, United States

REVIEWED BY
Shivam Priya,
The Ohio State University, United States
Alejandra Dagrosa,
National Atomic Energy Commission, Argentina

*CORRESPONDENCE
Malik Hamaidia
mhamaidia@uliege.be

†These authors have contributed equally to this work

RECEIVED 17 October 2023
ACCEPTED 19 January 2024
PUBLISHED 06 February 2024

CITATION
Sriramareddy SN, Jamakhani M, Vilanova L, Brossel H, Staumont B and Hamaidia M (2024) Selective inhibition of DNA ligase IV provides additional efficacy to the treatment of anaplastic thyroid cancer.
Front. Oncol. 14:1323313.
doi: 10.3389/fonc.2024.1323313

Selective inhibition of DNA ligase IV provides additional efficacy to the treatment of anaplastic thyroid cancer

Sathya Neelature Sriramareddy[1,2†], Majeed Jamakhani[1,2†], Léa Vilanova[1,2], Hélène Brossel[1,2], Bernard Staumont[1,2] and Malik Hamaidia[1,2*]

[1]Molecular and Cellular Epigenetics, Interdisciplinary Cluster for Applied Genoproteomics (GIGA), University of Liège, Liège, Belgium, [2]Molecular Biology (TERRA), University of Liege, Gembloux, Belgium

Background: Although the incidence of anaplastic thyroid carcinoma (ATC) is low (2.5% of thyroid cancer cases), this cancer has a very poor prognosis (survival rates < 5 months) and accounts for 14–39% of deaths. Conventional therapies based on surgery in combination with radiotherapy or chemotherapy showed limited effectiveness primarily due to the robust and protective DNA damage response in thyroid cancer cells.

Methods: We used single-cell transcriptomic data from patients with different subtypes of thyroid cancer to study expression of genes involved in homologous recombination (HR) and non-homologous end joining (NHEJ) pathways. Then, we investigated the mechanisms of DNA damage and repair in anaplastic (C643 and Hth74) and papillary (TPC-1) thyroid cancer cell lines. The effect of caffeine (inhibitor of ATM and ATR) and UCN-01 (CHK1 inhibitor) was evaluated in cell cycle progression of thyroid cancer cells after γ-radiation or doxorubicin treatment. The DNA damage response was monitored after staining of phosphorylated γ-H2AX and 53BP1. Reporter plasmids were used to determine the efficacy of double-strand DNA breaks (DSBs) repair by HR and NHEJ in thyroid cancer cells. We evaluated the combination of selective inhibition of the DNA ligase IV by SCR7 and doxorubicin on cellular apoptosis and tumor growth in xenograft murine models of anaplastic thyroid cancer.

Results: Single-cell RNA-Seq showed that NHEJ- and HR-related genes are expressed in ATC and PTC patients. We showed that ATC cells undergo mitosis in the presence of unrepaired DNA damage caused by γ-radiation and doxorubicin treatment. To proliferate and survive, these cells efficiently repair DNA lesions using homologous recombination (HR) and non-homologous end joining (NHEJ). The combination of SCR7 with doxorubicin, significantly increased apoptosis and impaired ATC tumor growth in a xenograft mouse model compared to doxorubicin monotherapy.

Conclusion: This study shows the therapeutic value of the combination of a DNA ligase IV inhibitor and DNA-damaging agents (doxorubicin and/or γ-radiation) for the treatment of anaplastic thyroid cancer.

KEYWORDS

anaplastic thyroid cancer, DNA ligase IV, homology directed repair, non-homologous end joining, radiotherapy, chemotherapy, single-cell RNA-seq

Introduction

Accounting for approximately 1% of newly diagnosed cancer cases, the incidence of thyroid cancer has increased over the past 3 decades by >5% per year (1–4). Thyroid cancers originate either from the follicular epithelium or from neuroendocrine C cells (i.e., follicular and medullary thyroid cancer, respectively). Follicular thyroid cancer can be subdivided into well-differentiated (WDTC), poorly differentiated (PDTC), and anaplastic (ATC) thyroid cancers (5). WDTC, which accounts for 90% of cases, includes papillary (PTC) and follicular (FTC) thyroid cancers. With long-term survival rates of 75-90%, the prognosis of medullary and WDTC thyroid cancers is relatively good (6–10). However, a significant proportion (10-35%) of patients relapse and lose the ability to uptake radioiodine-131 in tumors (5, 11–14). The main treatment for ATC and relapsing WDTC includes surgery, cytotoxic treatment (e.g., doxorubicin or cisplatin), and external beam radiation therapy (EBRT). Therapies that target cancer cells carrying the BRAFV600E mutation (dabrafenib/trametinib) have been recently approved for ATC but are associated with significant toxicities (15, 16). Although frequent in PTC, other genomic modifications, such as RET/PTC rearrangement, are uncommon in ATC. With median survival rates varying from 9 weeks to 5 months (5, 11–13, 17, 18), ATC is highly lethal and requires more efficient therapies.

Radiation therapy and topoisomerase inhibitors (e.g., doxorubicin) mainly induce DNA double-strand breaks (DSBs) in tumors. A critical component of radio resistance and chemoresistance is the ability of cancer cells to repair DNA damage. Indeed, DSBs initiate signaling and repair pathways orchestrated by sensors, transducers, and effectors of the DNA damage response (DDR) (19–21). DSBs induced by ionizing radiation and topoisomerase inhibitors can be repaired by homologous recombination (HR) and non-homologous end joining (NHEJ). HR is error-free repair pathway and requires DNA pairing with a homologous chromatid that is only available in late S and G2 phases of the cell cycle. However, NHEJ pathway can be initiated outside S and G2 phase and require a limited sequence homology. The NHEJ is initiated by the Ku70/Ku80 complex, which interacts with DSBs and recruits other components of the repair pathway, including the DNA-dependent protein kinase catalytic subunit (DNA-PKcs), endonuclease Artemis, DNA ligase IV, X-ray repair cross-complementing protein 4 (XRCC4) and polymerases μ and λ (Pol μ and Pol λ) (22). Upon recruitment to the DSB, DNA-PKcs undergoes autophosphorylation and activates Artemis, which then degrades DNA ends to produce short overhangs (≤4 nucleotides) between the strands that facilitate end joining. Upon activation by XRCC4, DNA ligase IV initiates end joining by transferring AMP to the 5′ end of one of the strands at the DSB. Covalent DNA ligation further requires the removal of AMP by aprataxin. Pol μ polymerizes short regions of microhomology for subsequent base pairing in a template-independent manner. Pol λ primarily promotes the ligation of terminally compatible overhangs that require fill-in synthesis (22). XRCC4-like factor (XLF) stimulates the ligation of short incompatible 3′ overhangs, while the paralog of XRCC4 and XLF (PAXX) promotes the joining of blunt ends. Therefore, NHEJ is the predominant mechanism to process most ionizing radiation-induced DSBs in thyroid cancer cells. However, NHEJ is error-prone process that can be responsible of genome instability or chromothripsis in response to DNA damaging therapies. These genomic rearrangements can increase thyroid cancer aggressiveness via the loss of a tumor suppressor gene and/or oncogene amplification (23). Therapeutic approaches that use pharmacological inhibitors targeting tyrosine kinase receptors (TKIs), BRAF V600E, Mitogen-activated kinases, mTOR, anaplastic lymphoma kinase, tropomyosin receptor kinases are proposed to reduce radio- and chemoresistance of thyroid cancer (14). Another strategy to increase tumor sensitivity to DNA damaging agents is to interfere DSBs repair pathways via the use

Abbreviations: ATC, anaplastic thyroid carcinoma; ATM, ataxia telangiectasia mutated; ATR, ataxia telangiectasia and Rad3-related protein kinases; CHK1/2, checkpoint kinase ½; DDR, DNA damage response; dHJ, double Holliday junction; DNA-PK, DNA-dependent protein kinase (DNA-PK); DSBs, DNA double-strand breaks; DSS1, deleted in spilt hand/spilt foot; EBRT, external beam radiation therapy; ERCC1, excision repair cross-complementation group 1; FTC, follicular thyroid cancer; HR, homologous recombination; LIG4, DNA ligase IV; MCM, minichromosome maintenance protein complex; NHEJ, non-homologous end joining; PARP1, poly(ADP-ribose) polymerase 1; PDTC, poorly differentiated thyroid cancer; PTC, papillary thyroid cancer; RPA, replication protein A; scRNA-seq, single cell RNA sequencing; SDSA, synthesis-dependent strand-annealing pathway; SSA, single-strand annealing; WDTC, well-differentiated thyroid cancer; XLF, XRCC4-like factor.XRCC, X-ray repair cross-complementing protein.

of selective inhibitors of PARP superfamily (e.g. Niraparib, Olaparib), DNA-PKcs (e.g. NU7441, M3814 or Nedisertib, AZD7648, M9831 or VX-984, KU-0060648), CHK1 (e.g. GDC-0575, MK-8776, Prexasertib), ATM (AZD0156, M3541), ATR (Ceralasertib, Berzosertib), WEE1 (Adavosertib) and DNA ligase IV (SCR7, NU7026) (24, 25). In this context, the objective of this study is (i) to evaluate the regulation of cell cycle and DSB repair activity (ii) to explore the therapeutic potential of DNA ligase IV selective inhibition after treatment of anaplastic thyroid cancer cells (C643 and Hth74) with conventional DNA damaging agents used for the treatment of thyroid cancer.

Methods

Cell cultures

Thyroid cancer cell lines C643 and Hth74 (anaplastic thyroid cancer) and TPC-1 (papillary thyroid cancer), provided by Karin Forsberg Nilsson (Uppsala University, Sweden), were grown in Dulbecco's modified Eagle's medium (DMEM) containing 100 units per ml penicillin, 100 µg/ml streptomycin and 10% fetal bovine serum (FBS). Cells were maintained at 37°C in a humidified incubator containing a 5% CO_2 atmosphere.

Cell cycle analysis

Thyroid cancer cells were seeded in 6-well plates (200,000 cells per well). Twenty-four hours later, the cells were γ-irradiated and/or incubated with checkpoint inhibitors (Sigma–Aldrich): UCN-01 (7-hydroxystaurosporin) resuspended in DMSO and caffeine (1,3,7-trimethylxanthine) dissolved in DMEM by heating (80°C) for 2 hours. After 24 hours, the cells were trypsinized and fixed in 300 µL of PBS-10% FBS and 700 µL of chilled ethanol. Following fixation overnight at -20°C, cells were incubated with RNase A solution (50 µg/mL in PBS with 0.1% Tween 20 (Sigma–Aldrich) for 30 minutes at 37°C. After suspension in propidium iodide (PI, 20 µg/L, Sigma–Aldrich), fluorescence was analyzed with a FACSCalibur flow cytometer (BD Biosciences) using BD CellQuest Pro software.

Mitotic trap assay

Three hours after γ-irradiation and/or incubation with UCN-01 or caffeine, thyroid cells were treated with 50 nM of Taxol (Bristol-Myers Squibb). After 16 hours of culture, cells were trypsinized, resuspended in PBS containing 10% FBS, and fixed overnight in 70% ethanol at -20°C. After removing ethanol, cells were labeled for 2 hours with an antibody specific for histone H3 phospho-Ser10 (Cell Signaling Technology, #9701, 1/200) and an anti-mouse immunoglobulin Alexa-488-conjugate (Invitrogen, 1/1000). After RNase A digestion and PI labeling, fluorescence was analyzed with a FACScanto II flow cytometer (BD Biosciences).

Confocal microscopy

Cells seeded on coverslips were fixed with 4% paraformaldehyde, permeabilized with 0.1% Triton X-100 for 10 minutes, and incubated with 5% bovine serum albumin (BSA). Cells were then labeled for 2 hours with primary antibodies specific for phospho-H2AX (Cell Signaling Technology, #2577, 1/400) or 53BP1 (Abcam, AB172580, 1/200). After nuclear staining with DAPI (Sigma), the cells were visualized with a Leica SP5 confocal microscope. Simultaneously, a similar experiment was conducted in parallel to analyze the mean fluorescence intensity of phospho-H2AX by FACScanto II flow cytometry.

Immunoblotting

At different times (2, 5, or 24 hours) after 10 Gy γ-irradiation, cells were lysed on ice with RIPA buffer (150 mM sodium chloride, 1% NP-40, 0.5% sodium deoxycholate, 0.1% SDS, 50 mM Tris pH 8.0) containing protease and phosphatase inhibitors: Halt Protease Inhibitor Cocktail (Thermo Fisher Scientific) and 1 mM phenylmethanesulfonyl fluoride (PMSF) (Sigma). After SDS-polyacrylamide gel electrophoresis (SDS–PAGE), proteins were transferred onto a nitrocellulose membrane and blocked for 1 hour with 5% BSA (Sigma–Aldrich) in TBS (Tris Buffered Saline) supplemented with 0.1% Tween 20. Proteins were labeled overnight at 4°C with antibodies directed against γ-H2AX (Cell Signaling Technology, #2577, 1/1000) or tubulin (Sigma, SAB4500087, 1/1000). After washing with TBS-Tween (0.1%), membranes were incubated with horseradish peroxidase (HRP)-conjugated secondary anti-rabbit antibody (Cell Signaling Technology, #7074, 1/1000) for 1 hour at room temperature. Luminescence was revealed with HRP substrate (Pierce ECL Western Blotting Substrate, Thermo Scientific) using a CCD camera (ImageQuant LAS4000 mini, GE Healthcare Life Sciences) and analyzed with ImageJ software.

Quantification of DNA repair efficiency

The quantification of DSB repair by HR and NHEJ was based on plasmid reporters provided by Vera Gorbunova (University of Rochester, USA)[37]. The GFP-Pem1 vector contains a GFP open reading frame interrupted by a 3 Kb intron from the Pem1 gene. In the NHEJ sensor, the Pem1 intron contains an additional adenoviral exon that is flanked by inverted HindIII/I-SceI restriction sites. Endonuclease cleavage leads to nonpalindromic incompatible DNA ends that are repaired by NHEJ. Cleavage of the adenoviral exon, transfection into cells, and repair by NHEJ restore GFP expression. In the HR reporter, the first exon of GFP-Pem1 has a 22 bp deletion flanked by I-SceI/HindIII/inverted I-SceI restriction sites. Due to the deletion, NHEJ repair of the restricted plasmid does not restore GFP expression. The HR reporter contains a second copy of the GFP first exon lacking an ATG. HR between

the deleted and ATG-mutated copy of GFP by gene conversion restores green fluorescence.

The HR and NHEJ reporter plasmids were digested overnight with I-SceI (VWR) and purified by gel electrophoresis using the QIAGEN gel extraction kit. Linearized plasmid (2 µg) was transfected with Lipofectamine (Thermo Fisher Scientific) into thyroid cancer cell lines together with 0.5 µg of pHcRed (Clontech). After 48 hours of culture under DNA-damaging conditions, cells were analyzed by flow cytometry. The efficiencies of HR and NHEJ pathways were calculated as ratios of GFP and HcRed fluorescence.

Analysis of apoptosis

TPC-1, C643, and Hth74 cells were cultivated for 48 hours in 6-well plates (10^5/well) in the presence of SCR7 (Xcess Bioscience), RI-1 (Axon MedChem), and/or doxorubicin (Sigma Aldrich, 200 nM). Cells were harvested, washed in cold PBS, suspended in 100 µL of binding buffer (PE Annexin V Apoptosis Detection Kit, BD Pharmingen), and labeled with 5 µL of Annexin-V FITC + 7-AAD for 15 minutes in the dark. For the analysis of genomic DNA fragmentation, 10^5 cells were washed twice in 10% FBS-PBS, resuspended in 300 µL of 10% FBS-PBS, and fixed with 700 µL chilled ethanol (100%) at -20°C. After overnight fixation, cells were recovered by centrifugation, washed twice, treated with RNase A (20 µg/ml) for 30 min, and stained for 10 min with PI (50 µg/ml). Fluorescence was analyzed with 585/42 filters in a FACSCalibur (Becton Dickinson).

Mouse models

Animal experimentation was approved by the Ethical Committee for the use of laboratory animals at the University of Liège (case number 14-1736) and performed according to the Federation of Laboratory Animal Science Association (FELASA) guidelines. The triple transgenic NOD. Cg-Prkdc^{scid} Il2rg^{tm1Wjl} Tg (CMV-IL3, CSF2, KITLG)1Eav/MloySzJ mice, also called NSG-SGM3 mice (provided by animal facility LA2610359), were inoculated subcutaneously into the right and left flanks with 2.10^6 C643 or Hth74 cells. A total of 200 µL medium suspension containing 50% v/v Matrigel (Basement Membrane Matrix, Corning) was injected in each flank using a 27G needle. Once the average tumor volume reached 50 mm^3, mice were randomized into 6 groups (n=5) to minimize weight and tumor size differences. Mice were mock-treated (vehicle) or injected intraperitoneally with doxorubicin (twice per week at 0.5 mg/kg) and/or SCR7 (10 mg/kg twice a week). Tumors were measured biweekly with a digital caliper, and tumor volume was estimated by using the formula (π x length x width^2)/6.

scRNA-Seq data processing

The publicly available scRNA-Seq data from 10 ATC tumors, 7 PTC tumors and 6 adjacent normal thyroid tissues with the GEO accession number GSE193581 were used for our study (26). Raw data composed of approximately 71,831 cells were filtered by using quality metrics (percentage of mitochondrial genes) with Scanpy (version 1.9.3). Single cells that had fewer than 200 genes or more than 6,000 genes detected were removed. Doublets were removed from each sample (Scrublet, version=0.2.3). Approximately 40,070 cells passed the quality control. The count matrix was log normalized and Z transformed (scanpy, version 1.9.3). The batch effect was evaluated and corrected (scanorama, version 1.7.3). The scanorama-corrected data were clustered by using the Elbow method, and 30 principal components were retained to determine the number of clusters (k) by using the k-means clustering algorithm. The k-mean value of 10 was used for our study. Clusters were automatically annotated for different cell types (CellTypist, version 1.5.2). Epithelial cells from k-mean clusters were extracted to perform differential gene expression between ATC, PTC and adjacent normal thyroid tissues (normal cells) within the epithelial cluster. Differential gene expression was performed by using the Wilcoxon rank sum test (scanpy, version 1.9.3) of 3 groups of ATC, PTC and normal cells.

Statistical analysis

Statistical relevance was determined using GraphPad Prism 8. The Shapiro–Wilk test was used to determine the normality of distribution, and the F test was used to determine the equality of variances. Means within a dataset with equal variance were compared by 1-way ANOVA followed by Tukey's multiple-comparisons test. Statistical significance between non-Gaussian paired distributions was calculated using the nonparametric Friedman's test followed by Dunn's multiple-comparisons test. The analysis of tumor growth was performed using 2-way ANOVA and Bonferroni's post-tests. Survival curves were compared by using a log-rank test ($\chi 2$). For Western blot and imaging data, statistical analysis was performed using the nonparametric Friedman's test followed by Dunn's multiple-comparisons test. Data were considered statistically significant (*), very statistically significant (**), and highly statistically significant (***) at $P < 0.05$, $P < 0.01$, and $P < 0.001$, respectively.

Results

NHEJ- and HR-related genes are differentially expressed in ATC and PTC tumors

We used a publicly available dataset of single-cell transcriptomes from 10 ATC tumors, 7 PTC tumors, and 6 adjacent normal thyroid tissues (GSE193581) to determine the expression of genes involved in NHEJ and HR pathways. A total of 40 070 cells out of 71 831 passed the quality control and were investigated for further analyses. We performed k-mean clustering (k-mean value 10) and automated identification of 10 major cell types found in the tumor microenvironment (Figures 1A, B). The

differential gene expression was investigated from the epithelial cluster because both normal thyroid cells and tumor cells are of epithelial origin (Figure 1C, Supplementary Table). We determined the differential expression of genes highly involved in NHEJ and HR pathways (KEGG references: K10980 and map03440, respectively) in tumors (PTC and ATC) and normal thyroid tissues (NORM). NHEJ- (*XRCC6, XRCC5, PRKDC*) and HR- (*SSBP1, SEM1, RPA2, RPA3*)-related genes were found to be expressed in both normal follicular and thyroid cancer cells. The mean expression of NHEJ-related genes (*XRCC6, XRCC5, PRKDC*) decreased in ATC epithelial cells compared to normal thyroid and PTC cells. The fraction of cells expressing HR-related genes (*SSBP1, SEM1, RPA2, RPA3*) was reduced but with a similar mean expression compared to normal cells and PTC (Figures 1D, E). These data suggest that both the HR and NHEJ pathways exist in ATC and cooperate and/or compete for DSB repair.

These results show that HR- and NHEJ-related genes are expressed by PTC and ATC cells from patients.

Cell cycle checkpoint inhibitors abrogate G2/M arrest in γ–irradiated thyroid cancer cells

To determine optimal experimental conditions, the cytotoxicity of checkpoint kinase inhibitors (caffeine, UCN-01) and γ-radiation was evaluated in 3 cell lines pertaining to different histological subtypes of thyroid cancer: C643, Hth74 (anaplastic) and TPC-1 (papillary) cells (27–29). Cells were cultivated for 24 hours in the presence of increasing concentrations of caffeine (an inhibitor of ATM and ATR: 0.5 mM-5 mM) or UCN-01 (an inhibitor of CHK1: 0-100 nM) and/or after γ-radiation (0-10 Gy). Based on the dose–

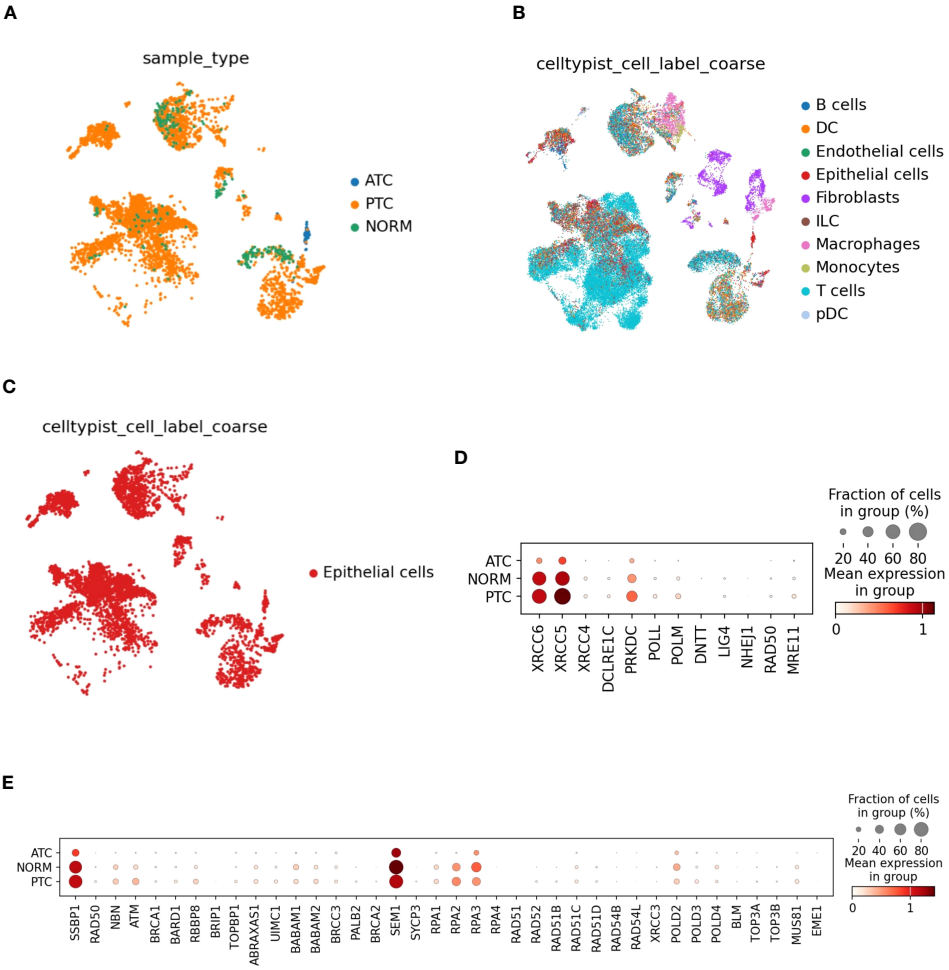

FIGURE 1
NHEJ- and HR-related genes are differentially expressed in ATC and PTC tumors. **(A)** The publicly available scRNA-Seq data from 10 ATC tumors, 7 PTC tumors, and 6 adjacent normal thyroid tissues with the GEO accession number GSE193581 were used for our study (26). Raw data composed of approximately 71,831 cells were filtered by using quality metrics, and approximately 40,070 cells passed the quality control. The scanorama-corrected data were clustered using the Elbow method, and 30 principal components were retained to determine the number of clusters (k) by using the k-means clustering algorithm (k-mean value 10). The k-mean value of 10 was used for our study. **(B)** Clusters were automatically annotated for different cell types by using CellTypist (version 1.5.2). **(C)** Clustering of cells expressing epithelial markers. **(D, E)** Plot showing mean expression in group and fraction of expressing cells within the epithelial cells cluster of genes involved in HR and NHEJ pathways. The differential gene expression was performed using scanpy (version 1.9.3) and the Wilcoxon rank sum test for 3 groups: ATC, PTC, and normal cells.

response relationship (Supplementary Figure 1), subtoxic concentrations were selected for further analyses (i.e., 50 nM for UCN-01 and 2.5 mM for caffeine).

To investigate checkpoint control, the 3 cell lines were exposed to 10 Gy of γ-irradiation (IR) and analyzed by flow cytometry (Figure 2A). After 24 hours, C643 cells accumulated in G2/M (arrows on Figure 2B), indicating that checkpoint control prevented entry into mitosis. DNA damage resulting from γ-irradiation blocked mitosis in C643 (78%), TPC-1 (43%), and Hth74 (44%) cells (Figure 2C, Supplementary Figures 2, 3). In the presence of caffeine, the percentages of γ-irradiated cells in G2/M were reduced to 39%, 21%, and 32% in C643, TPC-1, and Hth74 cells, respectively (Figure 2C, Supplementary Figures 2, 3). A similar effect was obtained with another checkpoint inhibitor (UCN-01), although less efficiently in TPC-1 cells. Under these conditions, apoptosis evaluated by DNA fragmentation (sub-G1 peak) and polyploidy (>G2/M) remained negligible (Figure 2D, Supplementary Figures 2–4).

These data thus suggest that checkpoint inhibitors allow γ-irradiated thyroid cells to escape G2/M arrest and enter the G1 phase.

γ–Irradiated thyroid cells undergo mitosis in the presence of caffeine and UCN-01

To confirm that γ-irradiated cells underwent effective mitosis in the presence of checkpoint inhibitors, C643 cells were labeled for histone 3 phosphoserine 10 (H3pSer10) and analyzed for their DNA content by flow cytometry (Figure 2E). γ-Irradiation increased the percentages of G2/M cells but did not significantly modify H3pSer10 labeling (4%). In contrast, the spindle inhibitor Taxol increased the percentages of H3pSer10-positive cells from 4% (control) to 41% (Figures 2F, G). Since Taxol inhibits the cytokinesis of mitotic cells, it is estimated that a significant proportion of C643 cells re-entered G1 after 24 hours. In the presence of UCN-01 and Taxol, 23% of γ-irradiated C643 cells were positive for H3pSer10. Checkpoint abrogation by UCN-01 thus allowed a significant proportion of γ-irradiated cells to undergo mitosis (20%, the difference between 23% and 3%) (Figures 2F, G). Similar conclusions were drawn using doxorubicin, a chemotherapeutic compound used in patients with advanced thyroid cancer (Figure 2H). It thus appears that when cell cycle checkpoints are inhibited by UCN-01, C643 cells divide during the 24-hour period despite being γ-irradiated. These conclusions were extended to another cell line (Hth74) treated with caffeine (Supplementary Figure 5).

γ–Irradiation is genotoxic to anaplastic thyroid cancer cells

Data from Figure 2 show that a significant proportion of γ-irradiated cells survive and undergo mitosis in the presence of checkpoint inhibitors. To evaluate the extent of DNA damage, cells were stained for Ser139 phosphorylation of H2AX (γ-H2AX). As shown in panel A of Figure 3, γ-irradiation induced a rapid increase of γ-H2AX foci in C643 cells, indicating the onset of DNA damage. The maximum number of γ-H2AX foci enumerated at 2 hours gradually decreased at 5 and 24 hours post-irradiation. Similar observations were confirmed by measuring the mean intensity of fluorescence (Figure 3B) and by immunoblotting (Figures 3C, D). Finally, another marker of DNA damage repair, 53BP1, further validated the conclusions (Figures 3E, F).

Taken together, these results show that, as expected, a γ-irradiation dose of 10 Gy induces significant damage, suggesting that thyroid cancer cells can efficiently repair their DNA in response to γ-irradiation.

DNA double-strand breaks are efficiently repaired in thyroid cancer cells

The efficiency of these 2 repair pathways was quantified using GFP-based reporter vectors in C643, TPC-1, and Hth74 cells. In these systems, functional GFP is expressed when a DSB (created *in vitro* by the I-SceI endonuclease) is repaired in cellulo by HR or NHEJ (Figure 4A). Flow cytometry data were normalized to an internal control (pHcRed) to eliminate variations in transfection efficiencies. Absolute rates of DNA repair efficiency were calculated based on the ratio between the number of GFP^+ cells generated by the HR and NHEJ reporters and the number of $HcRed^+$ cells. Relative repair efficiencies were obtained by normalizing these ratios with a control GFP plasmid. As predicted, C643, TPC-1, and Hth74 cells efficiently repaired the DNA lesions induced by γ-irradiation using both HR and NHEJ pathways (Figures 4B–G). Repair efficiencies significantly increased in most experimental settings after γ-irradiation except for NHEJ in TPC-1 cells and HR in Hth74 and TPC-1 cells. Similar conclusions were obtained with another DNA-damaging agent (doxorubicin), except for HR in C643 and TPC-1 cells.

These results show that thyroid cells are able to actively repair genomic lesions by HR and NHEJ.

Inhibition of double-strand break repair induces apoptosis of thyroid carcinoma cells

Since thyroid cancer cells require efficient DNA repair, we evaluated the effect of NHEJ and HR inhibitors in the presence of agents inducing DSBs, such as doxorubicin. RI-1 is a small molecule that inhibits the central recombination protein RAD51 involved in the gene conversion pathway of HR (RI-1) (31). SCR7 interferes with the binding of DNA ligase IV (LIG4) to DNA and thereby inhibits NHEJ (32). The pro-apoptotic effect of these 2 inhibitors on thyroid cell lines was evaluated by Annexin V and 7-AAD labeling. Each inhibitor used alone had only a minor effect on the survival of C643, TPC-1, and Hth74 cells (Figures 5A–C). Similarly, RI-1 was inefficient in significantly increasing doxorubicin-induced apoptosis in C643 and TPC-1 cells. In contrast, SCR7 combined with

10.3389/fonc.2024.1323313

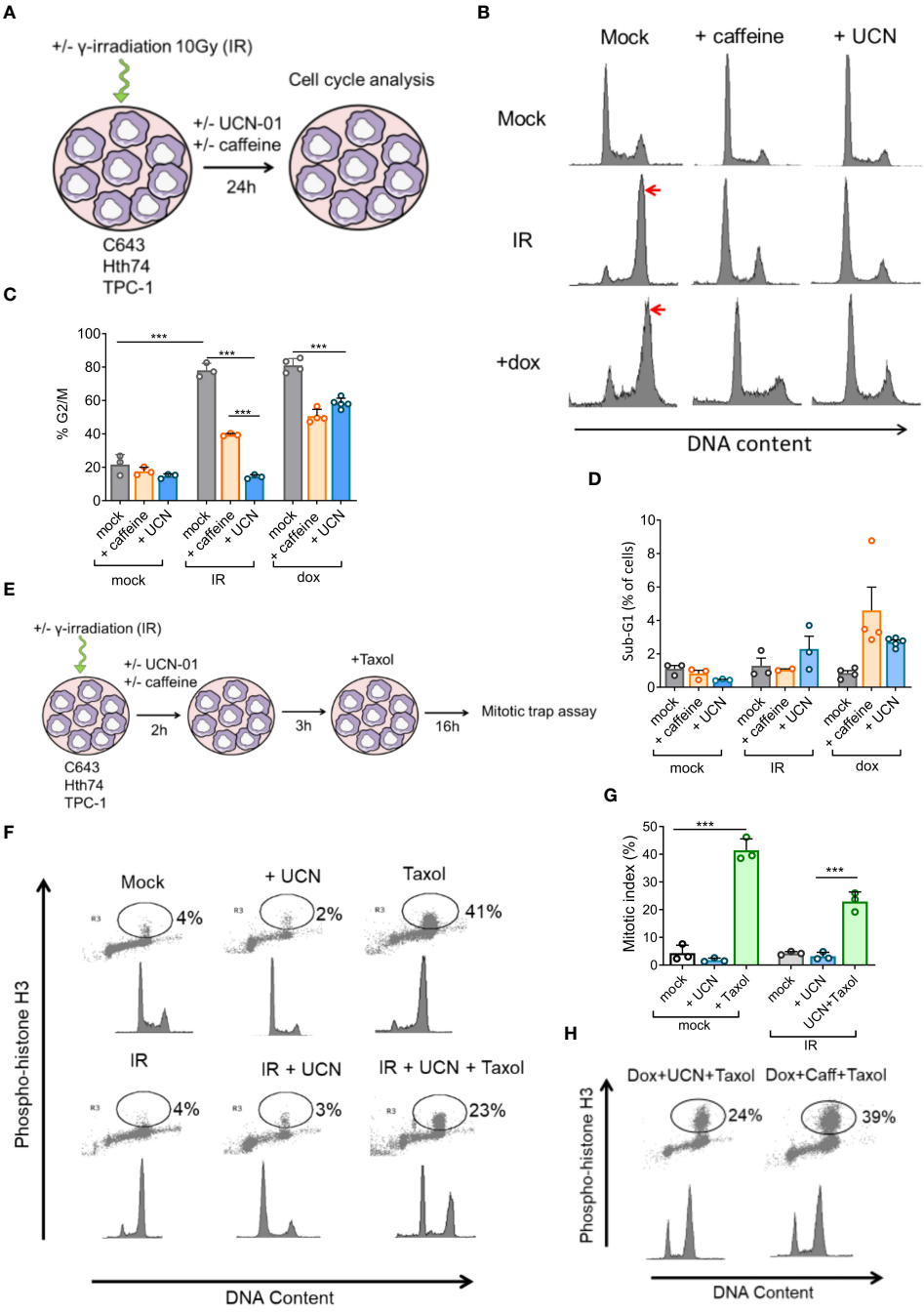

FIGURE 2
Thyroid cancer C643 cells bypass the mitotic checkpoint induced by γ–irradiation in the presence of UCN-01 or caffeine. **(A)** Thyroid carcinoma cells (C643) were γ-irradiated with 10 Gy and/or cultivated with caffeine (2.5 mM) or UCN-01 (50 nM). After 24 hours, the cells were fixed and permeabilized with ethanol and labeled with propidium iodide. **(B)** The cell cycle profiles were analyzed by flow cytometry and histograms indicating the fluorescent profile of propidium iodide (PI) corresponding to cell DNA content (x-axis) and the cell count (y-axis). **(C, D)** Histogram showing percentages of cells in G2/M and sub-G1 calculated from 4 independent experiments. **(E)** Mitotic trap assay. Three hours after γ-irradiation (IR), UCN-01 (50 nM, UCN-01), and/or caffeine (2.5 mM, Caff), C643 thyroid cells were incubated with taxol at 50 nM. Sixteen hours later, the cells were fixed and permeabilized with ethanol. Cells were stained with a histone 3 anti-phosphoserine 10 (H3pSer10) antibody and PI and analyzed by flow cytometry. **(F)** Histogram and dot plot indicating on the x-axis fluorescence associated with PI (DNA content) and on the y-axis the fluorescence associated with staining of anti-H3pSer10. **(G)** Histogram indicating the percentage of H3pSer10-positive cells from three independent experiments. **(H)** C643 cells were analyzed for the staining of H3pSer10 and PI as described in panel A except that doxorubicin (500 nm) was used instead of γ-irradiation. Each bar represents the mean +/- SD. Statistical significance was determined by one-way analysis of variance (ANOVA) followed by Tukey's multiple comparisons test. Data were considered statistically significant (*), very statistically significant (**), and highly statistically significant (***) at $P < 0.05$, $P < 0.01$, and $P < 0.001$, respectively.

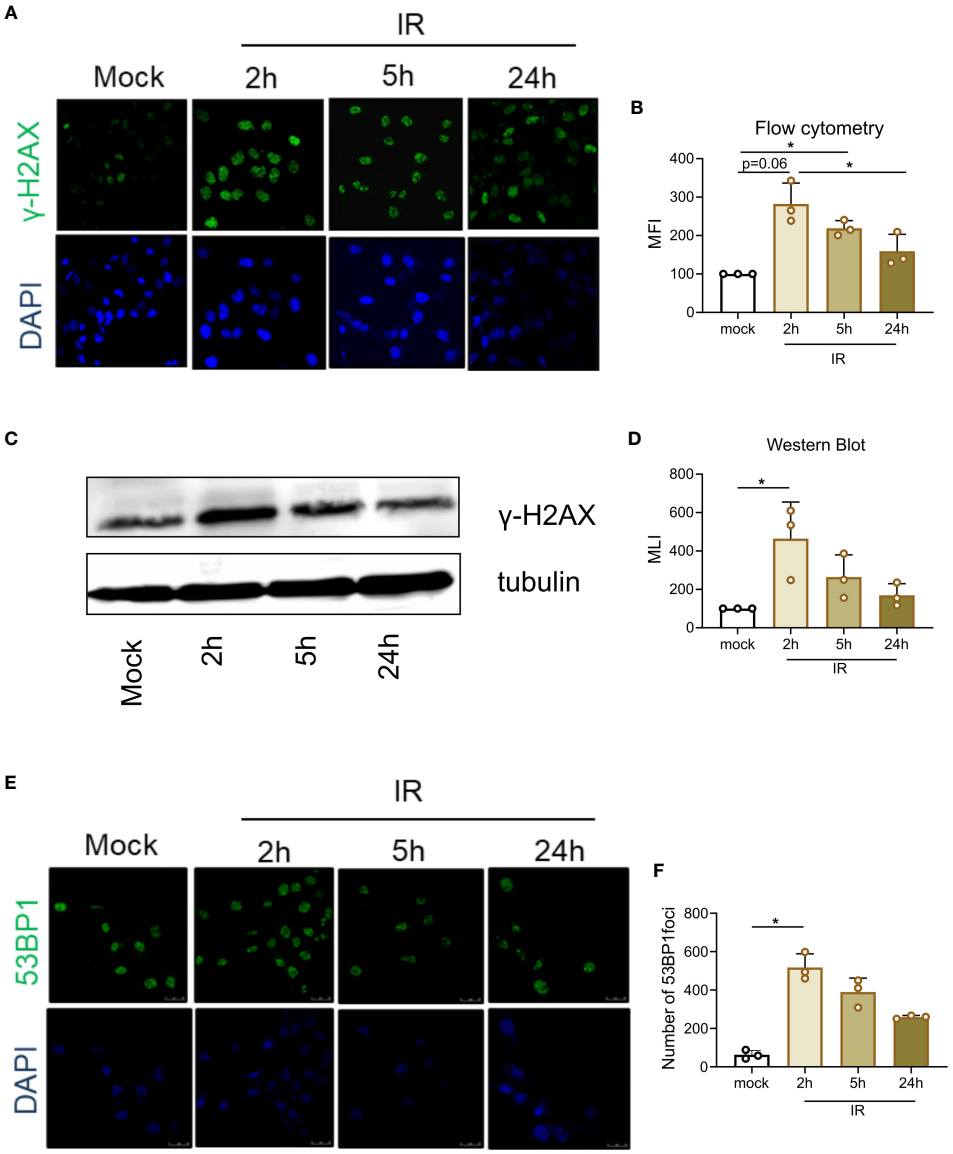

FIGURE 3
γ–Irradiation is genotoxic to thyroid cancer cells. **(A)** At 0, 2, 5, and 24 hours post-irradiation, C643 cells were analyzed by confocal microscopy after labeling with an anti-γ-H2AX antibody and an Alexa Fluor 488 conjugate (green fluorescence). Nuclei were stained with DAPI (blue fluorescence). **(B)** C643 cells were treated as described in panel A and analyzed by flow cytometry. The mean fluorescence intensities (MFI) of γ-H2AX foci were normalized to the control arbitrarily set to 100. Data represent the means of three independent experiments. Statistical significance was determined by using the nonparametric Friedman test followed by Dunn's multiple comparisons. **(C)** Immunoblot analysis of γ-irradiated C643 cells labeled with antibodies directed against γ-H2AX and tubulin. **(D)** Quantification of immunoblot luminescence intensities normalized to mock calculated from 3 independent experiments. Statistical significance was determined by using the nonparametric Friedman test followed by Dunn's multiple comparisons. **(E)** Cells were γ-irradiated and analyzed by confocal microscopy after labeling with an anti-53BP1 antibody and an Alexa Fluor 488 conjugate (green fluorescence). Nuclei were stained with DAPI (blue fluorescence). **(F)** 53BP1 foci were quantified at 0-24 hours post-irradiation from 3 independent experiments. Each bar represents the mean +/- SD. Statistical significance was determined by using the nonparametric Friedman test followed by Dunn's multiple comparisons. The data represent the means of three independent experiments. Data were considered statistically significant (*) at $P < 0.05$.

doxorubicin efficiently promoted apoptosis of C643 and TPC-1 cells (Figures 5A, B). However, the combination of doxorubicin with selective inhibitors did not significantly affect the apoptosis of Hth74 cells (Figure 5C). The onset of apoptosis evaluated by Annexin-V and 7-AAD labeling was confirmed by measuring DNA fragmentation (sub-G1 peak) in different cell lines (Supplementary Figure 6).

Taken together, these results demonstrate that apoptosis can be induced in thyroid cells by a combination of a DSB-inducing agent and inhibitors of DNA repair.

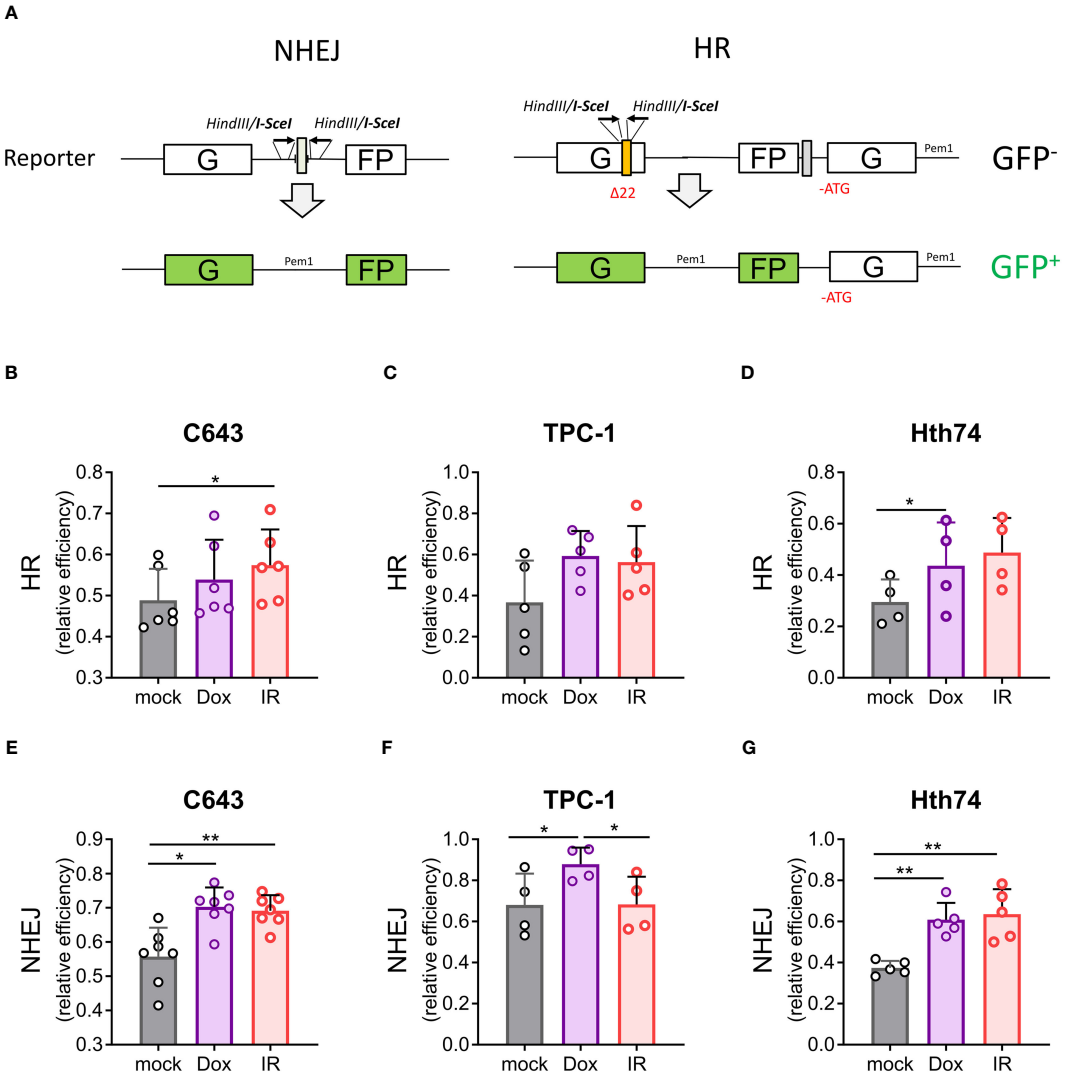

FIGURE 4
ATC and PTC cells efficiently repair DNA double-strand breaks caused by γ-irradiation and doxorubicin. **(A)** Reporter constructs for the analysis of DNA DSB repair by NHEJ and HR as described in (30). C643, Hth74, and TPC-1 cells were transfected with HR or NHEJ reporter plasmids. DNA double-strand breaks were induced by γ-irradiation or treatment with doxorubicin (300 nM). **(B–G)** Quantification of HR and NHEJ repair efficiencies was based on GFP reporter plasmids and calculated as described in the Materials and Methods. The data represent quantification from n>4 independent experiments. Each bar represents the mean +/- SD. Statistical significance was determined by one-way analysis of variance (ANOVA) followed by Tukey's multiple comparisons test. Data were considered statistically significant (*), and very statistically significant (**), at $P < 0.05$, and $P < 0.01$ respectively.

Inhibition of DNA repair impairs tumor growth in mouse models

Since the pro-apoptotic activity of SCR7 in combination with doxorubicin depends on the cell type, its therapeutic potential was evaluated in 2 mouse models of ATC. Immunodeficient NSG-SGM3 mice were inoculated subcutaneously with anaplastic C643 and Hth74 thyroid cancer cells. Once the tumor reached a mean volume of 50 mm^3, mice were injected twice per week with SCR7 (10 mg/kg) or/and doxorubicin (0.5 mg/kg) (Figure 6A). When used as a single agent, doxorubicin showed no antitumor activity compared to the vehicle (Figures 6B, C, E, F). In contrast, the combination of SCR7 with doxorubicin reduced tumor growth and prolonged the survival of C643-inoculated mice (Figures 6B–D). The combination of SCR7 and doxorubicin caused a minor tumor reduction but significantly increased Hth74-inoculated mice survival compared to doxorubicin alone (Figures 6E–G).

We conclude that the inhibition of DNA ligase IV increased the control of tumor growth after doxorubicin treatment in xenograft murine models of ATC.

Discussion

Thyroid tumors are commonly treated by radiotherapy by using radioactive iodine (RAI) to cause double-strand breaks (DSBs) (20, 21, 33). The elevated number of DSBs destroys the genome integrity of cancer cells and causes their elimination. However, non-

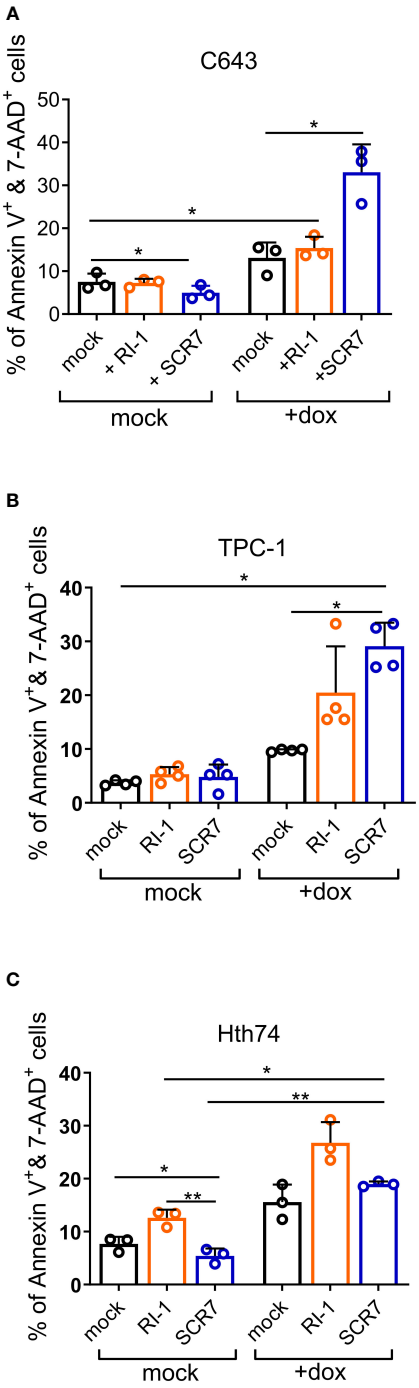

FIGURE 5
Inhibition of double-strand break repair induces apoptosis of thyroid carcinoma cells. **(A)** C643, **(B)** TPC-1 and **(C)** Hth74 74 cells were treated with LIG4 inhibitor (SCR7; 200 µM) or RAD51 inhibitor (RI-1; 100 µM) and/or doxorubicin (200 nM, Dox). After 48 hours, apoptotic cells were labeled with Annexin V FITC and 7AAD and analyzed by flow cytometry. The data represent the mean from 3 independent experiments. Each bar represents the mean +/- SD. Statistical significance was determined by one-way analysis of variance (ANOVA) followed by Tukey's multiple comparisons test. Data were considered statistically significant (*), and very statistically significant (**) at $P < 0.05$, and $P < 0.01$, respectively.

homologous end joining (NHEJ) and homologous recombination (HR), 2 representative DSB repair pathways, are effective in maintaining genetic information and favor thyroid cancer resistance to therapies using DNA damaging factors. Radiotherapy and chemotherapy resistance have been shown to lead to cancer relapse and poor prognosis of cancer patients (34, 35). The identification of DSB repair inhibitors is urgently needed to improve the outcomes of these therapies. In principle, inhibition of cell cycle checkpoint kinases is thus predicted to ameliorate radiosensitization (36–39).

In this context, we evaluated the effect of 2 checkpoint inhibitors, caffeine (a methylxanthine alkaloid) and UCN-01 (an indolocarbazole ATP analog), on thyroid cancer cell lines (38–40). We used C643, Hth-74 and TPC-1 cell lines cells that are respectively characterized by *HRAS* mutation, *NF1* mutation and *RET/PTC1* rearrangement (29). *HRAS* and *NF1* mutations are commonly detected in ATC (respectively 10-20% and 9% of ATC tumors) (41, 42). These cells are also found to be mutated for *TP53* gene (29). Previous studies showed that both UCN-01 and caffeine increased the sensitivity of tumor cells to chemotherapy (cisplatin, camptothecin, doxorubicin) and γ-radiation (43–46). Our present study shows that despite successful checkpoint abrogation, γ-radiation in combination with caffeine or UCN-01 has a minor effect on cell survival. We observed that a significant fraction of thyroid cancer cells resumed the cell cycle and survived, thus extending observations in different cancer types (47–49). When thyroid tumor cells are released from G2 arrest by checkpoint inhibitors, cells have the possibility either to repair DNA damage before entering mitosis or to undergo polyploidy. If cells bypass the mitotic checkpoint without repairing DNA lesions, they undergo mitotic catastrophe and cell death due to improper segregation of fragmented chromosomes (50–52). Unexpectedly, we did not observe significant levels of micronuclei or polyploidy in any of the treatment combinations (Supplementary Figures 2, 3). In the absence of apoptosis, mitotic catastrophe, or polyploidy, we hypothesized that thyroid cancer cells may bypass mitotic checkpoints and survive. Using a mitotic trap assay, we demonstrated that a significant proportion of cells successfully underwent mitosis in the presence of caffeine or UCN-01 (Figure 2, Supplementary Figure 5). The kinetics of γ-H2AX and 53BP1 labeling indicated that double-strand DNA lesions induced by irradiation are rapidly resolved (Figure 4), consistent with other reports (47–49).

We used publicly available scRNA-seq data to analyze the expression of key genes involved in the HR and NHEJ pathways (26). NHEJ- (*XRCC6, XRCC5, PRKDC*) and HR- (*SSBP1, SEM1, RPA2, RPA3*) related genes are expressed by both normal follicular and thyroid cancer cells. NHEJ-related genes are more highly expressed in PTC than in ATC. However, the level of HR-related gene expression is similar between PTC and ATC. These data suggest that both HR and NHEJ pathways exist in ATC and cooperate and/or compete for DSB repair in patients. We observed that the DSB repair capacity using HR and NHEJ globally increased after γ-radiation or

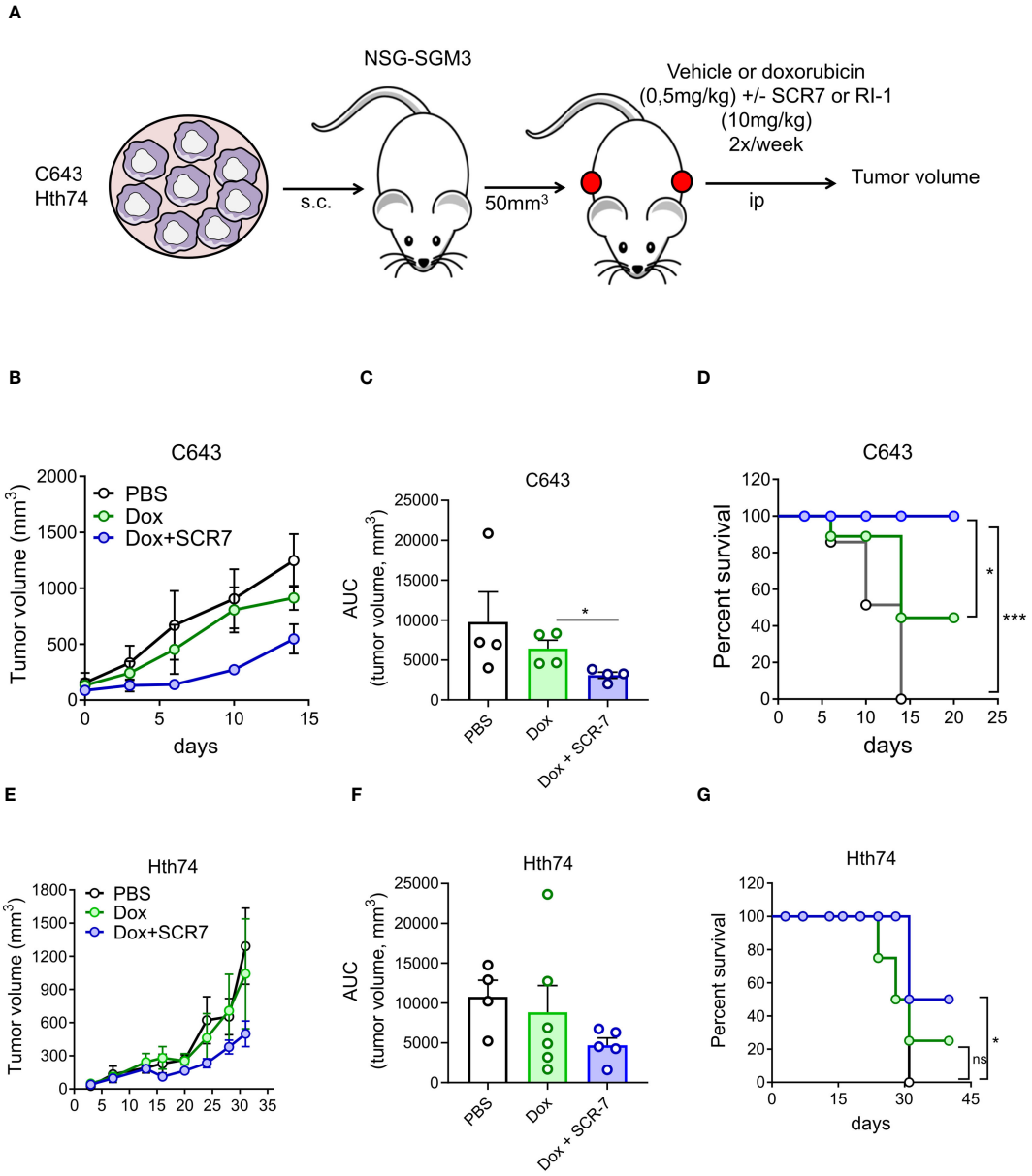

FIGURE 6
SCR7 combined with doxorubicin inhibits tumor growth in a thyroid carcinoma xenograft mouse model. **(A)** Tumor growth of C643 and Hth74 thyroid carcinoma cells was evaluated after subcutaneous injection in immunocompromised NSG3GS mice in each flank. Mice were treated intraperitoneally with PBS, doxorubicin (0.5 mg/kg twice a week, Dox), or SCR7 (10 mg/kg twice a week). **(B, E)** Graph indicating the mean tumor volume (mm^3) measured bi-weekly over the time from n=5 mice. **(C, F)** Histogram showing the mean area under individual tumor growth curves (AUCs). Statistical significance was determined by the nonparametric Kruskal–Wallis test followed by Dunn's multiple comparisons. **(D, G)** represent the corresponding survival curves. Statistical significance was determined by performing a chi-square log-rank (Mantel–Cox) test. Each bar represents the mean +/- SEM. Data were considered statistically significant (*), and highly statistically significant (***) at $P < 0.05$, and $P < 0.001$, respectively.

doxorubicin treatment in ATC and PTC cells. HR requires a template and numerous enzymes and can perform an error-free DDR compared to NHEJ (53). Template-independent NHEJ is predominant and can lead to mutations (error-prone) in genes involved in negative regulation of the cell cycle, thus promoting therapy resistance. NHEJ is initiated by XRCC5 (Ku80) and XRCC6 (Ku70), which directly interact with DSB ends (54). DSB ends are protected by DNA-dependent protein kinase (DNA-PKcs) before ligation by the XRCC4-XLF complex and DNA ligase IV (LIG4) (Figure 7) (53). Mutations and/or the loss of factors directly involved in the NHEJ pathway have been associated with increased sensitivity to DNA-damaging agents (55). The use of selective inhibitors of NHEJ repair is a groundbreaking therapeutic approach to promote genome instability by minimizing the dose of chemotherapy and radiation therapy. In fact, overexpression of DNA-PKcs, LIG4 and XRCC4 is correlated with poor prognosis in several cancer types, such as esophageal cancer, colorectal cancer, bladder cancer, ovarian cancer, and hepatocellular cancer (56–60). Targeting DNA-PKcs

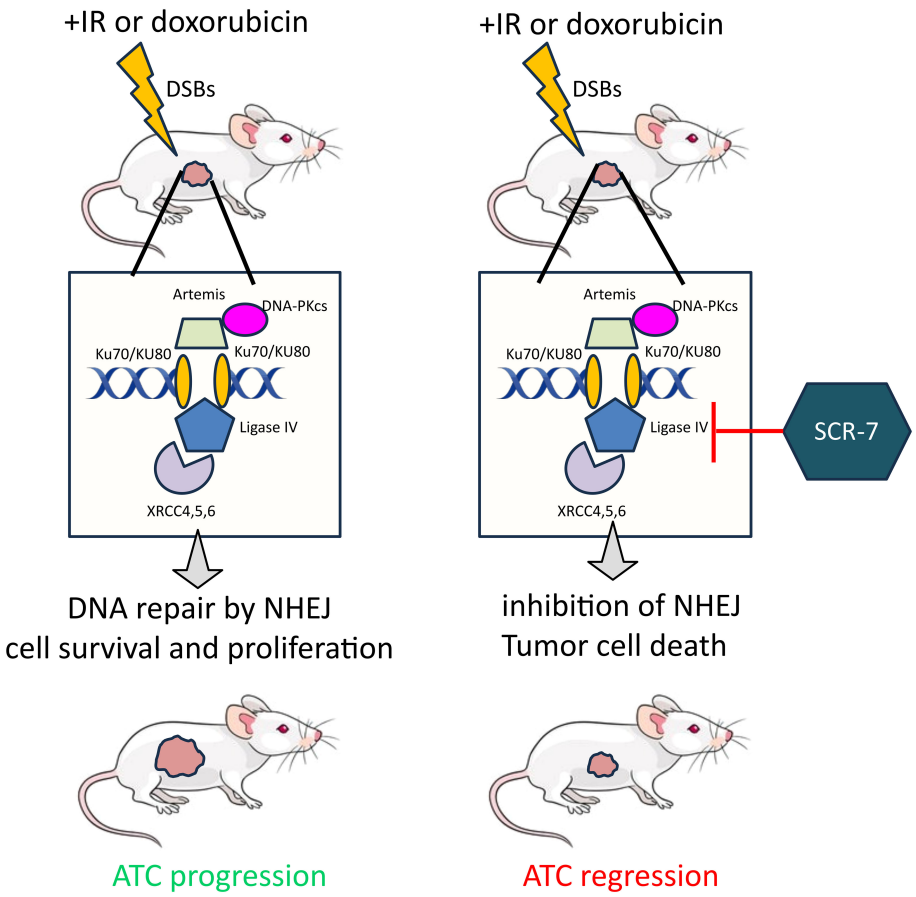

FIGURE 7
A model showing tumor control after the combination of a selective LIG4 inhibitor (SCR7) and doxorubicin in a mouse xenograft model of anaplastic thyroid cancer. Treatment with doxorubicin causes double-strand DNA breaks (DSBs) which are rapidly repaired by the non-homologous end-joining pathway (NHEJ). NHEJ is initiated by the recruitment of the Ku complex composed of Ku70 and Ku80 to double-strand DNA ends. Once attached, DNA-PKcs is recruited for the protection of DNA ends and the formation of the DNA-PK holoenzyme. DNA-PK activates the XRCC4-LIG4-XLF complex for the final ligation of DNA ends. Once repaired, thyroid cancer cells resume the cell cycle, causing tumor progression. The combination of doxorubicin and selective inhibitor of DNA ligase IV (SCR7) reduced tumor growth by impairing the NHEJ repair pathway of DSBs caused by doxorubicin. The accumulation of DSBs causes cell death and tumor regression.

catalytic activity with potent selective inhibitors (NU7441 and KU-0060648) to increase efficacy of radiotherapy was extensively evaluated in pre-clinical and clinical trials (NCT02516813, NCT03770689, NCT04555577, NCT04533750, and NCT03907969) (61). However, the use of DNA ligase IV inhibitors for cancer sensitization to DNA damaging agents is poorly exploited (53). It has been shown that patients with homozygous mutations in DNA ligase IV are characterized by hyper-radiosensitivity (62–64). scRNA-seq analysis showed reduced expression of the *LIG4* gene at the mRNA level in normal follicular thyroid cells and thyroid cancer cells, but its activity is tightly regulated at the protein level by XRCC4 and DNA-PKcs (65). Furthermore, the DNA ligase IV is detected at protein level in 50% of thyroid cancer patients (https://www.proteinatlas.org/ENSG00000174405-LIG4/pathology) thus making DNA ligase IV an attractive target to develop new antiproliferative agents. The first generation of DNA ligase IV inhibitors (L189, IC50 value 5+/- 2μM) showed low inhibition efficacy and specificity compared to SCR7 inhibitor (32, 66). Recently, it has been shown that SCR7 can also inhibit the DNA ligase IIIα/XRCC1 (67). The combination therapy of SCR7 and chemotherapy was shown to enhance melphalan cytotoxicity in patients with multiple myeloma (68). Doxorubicin when administered with SCR7 showed an increased efficacy in cervical cancer compared to monotreatment (69). In this report, we evaluated the combination therapy SCR7/doxorubicin for the treatment of thyroid cancer. Doxorubicin monotherapy showed effective control of ATC growth in patients when used in the initial stages. However, repeated administration of doxorubicin is commonly associated with cancer drug resistance and adverse effects (e.g. cardiotoxicity, stomatitis, bone marrow aplasia) (70, 71). NSG immunocompromised mice were shown to be sensitive to doxorubicin therapy and resulted in gastrointestinal and hepatic injuries and cardiotoxicity (72). Our preclinical study was conducted by a well-tolerated dose of doxorubicin (0.5 mg/kg, twice a week) which represents 1/8 the dose of studies using xenograft models (72). We showed that the combination of a low dose of doxorubicin with SCR7 significantly increased cell apoptosis and enhanced tumor control in C643 xenograft model. The drug resistance associated with Hth74 cells is not understood and is probably caused by the presence of *NF1* and *TP53* mutations (73).

Our data showed an increased sensitivity of TPC-1 cells (*RET/PTC1* rearrangement) to doxorubicin in presence of the DNA ligase IV inhibitor *in vitro*. The therapeutic potential of the DNA ligase IV inhibitor should need further validation on thyroid cancer cell lines characterized by different cancer genetic drivers (e.g. BRAF p.V600, NRAS p.Q61K) (29). A broader panel of cell lines, in particular BRAFV600E positive ATCs (e.g. 8505C, SW1736), would increase the relevance of the study. By increasing DSBs, the combination therapy doxorubicin/SCR7 can be used to increase the tumor mutational burden thereby supporting anti-tumor immunity (74, 75). We showed that the administration of SCR7 and doxorubicin offers a promising strategy for the treatment of papillary and anaplastic thyroid cancer.

Conclusions

Taken together, this evidence suggests that SCR7 is a promising candidate to reduce thyroid cancer resistance to multimodal therapy. Of note, adequate timing and dosage of combination therapy is required to prevent therapy-related secondary cancers. While new inhibitors are becoming available and are currently evaluated in clinical trials, our results support the proof-of-concept of a strategy interfering with NHEJ repair in advanced thyroid cancer.

Data availability statement

The datasets presented in this study can be found in online repositories. The names of the repository/repositories and accession number(s) can be found in the article/Supplementary Material. We used a publicly available dataset of single-cell transcriptomes (GSE193581): https://www.ncbi.nlm.nih.gov/geo/query/acc.cgi?acc=GSE193581.

Ethics statement

Ethical approval was not required for the studies on humans in accordance with the local legislation and institutional requirements because only commercially available established cell lines were used. The animal study was approved by Ethical Committee for the use of laboratory animals at the University of Liège. The study was conducted in accordance with the local legislation and institutional requirements.

Author contributions

SS: Conceptualization, Investigation, Writing – review & editing, Methodology. MJ: Investigation, Methodology, Writing – review & editing. LV: Writing – review & editing. HB: Writing – review & editing. BS: Writing – review & editing. MH: Conceptualization, Funding acquisition, Investigation, Methodology, Supervision, Writing – original draft, Writing – review & editing.

Funding

The author(s) declare financial support was received for the research, authorship, and/or publication of this article. This work received financial support from the "Fonds National de la Recherche Scientifique" (FNRS), the Télévie, the Belgian Foundation against Cancer (FBC), and the "Fondation Léon Fredericq" (FLF). SS, MJ, LV, HB, BS, and MH are supported by grants from FNRS and the FBC. The funders had no role in the study design, data collection and analysis, decision to publish, or preparation of the manuscript.

Acknowledgments

We thank Pr. Karin Forsberg Nilsson (Uppsala University, Sweden) for cell lines and Vera Gorbunova (University of Rochester, USA) for reporter plasmids. We thank Pr. Luc Willems (University of Liege and FNRS) for scientific input and financial support. We thank Jean-Rock Jacques for his technical expertise. We thank the GIGA Imaging technology platforms for their advice and support.

Conflict of interest

The authors declare that the research was conducted in the absence of any commercial or financial relationships that could be construed as a potential conflict of interest.

Publisher's note

Supplementary material

The Supplementary Material for this article can be found online at: https://www.frontiersin.org/articles/10.3389/fonc.2024.1323313/full#supplementary-material

References

1. Lamartina L, Grani G, Durante C, Borget I, Filetti S, Schlumberger M. Follow-up of differentiated thyroid cancer – what should (and what should not) be done. *Nat Rev Endocrinol* (2018) 14:538–51. doi: 10.1038/s41574-018-0068-3

2. Molinaro E, Romei C, Biagini A, Sabini E, Agate L, Mazzeo S, et al. Anaplastic thyroid carcinoma: From clinicopathology to genetics and advanced therapies. *Nat Rev Endocrinol* (2017) 13:644–60. doi: 10.1038/nrendo.2017.76

3. Kuo JH, Chabot JA, Lee JA. Breast cancer in thyroid cancer survivors: An analysis of the Surveillance, Epidemiology, and End Results-9 database. *Surgery* (2016) 159:23–9. doi: 10.1016/j.surg.2015.10.009

4. Bible KC, Kebebew E, Brierley J, Brito JP, Cabanillas ME, Clark TJ, et al. 2021 American thyroid association guidelines for management of patients with anaplastic thyroid cancer. *Thyroid* (2021) 31:337–86. doi: 10.1089/thy.2020.0944

5. Gu L, Sun W. MiR-539 inhibits thyroid cancer cell migration and invasion by directly targeting CARMA1. *Biochem Biophys Res Commun* (2015) 464:1128–33. doi: 10.1016/j.bbrc.2015.07.090

6. Nagaiah G, Hossain A, Mooney CJ, Parmentier J, Remick SC. Anaplastic thyroid cancer: a review of epidemiology, pathogenesis, and treatment. *J Oncol* (2011) 2011:542358. doi: 10.1155/2011/542358

7. Gandhi M, Evdokimova V, Nikiforov YE. Mechanisms of chromosomal rearrangements in solid tumors: The model of papillary thyroid carcinoma. *Mol Cell Endocrinol* (2010) 321:36–43. doi: 10.1016/j.mce.2009.09.013

8. Pellegriti G, Frasca F, Regalbuto C, Squatrito S, Vigneri R. Worldwide increasing incidence of thyroid cancer : update on epidemiology and risk factors. *J Cancer Epidemiol* (2013) 2013:. doi: 10.1155/2013/965212

9. Xing M, Haugen BR, Schlumberger M. Progress in molecular-based management of differentiated thyroid cancer. *Lancet* (2013) 381:1058–69. doi: 10.1016/S0140-6736(13)60109-9

10. Chintakuntlawar AV, Foote RL, Kasperbauer JL, Bible KC. Diagnosis and management of anaplastic thyroid cancer. *Endocrinol Metab Clin North Am* (2019) 48:269–84. doi: 10.1016/j.ecl.2018.10.010

11. Hoang JK, Nguyen XV, Davies L. Overdiagnosis of thyroid cancer. Answers to five key questions. . *Acad Radiol* (2015) 22:1024–9. doi: 10.1016/j.acra.2015.01.019

12. Tsumagari K, Abd Elmageed ZY, Sholl AB, Friedlander P, Abdraboh M, Xing M, et al. Simultaneous suppression of the MAP kinase and NF-κB pathways provides a robust therapeutic potential for thyroid cancer. *Cancer Lett* (2015) 368:46–53. doi: 10.1016/j.canlet.2015.07.011

13. Gao X, Wu X, Zhang X, Hua W, Zhang Y, Maimaiti Y, et al. Inhibition of BRD4 suppresses tumor growth and enhances iodine uptake in thyroid cancer. *Biochem Biophys Res Commun* (2016) 469:679–85. doi: 10.1016/j.bbrc.2015.12.008

14. Fullmer T, Cabanillas ME, Zafereo M. Novel therapeutics in radioactive iodine-resistant thyroid cancer. *Front Endocrinol (Lausanne)* (2021) 12:720723. doi: 10.3389/fendo.2021.720723

15. Crispo F, Notarangelo T, Pietrafesa M, Lettini G, Storto G, Sgambato A, et al. Braf inhibitors in thyroid cancer: Clinical impact, mechanisms of resistance and future perspectives. *Cancers (Basel)* (2019) 11. doi: 10.3390/cancers11091388

16. Bonhomme B, Godbert Y, Perot G, Al Ghuzlan A, Bardet S, Belleannée G, et al. Molecular pathology of anaplastic thyroid carcinomas: A retrospective study of 144 cases. *Thyroid* (2017) 27:682–92. doi: 10.1089/thy.2016.0254

17. Gustavsson B, Hermansson A, Andersson A-C, Grimelius L, Bergh J, Westermark B, et al. Decreased growth rate and tumor formation of human anaplastic thyroid carcinoma cells transfected with a human thyrotropin receptor cDNA in NMRI nude mice treated with propylthiouracil. *Mol Cell Endocrinol* (1996) 121:143–51. doi: 10.1016/0303-7207(96)03859-2

18. Neff RL, Farrar WB, Kloos RT, Burman KD. Anaplastic thyroid cancer. *Endocrinol Metab Clin North Am* (2008) 37:525–38. doi: 10.1016/j.ecl.2008.02.003

19. Bartek J, Lukas J. Chk1 and Chk2 kinases in checkpoint control and cancer. *Cancer Cell* (2003) 3:421–9. doi: 10.1016/S1535-6108(03)00110-7

20. Jackson SP, Bartek J. The DNA-damage response in human biology and disease. *Nature* (2010) 461:1071–8. doi: 10.1038/nature08467.The

21. Pearl LH, Schierz AC, Ward SE, Al-lazikani B, Pearl FMG. Therapeutic opportunities within the DNA damage response. *Nat Rev Cancer* (2015) 15:166–80. doi: 10.1038/nrc3891

22. Chang HHY, Pannunzio NR, Adachi N, Lieber MR. Non-homologous DNA end joining and alternative pathways to double-strand break repair. *Nat Rev Mol Cell Biol* (2017) 18:495–506. doi: 10.1038/nrm.2017.48

23. Cortés-Ciriano I, Lee JJK, Xi R, Jain D, Jung YL, Yang L, et al. Comprehensive analysis of chromothripsis in 2,658 human cancers using whole-genome sequencing. *Nat Genet* (2020) 52:331–41. doi: 10.1038/s41588-019-0576-7

24. Boeckman HJ, Trego KS, Turchi JJ. Cisplatin sensitizes cancer cells to ionizing radiation via inhibition of nonhomologous end joining. *Mol Cancer Res* (2005) 3:277–285. doi: 10.1158/1541-7786.MCR-04-0032

25. Feng W, Smith CM, Simpson DA, Gupta GP. Targeting non-homologous and alternative end joining repair to enhance cancer radiosensitivity. *Semin Radiat Oncol* (2022) 32:29–41. doi: 10.1016/j.semradonc.2021.09.007

26. Lu L, Wang JR, Henderson YC, Bai S, Yang J, Hu M, et al. Anaplastic transformation in thyroid cancer revealed by single-cell transcriptomics. *J Clin Invest* (2023) 133. doi: 10.1172/JCI169653

27. Lee JJ, Foukakis T, Hashemi J, Grimelius L, Heldin NE, Wallin G, et al. Molecular cytogenetic profiles of novel and established human anaplastic thyroid carcinoma models. *Thyroid* (2007) 17:289–301. doi: 10.1089/thy.2006.0246

28. Schweppe RE, Klopper JP, Korch C, Pugazhenthi U, Benezra M, Knauf JA, et al. Deoxyribonucleic acid profiling analysis of 40 human thyroid cancer cell lines reveals cross-contamination resulting in cell line redundancy and misidentification. *J Clin Endocrinol Metab* (2008) 93:4331–41. doi: 10.1210/jc.2008-1102

29. Landa I, Pozdeyev N, Korch C, Marlow LA, Smallridge RC, Copland JA, et al. Comprehensive genetic characterization of human thyroid cancer cell lines: A validated panel for preclinical studies. *Clin Cancer Res* (2019) 25:3141–51. doi: 10.1158/1078-0432.CCR-18-2953

30. Seluanov A, Mao Z, Gorbunova V. Analysis of DNA double-strand break (DSB) repair in mammalian cells. *J Vis Exp* (2010) 43:2002. doi: 10.3791/2002

31. Budke B, Logan HL, Kalin JH, Zelivianskaia AS, Cameron W, Miller LL, et al. RI-1 : a chemical inhibitor of RAD51 that disrupts homologous recombination in human cells. *Nucleic Acids Res* (2012) 40:7347–57. doi: 10.1093/nar/gks353

32. Srivastava M, Nambiar M, Sharma S, Karki SS, Goldsmith G, Hegde M, et al. An inhibitor of nonhomologous end-joining abrogates double-strand break repair and impedes cancer progression. *Cell* (2012) 151:1474–87. doi: 10.1016/j.cell.2012.11.054

33. Lord C. The DNA damage response and cancer therapy. *Nature* (2012) 481:287–94. doi: 10.1038/nature10760

34. Lee JW, Wernicke AG. Risk and survival outcomes of radiation-induced CNS tumors. *J Neurooncol* (2016) 129:15–22. doi: 10.1007/s11060-016-2148-3

35. Seo YS, Ko IO, Park H, Jeong YJ, Park JA, Kim KS, et al. Radiation-induced changes in tumor vessels and microenvironment contribute to therapeutic resistance in glioblastoma. *Front Oncol* (2019) 9:1259. doi: 10.3389/fonc.2019.01259

36. Yang Y, Luo J, Chen X, Yang Z, Mei X, Ma J, et al. CDK4/6 inhibitors: A novel strategy for tumor radiosensitization. *J Exp Clin Cancer Res* (2020) 39. doi: 10.1186/s13046-020-01693-w

37. Petroni G, Buqué A, Yamazaki T, Bloy N, Di Liberto M, Chen-Kiang S, et al. Radiotherapy delivered before CDK4/6 inhibitors mediates superior therapeutic effects in ER+breast cancer. *Clin Cancer Res* (2021) 27:1855–63. doi: 10.1158/1078-0432.CCR-20-3871

38. Kim YM, Jeong IH, Pyo H. Celecoxib enhances the radiosensitizing effect of 7-hydroxystaurosporine (UCN-01) in human lung cancer cell lines. *Int J Radiat Oncol Biol Phys* (2012) 83:e399–407. doi: 10.1016/j.ijrobp.2012.01.001

39. Mack PC, Jones AA, Gustafsson MH, Gandara DR, Gumerlock PH, Goldberg Z. Enhancement of radiation cytotoxicity by UCN-01 in non-small cell lung carcinoma cells. *Radiat Res* (2004) 162:623–634. doi: 10.1667/RR3253

40. Sinn B, Tallen G, Schroeder G, Grassl B, Schulze J, Budach V, et al. Caffeine confers radiosensitization of PTEN-deficient Malignant glioma cells by enhancing ionizing radiation-induced G1 arrest and negatively regulating akt phosphorylation. *Mol Cancer Ther* (2010) 9:480–8. doi: 10.1158/1535-7163.MCT-09-0498

41. Landa I, Ibrahimpasic T, Boucai L, Sinha R, Knauf JA, Shah RH, et al. Genomic and transcriptomic hallmarks of poorly differentiated and anaplastic thyroid cancers. *J Clin Invest* (2016) 126:1052–66. doi: 10.1172/JCI85271

42. Xing M. Clinical utility of RAS mutations in thyroid cancer: A blurred picture now emerging clearer. *BMC Med* (2016) 14. doi: 10.1186/s12916-016-0559-9

43. Kawabe T. G 2 checkpoint abrogators as anticancer drugs Minireview G 2 checkpoint abrogators as anticancer drugs. *Mol Cancer Ther* (2004), 513–9.

44. Wang Q, Fan S, Eastman A, Worland PJ, Sausville EA, O'Connor PM. UCN-01: A potent abrogator of G2 checkpoint function in cancer cells with disrupted p53. *J Natl Cancer Inst* (1996) 88:956–65. doi: 10.1093/jnci/88.14.956

45. Monks A, Harris ED, Vaigro-Wolff A, Hose CD, Connelly JW, Sausville EA. UCN-01 enhances the in *vitro* toxicity of clinical agents in human tumor cell lines. *Invest New Drugs* (2000) 18:95–107. doi: 10.1023/A:1006313611677

46. Petersen L, Hasvold G, Lukas J, Bartek J, Syljuåsen RG. P53-dependent G1 arrest in 1st or 2nd cell cycle may protect human cancer cells from cell death after treatment with ionizing radiation and Chk1 inhibitors. *Cell Prolif* (2010) 43:365–71. doi: 10.1111/j.1365-2184.2010.00685.x

47. Doai M, Watanabe N, Takahashi T, Taniguchi M, Tonami H, Iwabuchi K, et al. Sensitive immunodetection of radiotoxicity after iodine-131 therapy for thyroid cancer using γ-H2AX foci of DNA damage in lymphocytes. *Ann Nucl Med* (2013) 27:233–8. doi: 10.1007/s12149-012-0678-0

48. Eberlein U, Scherthan H, Bluemel C, Peper M, Lapa C, Buck AK, et al. DNA damage in peripheral blood lymphocytes of thyroid cancer patients after radioiodine therapy. *J Nucl Med* (2015) 57:173–80. doi: 10.2967/jnumed.115.164814

49. Nakazawa Y, Saenko V, Rogounovitch T, Suzuki K, Mitsutake N, Matsuse M, et al. Reciprocal paracrine interactions between normal human epithelial and mesenchymal cells protect cellular DNA from radiation-induced damage. *Int J Radiat Oncol Biol Phys* (2008) 71:567–77. doi: 10.1016/j.ijrobp.2007.10.036

50. Castedo M, Perfettini JL, Roumier T, Andreau K, Medema R, Kroemer G. Cell death by mitotic catastrophe: a molecular definition. *Oncogene* (2004) 23:2825–37. doi: 10.1038/sj.onc.1207528

51. Vitale I, Galluzzi L, Castedo M, Kroemer G. Mitotic catastrophe: a mechanism for avoiding genomic instability. *Nat Rev Mol Cell Biol* (2011) 12:385–92. doi: 10.1038/nrm3115

52. Vakifahmetoglu H, Olsson M, Zhivotovsky B. Death through a tragedy: mitotic catastrophe. *Cell Death Differ* (2008) 15:1153–62. doi: 10.1038/cdd.2008.47

53. Huang RX, Zhou PK. DNA damage response signaling pathways and targets for radiotherapy sensitization in cancer. *Signal Transduct Target Ther* (2020) 5. doi: 10.1038/s41392-020-0150-x

54. Mimitou EP, Symington LS. Ku prevents Exo1 and Sgs1-dependent resection of DNA ends in the absence of a functional MRX complex or Sae2. *EMBO J* (2010) 29:3358–3369. doi: 10.1038/emboj.2010.193

55. Van Der Burg M, Van Dongen JJM, Van Gent DC. DNA-PKcs deficiency in human: Long predicted, finally found. *Curr Opin Allergy Clin Immunol* (2009) 9:503–9. doi: 10.1097/ACI.0b013e3283327e41

56. Hosoi Y, Watanabe T, Nakagawa K, Matsumoto Y, Enomoto A, Morita A, et al. Up-regulation of DNA-dependent protein kinase activity and Sp1 in colorectal cancer. *Int J Oncol* (2004) 25:461–468. doi: 10.3892/ijo.25.2.461

57. Damia G. Targeting DNA-PK in cancer. *Mutat Res - Fundam Mol Mech Mutagenesis* (2020) 821. doi: 10.1016/j.mrfmmm.2020.111692

58. Xie R, Cheng L, Huang M, Huang L, Chen Z, Zhang Q, et al. NAT10 drives cisplatin chemoresistance by enhancing ac4C-associated DNA repair in bladder cancer. *Cancer Res* (2023) 83:1666–83. doi: 10.1158/0008-5472.CAN-22-2233

59. Assis J. Ovarian cancer and DNA repair: DNA ligase IV as a potential key. *World J Clin Oncol* (2013) 4:14–24. doi: 10.5306/wjco.v4.i1.14

60. Jun S, Jung YS, Suh HN, Wang W, Kim MJ, Oh YS, et al. LIG4 mediates Wnt signaling-induced radio resistance. *Nat Commun* (2016) 7. doi: 10.1038/ncomms10994

61. Willoughby CE, Jiang Y, Thomas HD, Willmore E, Kyle S, Wittner A, et al. Selective DNA-pkcs inhibition extends the therapeutic index of localized radiotherapy and chemotherapy. *J Clin Invest* (2020) 130:258–271. doi: 10.1172/JCI127483

62. Yin M, Liao Z, Liu Z, Wang LE, O'Reilly M, Gomez D, et al. Genetic variants of the nonhomologous end joining gene LIG4 and severe radiation pneumonitis in non-small cell lung cancer patients treated with definitive radiotherapy. *Cancer* (2012) 118: e537–43. doi: 10.1002/cncr.26214

63. Gomes BC, Silva SN, Azevedo AP, Manita I, Gil OM, Ferreira TC, et al. The role of common variants of non-homologous end-joining repair genes XRCC4, LIG4 and Ku80 in thyroid cancer risk. *Oncol Rep* (2010) 24:1079–85. doi: 10.3892/or-00000958

64. Riballo E, Doherty AJ, Dai Y, Stiff T, Oettinger MA, Jeggo PA, et al. Cellular and biochemical impact of a mutation in DNA ligase IV conferring clinical radiosensitivity. *J Biol Chem* (2001) 276:31124–32. doi: 10.1074/jbc.M103866200

65. Critchlow SE, Bowater RP, Jackson SP. Mammalian DNA double-strand break repair protein XRCC4 interacts with DNA ligase IV. *Curr Biol* (1997) 7:588–98. doi: 10.1016/S0960-9822(06)00258-2

66. Saquib M, Ansari MI, Johnson CR, Khatoon S, Kamil Hussain M, Coop A. Recent advances in the targeting of human DNA ligase I as a potential new strategy for cancer treatment. *Eur J Med Chem* (2019) 182. doi: 10.1016/j.ejmech.2019.111657

67. Greco GE, Matsumoto Y, Brooks RC, Lu Z, Lieber MR, Tomkinson AE. SCR7 is neither a selective nor a potent inhibitor of human DNA ligase IV. *DNA Repair (Amst)* (2016) 43:18–23. doi: 10.1016/j.dnarep.2016.04.004

68. Gkotzamanidou M, Terpos E, Bamia C, Munshi NC, Dimopoulos MA, Souliotis VL. DNA repair of myeloma plasma cells correlates with clinical outcome: The effect of the nonhomologous end-joining inhibitor SCR7. *Blood* (2016) 128:1214–1225. doi: 10.1182/blood-2016-01-691618

69. Manjunath M, Choudhary B, Raghavan SC. SCR7, a potent cancer therapeutic agent and a biochemical inhibitor of nonhomologous DNA end-joining. *Cancer Rep* (2021) 4. doi: 10.1002/cnr2.1341

70. Szakács G, Paterson JK, Ludwig JA, Booth-Genthe C, Gottesman MM. Targeting multidrug resistance in cancer. *Nat Rev Drug Discovery* (2006) 5:219–34. doi: 10.1038/nrd1984

71. Zhang S, Liu X, Bawa-Khalfe T, Lu LS, Lyu YL, Liu LF, et al. Identification of the molecular basis of doxorubicin-induced cardiotoxicity. *Nat Med* (2012) 18, 1639–42. doi: 10.1038/nm.2919

72. Favreau-Lessard AJ, Blaszyk H, Jones MA, Sawyer DB, Pinz IM. Systemic and cardiac susceptibility of immune compromised mice to doxorubicin. *Cardio-Oncology* (2019) 5. doi: 10.1186/s40959-019-0037-6

73. Philpott C, Tovell H, Frayling IM, Cooper DN, Upadhyaya M. The NF1 somatic mutational landscape in sporadic human cancers. *Hum Genomics* (2017) 11. doi: 10.1186/s40246-017-0109-3

74. Brossel H, Fontaine A, Hoyos C, Jamakhani M, Willems M, Hamaidia M, et al. Activation of DNA damage tolerance pathways may improve immunotherapy of mesothelioma. *Cancers (Basel)* (2021) 13. doi: 10.3390/cancers13133211

75. Hamaidia M, Gazon H, Hoyos C, Hoffmann GB, Louis R, Duysinx B, et al. Inhibition of EZH2 methyltransferase decreases immunoediting of mesothelioma cells by autologous macrophages through a PD-1-dependent mechanism. *JCI Insight* (2019) 4. doi: 10.1172/jci.insight.128474

Frontiers in Endocrinology

Explores the endocrine system to find new therapies for key health issues

The second most-cited endocrinology and metabolism journal, which advances our understanding of the endocrine system. It uncovers new therapies for prevalent health issues such as obesity, diabetes, reproduction, and aging.

Discover the latest Research Topics

See more →

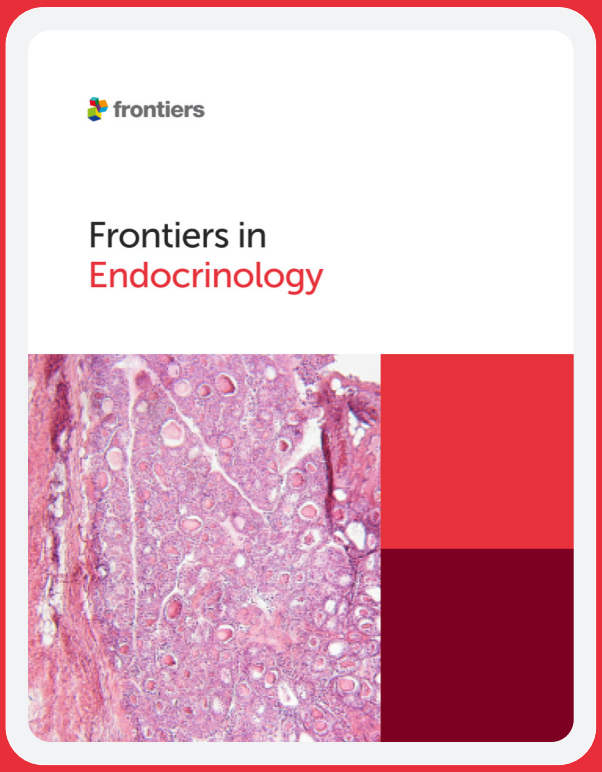

Frontiers

Avenue du Tribunal-Fédéral 34
1005 Lausanne, Switzerland
frontiersin.org

Contact us

+41 (0)21 510 17 00
frontiersin.org/about/contact